The Dark Secrets of Fluorescent Proteins : Manipulating Fluorophore Photophysics to Boost Quantitative SMLM

Jip Wulffele

THÈSE

Pour obtenir le grade de

DOCTEUR DE L'UNIVERSITÉ GRENOBLE ALPES

École doctorale : CSV- Chimie et Sciences du Vivant
Spécialité : Biologie Structurale et Nanobiologie
Unité de recherche : Institut de Biologie Structurale

Les secrets obscurs des protéines fluorescentes : manipulation de la photophysique des fluorophores pour améliorer la SMLM quantitative

The Dark Secrets of Fluorescent Proteins: Manipulating Fluorophore Photophysics to Boost Quantitative SMLM

Présentée par :

Jip WULFFELE

Direction de thèse :

Dominique BOURGEOIS — Directeur de thèse
DIRECTEUR DE RECHERCHE, Université Grenoble Alpes

Joanna TIMMINS — Co-directrice de thèse
DIRECTRICE DE RECHERCHE, Université Grenoble Alpes

Rapporteurs :

Christian LESTERLIN
DIRECTEUR DE RECHERCHE, CNRS délégation Rhône Auvergne

Mike HEILEMANN
FULL PROFESSOR, Johann Wolfgang Goethe University

Thèse soutenue publiquement le **21 novembre 2023**, devant le jury composé de :

Antoine DELON PROFESSEUR DES UNIVERSITES, Université Grenoble Alpes	Examinateur
Christian LESTERLIN DIRECTEUR DE RECHERCHE, CNRS délégation Rhône Auvergne	Rapporteur
Juliette GRIFFIE ASSISTANT PROFESSOR, Stockholms Universitet	Examinatrice
Cécile MORLOT DIRECTRICE DE RECHERCHE, CNRS délégation Alpes	Présidente
Jérôme DUPUY MAITRE DE CONFERENCES, Université Grenoble Alpes	Examinateur
Mike HEILEMANN FULL PROFESSOR, Johann Wolfgang Goethe University	Rapporteur

Acknowledgements

First and foremost, I have to thank my supervisors Dominique and Joanna for their support, and invaluable insights throughout the entire journey of my PhD. You taught me countless of new things about photophysics, MATLAB and the ins and outs of doing science in general. I appreciate your honesty and critical feedback, always motivating me to achieve my best. Dominique, I enjoyed every photophysics lunch discussion and hereby promise that I will climb the Neron before leaving IBS.

Off course an immense thank you to all the members of the I2SR group! Lianne, Ahmed, Arijit, Sasha, Angela, Mohammed, Pascale, Françoise, Salvatore, Virgile, Jean-Philippe, Philippe, Pierre and Fabienne, I thank you for all your support, advice and the good time in and out the lab. A special thank you goes to my office mates Arijit, Sasha, Angela, Lianne and Ahmed for their friendship and all the delicious snacks in the office. My sincere apologies for all the photophysics lunch sessions you had to endure. Another special thank you goes to Pascale and Françoise, Salvatore, Virgile, Sasha and Jean-Philippe for always being there to help on the microscope and in the lab.

This thesis would not have been the same without all the collaborations. Many thanks to Julian Bauer, Michael Scheckenbach, Prof. Phillip Tinnefeld and the rest of the Tinnefeld team for their warm welcome and teaching me about DNA-origamis. I would also like to thank Dr. Bernard Brutscher, Dr. Martin Byrdin, Dr. Jean-Baptiste Siberata, Dr. Matthieu Sainlos, Dr. Magali Mondin, Dr. Florian Levet, Lorris Verron, Dr. Remi Galland, Abdelghani Neuhaus, Dr. Agate Espagne and Dr. Thomas Le Saux for all the engaging discussions.

I would like to express my sincere gratitude to the members of my CSI committee Dr. Celice Morlot, Prof. Yves Bollen and Dr. Jean-Bernard Fiche for their insightful feedback and advice during this journey.

I would also like to thank my jury members Prof. Mike Heilemann, Dr. Christian Lesterlin, Prof. Juliette Griffié, Dr. Celice Morlot, Prof. Antoine Delon and Dr. Jérôme Dupuy for dedicating their time and expertise to review my work

Lastly, I am immensely grateful to my family for their love and encouragement. Mam and pap, ik had dit niet gekund zonder jullie aanmoediging vanaf mijn eerste spinnen spreekbeurt. Grootje en opa, jullie waren mijn inspiratie om biologie te studeren. En natuurlijk Lot, Pim and Saar, mijn grote motivatie om naar Frankrijk (lees: ver weg) te verhuizen (maar ik houd nog steeds van jullie). Nico, I thank you for all your refreshing insights that kept me grounded and I look forward to our future. Ma nouvelle famille française, je vous remercie de m'avoir accueillie dès le premier instant. Votre accueil m'a permis de me sentir chez moi dès le début.

Contents

Abstract in English

Fluorescence single-molecule localization microscopy (SMLM) has become an indispensable tool in integrated structural and cell biology, providing insights into macromolecular organizations and dynamics at the nanoscale *in cellulo*. A popular SMLM technique is photoactivated localization microscopy (PALM), which relies on the 'smart' photophysical behavior of phototransformable fluorescent proteins (PTFPs). Yet, the complex photophysical behaviors of PTFPs hinder quantitative PALM applications, such as counting (qPALM) and single-particle tracking (sptPALM). Besides suboptimal fluorophore behaviors, imaging artifacts and the necessity for sophisticated data analysis contribute to the still limited usage of quantitative PALM techniques. Aiming to push the application of quantitative PALM, my PhD work consists of two projects, dealing with different aspects of quantitative PALM.

The first project is focused on the characterization of PTFPs, aiming to develop strategies to improve their behavior for SMLM. This work starts with a comparison between different protein immobilization platforms for the photophysical characterization of PTFPs. Next, follows an investigation of the effects of different illumination conditions on the behavior of the popular green-to-red photoconvertible FP mEos4b, using a combination of single-molecule and ensemble fluorescence microscopy and simulations. Lastly, my thesis contributes to the development of a new photophysical model describing the behavior of the reversibly photoswitchable FP rsEGFP2 at cryogenic temperature. Altogether, this work contributes to a deeper understanding of the photophysical behavior of PTFPs and provides guidelines for optimized imaging schemes for PALM imaging.

The second project involves the application of sptPALM to study stress-induced nucleoid remodeling in *Deinococcus radiodurans*, one of the most radioresistant bacterium known today. By monitoring the diffusion dynamics of the mEos4b labeled nucleoid associated protein HU, this work reveals that nucleoid remodeling proceeds differently in response to different stresses. Using simulations, it discusses how the small size of bacteria complicates the interpretation of sptPALM data. The work highlights the value of sptPALM for the study of bacteria but also identifies weaknesses in current analysis pipelines that may lead to erroneous data interpretation.

Abstract in French

La microscopie de localisation à molécule unique par fluorescence (SMLM) est devenue un outil indispensable en biologie structurale et cellulaire intégrée, permettant de mieux comprendre les organisations et dynamiques macromoléculaires à l'échelle nanométrique in cellulo. La microscopie de localisation photoactivée (PALM), qui repose sur le comportement photophysique "intelligent" des protéines fluorescentes phototransformables (PTFP), est une technique SMLM très répandue. Cependant, les comportements photophysiques complexes des PTFP entravent les applications quantitatives de la PALM, telles que le comptage (qPALM) et le suivi d'une seule particule (sptPALM). Outre les comportements suboptimaux des fluorophores, les artefacts d'imagerie et la nécessité d'une analyse sophistiquée des données contribuent à l'utilisation encore limitée des techniques PALM quantitatives. Dans le but d'étendre l'application de la technique PALM quantitative, mon travail de doctorat consiste en deux projets, qui traitent de différents aspects de la technique PALM quantitative.

Le premier projet est axé sur la caractérisation des PTFP, dans le but de développer des stratégies visant à améliorer leur comportement pour SMLM. Ce travail commence par une comparaison entre différentes plateformes d'immobilisation des protéines pour la caractérisation photophysique des PTFP. Ensuite, nous étudions les effets de différentes conditions d'illumination sur le comportement du populaire FP photoconvertible vert-rouge mEos4b, en utilisant une combinaison de microscopie de fluorescence à molécule unique et d'ensemble, ainsi que des simulations. Enfin, ma thèse contribue au développement d'un nouveau modèle photophysique décrivant le comportement du FP réversiblement photoswitchable rsEGFP2 à température cryogénique. Dans l'ensemble, ce travail contribue à une meilleure compréhension du comportement photophysique des PTFPs et fournit des lignes directrices pour des schémas d'imagerie optimisés pour l'imagerie PALM.

Le second projet concerne l'application de sptPALM pour étudier le remodelage des nucléoïdes induit par le stress chez Deinococcus radiodurans, l'une des bactéries les plus radiorésistantes connues à ce jour. En surveillant la dynamique de diffusion de la protéine HU associée au nucléoïde et marquée au mEos4b, ce travail révèle que le remodelage du nucléoïde se déroule différemment en réponse à différents stress. À l'aide de simulations, il montre comment la petite taille des bactéries complique l'interprétation des données sptPALM. Ce travail met en évidence la valeur de sptPALM pour l'étude des bactéries, mais identifie également les faiblesses des pipelines d'analyse actuels qui peuvent conduire à une interprétation erronée des données.

List of Abbreviations

APS Ammonium PerSulfate
CT Cryogenic Temperature
Dapp apparent Diffusion coefficient
DNA DeoxyriboNucleic Acid
DTT DithioThreiTol
ELE Effective Labeling Efficiency
EM Electron Microscopy
EMCCD Electron Multiplying Charge-Coupled Device
ESPT Excited State Proton Transfer
FISC Forward Inter Sytem Crossing
FP Fluorescent Protein
FRAP Fluorescence Recovery After Photobleaching
FRET Forster Resonance Energy Transfer
GFP Green Fluorescent Protein
HU Heat-Unstable protein
ISC Inter System Crossing
JD Jump Distance
LEA Least Envolved Ancestor
MINFLUX MINimal photon FLUX
MJD Mean Jump Distance
MSD Mean Squared Displacement
NA Numerical Aperture
NADH Nicotinamide Adenine Dinucleotide (NAD) + Hydrogen (H)
NAP Nucleoid Associated Protein
NIR Non-IRradiated
NMR Nuclear Magnetic Resonance
NPC Nuclear Pore Complex
NRO New Rectangular Origami
PAA Polyacrylamide
PAFP Photoactivatable Fluorescent Protein
PAINT Point Accumulation for Imaging in Nanoscale Topography
PALM PhotoActivated Localization Microscopy
PCE PhotoConversion Efficiency
PCFP PhotoConvertible Fluorescent Protein
PSF Point Spread Function
PTFP PhotoTransformable Fluorescent Protein
PVA PolyVinyl Alcohol
qPALM quantitative PALM
QY Quantum Yield
RESOLFT REversible Saturable or switchable OpticaL Fluorescence Transitions
RFP Red Fluorescent Protein
ROS Reactive Oxygen Species
RSFP Reversibly Switchable Fluorescent Protein
RT Room Temperature
sCMOS scientific Complementary Metal Oxide Semiconductor
SIM Structured Illumination Microscopy
SMC Structural Maintenance of Chromosomes
SMLM Single Molecule Localization Microscopy

SMIS Single-Molecule Imaging Simulator
sptPALM single particle tracking PALM
SRM Super-resolution microscopy
ssDNA single stranded DNA
STED Stimulated Emission Depletion
STROM Stochastic Optical Reconstruction Microscopy
TCEP Tris(2-CarboxyEthyl)Phosphine
TEMED TEtraMethylEthyleneDiamine
TIRF Total Internal Reflection Fluorecsnce
XFEL X-Ray Free Electron Laser
YFP Yellow Fluorescent Protein

List of Figures

List of Tables

1 Introduction

1.1 Quantitative super-resolution microscopy in biological research

Super-resolution microscopy (SRM) offers the ability to look at biological structures beyond the diffraction limit of light. Before the rise of SRM, optical imaging was limited by light diffraction to resolutions about half the wavelength of light. Consequently, details smaller than ~250 nm could not be resolved. Nowadays, resolutions of 10-30 nm are routinely achieved by SMR techniques, uncovering biological structures that were previously hidden. In 2014, Eric Betzig, Stefan Hell and William Moerner were awarded the Nobel Prize in Chemistry for the development of SRM. But the success of SMR would not be as big as it is today without the discovery of fluorescent proteins (FPs).

The Green Fluorescent Protein (GFP) was discovered by Shimomura and colleagues in 1962 in the jellyfish *Aequora Victoria*. It was not until 1994, however, that Chalfie et al. demonstrated that GFP can be genetically fused to any protein of interest and used as a fluorescent protein marker for live-cell imaging[1], which really started the 'green revolution' in fluorescence microscopy[2]. The discovery and development of GFP as a fluorescent protein marker was acknowledged in 2008 with the Nobel Prize in Chemistry to Osamu Shimomura, Martin Chalfie and Roger Tsien.

SRM can be performed using different types of fluorophores but the fact that FPs are genetically encoded offers specific advantages for live-cell imaging and quantitative applications. SRM is developing more and more into a quantitative technique building on advancements in fluorophores, instrumentation and software. Quantitative SMR can be used to assess clustering and oligomerization of the protein of interest, or to monitor its diffusion dynamics. These quantitative applications are mostly based on Single Molecule Localization Microscopy (SMLM), a variant of SRM, which relies on the 'smart' photophysical behavior of the used fluorophores. However, the wide-spread application of quantitative SMR is currently limited by suboptimal fluorophore behaviors and imperfect analysis tools. My PhD work aims to participate in addressing these limitations and boost the application of quantitative SMR.

1.2 Fluorescent markers for biological research

1.2.1 Basic principles of fluorescence

Fluorescence is the emission of a photon by a molecule shortly following the absorption of a photon of a shorter wavelength (i.e. higher energy). **Figure 1.1A** shows a Jablonksi diagram describing the energy transitions of a basic fluorophore. Absorption of a photon excites the molecule from the singlet ground state (S_0) into a vibrationally-coupled excited state (S1, S2…), according to the Frank-Condon principle (**Figure 1.1B**). From this state, the excited electron quickly relaxes to the lowest vibrational state of S_1 by vibrational relaxation and internal conversion. From here, decay back to S_0 can occur by emission of a photon (fluorescence) or by non-radiative decay. The probability that a fluorophore emits a photon after excitation is given by its fluorescence quantum yield (Φ = # emitted photons / # absorbed photons), which is typically between 0.5 and 0.9 for good fluorophores.

Instead of relaxing to S_0, an excited molecule can also undergo Inter System Crossing (ISC) and enter the triplet state (T_1). Transition to T_1 is accompanied by a 'forbidden' spin conversion of the electron and is thus less likely to occur than decay to S_0 (quantum yield of T_1 formation ~10^{-3}-10^{-2}). Decay from T_1 back to S_0 can occur by emission of a photon (phosphorescence) or by non-radiative decay. This transition again involves a 'forbidden' spin change which makes T_1 longer-lived (µs-ms) than S_1 (ns).

Due to its long live-time and reactivity, the triplet state is the starting point of photochemical processes leading to the formation of long-lived dark states and bleached states.

In addition to ISC, some fluorophores can undergo a variety of other photo-induced transformations, such as photoactivation and photoconversion. All these phototransformations have corresponding quantum yields, typically much lower than the fluorescence quantum yield.

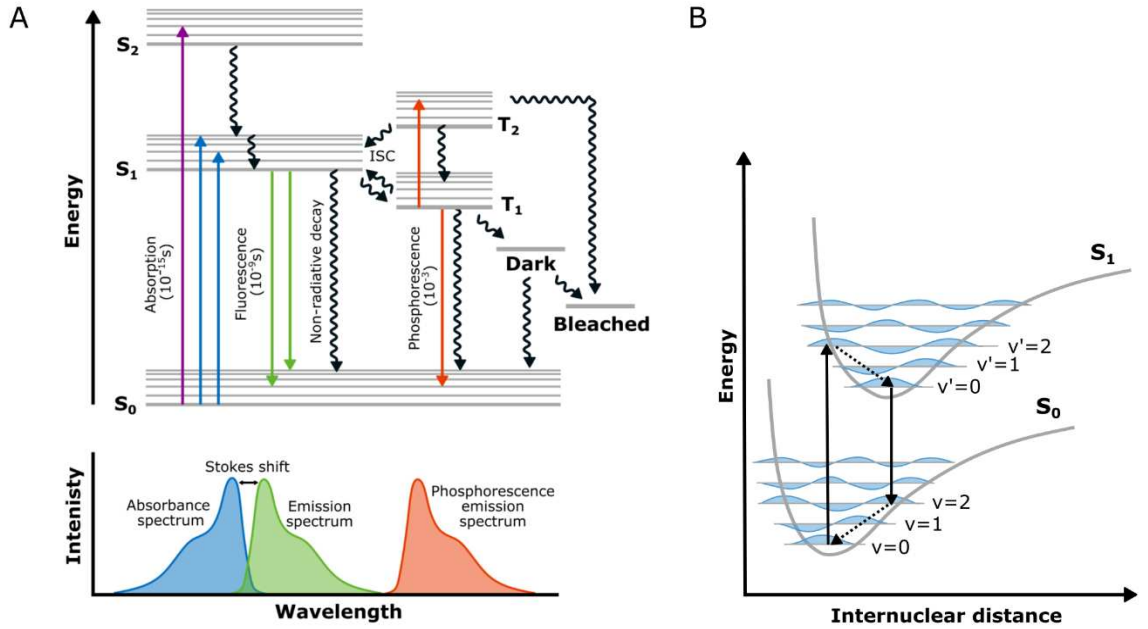

Figure 1.1 Basics of fluorescence. *A) Jablonksi diagram showing the energy transitions of a basic fluorophore. Absorption of a photon brings the molecule from the ground state (S_0) into an excited state (S_1 … S_n). From the excited state, the molecule can relax back to the ground state by emission of a photon (fluorescence) or by internal conversion. Alternatively, the molecule can access the excited triplet state (T_1) by inter system crossing (ISC). From the excited triplet state the molecule can relax back to S_0 by emission of a photon (phosphorescence) or by internal conversion. Additionally, the triplet state is the starting point of biochemical processes leading to the formation of long-lived dark states and bleached states. B) Franck-Condon principle energy diagram (see text for details). The blue waves illustrate the probability of nuclei to be at a certain internuclear distance at a given vibrational level (v=0, v=1, …). C) The absorption rate of a fluorophore depends on the orientation of its transition dipole relative to the polarization of the incoming light.*

The ability of a fluorophore to absorb photons of a given wavelength is described by its extinction coefficient (ε in $M^{-1}cm^{-1}$). The extinction coefficient together with the fluorescence quantum yield determine the theoretical brightness of a fluorophore (brightness = Φ * ε). While the extinction coefficient sets the upper limit of the light absorption rate, the actual rate at which a fluorophore absorbs depends on its orientation relative to the incoming light[3,4]. The more parallel the alignment of the dipole of the fluorophore is to the polarization of the light, the higher the absorption rate (**Figure 1.1C**). Practically speaking, the excitation rate of a tumbling fluorophore (isotropic orientation) can be calculated by[4]:

$$k = \varepsilon P \lambda \frac{(10^{-6}) Ln(10)}{N_A hc}$$

where ε is the extinction coefficient ($M^{-1}cm^{-1}$) of the fluorophore at wavelength λ (nm), P the power density of the incoming light (Wcm^{-2}), N_A the Avogadro number, h the Planck constant and c the speed of light. For a fluorophore with a fixed orientation with spherical coordinates θ and φ, the

excitation rate is calculated by[4]: $k_\theta = \frac{3}{2}kcos^2\theta$, when the fluorophore is illuminated with circularly polarized light, or, when illuminated with linear polarized light, by[4]: $k_{\theta,\varphi} = 3kcos^2\theta cos^2\varphi$.

The absorption spectrum of a fluorophore is dependent on the size of the energy gap between S_0 and S_1. The larger the energy gap, the more energy is required to excite an electron and thus the more blue-shifted the absorption spectrum. The size of the energy gap between S_0 and S_1 is dependent on the extent of delocalization of the electrons. Delocalized electrons are electrons that do not belong to a unique atom or covalent bond. This is seen in molecules with alternating double and single bonds (see for example the organic dyes in **Figure 1.2** and the FP chromophores in **Figure 1.8**), which form a conjugated π-system in which the electrons are shared (i.e. delocalized) between all atoms.

The emission spectrum of a fluorophore is red shifted compared to its absorption spectrum. The difference in wavelength between the absorption and emission peaks is called the Stokes shift (usually ~10 - 45 nm). This shift is due to non-radiative energy loss during the decay from the excited state to S_0. The Stokes shift of FPs is influenced by solvent relaxation, and structural changes and rearrangements in the H-bond network around the chromophore happening in the excited state[5]. Some fluorophores have an extremely large Stokes shift (> 100 nm), which can be caused by Excited State Proton Transfer (ESPT), as can be seen in wtGFP[6]. In addition, the Franck-Condon principle also contributes to the Stokes shift of FPs. The Franck-Condon principle states that electronic transitions are much faster than nuclear motions so that when an electron is excited it will enter an excited state vibrational level with minimal change in nuclear coordinates (**Figure 1.1B**). Because the nuclear coordinates in the excited state are usually different than in the ground state, the electron will be excited to a higher vibrational level of S_1. From there, the electron will quickly relax to the lowest vibrational level of S_1, loosing part of its energy. The transition from the lowest vibrational level of S_1 to S_0 is similarly affected by the Frank-Condon principle.

1.2.2 Fluorescence labelling strategies

Various methods have been developed to fluorescently label specific biological structures. These methods differ in the type of fluorophore that is used and in how the fluorophore is attached to the structure of interest. Based on the type of fluorophore that is used, labelling strategies can be classified into three categories (**Figure 1.2**): fluorescent proteins, organic dyes and fluorescent nanoparticles such as quantum dots. Each of these strategies has its own strengths and weaknesses; there is no single best method that fits all applications.

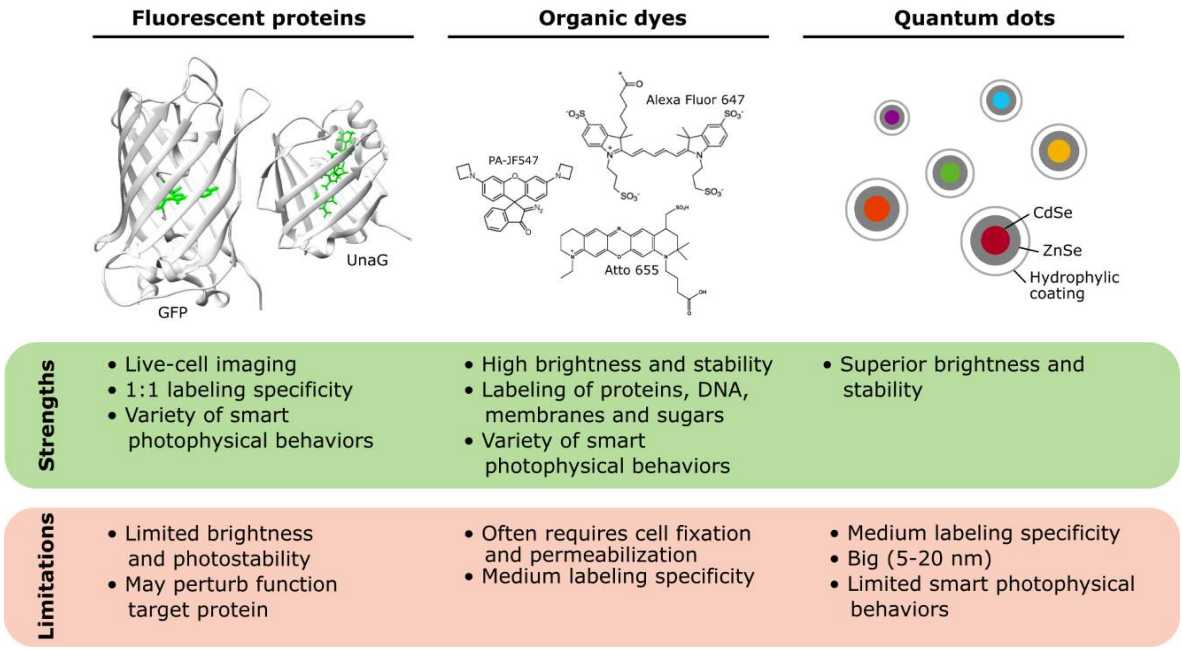

Figure 1.2 Fluorescent labels for biological research*. Three types of fluorophores can be distinguished: fluorescent proteins, organic dyes and nanoparticles. Listed are the main strengths and weaknesses of these markers. Protein structures of EGFP (PDB: 4EUL) and UnaG (PDB: 413B) are shown with the chromophores colored in green. Figure not to scale.*

Fluorescent proteins of the GFP-family have revolutionized biological research. They are the most popular choice for live-cell imaging because they are genetically encoded, do not require external factors to acquire fluorescence except O_2, and are generally not cytotoxic. FPs are available spanning the entire visible spectrum. Moreover, FPs exhibiting 'smart' photophysical behaviors, such as photoactivation and photoconversion, are available for SRM and other advanced applications. The main weakness of GFP-like FPs lies in their limited photostability compared to organic dyes. Other limitations of GFP-like FPs are that there are no variants emitting in the near infrared (NIR), which is desired for deep tissue imaging, and that they are not suitable to study anaerobic environments. These latter two limitations can be overcome by the use of other classes of FPs, which rely on the binding of flavins or linear tetrapyrroles. These FPs do not require O_2 for maturation but instead acquire fluorescence by binding of an exogenous chromophore. These chromophores might be covalently or noncovalently bound depending on the FP, and might be naturally present in the cells or supplemented to the imaging buffer. FP variants emitting in the NIR have been developed from bacterial phytochromes, which covalently bind a biliverdin (BV) chromophore. BV is an intermediate of heme degradation and is naturally produced in mammalian cells. NIR FPs have been successfully used for deep tissue imaging in mice[7–9]. Furthermore, recent reports have demonstrated the use of these non-GFP-type FPs for SRM[9,10], although the number of 'smart' controllable variants remains limited compared to the number of available GFP-type variants.

Organic dyes are widely used in biological research. They are often more photostable than FPs, are available in colors covering the entire visible spectrum and the NIR, and have been developed to display a board range of 'smart' photophysical behaviors.[11,12] However, organic dyes are not genetically encoded, so the challenge is to target them to the structure of interest (**Figure 1.3**). Most commonly this is achieved by immunolabeling using primary and secondary antibodies, which are generally commercially available. These antibodies, however, create a large distance between the fluorophore and the actual target (~ 10 nm). Smaller alternatives for antibodies include nanobodies[13], affimers[14] and aptamers[15], but these methods need to be adopted to each new target, which can be extensive work. Immunolabelling is never 100% specific and usually requires fixation and permeabilization of the cell to allow the dye and antibodies to enter the cell, which restricts its

use for live-cell imaging. An alternative to immunolabeling is the use of self-labelling tags, such as the SNAP, CLIP and Halo-tags, which allows combining the strengths of FPs and dyes[16,17]. These tags are proteins that can be genetically fused to the protein of interest, similarly as FPs, and bind a specific dye that is exogenously supplied. The use of dyes that can cross the cell membrane makes this strategy suitable for live-cell imaging[18]. The choice of dyes that compatible with self-labelling tags, however, is limited, especially for dyes with smart photophysical behaviors. Instead of using self-labeling tags, it is also possible to attach the dye directly to the target protein by the use of unnatural amino acids and click chemistry[19]. Finally, there is a selection of dyes that has been developed to exhibit a natural affinity for a particular protein or structure. This affinity can be based on the dye itself, for example dyes that intercalate with DNA, or by fusion of the dye to a peptide that exhibits a natural affinity for a particular target, for example Lifeact[20,21], which is used to stain actin.

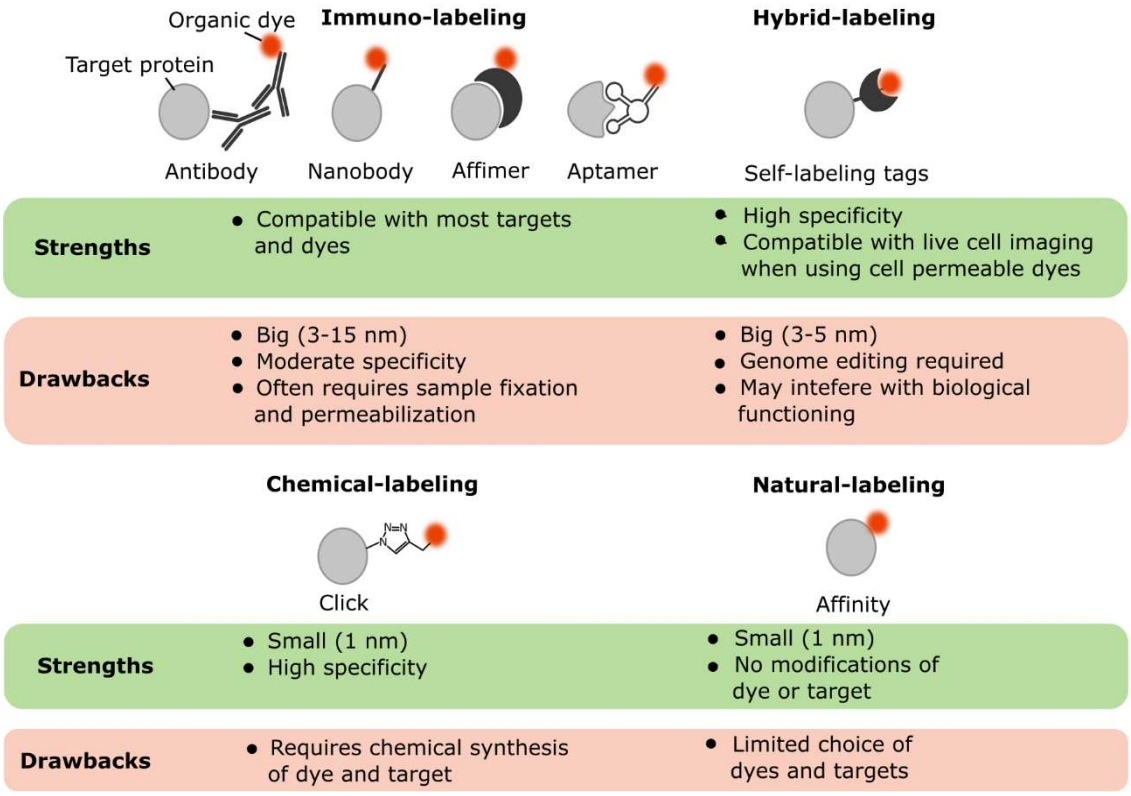

Figure 1.3 Labelling strategies with organic dyes. *Several methods have been developed to target organic dyes to specific structures. Listed are the different methods with their main strengths and drawbacks.*

Quantum Dots (QDs) are superior to FPs and organic dyes in terms of brightness and photostability[22]. Most widely used QDs are composed of a cadmium selenide (CdSe) core and a zinc sulfide (ZnS) shell, which is surrounded by a hydrophilic coating necessary for biological applications. The size of the CdSe core determines the excitation and emission spectrum, with larger cores exhibiting more red shifted profiles. The targeting of QDs to specific biological structures remains challenging. Although QDs can be conjugated to antibodies, similar as organic dyes, there are usually multiple antibodies attached to a single QD, which can lead to artificial clustering of the target protein. There are various protocols available nowadays to generate monovalent QDs, but their production is elaborate[23,24]. Another challenge arises from the large size of QDs, which can hinder their penetration into subcellular compartments[25]. QDs that exhibit the same variety of 'smart' photophysical behaviors as FPs and organic dyes have not been developed yet, although QDs have been demonstrated to switch between fluorescent and non-fluorescent states in a way that can be used for SRM[26]. Due to the multiple issues associated with QDs, their application in cell imaging is not as widespread as that of

FPs and organic dyes. Nevertheless, the high photostability of QDs has proven very useful for the long-term tracking of particles, such as viruses and membrane receptors[27,28].

While all types of labelling strategies have their advantages, my PhD work has focused on GFP-like FPs. The reason for this being that my thesis is centered on the application of quantitative SRM, in particular molecular counting and particle tracking. These methods rely on smart photophysical behaviors, are often performed in live cells (particle tracking is exclusively performed in live cells) and benefit from the 1:1 labelling specificity offered by FPs. For simplicity, I will refer to GFP-like FPs as just 'FPs' throughout this manuscript.

1.2.3 General properties of fluorescent proteins

There exists no single best FP that is the perfect choice for every experiment. Depending on the application, there are different requirements for the characteristics of the FP. Moreover, some characteristics that negatively affect standard imaging may be exploited for specific applications. Examples of this include the environmental sensitivity of FPs that is used for the development of biosensors, and photochromism that is at the heart of SRM. In this section I outline different properties of FPs, emphasizing factors that are important to consider when choosing a FP for a given experiment.

1.2.3.1 Protein structure and chromophore properties

All GFP-like FPs share a similar structure consisting of an 11-stranded β-barrel surrounding a central α-helix that bears the chromophore (**Figure 1.4A**). Flexible loops cap the β-barrel at both ends. There are slight variations in the overall shape of the β -barrel, with FPs originating from Anthozoa species being slightly more oval than FPs originating from Hydrozoa species (**Figure 1.4B**). This overall β-barrel structure is critical for the fluorescence of FPs as it stabilizes the chromophore, resulting in a high fluorescence quantum yield (~0.5-0.9, **Figure 1.4C**). In fact, the free GFP chromophore in solution is non-fluorescent due to extensive twisting favoring non-radiative decay[29,30]. Inside the β -barrel, the chromophore forms auto-catalytically from three amino acids (Ser65, Tyr66 and Gly67 for wtGFP) only requiring oxygen.

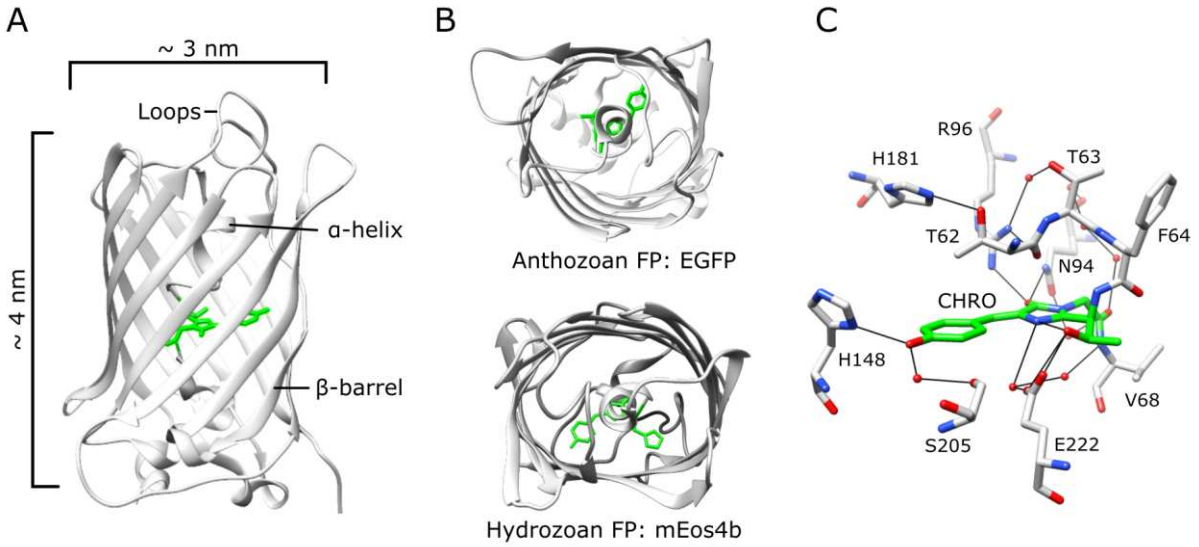

Figure 1.4 Architecture of GFP-like fluorescent proteins. *A) Side view of EGFP (PDB: 4EUL) with the overall protein structure in grey and the chromophore in green. B) Top view of the Anthozoan FP EGFP and the Hydrozoan FP mEos4b (PDB: 6GOY). C) The GFP chromophore is stabilized inside the β-barrel by an extensive hydrogen bond network (black lines), van der Waals interactions and π-stacking interactions. These interactions*

are critical for a high fluorescence quantum yield and determine to a large extend the fluorescent color and photophysical behavior of the FP.

Most natural FPs have a tendency to form oligomers. This is especially the case for Anthozoan FPs, which are obligate tetramers and are prone to aggregation[31]. This is a problem for the design of FP-fusions as it may affect the localization and functioning of the labeled protein. Luckily nowadays, the oligomerization of FPs is quite well understood and most FPs have been successfully engineered (through site-directed mutagenesis) to be monomeric while preserving their high fluorescence quantum yield and other desired properties. The oligomerization tendency of FPs is usually assessed by *in vitro* methods, such as ultracentrifugation, gel filtration and native electrophoresis. *In vivo* methods to examine the oligomerization prospensity of FPs include yeast-two-hybrid approaches and the OSER (organized smooth endoplasmic reticulum) assay[32,33]. When it is not possible to monomerize a particular FP, an alternative option is to create a tandem version by fusing two copies of the FP by a flexible linker[34–36]. This will minimize unwanted oligomerization of the target protein but increases the size of the label by a factor of two.

Other important biochemical properties of FPs are their ability to fold in diverse cellular environments and their tolerance to N-and C-terminal fusions. The proper folding of FPs in different cellular conditions is not straightforward. Firstly, FPs are derived from organisms that live in cold environments, while most bacteria and mammalian cells in the lab are cultured at 37°C[36,37]. This temperature difference can lead to poor expression and maturation, and several rounds of mutagenesis might be necessary to enhance the expression of a particular FP at 37°C[37,38]. Secondly, inappropriate modifications, such as glycosylation and the formation of disulphide bonds, can affect the folding, fluorescence and localization of FPs[39–42]. This is especially a concern when targeting proteins along the eukaryotic secretory pathway or in the bacterial periplasm[39–42]. To overcome these problems, several 'oxFPs' or 'moxFPs' have been designed for expression in such environments by removal of glycosylation sites and cysteines[35,39–42]. The tolerance of FPs to N-and C-terminal fusions is important as FPs are often used to label other proteins. This has been shown to be a problem with some Anthozoan derived FPs[34,43]. Interestingly, Shaner et al showed that this problem can be overcome by extension of the FP with GFP-like (Hydrozoa origin) N- and C-termini[34].

The chromophore of FPs forms autocatalytically from three amino acids located on the central α-helix (typically XYG or XWG, where X can be any amino acid (but exceptions exist, see[44–47])), in a reaction known as maturation. Chromophore maturation can be divided into three steps: cyclization, dehydration and oxidation (**Figure 1.5**). The order of these steps, however, remains debated[48–53]. Efficient maturation of the chromophore is strongly dependent on the protein matrix around the immature chromophore. Especially R96 and E222 (GFP numbering) are well-known to play critical roles in the maturation process[51,54,55]. Maturation times of FPs range from ~10 to ~500 minutes, depending on the FP and environmental factors[56]. Because fast maturation is desired for most experiments[56,57], many mutational studies have focused on the design of fast maturing variants (for example[58]). In addition to being slow, maturation of FPs can also be inefficient[52,59]. For example, the maturation efficiency of the RFP FusionRed has been estimated to be only 60% due to cleavage of the protein backbone preventing maturation[59]. Yet another maturation related problem is the formation of fluorescent maturation intermediates. This is seen in DsRed-like FPs, which form a blue emitting state before reaching the final mature red emitting state, or may be trapped in a green emitting state and never reach the red emitting state[33,52,60,61]. While the formation of fluorescent intermediates may pose problems for multicolor experiments, it has also been utilized for the development of fluorescent timers, which can be used, for example, to monitor different phases of the cell cycle[60,61]. Altogether, maturation is a very complex process, which remains incompletely understood. Care should be taken to select sufficiently fast and efficient maturing variants to avoid artifacts, in particular for multicolor and quantitative experiments.

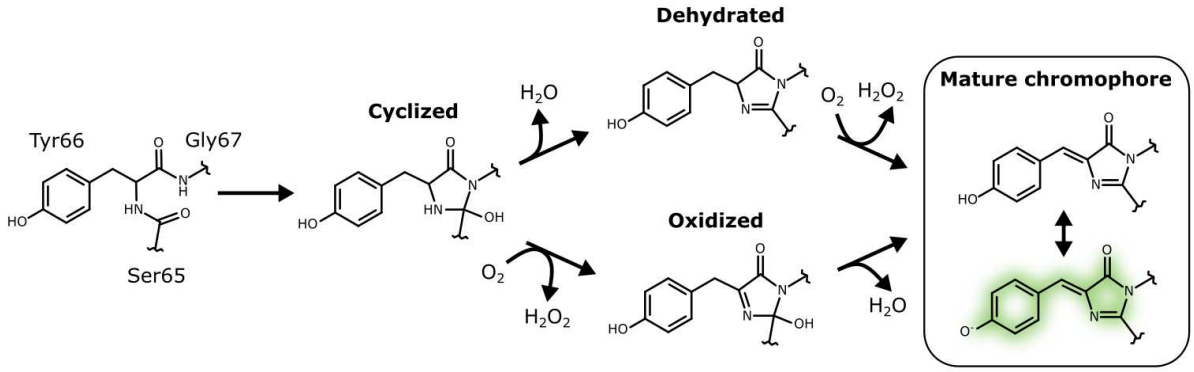

Figure 1.5 Formation of the GFP chromophore. *The GFP chromophore forms autocatalytically, only requiring oxygen. Chromophore formation involves sequential cyclization, dehydration and oxidation, although the order of these steps remains debated. The mature chromophore can be either protonated or deprotonated in a pH dependent manner. The deprotonated anionic state is generally the fluorescent state of the chromophore (see section 1.2.3.4).*

The mature chromophore can adopt either a *cis* or *trans* conformation (**Figure 1.6**). In most FPs, the *cis* conformation is the fluorescent state of the chromophore, while the *trans*-state is non-fluorescent. There are some exceptions to this rule, including the Red FPs (RFPs) PAmCherry[62] and eqFP611[63], and the GFP Gamillus[64,65]. Light induced switching between the *cis* and *trans* conformation has been observed in many FPs and is utilized in advanced imaging applications. This behavior will be discussed in more detail in sections **1.2.3.3** and **1.3.1**. It should be noted that strictly speaking the two isomeric states of the chromophore should be referred to as the *Z*- and *E*-state, rather than the *cis*- and *trans*-state (see for example[66]). This is because the terms *cis/trans* can only be used when both the carbon atoms involved in the double bond have a hydrogen group and one other functional group, which is not the case for the chromophores of FPs in which the Cα atom is connected to a nitrogren atom and another carbon atom. However, to avoid confusion with most existing literature, I will refer to these states as *cis* and *trans* throughout my thesis.

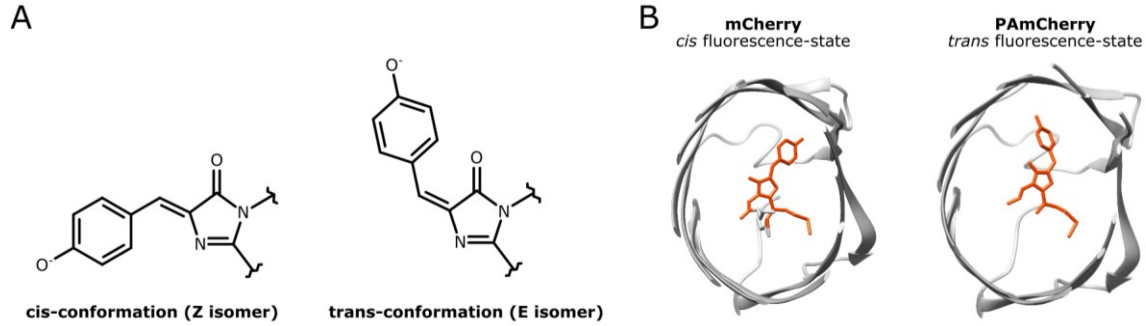

Figure 1.6 The mature chromophore can adopt a cis or trans conformation. *A) Cis- and trans-conformations of the GFP chromophore. B) Cross-sections of the FPs mCherry (PDB: 2H5Q) and PAmCherry (PDB: 3KCT) in the fluorescence states revealing that the chromophore adopts a cis conformation in mCherry but a trans conformation in PAmCherry.*

1.2.3.2 Color and brightness

Color and brightness are key properties of FPs for research applications. FPs are available spanning the entire visible spectrum but these FPs are not all equally bright. The brightest FPs are found in the green/yellow range, while the FPs at both ends of the spectrum (violet/blue and red) show a reduced brightness (**Figure 1.7A**)[67]. Ongoing efforts are focused on the development of brighter FPs covering the whole range of the visible spectrum, even reaching into the NIR, by mutating the chromophore itself and the surrounding protein matrix.

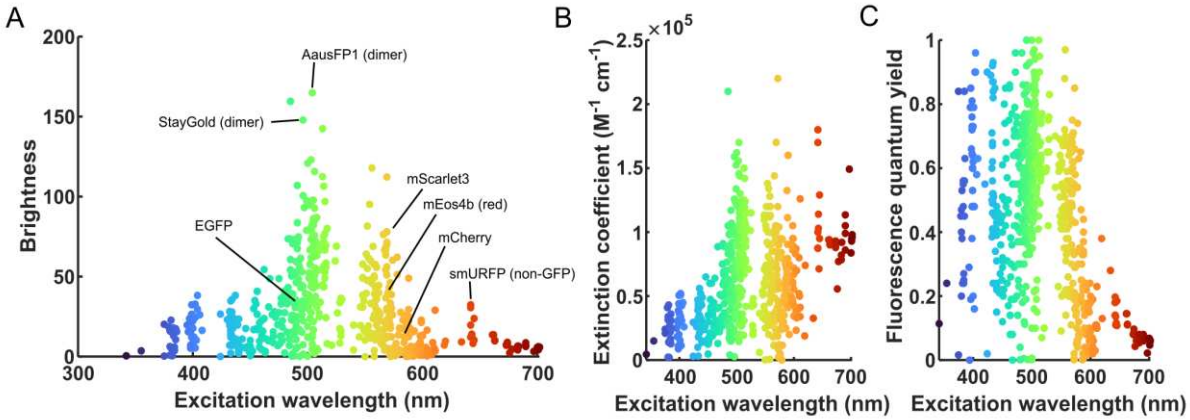

Figure 1.7 Color and brightness of FPs. *A) The theoretical brightness of FPs against their maximum excitation wavelength. Data extracted from FPbase[68] and includes nonGFP-like FPs (e.g. smURFP). Highlighted are a selection of popular FPs and FPs with extraordinary brightness. The extinction coefficients and fluorescence quantum yields of the same FPs are shown in B) and C), respectively.*

The fluorescence color of FPs can be tuned by either shortening or extending the π -conjugated system of the chromophore, or by changing the interactions between the chromophore and the protein matrix. Shortening or extending the chromophore's π -conjugated system will result in a blue shift or a red shift, respectively (**Figure 1.8**). This can be achieved by changing the first or second residue of the chromophore[69,70] or by changing the oxidation, protonation and/or hydration status of the chromophore[52,71,72]. In addition to changing the chromophore itself, color tuning can be achieved by changing residues near the chromophore[5,73]. For example, the FPs mTFP1.0 and Citrine have the same chromophore but their peak absorption differs by 65 nm[73]. Such effects are attributed to π-stacking and electrostatic interactions between the chromophore and nearby residues, affecting the extent of electron delocalization[5,73].

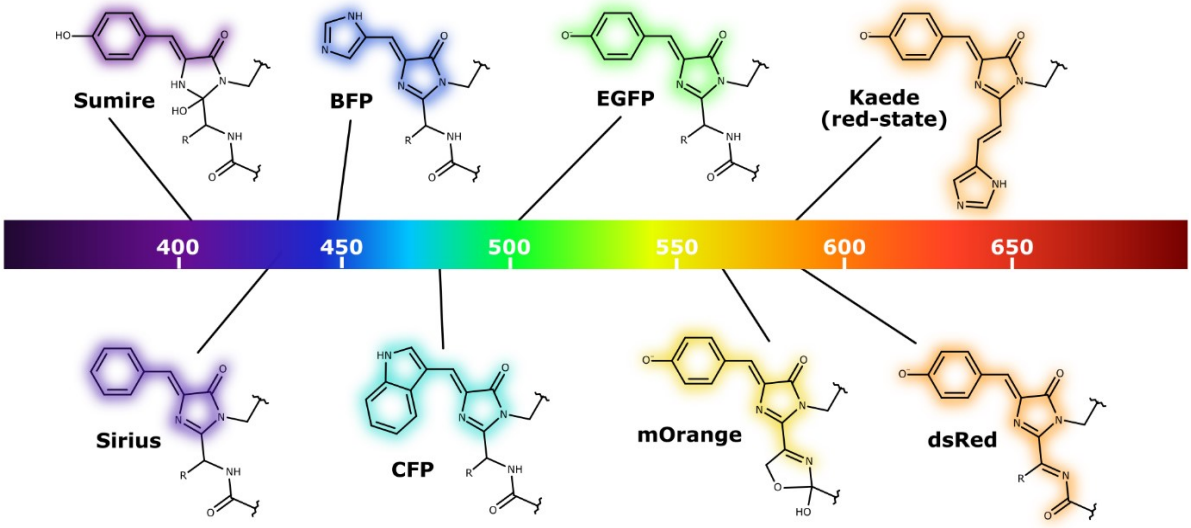

Figure 1.8 Color tuning of FPs by changing the chromophore. *Displayed are various chromophores sorted by emission wavelength.*

The theoretical brightness of FPs is the product of their extinction coefficient and fluorescence quantum yield. This largely explains why green/yellow FPs are generally the brightest: at this spectral range there is the optimal balance between a high extinction coefficient and a high fluorescence quantum yield (**Figure 1.7**). The reduced brightness of RFPs is for a big part explained by a low fluorescence quantum yield, meaning that there is a lot of nonradiative decay from the S_1 to the S_0

state. There are several factors that have been proposed to contribute to this effect, such as the reduced energy gap between the S_0 and S_1 states and increased structural flexibility of the RFP chromophore, both facilitating nonradiative decay[67,74,75]. The relatively low brightness of violet/blue FPs, on the other hand, is related to a low extinction coefficient, which has been attributed to the smaller size of blue absorbing chromophores[67].

Efforts to create brighter FPs are mostly focused on increasing the extinction coefficient and the fluorescence quantum yield by reducing nonradiative decay. This is typically done by directed evolution: a repetitive process of creation of large protein 'libraries' by random and/or site directed mutagenesis and selection of the best variants. A popular criterium to identify brighter variants is the fluorescence live-time because it is independent of the protein concentration and in often scales with brightness (less nonradiative decay -> longer lifetime)[76–79]. The mutation process is generally not completely random but structure guided, targeting residues that are expected to optimize the planarity and rigidity of the chromophore[77,78,80]. Such optimization processes have led to, for example, the creation of mTQ2[80], a cyan FP with an impressive fluorescence quantum yield of 0.93, and mCherry-XL[78], a RFP that is three times as bright as its precursor mCherry.

A high theoretical brightness does not always mean a high apparent brightness when the FP is expressed in cells. The apparent brightness, also called practical brightness, of FPs is dependent on many factors including efficient expression, folding and maturation, low degradation, various environmental conditions (see section **1.2.3.4**) and formation of short-lived nonfluorescent states. There are many examples of FPs whose apparent brightness has been increased, not by enhancement of their theoretical brightness, but by improvement of their expression efficiency (for example[81,82]). For optimal expression, the genetic sequence of the FP should be codon optimized for the host organism[83].

Finally, it is important to note that the appearent brightness of FPs is, of course, dependent on the applied laser power, and, in view of this, to distinguish between 'brightness' and 'photon budget'. The photon budget is the number of photons that can be emitted by a fluorophore before it is irreversibly destroyed (i.e. bleached, see **section 1.2.3.3.1**). Consider two fluorophores: one fluorophore with a high brightness but a low photon budget (fluorophore 1) and one fluorophore with a low brightness but a high photon budget (fluorophore 2). Using a given laser power that bleaches fluorophore 1 in a single frame, fluorophore 1 will appear brighter (i.e. emit more photons during a single frame) than fluorophore 2 but fluorophore 2 will be fluorescent for many more frames (emitting more photons in total). If the laser power is now increased so that fluorophore 2 is bleached in a single frame, fluorophore 2 will appear much brighter than fluorophore 1 because in this situation the appearent brightness of both fluorophores is limited by their photon budget. Both brightness and photon budget should thus be considered when searching for a bright appearing FP. It should be mentioned, however, that there are practical limitations to increasing the laser power, especially for experiments with living cells in which phototoxcicity is a concern (see **section 1.2.3.5**). Aditionally, increasing the laser power to increase the apparent brightness does not work efficienctly in situations where the brightness is limited by the formation of short-lived non-fluorescent states (see **sections 1.2.3.3.2, 1.6.4.2.1** and **3.1.4.2**).

1.2.3.3 Photostability

Photostability refers to the stability of the fluorescence signal of a fluorophore over time. The photostability of a FP includes its resistance to irreversible photobleaching, which is critical for long-term imaging, but also its propensity for other light-induced transformations, such as dark state formation, photoswitching, photoactivation and photoconversion. FPs displaying light induced transformations, other than photobleaching, are referred to as 'photochromic FPs' or

'phototransformable FPs' (PTFPs)[83,84]. Some FPs have been specifically designed and optimized to exhibit certain photochromic behaviors. These FPs are at the heart of SRM and will be discussed in detail in **section 1.3**. Many 'standard' FPs also exhibit some degree of photochromic behavior, which can be problematic in fluorescence techniques such as FRET and FRAP[85]. **Figure 1.9** provides an overview of common photochromic behaviors found in FPs.

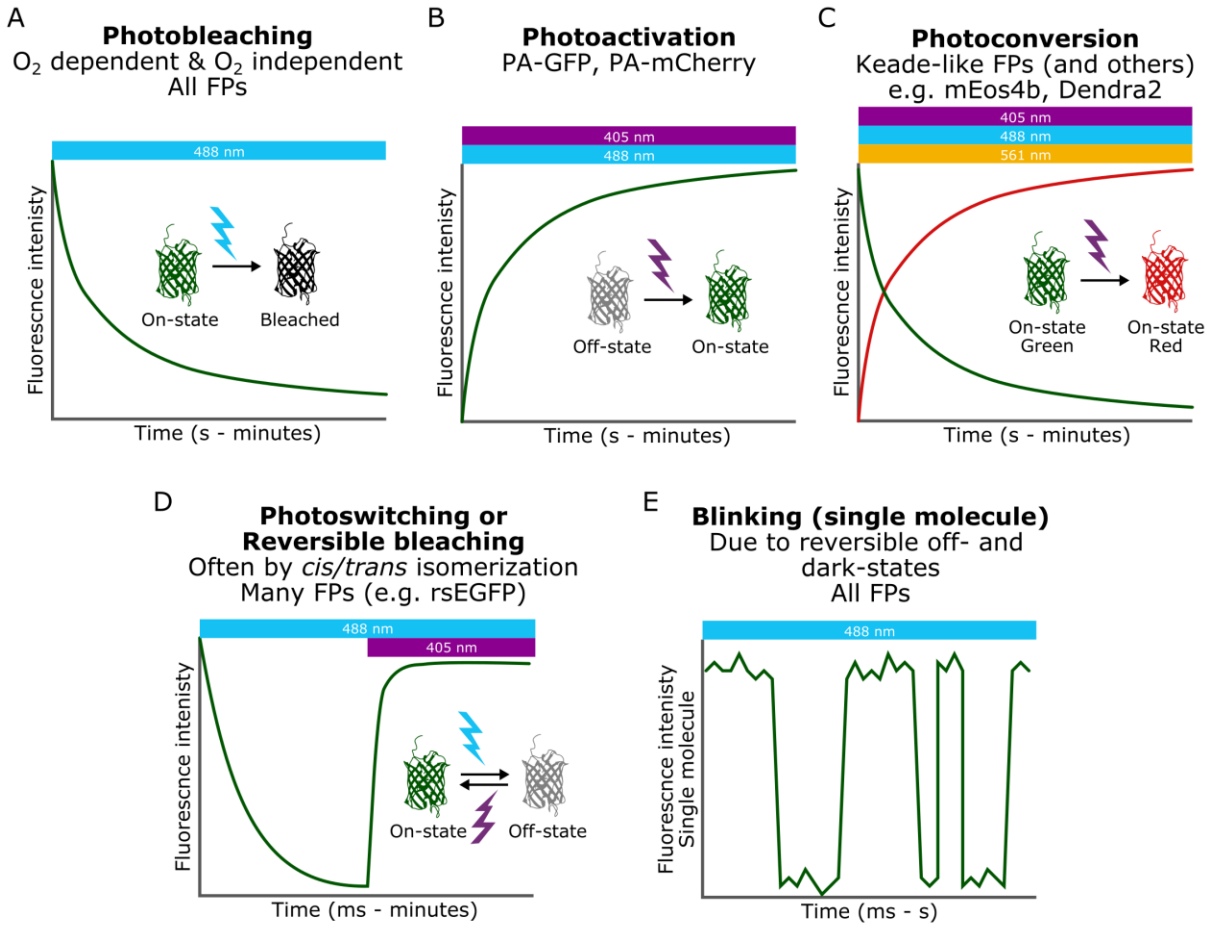

Figure 1.9 Common phototransformations of FPs. *A) All FPs are susceptible to irreversible photobleaching, which may proceed via O_2 dependent or independent mechanisms. B) Photoactivation is the irreversible conversion of FPs from a non- or weakly-fluorescent state into a fluorescent state. Typical examples are PAGFP and PAmCherry, which are activated by 405 nm light. C) Photoconversion is the light induced change in absorption and emission spectra of a FP. Typical examples are Keade-like FPs, such as mEos4b and Dendra2, which convert from a green emitting into a red emitting state upon excitation with 405 nm light. D) Photoswitching or reversible bleaching is the reversible loss of fluorescence, often by cis/trans isomerization of the chromophore. The fluorescent on-state can typically be recovered by excitation of the off-state with blue-shifted light. E) The formation of transient dark states (photoswitching/reversible photobleaching) gives rise to blinking at the ms to s time scale. Figure inspired by[86].*

1.2.3.3.1 Photobleaching

Photobleaching is the irreversible loss of fluorescence by light-induced destruction of the chromophore or chromophore pocket locking the chromophore in a non-fluorescent state (**Figure 1.9A**). As mentioned above, the number of photons emitted by a fluorophore before it is bleached is called the photon budget. The photobleaching mechanisms of FPs are not fully understood. It has been shown that FPs can bleach in O_2 dependent and independent manners and that the applied laser intensity affects the bleaching mechanism[87–89]. Duan et al. demonstrated that the fluorescent protein IrisFP bleaches in a O_2 dependent manner under low intensity illumination due to oxidation

of residues in the chromophore pocket, while that under high intensity illumination bleaching proceeds in an O_2 independent manner through decarboxylation of E212[89]. The bleaching rate often scales nonlinearly with the laser power, indicating that photobleaching can involve two or more photons[67]. It is also important to note that while photobleaching is expected to be monophasic, many FPs show multiphasic bleaching behaviors[35,90–92]. This might in part be due to the formation of reversible dark states (discussed below)[90,93] or due to immobilization techniques that fix the dipole orientation of the FP so that not all molecules experience the same light dose, but more complex scenarios, such as the existence of multiple subpopulations with different photo-resistance properties, are not excluded.

1.2.3.3.2 Reversible photobleaching, photoswitching and blinking

In addition to irreversible photobleaching, many FPs can bleach in a reversible manner[43,58,76,85,87,94,95]. This process is referred to as reversible photobleaching, photoswitching, kindling or dark state formation. With reversible photobleaching, the lost fluorescence can be recovered in the dark and/or by illumination with light of a specific wavelength (**Figure 1.9D**). At the single molecule level, reversible photobleaching gives rise to a phenomenon named blinking or flickering (**Figure 1.9E**). A common mechanism of reversible photobleaching is *cis*/*trans* isomerization coupled with (de)protonation of the chromophore (see **section 1.3.1**). Typically, the *cis*-state is the fluorescent state of the chromophore, while the *trans*-state is non-fluorescent. The *trans* configuration of the chromophore is often quite stable so that thermal recovery back to the *cis*-state can take seconds to hours but this process can be accelerated by excitation of the *trans*-state with cyan/violet light. Non-fluorescent states that are sensitive to light, such as the *trans*-state, are generally referred to as 'off-states', while non-fluorescent states that are not light sensitive are named 'dark-states' (but note: this terminology is not consistently used in the literature).

In addition to *cis*/*trans* isomerization, other off- and dark-states with a radical nature may be formed, suspectedly down-stream of the triplet state[96]. By itself, the triplet state does not live long enough (~1-5 ms) to be detected as reversible photobleaching or blinking under standard imaging conditions[88,97,98]. However, the formation quantum yield of triplet state is large (~0.1-1%) so that triplet state formation lowers the overall fluorescence intensity in both ensemble and single molecule imaging (**Figure 1.10**)[88,99]. Furthermore, the triplet state provides a starting point for diverse photochemical reactions, which may lead to the formation of longer-lived dark states and irreversible photobleaching[88].

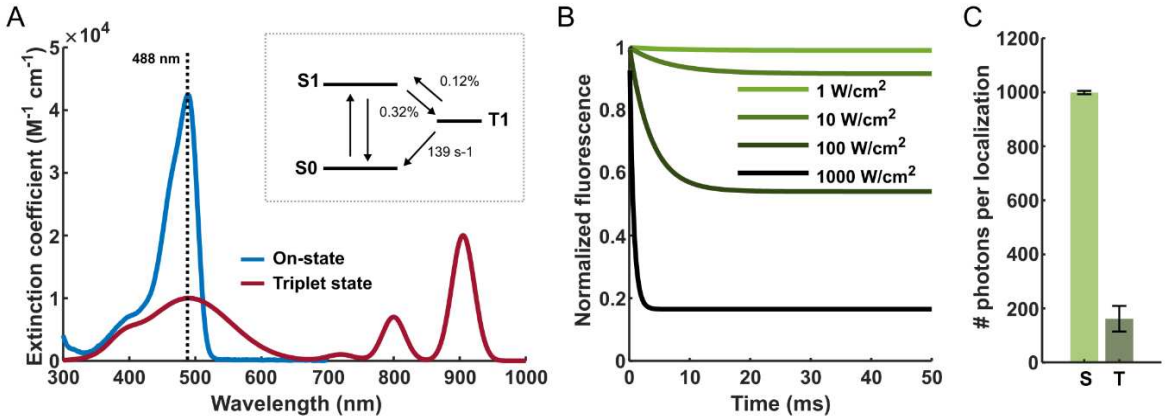

Figure 1.10 Triplet state formation lowers the apparent brightness of FPs. *The fluorescence signal of a GFP was simulated under* continuous *illumination with 488 nm light using SMIS. The fluorophore model is based on Rane et al.[100], consisting of a fluorescent state and triplet state. The quantum yield of forward ISC is 0.32%, while the quantum yield of reverse ISC is 0.12%. Thermal recovery from the triplet state happens with a rate of 139 s^{-1} (half-life 5 ms). A) Absorption spectra used for the simulations. Inset shows the photophysical model. B)*

Simulated ensemble fluorescence signal under continuous *illumination with 1-1000 W/cm^2 488 nm light, showing a sharp decay during the first ms due to saturation of the triplet state. C) The number of detected photons per simulated single molecule under* continuous *illumination with 1000 W/cm^2 488 nm light using a frame time of 100 ms, assuming that there is no triplet state formation (S, FISC=0%) or that there is triplet state formation as in B (T, FISC=0.32%).*

1.2.3.3.3 Photoactivation

In contrast to reversible and irreversible photobleaching, photoactivation is the irreversible gain in fluorescence intensity upon illumination. Typical examples of photoactivatable FPs are PA-GFP and PAmCherry, which are widely used for SMLM (**Figure 1.9B**)[101,102]. These PA-FPs start out from a non-fluorescent state and become highly fluorescent upon excitation with violet (405 nm) light, which causes decarboxylation of Glu222 (PA-GFP numbering), favoring the fluorescent state of the chromophore (see **section 1.3.2**) [62,101–103].

In addition to true photoactivatable-FPs, various FPs show transient photoactivation under illumination with their typical excitation wavelength or under dual illumination with blue shifted light. This transient activation can be seen in a diverse set of FPs, including mStable[104], mKate2[58,76], mRuby2[83], mOrange2[43], TagRFP-T[58,83] and mBlueberry2[105]. In mStable, the transient photoactivation is due to oxidation of a cysteine residue near the chromophore (C143) , which stabilizes the *cis* conformation of the chromophore, enhancing the fluorescence signal and photostability of the FP[104]. In the other FPs, the mechanisms underlying the observed photoactivation remain poorly understood and the observed photoactivation may possibly result from other photochromic events occurring under specific imaging conditions. For example, a fraction of FPs might start in a reversible off-state (due to a thermal equilibrium or off-switching by ambient light) and be progressively recovered under illumination thereby transiently increasing the fluorescent signal, as was proposed by Botman et al[83]. This explanation would be especially applicable to FPs that are known to photoswitch, such as mRuby2 and TagRFP[58,76]. The apparent photoactivation of mOrange2 under confocal excitation seen in ref[43] could maybe be explained by orange-to-red photoconversion of the FP[106] increasing the detected fluorescence due to the presence of a 656 nm long-pass filter in the detection path.

1.2.3.3.4 Photoconversion

Photoconversion is a light-induced change in absorption and emission spectra of the fluorophore. Photoconvertible FPs (PCFPs) are popular markers for SMLM. Among the different types of photoconvertible FPs, Kaede-like PCFPs are most commonly used (**Figure 1.9C**). These PCFPs are characterized by a histidine as first amino acid of the chromophore and undergo irreversible green-to-red photoconversion upon irradiation with violet light (typically 405 nm) in a single photon process[107]. This photoconversion is mediated by extension of the π-conjugated system of the chromophore through cleavage of the protein backbone. The photoconversion mechanism of Kaede-like PCFPs will be discussed in more detail in **section 1.3.3**. PS-CFP(2) is another type of PCFP that converts from a cyan- into a green-emitting state in response to ~405-nm irradiation (note: PS stands for photoswitchable but means photoconvertible)[108,109]. The conversion mechanism of PS-CFP was proposed to be similar as the activation mechanism of PA-GFP: decarboxylation of Glu222, favoring the anionic green-emitting state of the chromophore[108]. Yet another type of PCFP that has been designed for SMLM is (PS)mOrange [43,106,110]. PSmOrange photoconverts from an orange to a far red state upon irradiation with blue-green light (~470-540 nm) in a two photon process[106]. Similarly as for Keade-like PCFPs, photoconversion of PSmOrange involves cleavage of the protein backbone, although the photoconversion mechanism is otherwise very different[106].

Green-to-red photoconversion is also observed in GFP and EGFP, in which case the conversion is referred to as 'redding'[111–113]. Redding of GFPs is a complex process resulting in multiple photoconverted states with slightly different emission spectra[111–113]. Two different mechanisms of redding have been described: one dependent on low oxygen concentrations[111] and another dependent on the presence of oxidants[112,113], the latter named oxidative redding. GFP redding is thus highly sensitive to the environmental conditions and may proceed differently depending on the cell type, cellular localization and culture conditions[113,114].

Finally, there is a heterogeneous group of FPs that have been reported to photoconvert into a blue shifted species[110,115,116]. For example, the RFP mKate(2) converts into green and blue species upon intense irradiation[110,117]. This effect was shown to be enhanced by incubation of the FP in sodium dithionite and was ascribed to a reversible reduction of the chromophore[117]. Another example is presented by NowGFP, a GFP that converts irreversibly from a green into a cyan emitting species by illumination with blue light, which has been related to *cis*/*trans* isomerization of the chromophore and decomposition of the side chain of K61[118].

1.2.3.3.5 Conclusion

In conclusion, FPs display a variety of photo-induced transformation, which are often incompletely understood and can be problematic for imaging. Extra complexity is added by environmental sensitivity of certain behaviors and the influence of the imaging conditions[87,110,113,114,118]. In particular, FPs may display a very different photostability under wide-field illumination conditions than under scanning confocal illumination conditions[43,76,87]. The reason for this is likely that the scanning of the confocal lasers allows short-lived dark states of some FPs to recover, enhancing their apparent photostability, while the high laser power might induce two photon processes in other FPs, accelerating their bleaching compared to wide field illumination conditions. As a consequence of this complexity, different studies may report different photostabilities and photochromic behaviors for the same protein, which may complicate the choice of a suitable FP for a given experiment. Despite all the issues arising for photochromism, phototransformable FPs are at the core of SRM techniques and are thus valuable for biological research.

1.2.3.4 Environmental sensitivity

FPs are highly sensitive to environmental conditions, such as pH, redox status, temperature, viscosity[119], protein crowding[120], pressure[121] and ion concentrations. This sensitivity can give rise to unwanted photochromic behaviors and lowered fluorescence intensity. To solve such issues, FPs with high pH and chemical resistance have been developed. At the same time, the environmental sensitivity of FPs is also a starting point for the development of biosensors.

All FPs are sensitive to the pH of their environment, which is mainly attributed to (de)protonation of the chromophore, with the protonated state being non-fluorescent (**Figure 1.11A**). The protonated state is non-fluorescent due to breakage of the H-bond network, which stabilizes the anionic chromophore, leading to increased dynamics favoring non-radiative decay[122]. The (de)protonation events of the chromophore are too fast (~µs-ms timescale) to be detected as blinking under typical imaging conditions but quench the overall detected fluorescence signal[122–125]. The absorbance of the protonated chromophore is blue shifted compared to the anionic state and can usually easily be recognized in the absorption spectrum (**Figure 1.11A**). Examples of FPs with high pH resistance include mCerulean3[126], rsGamillus[65] and TagRFP[127], which all have a pKa below 4. The pH sensitivity of FPs is commonly described by a Hill equation, describing their pKa and Hill coefficient (**Figure 1.11B**). In theory, the Hill coefficient should equal 1, assuming that chromophore protonation occurs in a simple one-step protonation process solely dependent on the environmental pH. In practice,

however, the pH sensitivity of FPs is very complex due to interactions between the chromophore and the rest of the protein matrix and due to (de)protonation of other residues nearby the chromophore, which may influence the emitted fluorescence[123,128]. Consequently, some FPs exhibit little pH sensitivity over a wide pH-range[123,129], while others show two distinct protonation steps[130–133]. Moreover, some FPs show a reverse pH dependence, meaning that the anionic (deprotonated) population increases as the pH decreases[134–136]. In the FP mKeima, this effect was ascribed to the protonation status of residue Asp157 in the chromophore pocket, stabilizing the anionic-*cis*-conformation at low pH and the protonated-*trans*-conformation at high pH[134]. It is also important to note that while the protonated chromophore is considered non-fluorescent, excitation of the neutral chromophore can in some FPs, including wtGFP, lead to fluorescence emission through formation of the anionic chromophore by Excited State Proton Transfer (ESPT)[6,137].

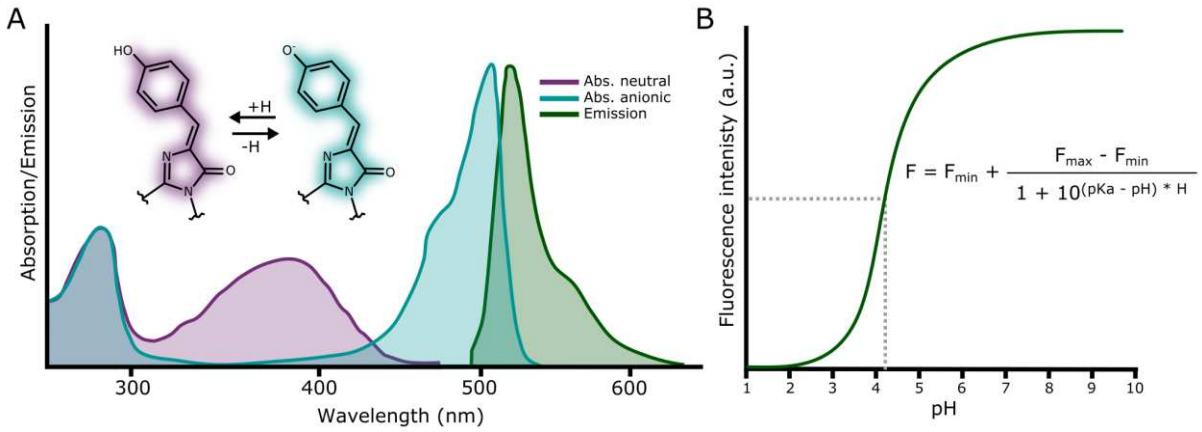

Figure 1.11 pH sensitivity of FPs. *A) Typical absorption spectra of the neutral (pronated) and anionic (deprotonated) states of a green FP. B) Generally, the fluorescence intensity of FPs is quenched at low pH due to protonation of the chromophore. The pH sensitivity can be described by a Hill equation, where H is the hill coefficient. The pKa is defined as the pH at which the FP is at the half max of its fluorescence intensity (grey dotted line).*

In addition to pH, FPs are sensitive to many other environmental factors. Many FPs are sensitive to chloride and other anions, which quench their overall fluorescence signal[138–142]. Examples of FPs with reduced chloride sensitivity are Citrine[138] and hyYFP[140]. The environmental viscosity can influence the photochromic behavior of FPs by modulating the flexibility of the protein matrix[119]. FPs are also senisitive to the redox status of their environment, which is mainly due to the relatively long lifetime of the singlet excited state (ns) and the triplet state (ms), which are both highly reactive. As described in section **1.2.3.3**, the redox environment is known to affect redding of GFPs[98,114] and the blueing of mKate[117]. In addition, the redox environment has been shown to affect the blinking and bleaching of certain FPs[143–147].

To summarize, FPs are highly sensitive to their environment. Consequently, the *in vitro* performance of a FP does not necessarily reflect its *in cellulo* performance. Moreover, the fluorescence properties of an FP can differ depending on the cell line in which it is expressed and the cellular localization. Besides live-cell imaging, the environmental sensitivity of FPs can pose problems for chemical fixation, as the fluorescence intensity of many FPs is reduced after fixation[140,148–152]. This problem has been dealt with by the development of several fixation resistant FP variants[82,140,149–151]. Although the environmental sensitivity of FPs can complicate experiments, it has also inspired the development of diverse FP-based biosensors, including pH-[133,135], chloride-[139,142] and redox-sensors[153,154].

1.2.3.5 Cytotoxicity

Low cytotoxicity is an important criterion for FPs since they are used to label and study living cells. Although FPs are generally considered to be nontoxic, FPs can be toxic and disturb biological systems through various mechanisms, including the production of reactive oxygen species (ROS) and interference with the functioning of the labeled protein.

Starting at the maturation process, one H_2O_2 molecule is generated during the maturation of each chromophore. This low level of H_2O_2 production has been reported to be within the normal cellular range and is thus not toxic[155]. However, maturation is not an instantaneous process and FPs may be in an immature state for minutes to hours. These immature FPs have been reported to produce continuously $O2^{\bullet-}$ and H_2O_2 in the presence of NADH in a catalytic manner, which was shown to activate stress response pathways in both *E. coli* and HeLa cells[156]. After maturation, FPs can produce ROS in a light dependent manner via type I and II photosensitization mechanisms[157]. This effect is particularly a concern for long-term live cell imaging. While ROS production is usually unwanted, some FPs have been engineered to produce large amounts of ROS upon excitation, such as KillerRed and SuperNova[157,158]. The structural basis for the high phototoxicity of KillerRed has been proposed to be a water channel connecting the chromophore to the solvent, facilitating exchange of O_2 and ROS molecules[159,160]. FPs, such as KillerRed, are used in research as photosensitizers to inactivate specific proteins and to kill cells in a controlled light-induced manner[158]. It is important to note that imaging induced toxicity is not necessarily dependent on ROS generation by FPs, but may also be a direct effect of the illumination. Violet and blue light are known to be phototoxic, while red shifted light has been reported to be less harmful[10,98,161]. The phototoxicity of UV and blue light is the result of the excitation of flavins and porphyrins, which are naturally present inside cells, leading to the generation of ROS[162].

Another potential source of toxicity is physical disturbance of the biological system[20,163]. This might be because the FP is not fully monomeric[164], does not fold properly and aggregates, or because the FP sterically hinders the activity of the labeled protein, which may activate stress response pathways or may alter the ability of the cell to respond to certain stimuli. For this reason, it is always important to validate that the cells expressing a fusion construct behave similarly as wild-type cells. A possible solution to oligomerization, when suitable FPs with high monomericity are not at hand, is the use of tandem FPs but this comes at the cost of a larger label size[34,35]. It is worth noting that FPs that perform well in one fusion construct or in one cell line, may be problematic in another. For example, mCherry, which has been widely used in biological studies, was reported to form large aggregates in neurons[165].

In conclusion, although FPs are widely used in biological research, labelling with FPs may lead to toxicity and disturbance of the biological system. To minimize toxicity, there are several factors that should be considered. Firstly, it is advisable to use readily folding, highly monomeric and fast-maturing FPs to minimize ROS production and aggregation. Secondly, imaging should preferably be performed using red shifted light and using as low doses as possible. Lastly, it important to validate that localization and functioning of the protein of interest is not affected by the fluorescent label.

1.3 Fluorescent proteins for super-resolution microscopy

Super-resolution microscopy techniques have pushed, and keep pushing, the resolution of optical microscopy into the nanometer range. There exists a variety of SMR methods which rely on advances in instrumentation and fluorophore developments. These techniques can be roughly divided into two major categories: those based on structured illumination (deterministic methods: e.g. SIM, STED and RESOLFT) and those based on stochastic single molecule activation/blinking (SMLM techniques:

PALM, STORM, PAINT and MINFLUX (also requires structured illumination))[166]. These different techniques require different types of fluorophores.

SIM is based on the use of periodic illumination patterns and sophisticated software to reconstruct the image through Fourier space[167]. Although the gain in resolution using SIM is limited compared to other SMR techniques (only up to 100 nm resolution), a big advantage is that it is performed using standard fluorophores[167]. STED microscopy utilizes the possibility to de-excite fluorophores by stimulated emission to increase the imaging resolution[168]. To this end, STED imaging is performed using two sequential laser pulses: firstly, a Gaussian beam to excite the fluorophores and secondly, a donut-shaped beam to de-excite the fluorophores at the edge of the Gaussian, thereby reducing the area of emitted fluorescence[168]. STED imaging requires fluorophores with a high photostability and that can be de-excited efficiently by stimulated emission, for which reasons organic dyes are more commonly used than FPs[168]. RESOLFT makes use of a similar illumination scheme as STED but uses photoswitchable fluorophores instead, switching the fluorophores into a non-fluorescent state instead of de-exciting them[169]. Reversibly photoswitchable FPs are highly suitable for this latter technique[169]. More detailed descriptions of these, and other, deterministic super-resolution methods can be found in recent reviews[166–168].

SMLM techniques rely on the stochastic activation or blinking of molecules, with the different SMLM methods relying on different types of fluorophores and different activation/blinking mechanisms[170]. PALM imaging makes use of the stochastic photoactivation or photoconversion of photoactivatable and photoconvertible FPs. Sometimes, PALM imaging is performed using reversibly photoswitchable FPs but this is less common[171,172]. STORM imaging relies on the stochastic blinking of organic dyes. PAINT imaging is based on the stochastic binding and unbinding of a fluorophore to its target. MINFLUX combines SMLM with a donut-shaped excitation beam to reach nanoscale precision while requiring only few photons[173]. A more detailed description of PALM, STORM and PAINT imaging is provided in **section 1.4.2**.

As a side note, the distinction between PALM and STORM imaging is not clear-cut. Historically, PALM imaging is performed using FPs, while STORM imaging is perfomed using organic dyes. However, one can also argue that the difference between PALM and STORM imaging is that PALM is based on irreversible phototransformations (photoconversion and photoactivation), while STORM is based on reversible phototransformations (photoswitching/blinking), in which case PALM and STORM can both be perfomed using FPs or organic dyes. Throughout my thesis I will use the first definition that PALM is performed using FPs, while STORM is performed using organic dyes.

In this section I give an overview of the different types of phototransformable fluorescent proteins used for super-resolution microscopy: reversibly photoswitchable FPs (RSFPs), photoactivatable FPs (PAFPs) and photoconvertible FPs (PCFPs). The main focus will be on photoconvertible FPs, especially those of the EosFP family, which are the FPs I have mostly worked with.

1.3.1 Reversibly photoswitchable fluorescent proteins

Reversibly photoswitchable fluorescent proteins (RSFPs) are FPs that can be repeatedly switched between a fluorescent on-state and a non-fluorescent off-state. Such light-induced switching was first reported by Dickson et al. in 1997, who observed single molecule blinking of GFP mutants under illumination with 488 and 405 nm light[174]. Since then, blinking has been observed in many FPs and FPs with enhanced switching behaviors have been developed for SRM application. Based on the wavelengths used for on/off-switching and fluorescence excitation, RSFPs can be grouped into three classes: negative RSFPs, positive RSFPs and decoupled RSFPs (**Figure 1.12**).

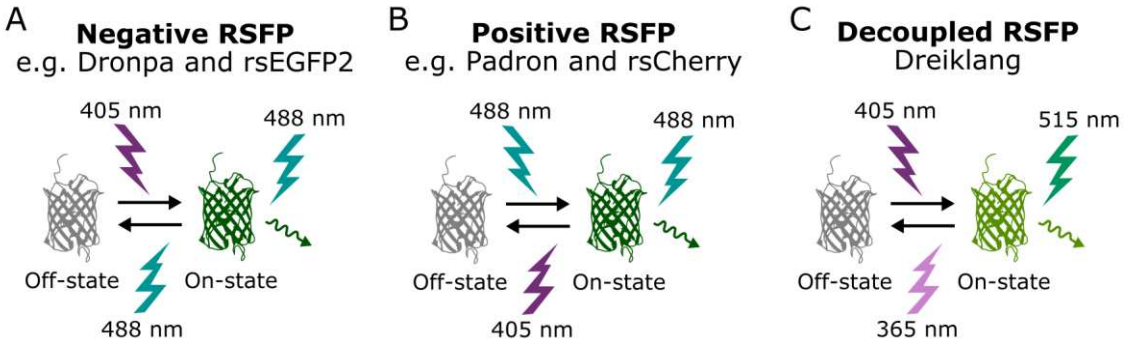

***Figure 1.12 Classes of Reversible Switchable Fluorescent Proteins (RSFPs**). RSFPs can be grouped into three classes based on the wavelengths used for on/off switching and fluorescence excitation. A) Negative RSFPs are switched off by the same wavelength used to elicit fluorescence and switched on by blue shifted light. B) Positive RSFPs are switched off by blue shifted light and switched on by the same wavelength used to elicit fluorescence. C) In decoupled RSFPs, on/off switching is decoupled from fluorescence excitation. Note that the wavelengths denoted in the figure are for illustrative purposes, representing common laser lines used for switching of common RSFPs.*

Photoswitching of both positive and negative RSFPs is based on changes in the *cis/trans* isomeric state and protonation state of the chromophore. Popular examples of positive and negative RSFPs include Padron[132,175,176] and rsCherry[177], and Dronpa[178] and rsEGFP(2)[179,180], respectively. The difference between positive and negative RSFPs is that in positive RSFPs the wavelength used to elicit fluorescence emission switches the FP to the on-state, while in negative RSFPs this wavelength switches the FP to the off-state (**Figure 1.13**). Underlying this difference are the pKa's of the *cis*- and *trans*-states, as photoswitching involves four chromophore species: *cis*-anionic, *cis*-protonated, *trans*-anionic and *trans*-protonated, with the *cis*- and *trans*-anionic states, and the *cis*- and *trans*-protonated states having similair absorption spectra (**Figure 1.13**). In negative RSFPs the pKa of the *cis*-state is much lower (~5-6) than the pKa of the *trans* state, which is generally >10[122,130,181]. Therefore, at physiological pH, the *cis*-state is mostly anionic while the *trans*-state is mostly protonated, absorbing blue-shifted light, so that excitation of the fluorescent *cis*-anionic state leads to off-switching, while excitation of the trans-protonated state with violet/blue light leads to on-switching (**Figure 1.13A&C**). In positive RSFPs, on the other hand, the pKa of the *trans*-state is lower than the pKa of the *cis*-state[132,181]. Consequently, efficient photoswitching of positive RSFPs happens at pH values lower than the *cis*-state pKa but higher than the *trans*-state pKa. In this situation, there is a mixture of anionic and protonated *cis*-state, which can be switched off by excitation of the protonated *cis*-state, while the mostly anionic *trans*-state can be switched on with the same excitation wavelength used to elicit fluorescence from the *cis*-anionic state (**Figure 1.13B&D**).

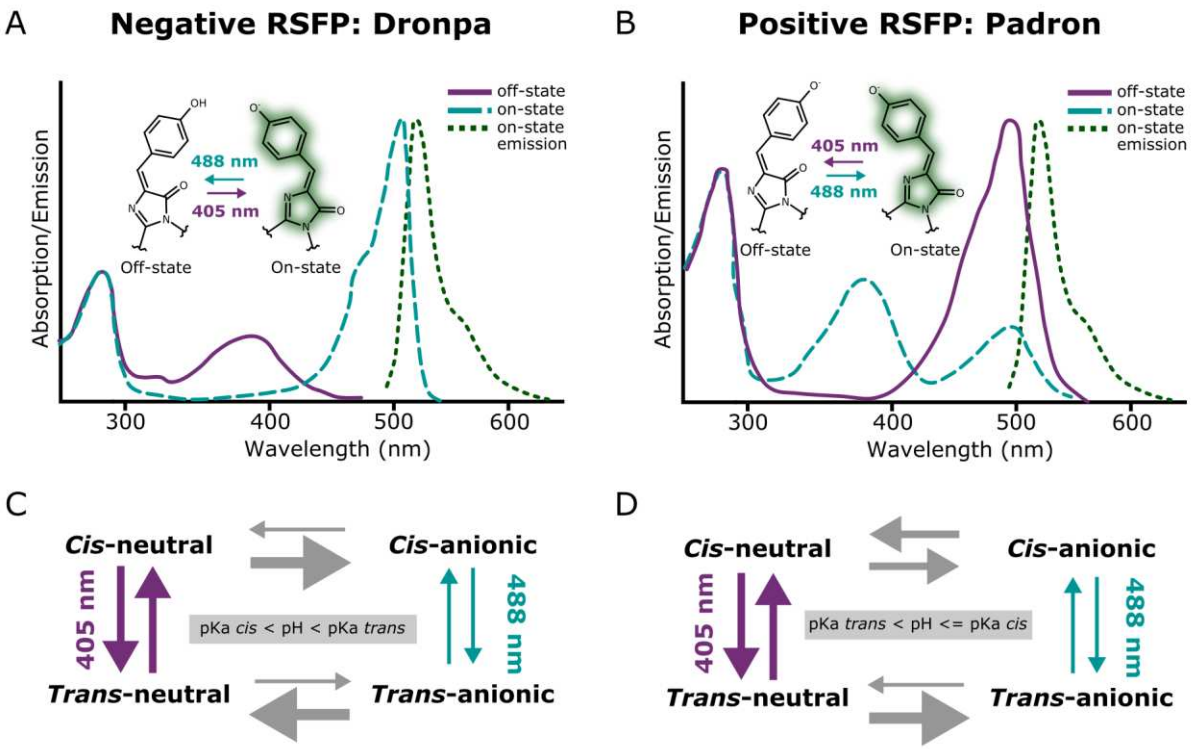

Figure 1.13 Photoswitching mechanisms of negative and positive RSFPs. *Photoswitching of both negative (A & C) and positive (B & D) RSFPs is based on changes in the cis/trans isomeric state and protonation state of the chromophore. Shown are the examples of Dronpa, a negative RSFP, and Padron, a positive RSFP. A & B) Cartoons of the emission and absorption spectra of Dronpa (A) and Padron (B) in the on and off states. C-D) Schematics of the photoswitching pathways in Dronpa (C) and Padron (D). The sizes of the arrows in C and D reflect the relative differences in quantum yields and rates. Colored arrows indicate light driven transitions (pruple = 405 nm, cyan = 488 nm), grey arrows indicate thermal transitions.*

In contrast to negative and positive RSFPs, decoupled RSFPs are FPs in which on/off switching is decoupled from fluorescence excitation. This class only contains a single FP: Dreiklang[171,182]. In Dreiklang, fluorescence emission is elicited by excitation with ~488-515 nm light, while on- and off-switching is achieved by excitation with ~365 nm and ~405 nm light, respectively[171,182]. This disconnection is due to the fact that off-switching occurs from the neutral state of the chromophore, which absorbs around 405 nm, while the off-state is a hydrated state of the chromophore, which absorbs around 340 nm, so that excitation of the on-state with 515 nm light has little effect on the switching[171]. A disadvantage of Dreiklang is that switching requires relatively high intensities of 365 and 405 nm light, which are highly phototoxic. To overcome this problem, Dreikling was subjected to random mutagenesis resulting in a FP which was named SPOON (SPOntaneous switching ON fluorescent protein)[183]. Compared to Dreiklang, spontaneous thermal recovery from the off-state is faster in SPOON and off-switching of SPOON can be efficiently achieved using 488 nm light alone so that SMLM imaging can be performed using only a single laser at 488 nm, which is a clear advantage for live-cell imaging[183]. A disadvantage of the strategy, however, is that there is limited control over the localization density.

In addition to photoswitchable RSFPs, switching of some FPs can be chemically induced. The addition of thiols, such as β-mercaptoethylamine (MEA) and β-mercaptoethanol (βME), has been shown to promote blinking of, for example, the popular red FP mCherry, and the photoconvertible mEos2 and mEos3.2[143–146]. The identification of such FPs that blink in a chemically induced manner opens up the possibility to use standard FPs for SMLM imaging and to multicolor imaging using both FPs and organic dyes under STORM-like conditions[143–146]. Cloin et al. revealed the mechanisms of βME induced dark state formation in mCherry, showing that βME can either covalently attach to the

chromophore or reduce the chromophore, both resulting in an off-state that can be recovered by washing out the βME or by excitation with 405 nm light[146]. Unfortunately, this quenching mechanism appeared unique to mCherry, so that this strategy cannot be widely used[146].

1.3.2 Photoactivatable fluorescent proteins

Photoactivatable FPs (PAFPs) can be irreversibly switched from a non-fluorescent (or very weakly fluorescent) state into a strongly fluorescent state. The lack of fluorescence from the initial non-fluorescent off-state of PAFPs can be an advantage over PCFPs for multicolor imaging. FPs in this category include PA-GFP, PAmCherry, PAmKate and PATagRFP.

In both PA-GFP and PAmCherry photoactivation was shown to involve UV-induced decarboxylation of E212 (GFP numbering), although the effect of E212 decarboxylation was shown to be strikingly different. In PA-GFP, E212 decarboxylation was reported to increase the pKa of the chromophore, favoring the fluorescent anionic state[102,103]. In PAmCherry, on the other hand, E212 decarboxylation was reported to promote double bond formation between the Cα and Cβ atoms of the tyrosine side chain in the chromophore, extending the π-conjugated system[62]. Interestingly, the on-state configuration of the PAmCherry chromophore was shown to be the *trans*-state, while the on-state configuration of the non-photoactivatable mCherry chromophore is the *cis*-state[62]. The photoactivation mechanisms of PAmKate and PATagRFP are not fully understood. Photoactivation of PAmKate was proposed to involve E212 decarboxylation and chromophore deprotonation as in PA-GFP, based on a similar changes in absorption spectra between the off-and on-states and similar photoactivation capabilities at cryogenic temperature[184,185]. Photoactivation of PATagRFP was proposed to be a two-step oxidation process, thus requiring two photons, with the second oxidation step being similar as in PAmCherry[186].

1.3.3 Photoconvertible fluorescent proteins

Photoconvertible FPs (PCFPs) can be converted irreversibly from one fluorescent color into another, typically red-shifted, color. An advantage of PCFPs over PAFPs is that the fluorescence of the initial state enables straightforward detection of successfully labeled samples. As discussed in **section 1.2.3.3**, there exist different types of PCFPs which have been developed for SMLM. Here, I will focus on Kaede-like PCFPs, which are the most widely used.

The protein Kaede was discovered in 2002 by Ando et al., who cloned the protein as a green-emitting FP from the stony coral *Trachyphyllia geoffroyi*[187]. The green-to-red photoconversion capabilities of the protein were discovered by chance when the protein was left overnight on the lab bench and was converted into a red-emitting FP by sunlight[187]. The FP was named 'Kaede', meaning maple leaf in Japanese[187]. Following the discovery of Kaede, different green-to-red PCFPs were found in other coral species, including EosFP, which was cloned from the stony coral *Lobophyllia hemprichii*[188]. The biological function of green-to-red PCFPs has been proposed to be the scavenging and conversion of blue light, which penetrates best in water, into red light, which is more useful for photosynthesis and is less phototoxic[189]. In addition to these naturally occurring PCFPs, Kaede-like green-to-red PCFPs have been created by directed molecular evolution from non-photoconvertible green FPs (KikGR[190] and mClavGR2[191]).

The photoconversion mechanism of Kaede-like PCFPs has been intensively investigated. All Keade-like PCFPs have a Histidine as first amino acid of the chromophore. Incorporation of this Histidine into the π-conjugated system of the chromophore is responsible for the green-to-red photoconversion (**Figure 1.14A**). This process is mainly triggered by excitation of the neutral green chromophore by UV light, which leads to breakage of the protein backbone in between F61 and H62

(**Figure 1.14A**). The exact reactions leading to this backbone cleavage remain incompletely understood. Various reaction mechanism have been proposed involving β-elimination via stepwise E1 or concerted E2 mechanisms[192–194], the triplet state[194], an intermediate radical state[195] and/or excited-state proton transfer[188]. A consensus between these different hypotheses is that the fully conserved E212 plays a critical role, although its exact function remains under investigation[192,194,195].

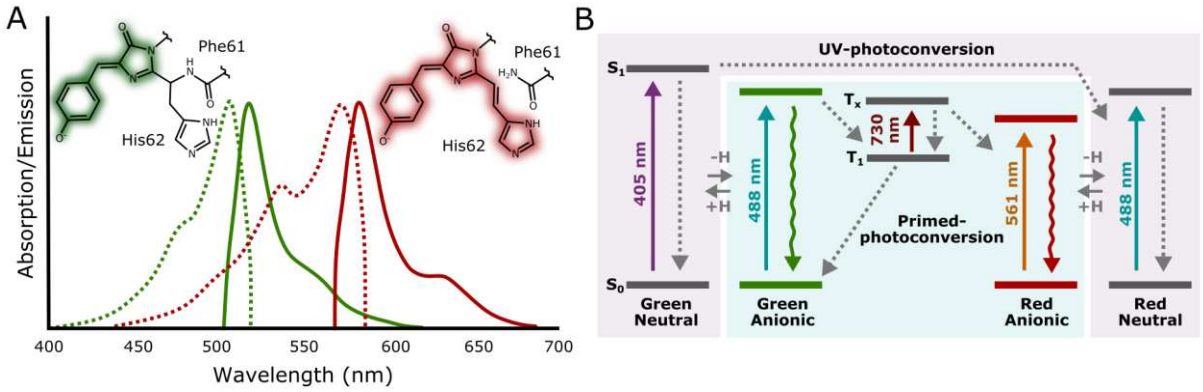

Figure 1.14 Photoconversion of Kaede-like PCFPs. *A) Absorption (dashed lines) and emission (solid lines) spectra of the green and red anionic states of the popular Kaede-like PCFP mEos4b. Green-to-red photoconversion is the result of incorporation of His61 (mEos4b numbering) into the conjugated system of the chromophore due to cleavage of the protein backbone at the level of Phe61. B) Jablonski diagram of the two photoconversion pathways: UV-photoconversion and primed-photoconversion. UV-photoconversion is a one photon process which is initiated from the green neutral chromophore by excitation with UV (typically 405 nm) light. Primed-photoconversion is initiated from the green anionic chromophore, which upon excitation with blue light can enter the triplet state from which photoconversion can occur upon excitation with red (650-800 nm) light. Primed photoconversion can also happen (although inefficienctly) under illumination with 488 nm light alone. Note that the primed photoconversion pathway is not efficient in all Kaede-like PCFPs. Solid lines indicate light induced processes, dashed lines indicate thermal processes, and wavy lines indicate fluorescence emission.*

To gain better understanding of the fundamental properties of PCFPs, Field and Matz traced back the evolution of green-to-red photoconversion[196]. Their efforts resulted in the design of ALL-GFP, a green non-convertible FP believed to be the common ancestor of Anthozoa FPs, and LEA (least involved ancestor), bearing a minimal number of 12 mutations necessary to engineer PC from ALL-GFP[196]. In following studies, LEA was subjected to extensive biochemical and photophysical characterizations to gain insight into the fundamentals of photoconversion[197–200]. Kim et al. (2013) showed that the pH-dependence of the photoconversion rate of LEA follows a bell-shaped spectrum with a maximal photoconversion quantum yield of 1.5×10^{-3} at pH 6.1[198]. Based on this finding and further structural characterization they proposed a critical role for the H-bond network around the chromophore involving residues E222, H203, E148, and R69[198]. Later Kim et al. (2015) showed that flexibility of the protein backbone is essential for efficient PC[197]. Krueger et al (2019) reported that dual illumination with 400 and 505 nm light enhances the photoconversion of LEA, which they proposed is due to an increased protonated green population (light-induced formation of the *trans*-protonated green off-state), suggesting that photoconversion may occur from both the *cis*-neutral and *trans*-neutral chromophore[199]. A limitation of all these studies on LEA is that they do not include any standard PCFPs for comparison, so that it remains unclear whether the properties of LEA are truly representative of Kaede-like PCFPs.

The photoconversion quantum yield of PCFPs by excitation of the green neutral state has been estimated to be in the order of 1×10^{-5} up to 1×10^{-3} (**Table 1.1**)[4,107,187,201,202]. In the PCFP Dendra, photoconversion was shown to also occur from the green anionic chromophore, although with a much lower quantum yield (~6×10^{-5} vs ~1.5×10^{-3})[107]. It is important to note that photoconversion from the green to the red state is not 100% efficient. The photoconversion efficiency (PCE) has been estimated between 1% and 90% (**Table 1.2**)[144,164,203–206], depending on the PCFP, the environmental

and illumination conditions, and the method used to estimate the PCE. There are several factors that have been proposed to contribute to the suboptimal PCE of PCFPs including bleaching of the green state, and the existence (or formation) of a green subpopulation that is unable to convert[199,203,204].

Table 1.1 List of reported photoconversion quantum yields.

Reference	PCFP	Photoconversion quantum yield	Notes
Adam et al. (2008)	IrisFP	1.8e-3	Purified protein, 405 nm light
	EosFP	8e-4	Purified protein, 405 nm light
Ando et al. (2002)	Kaede	2.4e-4	*In cellulo,* 365 and 400 nm light
Avilov et al. (2014)	Dendra2	1.4e-5	*In cellulo*, 405 nm light
Habuchi et al. (2008)	mKikGR KikGR	7.5e-3 4.7e-3	Purified protein, 405 nm light
Makarov et al. (2014)	Dendra2	1.5e-3	From the neutral chromophore (400 light) Purified protein
		6e-5	From the anionic chromophore (488 nm) Expectedly via the same pathway as primed photoconversion (see below)

Table 1.2 List of reported photoconversion/effective labeling efficiencies. *Depending on the method, is is difficult to distinguish the PCE from the effective labelling efficiency (ELE) or the detection efficiency. For a more detailed discussion on the differences between the PCE, the ELE and the detection efficiency see* ***section 1.6.1****. A detailed explanation of the different counting methods (off-time tresholding and blinking statistics) can be found in* ***section 1.5.2****.*

Reference	PCFP	PCE/ELE	Method	Notes
Baldering et al. (2019)	mEos3.2	64%	Blinking statistics	Purified protein, genetic and synthetic dimers (61% *in cellulo*) 210 W/cm^2 568 nm light and 0-30 mW/cm^2 405 nm light.
Baldering et al. (2021)	mEos4b	79%	Blinking statistics	FP fusion to membrane protein 0-30 mW/cm^2 405 nm, 210 W/cm^2 568 nm and 4.6 W/cm^2 638 nm
Durisic et al. (2014)	mEos2 mEos3.2 mClavGR2 mMaple Dendra2	60% 42% 56% 51% 54%	Stepwise photobleaching	FP fusion to membrane protein on Xenopus oocyte 405 nm light 1-10 W/cm2 for 2-15 s dependeing on the fluorophore
	mEos2 mEos3.2 mClavGR2 mMaple Dendra2	61% 41% 53% 54% 48%	Single molecule counting (off-time tresholding)	FP fusion to membrane protein on Xenopus oocyte 0-10 W/cm2 405 nm light and 1 kW/cm^2 560 nm light
Fricke et al. (2015)	Eos2	90%	Blinking statistics	Fusion to membrane protein

				0-10 W/cm^2 405 nm light and 500 W/cm^2 568 nm light PCE overestimated due to a shortcoming in the counting model (see **section 1.5.2.2**)
Puchner et al. (2013)	mEos2	59%	Single molecule counting (off-time tresholding)	*In cellulo*, fused to membrane protein, dimers and trimers 0.06-10 W/cm^2 405 nm and 1 kW/cm^2 561 nm
Thédié et al. (2017)	mEos2	25%	Comparison of the photoconversion rate with the green decay rate	561 nm light only (2400 W/cm^2)
Thevathasan et al. (2019)	mMaple	55-58%	ELE estimation using the NPC template (see **section 3.1.2.2**)	27.5 W/cm^2 405 (increasing pulse length) and 3.5 kW/cm^2 561 nm Fixed and live cells
Wang et al. (2014)	Dendra2 mEos2 mEos3.2 tdEos mKikGR mMaple mMaple2 mMaple3	3.9% 1.0% 1.7% 4.0% 2.7% 20% 18% 10%	Comparision of the number of localizations (corrected for blinking) with the expression level of the fusion protein (determined by quantitative westen blot)	Expressed in *E.coli*, fused to hupA gene Reported is the 'signaling efficiency' Low signaling efficiencies may be explained by slow maturation of the PCFPs in the rapidly dividing *E.coli* cells 0-1 kW/cm^2 405 nm and 1.8 kW/cm^2 561 nm

A disadvantage of Kaede-like FPs for live-cell imaging is the need for phototoxic UV light for efficient photoconversion[98,161]. In addition, photoconversion by UV cannot easily be axially confined, limiting single cell imaging *in vivo*[207]. Dempsey et al. discovered that these limitations can be overcome by the use of primed photoconversion (**Figure 1.14**)[207]. In contrast to UV-induced photoconversion, primed photoconversion initiates from the anionic green chromophore by excitation with blue light. Excitation of the anionic chromophore was found to lead to the formation of an intermediate 'primed' state, from which photoconversion can be induced by excitation with ~650-800 nm light[97,98,207]. This 'primed' state, was later proposed to be the triplet state[97]. It should be noted that not all UV-convertible PCFPs are convertible by primed photoconversion. One key residue for primed photoconversion is T69 (or S69), which controls the conformation of R66 (**Figure 1.15**), which was proposed to influence triplet state formation and flexibility of the chromophore[97,98,147]. The fact that not all PCFPs are convertible by primed photoconversion has opened the possibility for pseudo two-color PALM imaging by combining primed- and UV- photoconvertible FPs[97,208]. There is, however, also a serious drawback of primed-photoconversion, which is that the PCE is expectedly significantly lower than with UV photoconversion[97]. This might be explained by increased bleaching of the green state by the applied 488 nm light. In addition, primed-photoconvertible FPs appear less bright than their UV-convertible variants because their chromophores have a higher pKa due to the T69 mutation[97].

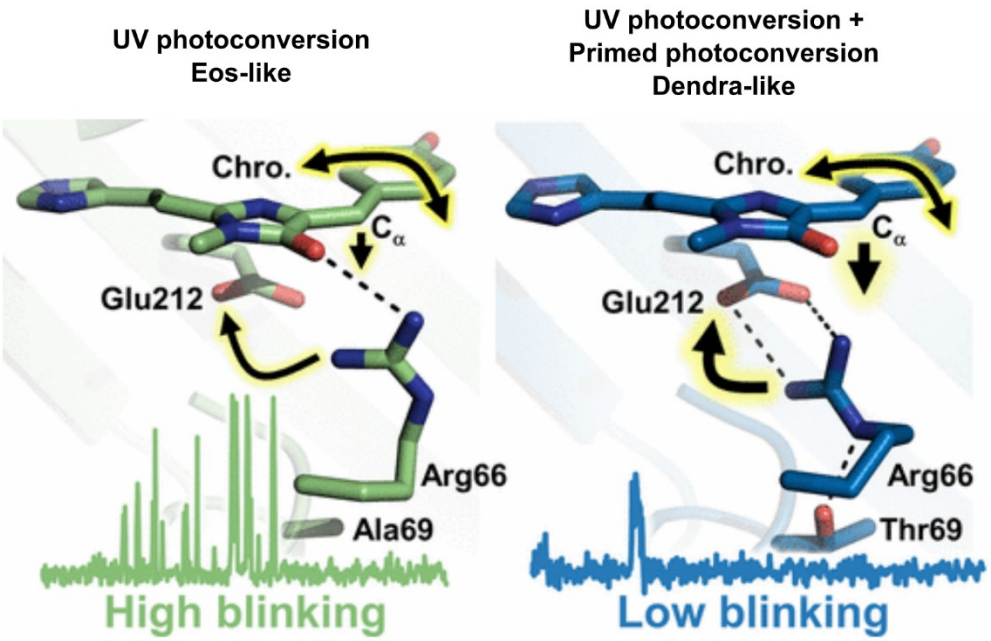

Figure 1.15 T69 facilitates primed photoconversion*. T69 controls the conformation of R66, which exerts strong effects on the photophysical properties of the FP. Figure adopted from*[147]*.*

1.3.3.1 The EosFP family

Members of the EosFP family are among the most popular PCFPs for SMLM imaging because of their relatively good brightness and photostability. Furthermore, some of the members were designed to have an exceptional resistance to chemical fixation, which is useful for correlative studies. In addition to PCFPs, the EosFP family contains efficient RSFPs and variants which both photoswitch and photoconvert efficiently. **Figure 1.16** shows an overview of the EosFP family.

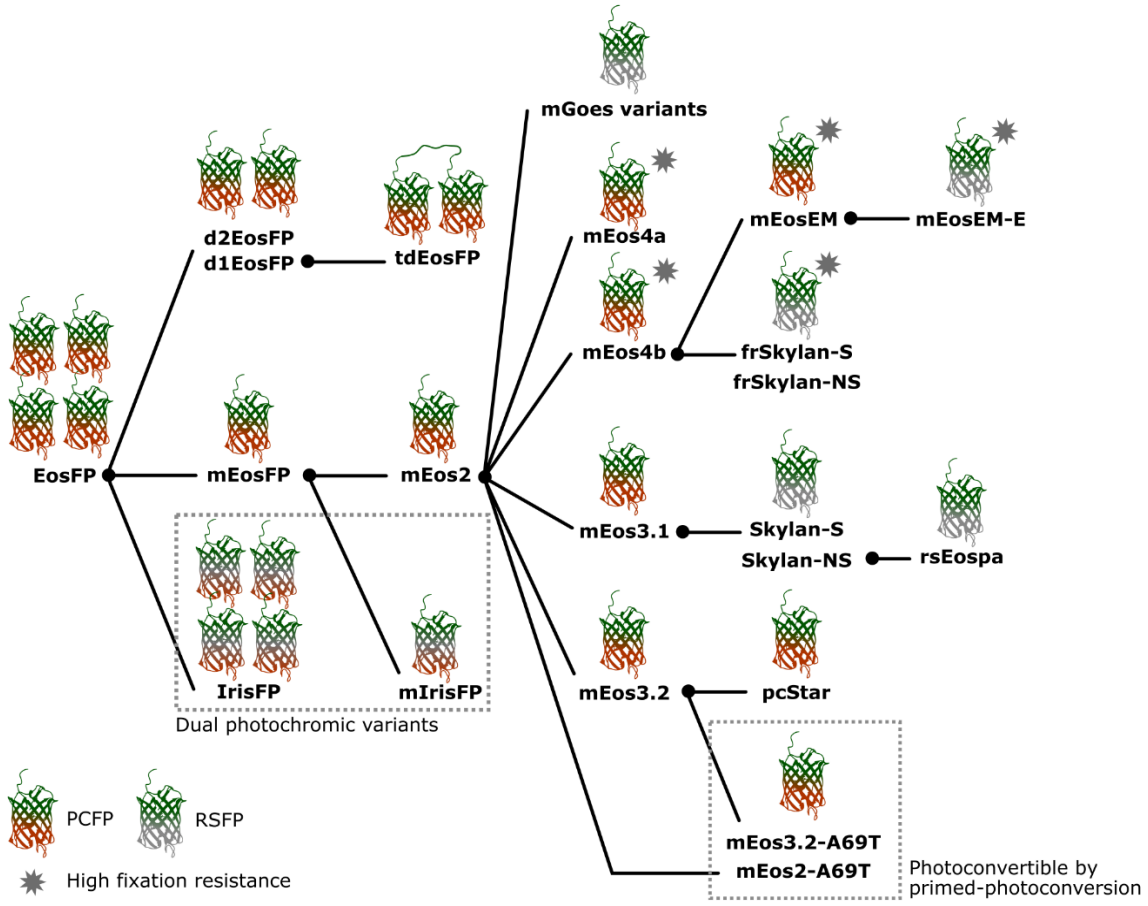

Figure 1.16 The EosFP family. *Overview of Eos variants derived from the naturally occurring EosFP. The oligomerization state of each variant is represented in the number of FP molecules. Note that this is not an exhaustive overview of all mutants.*

Like all other anthozoan FPs, the original EosFP is an obligate tetramer[188], which is not practical for its use in biological research. Monomerization of EosFP was achieved by introducting two mutations, V123T and T158H, that disrupt the two dimer interfaces, resulting in mEosFP[188]. Unfortunately, mEosFP showed poor maturation at 37°C[36]. As a temporary solution, a tandem dimer, tdEosFP, was designed from the dimeric d2EosFP (EosFP- T158H), which exhibited efficient maturation at 37°C[36]. Later, three additional mutations were found that restored efficient maturation of mEosFP at 37°C (N11K, E70K and H74N), resulting in mEos2[38]. However, mEos2 appeared to be only partially monomeric, so more efforts followed to design truly monomeric EosFP variants, resulting in mEos3.1 (mEos2 - I102N, I157V, H158E, Y189A) and mEos3.2 (mEos3.1 - V157I)[164,209]. Importantly, when mEos4a and mEos4b were designed from mEos2, the mutations responsible for the high monomeric quality of mEos3.2 were maintained to create again truly monomeric variants[150]. Finally, pcStar (mEos3.2 – D28E, L93M and N166G) was derived from mEos3.2 by site directed and semi-random mutagenesis, creating a FP with improved maturation and photoconversion[210].

Members of the EosFP family display a variety of photochromic behaviors. EosFP is naturally photoconvertible from the green neutral state by excitation with UV light[188]. In addition, photoconversion may also occur by excitation with 488 or 561 nm light (readout photoconversion), although this pathway is much less efficient and the mechanism of this pathway remains unclear[204]. EosFP originally caries an alanine at position 69 and is thus not efficiently convertible by primed-photoconversion. Variants with efficient primed-photoconversion were derived from mEos2 and mEos3.2 by introduction of A69T[98,209]. Mutation of H62, the first residue of the chromophore, in mEos2 and mEos3.1 yielded the non-photoconvertible mGoes[211] and Skylan[212] variants, which are efficient negative RSFPs. Furthermore, dual photochromic variants (IrisFP and mIrisFP) were

developed from EosFP and mEosFP by mutation of F173S, introducing efficient *cis-trans* photoswitching while preserving the green-to-red photoconversion capabilities of the FP[201,213]. Finally, the intriguing RSFP rsEospa was derived from Skylan-NS, showing the formation of a rare cationic chromophore in a pH and light dependent manner[214]. It should be noted that likely all EosFP variants exhibit some degree of photoswitching by *cis-trans* isomerization, although much less efficiently than true RSFPs. This may be explained by the fact that both photoswitching and photoconversion require flexibility of the protein matrix [119,197], so that the ability to photoswitch may be an unavoidable side-effect of the ability to photoconvert.

The increasing interest in Correlative Light and Electron Microscopy (CLEM) has motivated the development of fixation resistant FPs, as chemical fixation reduces the fluorescence intensity of many standard FPs. To this end, mEos4a and mEos4b were designed to withstand osmium tetroxide (OsO_4) embedding, typically used for sample preparation in electron microscopy (EM)[150]. The increased fixation resistance of mEos4a and mEos4b was achieved by mutating reactive surface exposed residues (Lys, Cys, His and Met) into less reactive residues with similar size and charge. Fu et al. later combined the mutations responsible for the fixation resistance of mEos4b with the mutations responsible for the increased performance of pcStar to create mEosEM, a variant with improved expression and fixation resistance (note: after Epon embedding mEosEM is no longer photoconvertible, only photoswitchable)[149]. Finally, fixation resistant RSFPs, frSkylan variants[151] and mEosEM-E[215], were derived from mEos4b and mEosEM by mutation of H62.

The utility of EosFP variants for super-resolution microscopy has driven many structural and photophysical studies to elucidate the molecular mechanisms driving their rich photochromic properties. Here, I compiled a photophysical model of mEos4b based on studies of various EosFP variants (**Figure 1.17**):

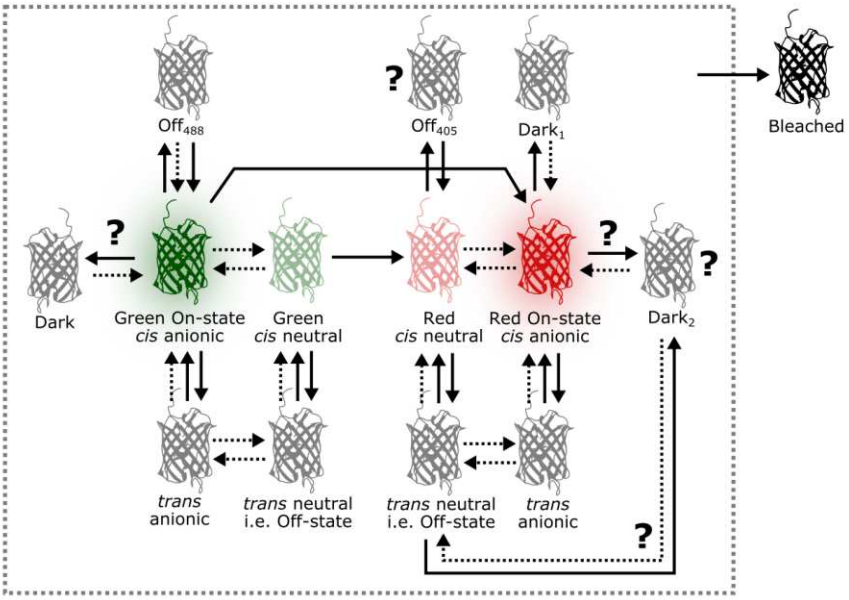

Figure 1.17 Tentative model of mEos4b photophysics. *Solid arrows indicate light induced processes, dashed lines indicate thermal processes. Question marks indicate states/transitions that remain poorly characterized. See text for details.*

- **Photoconversion:** mEos4b is UV-photoconvertible from the green neutral state into the red neutral state. Photoconversion can also be elicit by excitation with 488 or 561 nm light, although inefficiently (presumably from the anionic chromophore, primed photoconversion?)[204]. The photoconversion efficiency of EosFP variants has been estimated to be between 25 and 80%, depending on the variant and the illumination/environmental

conditions (see **Table 1.2**)[144,203–206,216]. mEos4b is not efficiently convertible by primed photoconversion because it carries a valine at position 69.

- **Photoswitching (i.e. *cis/trans* isomerization):** In both the green and red state, the chromophore of mEo4b is able to *cis/trans* isomerize in a light induced manner, with the *trans* neutral state referred to as the '(long-lived) Off-state'[217,218]. As such, mEos4b behaves as an inefficient negative RSFP, with on- and off-switching induced by 405 and 488 nm light, and 405/488 and 561 nm in the green and red states, respectively. The *cis* conformation (On-state) of the chromophore is the thermally favored conformation so that the Off-state will relax back to the On-state in the dark with a half-time of ~2.8 hours and ~2 hours for the green and red states, respectively[217,218]. It is worth noting that, although the absorption spectrum of the green state shows no significant absorption around 561 nm, intense illumination with 561 nm light was shown to switch and bleach the green state of mEos variants, including mEos4b, due to the so-called Urbach tail effect[204,219]. This behavior was shown to affect the photoconversion kinetics under SMLM imaging conditions, which typically require intense 561 nm light for readout of the red fluorescence[204].

- **Formation of short-lived green dark- and off-states:** A short-lived off-state sensitive to 488 nm light was identified in green mEos4b by De Zitter et al (Off_{488})[218]. In addition, Thédié et al. reported the formation of a non-absorbing short-lived green dark state (Dark, half-time ~400 ms) in mEos2, which they proposed to be a radical state similar to a state previously reported in IrisFP[96,204]. It is unclear whether Off_{488} and Dark could refer to the same state. Although, Thédié et al. reported that Dark is insensitive to 561 nm light, the recovery rate from Dark was reported to be ~5 times faster under 488 nm light than under 561 nm light even though the 488 nm light intensity was more than 100 lower than the 561 nm light intensity[204], suggesting that this state is likely sensitive to 488 nm light. Furthermore, the recovery rate reported for Dark under 10 W/cm^2 488 nm light (0.18 s^{-1}) is comparable to that reported for Off_{488} under 7 W/cm^2 488 nm light (0.32 s^{-1}) and also the off-switching rates of Dark and Off_{488} appear comparable[204,218]. To indicate the possibility that Off488 and Dark might be the same state, Dark is highlighted with a question mark in **Figure 1.17**.

- **Formation of short-lived red dark- and off-states:** De Zitter et al. showed that the red state of mEos4b contains at least one but probably two light insensitive dark states ($Dark_1$ and $Dark_2$)[217]. $Dark_1$ (half-time ~40 ms) was proposed to be of radical nature, similar to the short-lived dark states found in IrisFP and mEos2[96,147,217]. $Dark_2$ was left uncharacterized[217]. In addition to these dark states, Sun et al. reported the formation of a red off-state driven by illumination with 405 nm light in mEos3.2[148]. They showed that this off-state could be recovered by illumination with 561 nm light[148]. Although the nature of this off-state remains elusive, it is most likely formed from the neutral state of the chromophore which absorbs strongly around 405 nm. It remains to be investigated whether this 405 nm induced off-state (Off_{405}) is also present in mEos4b.

- **Photobleaching:** Photobleaching can occur from every light sensitive state. Duan et al. characterized in detail the photobleaching mechanisms of the green state of IrisFP[89]. They found that under low laser-light intensities (<<100 W/cm^2) bleaching happened in an O_2 dependent manner by sulfoxidation of M159 and C171, locking the chromophore in a non-fluorescent state[89]. Under conditions with high (>100 W/cm^2) laser intensities, they found that bleaching mainly happened in an O_2 independent manner by decarboxylation of E212[89]. Both bleaching pathways were proposed to proceed via the triplet state[89]. In line with this hypothesis, the bleaching quantum yield of mEos2 was shown to be increased in the absence of O_2, which prolongs the lifetime of the triplet state[147]. It is likely that similar bleaching pathways are present in mEos4b.

In conclusion, members of the EosFP family exhibit rich photochromic behaviors. The relatively high brightness, good photostability and fixation resistance (of some of the members) make EosFP variants popular markers for super resolution imaging and fluorescence - EM correlative studies. The highly complex and still incompletely understood photophysical behaviors, however, can cause artifacts, especially in quantitative experiments.

1.3.4 FPs for SMLM at cryo-temperature

There is growing interest in SMLM imaging at cryogenic temperature (CT), also referred to as cryoPALM[220]. There are several reasons for this. Firstly, chemical fixation is known to disturb various biological structures, while these structures can be well-preserved by cryofixation[221–223]. Secondly, SMLM imaging at CT opens the possibility for correlative imaging with cryo-electron microscopy (cryoCLEM)[223–225]. Lastly, at CT, the emission spectrum of FPs is narrowed, which is advantageous for multicolor imaging, and photobleaching is reduced, which means more photons and thus a better localization precision[185,224–227]. A hurdle, however, for cryoPALM imaging is the limited number of available fluorophores that efficiently switch or activate at CT.

Diffusion and protein motions are restricted at CT. Consequently, many organic dyes, whose blinking relies on the diffusion of buffer molecules, cannot be used at CT. Furthermore, many standard PTFPs that are used at RT do not photoswitch, -activate or –convert at CT because their activation mechanism requires large structural rearrangements. Numerous FPs have been tested for their ability to switch at CT, which has led to the identification of a diverse set of cryo-switchable FPs, including RT PTFPs and standard FPs. However, the photoswitching efficiency is often limited compared to RT and the underlying mechanisms remain poorly understood.

Typical RSFPs that have been reported to also photoswitch at CT include Dronpa[224,228,229] and rsEGFP2[229]. These FPs have been shown to maintain their behavior as negative photoswitchers, albeit with slower and less efficient switching kinetics[224,228,229]. It is unclear whether the photoswitching of these FPs at CT proceeds via the same *cis*-*trans* isomerization mechanism as at RT. *trans*-to-*cis* isomerization has been shown to be maintained in the RSFP Padron at CT[230]. However, in other RSFPs, including Dronpa, *cis/trans* isomerization has not been observed at CT[230]. A recent study discovered a novel cryo-switching mechanism in the RFP mApple[227], a FP which exhibits complex photochromic behaviors at RT[43]. They found that, at CT, off-switching requires dual illumination with 561 and 405 nm light and that mApple can access two distinct on-states in a pH dependent manner[227]. This work highlights how different the photochromic behavior of FPs can be at CT.

Photoactivation at CT has been seen in the classical PAFPs PAGFP[185,231] and PAmKate[185]. This activation was proposed to proceed via the same decarboxylation mechanism as at RT[185]. Moreover, photoactivation of these FPs appeared equally efficient at CT as at RT[185]. In contrast, no activation was observed in PAmCherry at CT[185,231]. This is likely attributed to the fact that photoactivation of PAmCherry requires decarboxylation, oxidation and *cis*-to-*trans* isomerization, the latter two presumably being restricted at CT[62,185]. Green-to-red photoconversion at CT has been observed in mEos3.2 but required ~100 times more 405 nm light than at RT[224]. Others have not seen green-to-red photoconversion at CT[231].

Various standard FPs that do not photoswitch or -activate at RT have been shown to be efficient negative photo-switchers at CT, including EGFP[223,224,229,232], EYFP[228] and mEmerald[223]. Furthermore, Padron, a positive RSFP at RT, and PAGFP, an irreversible PAFP, have also been shown to behave as negative RSFPs at CT[229]. Altough the exact photoswitching mechanisms of these FPs remains unclear, protonation[228] and triplet state formation[223] have been proposed to be involved. It is conceivable

that these standard FPs exhibit the same cryo-switching mechanism as typical RSFPs, such as Dronpa and rsEGFP2[229], assuming that *cis-trans* isomerization is restricted at CT.

1.4 Single molecule localization microscopy

1.4.1 Breaking the diffraction limit with SMLM

The spatial resolution of standard optical microscopy is limited by the diffraction of light. Due to diffraction, an infinitely small light source does not appear as a point but as a point spread function (PSF) when imaged on an optical microscope. For a circular aperature, the shape of the PSF is an Airy pattern. The width of the central peak of the Airy disk is approximately 200-300 nm and sets the resolution limit for optical microscopy. This diffraction theory was developed by the German physicist Ernst Abbe in 1873, who found that the minimal distance (d, which equals the width of the central peak of the Airy disk) that is required to be able to separate two objects can be approximated by $\lambda/2NA$, where λ is the wavelength of the light and the NA is the numerical aperture of the microscope. Considering a red emitting FP (~600 nm) and an oil immersion objective with a NA of 1.4, the smallest distance over which two objects can be identified is ~210 nm. This can pose a clear problem for the study of cells, especially bacterial cells, which are typically only several hundreds of nanometers in size.

During the past decades, various microscopy techniques have been developed that are able to circumvent the resolution limit set by Abbe's theorem. These techniques are collectively referred to as super-resolution microscopy techniques. A brief overview of the different SRM techniques is provided in **section 1.3**. Here, I will focus on SMLM, which can improve the resolution up to ~5-30 nm.

SMLM relies on the ability to localize single molecule light emitters with high precision when their PSFs are isolated. To create isolated PSFs on a densely labeled structure, SMLM separates the emission of single fluorophores by time. This temporal separation is achieved by the use of fluorophores whose fluorescent properties can be controlled by illumination, buffer conditions (see **section 1.3**), or their ability to bind and unbind to a particular structure. A typical SMLM experiment thus consists of the acquisition of several thousand images of a single structure, on each frame only imaging a subset of fluorophores (**Figure 1.18**). After the acquisition, the fluorophores on each frame are precisely localized using software's, such as Thunderstorm[233] or SMAP[234], to generate a super-resolved image of the structure (**Figure 1.18**).

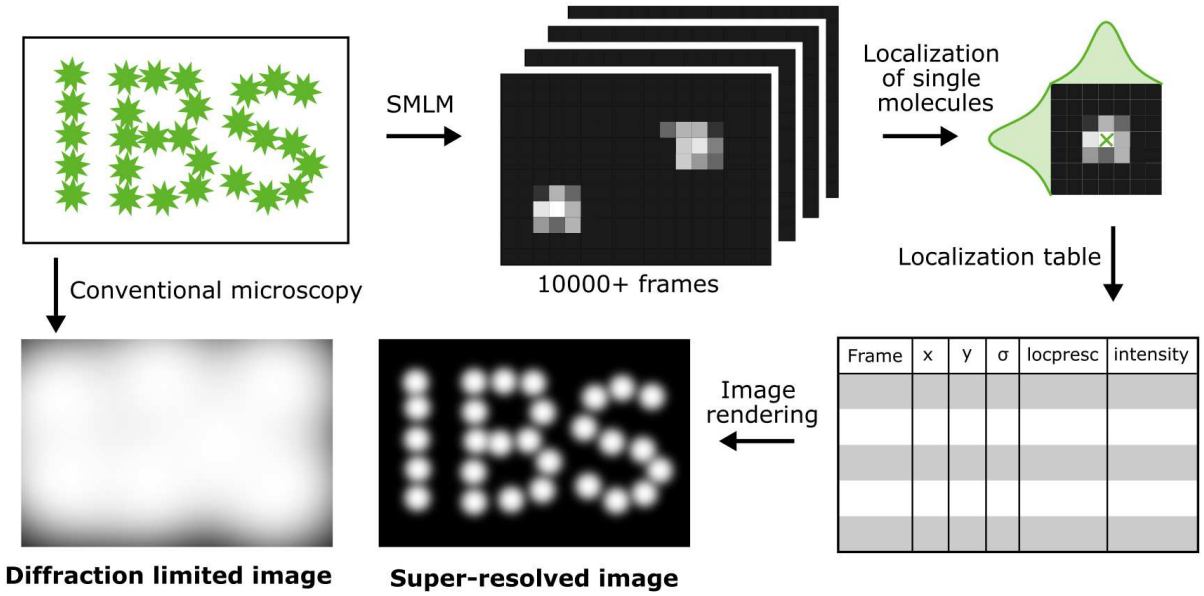

Figure 1.18 Breaking the diffraction limit by SMLM. *The resolution of conventional light microscopy is limited by the diffraction of light to ~200-300 nm. SMLM circumvents this limit by separating the emission of individual fluorophores in time, which enables their localization with an improved resolution of ~5-30 nm. (Illustrations not to scale)*

1.4.1.1 Localization properties

To localize single fluorophores, their PSFs are generally approximated with a 2D Gaussian function. Some programs allow the fitting of experimental PSFs, which is particularly useful for 3D SMLM (see for example SMAP[234]). This fitting provides an estimation of the subpixel x and y (and z if 3D) coordinates of the fluorophore. In addition, other important information is usually provided, including the uncertainty, the sigma and the intensity of the localizations.

- **The intensity** of a localization reflects the number of collected photons from the fluorophore. This is calculated from the integrated intensity of the fitted PSF, taking into account the camera specificities (gain, conversion factor, noise).

- **The localization uncertainty**, also called localization precision, reflects the (theoretical) spread of multiple localizations from a single emitter. Localization programs typically provide a localization uncertainty for each localization, calculated as[235]:

$$< (\Delta x)^2 > = \frac{s^2 + \frac{a^2}{12}}{N} + \frac{8\pi s^4 b^2}{a^2 N^2}$$

or, taking into account the EM GAIN of an EMCCD camera, as[236]:

$$< (\Delta x)^2 > = \frac{2s^2 + \frac{a^2}{12}}{N} + \frac{8\pi s^4 b^2}{a^2 N^2}$$

where s is the standard deviation (sigma) of the fitted PSF, a is the pixel size, N is the number of collected photons and b is the background. So, the more photons, the lower the localization uncertainty.

- **The sigma** reflects the width of the fitted Gaussian functions and is typically between 100 and 200 nm. A sigma below 100 nm usually arises from the detection of noise in the form of single bright pixels. A sigma above 200 nm may be the result of either overlapping PSFs that are fitted as a single localization or molecules that are out of focus. It is generally advisable to remove localizations with a suspiciously low or high sigma from the localization list.

1.4.1.2 Post-processing of SMLM data

After the localization of all fluorophores typically follows a series of post-processing steps:

- **Lateral drift correction**: SMLM experiments, which can take minutes-to-hours to acquire, often suffer from lateral drift. There are two ways to correct for this drift: by the use of fiducials or by cross-correlation. Fiducial markers are bright and stable fluorescent particles, such as nanodiamonds, whose localization can be tracked over the entire experiment to monitor and correct for drift. Cross-correlation methods divide the localizations into multiple temporal bins, from which individual super-resolved images are reconstructed. The drift is then determined based on the lateral shift between the images from subsequent bins. To function properly, cross-correlation methods require relatively well-defined structures and high numbers of localizations.

- **Merging of localizations**: A fluorophore might emit photons during multiple sequential frames or during multiple frames separated by gaps due to blinking. This results in multiple localizations belonging to a single fluorophore. These localizations can be merged based on temporal and spatial constraints into a single localization with an improved localization precision.

- **Filtering of poor localizations**: Some localizations might belong to noise, to molecules that are out of focus, to molecules only emitting few photons or multiple molecules with overlapping PSFs. These localizations degrade the quality of the reconstructed image. Therefore, these localizations are often removed by filtering on the localization precision, sigma and intensity.

1.4.1.3 SMLM in multicolor and 3D

Building on the basic principles of SMLM, advanced modules have been developed to perfom SMLM in multicolor and in 3D.

There exist various methods to do (pseudo-)multicolor SMLM. One option is to use fluorophores that can be activated using different laser wavelengths so that the fluorophores can be imaged sequentially (e.g. using a primed-photoconvertible and a UV-convertile PCFP[208]). This strategy, however, restricts multicolor imaging to only 2 to 3 colors and increases the duration of the acquisition by a factor of 2 to 3. Spectral demixing presents a more sophisticated approach to multicolor SMLM[237]. In this approach, all fluorophores (2 to 3) are imaged at the same time using a single laser. To distinguish between the different fluorophores, the fluorescence emission is split by a long-pass dicroic and collected on two cameras (or differents sections of the same camera). The ratio of the number of photons collected on one camera compared to the other camera encodes the identity of the fluorophore, given that the fluorophores have sufficiently different emission maxima. Fluorophores that can be used for spectral demixing include AF647, CF660 and CF680. Note that when choosing fluorophores for multicolor imaging, it is important to consider not only their 'color' but also their buffer requirements (i.e. can they blink in the same buffer?)[238]. Yet another approach to multicolor SMLM is multiplexed imaging. In multiplexed imaging, the sample is stained and imaged

multiple times in a sequential manner to enable the visualization of different structures, without beining limited by the restricted number of available fluorophores. Using this strategy, Klevanski et al. could image 15 targets in a single U2OS cell[239]. Finally, an alternative option is to use a reference structure to combine dinstinct dual-color images into one multicolor image, but this approach only works for well-defined structures[240].

SMLM can be performed in 2D or in 3D. For 3D SMLM, the axial position of the fluorophores can be encoded in the PSF by PSF engineering, which introduces an axial asymmetry in the PSF[241]. Although PSF engineering is very powerful, a disadvantage is that the engineered PSF is spread out over a bigger area than the normal PSF, which means that the localization density needs to be sparser to prevent overlap (which means longer acquisition time) and that more photons are required to achieve the same signal-to-noise ratio. For the latter reason, 3D SMLM is mostly restricted to organic dyes, which generally have a higher photon budget than FPs. Besides the 3D coordinates, it is also possible to extract the 3D orientation of molecules by SMLM using PSF enginering[242,243]. This requires the fluorophore to be rigidly attached to the taget structure so that the dipole orientation of the fluorophore is fixed relative to the structure of interest.

1.4.2 SMLM imaging techniques

There exist three main variations of SMLM: PALM, (d)STORM and PAINT. These variations differ from each other in the types of fluorophores that are used and in the way that single molecule blinking is achieved.

1.4.2.1 PALM

In Photo-Activated Localization Microscopy (PALM) relies on the light-controllable fluorescence properties of PTFPs, mostly PAFPs and PCFPs (see **section 1.3**). These fluorophores can be 'activated' by excitation with UV light and subsequently imaged and bleached using a laser with an appropriate wavelength (**Figure 1.19**). The activation rate, or localization density, can be controlled by changing the UV intensity. Often, the UV intensity is gradually increased during the acquisition to keep a constant localization density while the pool of native fluorophores decreases.

One of the main advantages of PALM imaging is that it is suitable for live-cell imaging because fixation and permeabilization are not necessary when working with FPs. However, because PALM imaging is relatively slow (tens of minutes), it is restricted to mostly immobile proteins in living cells (e.g. proteins of the nuclear pore complex[244]), unless the mobility of the protein is of interest (see sptPALM). Another advantage of PALM is the 1:1 labeling specificity that is ensured when working with FPs. A drawback, however, is the relatively low brightness and stability of FPs compared to organic dyes, which usually results in a lower spatial resolution of the final reconstructed image.

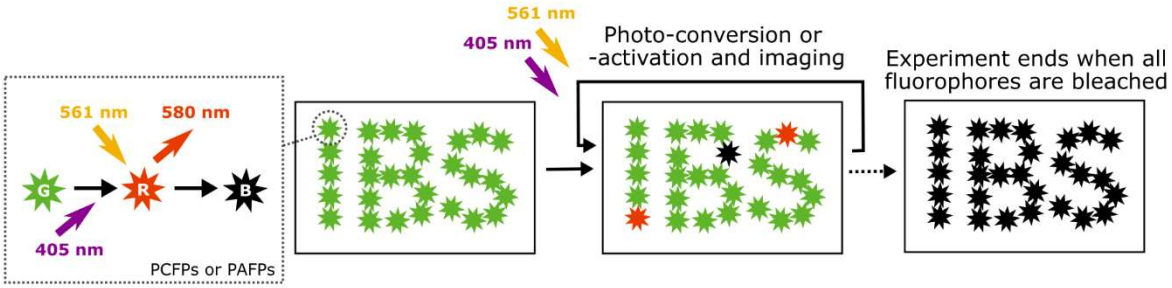

Figure 1.19 PALM imaging. *In Photo-Activated Localization Microscopy (PALM) the fluorescent properties of the fluorophores are controlled by illumination. These fluorophores, mostly PCFPs or PAFPs, are sequentially*

activated/converted, imaged and bleached. The illustration shows a simplified photophysical scheme of a green-to-red PCFP.

1.4.2.2 STORM

There exist two variations of Stochastic Optical Reconstruction Microscopy (STORM) microscopy: STORM and direct STORM (dSTROM). STORM microscopy makes use of a pair of activator-receptor dyes, while dSTORM only involves a single dye, which is inherently capable of blinking. Here, I will focus on dSTORM, which is more commonly used nowadays.

In dSTORM, single molecule blinking is usually induced by a combination of buffer and illumination conditions (**Figure 1.20**). In a dSTORM experiment, the fluorophores are often initially fluorescent. Therfore, a typical dSTORM experiments starts by switching the fluorophores into a long-lived non-fluorescent state, usually a radical or adduct state, using high intensity illumination. Typical dSTORM buffers are depleted of O_2 and contain reducing agents to stabilize the non-fluorescent state. Return from the non-fluorescent state back to the singlet ground state can be spontaneous or can be promoted by excitation of the off-state by UV light. After the switching phase follows the single molecule blinking phase during which the localizations are made. The localization density during this phase can be controlled by the illumination intensity (higher intensity -> shorter on-times), the UV intensity or the buffer conditions. While typical dSTORM experiments rely on the stochastic blinking of fluorophore, there also exist photoactiovatable dyes which can be activated irreversibly from a non-fluorescent into a fluorescent state, similarly as PAFPs.

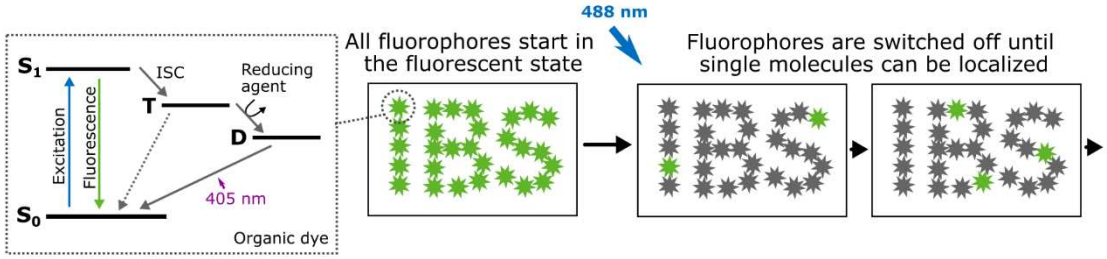

Figure 1.20 dSTORM imaging. *dSTORM imaging relies on the stochastic blinking of organic dyes. At the start of a typical experiment, the fluorophores are driven into a long-lived non-fluorescent state by intense illumination. After this initial switching phase, single molecule blinking can be detected.*

An advantage of STORM imaging is that organic dyes generally have a higher photon budget than FPs, resulting in a higher localization precision and thus a higher spatial resolution. Furthermore, the higher photon budget facilitates 3D SMLM imaging. A disadvantage of STORM imaging is that the use of organic dyes comes at the cost of some unspecific staining, which is not the case when using FPs that are genetically fused to the POI.

1.4.2.3 PAINT

Point Accumulation in Nanoscale Topography (PAINT) imaging relies on the binding and unbinding of fluorophores to the target structure (**Figure 1.21**): fluorophores that are unbound are rapidly diffusing, which blurs their intensity over multiple pixels per frame making it impossible to detect them, while fluorophores that are bound emit many photons at the same location, which enables their detection. This technique, thus, does not require photoswitchable fluorophores but can be done with any fluorophore that is sufficiently bright. One option for PAINT is to use a fluorophore that exhibits a natural affinity for a particular structure, such as NileRed for the cell membrane[245]. Alternatively, any arbitrary protein can be targeted by the use of DNA-PAINT. In DNA-PAINT, the target protein is immunolabeled with an antibody caring a single-stranded DNA oligonucleotide, called the docking strand, while the fluorophore is labeled with a complementary DNA strand (**Figure**

1.21). Nowadays there exist various variations of DNA-PAINT, using nanobodies or self-labelling tags (e.g. Halo or SNAP), which reduce the linkage error and/or increase the labelling specificity.

A strong advantage of PAINT imaging is that it does not suffer as much from bleaching as do PALM and STORM imaging because a particular location can be imaged numerous times by the binding of new unbleached fluorophores. Disadvantages of PAINT, however, are that it is usually not compatible with live-cell imaging and that it can suffer from a high background arising from the unbound fluorophores. This background problem can be alleviated by the use of TIRF or HiLo imaging modes, or can be circumvented by the use of fluorogenic probes that only become fluorescent after binding to their target[246].

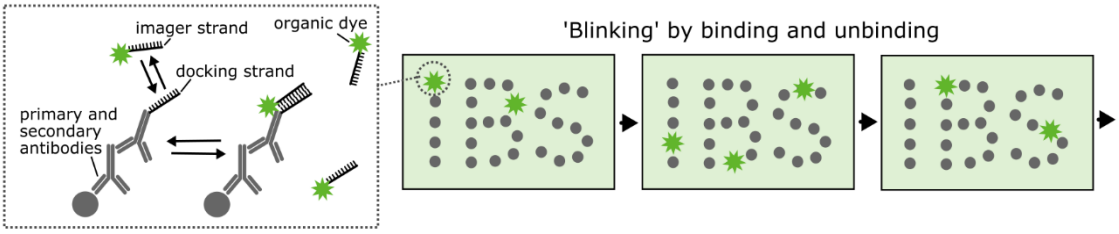

Figure 1.21 PAINT imaging. *PAINT relies on the binding and unbinding of the fluorophore to the target structure. This binding can be based on a natural affinity of the dye for the target or on the use of complementary DNA strands (DNA-PAINT) as depicted in the scheme.*

1.5 Quantitative analysis of SMLM data

There is increasing interest in the use of SMLM as a quantitative tool to extract biological information. Quantitative SMLM methods can be grouped into three categories: cluster analysis, molecular counting and single particle tracking.

1.5.1 Cluster analysis

Two types of SMLM cluster methods can be distinguished:

1. The spatiotemporal clustering of localizations that belong to a single fluorophore to improve the image resolution or characterize the blinking behavior of the fluorophore (**Figure 1.22A**).
2. The spatial clustering of localizations that belong to different fluorophores to assess whether the protein of interest forms clusters (**Figure 1.22B**).

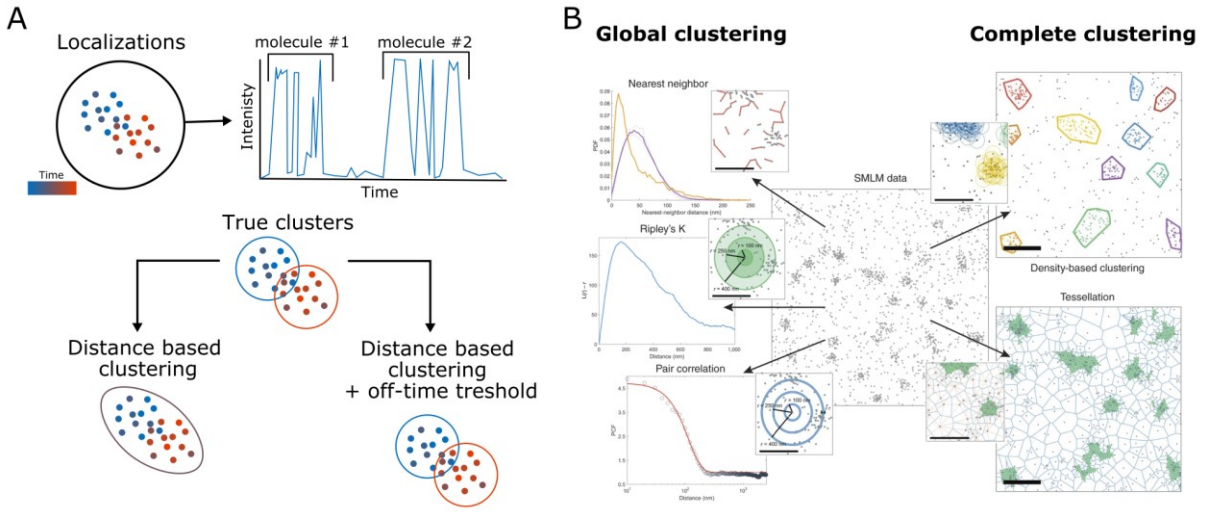

Figure 1.22 Clustering. *A) Schematics of the spatiotemporal clustering of localizations that belong to a single fluorophore. Simple distance-based clustering fails at high molecule densities. Taking into account the temporal component of the localizations by an off-time threshold can improve the clustering in such situations. B) Several clustering methods have been developed to assess the spatial distribution of labeled proteins. These methods can be classified as either global or complete clustering methods. (B adopted from[247])*

A single fluorophore can be fluorescent for multiple frames, separated by blinks or not. This results into multiple localizations belonging to the same fluorophore. It is important to cluster these localizations together to make optimal use of the photon budget of the fluorophore (see **section 1.4.1.2**). In addition, this clustering is essential for characterization of the blinking behavior of fluorophores. A naïve clustering approach would be to group together all localizations that are within a certain spatial distance from each other. This strategy, however, quickly fails when the underlying protein density is high and the fluorophore experiences long-lived blinks. Many different methods have been proposed to facilitate clustering at higher protein densities involving distance-based methods combined with off-time thresholding[4], data driven determination of grouping parameters[223], linear assignment[248], tessellation[249], or Bayesian statistics[250]. In practice, these sophisticated methods are not widely used. Instead, most studies rely on relatively simple in-house clustering algorithms or on algorithms available in well-known software such as Thunderstorm[233]. How to best cluster the localizations of a single fluorophore remains a question for future work.

SMLM cluster analysis can also be used to examine whether the protein of interest forms clusters. This is a different question from the clustering of localizations from a single fluorophore and typically has no temporal component. Again, there exist many different clustering algorithms[247,251,252]. These algorithms fall into two groups: global clustering methods and complete clustering methods (**Figure 1.22B**). Global clustering methods, such as Ripley's K function and nearest neighbor analysis, provide an overall description of the spatial distribution of the protein of interest. These methods can be used to answer questions such as, does my protein form clusters, and if so, how big? However, global clustering is an ensemble method and does not provide information about individual clusters. In contrast, complete clustering approaches assign each localization to a cluster and thus provide a more detailed description of the data. Nieves et al. recently published a comparison of several complete clustering algorithms, showing that there is no single best algorithm, but that algorithm performance depends on the distribution of the localizations[251]. They also provide guidelines on how to choose the most suitable clustering algorithm, which can help future studies[251].

1.5.2 Molecular counting (qPALM)

Molecular counting is used to gain information about the oligomeric state of protein complexes. Counting is often done using PAFPs or PCFPs in a PALM fashion, in which case it is also referred to as quantitative PALM (qPALM). The data acquisition in a counting experiment proceeds similar as in a normal PALM experiment. After the acquisition and localization of the single molecules, the SMLM data is further processed to count the number of fluorophores and deduce the oligomeric state(s) of the underlying protein complex. To this end, the localizations are first spatially grouped into clusters of localizations belonging to single oligomers. Ideally, each fluorophore is activated, detected, and bleached so that each localization corresponds to a unique fluorophore, in which case the stoichiometry can be directly deduced from the number of localizations per cluster. Unfortunately, this is not the case in practice where a single fluorophore might emit photons in multiple frames. If not corrected for, this leads to overcounting. Another problem arises from the incomplete photoactivation efficiency of PAFPs and PCFPs, which leads to undercounting. Several strategies have been proposed to correct for under- and overcounting. These methods are mainly based on off-time thresholding[203,205,253] or analysis of the blinking statistics[144,206,254,255].

1.5.2.1 Counting by off-time thresholding

Off-time thresholding-based methods account for blinking by grouping the localizations in spatially grouped clusters into subclusters of localizations belonging to a single fluorophore by use of a temporal cutoff (**Figure 1.23A**). So, localizations that appear in sequential frames or in frames separated by less than the temporal cutoff are assigned to the same fluorophore, while localizations that are separated by a time exceeding the temporal cutoff are assigned to different fluorophores (**Figure 1.23A**). There are different ways to choose the duration of the cutoff. A seemingly straightforward solution is to choose the threshold based on the off-time duration of the used fluorophore so that only a minor fraction of off-times exceeds the threshold[203,205]. This solution, however, is not optimal because if the off-times are relatively long compared to the time in between the activation of different molecules, for example at high stoichiometries, this can lead to undercounting.

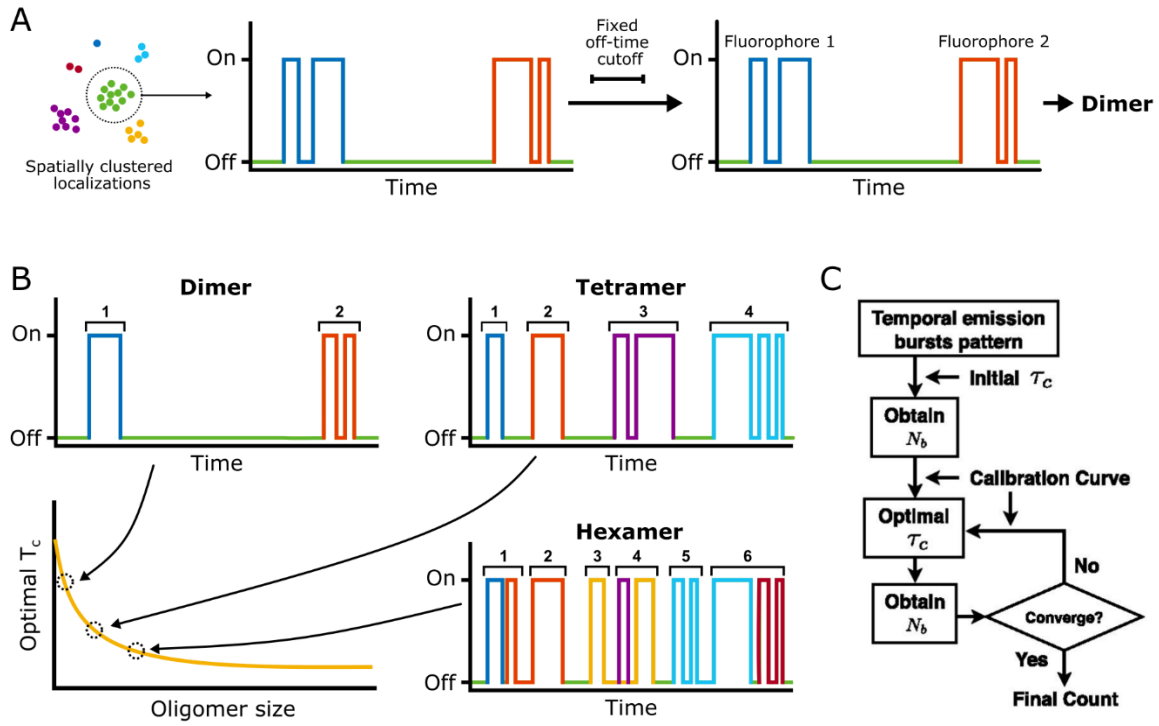

Figure 1.23 Molecular counting by off-time tresholding. *A) The fluorescence time-traces of spatially clustered locatizations are divided based on a fixed off-time cutoff to count the number of fluorophores per cluster. B-C) According to Lee et al., the optimal off-time cutoff (T_c) depends on the stoichiometry of the complex. Therefore, counting proceeds via an iterative processes (C) using a calibration curve (B) of the optimal off-time cutoff (see text for details). C adopted from Lee et al*[253]*.*

To balance the off-time duration and the activation rate, Lee et al. developed a method that determines the oligomeric state and optimal threshold for each individual cluster in a iterative fashion by use of a calibration curve generated from artificial oligomers with known stoichiometries (**Figure 1.23B,C**)[253]. The calibration curve shows that the optimal off-time cutoff is smaller for larger oligomers, which is because the time in between the activation of different molecules is shorter (**Figure 1.23B**). Note that this strategy is designed to count the correct number of molecules but does not necessarily group the localizations correctly into groups belonging to unique fluorophores (see **Figure 1.23B**). Using this strategy, Lee et al. were able to count complexes with a stoichiometry of 34[253].

Undercounting in off-time thresholding-based methods can be corrected for by calibration of the detection efficiency of the used fluorophore using oligomers of a known stoichiometry[205].

1.5.2.2 Counting by blinking statistics

Counting methods based on blinking statistics do not correct for blinking, but rather use the blinking behavior of the fluorophore to deduce the oligomeric state (**Figure 1.24**). These methods are based on the idea that a fluorophore can either blink or bleach, from which follows that the probability to blink N_{blinks} times for a single fluorophore is given by a geometric distribution[206]:

$$P_p(N_{blinks}) = p(1-p)^{N_{blinks}}$$

where p is the probability to bleach without blinking. For a given fluorophore, p can be determined by fitting the blinking histogram of the (monomeric) fluorophore with this model (**Figure 1.24A**).

Knowing p, the probability to detect N_{blinks} blinks for an oligomer of size r can be described by a negative binomial distribution[144]:

$$P_{p,r}(N_{blinks}) = \binom{N_{blinks}}{r-1} p^r (1-p)^{N_{blinks}-r+1}$$

Using this model, the blinking histogram of the complex of interest can be fitted to determine the stoichiometry (**Figure 1.24B**). Note that this model takes into account the apparent blinking that arises from the activation of subsequent fluorophores, which right-shifts the N_{blink} distribution of oligomers by r-1 (**Figure 1.24B**). This subtlety was not taken into account in the original paper by Fricke et al.[206], resulting in an overestimation of the PCE of mEos2 (see **Table 1.2**). This model can be further extended to take into account incomplete photoactivation and labeling[144], complicated photophysical models[255] and mixtures of different oligomeric states[216,254]. This blinking-based method has been shown to work well for the estimation of the size of small oligomers (dimers up-to tetramers). However, this method is expectedly less suitable for the counting of large complexes because it strongly relies on accurate estimation of the probability to bleach without blinking (p), which can be challenging because the blinking histograms are often polluted by noise, processing errors and possibly the existence of multiple fluorophore population (further discussed in **section 3.1.3.1**).

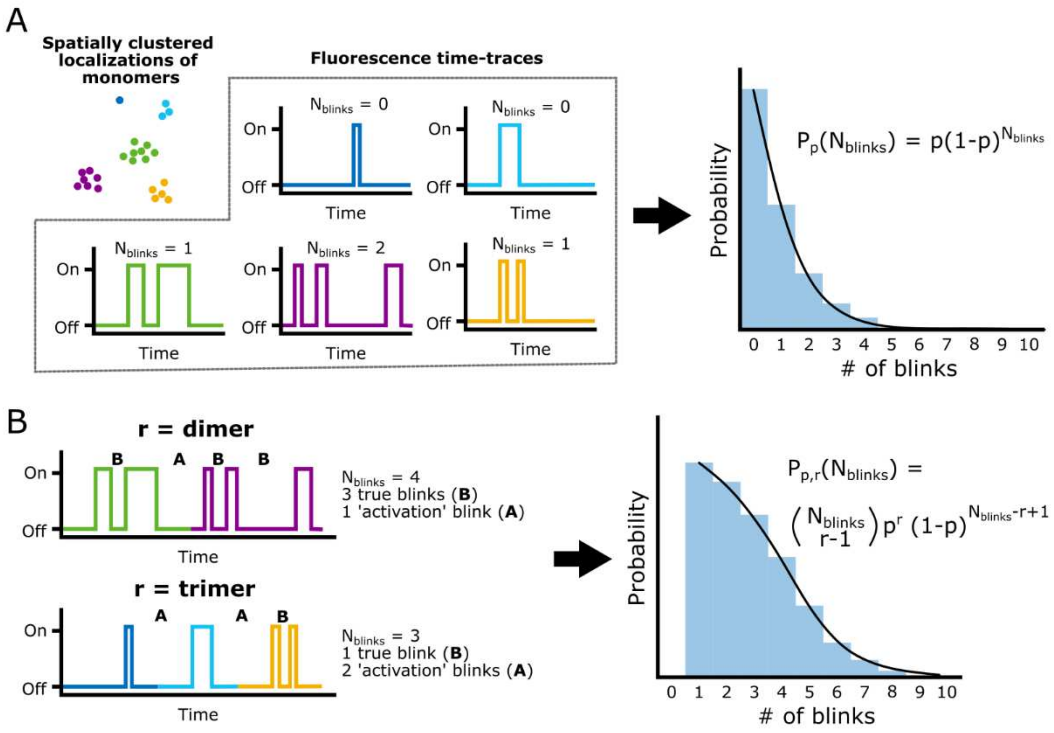

Figure 1.24 Molecular counting by blinking statistics. *A) The the probability of a fluorophore to blink (1-p) can be determined by analysis of the blinking histogram of the monomeric fluorophore. B) Knowing p, the unknown stoichiometry (r) of a complex can be estimated from the blinking histogram of the complex. Note that for oligomers the blinking histogram is right shifted by r-1 because the activation of each fluorophore, except the first fluorophore of the complex, results in a 'fake' blink (activation blink). This model assumes a 100% effective labelling efficiency (PCE + labelling efficiency + detection efficiency). More sophisticated models can handle incomplete labelling, complicated photophysical models and mixtures of oligomeric states as referenced in the text.*

A variation on counting the number of blinks is counting the number of localizations, which has been shown to be suitable for the counting of large oligomers (10 - 40 subunits). The average number of localization per fluorophore can be calibrated using oligomers of known stoichiometries, to correct

for both blinking and incomplete detection[244,256–258]. This calibration can then be used to deduce the oligomeric state of the protein complex of interest from the histogram of the number of localizations per cluster[244,256–258].

1.5.2.3 Other counting strategies

In addition to off-time thresholding and modeling of the blinking statistics, there exists a variety of other counting methods.

One challenge of both counting techniques described above is that they rely on accurate spatial clustering of localizations belonging to the same fluorophore or complex. This can be a difficult task, especially when the density of complexes is high. In addition, these methods depend on precise characterization of the photophysical behavior of the used fluorophore, require fluorophores with a relatively good activation/detection efficiency and are sensitive to background noise. Tan et al. recently developed a counting method that could avoid all of these difficulties by use of a dual-color colocalization strategy[152]. They show that their technique can handle FPs with a detection efficiency as low as 10-20% and is very resistant to noise[152]. A limitation of their method, however, is that it cannot handle mixtures of different oligomeric states and that the complexes need to be relavively sparse (>100 nm distance)[152].

Molecular counting can also be done using STORM or DNA-PAINT imaging modalities. Using STORM, counting can be done by counting the number of blinks or localizations per cluster in a similar fashion as when using PALM[254,259]. In contrast to counting by PALM or STORM, counting by DNA-PAINT (qPAINT) is independent of the fluorophore photophysics and instead relays on the binding kinetics between the fluorophore and the target site[260,261]. An advantage of qPAINT is that it is less affected by bleaching and other complex photophysical behaviors.

Finally, it is important to note that there also exists a variety of diffraction limited (non-SMLM) molecular counting approaches. One option is to look at the total brightness of the complex. The idea behind this strategy is that the brightness scales with the number of fluorophores, which scales with the oligomeric state of the complex[244,256]. This relation is not linear, probably due to a fraction of fluorophores residing in a non-fluorescent state, but can be calibrated using oligomers of known stoichiometries[244,256]. Another option is to perform stepwise photobleaching and count the number of bleaching events[203,262]. Advantages of these diffraction limited techniques are that they are fast (no need to collect >20000 frames as in SMLM) and use standard FPs. A disadvantage is that the oligomers need to be relatively sparse so that they can be identified under diffraction limited conditions (at least >300 nm distance).

1.5.3 Single particle tracking PALM

sptPALM is a powerful tool to monitor the diffusion of abundant proteins at a high spatial and temporal resolution inside living cells. sptPALM can, for example, be used to follow the dynamics of DNA repair proteins before and after the administration of genotoxic compounds to gain insight into the DNA repair process (see e.g.[263]), or to monitor the behavior of membrane receptors upon ligand stimulation (see e.g.[216,264]).

The general workflow of sptPALM experiments is shown in **Figure 1.25**.

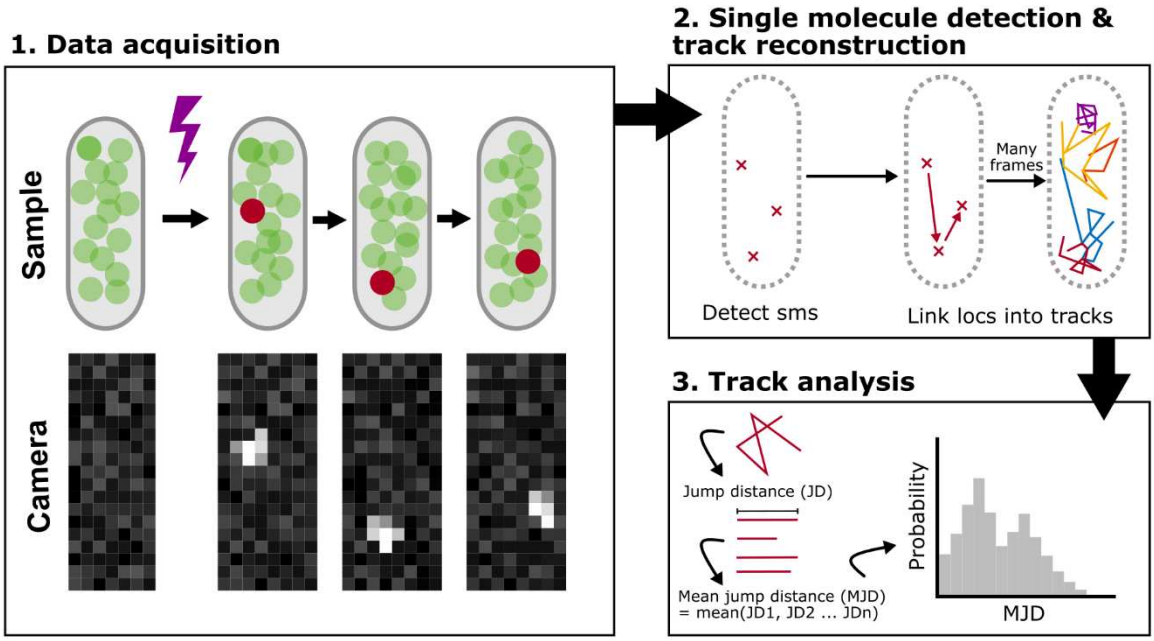

Figure 1.25 sptPALM workflow. *First, single molecule data are acquired on living cells by PALM imaging (1). Next, single molecules (sms) are localized after which the localizations (locs) are linked in time to reconstruct tracks belonging to unique molecules (2). Finally, the tracks are analyzed to extract the diffusion dynamics of the studied protein (3). Shown is an example of MJD analysis but there are different methods to analyze the tracks as explained in the text.*

sptPALM imaging proceeds similar as standard PALM imaging with only slight adjustments. The UV intensity is typically lower in sptPALM experiments to keep the localization density sufficiently low for accurate track reconstruction. In addition, the intensity of the read-out laser (561 nm in case of EosFP variants) is usually lower in sptPALM to reduce the photobleaching rate and create longer tracks, compromising localization precision for track length. Finally, the frame time is often reduced (5-20 ms) to limit motion blur, especially when studying fast diffusing proteins.

After the data acquisition and localization of the molecules, the localizations are linked together in time into trajectories belonging to unique molecules. To facilitate track reconstruction, various algorithms have been developed. Classical algorithms are based on nearest neighbor analysis, searching for the nearest localizations in consecutive frames. Such algorithms, however, lose accuracy at medium localization densities where tracks can cross and multiple localizations are close enough to conceivably belong to the same track[265]. Furthermore, such algorithms often do not correct for fluorophore blinking which can temporarily disrupt tracks. More advanced algorithms aim to address these issues by taking into account the information of multiple frames, the diffusion dynamics of individual tracks and even the expected fluorophore behavior in terms of blinking and bleaching[265]. However, even these advanced methods do not perform perfectly as has been demonstrated by the analysis of simulated data[217,265,266]. Nevertheless, even though track reconstruction is usually not perfect, these algorithms perform well enough to derive biologically meaningful information in most situations.

The final step in sptPALM is to analyze the trajectories and extract information regarding the underlying diffusion dynamics.

1.5.3.1 Analysis and interpretation of spt data

Several methods have been developed to analyze single particle tracks. These methods can answer different questions, such as ‘what is the diffusion coefficient?’, ‘Is the diffusion free, confined,

directed or anomalous?' and 'How many populations with different diffusion behaviors are present and what are the exchange rates between these populations?'

1.5.3.1.1 Mean Squared Displacement

The classical approach to analyze tracks is based on the Mean Squared Displacement (MSD). The MSD($n\Delta t$) of a 2D trajectory is defined by the average of all squared distances between two localizations with a certain lag time ($n\Delta t$) (**Figure 1.26**)[267,268]:

$$MSD(n\Delta t) = \frac{1}{l-n}\sum_{i=1}^{l-n}(x(i+n)-x(i))^2 + (y(i+n)-y(i))^2$$

where l is the length of the trajectory, $x(i)$ and $y(i)$ are the coordinates at time i and Δt is the time step between frames. The diffusion coefficient (D) can be determined from the slope of the MSD plot. For Brownian diffusion, the D can be fitted by: $\mathrm{MSD}(n\Delta t) = 4\mathrm{D}n\Delta t$. In theory, the MSD should equal 0 when $n\Delta t$=0. In practice, however, this is not the case because the localization uncertainty (σ) introduces an offset of $4\sigma^2$, which needs to be taken into account: $\mathrm{MSD}(n\Delta t) = 4\sigma^2 + 4\mathrm{D}n\Delta t$.

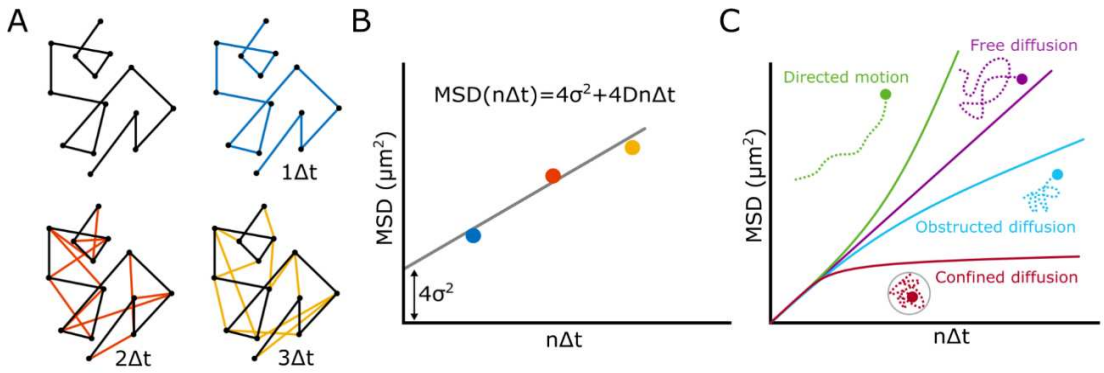

Figure 1.26 Principles of MSD analysis. *A) The Mean Squared Displacement (MSD(nΔt)) of a 2D trajectory is defined by the average of all squared distances between two localizations with a certain lag time of $n\Delta t$. B) For freely diffusing molecules, the MSD scales linearly with the lag time and is offset by the localization uncertainty ($4\sigma^2$). The slope of the MSD curve scales with the diffusion coefficient of the molecule. C) The relation between the MSD and the lag time encodes information about the type of diffusion underlying the dynamics.*

There are two approaches to MSD analysis. The first approach is to fit the MSD plots of individual tracks and compose a histogram of the fitted diffusion coefficients (**Figure 1.26B**). From this histogram, the number of diffusive populations can be estimated and the underlying diffusion coefficients can be extracted. This approach works well in situations with long tracks and freely diffusing molecules, but is strongly affected by confinement. The second approach is to calculate the MSD($n\Delta t$) over all tracks to gain information about the diffusion behavior of the molecule (**Figure 1.26C**). For a freely diffusing molecule, the MSD increases linearly with $n\Delta t$. When the relation between the MSD and the lag time is not linear, this indicates confined-, directed- or anomalous diffusion (**Figure 1.26C**). For anomalous diffusion, D can be fitted by: $\mathrm{MSD}(n\Delta t) = 4\sigma^2 + 4\mathrm{D}n\Delta t^a$, with a<1 and a>1 indicating obstructed diffusion and directed motion respectively. For confined diffusion, D and the width of the confinement area (L) can be estimated using[269]:

$$MSD(n\Delta t) = L^6 + \frac{16\,L^2}{\pi^4}\sum_{i=1}^{\infty} e^{\frac{-(i\pi\varsigma)^2}{L^2 n\Delta t}}$$

where $D = \varsigma^2/2$. It is important to note that this second approach cannot be used on individual tracks because these contain too little information to be fitted accurately.

An alternative method to extract the diffusion coefficient is one-step MSD analysis, which is less affected by confinement and short track lengths than classical MSD analysis[270]. The one-step MSD only considers displacements between consecutive frames and is calculated as:

$$MSD(\Delta t) = \frac{1}{n}\sum_{i=1}^{n}(x(i\Delta t + \Delta t) - x(i\Delta t))^2 + (y(i\Delta t + \Delta t) - y(i\Delta t))^2$$

where Δt is the time between frames, n is the number of frames over which the molecule is tracked and x(t) and y(t) are the coordinates at time t. n should be kept constant for all tracks to later enable fitting of the distribution of diffusion coefficients. The diffusion coefficients can be calculated from the $MSD(\Delta t)$ by: $D_i = \frac{MSD(\Delta t)}{4\Delta t}$. Lastly, the distribution of diffusion coefficients can be fitted by:

$$p(D_i) = \sum_{m=1}^{k} \frac{p_m}{(n-1)!} * \left(\frac{n}{D_m}\right)^n * (D_i)^{n-1} * exp\left(\frac{-nD_i}{D_m}\right)$$

where k is the number of diffusive states present in the data, D_m is the diffusion coefficient of diffusive state m and p_m is the fraction of molecules in state m.

The one-step MSD presents a suitable solution to analyze individual tracks and extract the diffusion coefficient. However, the one-step MSD does not provide insight into the diffusion behavior of the molecule. To obtain this information, classical MSD analysis can be applied to the ensemble of tracks. One-step MSD analysis can account for the presence of multiple diffusive states when fitting the distribution of diffusion coefficients but it can be challenging to determine how many diffusive states are present. Another challenge related to the potential presence of multiple populations is that MSD analysis is not able to deal with changes in diffusion dynamics within single tracks.

1.5.3.1.2 Jump distance and mean jump distance

Jump Distance (JD) and Mean Jump Distance (MJD) analyses are based on the distances between consecutive localizations whitin trajectories. The JD is defined as the distance between two consecutive localizations, while the MJD is defined as the mean JD of a trajectory. The diffusion coefficient can be extracted from the distribution of JDs by:

$$p(r) = \sum_{i=1}^{n} \frac{p_i}{\sqrt{4\pi D_i t}} e^{\frac{-r^2}{4D_i t}}$$

where r is the JD, n is the number of diffusive states present in the data, D_i is the diffusion coefficient of state i and p_i is the fraction of molecules in state i. Because JD analysis is based on individual displacements, it is less affected by changes in diffusion regimes within single tracks. Using simulated data, Weimann et al. showed that JD analysis may be better suited than MSD analysis when multiple (exchanging) populations are present[267].

It is often challenging to decide how many populations are present in the data based on the JD distribution because the populations are generally not well-defined in the histogram. In this situation, it can be helpful to look at the distribution of MJDs, which is typically better resolved, especially when only selecting relatively long tracks. The MJD distribution cannot be analytically

described because it includes tracks of different lengths, although for sufficiently long tracks the distribution can be approximated by a Gaussian model (central limit theorem)[271].

Overall, JD and MJD analyses are very comparable to one-step MSD analysis. One-step MSD analysis is basically MJD analysis with a defined track length. Because the one-step MSD includes multiple displacements per data point, its distribution can be expected to be better resolved than the JD distribution. Similar as the MJD distribution, the resolution of the on-step MSD distribution can be increased by increasing the number of frames over which is averaged (n), which can facilitate identification of the different diffusive state. This, however, requires sufficiently long tracks and state transitions within single tracks can become problematic.

1.5.3.1.3 Bayesian modeling and deep learning

The potential presence of multiple diffusive states presents a problem for both (one-step) MSD and JD/MJD analysis. In recent years, several methods have been developed to overcome this problem by use of Bayesian modeling[272–274] or deep learning[275–277]. These methods are not yet widely used, but they are gaining popularity.

vbSPT (variational Bayes SPT) is a tool based on Bayesian modeling developed by Persson et al. This tool is able to determine how many diffusive populations are present, the diffusion coefficients of these populations and the transition rates between them. This tool has already been used to unravel the role of histone-like protein HU in nucleoid organization in *E. coli*[278] and to reveal the dynamics of DNA-repair proteins in *B. subtilis*[263]. Still, care should be taken when using vbSPT because it is prone to over-fitting and is sensitive to confinement[266].

1.5.3.1.4 Challenges and solutions for analysis of spt trajectories

Most studies refer to the diffusion coefficient derived from MSD or JD analysis as the 'apparent diffusion coefficient' (Dapp). This is because the observed diffusion coefficient is affected by many factors, which hide the 'true' diffusion coefficient (**Figure 1.27**). Listed below are the different factors that affect the observed diffusion coefficient together with strategies that can minimize the effects of these factors.

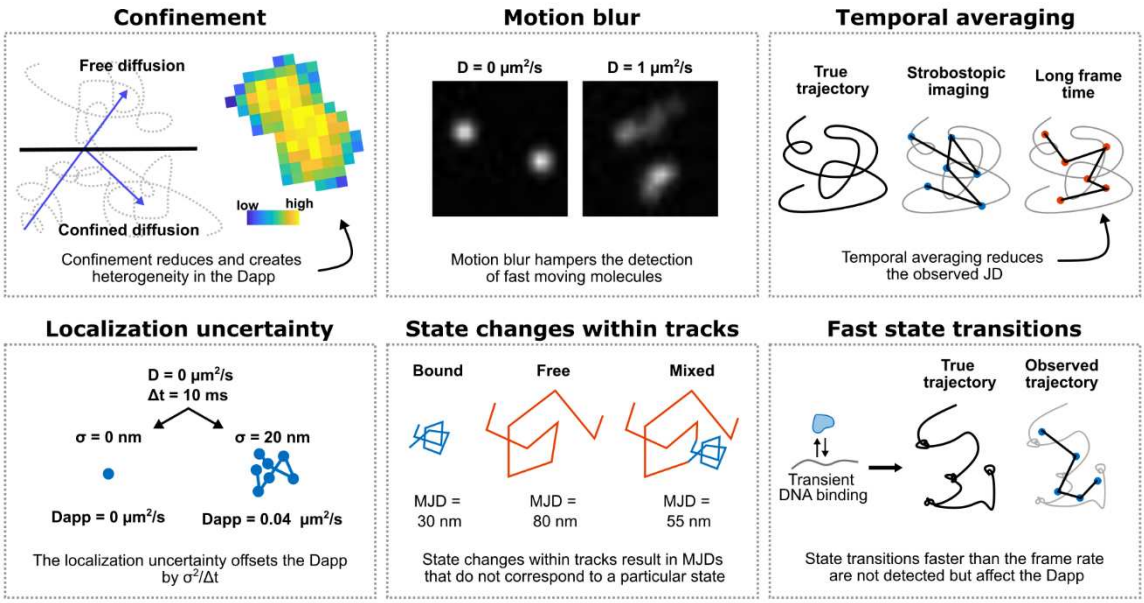

Figure 1.27 Challenges in spt analysis. *See text for details. Confinement: shown is a heatmap of the average JD per pixel of simulated molecules diffusing with D = 1 μm²/s in a nucleoid shaped volume (~1-3 μm diameter). Motion blur: Shown are simulated images of molecules diffusing with D = 0 μm²/s and D = 1 μm²/s imaged with an exposure time of 50 ms. Simulation performed in SMIS.*

- **Confinement:** Confinement has two effects on the observed diffusion coefficient. First of all, confinement lowers the observed D. This effect becomes stronger the larger the diffusion coefficient compared to the confinement area[279–281]. To correct for this effect, simulations can be used to calibrate the effect of confinement given a diffusion coefficient and confining volume[279]. This can be an effective strategy when the confining volume is known and relatively uniform but it is less suitable for irregular volumes with poorly defined bounderies. Another strategy to deal with confinement that is frequently used in studies in *E.coli* is to only consider displacements along the long axis of the cell (see e.g.[278]). The second consequence of confinement is that it creates a heterogeneity in the observed diffusion coefficient[280]. This can result in the appearance of two diffusive states, eventhough there truly is only one population[280]. So far, no satisfying solution has been found to address this issue, but it can be minimized by only considering displacements that are far away from the confining boundary[280].

- **Motion blur and temporal averaging:** Diffusion of the protein during the camera exposure blurs the PSF, which makes the localization less accurate. Moreover, the PSF of fast-moving molecules might be so blurred that they cannot be detected. Additionally, it is not the true position of the molecule that is detected but rather the average position of the molecule during the camera exposure time (temporal averaging), which results in an underestimation of the true jump distance and consequently an underestimation of the diffusion coefficient when using a JD-based analysis method[266,282]. Motion blur and temporal averaging can be limited by the use of stroboscopic imaging, which means that the camera exposure time is minimized as much as possible (~ 1 ms) while the frames are interleaved by dark periods to adjust the sampling rate[280].

- **Localization uncertainty:** The apparent diffusion of molecules is offset by the localization uncertainty, meaning that even molecules that are truly immobile have a Dapp>0. The localization uncertainty (σ) results in an offset of $\sigma^2/\Delta t$, where Δt is the frame time. In theory, the localization uncertainty can simply be corrected for. However, in practice precise estimation of the localization uncertainty can be challenging (see **section 3.2.2.1**), which

becomes especially problematic when studying slow diffusing molecules because in those situations the contribution of the localization uncertainty to the Dapp is relatively large.

- **State changes within tracks:** MSD and MJD analyses cannot deal with state transitions within single tracks. If the exchange rates are relatively low compared to the track lengths, this is not such a problem. However, when the exchange rates are relatively high, this becomes a significant problem because the MSD/MJD will report an average value of the different states. Some tracking software can solve this problem by splitting the tracks into segments with unique diffusion behaviors before proceeding with MJD/MSD analysis[264]. Another solution is to use software such as vbSPT (discussed above).

- **Fast state transitions:** The ability to detect state transitions depends on the ratio between the exchange rates and the sampling frequency (i.e. frame time). To accurately detect the exchange between different populations it is advisable to acquire acquisitions at different frame rates to capture dynamics at different time scales[266,272]. Still, some transitions might be too fast to be observed, for example the transient interaction between DNA binding proteins and DNA in bacteria[279]. In such a situation, it is still possible to estimate the relative populations of the exchanging states, as long as the diffusion coefficients of both states are known[279].

- **Labeling:** In sptPALM, it is not the endogenous protein that is tracked but rather the protein labeled with a fluorophore. This increases the size of the protein and thus slows down its diffusion. In addition, different fluorophores might interact differently with other cellular components thereby further modifying the observed diffusion dynamics[281]. For this reason, it is important to select inert fluorophores with a high monomeric quality.

Altogether, it is very challenging, not to say impossible, to extract true diffusion coefficients from sptPALM data. Therefore, extracted diffusion coefficients are generally referred to as apparent diffusion coefficients. In addition, it is advisable to use sptPALM mostly as a qualitative technique to compare dynamics under different conditions, rather than to use sptPALM to report absolute values.

1.6 Characterization and optimization of FPs for (quantitative) SMLM

Natural FPs are usually not directly usable in biological research because of suboptimal properties, such as a low monomeric quality, slow maturation and low photostability. Therefore, extensive characterization and optimization of FPs is critical.

1.6.1 Important fluorophore properties for SMLM

The suitability of fluorophores for SMLM imaging depends on various characteristics. Firstly, general properties, such as a low toxicity, fast maturation and a good monomeric quality are important. Secondly, there are sereval more specific criteria for SMLM, including a high brightness and photostability. Finally, there is a set of properties that is only applicable to specific types of PTFPs, such as a high photoconversion or –activation efficiency for PCFPs and PAFPs, and a high switching contrast and efficiency for RSFPs. What properties are most important depends on the intended application (PALM, qPALM or sptPALM).

A high apparent brightness and photon budget are critical for all SMLM applications because a single FP needs to emit enough photons to be detected. Under single molecule conditions, the apparent

brightness is dependent on the theoretical brightness, environmental conditions, and the formation of short-lived non-fluorescent states, such as the triplet state. The formation of short-lived non-fluorescent states is especially a concern for single molecule imaging because of the high laser powers that are typically used (see **Figure 1.10**!). Maturation and expression efficiency, which are important factors for the apparent brightness at the ensemble level, do not affect the apparent brightness at the single molecule level since a single FP is mature and fluorescent or not.

A high photostability of PCFPs and PAFPs is important for multiple reasons. Firstly, the initial non-activated/non-converted state needs to be resistant to irreversible photobleaching to ensure a high photoactivation efficiency (**Figure 1.28**). Secondly, the activated/converted state needs to be resistant to irreversible bleaching (i.e. high photon budget) and reversible bleaching/photoswitching. Resistance to reversible bleaching limits blinking and thereby facilitates merging of multiple localization, molecular counting and particle tracking. In addition, the formation of short-lived non-fluorescent states can lower the photon count per frame and decrease the apparent brightness as discussed above. Of course, for PALM applications, the activated fluorophores need to bleach eventually because PALM imaging would otherwise be impossible (activated molecules would just accumulate to a level where single molecules can no longer be distinguished). Considering the current performance of PTFPs, however, this is not an urgent concern.

For PCFPs and PAFPs, their photoconversion or –activation efficiency is one of their most important properties. For a standard PALM experiment, a high activation efficiency is important to satisfy the Nyquist criterion, which states that you need to sample at a frequency that is at least two times higher than the frequency you aim to observe (spatial resolution)[283,284]. A low activation efficiency will lower the sampling frequency and thereby thus the achievable spatial resolution. For qPALM experiments a high activation efficiency is important because it minimizes undercounting. For sptPALM, the activation efficiency is less critical because it is not necessary to image all FPs. Of note, the activation efficiency of PTFPs is not just an intrinsic property of the FP but strongly depends on the environmental and illumination conditions (see for example[203,285]).

When talking about the photoconversion efficiency (or -activation efficiency), it is important to distinguish between the PCE and the effective labelling efficiency (ELE) (**Figure 1.28**). The PCE strictly refers to the fraction of green molecules that is able to reach the photoconverted red state. The ELE, on the other hand, refers to the fraction of target proteins for which a fluorescent signal is detected. The ELE, thus, includes bleaching of the red state before a detection can be made and incomplete labeling of the protein of interest, for example, due to expression of the endogenous unlabeled protein or due to immature or misfolded FPs. Practically speaking, a high overall ELE is more interesting than a high PCE alone. Here, the maturation and expression efficiency of the PTFP become important.

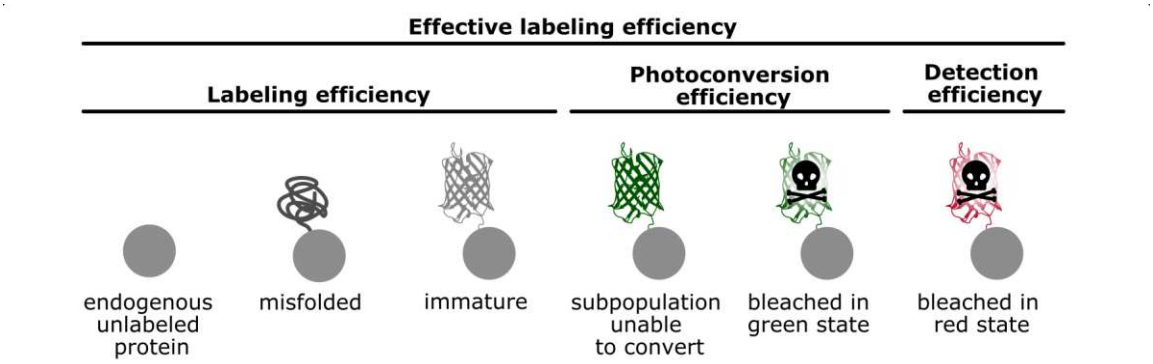

Figure 1.28 The effective labeling efficiency. *The ELE refers to the fraction of target proteins for which a fluorescent signal is detected. This fraction is lowered by an incomplete labelling efficiency due to endogenous protein and misfolded or immature FPs, by an incomplete photoconversion efficiency due to green proteins*

unable to convert and bleaching of the green state, and by bleaching of the red state before a detection can be made. Note that in literature other definitions might be used.

Finally, two properties that are specific to RSFPs are switching contrast and switching fatigue. The switching contrast is defined as the fraction of the fluorescent signal that remains when the protein is switched off. This residual fluorescence might originate from incomplete off-switching or from weak fluorescence coming from the off-state molecules. The switching fatigue refers to the loss in fluorescence signal due to photobleaching when the FP is switched back-and-forth between the On- and Off-state. RSFPs that switch faster (i.e. have a higher switching quantum yield) typically have a lower switching fatigue because they spent less time in the On state reducing the chance to photobleach[81]. Although RSFPs are mostly used for RESOLFT imaging, these properties are also applicable to PALM/STORM imaging with RSFPs: a high switching contrast is necessary to reach densities appropriate for single molecule imaging; a high on-switching efficiency is important to have a high labeling efficiency, similar as a high PCE for PCFPs. A difference in the requirements for RESOLFT and SMLM imaging, however, is that for SMLM imaging the off-switching quantum yield should not be too high to enable the collection of sufficient photons before the FP switches off.

1.6.2 FP immobilization strategies for photophysical studies

To study the photophysical properties of FPs under the microscope, FPs need to be immobilized in a sample suitable for microscopy. Various immobilization platforms have been developed but their suitability for the characterization of FPs has rarely been addressed. There are many factors to take into account when developing or using a specific platform. Ideally, sample preparation should be fast and cheap, and the platform should be easily adaptable to different FPs and fluorophore densities (ensemble and single molecule level). Additionally, it is desirable that the buffer conditions can be varied easily and the FPs can tumble (isotropic orientation). Finally, it is important that the sample does not contain any fluorescent impurities, or provides a way to distinguish between impurities and signal coming from the FP. The most commonly used immobilization strategies can be roughly divided into three categories: polymer gels, (non-)covalent attachment to cover glasses and cell-based platforms. An overview of these immobilization methods, including their strengths and limitations, is provided in **Table 1.3**.

Table 1.3 FP immobilization platforms.

	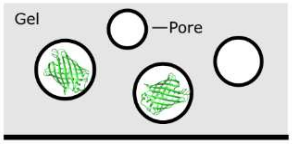 **Polymer gels**	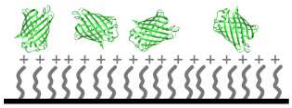 **Poly-lysine coating**	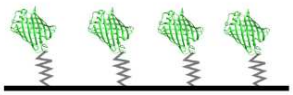 **Covalent attachment**
Single molecule or ensemble	Single molecule and ensemble	Single molecule (and ensemble?[1])	Single molecule (and ensemble?[1])
Modifications FP	Purified protein	Purified protein	Purified protein
Environment	Polymer gel (pH? redox?)	Aqueous, buffer of choice	Aqueous, buffer of choice
FP orientation	Anisotropic	Anisotropic	Anisotropic
Impurities and background	Minimal	Minimal	Minimal
References	Dickson et al. (1996); Garcia-Parajo et al. (2000); Avilov et al. (2014); Zondervan et al. (2003)	Baldering et al. (2019); Fricke et al. (2015); Mehta et al. (2016)	Golfetto et al. (2018); Berardozzi et al. (2016)

	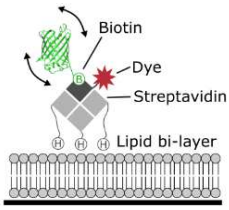 **Bition-streptavidin[3]**	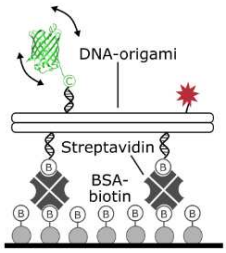 **DNA-origami**	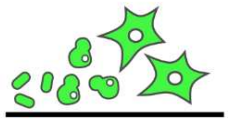 **Cell-based**	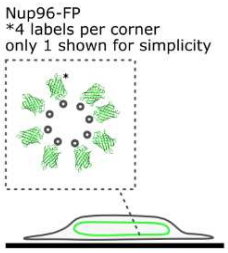 **Nuclear pores**
Single molecule or ensemble	Single molecule	Single molecule	Ensemble	Single molecule (and ensemble?[1])
Modifications FP	Purified protein Linker-biotinylated	Purified protein Linker-cysteine Attached to DNA	Cyctosolic expression	Genetic fusion to nucleoporin
Environment	Aqueous, buffer of choice	Aqueous, buffer of choice	Cellular	Cellular (or buffer of choice when fixed)
FP orientation	Isotropic (??[2])	Isotropic (??[2])	Isotropic	Isotropic (??[2])
Impurities and background	FP signals can be distinguished from impurities by colocalization with dye		Cellular autofluorescence	Cellular autofluorescence
References	Platzer et al. (2020); Henrikus et al. (2021); Endesfelder et al. (2014)	Jusuk et al. (2015); Zanacchi et al. (2017)	Gadella et al. (2023); Botman et al. (2019)	Thevathasan et al. (2019)

1. These platforms can in principle be used for ensemble measurements, given that enough signal can be obtained from a single layer of FPs
2. The orientation of the FPs in these platforms is not fully fixed because of a flexible linker connecting the FP to the platform but it is unclear whether it is truly isotropic
3. Different streptavidin-biotin based platforms have been designed. Shown is the platform developed by Platzer et al.

Polymer gels, such as polyacrylamide (PAA) and poly-vinyl alcohol (PVA) gels, are widely used for the characterization of FPs, both at the single molecule as well as the ensemble level[4,67,217,286–289]. Their main advantages are that their preparation is fast, cheap and easy, and that they can be used for any FP without requiring specific modifications. Furthermore, these gels have been shown to contain minimal fluorescent impurities[4]. Disadvantages, however, are that the dipole orientation of the FPs is fixed in the gel[287] and that the buffer conditions can be challenging to control, notably in terms of pH and redox environment[288–290]. Despite these drawbacks, polymer gels are very convenient for initial characterizations and screening of multiple FPs.

Attachment of FPs to the cover glass is another popular *in vitro* immobilization strategy. There are many ways to do this. One of the simplest methods is to deposit FPs on poly-lysine coated cover glasses[144,206,254,291]. This way, the FPs become immobilized by electrostatic interactions with the positively charged poly-lysine. This method is simple and allows control over the buffer conditions[144,254], but also fixes the dipole orientation of the FPs[291]. More complex methods make use of biotin-streptavidin complexes[292–294] or DNA origamis to immobilize FPs[258,295]. These methods are more elaborate but provide better control over how the FP is immobilized and also enable the incorporation of a second control fluorophore to distinguish fluorescent impurities[292,295]. Finally, another possibility is to attach the FP covalently to the cover glass, which can be achieved by specific chemistry targeting primary amines (N-terminus and surface exposed lysine and arginine residues), cysteines or histidines[147,296]. These methods are easily adaptable to different FPs and allow full control over the buffer conditions.

Finally, there are different cell-based platforms that allow the characterization of FPs directly inside cells. These cell-based platforms are useful because FPs can behave differently in cellular environments than *in vitro* because of a multitude of factors[4,83]. There exist different cell-based immobilization strategies for different purposes. The simplest strategy is to overexpress the FP as a cytosolic protein, which allows characterization of the ensemble florescence behavior[58,83]. This method has been used to characterize the behavior of FPs in mammalian, yeast and bacterial cells[58,83,297]. To characterize the single molecule behavior, however, the FP needs to be really immobilized. This can be done by fusing the FP to a mostly immobile cellular protein or by fixing the cells[4,244]. Thevathasan et al. recently introduced the usage of nuclear pores as a platform to assess the performance of FPs (and fluorescent dyes) in single molecule imaging conditions[244]. To this end they tagged the nucleoporin Nup96, which is present in 32 copies per NPC and organized into eight corners[244]. They showed that this well-defined morphology and stoichiometry enables quantitative assessment of the labelling efficiency of the FP under different illumination and environmental conditions[244].

1.6.3 Structural characterization of fluorescent proteins

In addition to photophysical characterization, structural characterization is valuable for the development of better performing FPs. During the last years, structural studies have provided insights into the mechanisms of photoactivation, -switching and -conversion in PTFPs and have guided the rational design of better FPs. The field of structural biology is dominated by three main techniques: X-ray crystallography, Nuclear Magnetic Resonance (NMR) and electron microscopy (EM). While FPs are too small to be studied by EM, X-ray crystallography and NMR spectroscopy have proven very useful for the characterization of the structural dynamics of FPs.

X-ray crystallography uses X-rays to determine the molecular structure of proteins with atomic resolution. The process from protein to structure can be divided into four steps (**Figure 1.29A**): First, the protein is crystallized. Second, the crystal is irradiated with X-rays, producing a diffraction pattern. By rotating the crystal, three-dimension information from the crystal is obtained. Third,

these diffraction patterns are used to compute an electron density map of the crystal. Fourth, a model of the protein is built and refined. Classical X-ray crystallography, as described above, has provided information about the overall protein and chromophore structure of various FPs (see for example[298]). A more dynamic view of FPs has come from kinetic crystallography[299].

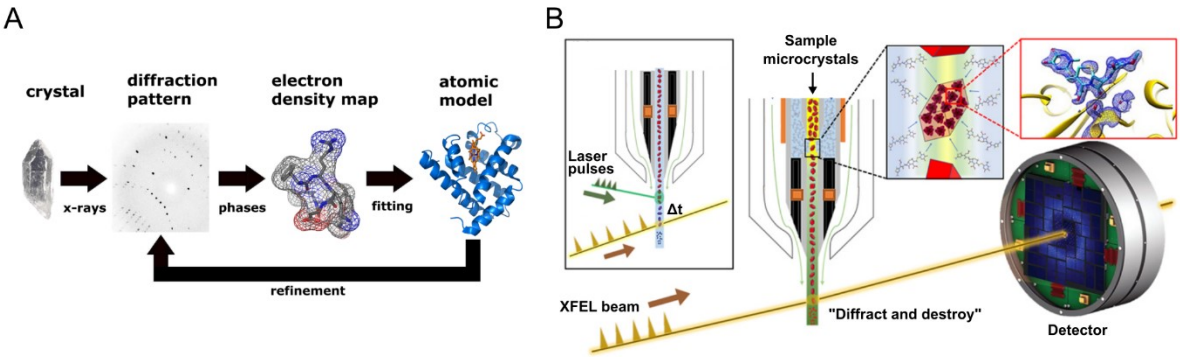

Figure 1.29 X-ray crystallography to gain structural insights into FPs. *A) Workflow of classical X-ray crystallography. See text for details. B) Structural dynamics of FPs can be monitored in real-time using XFEL-sources. Inset: the crystal is first 'pumped' by a laser pusle and then 'probed' by the XFEL beam. Δt can be varied to reconstruct a molecular movie of the dynamics of the protein. A adapted from www.creativebiomart.net, B adapted from Fromme et al.*[300]

Kinetic crystallography is used to capture conformational changes in FPs in response to illumination. Examples include the differences between the initial green and photoconverted red state of PCFPs, and the on- and off-state of RSFPs. Kinetic crystallography can be performed by either trapping an intermediated state of the protein inside the crystal or by monitoring the dynamics of the crystalized protein in real-time using X-ray Free Electron Lasers (XFEL) sources (**Figure 1.29B**)[299]. To trap an intermediate state (e.g. the *trans*-protonated off-state of negative RSFPs) inside a crystal, the crystal is illuminated to populate the intermediate state after which it is frozen so that the intermediate state cannot relax back and a structure can be obtained. Alternatively, the crystal is first frozen and then illuminated. This approach of kinetic crystallography is most widely used because it is relatively simple. The use of XFEL sources to monitor protein dynamics in real-time, however, has some clear advantages over the 'trapping' approach: it provides information about the kinetic rates and does not require freezing, which may affect the structure. In this technique, real-time monitoring is achieved by a 'pump-probe' approach. First, the structural response is triggered by illumination with UV-visible light ('pump'). Second, after a well-defined time-delay (ps to ns), a diffraction pattern is obtained to 'probe' the structure of the protein. This way, by changing the time delay between 'pumping' and 'probing' (Δt), it is possible to reconstruct a movie of the conformational changes in the protein with picosecond resolution. Woodhouse et al., for example, used this time-resolved approach to capture the off-to-on photoswitching pathway of rsEGFP2[301]. Disadvantages of this technique, however, are that it requires large amounts of microcrystals since only one diffraction pattern can be obtained per crystal due to immediate destruction of the crystal by the XFEL beam, and that there are only few XFEL sources.

NMR makes use of the nuclear spin of certain nuclei (typically ^{1}H, ^{13}C and/or ^{15}N) to gain information about the structure and dynamics of proteins. A basic NMR experiment can be divided into three steps: preparation of an isotope-labeled protein sample (^{13}C and /or ^{15}N); NMR data collection; assignment of the chemical shift to atoms in the protein. A common NMR experiment is to acquire a 2D spectrum of the ^{1}H and ^{15}N chemical shifts, which gives one peak for each amino acid of the protein backbone (except for proline) (**Figure 1.30B**). Conformational changes, such as photoconversion, or chemical changes, such as protonation, lead to changes in the chemical environment of certain nuclei, modifying their chemical shifts (i.e. location of the peak) (**Figure 1.30B**). NMR is sensitive to changes happening at time scales ranging from picoseconds to hours and

can detect protein states with low occupancy (as low as 1%). Furthermore, recent developments have enabled *in situ* illumination of protein samples inside the NMR tube, which enables the monitoring of photoswitching and photoconversion of FPs in real-time (**Figure 1.30A**)[122,302].

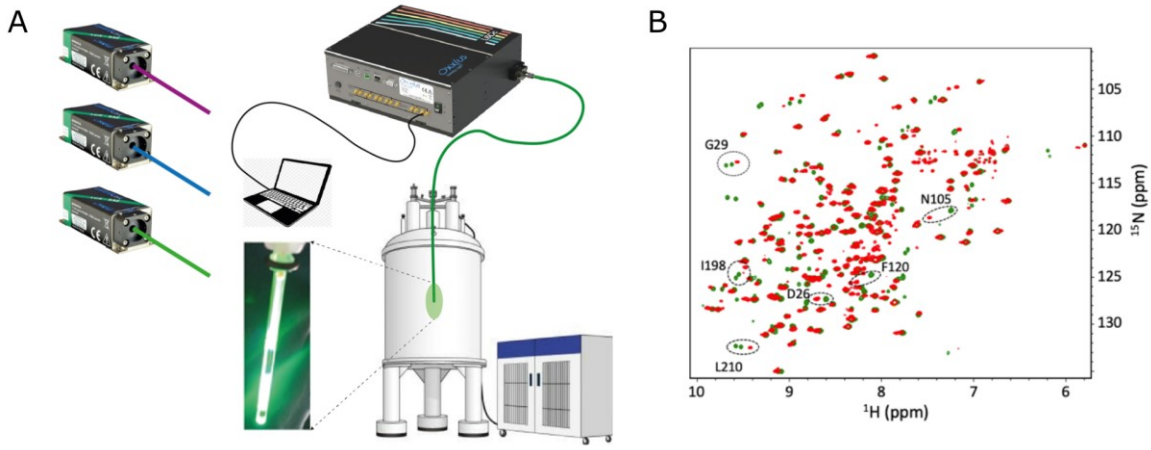

Figure 1.30 NMR spectroscopy for the structural characterization of FPs. *A) Schematics of the NMR set-up present at IBS, showing the three available laser lines (405, 488 and 561 nm) and the illumination of the protein sample (photo). B) 2D NMR spectra of green state (green) and red state (red) mEos4b. Highlighted are a selection of amino acids which show a large chemical shift difference between the green and red state. Figure prepared by Arijit Maity.*

To summarize, X-ray crystallography and NMR spectroscopy are both valuable techniques for the structural characterization of FPs with complementary strengths. X-ray crystallography provides structural information and can reveal the structural arrangements in FPs in response to irradiation. However, for this, the FP needs to be crystallized which might affect its dynamic properties (see for example[303]). In addition, small structural changes can be difficult to detect, as well as states with a low occupancy (but see[304]). With NMR, on the other hand, the FPs are kept in solution providing a more native environment. Furthermore, NMR is sensitive to changes in the chemical environment around nuclei, not necessarily requiring large structural rearrangements. What remains challenging with NMR, however, is to translate the chemical shifts into a structural model.

1.6.4 Optimizing FP performance

The perfect PTFP for SMLM has not been developed yet. To improve the performance of FPs there are two options: introduce mutations that suppress suboptimal behaviors (thus creating new FPs), or tune the experimental conditions to enhance desirable properties and suppress unwanted behaviors.

1.6.4.1 Development of new FPs by structure-guided and random mutagenesis

Seemingly the most straightforward approach to eliminate suboptimal behaviors is to develop new FPs that do not display these behaviors. This strategy is often guided by structural studies, which provide clues about which residues to target to improve particular behaviors. In practice, development of better FPs is often done by a combination of site-directed and random mutagenesis. This is because it is very difficult to predict the consequences of specific mutations. It is not uncommon that mutations far away from the chromophore have a big effect on the photophysical behavior of the FP. Furthermore, sometimes specific mutations to optimize one characteristic, such as monomeric quality, degrade other properties, such as brightness. In such situations, other mutations need to be introduced to rescue degraded properties. Another challenge for the development of new PTFPs is the screening of the huge protein libraries that are created by random mutagenesis. There exist various high throughput workflows that have been designed to screen FP

libraries for properties such as brightness, fluorescence lifetime, and photostability (for example[305,306]), but these workflows are often not adapted to test for PTFP specific properties, such as photoconversion efficiency and blinking behavior. Despite these challenges, mutagenesis is an essential step in the development of better performing PTFPs, especially to address problems that cannot be manipulated by changing the experimental conditions, such as poor monomeric quality and slow maturation.

1.6.4.2 Manipulating FP photophysics

Mutagenesis is not always the best approach to increase FP performance. One major concern is the intrinsic limit of GFP-like FPs: 'Is it possible to create monomeric FPs that are as bright and stable as organic dyes or is this physically impossible? ', and, 'Is it possible to create PCFPs that are as stable as the best standard FPs or does the ability to photoconvert always come at the cost of decreased stability?' Various recent studies report on the discovery and development of new FP variants with outstanding qualities in terms of brightness and stability, showing that improvements are still possible[35,307]. However, mutagenesis studies are often unsuccessful and the development of improved FPs can take many years. Therefore, it is important to invest in strategies to optimize the performance of existing FPs. An additional argument in favor of this strategy is that it can be a lot of work to create a fusion construct or even a stable cell-line. So, approaches that are based on changes in the experimental conditions may be more easily implemented than new FPs.

1.6.4.2.1 Increasing brightness

Brighter fluorophores with a higher photon budget are always desired for SMLM because the more photons, the higher the localization precision.

One approach to increase the appearent brightness is to use heavy water (D_2O) instead of ordinary water (H_2O), which has been shown to improve the photon count of both FPs and organic dyes[244,308–310]. Ong et al. showed that the use of D_2O increases the number of detected photons of mEos2 by 31%, increasing the localization precision from ~40 nm to ~20 nm[308]. Importantly, this approach is compatible with live-cell imaging (at least for limited durations)[308]. How exactly D_2O increases the photon count of fluorophores is not fully understood. Maillard et al. proposed that H_2O, but not D_2O, quenches the excited state or organic dyes thereby reducing their fluorescence quantum yield and hence their brightness[309]. Ong et al, on the other hand, found that the increased photon counts of FPs in D_2O result from decreased bleaching (i.e. higher photon budget) rather than from increased brightness[308]. In any case, regardless of the exact mechanism, the use of D_2O appears highly beneficial for SMLM.

Another approach to increase the brightness of FPs is to reduce the formation and lifetime of the triplet state. There have been many efforts to reduce the lifetime of the triplet state, not only in PTFPs but also in standard FPs. Different studies have shown that the triplet state lifetime can be reduced by illumination with near infrared light (NIR)[99,311,312], which matches with the triplet state absorption spectrum of (E)GFP[88,100]. Reduction of the triplet state lifetime by NIR light has been shown to increase the ensemble fluorescent signal of EYFP[99,311]. Furthermore, recent work by Ludvikova et al. showed that NIR light reduces bleaching of various green and yellow emitting FPs, although, in contrast to previous work, no increase in brightness was reported[312]. Alternatively, Donnert et al. proposed a pulsed illumination strategy that they suggested allows relaxation of the triplet state[313]. They showed that pulsed illumination significantly increases the fluorescent signal of GFP and a YFP (Venus)[313]. However, although their strategy appears successful, it is unclear whether this is really due to relaxation of the triplet state, since recent literature suggests that the lifetime of the triplet state of FPs is 1-5 ms[88,97,98], while they used dark intervals of only 2 µs. Whether these

approaches are usable for SMLM remains to be tested. It should be noted that acting on the triplet state does not only affect brightness but also other photophysical properties that are related to the triplet state, such as bleaching and blinking. Although the reduction of blinking and bleaching would be beneficial for SMLM, one concern is that photoconversion could be affected, given that this might also proceeds via the triplet state (see[194]).

Finally, it is possible to improve the brightness of FPs by changing the redox environment[144,293,314]. For example, Baldering et al. showed that the reducing agent β-mercaptoethylamine (MEA) increases the photon count per localization of mEo3.2 and mMaple3 by 20-50%[144]. This strategy, however, might not be compatible with live-cell imaging.

1.6.4.2.2 Limiting photobleaching

Photobleaching affects SMLM in two ways: photobleaching of the non-activated/non-converted state lowers the PCE; photobleaching of the activated/converted state lowers the total photon count and limits the track length in sptPALM.

Most of the strategies that have the potential to increase the brightness of PTFPs also have the potential to reduce photobleaching. This is because both (apparent) brightness and photobleaching are related to the photon budget and because the triplet state plays an important role in both properties. So, approaches to reduce photobleaching include the use of D_2O[308] or antifading agents[4,314], and reduction of the triplet state lifetime[99,311,313].

Another approach to reduce the photobleaching rate is to reduce the laser power. This can be an acceptable approach in sptPALM where long tracks are more important than a very high localization precision. This strategy does not increase the photon budget of the FP (not considering nonlinear effects), but spreads the available photons over more frames. For normal PALM experiments this is not beneficial, although very high laser intensities (>10kW/cm^2) should still be avoided to avoid strong nonlinear bleaching[315]. For experiments in which a high photoactivation efficiency is important (e.g. qPALM) it is worth optimizing the intensity of the UV laser. The use of lower doses of 405 nm light has been shown to be beneficial for the activation efficiency of various PCFPs and PAFPs[203,285]. However, it is not advisable to abolish all UV light because this will also lead to a suboptimal activation efficiency, at least in PCFPs, due to bleaching of the initial green state by the laser used to excite the red state (typically ~561 nm)[204]. How exactly the PCE of PCFPs scales with different 405 and 561 nm laser intensities requires more in-depth investigation.

1.6.4.2.3 Reducing blinking

Long-lived blinks are one of the major problems of PCFPs because they hinder the clustering, counting and tracking of molecules.

De Zitter et al. showed that the addition of weak 488 nm light largely eliminates long-lived blinks in photoconverted mEos4b and other EosFP variants, which they show is because of accelerated recovery of the red Off-state (*trans* neutral chromophore)[217]. Most interestingly, they show that this dual illumination strategy can be used to increase the track length in sptPALM experiments and only minimally affects photoconversion[217]. Whether this approach could also benefit counting remains to be investigated. Unfortunately, this strategy does not remove all long-lived blinks and does not work with other FP variants, indicating the presence of other blinking mechanisms[217].

Another interesting strategy to increase the track length in spt experiments was developed by Basu et al., who showed that the photostability of mEos3.2 can be improved by the close proximity of a

FRET acceptor (JF_{549})[316]. They show that this enhancement is due to energy transfer from mEos3.2 to the FRET acceptor, which reduces the excited state lifetime and thereby the probability of phototransformations, such as blinking and bleaching, to occur[316]. Using this approach, they increase the average track length by a factor of 7[316]. It should be noted, however, that this approach comes at the cost of a bigger label size (FP + FRET acceptor) and a lower photon count per localization.

1.7 A biological application of sptPALM: the study of stress-induced nucleoid remodeling

In addition to photophysical studies, my thesis includes the application of sptPALM to investigate stress-induced nucleoid remodeling in bacteria. Stress-induced nucleoid remodeling is a wide-spread phenomenon in bacteria, which helps them to survive hostile conditions. To gain insight into this behavior we used a combination of confocal microscopy and sptPALM to monitor changes in overall nucleoid morphology and diffusion behavior of histone-like protein HU, a multifunctional nucleoid associated protein (NAP). In this section, I will provide some background on nucleoid organization in bacteria under normal growth conditions and under stressed conditions with a special focus on the implication of HU in this process. Furthermore, I will discuss the use of the bacterium *Deinococcus radiodurans* as a model system.

1.7.1 Organization of the bacterial nucleoid

Genomic DNA needs to be condensed several orders of magnitude to fit inside the dedicated subcellular space in both eukaryotic and prokaryotic cells. Condensation alone, however, is not sufficient because at the same time the DNA needs to be accessible for protein complexes involved in DNA replication, transcription and repair. This balance between compaction and accessibility is achieved by highly ordered but dynamic packing of the DNA (**Figure 1.31**). In eukaryotic cells the genomic DNA is stored in the nucleus, separated from the cytosol by the nuclear membrane. In the nucleus, the DNA is organized in a hierarchical manner, starting with the wrapping of the DNA around histones to form nucleosomes, which are subsequently organized into higher order chromatin structures[317]. In bacteria, on the other hand, the genomic DNA is stored in a membrane-less organelle inside the cytosol, named the nucleoid. While bacteria do not have histones, they also have a hierarchical and highly structured DNA organization[318–320]. This organization is achieved by a combination of physical forces, such as confinement, crowding and supercoiling, and nucleoid associated proteins (NAPs), small DNA binding proteins that have histone-like functions[320–322].

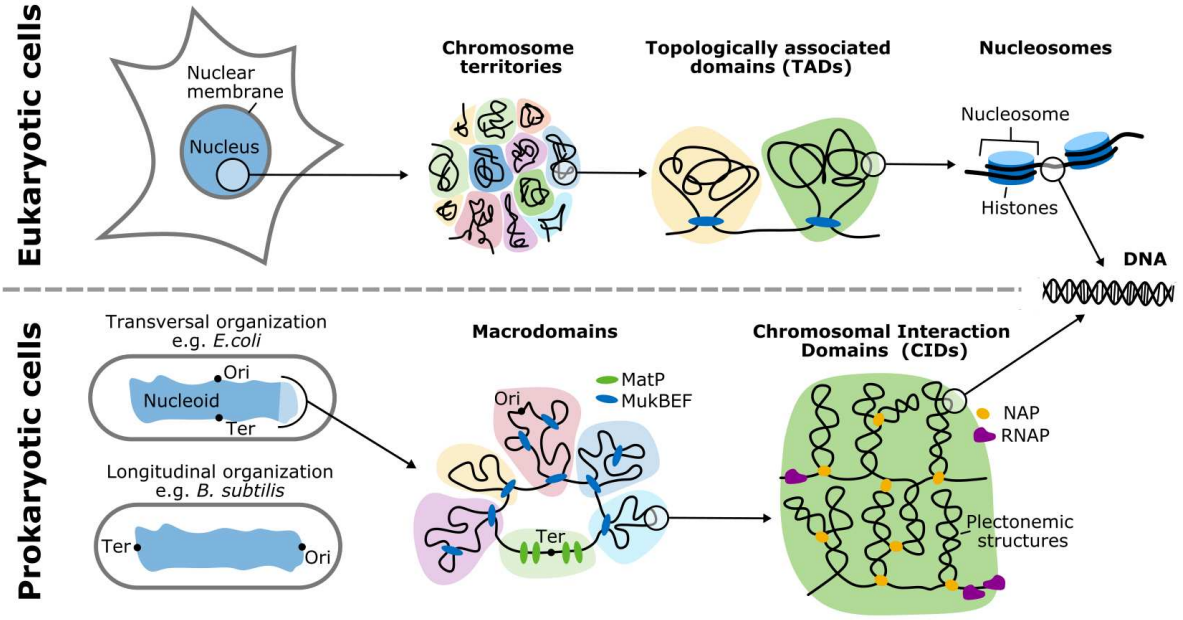

Figure 1.31 DNA organization in eukaryotic and prokaryotic cells. *In eukaryotic cells the genomic DNA is stored inside the nucleus, enclosed by the nuclear membrane. Eukaryotic cells typically have multiple chromosomes, which all occupy a distinct territory within the nucleus. Subdomains within chromosomes with many DNA-DNA interactions are called TADs. These regions play an important role in gene regulation. Inside the TADs, the DNA is organized in the form of nucleosomes. In prokaryotic cells the DNA is stored inside a membrane-less organelle called the nucleoid. Bacteria often have only one circular chromosome, which is organized into macrodomains by the actions of SMCs (MukBEF in E. coli). Inside the cell, the chromosome can adopt a transversal or longitudinal disposition, depending on the species. The macrodomains can be further subdivided into CIDs, which are functionally equivalent to TADs in eukaryotic cells.*

Most of our knowledge of nucleoid organization comes from studies in *E. coli*. Although our understanding of nucleoid organization remains incomplete, the emerging picture is that the nucleoid as a whole is phase separated from the cytosol, providing spatiotemporal control over cellular processes happening in the nucleoid and cytosol without the need for a separating membrane[323,324]. The nucleoid itself appears structurally and functionally organized into macrodomains (~ 1Mbp), which are further subdivided into subdomains, named Chromosomal Interaction Domains (CIDs), functionally comparable to Topologically Associated Domains (TADs) in eukaryotic cells[319,325,326]. Macrodomains and CIDs are characterized by having more physical interactions between DNA segments within the domain than with DNA segments in other domains[325,326]. Six macrodomains are recognized in *E. coli*: the Ori domain, surrounding the origin of replication; the Ter domain, surrounding the replication terminus; the Right and Left domains, flanking the Ter domain; the NS-right and NS-left domains, non-structured domains flanking the Ori domain. The formation and maintenance of these macrodomains is driven by protein complexes of the Structural Maintenance of Chromosomes family (SMCs) (MukBEF in *E.coli*, with MatP defining the Ter region)[319,327–329]. How these macrodomains are positioned inside the bacterium differs between species. In some species, such as *B. subtilis*, the chromosome adopts a longitudinal configuration, while in others, including *E. coli*, the chromosome adopts a transversal configuration[330].

CIDs are smaller interaction domains within the macrodomains. 31 CIDs have been identified in exponentially growing *E.coli* cells, ranging in size from 30 to 400 kb[325]. DNA supercoiling appears to be at the basis of CID formation[319]. Supercoiling is caused by the under- and over-winding of the DNA helix relative to its relaxed conformation (~10.5 bp per turn), which in bacteria leads to DNA condensation due to the formation of plectonemic structures, meaning that the DNA interwinds with itself[319]. The supercoiled status of the bacterial chromosome is regulated and maintained by enzymes called topoisomerases, which act by cutting the DNA after which they create or relax supercoils

before re-ligating the DNA back together. It is not fully understood how the boundaries of individual CIDs are defined. Probably there exist multiple mechanisms, including effects from DNA transcription and regulation by NAPs[325,331,332]. In addition to CIDs, it has been proposed that small sub-compartments with specialized functions, such as transcription, can be formed by liquid-liquid phase separation[323,324,332–334].

Fluorescence imaging of the bacterial nucleoid has revealed that its organization is highly dynamic. By creation of widened *E. coli* cells, Wu et al. imaged the organization of the genomic DNA into distinct domains[327]. They found that the DNA is organized into, on average, 4 major domains ('blobs') which merge, split and rearrange at a minute time scale[327]. Similar dynamics of 'blob-like' regions in the *E.coli* nucleoid were observed by Gupta et al[323]. Local dynamics of the chromosome have been measured by tracking of individual loci on the chromosome. The motion of loci on the chromosome is sub-diffusive, which is largely due to the polymeric nature of the DNA, but also due to other factors, such as confinement within the nucleoid and molecular crowding[335]. It is important to note that the nature of the dynamics of the DNA is dependent on the timescale of the experiment. At a short time scale (< 10 s) the dynamics are dominated by local movements of the DNA, while at a larger time scale (> minutes) the dynamics are dominated by cell-division and chromosome segregation[335,336]. Probably as a consequence of this complexity, different studies, using different experimental conditions, time intervals and analyses, have reported widely different diffusion coefficients for loci on the genomic DNA, ranging from 10^{-5} up to 10^{-2} $\mu m^2/s$[278,337–341]. In addition, studies monitoring the motion of various loci have revealed that their respective mobilities are strongly dependent on their position along the chromosome[339,341–344]. In particular, the Ter region has been reported to be less mobile than the rest of the chromosome[339,341–344], which might be explained by tethering of the Ter site to the cell-division machinery[345,346], restricting its movement. How this dynamic view of the nucleoid relates to the rather static hierarchical macrodomain model explained above requires further study.

Nucleoid associated proteins (NAPs) play important roles in nucleoid organization. NAPs are small basic (positively charged) DNA binding proteins, which are usually highly abundant and perform histone-like functions. NAPs contribute to nucleoid organization by bending, bridging and bunching the DNA by specific (sequence- or structure-specific) and non-specific interactions. Thereby, they contribute to nucleoid condensation, domain formation and regulation of gene expression[278,319,325,327]. There exists a variety of NAPs, some of which are highly conserved, while others are less conserved between species. 12 different NAPs have been identified in *E. coli*[347]. The most conserved NAP is histone-like protein HU (heat-unstable protein) whose properties and functions will be discussed in detail below.

1.7.1.1 Histone-like protein HU

HU is a key player in nucleoid organization and is associated with diverse biological processes including the regulation of overall nucleoid compaction[278], the formation and maintenance of nucleoid domains[325,327], the regulation of gene expression[348–351], the control of stress-response pathways and DNA repair[350,352], and even in biofilm formation[353]. HU molecules form dimers, which can interact with the DNA in structure specific and non-specific manners. *E. coli* expresses two HU variants, HUα and HUβ, which form HUαα homodimers and HUαβ heterodimers[350,354]. The expression of these two HU variants is dependent on the growth phase and external stress factors, with HUαα being most abundant during exponential phase and HUαβ being most abundant during stationary phase and under stressed conditions[350,354]. Although HU is not essential for *E. coli*, cells deficient in HU have been reported to show expanded nucleoids, altered transcription profiles[348–350] and increased sensitivity to UV[352,355] and gamma irradiation[356], highlighting the importance and versatility of HU.

The different physiological roles of HU are regulated trough different modes of interaction with the genomic DNA. Two DNA binding modes have been reported for HU: transient non-specific binding and structure-specific binding (**Figure 1.32**). The non-specific binding mode is the most abundant, causing HU to uniformly distribute over the whole nucleoid[278,348,349]. This non-specific binding is critical for maintenance of the overall compaction status of the nucleoid and is mediated by three conserved lysine residues located on the sides of the HU α-helical 'body'(**Figure 1.32**)[278,348]. Furthermore, these lysines enable HU to bridge different DNA segments since they are located on both sides of the HU body[357,358], which could contribute to the capability of HU to promote long-range DNA contacts and domain formation[325,326]. In vitro studies have revealed that the effect of HU on DNA compaction is dependent on the protein concentration: while at low concentrations HU was shown to promote overall DNA condensation by creation of flexible bends, at high concentrations, HU was shown to promote the formation of rigid filaments by multimerization of HU molecules[357–360]. The biological relevance of HU multimerization, however, remains to be established, as such high concentration are usually not found inside cells, although it is not excluded that local conditions might favor multimerization[319]. Besides this non-specific binding mode, HU has been shown to bind DNA in a structure-specific manner, recognizing structures such as kinks, nicks, gaps, and cruciform structures. This structure-specific binding is mediated by proline residues located on the HU β-hairpin 'arms', which intercalate into the minor groove of the DNA (**Figure 1.32**)[361]. Structure-specific binding has been shown to be involved in maintenance of the supercoiled status of the DNA and regulation of gene transcription[348].

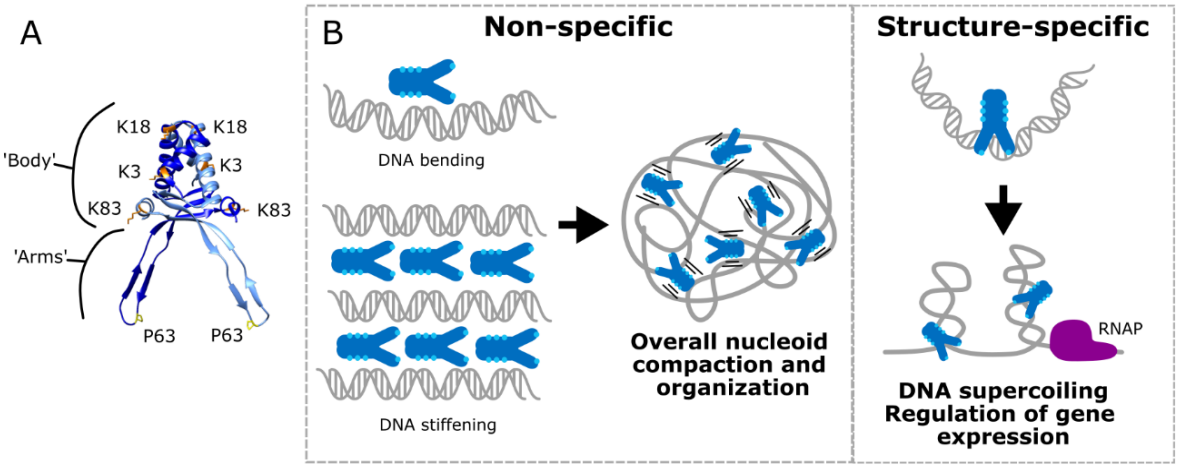

Figure 1.32 HU is a key player in nucleoid organization. *A) Structure of HUαα from E. coli (PDB 6O8Q) with the lysines and prolines involved in non-specific and structure-specific DNA binding highlighted in orange and yellow, respectively. B) Non-specific interactions between HU and DNA can lead to DNA bending or DNA rigidification by multimerization of HU molecules, depending on the HU concentration. These non-specific interactions contribute to the overall compaction and organization of the nucleoid. Structure-specific interaction between HU and the DNA have been proposed to be involved in regulation of the supercoiled state of the DNA and gene expression.*

In addition to the two intrinsic DNA binding modes of HU, there is increasing evidence that the interaction between HU and the DNA is modulated by post-translational modification (PTMs). In eukaryotic cells, many activities around the DNA are regulated by PTMs on the histone tails, which are collectively referred to as the 'histone-code'[362,363]. Based on the various PTMs found on NAPs, Carabetta coined the hypothesis of the existence of a histone-like code in bacteria[352]. For example, HU has been reported to be acetylated, phosphorylated and succinylated in various bacterial species[352,364–367]. These modifications have been shown to influence the DNA binding affinity of HU and have been proposed to contribute to fine-tuning the overall nucleoid architecture, regulation of gene expression and adaptation to environmental stress[364,365,367].

1.7.1.2 Single particle tracking of HU

Single-particle tracking of HU molecules has significantly contributed to our understanding of the activities of HU in living cells. **Table 1.4** provides a list of studies that used sptPALM to investigate the behavior of HU in various bacterial species.

Most studies identified two HU populations: one slow diffusing, seemingly immobile, population (≤ 0.15 $\mu m^2/s$)[278,279,368]; one faster diffusing population (~0.3-0.5 $\mu m^2/s$)[278,279,368]. Although it is tempting to speculate that these two states correspond to the specific- and non-specific DNA-binding modes of HU, Bettridge et al. showed that the dwell-time of the slow diffusing population is too short compared to what would be expected for HU molecules structure-specifically binding to the DNA[278,369]. Instead, they proposed that the slow population corresponds to the non-specific DNA binding mode of HU mediated by the lysine residues located on the HU body[278]. The apparent diffusion of the 'immobile' population results from motion of the DNA[278,337] and the localization uncertainty[279]. The size of the HU population structure-specifically binding to the DNA is possibly too low to be detected. The diffusion coefficient of the faster diffusing population is too low to represent a freely diffusing population. Rather, this population has been proposed to interact with the DNA in a transient manner with a dwell time too low to be detected by sptPALM (see **Figure 1.27**)[278,279]. In fact, using a combination of DNA free cells and simulations, Stracy et al. estimated that the HU molecules in this population spend 99% of their time (transiently) bound to the DNA[279].

In addition to WT HU, Bettridge et al. also studied the diffusion of two HU mutants: HUα(triKA), lacking the three lysine residues located on the HU body, and HUα(P63A), lacking the proline located on the HU arm (**Figure 1.32A**)[278]. They found that both mutants diffuse faster than WT HU, suggesting that these mutants bind less to the DNA[278]. Interestingly, they also showed that while the nucleoids in HUα(triKA) cells are hyper compacted, the nucleoids in HUα(P63A) cells are expanded[278]. They attributed this observation to a dual role of HU in nucleoid compaction, balancing compaction and expansion through differential interactions with the DNA[278].

While most studies found two HU populations, others found one[337,370] or three[371] populations. The appearance of only a single HU population was ascribed to fast exchange between the DNA-bound and unbound states[370]. The biological meaning of the three populations identified by Kamagata et al. is unclear. Their fitted diffusion coefficients, however, are very close to those reported in refs[278,279,368].

Table 1.4 Single particle tracking of HU. *Listed are studies performing spt of HU in various species.*

Reference	**Species[1]**	**HU fusion**	**Frame time (ms) + interval (ms)[2]**	**SPT analysis**	**Diffusion coefficient ($\mu m^2/s$); population (%); dwell time (ms)**
Bettridge et al. (2020)[278]	*E.coli*	Huα-PAmCherry	6.74	vbSPT[272]	0.39 (57%); 74 0.14 (43 %); 100
		HUα(triKA)-PAmCherry			1.1 (95%); 852 0.18 (5%); 107
		HUα(P63A)-PAmCherry			0.84 (68%); 114 0.25 (32%); 129
Floc'h et al. (2019)[370]	*D. radiodurans*	HU-PAmCherry	30	Classical MSD analysis	0.32 (100%)

Kamagata et al. (2021)[371]	*E.coli*	HUβ-eGFP	10 + 30.8	Classical MSD analysis	0.54 (20%) 0.17 (49%) 0.071 (31%)
Stracy et al. (2021)[279]	*E.coli*	HUβ-PAmCherry	15 + 0.48	One-step MSD analysis	0.41 (23%) 0.11 (73%)
Strzałka et al, (2022)[368]	*S. coelicolor*	Huα-PAmCherry	30	Gaussian mixture model[372]	0.40 (25%) 0.015 (75%)
Zhu et al. (2020)[337]	*E.coli*	Huα-PAmCHerry	30 + 2.5	Classical MSD analysis	0.098 (100%)

1. All measurements were performed in exponential phase cells
2. The frame time refers to the exposure time of the camera; the interval refers to additional time in between frames

1.7.2 Stress-induced nucleoid remodeling

Bacteria have the ability to swiftly adapt to changing environmental conditions, which is crucial for their survival. Among the different adaptation strategies bacteria have developed, reorganization of the nucleoid architecture appears to be a wide-spread mechanism. Nucleoid remodeling has been observed in cells entering stationary phase and in acute response to osmotic stress[373], oxidative stress[374], nutrient starvation[337,375], antibiotics[375–378] and gamma-[379] and UVC irradiation[380–383]. This reorganization is typically observed as a hyper-condensation of the nucleoid, which is reversed when the stress factor is removed or when the cells have recovered or adapted[376,380–383]. The function of stress-induced nucleoid remodeling has been proposed to be threefold: protection of the genomic DNA from further damage; facilitation of DNA repair by the alignment of sister chromosomes to facilitate homologous recombination[376,378]; regulation of gene expression to upregulate the production of proteins that help cope with stress[384].

The molecular mechanisms driving stress-induced nucleoid remodeling have been intensively investigated (**Figure 1.33**). Recent studies suggest that nucleoid condensation might be partly ascribed to the intrinsic capability of homologous DNA strands to find each other and align[376,385,386]. Prolonged nucleoid compaction, however, does appear to be dependent on the activity of specific proteins[376,378,382,383]. Studies in *E. coli*, and other bacteria, have shown that RecA and RecN are key players in nucleoid remodeling[376,378,382,383]. RecA is a multifunctional protein which is involved in DNA repair and activation of the SOS response. The SOS response is a common stress response in bacteria, driving upregulation of proteins involved in DNA repair (i.e. the SOS-genes)[387,388]. This response is triggered by the binding of RecA to single stranded DNA (ssDNA), which subsequently triggers autoproteolysis of LexA. LexA is a transcriptional repressor, which, under normal growth conditions, is bound to the promoter regions of the SOS-genes, thereby suppressing their expression. Upon proteolysis, LexA is unable to bind the DNA and the SOS-genes are expressed. Activation of the SOS-response has been shown to be essential for prolonged nucleoid compaction[381,383], although it remains unclear how exactly this is mediated. It remains also unclear whether RecA, in addition to SOS activation, plays a more direct role in nucleoid remodeling[381,383]. RecN is one of the proteins that is upregulated by the SOS response[387]. RecN is a member of the SMCs family and has been shown to act as a cohesin-like protein, promoting DNA-DNA interactions[389]. RecN has been shown to contribute to DNA compaction in response to UV irradiation[382,383]. Furthermore, Vickridge et al showed that RecN promotes the alignment of sister chromosomes in response to DNA damage[378].

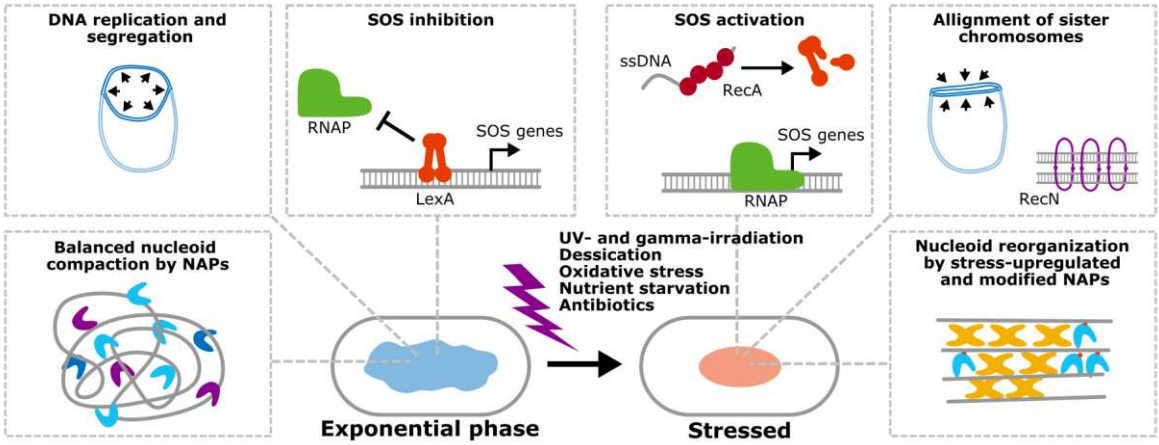

Figure 1.33 Molecular mechanisms driving stress-induced nucleoid remodeling. *Stress-induced nucleoid remodeling is typically characterized by a transient compaction of the nucleoid. Several factors have been proposed to contribute to this reorganization: RecA mediated SOS activation resulting in the expression of proteins involved in recovery from DNA damage; Alignment of sister chromosomes by intrinsic abilities of homologous DNA segments to recognize each other and by the action of the cohesin–like protein RecN; Tight packing of the nucleoid by stress-upregulated and modified NAPs.*

An increasing number of studies indicates that NAPs play an important role in stress-induced nucleoid remodeling[384]. In eukaryotic cells, it is well-known that changes in histone composition and histone modifications are involved in stress signaling and the regulation of DNA repair processes. In particular, phosphorylation of H2AX is a well-known marker of DNA damage and has been shown to recruit DNA repair proteins and modulate the mobility of the DNA[390–392]. Moreover, Hauer et al showed that, in yeast, overall histone levels drop in response the DNA damage leading to increased DNA mobility, facilitating homology search[393]. Similarly, in bacteria, modifications of NAPs and changes in the expression levels of different NAPs have been shown to contribute to a swift stress response. Dps (DNA-binding protein from starved cells) is a multifunctional NAP that is upregulated under stressed conditions, including oxidative stress and nutrient starvation. In addition, there is likely an important role for HU in stress-induced nucleoid remodeling. *E. coli* cells deficient in HU show increased sensitivity to UV-[352,355,369] and gamma-irradiation[356], which has been attributed to the role of HU in DNA repair[369] and SOS activation. Furthermore, Remesh et al. showed that HU mediates nucleoid remodeling in *E. coli* under acid stress[357]. Finally, recent studies suggest that phosphorylation and acetylation of HU could play a role stress-resistance[365,375,394].

In my thesis, I will focus on two sources of stress: entry into stationary phase and exposure to high doses of UVC irradiation.

1.7.2.1 Nucleoid reorganization during stationary phase

Stationary phase is a bacterial growth phase in which the rate of cell growth is equal to the rate of cell-death. This phase is characterized by a high cell density, restricted nutrient availabilities and/or other growth limiting factors. In order to survive, bacteria lower their metabolic activity and adopt specific morphological changes, which protect them from starvation and also render them more resistant to other sources of stress. Nevertheless, stationary phase bacteria still suffer from oxidative stress, which limits their ability to restart growth when fresh nutrients are provided[395].

Investigations of the stationary phase nucleoid have revealed that it is more compact and less mobile than the exponential phase nucleoid[337]. One of the key regulators of this compaction in *E. coli* is Dps, whose expression is drastically upregulated in stationary phase[396]. Dps is a dodecameric protein, which, like HU, binds the DNA mostly in a non-specific manner and has the ability to condense the

DNA[323,396,397]. Surprisingly, DNA condensation by Dps has little effect on gene transcription during stationary phase[397]. In addition to its DNA-binding capabilities, Dps exhibits ferroxidase activity which contributes to the neutralization of toxic chemical species. Both these activities of Dps, DNA-binding and ferroxidase activity, have been shown to be essential for its protective abilities[398]: Dps mutant cells have worse survival during stationary phase and are more sensitive to oxidative-, temperature- and pH stress, and UV-and gamma-irradiation[398,399]. HU has also been shown to play a role in the reorganization of the stationary phase nucleoid. In *E.coli* cells entering stationary phase, there is a shift from HUαα homodimers to HUαβ heterodimers, which has been associated with increased DNA condensation and the maintenance of negative supercoiled regions[331,358,400].

1.7.2.2 Nucleoid remodeling in response to UVC irradiation

UVC (200-280 nm) irradiation is a popular method used to induce DNA damage in laboratory settings. Natural UVC light, coming from the sun, is mostly retained by the ozone layer so that it does not reach earth. Luckily, because it is highly mutagenic. UV irradiation damages the DNA via both direct and indirect effects[401]. Direct damage is the result of absorption of UVC photons by the DNA bases, which leads to the formation of pyrimidine dimers, 6-4 photoproducts and Dewar isomers[402,403]. Such structures distort the DNA helix hindering DNA replication and transcription, and are lethal if not repaired. Indirect damage is the result of UVC induced ROS formation, mainly singlet oxygen, which leads to the oxidation of guanine bases creating 8-Oxoguanine lesions[404,405]. In addition, ROS can contribute to the formation of single-strand breaks. Double-strand breaks may also be formed after UV irradiation, not as a direct effect of the irradiation but as a consequence of DNA repair and stalled DNA replication[406,407]. In addition to DNA damage, UVC induced ROS formation may also lead to protein damage[408].

In response to UVC irradiation, bacteria activate their SOS response, upregulating the production of DNA repair proteins, such as RecA and UvrA[382,383]. Studies in *E. coli* revealed that, after sub-lethal irradiation, the nucleoid first adopts a highly compacted organization after which it becomes dispersed along the cell before it recovers its normal morphology and the cells restart growth[380,382,383]. This remodeling was shown to be dependent on SOS activation as described above. It is not fully understood how these different stages of nucleoid remodeling are related to DNA repair and recovery. Odsbu and Skarstad proposed that the initial compaction phase serves to stabilize the damaged DNA and repair severe lesions, such as double stranded breaks, while the repair of other lesions happens during the dispersed stage[383]. This hypothesis is in line with the observation that cells deficient in DNA repair proteins reach the dispersed stage but are unable to restart growth[382,383]. HU likely plays a role in the nucleoid reorganization and DNA repair following UVC irradiation as cells deficient in HU show increased sensitivity to irradiation[352,355]. A possible activity of HU could be the stabilization of damaged DNA[369].

1.7.3 Deinococcus radiodurans as model system for nucleoid remodeling

Deinococcus radiodurans is a relatively large spherical non-pathogenic bacterium with an extraordinary capacity to survive extremely harsh conditions. *D. radiodurans* was discovered in 1956 after it had spoiled a can of meat that had been sterilized by X-rays[409]. Further studies revealed that *D. radiodurans* can survive diverse types of genotoxic stress, including high doses of ionizing- and UV-radiation, desiccation and oxidizing agents. Why *D. radiodurans* has evolved such an extreme resistance to radiation remains unclear, as such conditions are not found on earth. One explanation is that its radiation resistance is simply a side-effect of its resistance to desiccation[410]. There are multiple factors that have been proposed to contribute to the remarkable stress-resistance of *D. radiodurans* including an efficient DNA repair machinery, an extensive antioxidant system protecting the proteome and a special nucleoid organization.

The genome of *D. radiodurans* is composed of two chromosomes (chromosome I and II), a megaplasmid and a small plasmid, which are all present in multiple copies per cell (4 - 10)[411,412]. This multiplicity has been proposed to facilitate DNA repair by homologous recombination, thereby contributing to the remarkable resistance of *D. radiodurans*. Harsojo et al, however, showed that the irradiation resistance of *D. radiodurans* is not influenced by its genome multiplicity (5 or 10 copies)[412], although this does not exclude that it is beneficial to have more than one copy. These chromosomes and plasmids are organized in the nucleoid inside an unusual ring-like configuration, which had originally been proposed to contribute to radioresistance[413,414]. Moreover, it had been speculated that inside this ring-like configuration the chromosome copies are pre-aligned to facilitate DNA -repair[415,416]. These two hypotheses, however, have since been proven wrong, although a transient alignment of chromosome I loci was observed after exposure to gamma-irradiation[411,417]. Nevertheless, it does appear that radioresistant species have more compact nucleoids than radiosensitive species, which has been proposed to limit diffusion of damaged DNA fragments[417].

In *D. radiodurans*, organization of the genomic DNA inside the nucleoid is achieved by a limited number of NAPs, with HU and DNA Gyrase (DrGyr) being the main regulators of nucleoid organization[418]. In contrast to *E. coli*, *D. radiodurans* only expresses one HU variant, which is essential for its viability[418,419]. Depletion of HU from *D. radiodurans* cells results in nucleoid expansion, DNA fragmentation and ends with cell lysis[419]. Studies on the activity of HU in D. radiodurans revealed that the interaction between HU and the DNA is mainly transient[370] and that HU can promote both DNA compaction as well as DNA stiffening in a concentration dependent manner[359]. DrGyr is a type II topoisomerase which is composed of two subunits GyrA and GyrB and mediates DNA relaxation and supercoiling[418,420]. In addition to HU and DrGyr, *D. radiodurans* expresses two Dps variants, Dps1 and Dps2. Dps1 is present independent of the growth phase[418], unlike Dps in *E.coli* which is mainly expressed during stationary phase. Dps2, on the other hand, is upregulated in response to oxidative stress[421,422]. These Dps variants are not essential for the viability of *D. radiodurans* but likely contribute to its extreme resistance by regulating the metal concentrations inside the cell[419,423,424].

The remarkable resistance of *D. radiodurans* has motivated many studies to investigate its stress-response. Proteomic studies show that in response to stress a large number of proteins are upregulated, including proteins involved in cell wall synthesis, transcription, iron homeostasis and DNA repair[422,425]. In *D. radiodurans*, this stress response is not regulated by the classical SOS response. Although *D. radiodurans* does express both functional RecA and LexA, these proteins do not control the upregulation of repair proteins in response to stress[426–428]. Instead, the expression of these genes is controlled by IrrE, also called PprI, and DdrO. IrrE is a metalloprotease that is activated by oxidative stress (and possibly other mechanisms) and subsequently cleaves DdrO, the transcriptional repressor of the radiation/dessication regulon (RDR)[428–430]. This regulon encodes classical DNA repair proteins, such as RecA, as well as *D. radiodurans* specific proteins, such as PprA and DdrC[379,430]. PprA is one of the proteins that is crucial for the stress-resistance of *D. radiodurans*. PprA has been shown to interact with DNA-gyrase and RecA and is expected to thereby regulate DNA repair and genome maintenance after irradiation[420,431,432]. DdrC is a DNA binding protein that has been shown to be rapidly recruited to the nucleoid in response to gamma-irradiation. The function of DdrC has been proposed to be multifold[379,433]: protection of the DNA against nucleases; compaction of the nucleoid to limit dispersion of fragmented DNA; facilitation of DNA repair.

Whether HU also plays a role in the stress-response of *D. radiodurans* remains to be investigated. Given that the activities of HU in *D. radiodurans* appear very similar to those of HU in other bacteria under normal growth conditions, its role under stressed-conditions is presumably also similair. Notably, Hou et al. showed that HU can be phosphorylated and that the phosphorylated status of HU in *Deinococcus* affects its UV- and oxidative stress resistance[365].

Although *D. radiodurans* is very resistant, it is not unbeatable. What happens when the DNA and protein damage is too severe and cells are unable to recover? Devigne et al. showed depletion of DdrO triggers an apoptotic-like cell death with fragmented DNA, misplaced nucleoid and blebbing membranes[434]. They propose that in conditions where recovery is impossible, IrrE activity is prolonged due to persisting oxidative stress, preventing recovery of normal DdrO levels thereby triggering an apoptosis-like cell death in *D. radiodurans*[434].

In additions to its own scientific interest, *D. radiodurans* presents a good model system to study stress-induced nucleoid remodeling. Firstly, it is a relatively large bacterium, which facilitates imaging studies. Secondly, *D. radiodurans* has a low number of NAPs, which facilitates the study of the role of these NAPs in nucleoid organization[418]. Thirdly, previous work of the lab has characterized in detail the organization of its nucleoid under normal growth conditions and various studies are available on the changes in the nucleoid in response to stress. Together, these factors make *D. radiodurans* a good model system to study stress-induced nucleoid remodeling.

1.8 Thesis objectives

The central theme of my PhD work was quantitative PALM. The wide-spread use of quantitative PALM is currently limited by suboptimal fluorophore behaviors and imperfect analysis tools. Aiming to boost the application of quantitative PALM experiments, most of my thesis work has been dedicated to the photophysical characterization of PTFPs with the goal to develop strategies to optimize their behavior for SMLM. In addition, I have worked on the application of sptPALM to study stress-induced nucleoid remodeling *D. radiodurans*, exploring different analysis strategies to unravel the role of HU in nucleoid organization.

1.8.1 Photophysical characterization of PTFPs

Most of my work has been focused on the popular PCFP mEos4b. This work builds on previous findings of the lab showing that 488 nm light can be used to suppress long-lived blinks and boost sptPALM[217], which inspired the idea that 488 nm light might also benefit qPALM (continuing the PhD work of Daniel Thédié). This idea motivated extensive characterization of the effects of 405 and 488 nm light on the blinking behavior and PCE of mEos4b. Furthermore, the team led by Bernard Brutsche uncovered by NMR spectroscopy that the ground-state of green-state mEos4b is heterogeneous, which motivated investigations of the effects of this heterogeneity on the photophysical behavior of mEos4b.

In addition to mEos4b, part of my thesis is dedicated to the study of the RSFP rsEGFP2, which has been identified as a promising candidate for cryoPALM. Investigation of the switching behavior of rsEGFP2 at CT was the PhD work of Angela Mantovanelli, who defended her thesis in March 2023. Her work, together with work by Oleksandr Glushonkov and Virgile Adam, revealed intriguing switching behaviors that could not be explained by existing photophysical models. In parallel to this project, work lead by Martin Byrdin revealed that the apparent brightness of EGFP and rsEGFP2 at CT is strongly affected by triplet state formation. I contributed to the development of a new photophysical model of rsEGFP2 by discussion and use of simulations to examine what models could explain the observed behaviors.

In support of these photophysical studies, my thesis starts with the discussion of the strengths and drawbacks of different immobilization strategies that can be used to study FP photophysics. This work benefited from a collaboration with the Tinnefeld lab (LMU, Munich), to explore the use of DNA-origamis for the photophysical characterization of mEos4b.

To sum up, the objectives of this part are the following:

1. Compare different immobilization platforms for the photophysical characterization of FPs
2. Characterize the effects of different illumination conditions on the blinking behavior and photoconversion efficiency of mEos4b to build a refined photophysical model
3. Develop a photophysical model explaining the photophysical behavior of rsEGFP2 at cryogenic temperature with the support of simulations

1.8.2 Application of sptPALM to study stress-induced nucleoid remodeling

In addition to photophysical studies, my thesis includes the application of sptPALM to the investigation of stress-induced nucleoid remodeling in *D. radiodurans*. Unraveling the molecular mechanisms driving nucleoid organization in response to DNA damage is one of the central themes in the lab. This work is mainly driven by Pierre Vauclare and Joanna Timmins, who characterized in detail the morphological changes if the nucleoid of *Deinococcus radiodurans* in response to UVC irradiation. This work also builds on previous work of the lab by Kevin Floc'h and Françoise Lacroix who characterized the cell and nucleoid morphology of *D. radiodurans* under normal growth conditions[370].

While this project is motivated by a biological question, namely how nucleoid remodeling is orchestrated in response to stress, my work is mainly focused on the practical aspect: analysis and interpretation of the sptPALM data.

So, the objectives of this part are the following:

1. Find the most appropriate methods to collect and analyze spt data in *D. radiodurans*
2. Characterize the diffusion dynamics of HU under normal growth conditions (exponential and stationary phase) and in response to UVC irradiation

2 Material and Methods

2.1 Fluorescent proteins

Plasmids encoding mEos4b, mEos3.2, pcStar and Dendra2 were available in the lab. Plasmids encoding mEos4b with an N-and C-terminal cysteine for maleimide labeling were designed and cloned by Virgile Adam. All protein constructs carried a His-Tag to facilitate purification. Proteins were expressed and purified as described previously[218] with the help of Salvatore De Bonis and Virgile Adam. Purified proteins were stored at -80°C.

2.2 Bacterial strains and culture conditions

A genetically-engineered *D. radiodurans* strain expressing HU-mEos4b from the endogenous HU promoter was prepared by Claire Bouthier de la Tour and Fabrice Confalonieri (Institute for Integrative Biology of the Cell, Gif-sur-Yvette, France). A WT strain (GY9613, ATCC 13939, strain R1) and *oriC/ter*-labeled strains[370,411] (GY15787 and GY15800) were available in the lab. All strains were grown in a shaking incubator at 30°C in 2xTGY broth (Tryptone-Glucose-Yeast extract) supplemented with the appropriate antibiotic (50 µg/ml hygromycin for the HU-mEos4b expressing strain and 3.4 µg/ml chloramphenicol for the *oriC/ter*-labeled strains). For microscopy experiments, a pre-culture was started in the morning the day before the experiment. Dilutions of this initial culture were then grown overnight to exponential phase (OD_{600} ~0.3-0.6) or early stationary phase (OD_{600} >3, ~24h culture). Alternatively, notably for *oriC/ter*-labeled strains, a pre-culture was grown overnight and was diluted 60 times in fresh 2xTGY the next morning and grown for approximately 5 hours to reach exponential phase for experiments in the afternoon.

The HU-mEos4b strain showed no growth defects or abnormal morphologies, and showed WT-like resistance to irradiation. Furthermore, imaging revealed that HU-mEos4b localized with the DNA (**Figure 2.1**), as is expected for HU. Given that HU is an essential protein in *D. radiodurans*, these findings indicate that HU-mEos4b is functional.

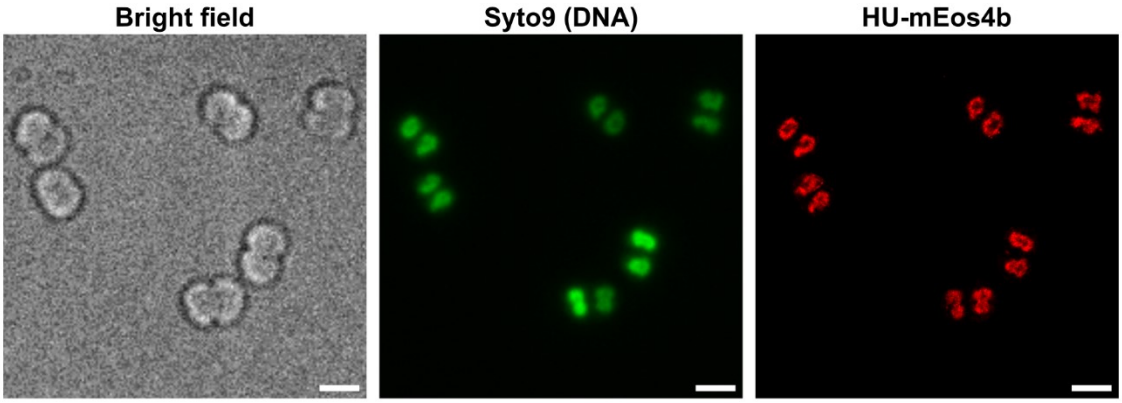

Figure 2.1 HU-mEos4b localizes to the nucleoid. *DR cells expressing HU-mEos4b were stained with the DNA stain Syto9 to evaluate the localization of HU-mEos4b. First, a bright field image was acquired, after which syto9 was imaged using 488 nm light, before HU-mEos4b was imaged using the typical sptPALM imaging scheme described below. Scale bar = 3 µm.*

Labeling of the *oriC* and *ter*-sites is based on the *parS*/ParB system (**Figure 2.2**). *parS* is a short DNA sequence that binds ParB. When bound to *parS*, ParB proteins spread on the DNA, forming complexes that can be seen as foci by fluorescence microscopy if the ParB protein is fused to a FP (**Figure 2.2B**). In *oriC- or ter*-labeled strains, multiple *parS* sites were inserted close to either the *oriC*

or the *ter* sites of chromosome I, and ParB-GFP was expressed from a plasmid under the control of a constitutive promoter. In addition, these strains expressed HU fused to mCherry for visualization of the nucleoid.

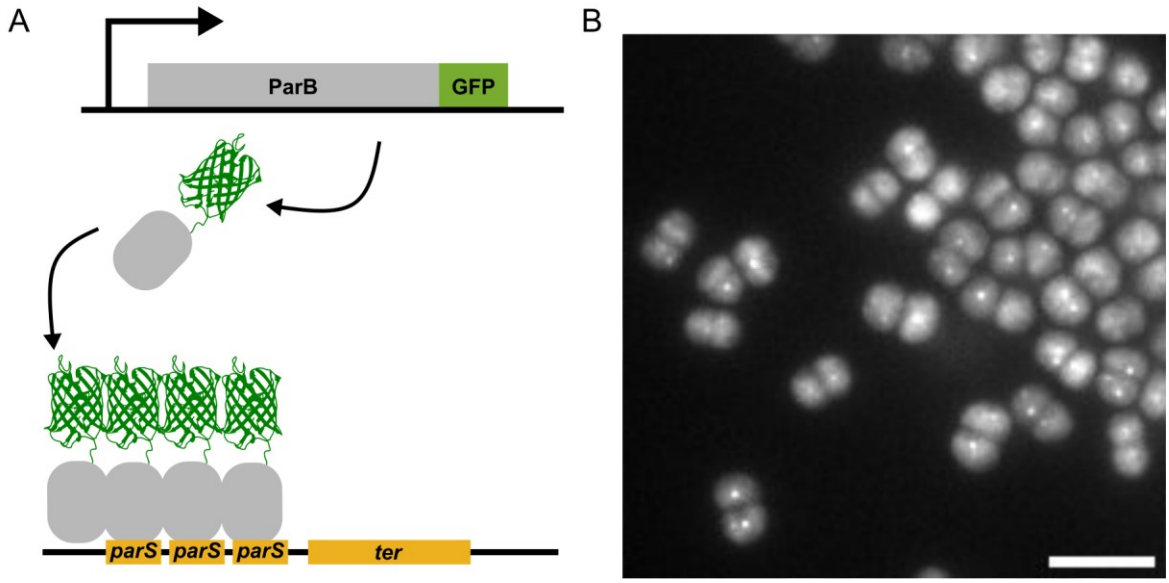

Figure 2.2 Labeling of the oriC and ter sites using the parS-ParB system. *A) Illustration of the usage of the parS/ParB system to label the oriC and ter sites. B) Fluorescence image of ter labelled D. radiodurans cells. The high fluorescence background in the cells arises from freely diffusing ParB-GFP expressed in excess from a plasmid. Scale bar = 5 µm.*

2.3 Mammalian cell lines and culture conditions

The U2OS CRISPR cell line expressing Nup96-mMaple was purchased from Cell Line Service. A U2OS cell line expressing Nup96-mEos4b was created by CRISPR technology by Pascale Tacnet, Philipe Frachet, Virgile Adam and Oleksandr Glushonkov. Cell cultures were maintained by Pascale Tacnet. Cells were grown at 37°C and 5% CO_2 in growth medium (DMEM containing Glutamax and 10% fetal calf serum). For microscopy experiments, cells were seeded on ozone cleaned high precision cover glasses (No. 1.5H, Marienfeld) and grown for two days to a confluency of ~60%.

2.4 Sample preparation for microscopy experiments

2.4.1 Preparation of polyacrylamide samples

Purified protein was diluted into a 1:1 mixture of 30% Acrylamide/Bis-acrylamide solution (29:1 v/v or 19:1 v/v, Invitrogen) and appropriate buffer (Tris buffer (1.5 M, pH 7-8.4) or McIlvaine (MI) buffer (1 M phosphate buffer and 0.5 M citric acid, pH 5-6)). The final FP concentration was in the µM range for ensemble measurements or in the nM range for single-molecule measurements. In addition, nanodiamonds (Adámas Nanotechnologies) were added to the mixture to serve as fiducial markers for single-molecule measurements. Polymerization was initiated by addition of ammonium persulfate (APS) and tetramethylethylenediamine (TEMED), after which 10 µl of sample was sandwiched between two ozone cleaned cover glasses. Samples were left to polymerize for 10 minutes at RT. The final thickness of the sample was ~10 µm.

Polyacrylamide samples contained minimal amounts of fluorescent impurities as shown in **Figure 2.3**. For comparison, on a typical sample, containing mEos4b, more than 10000 clusters (often containing multiple localizations) were detected during a 20-minute acquisition.

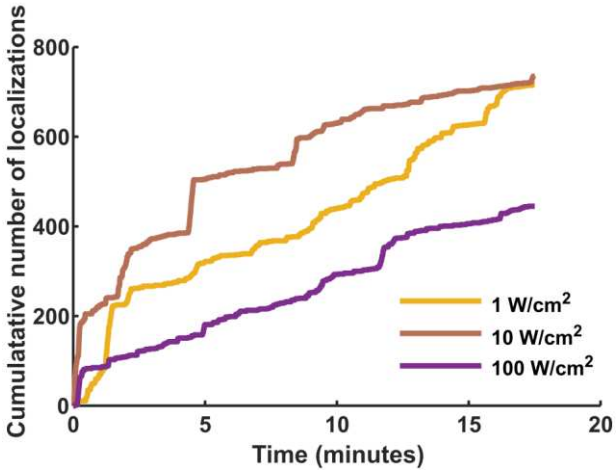

Figure 2.3 Polyacrylamide samples contain minimal fluorescent impurities*. Cumulative number of localizations detected on a PAA sample without any mEos4b molecules using 500 W/cm^2 561 nm light and 1-100 W/cm^2 405 nm light.*

2.4.2 Preparation of DNA origami samples

2.4.2.1 Sample design

In collaboration with the Tinnefeld lab (LMU, Germany), we set-out to develop a protocol to immobilize mEos4b using DNA-origamis for photophysical studies. The sample design is shown in **Figure 2.4A**. We chose to use the new rectangular origami (NRO) as a template structure because we hypothesized that the shape of the rectangular origami would provide a barrier between mEos4b and the cover glass, preventing unwanted interactions. The basic NRO template was modified to have a 21nt docking strand to bind DNA-labeled mEos4b and three 21nt docking strands to bind DNA labeled dye molecules (so called 'reference dye'). The distance between the docking strands for the FP and dye molecules was set to be 35 nm to prevent unwanted interactions. For immobilization of the origami on a BSA-biotin – streptavidin surface, six biotinylated strands were incorporated into the origami design.

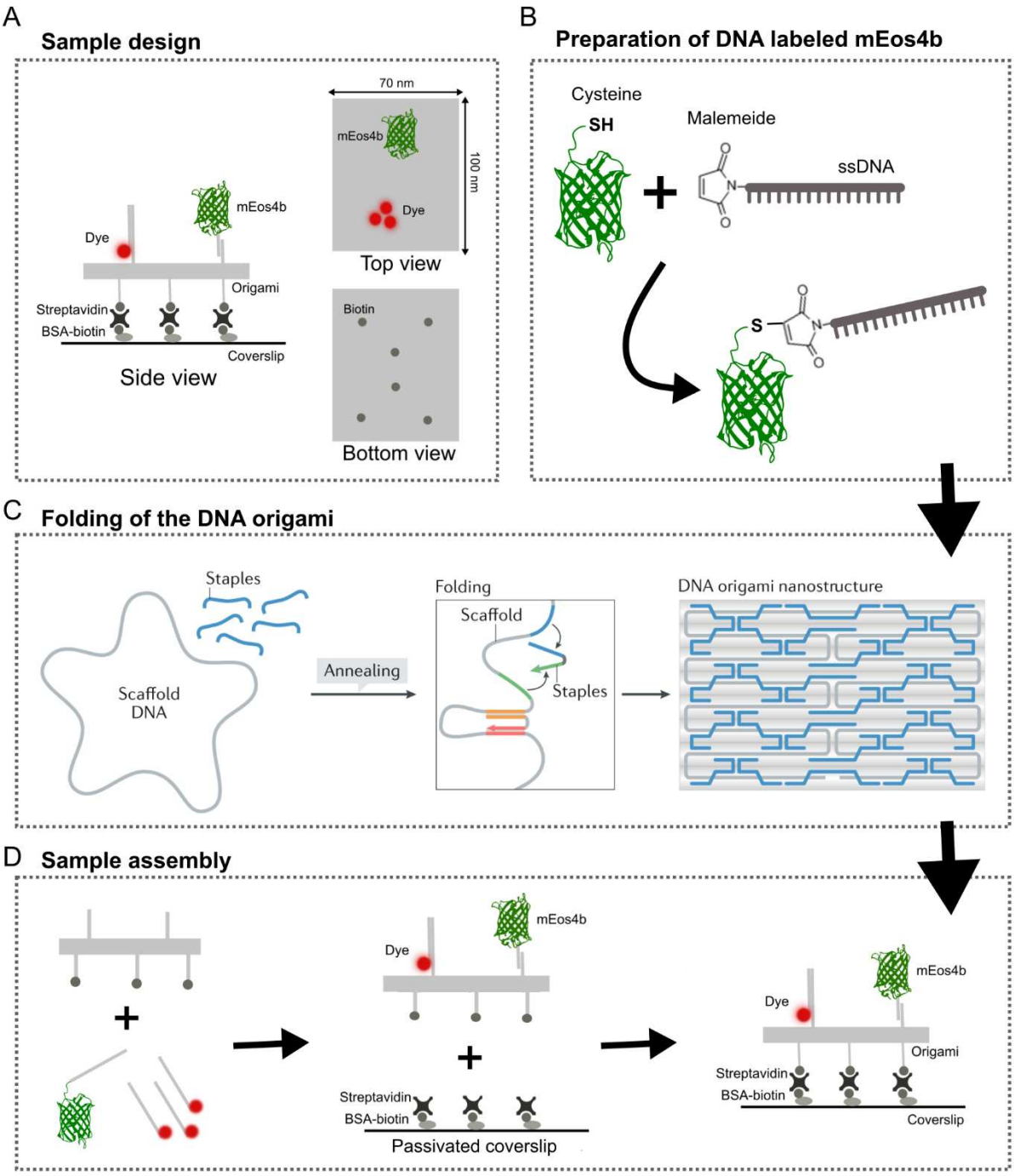

Figure 2.4 A DNA-origami based platform for photophysical studies. *A) Sample design based on the NRO. B) Labeling of mEos4b with ssDNA via maleimide chemistry. C) Folding of DNA origamis (figure adapted from[435]). D) Sample assembly for microscopy experiments. See text for details.*

2.4.2.2 Preparation of DNA labeled mEos4b

Purified mEos4b (100 µM) containing a free cysteine at its N- or C-terminus was incubated with 5 mM TCEP (tris(2-carboxyethyl)phosphine) at neutral pH to reduce the free cysteine making it available for reaction with maleimide. After 30 minutes, 1 mM of maleimide labeled ssDNA (Biomers, TTTGTGATGTAGGTGGTAGAGGAA) was added to the mixture and left to incubate for 3 hours at RT (**Figure 2.4B**). We attempted to remove the excess ssDNA from the sample by loading the His-tagged protein construct on a nickel column to wash out the free ssDNA. However, this step was complicated by poor binding of the protein construct to the nickel column (discussed in Results).

Alternatively, we tried to remove the free DNA by ion exchange but the DNA labeled protein aggregated on the column (see Results).

2.4.2.3 Folding and purification of the DNA origamis

All DNA was available in the Tinnefeld lab. NRO DNA origamis were produced by mixing p7249 scaffold with unmodified staples and biotinylated staples (10x molar excess) in folding buffer (5 mM Tris-HCl pH 8, 1 mM EDTA, 20 mM $MgCl_2$) (**Figure 2.4C**). The folding reaction was carried out in a thermocycler, which was first heated to 80°C to denature the DNA after which the temperature was gradually decreased from 60°C to 4°C (3 min 12 s per °C) to promote annealing. After the folding was completed, excess staples were removed using 100k Amicon spin filters.

2.4.2.4 Sample assembly

DNA origamis were assembled by mixing 1nM folded origamis with 50 nM DNA-labeled AF647 and 50 nM DNA-labeled mEos4b. AF647 was chosen as reference dye because it exhibits minimal photobluening compared to other organic dyes, including ATTO647N, which was used in the original eYFP study[295,436]. After 2-3 hours of incubation at RT, unbound dye molecules and proteins were removed using 100k Amicon spin filters. It is important to remove the excess dye and FP from the sample because these may stick non-specifically to the BSA-biotin – streptavidin surface and appear as impurities.

Flow chambers were constructed from a glass slide, double sided scotch tape (or parafilm) and a high precision cover glass (**Figure 2.5**). The chambers were passivated with biotinylated BSA (0.5 mg/ml in PBS, 3 min at RT). Next, after the chambers were washed 3 times using PBS, Streptavidin (0.5 mg/ml) was loaded into the chambers. After 3 minutes of incubation, the chambers were washed with imaging buffer (50 mM Tris-HCl pH 7.4, 20 mM $MgCl_2$, 5 mM NaCl) and the assembled DNA-origamis were loaded on the sample. After 5 minutes of incubation, unbound origamis were removed by washing 3 times with imaging buffer, after which the chambers were sealed using picodent.

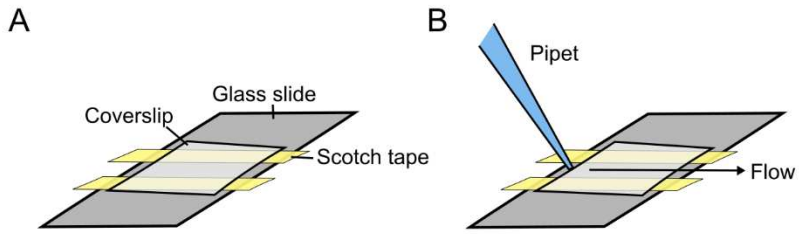

Figure 2.5 Flow chambers. *A) Flow chambers were constructed from a glass slide, double sided scotch tape and a coverslip. B) Samples were applied on one side of the chamber and aspirated through the chamber by use of a tissue (not shown in the scheme).*

We verified by Atomic Force Microscopy (AFM, Germany) that the origamis were folded properly (**Figure 2.6A**). Furthermore, we evaluated the incorporation and accessibility of the docking strands on the origamis by labeling the origamis with Atto647N as a reference dye and Cy3B substituting mEos4b (**Figure 2.6B**). Fluorescence imaging revealed that the dyes co-localized (**Figure 2.6B**), verifying the incorporation and accessibility of the docking strands in the origamis.

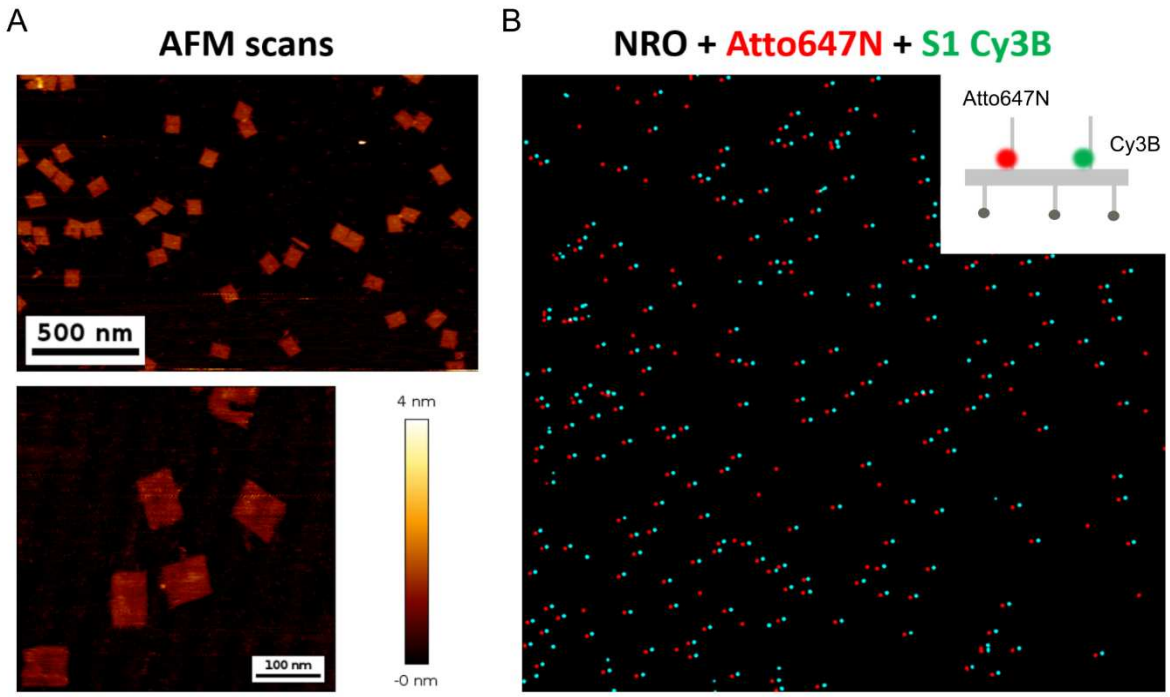

Figure 2.6 Evaluation of the DNA origamis by AFM and fluorescence imaging. *A) AFM scans of assembled DNA origamis validating that the origamis are properly folded. B) Colocalization of Atto647N (as reference dye, red) and Cy3B (as FP substitution, blue) verifies the incorporation and accessibility of the docking strands on the origamis. Note that the distance between the Atto647 and Cy3B localizations does not reflect the distance between the dyes on the origamis but is due to a chromatic shift.*

2.4.3 Preparation of U2OS Nup96-FP samples

U2OS cells expressing Nup96-mEos4b or Nup96-mMaple were grown directly on ozone cleaned cover glasses. After the cells had reached a confluency of ~60%, they were fixed according to a previously published protocol[244]. In brief, samples were rinsed 3 times with PBS after which they were prefixed for 30 s in 2.4% paraformaldehyde (PFA, w/v, Electron Microscopy Sciences) in PBS. Next, samples were permeabilized for 3 minutes in 0.4% (v/v) Triton X-100 in PBS and subsequently fixed for 30 minutes at 37°C in 2.4% PFA. Finally, after blocking the PFA using 100 mM NH4Cl solution, samples were rinsed with PBS and stored in the fridge for up to a week.

Although we did not perform immuno-labeling, we noticed that permeabilization of the cells with Triton X-100 was still useful to reduce the auto-fluorescence from the cells.

To prepare the samples for imaging, the coverslips with cells were placed on top of concave glass slides (Sigma Aldrich) containing 100 µl PBS or Tris-HCl buffer (50 mM, pH 7-8). Excess liquid was removed by gently pressing the coverslip while taking care not to trap any air bubbles. Samples were sealed with picodent twinsil.

2.4.4 Preparation of *D. radiodurans* samples

Bacterial cultures in exponential (OD_{600} between 0.3 and 0.6) or stationary phase (24h growth, OD_{600} >3) were washed 3 times by centrifugation (3000g for 3 minutes) and resuspension of the cell pellet in M9DR minimal medium (45.5 mM Na_2HPO_4, 22 mM KH_2PO_4 and 15.1 mM $(NH_4)_2SO_4$, pH 7.3). Following the final washing step, the cells were resuspended in 20-100 µl M9DR, depending on the size of the pellet. 10 µl of cell suspension was then placed on an ozone cleaned coverslip and the cells were left to sediment for 2 minutes, after which the excess liquid was removed. After the

samples had dried (2-4 minutes), 10 µl 1.5% (w/v) low melting agarose (LMA, Biorad) in M9DR was placed on top of the sedimented cells and a glass slide was placed on top to evenly distribute the LMA. Samples were sealed with picodent twinsil and imaged within 20 minutes.

For estimation of the contribution of the localization uncertainty to the apparent diffusion of HU-mEos4b, exponential phase cells expressing HU-mEos4b were chemically fixed by incubation in 3.7% PFA for 1 hour at RT, before proceeding with the sample preparation as described above.

The washing steps were necessary to limit autoblinking, as described previously[437]. Nevertheless, despite the washing, some samples still showed strong autoblinking (**Figure 2.7**). The reason for this is not understood. Cells with strong autoblinking were discarded from the analysis.

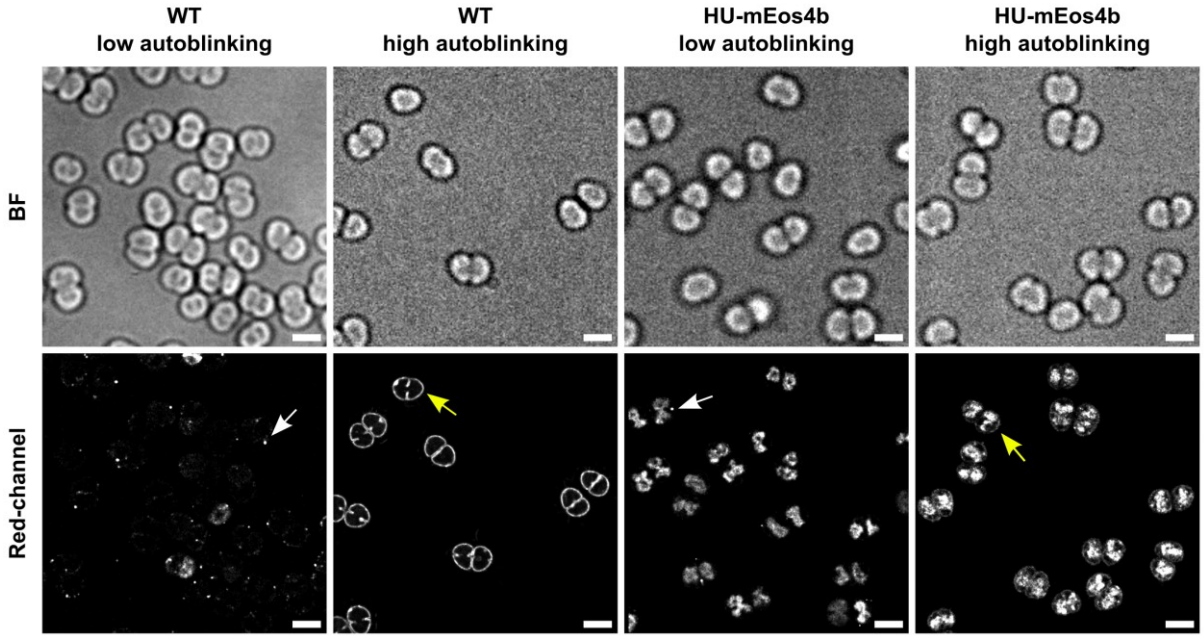

Figure 2.7 Autoblinking of Deinococcus radiodurans. *PALM data of WT and HU-mEos4b labeled DR cells were collected under standard imaging conditions (see below, 40,000-60,000 frames). Autoblinking levels were highly variable between samples, but could be controlled, to some extent, by washing the cells in M9DR medium prior to imaging. Autoblinking sometimes appeared as isolated clusters of localizations (white arrows) and sometimes as a smooth staining of the cell membrane (yellow arrows). Scale bar = 2 µm.*

We noticed that it was important to image the samples directly after their preparation, because the diffusion behavior of HU-mEos4b changed (increased slightly) with time (**Figure 2.8**). This effect was independent of whether it were the same cells (as in **Figure 2.8**), different cells or even different samples that were imaged at different times. This could potentially be explained by the absence of nutrients inside the M9DR, causing the cells to starve; or by the limited availability of O_2 inside the mounted sample, potentially acting as a source of stress.

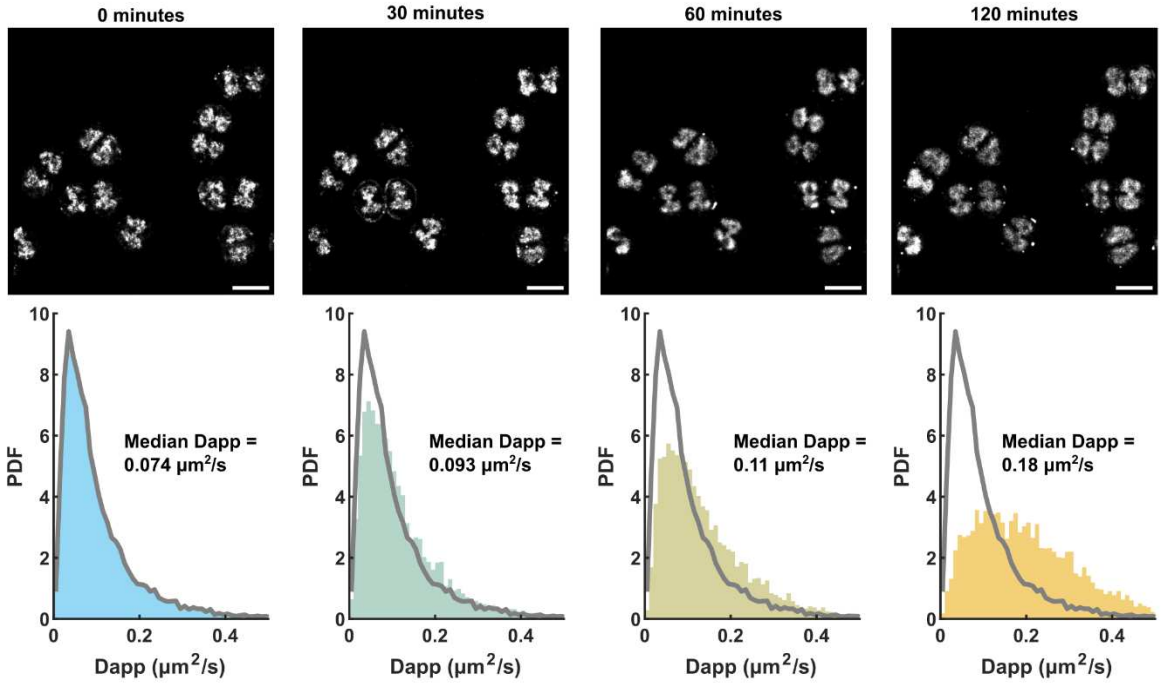

Figure 2.8 HU-mEos4b diffusion is affected by the sample age. *SptPALM data was collected directly after sample preparation (0 minutes) and after 30, 60 and 120 minutes. Shown are super- resolved images and histograms of the extracted diffusion coefficients. The grey lines in the histograms correspond to the distribution of diffusion coefficients at 0 minutes. Scale bar = 3 µm.*

2.4.4.1 UVC irradiation

To prepare *D. radiodurans* cells for irradiation experiments, exponential or stationary phase bacteria were washed two times with M9DR medium as described above, after which they were diluted to an OD_{600} in between 0.3 and 0.5 in M9DR and transferred into a 6-well plate (1 ml per well). It was important to wash the cells because TGY medium strongly absorbs UVC light. Cultures were diluted to the same OD_{600} (~0.3) to minimize shielding effects (multiple layers of cells with the top layer shielding the bottom layers from irradiation). The cells were irradiated with UVC light at a dose rate of approximately 24 J/m^2/sec using a Stratalinker UV crosslinking oven equipped with G5 Tube 8W TUV Germicide 254nm UVC Osram lamps. The total irradiation dose was 1.9 KJ/m^2 (sub-lethal dose) or 12 KJ/m^2 (lethal dose). Importantly, the UVC irradiation appeared to have only minimal effect on the fluorescence of mEos4b (**Figure 2.9**), indicating that the FP was not bleached nor severly damaged. After irradiation, the cells were spun down and resuspended in fresh 2xTGY medium and returned to the shacking incubator for recovery. A sample was taken immediately after irradiation (T0) and then after 1, 2, 3, 6 and 24 hours of recovery for imaging and prepared as described above.

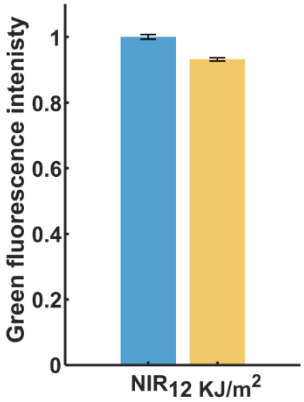

Figure 2.9 UVC irradiation has minimal effect on the fluorescence of mEos4b. *Purified mEso4b was diluted in M9DR medium (final concentration 1.5 mg/ml) and the green fluorescence intensity (excitation 470-489 nm, emission 510-550 nm) of the sample was measured before and after irradiation with 12 KJ/m^2 UVC light ('lethal' dose) using a plate reader (CLARIOstar). A blank sample (M9DR only) was used for background substraction.*

2.5 Microscopy

2.5.1 Microscope set-up

Experiments were performed on a home-built PALM set-up (single-molecule photophysics and ensemble measurements) or on a commercial Abbelight set-up (sptPALM experiments) (**Figure 2.10**).

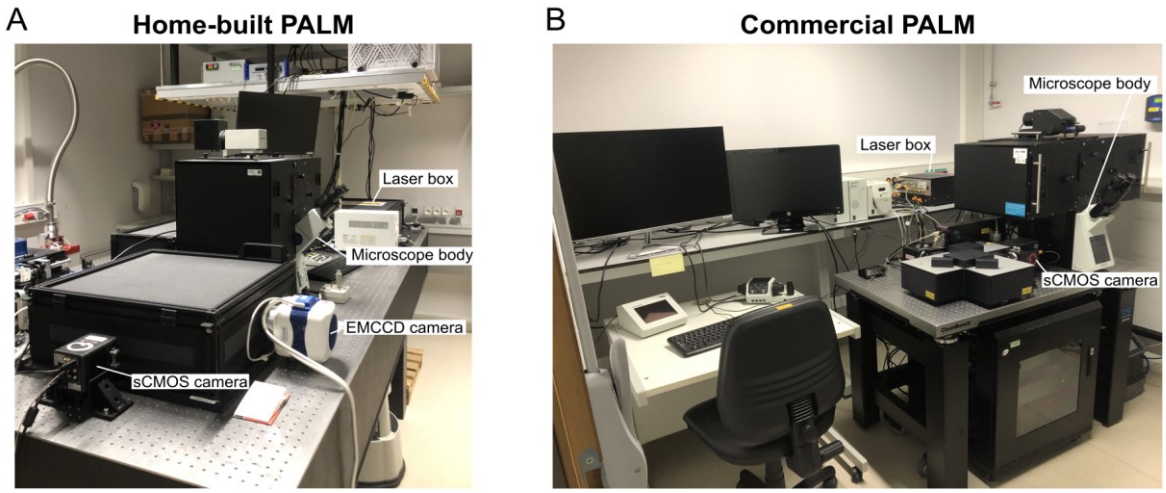

Figure 2.10 PALM microscopes*. Overviews of the home-built (A) and commercial PALM (B) set-ups, with their main components labeled (laser box, camera and microscope body).*

The home-built PALM set-up is based on a commercially available Olympus IX81 inverted microscope equipped with a x100 1.49 NA oil-immersion apochromatic objective lens (Olympus). Widefield illumination is achieved by focusing of the laser beams at the back focal plane of the objective. A continuous focus system (ZDC, Olympus) is available to maintain a constant focus during long acquisitions. The lasers are localized in a laser box; six lasers are available: 405-nm (CrystaLaser), 488-nm (Oxxius), 532 nm (Cobolt), 561 nm (Cobolt), 643 nm (Oxxius) and 730 nm (Obis). The lasers are co-aligned and directed through a multimode optical fiber to create equal beam sizes for all lasers. To control the illumination of the sample, the 561 and 532 lasers are directed through an acousto-optic tunable filter (AOTF) (AA Opto Electronic), which is controlled by LabVIEW, while the other lasers are directly controlled by LabVIEW. There are two cameras available on this set-up: an Evolve

512 back-illuminated EMCCD camera (Photometrics, USA) and a sCMOS camera (ORCA-Fusion BT, Hamamatsu, since April 2023). Most experiments in this thesis have been performed using the EMCCD-camera. Both cameras are controlled by Micro-Manager and LabVIEW software. The use of Micro-Manager and LabVIEW software enables the design of customized illumination schemes and laser sequences, which is essential for photophysical studies. Another advantage of this set-up is that the effective power densities of the lasers can be tuned over a wide range (~100 mW/cm^2 up to ~2 kW/cm^2 depending on the laser) by the use of optical density filters, which is also useful for photophysical studies.

The commercial Abbelight PALM system is the SAFe360 system. This set-up is based on an Olympus IX83 inverted microscope equipped with a 100x oil immersion 1.5 NA objective lens (UPLAPO100XOHR). An axial drift correction unit (IX3-ZDC2-830) ensures a constant focus during long acquisitions. Six lasers are available in an Oxxius laser combiner (405, 488, 532, 561, 643 and 730 nm). Homogenous illumination of a large field of view (up to 100x100 µm) is achieved by ASTER technology[438]. Images are acquired on an Orca Fusion sCMOS camera (Hamamatsu). The lasers and cameras are controlled by NEO Live imaging software (Abbelight). There are several advantages of this set-up: a large field of view with homogenous illumination, real time analysis provided by the NEO software, the possibility for 3D and multicolor imaging (not used in this thesis) and a sCMOS camera allowing fast acquisitions (which was previously not present on the home-built PALM set-up). Disadvantages of this set-up, however, are that the NEO Live imaging software does not enable the design of complicated imaging schemes and that the range over which the laser intensities can be tuned is limited.

2.5.2 PALM data collection

PALM data were acquired on the home-built PALM set-up, which allows the design of customized imaging schemes.

2.5.2.1 PAA samples

Single-molecule data of mEos4b molecules embedded in PAA were acquired using a frame time of 70 ms and 500 W/cm^2 561 nm light. Frames were interleaved by 12 ms 'add' time during which 405 and/or 488 nm light was applied for 8.2 ms at 0-100 W/cm^2 (**Figure 2.11A**).

To test whether 405 nm light bleaches mEos4b in a non-linear manner, frames (70 ms, 500 W/cm^2 561 nm) were interleaved by 82 ms 'add' time during which 405 nm light was applied for 82 or 8.2 ms at 10 or 100 W/cm^2, respectively (**Figure 2.11B**).

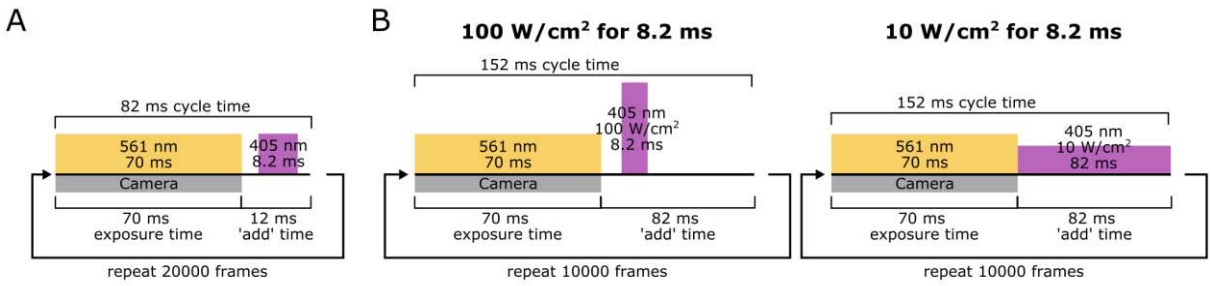

***Figure 2.11 PALM imaging schemes**. A) Standard PALM imaging scheme. B) PALM imaging schemes to test whether 405 nm light bleaches PCFPs in a nonlinear manner.*

2.5.2.2 NPC samples

Single-molecule data of Nup96-mEos4b and Nup96-mMaple were collected using a frame time of 100 ms and 500 W/cm^2 561 nm light. Frames were interleaved by 12 ms 'add' time during which 5 W/cm^2 405 nm light was applied for 5 ms. Frames were collected until (almost) no more localization appeared (20000 frames).

To examine the effect of the 405 nm light power density on the PCE of mEos4b, frames were interleaved by 12 ms 'add' time during which 405 light was applied for 3.5 or 0.35 ms at 10 or 100 W/cm^2, respectively.

2.5.2.3 DNA-origami samples

DNA origami samples labeled with AF647 and mEos4b were imaged in two steps. Firstly, AF647 was imaged using a 647 nm laser (20% laser power, 70 ms exposure time) to localize the DNA origamis. Secondly, PALM imaging was performed as described before using 500 W/cm^2 561 nm light and 0-10 W/cm^2 405 nm light (70 ms frames time, 12 ms 'add' time).

2.5.3 SptPALM data collection

SptPALM acquisitions were collected on the Abbelight set-up.

SptPALM data of *D. radiodurans* cells expressing HU-mEos4b were collected at 27°C under continuous illumination with 400 W/cm^2 561 nm light and a frame time of 10 ms. The intensity of the 405 nm laser was manually increased during the acquisition to maintain a constant localization density. 40000 - 60000 frames were acquired per acquisition. A transmission light image was acquired for segmentation of the cells. For cells labeled with syto9, a snapshot was taken prior to PALM imaging using 488 nm light.

2.5.4 Imaging of the *oriC* and *ter* labeled cells

oriC and *ter* labeled cells were imaged on the home-built PALM set-up.

First, a bright field image and an image of HU-mCherry were collected (100 ms exposure time, 10 W/cm^2 561 nm light). Second, the *oriC* or *ter* sites (ParB-GFP) were imaged every second using an exposure time of 100 ms and 10 W/cm^2 488 nm light, until all sites had bleached (~100-500 frames).

2.5.5 Ensemble fluorescence experiments

Ensemble experiments were performed on the home-built PALM set-up.

Ensemble measurements of the photoconversion kinetics of mEos4b and other PCFPs (**Section 3.1.3**) were acquired using an exposure time of 20 ms and a total cycle time of 500 ms (**Figure 2.12A**). During the 20 ms camera exposure time, 8 W/cm^2 561 nm light was applied for readout of the red fluorescence intensity. During the remaining time, 405 nm light was applied (1-100 W/cm^2 for 400 ms). To test whether 405 nm light bleaches PCFPs in a non-linear manner, experiments were performed applying 10 W/cm^2 405 nm light for 82 ms or 100 W/cm^2 for 8.2 ms (**Figure 2.12A**).

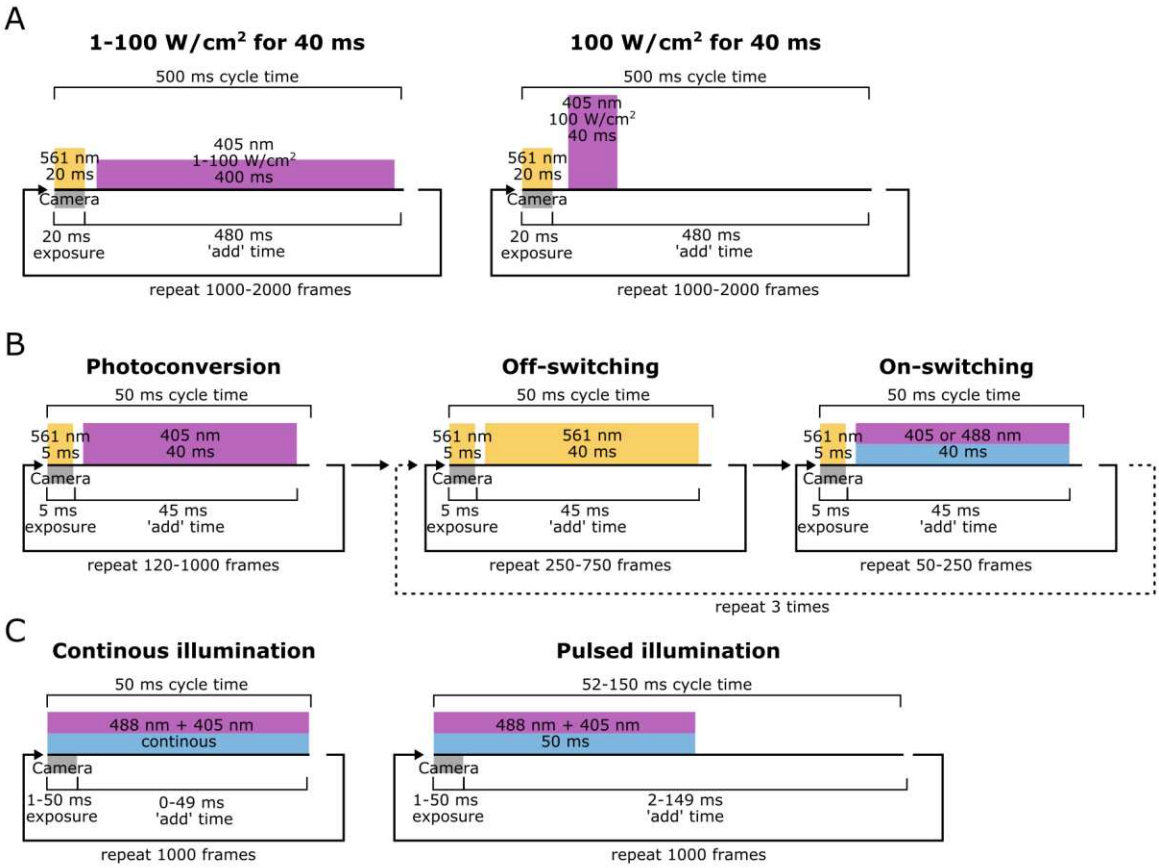

Figure 2.12 Illumination schemes used for ensemble fluorescence measurements. *A) Illumination schemes to monitor photoconversion kinetics. B) Illumination scheme to monitor red state photoswitching. C) Illumination schemes to monitor green state photoswitching.*

Ensemble measurements of the photoswitching behavior of red-state mEos4b (**Section 3.1.4.3**) were acquired using an exposure time of 5 ms and a total cycle time of 50 ms (**Figure 2.12B**). During the 5 ms exposure time, 10 W/cm^2 561 nm light was applied for readout of the red fluorescence. During the remaining time, 405 or 488 nm light (0.1-100 W/cm^2, on-switching and photoconversion) or 561 nm light (10 W/cm^2, off-switching) was applied. Each experiment started with a photoconversion period (10 W/cm^2 405 nm). The duration of this period was chosen to optimize photoconversion efficiency while minimizing bleaching or switching by the 405 nm laser. Consequently, the duration of this period varied with pH (**Figure 2.13A**). After the photoconversion periods, off- and on- switching cycles were alternated (30 s - 60 s depending on the illumination intensities) (**Figure 2.12B, Figure 2.13B**).

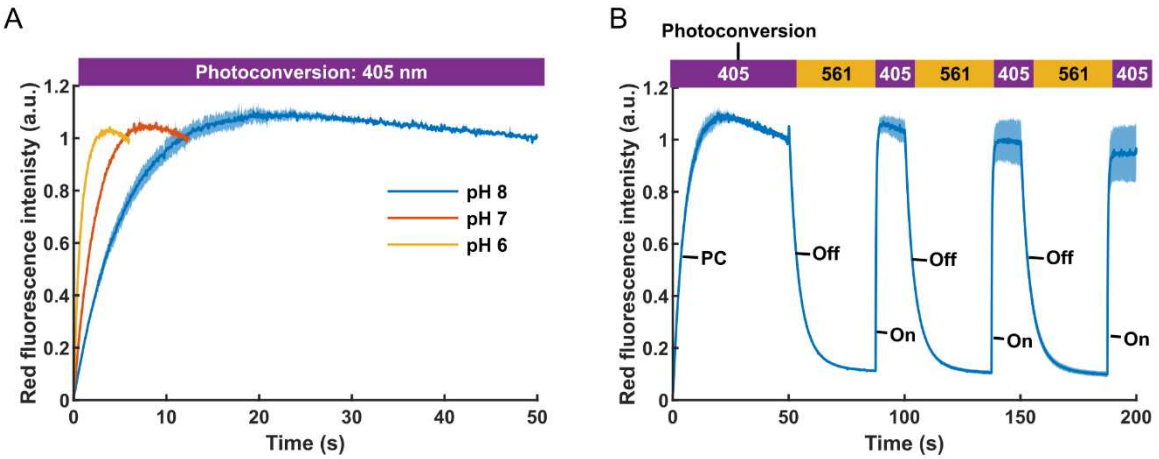

Figure 2.13 Photoconversion of mEos4b before photoswitching experiments. *A) Photoconversion of mEos4b molecules embedded in PAA gel at pH 6.4, pH 7.4 and pH 8. 405 nm light was applied at 10 W/cm^2 for 120, 250 or 1000 frames (40 ms per frame) depending on the pH. Data are normalized to the final intensity. B) Entire photoswitching experiment of mEos4b molecules at pH 8. Off-switching is induced by illumination with 561 nm light while on-switching is induced by illumination with 405 nm (1 W/cm^2) light as explained in the text. Data are normalized to the final intensity after the photoconversion period.*

Ensemble measurements of the photoswitching behavior of green-state mEos4b (**Section 3.1.4.2**) were acquired using an exposure time of 1-50 ms and a total cycle time of 50 ms (**Figure 2.12C**). Measurements were made under continuous illumination with 488 nm light (100 mW/cm^2 - 1 W/cm^2) and 405 nm light (0 - 500 mW/cm^2) or frames (50 ms) were interleaved by a dark period (10-500 ms) (**Figure 2.12C**).

2.5.6 Spectroscopic measurements

Absorption and emission spectra of mEos4b were collected on a home-built microspectrophometer (the CAL(AI)^{2}DOSCOPE) with the help of Virgile Adam. The CAL(AI)^{2}DOSCOPE enables time-resolved collection of fluorescence emission and absorption spectra, at RT and CT, under diverse illumination conditions.

To investigate the formation of a 405 nm light induced off-state in red state mEos4b, molecules were embedded in PAA gel (pH 6.4) or in 50% glycerol diluted in MES buffer (pH 6) at a concentration of 1 or 10 mg/ml, respectively. These high concentrations were required to collect high signal-to-noise absorption spectra. Samples were illuminated and data were collected according to the scheme presented in **Figure 2.14A**. During each cycle (1 s cycle time), the sample was illuminated for 5 ms with 14 W/cm^2 561 nm light during which the fluorescence emission was collected, after which the sample was illuminated for 40 ms with 8 W/cm^2 405 nm light. Following the second illumination period, an absorption spectrum was collected (integration time 500 ms). During the experiments, lasers were manually switched off or blocked physically when desired. Physical blockage was required to collect complete absorption spectra because of leakage of laser light (**Figure 2.14B**). In PAA gel samples, this leakage resulted in broad negative absorption bands covering the whole visible spectrum (**Figure 2.14C**). The underlying mechanism of this effect remains unclear.

Raw fluorescence and absorption data were processed in MATLAB, where they were background subtracted and smoothed.

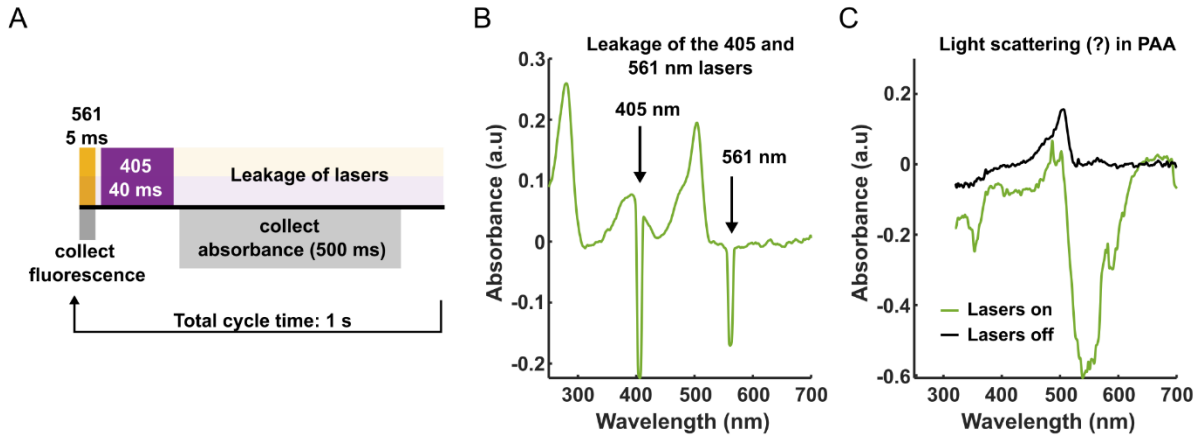

Figure 2.14 Spectroscopic experiments. *A) Illumination and data collection scheme used for spectroscopic measurements of mEos4b. B) Absorption spectrum of green state mEos4b molecules embedded in 50% glycerol showing the leakage of the 405 and 561 nm lasers. C) Absorption spectra of green state mEos4b molecules embedded in PAA gel, with (Lasers off, black line) and without (Lasers on, green line) physical blockage of the 405 and 561 nm lasers.*

2.6 Data analysis and statistics

2.6.1 PALM data analysis

Single molecules were localized using the Thunderstorm[233] plugin in ImageJ. Drift correction was performed using fiducials. Localizations were clustered using a custom written MATLAB routine[4] based on spatiotemporal clustering followed by k-means clustering to reconstitute the fluorescence time traces of single mEos4b molecules. A maximal dark time of 30 s was allowed between localizations of a single cluster. This dark time was chosen so that the off-time histograms under different 405 nm light power densities had reached the same value (see **Figure 3.15A**). Spurious localizations and clusters were removed based on their intensity or sigma, or photon budget or shape (ellipticity), respectively. From the clusters, the blinking characteristics (on-times, off-times, bleaching-times, numbers of blinks and photon budgets) were extracted and plotted as histograms.

To examine the relative PCE of mEos4b and pcStar under different illumination conditions, the cumulative number of clusters were extracted. To correct for differences in protein concentration between samples, two datasets with 10 W/cm^2 405 nm light were acquired on each sample to which all other datasets were normalized.

2.6.2 Estimation of the effective labeling efficiency using the Nup96-FP cell lines

To extract the effective labelling efficiencies of Nup96-mEos4b and Nup96-mMaple, localized single molecule data were analyzed in SMAP[234,244]. We followed a similar workflow as described by Thevathasan et al[244].

Localizations were filtered by localization uncertainty (<25 nm) and sigma (50-150 nm) to exclude dim localizations, localizations out of focus and localizations that might have been the result of two or more overlapping molecules. After automatic segmentation of the NPCs, spurious NPCs were removed based on their fitted radius (<40 nm or >70 nm) or on the presence of more than 25% of the localizations in the center of the structure (<40 nm radius) or the presence of more than 40% of the localizations far away from the center of the structure (>70 nm radius).

For counting purposes, only localizations within a radius of 30 to 70 nm were considered. The ELE was estimated by counting the number of detected corners per NPC and fitting the resulting distribution to a probabilistic model[244]. This probabilistic model is based on a binominal probability density function, which describes the probability of observing k successes in n independent trials, where p is the probability of success in each trial:

$$B(k|n,p) = \binom{n}{k} p^k (1-p)^{n-k}$$

From this distribution follows that the probability of not detecting a corner of an NPC (k=0) that carries 4 labels (n=4) is $p_{dark} = B(0|4, p_{label})$, where p_{label} is the labeling efficiency. Consequently, the probability of successfully detecting a coner is $p_{bright} = 1 - p_{dark} = 1 - B(0|4, p_{label})$. Thus, the probability of observing N out of 8 coners, given a labeling efficiency of p_{label}, is given by:

$$p(N|p_{label}) = B\big(N\big|8, p_{bright}\big) = B(N|8,1 - B(0|4, p_{label}))$$

2.6.3 spt data analysis

2.6.3.1 HU-mEos4b

Nucleoids were manually segmented and classified from an overlay of the bright field and super-resolved images of HU-mEos4b. Only cells with well-defined nucleoid morphologies that were also observed by confocal imaging of syto9 labeled WT cells (experiments by Pierre Vauclare) were included in the analysis. Sometimes, mostly after UVC irradiation, we observed apparent clustering of HU-mEos4b at the edge of the cells (**Figure 2.15**), a phenomenon that was never observed in WT or HU-mCherry expressing cells under the confocal microscope. These cells were therefore excluded from further analysis. It remains unclear what caused this effect and whether it represents a real biological response or an artifact. We did not observe this effect in every experiment; it was possibly related to a specific glycerol stock. This remains to be further investigated.

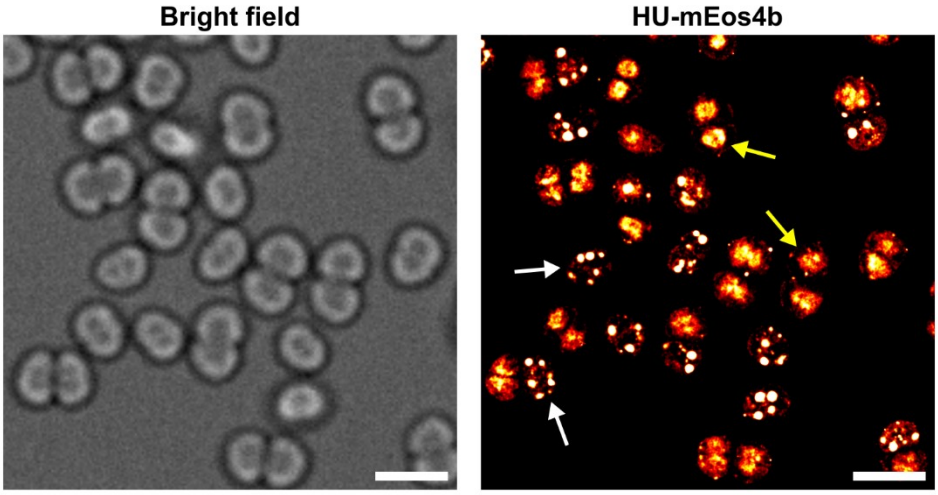

Figure 2.15 Apparent clustering of HU-mEos4b. *Bright field and super-resolved images of DR cells expressing HU-mEos4b 1 hour after irradiation with 1.9 KJ/m² UVC. Yellow arrows indicate cells with a 'normal' rounded nucleoid, white arrows indicate cells with apparent clusters of HU-mEos4b. Scale bar = 3 µm.*

Single molecules were localized using the Thunderstorm[233] plugin in ImageJ. Trajectories of single molecules were obtained using *swift* tracking software (Endesfelder et al., manuscript in prep (see[264])), using the following tracking parameters: 'exp_displacement = 60 nm', 'p_bleach = 0.1',

'p_blink = 0.2', 'p_reappear = 0.5', 'precision = 22 nm', 'max_displacement = 250 nm', 'max_displacement_pp = 250 nm' and 'max_blinking_duration = 2 frames'. Default values were used for the other parameters. The expected displacement (exp_displacement) was chosen to correspond approximately the peak of the mean jump distance histogram in NIR cells. The probability to bleach, blink and reappear (p_bleach, p_blink, p_reappear and max_blinking_duration) were chosen to approximately correspond to the observed track lengths and blinks. It is important to note that here the probability to blink does not soley refer to the intrinstic blinking prospensity of the FP but also to missing localizations, which may be due to diffusion of the protein out of the focus. The average localization uncertainty ('prescision') was estimated from the localizations. The maximum allowed displacement (max_displacement and max_displacement_pp) were chosen considering the size of the nucleoids and the right tail of the jump distance histogram in irradiated cells. *Swift* splits tracks, which contain motion changes (i.e. immobile -> diffusive), into segments containing unique behaviors. These segments were considered as trajectories for further analysis. Of note, only a small fraction of the tracks of HU-mEos4b contained multiple segments (~1-2%) suggesting that either HU-mEos4b only had 1 diffusive state or that the time HU-mEos4b spends in given state is relatively long compared to the average track length.

Trajectories were further analyzed in MATLAB. Trajectories were assigned to specific nucleoids based on the segmentation and the apparent diffusion coefficients were calculated. Apparent diffusion coefficients of single trajectories (D_i*) were calculated from the one-step mean squared displacement (MSD) as described by Stracy et al. using[279]:

$$D_i^* = \frac{1}{4n\Delta t}\sum_{i=1}^{n}[x(i\Delta t) - x(i\Delta t + \Delta t)]^2 + [y(i\Delta t) - y(i\Delta t + \Delta t)]^2$$

where n is the number of displacements over which the MSD is calculated, $x(t)$ and $y(t)$ are the coordinates of the molecule at time t and Δt is the frame time. Unless stated otherwise, four displacements per track were taken into account (n = 4).

The probability of measuring D_i* for a molecule that diffuses with an apparent diffusion coefficient D* is given by[270]:

$$p(D_i^*) = \frac{1}{(n-1)!} * \left(\frac{n}{D^*}\right)^n * (D_i^*)^{n-1} * exp\left(\frac{-nD_i^*}{D^*}\right)$$

This model can be extended to include two populations with apparent diffusion coefficients D_1^* and D_2^* and relative populations of A_1 and $(1 - A_1)$:

$$p(D_i^*) = \left[\frac{A_1}{(n-1)!} * \left(\frac{n}{D_1^*}\right)^n * (D_i^*)^{n-1} * exp\left(\frac{-nD_i^*}{D_1^*}\right)\right] + \left[\frac{(1-A_1)}{(n-1)!} * \left(\frac{n}{D_2^*}\right)^n * (D_i^*)^{n-1} * exp\left(\frac{-nD_i^*}{D_2^*}\right)\right]$$

Distributions of the D_i* were fitted in MATLAB using the one- or two-population model using nonlinear least squares.

2.6.3.2 Estimation of the localization uncertainty

Localization uncertainty (σ) offsets the apparent diffusion of molecules as measured by sptPALM by $\sigma^2/\Delta t$, where Δt is the frame time. We estimated this offset using three different methods: by single particle tracking of HU-mEos4b in chemically fixed cells and computation of the Dapp histogram (as

described above); from the localization uncertainty provided by Thunderstorm; from the average localization uncertainty extracted from the sptPALM data in chemically fixed cells, according to the method described by Endesfelder et al[294].

2.6.3.3 Tracking of *oriC* and *ter* sites

Loci were localized using Thunderstorm, similarly as single molecule data. Trajectories were obtained using *swift* tracking software (Endesfelder et al., manuscript in prep), using the following tracking parameters: 'exp_displacement = 50 nm', 'p_bleach = 0.001 ', 'precision = 50 nm', 'max_displacement = 250 nm', 'max_displacement_pp = 250 nm'. Default values were used for the other parameters.

Trajectories were further analyzed in MATLAB to calculate the apparent diffusion coefficients. Only trajectories with >10 localizations were considered.

2.6.4 Analysis of ensemble fluorescence measurements

Time-traces of the fluorescence intensity were extracted from a small region in the center of the field of view (FOV) using the 'Plot Z-axis Profile' function in ImageJ. Data were further processed in MATLAB, where they were background subtracted (background taken as the fluorescence intensity measured on a sample without any FP) and normalized either to the signal in the first frame, to the highest signal reached under the most intense illumination conditions or to the signal after photoconversion. Results are plotted as the mean ± sd of ≥3 measurements on ≥2 distinct samples, unless noted otherwise.

Due to a bug in the LabVIEW or Micro-Manager software, the collection of the fluorescence signal was incomplete in a fraction of the frames. This effect was only seen in acquisitions with short frame times and little dark times in between subsequent frames (for example in the green and red state photoswitching experiments, **Figure 2.16A**). Importantly, this effect was not notable in any of the single molecule data. To correct for this effect, erroneous low intensity values (less than 95% of the intensity of both the adjacent frames) were replaced by the average intensity value of the adjacent frames (**Figure 2.16B**).

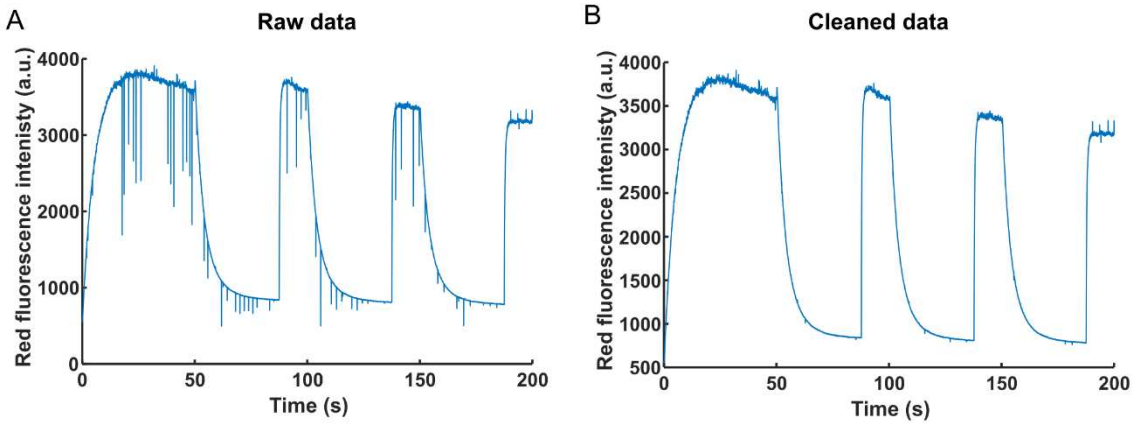

Figure 2.16 Cleaning of the ensemble fluorescence data. *A) Raw data of a red state photoswitching experiment at pH 8. B) The same data after replacement of erroneous low intensity values.*

2.7 Simulations

All simulations were performed using a recently developed simulation software developped in the lab: Single-Molecule Imaging Simulator (SMIS)[266]. This simulator takes as input a detailed photophysical model of the (hypothetical) fluorophore, including absorption and emission spectra, brightness and pH sensitivity. This information was either available in the lab, or taken from publications or FPbase:

- Absorption and emission spectra of the different states of the different fluorophores were available in the lab unless stated otherwise. The extinction coefficients, fluorescence quantum yields and pH sensitivity of the fluorescent states were taken from FPbase (https://www.fpbase.org/). All simulations were performed assuming a pH of 7.5.
- Phototransformation quantum yields and thermal exchange rates between different states were based on published models or experimental data obtained during this thesis.
- The anionic and neutral states (of all states of the chromophore, i.e. green anionic/neutral, red anionic/neutral, *cis* anionic/neutral…) are assumed to be in fast exchange. These states are treated as a single state by SMIS, whitout the need to specify thermal exchange rates (hence, no rates are specified in the tables below).

All tables listing termal exchange rates and phototransformation quantum yields have the following format:

Table 2.1 Used table format.

		To	
From		**State 1**	**State 2**
	State 1	-	x
	State 2	x	-

Note:
All phototransformation quantum yields and thermal exchange rates used for the simulations should be interpreted as qualitative estimates, rather than as absolute values, of the true quantum yields and rates. This is because, although all values are based on experimental data, it is difficult to extract absolute values due to the multitude of photophysical states. Furthermore, quantum yields and rates can be affected by environmental conditions (in particular pH and redox environment) so that the estimated values might only be applicable to a range of experimental conditions.

2.7.1 Single molecule simulations of mEos4b for molecular counting

For counting purposes, single-molecule PALM data of mEos4b were simulated using a simplified photophysical model, excluding green state photophysics (**Table 2.2**, and see **Figure 3.8**). Green state photophysics were omitted to facilitate the interpretation of the effect of different illumination schemes on the photophysical behavior of the red state. Simulations were performed using 70 ms frame time, 12 ms add time in between frames, 500 W/cm^2 561 nm light, 1 W/cm^2 405 nm light and 0-10 W/cm^2 488 nm light, comparable to real PALM experiments. Over 20000 molecules were simulated for each illumination condition.

The simulated data were processed like normal PALM data using Thunderstorm and Matlab as described above. For counting, fluorescence time traces of simulated monomers were merged randomly to create fluorescence time traces of oligomers of various stoichiometries (dimers, tetramers, octamers and 16-mers). These reconstituted oligomers were then subjected to molecular

counting by the two different methods developed by Lee et al.[253] and by Fricke et al. (corrected model, see **section 1.5.2.2**)[206].

Table 2.2 Phototransformation quantum yields and thermal exchange rates used for single molecule simulations of mEos4b. *Simulations were performed using a simplified model of mEos4b, omitting green state photophysics.*

	Red anionic	**Red neutral**	**Red dark**	**Red off**	**Red bleached**
Green anionic	5e-7	-	-	-	-
Green neutral	-	1e-4	-	-	-
Red anionic	-	-	5e-6	1.5e-5	1e-5
Red neutral	-	-	-	-	1e-5
Red dark	1e-4 20*	-	-	-	1e-5
Red off	0.02 1e-3*	-	-	-	1e-5

** Thermal exchange rates (s^{-1})*

2.7.2 Ensemble simulations of the PCE of mEos4b under various illumination conditions

To examine the effect of green state photobleaching on the PCE, photoconversion was simulated using the complete photophysical model of mEos4b available in SMIS, including green state photobleaching and photoswitching (**Table 2.3**). Simulations were performed using 70 ms frame time, 12 ms add time in between frames, 500 W/cm^2 561 nm light, 0-1 W/cm^2 405 nm light and 0-100 W/cm^2 488 nm light. The photoconversion efficiency was directly extracted from the ground-truth data provided by SMIS.

Table 2.3 Phototransformation quantum yields and thermal exchange rates used for ensemble simulations of mEos4b. *Simulations were performed using a complete photophysical model of mEos4b.*

	Green anionic	**Green dark**	**Green off**	**Green bleached**	**Red anionic**	**Red neutral**	**Red dark**	**Red off**	**Red bleached**
Green anionic	-	3.5e-5	5e-5	2.5e-6	5e-7	-	-	-	-
Green neutral	-	-	-	2.5e-6	-	1e-4	-	-	-
Green dark	1e-3 0.1*	-	-	2.5e-6	-	-	-	-	-
Green off	0.01 1e-3*	-	-	2.5e-6	-	-	-	-	-
Red anionic	-	-	-	-	-	-	5e-6	1.5e-5	1e-5
Red neutral	-	-	-	-	-	-	-	-	1e-5
Red dark	-	-	-	-	1e-4 20*	-	-	-	1e-5
Red off	-	-	-	-	0.02 1e-3*	-	-	-	1e-5

** Thermal exchange rates (s^{-1})*

2.7.3 Ensemble simulations of mEos4b photoconversion with two fluorescent green states

Simulations were performed using a simplified photophysical model (**Table 2.4**) of green-state mEos4b based on NMR data. This model consisted of two green states, A and B, with both the possibility to have an anionic or neutral chromophore. These states were assumed to have the same absorption and emission spectra (anionic states: mEos4b, FPbase; neutral states: mEos2[147]), extinction coefficients, fluorescence quantum yields, pKa's (5.5) and Hill coefficients (0.74)[150]. The thermal exchange rates of the A and B states were extracted from the NMR data ($k_{ex} = k_{AB} + k_{BA}$ = 2e-2 s^{-1} and $P_A/P_B = k_{BA}/k_{AB}$ = 1.33 so that k_{AB} = 0.0114 s^{-1} and k_{BA} = 0.0086 s^{-1}). Photoconversion was assumed to only happen from the A state (neutral chromophore). The photoconversion quantum yield and photobleaching quantum yields from the green anionic states were based on previously published data[187,201,204]. The photobleaching quantum yields of the green neutral states were adjusted to reproduce the UV-light-dependence of the PCE, after the quantum yields of the A-B exchange were adjusted to reproduce the UV-light-dependence of the AB equilibrium, as observed by NMR. Photoconversion was simulated for 10^4 minutes under continuous illumination with 2.5 mW/cm^2 - 100 W/cm^2 405 nm light.

Table 2.4 Phototransformation quantum yields and thermal exchange rates used for ensemble simulations of mEos4b photoconversion with two fluorescent green states.

	Green A anionic	**Green A neutral**	**Green B anionic**	**Green B neutral**	**Green bleached**	**Red neutral**
Green A anionic	-	-	0.0086*	-	2.5e-6	-
Green A neutral	-	-	-	0.3015 0.0086*	3.5e-6	5e-4
Green B anionic	0.0114*	-	-	-	2.5e-6	-
Green B neutral	-	0.0707 0.0114*	-	-	5.0e-4	-

** Thermal exchange rates (s^{-1})*

To explore the possibility that photoconversion happens from both the A-and the B-state, simulations were performed in which the photoconversion quantum yield of the B state was 10% or 100% of the photoconversion quantum yield of the A-state. To optimize the other phototransformation quantum yields, a fitting procedure was set-up, in which the bleaching quantum yields of the model were fitted to reproduce as close as possible the light-dependent PCE and A-state population under a range of 405 nm light intensities. Fitting was performed using nonlinear least squares in MATLAB. The final quantum yields that were used for the simulations are shown in **Table 2.5**.

Table 2.5 Phototransformation quantum yields and thermal exchange rates used for ensemble simulations of mEos4b photoconversion with two fluorescent green states assuming photoconversion from both the A- and B-state.

	Green A anionic	**Green A neutral**	**Green B anionic**	**Green B neutral**	**Green bleached**	**Red neutral**
Green A anionic	-	-	0.0086*	-	2.5e-6	-
Green A neutral	-	-	-	0.3015 0.0086*	1e-6 [A,B]	5e-4

Green B anionic	0.0114*	-	-	-	2.5e-6	-
Green B neutral	-	0.0707 0.0114*	-	-	5.9e-4 [A] 1.3e-3 [B]	5e-5 [A] 5e-4 [B]

** Thermal exchange rates (s^{-1})*

[A] *Phototransformation quantum yields used for simulations where the PC quantum yield of the B-state was 10% of the phototransformation quantum yield of the A-state*

[B] *Phototransformation quantum yields used for simulations where the PC quantum yields of the A-and B-state were equal*

2.7.4 Ensemble simulations of mEos4b red state photoswitching

Photoswitching of red state mEos4b was simulated using the default photophysical model of mEos4b provided in SMIS (**Table 2.3**) or the adjusted model shown in **Table 2.6** (see **section 3.1.4.3.1**). Simulations were started from the red fluorescent state, ignoring green state photophysics. Three consecutive off-and on-switching cycles were simulated using 750 frames for off-switching and 250 frames for on-switching. Each frame (50 ms cycle time) consisted of 5 ms exposure time during which 10 W/cm^2 561 nm light was applied and 40 ms 'add' time during which 10 W/cm^2 561 nm light (off-switching) or 1-100 W/cm^2 405 or 488 nm light (on-switching) was applied. Relative populations were extracted from the simulated data provided by SMIS.

Table 2.6 Adjusted phototransformation quantum yields and thermal exchange rates used for ensemble simulations of red state photoswitching of mEos4b.

	Red anionic	**Red neutral**	**Red dark**	**Red off**	**Red bleached**
Red anionic	-	-	5e-6	6e-5	3.2e-6
Red neutral	-	-	-	-	1e-5
Red dark	1e-4 20*	-	-	-	1e-5
Red off	0.1 1e-3*	-	-	-	1e-5

2.7.5 Ensemble and single molecule simulations of rsEGFP2 photoswitching at cryogenic temperature

A simplified photophysical model of rsEGFP2 at cryogenic temperature was designed based on ensemble and single molecule measurements (**Table 2.7** and see **Figure 3.49**). This model consisted of two non-exchanging on-states (On_1 and On_2) with corresponding long-lived off-states (Off_1 and Off_2). The photoswitching quantum yields of these states (On_1 - Off_1 and On_2 - Off_2) were estimated from the switching rates extracted from the experimental ensemble data, taking into account the laser intensities and extinction coefficients. The wavelength dependence of the on-switching quantum yields of Off_1 and Off_2 were incorporated into the model by an artificial scaling of the absorption spectra, which were obtained from experimental data in the lab (see **Figure 3.49**). Two short-lived dark states ($Off_{short\text{-}lived}$, thermal recovery rate 9.1 s^{-1}) were added to the model to account for short-lived blinks observed at the single molecule level and for some thermal recovery observed at the ensemble level. The formation quantum yield and recovery rate of these dark states were estimated from the fast-phase of the on- and off-time histograms from the single molecule

measurements. The photobleaching quantum yields and relative populations of On_1 and On_2 (70:30) were empirically estimated using photofatigue experiments (sequential on- and off-switching cycles).

Ensemble simulations were performed to validate that the proposed photophysical model was able to explain all the experimentally observed photoswitching behaviors. Simulations were performed using the following simulation parameters: 700 ms exposure time, 300 ms add time in between frames, 400-1000 W/cm^2 488 nm light, 10-30 W/cm^2 355 nm light and 200-300 W/cm^2 488 nm light. These laser intensities were the same as those in the experimental measurements. 488 nm light was applied during the frame time, while 355/405 nm light was applied during the add time.

After the photophysical model was successfully tested by ensemble simulations, single-molecule simulations were performed to examine the effects of 405 and 355 nm illumination on the on-switching efficiency at the single molecule level. To determine the on-switching efficiency, single molecule simulations were performed in 2D using Nuclear Pore Complexes (NPCs) with the Nup96 nucleoporin virtually labelled with rsEGFP2 (8 corners per NPC, 4 molecules per corner). The following simulation parameters were used: 100 ms frame time, 20 ms add time in between frames, 400 W/cm^2 488 nm light for off-switching and readout of green fluorescence, and 0.04 W/cm2 355 nm light or 0.8 W/cm^2 405 nm light for on-switching. The power densities of the 355 and 405 nm lasers were set to have sufficiently sparse localization density. 488 nm light was applied during the frame time, while 355/405 nm light was applied during the add time. For each condition, 1 simulation of 1 million frames with 100 NPCs was run. Molecules were localized using Thunderstorm and the effective labeling efficiency was determined using SMAP.

Table 2.7 Phototransformation quantum yields and thermal exchange rates used for ensemble and single molecule simulations of rsEGFP2 photoswitching at cryogenic temperature.

	On_1	**On_2**	**Off_1**	**Off_2**	**$Off_{short\text{-}lived\ (1)}$**	**$Off_{short\text{-}lived\ (2)}$**	**Bleached**
On_1	-	-	1.8e-7	-	1.4e-5	-	1.8e-7
On_2	-	-	-	1.8e-7	-	1.4e-5	2.6e-8
Off_1	2.9e-5	-	-	-	-	-	2.4e-5
Off_2	-	2.1e-5	-	-	-	-	1.0e-6
$Off_{short\text{-}lived\ (1)}$	9.1*	-	-	-	-	-	-
$Off_{short\text{-}lived\ (2)}$	-	9.1*	-	-	-	-	-

** Thermal exchange rates (s^{-1})*

2.7.6 sptPALM simulations

sptPALM simulations were performed in 3D using virtual samples based on segmented DR nucleoids (exponential phase), *E.coli* shaped volumes (rod of 2 x 0.5 µm) or a large 3D box (67 µm x 67 µm x 3 µm). To speed up the simulations and maintain a homogenous localization density over time, simulations were performed using a hypothetical fluorophore thermally switching between a fluorescent and non-fluorescent state to create short tracks as in sptPALM (**Table 2.8**). The diffusion coefficient was varied between 0.05 and 10 µm^2/s to assess the effect of confinement on the extracted diffusion coefficient. Simulations were performed with one or two diffusive populations. To include the effect of temporal averaging, simulations were performed using subframe diffusion (10 nm resolution).

Simulated data were analyzed using the same workflow as for experimental data (Thunderstorm -> swift -> MATLAB).

Table 2.8 Fluorophore model with thermal exchange rates (s^{-1}) used for spt simulations.

	On	**Dark**
On	-	1
Dark	0.1	-

3 Results and Discussion

3.1 Manipulating FP photophysics to boost quantitative SMLM

3.1.1 Introduction

The complex photophysics of PTFPs hinders quantitative SMLM experiments, including molecular counting and single particle tracking. Therefore, the goal of the work presented in this section was to gain a better understanding of the photophysical behavior PTFPs and investigate strategies to manipulate their behavior by changing the illumination and/or the environmental conditions.

3.1.2 FP immobilization platforms for photophysical studies

Photophysical studies of FPs rely on properly functioning immobilization platforms for microscopy experiments. Several of such platforms have been developed but the suitability of these platforms is rarely addressed.

3.1.2.1 Advantages and disadvantages of PAA gel

Polyacrylamide gel is a popular platform for photophysical characterization of FPs at both the single molecule and ensemble level. The usage of PAA gel is convenient because its preparation is easy and fast, it is available in every biochemical lab and it does not require specific modifications of the FP. For these reasons, PAA gel has been frequently used in the lab, for example to investigate the usage of 488 nm light to reduce the off-time durations of mEos4b[217] and to study the photoswitching behavior of the RSFP rsFolder[122]. However, the usage of PAA gel does also have several drawbacks, which we encountered during the photophysical characterization of mEos4b.

The first problem that we encountered was that the mEos4b molecules appeared to stick to the ozone cleaned cover glasses, which were used to sandwich the PAA gel. It is unclear whether other FPs are also 'sticky' like mEos4b or whether this is a protein specific problem. This 'sticking' could be due to electrostatic interactions between the negatively charged glass slide and positively charged residues on the FP. Comparing the theoretical isoelectric points (pI, calculated on https://web.expasy.org/) of EosFP variants with othe FPs, the pI's of EosFP proteins are relatively high (7.13 and 7.12 for mEos4b and mEos3.2, repectively, versus 5.58 and 5.62 for eYFP and mCherry, respectively), meaning that EosFP variants cary relatively more positive charge than many other FPs at the same pH, which could potentially explain the 'sticking' of mEos4b to the glass surface. The problem of proteins interacting with the cover glass is that we do not know how this interaction is mediated and whether it affects the behavior of the FP. A solution to this problem could be to coat the cover glass with a substance that does not interact with mEos4b. Substances that could, for example, be tested are PEG and BSA.

The second problem that we ran into, was that the FPs were not tumbling but had a fixed orientation. Although, we initially assumed that the proteins would be able to tumble inside of the pores of the gel, defocused imaging revealed that this is not the case (**Figure 3.1**), in agreement with a previsous study[287]. The interaction between the mEos4b molecules and the cover glass likely also contributed to this issue. A fixed orientation does not prohibit photophysical characterization but it does complicate the extraction of phototransformation rates because molecules will be excited at different rates depending on their orientation. Theoretically, this problem could be solved by increasing the pore size of the gel to provide enough space for the proteins to tumble, which can be

achieved by adjusting the cross-linker concentration. However, since the pores of PAA gel are interconnected[286], increasing the pore size comes at the risk of diffusion of the proteins inside the gel. In fact, we already noticed that FPs were sporadically diffusing inside the gel. The fact that we saw both proteins with a fixed orientation and diffusing proteins suggests that the PAA gel was heterogeneous in pore size.

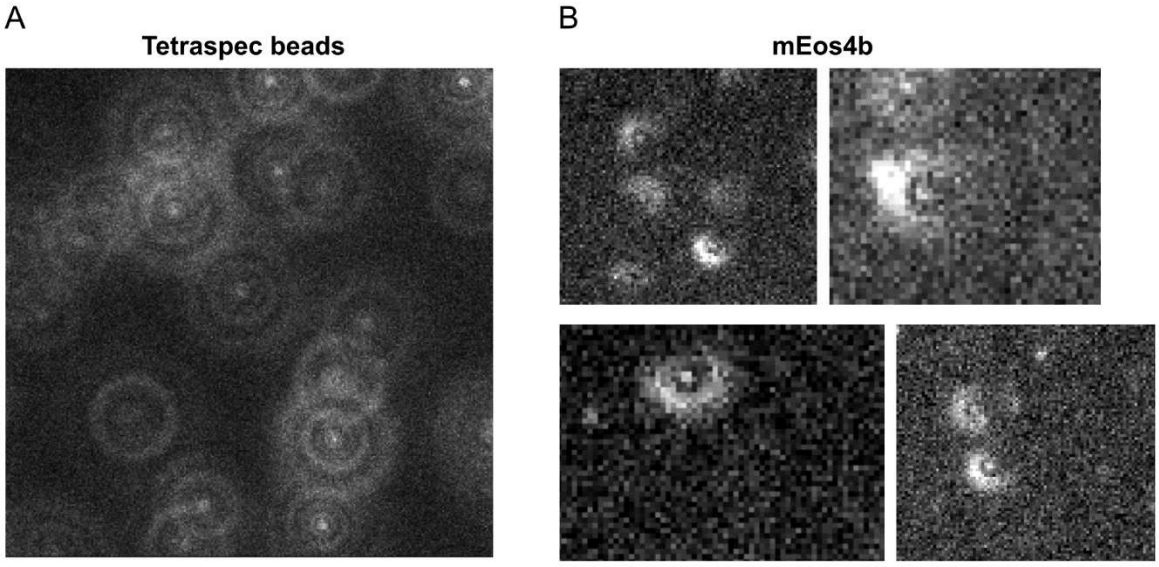

Figure 3.1 mEos4b molecules embedded in PAA gel have a fixed orientation*. Representative defocused images of Tetraspec beads (A) or mEos4b molecules (B) embedded in PAA gel. Both the Tertaspec beads and the mEos4b molecules have a fixed orientation but because a single Tetraspec bead contains many fluorophores, with different orientations, its PSF appears anisotropic. Images not the same scale.*

Another difficulty with PAA gel is that it can be difficult to control the buffer conditions, notably in terms of pH and redox environment, two factors that are known to have a big influence on the behavior of FPs. Polymerization of PAA gel is based on the production of free radicals, which interact with the acrylamide monomers. It is unclear whether this affect the FPs, which are mixed in to the sample before polymerization is initiated.

Finally, immobilization with PAA gel is not suitable for determination of the photoconversion or labeling efficiency of the FP because the true number of FPs is unknown.

Altogether, despite its convenience, PAA gel suffers from several limitations that restrict its usability as immobilization platform for the photophysical characterizations of FPs. Therefore, we decided to explore other immobilization techniques to find an alternative or complementary method to PAA gel.

3.1.2.2 Nuclear pore complexes as platform to optimize the imaging conditions *in cellulo*

Nuclear pores have recently been established as an *in cellulo* template to examine the performance of fluorescent dyes and proteins for quantitative PALM imaging (**Figure 3.2**)[244]. The well-known structure, symmetry, and robust stoichiometry of the nuclear pore complex (NPC) enables assessment of the image quality and the ELE of the used labeling technique[244]. The imaging of NPCs is facilitated by the flat nuclear membranes of U2OS cells resulting in hundreds of NPCs per cell being in a single focal plane[244]. Because NPCs were shown to be usable for the optimization of the imaging conditions and for quantitative applications[244,315], we decided to test the usage of the NPC template for the characterization of mEos4b.

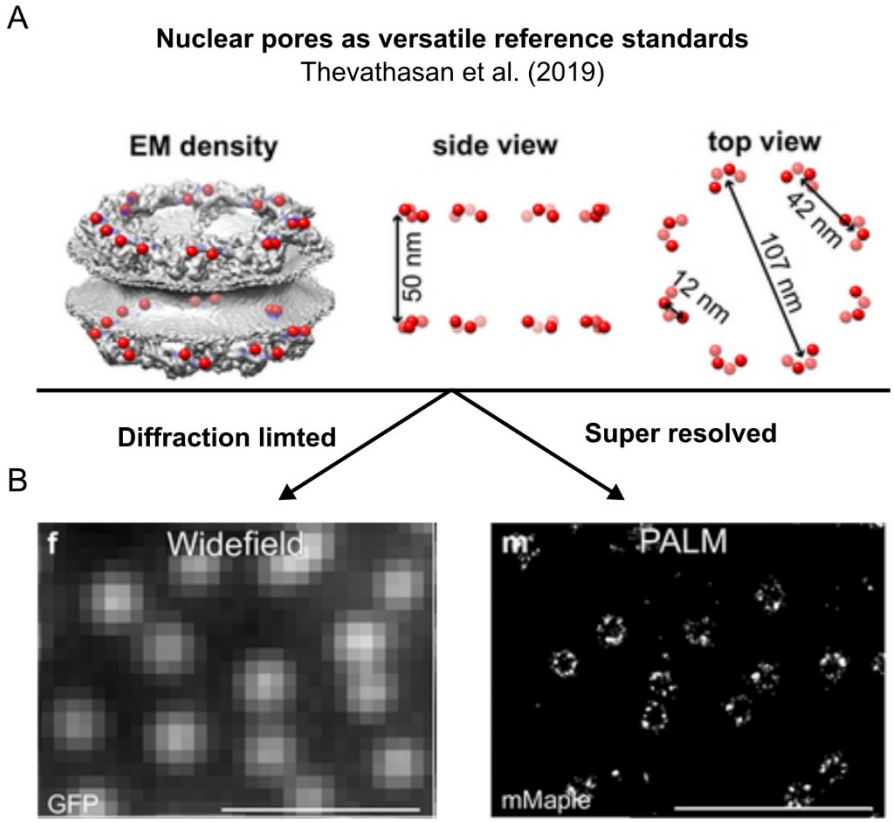

Figure 3.2 Nuclear pores as versatile reference standard. *Thevathasan et al recently introduced nuclear pores as versatile reference standard for quantitative super-resolution microscopy. A) EM density of the nuclear pore complex. Red dots indicate the C-termini of Nup96. B) Widefield and PALM images of Nup96-GFP and Nup96-mMaple respectively. Figure adopted from*[244].

NPCs consists of ~30 proteins (nucleoporins), which are organized into a symmetrical ring-like structure spanning the nuclear membrane. Of all the different nucleoporins, Thevathasan et al. identified Nup96 as a good reference protein for labeling[244]. Nup96 is present in 32 copies per NPC, forming a cytoplasmic and a nucleoplasmic ring (~ 110 nm diameter) with each 16 copies divided over eight corners. When imaged in 2D, Nup96 labeled NPCs appear as circular structures with eight corners each containing four fluorophores (**Figure 3.2**). Thevathasan et al. created a CRISPR cell-line expressing Nup96-mMaple suitable for PALM imaging, which is commercially available. For study of mEos4b, we created a cell-line expressing Nup96-mEos4b (work by Pascale Tacnet, Philipe Frachet, Virgile Adams and Oleksandr Glushonkov).

To validate the usability of NPCs for the characterization of mEos4b, we first compared the performance of mEos4b and mMaple, a Dendra-like PCFP (T69) (**Figure 3.3**). Cell expressing Nup96-mMaple and Nup96-mEos4b were imaged using alternating illumination with 500 W/cm^2 561 nm and 5 W/cm^2 405 nm light for 100 ms and 5 ms, respectively. The 405 nm light dose was chosen to ensure single molecule sparsity while imaging mMaple, which showed faster photoconversion than mEos4b (**Figure 3.3C**). Super-resolved images of Nup96-mMaple and Nup96-mEos4b are shown in **Figure 3.3A**, with both fusions revealing the ring-like organization of the NPC. The localization uncertainty with mEos4b (mean = 24 nm) was better than with mMapple (mean = 28 nm) (**Figure 3.3B**), which is likely due to the lower brightness and higher pKa of the red state of mMaple compared to the red state of mEos4b, resulting in a lower photon count per localization[150,439]. Assuming that mMaple and mEos4b have similar photoconversion quantum yields, the higher pKa of the green state of mMaple also explains its faster photoconversion rate (**Figure 3.3C**).

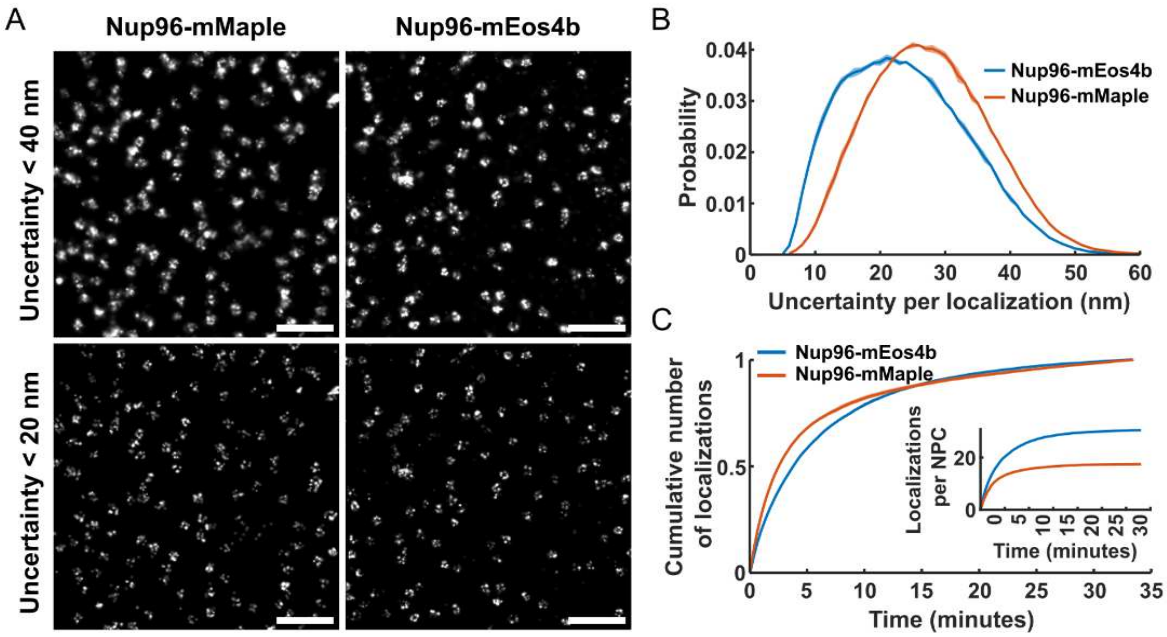

Figure 3.3 Nup96-mMaple and Nup96-mEos4b cell lines*. A) Super-resolved images of Nup96-mMaple and Nup96-mEos4b. Localizations are filtered by a localization uncertainty < 40 nm (top row) or < 20 nm (bottom row). Scale bar = 1 µm. B) Histograms of the localization uncertainty (nm) of unmerged localizations. C) Cumulative number of localizations. Data are normalized to the final cumulative number of localizations.* Inset show the cumulatative number of localizations normalized to the number of NPCs. *n = 2 cells.*

Next, we estimated the ELE of mMaple and mEos4b. The ELE can be estimated by counting the number of detected corners per NPC (**Figure 3.4A**) and fitting the resulting distribution with a probabilistic model, taking into account that each corner has 4 labels. Before counting, we merged localizations that were within a radius of 50 nm from each other and were separated by maximal 1 frame, after which we removed localizations with an uncertainty larger than 20 nm. These merging and filtering steps are important to increase the localization precision and prevent overcounting (see discussion below). Using this method, we found that the ELE of mMaple was slightly lower than with mEos4b (~27% vs ~29%) (**Figure 3.4B**). It is important to note that the ELE's of 27% and 29% may not reflect the relative PCE's of both PCFPs due to the lower localization presicion of mMaple (**Figure 3.3B)**, resulting in the removal of more localizations. Interestingly, although mEos4b and mMaple have a comparable ELE, the number of localizations per NPC is significatly lower with mMaple than with mEos4b, indicating that mEos4b gives more localizations per FP, in line with previsous studies, given that mMaple is a Dendra-like PCFP (**Figure 3.3C, inset**)[147,253]. The ELE's found in this work are notably lower than the ELE of Nup96-mMaple reported by Thevathasan et al. (58%). This difference could be partly due to the usage of D_2O and higher laser intensities by Thevathasan et al. resulting in a higher photon count per merged localization (~1621 photons compared to ~560 photons under our conditions) and thus a higher localization precision.

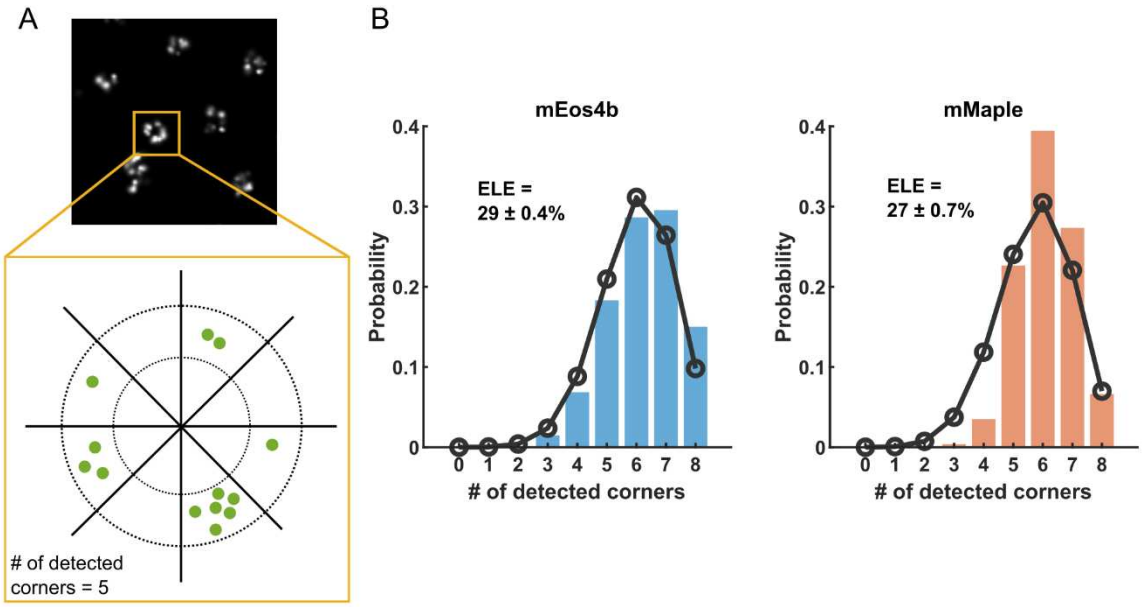

Figure 3.4 Effective labeling efficiencies with mEos4b and mMaple. *A) For each NPC, the number of detected corners is determined by alignment of the localizations belonging to that NPC to a template with 8-fold symmetry. B) Effective labeling efficiencies of Nup96-mEos4b and Nup96-mMaple (n = 400-800 NPCs from 2 cells) using alternating illumination with 500 W/cm^2 561 nm light (100 ms) and 5W/cm^2 405 nm (5 ms) light (Tris buffer, pH 8).*

Thevathasan et al. noted that accurate estimation of the ELE requires a high photon count. This is because NPCs are relatively small so that localizations with a low photon count, and consequently a poor localization precision, might end up up outside of what would be considered 'the NPC', which could lead to underestimation of the ELE, or might end up in a wrong corner, which could lead to overestimation of the ELE. Removal of localizations with a high uncertainty, may prevent overestimation of the ELE but comes at the risk of underestimation. This requirement for a high photon count is potentially problematic for the study of FPs, which typically have a lower photon budget than fluorescent dyes. To investigate the importance of a high localization precision, we considered a corner of a NPC (radius = 55 nm, theta=180) and simulated 100000 localizations belonging to that corner with a given localization uncertainty by sampling the error in x and y from a Gaussian distribution with σ = uncertainty (**Figure 3.5**). For each localization, we determined whether it was located in the correct corner (radius>30 nm & radius<70 nm and theta>157.5 & theta<202.5), in a wrong corner (radius>30 nm & radius<70 nm and theta<157.5 | theta>202.5), or outside of the theoretical NPC (radius<30 nm | radius>70 nm). The simulations revealed that up to 10 nm uncertainty, most localizations end up in the correct corner but that this accuracy quickly degrades at higher uncertainties (**Figure 3.5B**). At uncertainties >30 nm, localizations were more often located in a wrong corner than in the correct corner (**Figure 3.5B**). These simulations indicate that care should be taken when working with fluorophores with a low photon budget.

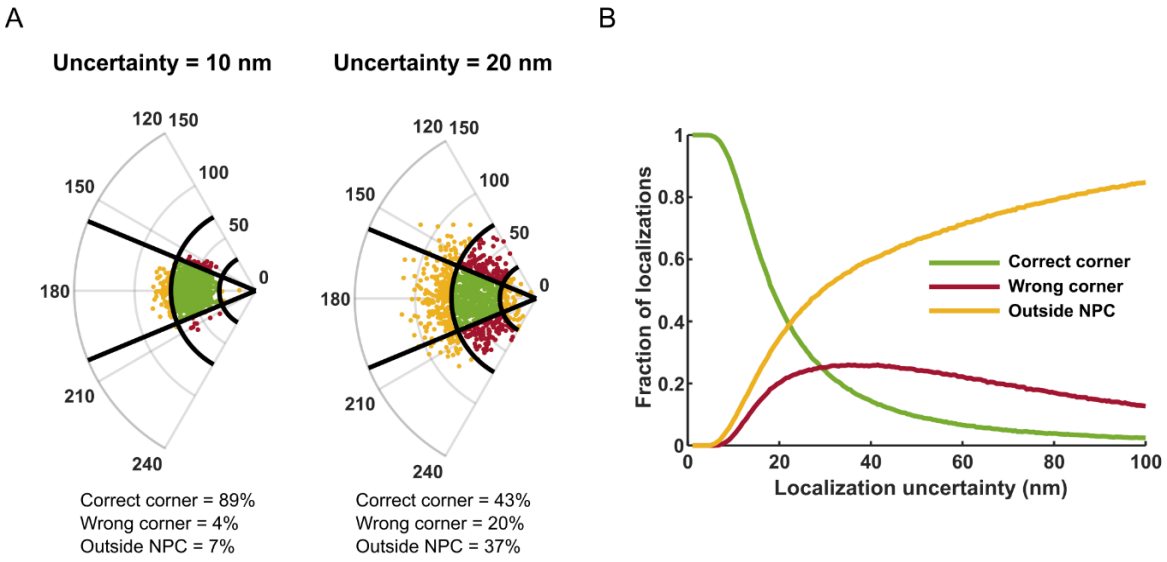

Figure 3.5 Estimation of the ELE is affected by the localization uncertainty. *A localization uncertainty (0=100 nm) was added to localizations belonging to a NPC corner (radius=55 nm, theta=180) by sampling from a Gaussian distribution. For each localization, we determined whether it was located in the correct corner (radius>30 nm & radius<70 nm and theta>157.5 & theta<202.5), in a wrong corner (radius>30 nm & radius<70 nm and theta<157.5 | theta>202.5), or outside of the theoretical NPC (radius<30 nm | radius>70 nm). 100000 localizations were simulated per uncertainty. A) Examples of simulated localizations with 10 nm and 20 nm uncertainty. Localizations that are located inside the correct comer are colored green, localization located in a wrong corner are colored red and localizations located outside the NPC are colored yellow. B) Relation between the localization uncertainty and the fraction of localizations which ends up in the correct corner (green), a wrong corner (red) or outside of the NPC (yellow).*

Altogether, the NPC appears to be a useful template to evaluate the performance of FPs and optimize imaging conditions. However, estimation of the ELE is probably only relevant under conditions with a good localization precision, which restricts the usability of NPCs to screen a wide range of experimental conditions. Furthermore, while NPCs are useful for optimization of imaging conditions, they are less suitable for the photophysical characterization of FPs due to their oligomeric nature. In addition, creation of a stable cell-line presents substantial work, which limits the usage of this template for the comparison of many FPs.

3.1.2.3 Immobilizing mEos4b using DNA-origamis

Searching for an *in vitro* immobilization platform that enables photophysical characterization and is easily adaptable to different FPs, we investigated the usage of DNA-origamis. DNA-origamis are frequently used for SMLM as nanorulers, easily applicable to DNA-PAINT. Jusuk et al. showed that DNA-origamis can also be used to study the photophysical behaviors of FPs[295]. FPs can be attached to DNA origamis via a piece of single stranded DNA (ssDNA) through maleimide chemistry, only requiring a surface exposed cysteine on the protein. The DNA origamis, in turn, can be attached to a coverslip via biotin-streptavidin interactions (**Figure 3.6A**). An advantage of this set-up is that a second fluorophore can be attached to the DNA-origamis to enable discrimination between fluorescent signals coming from the FP and signals coming from impurities. In addition, this second fluorophore could enable assessment of the PCE or ELE of the FP. For this project we worked in collaboration with the Tinnefeld lab (LMU München, Germany), who published the original paper on the usage of DNA-origamis to study FP photophysics.

Figure 3.6 shows the DNA-origami design with mEos4b and a reference dye. Because mEos4b has no available cysteine for maleimide labeling we designed a mEos4b construct in which we added a cysteine on the C-terminus (mEos4b-C). A His-Tag was present on the N-terminus to facilitate

purification (His6-mEos4b-C). During the purification, however, we noticed that the protein, despite its His-Tag, had a poor affinity for nickel columns and was already eluted by 25 mM imidazole, restricting the washing steps to < 5mM Imidazole. Evaluation of the purified sample by denaturing SDS-PAGE revealed that a fraction of the protein was dimeric (**Figure 3.6B**, lane 1). Incubation of the protein with a reducing agent (DTT or TCEP, lane 3 and 5) removed this dimeric fraction, suggesting that dimerization was mediated by disulfide bond formation between the C-terminal cysteines. Incubation of mEos4b-C with an excess of TCEP and maleimide labeled ssDNA resulted in labeling of ~40% of the proteins (lane 6). On the other hand, DTT prevented labeling of the protein, presumably because the DTT inactivated the maleimide (lane 4). Surprisingly, addition of maleimide labeled ssDNA to the protein sample in the absence of any reducing agent resulted in the formation of many high molecular weight species (lane 2). The origin of these species is unclear.

Next, we proceeded with the DNA-origamis. We choose to use the new rectangular origami (NRO)[440] as template structure. On this template, we added three 21nt docking strands to bind the ssDNA labeled reference dye (AF647) and, at 35 nm distance, a docking strand for the ssDNA labeled FP (**Figure 3.6A**). In addition, six biotinylated strands were incorporated into the origami for attachment to the coverslip (**Figure 3.6A**). Folded origamis were incubated with the DNA labeled protein and dye for 2-3 hours after which unbound proteins and dye molecules were removed using a 100k spin filter. After assembly, the labeled DNA origamis were loaded onto streptavidin coated cover glasses for PALM imaging.

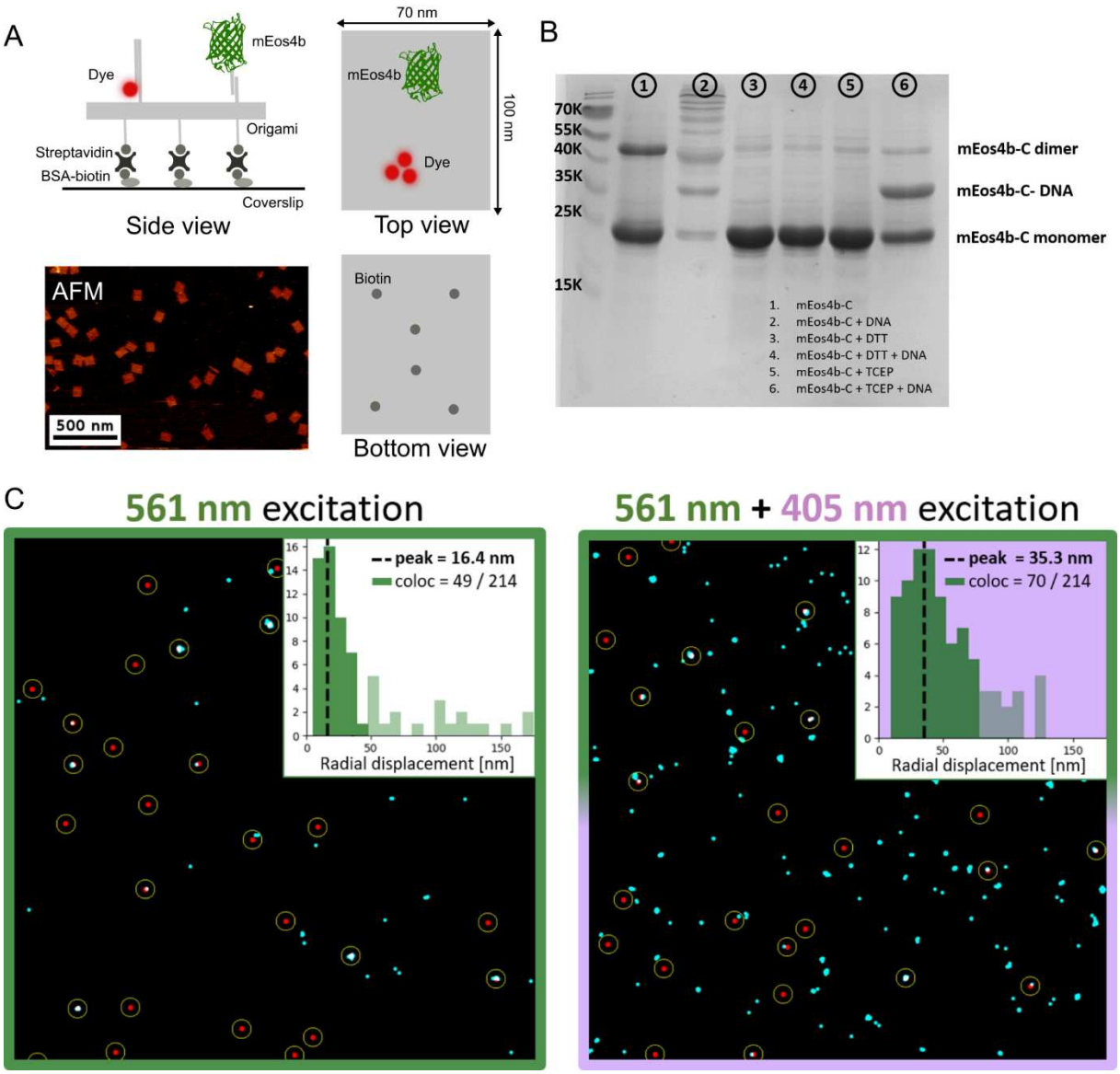

Figure 3.6 Using DNA-origamis to study FP photophysics. *A) Illustration of the DNA-origami design and AFM image of folded origamis. B) SDS-PAGE showing attachment of ssDNA to mEos4b-C after treatment by TCEP (lane 6) to reduce the cysteine making it available for reaction with the maleimide attached to the ssDNA. C) DNA-origamis labeled with AF647 and mEos4b were imaged under 561-nm light only (left) and 561-nm + 405-nm light (right). mEos4b molecules were identified by co-localization with the reference dye (AF647) imaged under 641-nm light. Histograms show the radial displacement between the AF647 signals and signals in the mEos4b channel. Noted are the mode radial displacement (peak) and number of dye signal co-localized with a mEos4b signal (coloc) (Figure C by Julian Bauer).*

Figure 3.6C shows the first imaging results of the DNA-origamis labeled with mEos4b and AF647. DNA-origamis where first localized by imaging the reference dye using 641-nm excitation, after which mEos4b was imaged using 405-nm and 561-nm light. In the absence of 405-nm light (**Figure 3.6C** left) there was minimal photoconversion of mEos4b. The signals co-localizing with the reference dye were probably resulting from photoblueing and direct excitation of AF647[436,441], given the close (~16 nm) distance between the two signals. Application of 405 nm light (**Figure 3.6C** right), resulted in signal presumably originating from mEos4b at the expected distance from the reference dye (~35 nm).

Although these first imaging results were promising, the samples at this state would not be usable for photophysical studies. The reasons for this being that photoblueing and/or direct excitation of AF647 prevented unambiguous identification of signals coming from mEos4b and that most of the

origamis (AF647 signals) did not co-localize with a mEos4b signal while the background contained many localizations in the Eos channel. The issues related to AF647 could maybe be solved by usage of another fluorophore or by increasing the distance between the dye and the FP to facilitate discrimination. The incomplete co-localization might be partly ascribed to incomplete photoconversion but the labeling of the DNA-origamis with the FP was likely incomplete due to the presence of free ssDNA inside the protein sample. Removal of free ssDNA from the protein sample was complicated by abnormal behaviors of the protein construct. Firstly, the protein construct showed poor affinity for nickel collumns (despite having a His-tag), limiting the uages of nickel collumns to wash out the unbound ssDNA. Secondly, when we tried to remove the free DNA by ion exchange chromatography (as in the eYFP paper[295]), the DNA labeled protein aggregated in the column, leaving the sample unusable (**Figure 3.7**).

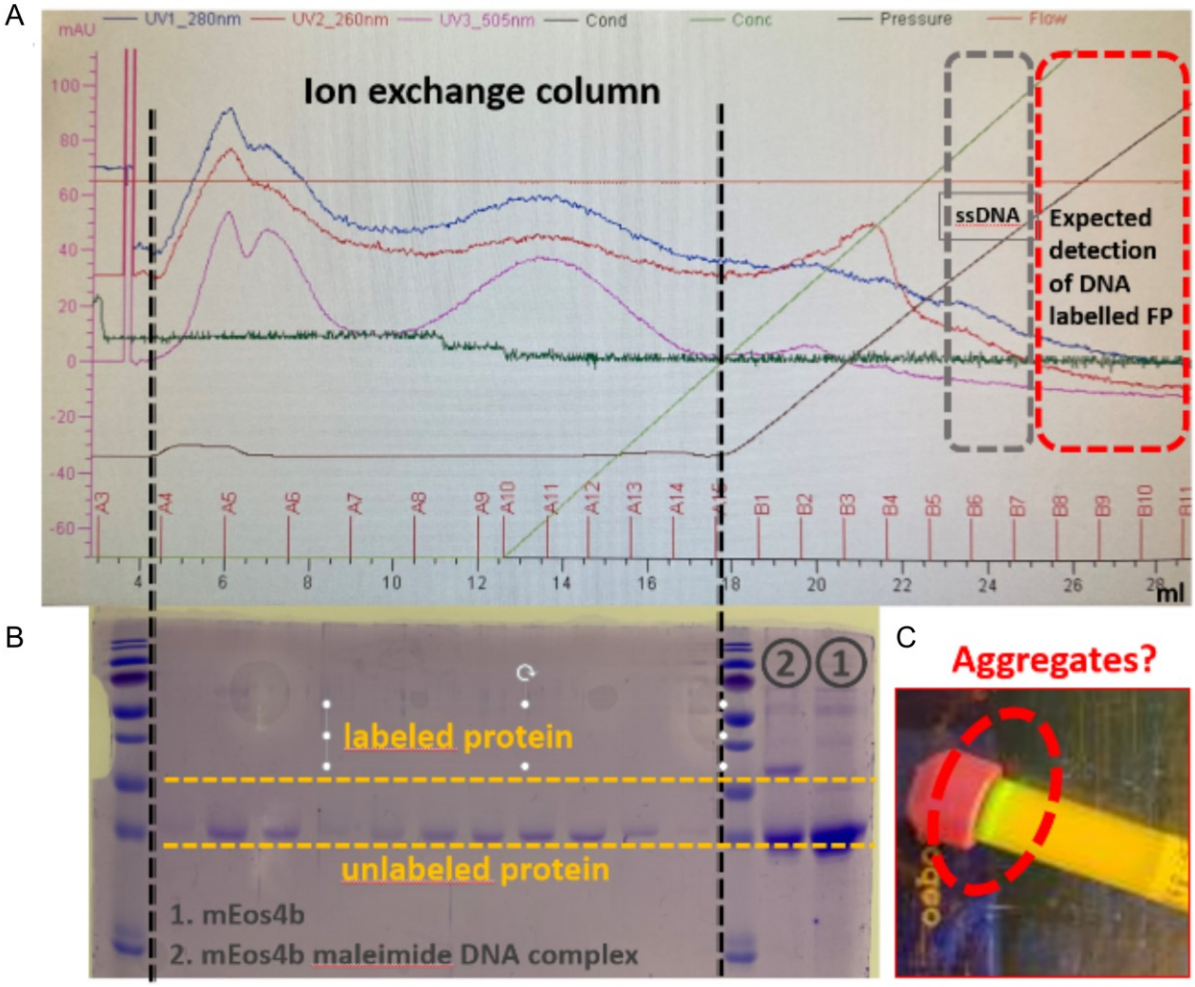

Figure 3.7 Aggregation of DNA-labeled mEos4b inside the ion exchange column. *Ion exchange chromatography was used in an attempt to purify DNA-labeled mEos4b from free ssDNA and unlabeled protein. However, the DNA-labeled protein did not elute from the column. A) Chromatogram of the sample with the corresponding fraction analyzed on SDS-PAGE in (B), showing elution of only unlabeled protein. C) Image of the column after the experiment showing the presence of fluorescent protein, presumably aggregates of the DNA-labeled mEos4b. Data and Figure by Julian Bauer.*

Given that the original mEos4b construct (His6-mEos4b) exhibits good affinity to nickel columns, we hypothesized that an interaction between N-terminal His-Tag and the C-terminal cysteine is responsible for the decreased affinity. Such an interaction could possibly also explain why the labeling efficiency of the protein with the DNA was relatively low (~40%). To investigate the possibility that our construct design was causing problems, we designed another FP construct in

which both the His-Tag and cysteine were located on the C-terminus (mEos4b-His6-C), similar as in the original FP construct used by Jusuk et al., hoping that this would improve its biochemical behavior. Unfortunately, although this construct did have a high affinity for nickel columns, DNA labeling remained inefficient and seemed to cause aggregation. Therefore, we decided not to continue this project with mEos4b.

3.1.2.4 Conclusion

Photophysical characterization of FPs requires a suitable immobilization platform. We found that, while convenient, PAA gel might not always be a good option, especially when aiming to extract information about the PCE or when full control over the environmental conditions is desired. The NPC presents a good alternative to study the effects of illumination and environmental conditions on the performance of FPs but is less suitable for photophysical studies due to its oligomeric nature. We tested the usage of DNA-origamis for photophysical studies of mEos4b but, unfortunately, we were unable to obtain a well-functioning sample. It remains to be tested whether the problems we encountered regarding labeling and aggregation are specific to mEos4b. Notably, Jusuk et al. did manage to study the behavior of eYFP attached to DNA-origamis.

Thus, the search for an alternative for PAA gel continues. Collaborators (J.B. Siberita and M. Sainlos, Bordeaux Neurocampus) are working on the development of a immobilization platform based on the SpyCatcher-SpyTag system[442]. Their preliminary results are promising, providing a platform which enables facile and specific immobilization of FPs and allows full control over the buffer conditions. This platform could present a suitable alternative for PAA gel.

3.1.3 Illumination conditions affect the photoconversion efficiency of mEos4b and other common PCFPs

Parts of the results of this section have been published in:

Jip Wulffele, Daniel Thédié, Oleksandr Glushonkov, and Dominique Bourgeois. ***mEos4b Photoconversion Efficiency Depends on Laser Illumination Conditions Used in PALM****. The Journal of Physical Chemistry Letters 2022 13 (22), 5075-5080. DOI: 10.1021/acs.jpclett.2c00933*

Green-to-red photoconvertible FPs from the EosFP family are popular fluorescent markers for PALM imaging. Their complex photophysical behavior, however, hinders their usability in quantitative applications. In particular blinking is a major source of error in molecular counting and single particle tracking experiments[144,218,253,254]. In spt experiments, blinking disrupts single particle tracks creating many truncated tracks, limiting the application of advanced analysis algorithms, which often require relatively long tracks[217]. In counting experiments, repetitive blinking causes overcounting errors if not properly corrected for[144,253,254]. Another key properties PCFPs is their photoconversion efficiency (PCE), which is the fraction of initial green proteins that reaches the photoconverted red state. This property is of less importance for spt but has great importance for molecular counting as incomplete photoconversion leads to undercounting[205,254]. In addition, the PCE is also a determining factor for the achievable spatial resolution in conventional PALM imaging as it affects the effective labeling efficiency (ELE) and thereby the Nyquist criterium[315].

Ongoing efforts are focused on improving the behavior of PCFPs, by both mutagenesis and optimization of experimental conditions, to boost their usage in quantitative applications. Previous work of the lab showed that application of low intensity 488 nm light during spt experiments increases the track length by suppression of long-lived blinks when using Eos-like FPs[218]. The

mechanistic explanation of this effect is that long-lived blinks in Eos-like proteins are largely due to light induced *cis-trans* isomerization of the chromophore, similar to off-switching in RSFPs, with the *trans* state being effectively switched back to the *cis* state by absorption of blue-shifted light[218]. Since long-lived blinks also hinder counting, we hypothesized that this strategy could also benefit molecular counting. This hypothesis was the motivation for the work described in this section, starting with an investigation of the effects of blinking on molecular counting, leading to the finding that the applied 405 power density in PALM experiments affects the PCE of many commonly used PCFPs.

3.1.3.1 Off-time reduction facilitates molecular counting

Before starting experiments, we investigated the effect of long-lived blinks on molecular counting by simulations. In particular, we wanted to test whether reduction of the off-time durations improves counting. To do this, we ran single molecule simulations in SMIS[266], using a simplified photophysical model of mEos4b (**Figure 3.8A**). We omitted green-state photophysics from the simulations to keep constant photoconversion kinetics to not confuse changes in blinking with altered photoconversion kinetics since both are known to affect counting. Simulations were run applying a typical PALM illumination scheme with 500 W/cm^2 561 nm and 1 W/cm^2 405 nm light. To test the effect of long-lived blinks on counting, simulations were performed with additional 488 nm light illumination, which strongly reduced the off-time durations (**Figure 3.8B**). Importantly, using these simulation conditions, 488 nm light did not affect the photoconversion kinetics nor changed the number of blinks (**Figure 3.8**). After processing of the simulated data and composing oligomers of various sizes as described in the materials and methods (**section 2.7.1**), counting was performed using two distinct methods: counting by off-time thresholding as described by Lee et al.[253] and counting by blinking statistics as described by Heilemann et al.[144,206,216,254].

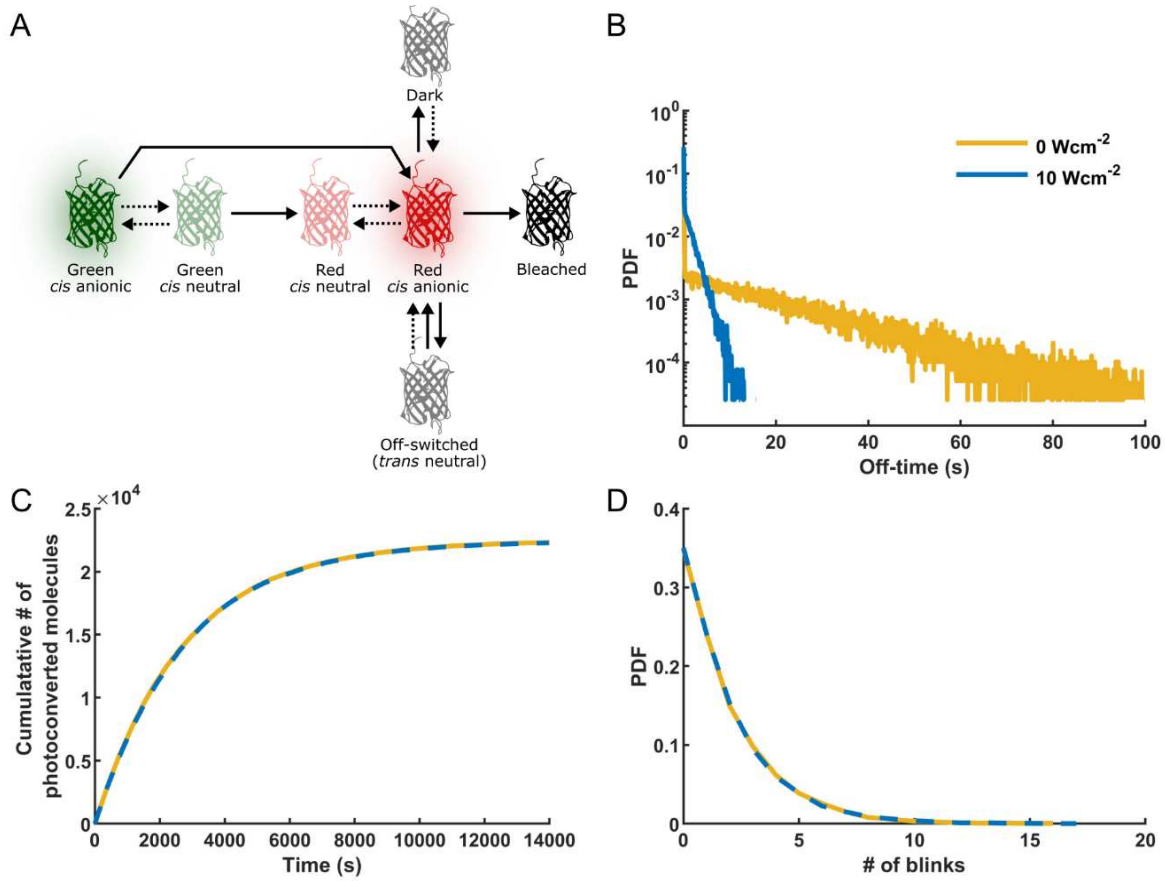

***Figure 3.8 Simulated single molecule data used for counting analysis**. Single molecule simulations where performed in SMIS using a simplified photophysical model of mEos4b (A), omitting green state photophysics. Single molecule traces were simulated under alternating illumination with 500 W/cm^2 561 nm and 1 W/cm^2 405 nm light, with and without 10 W/cm^2 488 nm light to reduce the red state off-times (B). Addition of 488 nm light had no effect on the photoconversion kinetics (C) and red state blinking histograms (D).*

The off-time based counting method developed by Lee et al. is based on the generation of a calibration curve from artificial oligomers to determine the optimal time threshold (τ_c) for a given stoichiometry (see **section 1.5.2.1**). The calibration curves of the simulated data are shown in **Figure 3.9A**. Both in the prescence and absence of 488 nm light, the optimal τ_c decreases with increasing stoichiometry to compensate for the decreased time between the acvtivation of different molecules. However, in the absence of 488 nm light the optimal τ_c is higher than in the prescence of 488 nm light because of longer off-time durations (**Figure 3.8B**). Given that the photoconversion kinetics are unaffected by the prescence of 488 nm light (**Figure 3.8C**), counting is consequently more precise in the prescence of 488 nm light (**Figure 3.9B** and **Supplementary Figure 1**) because there is less mixing of the fluorescence traces of different fluorophore. It should be noted, however, that while off-time reduction by 488 nm light reduced the spread of the distribution of retrieved stoichiometries, the average retrieved stoichiometry was always correct, also in the condition with long off-times (**Figure 3.9B**). However, contrary to in these simplified simulations, in real experiments, the retrieved average stoichiometry is likely to differ from the true stoichiometry because of noise, an incomplete labeling efficiency and possibly a mixture of oligomers of different sizes. Under these conditions, we expect the reduced distribution by off-time reduction to be highly beneficial for counting.

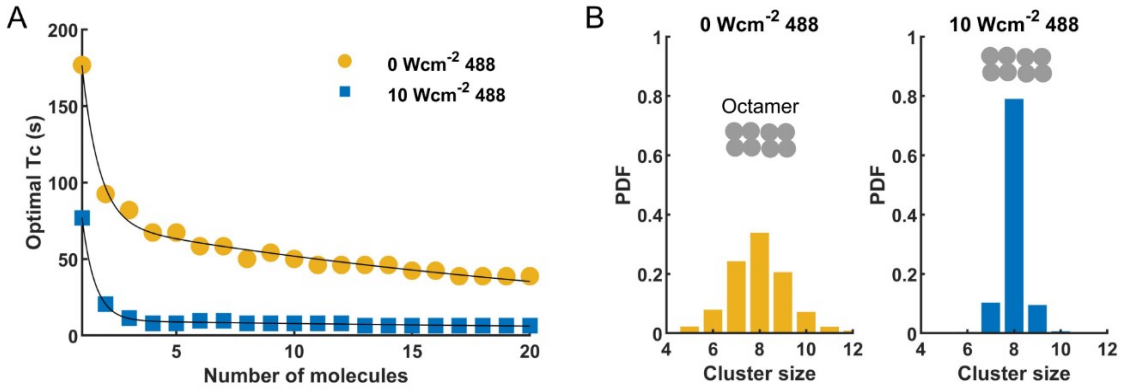

Figure 3.9 Off-time reduction facilitates molecular counting by off-time thresholding. *Molecular counting of simulated oligomers was performed as described by Lee et al. Optimal τ_c curves (A) were calculated from fluorescence traces of simulated monomers under typical PALM illumination with and without 10 W/cm^2 488 nm light. These optimal τ_c curves were used to count fluorescence traces of simulated octamers (B) with a labelling efficiency of one under the same illumination conditions as (A).*

The counting method developed by Heilemann et al. is based on the statistical analysis of the blinking histograms (nBlink histograms) of the fluorescent protein (see **section 1.5.2.2**). This method first calibrates the blinking propensity of the employed FP, denoted as the p-value, by fitting a geometric distribution to the nBlink histogram of the monomeric protein (**Figure 3.10A**). This p-value is then used to deduce the stoichiometry of unknown oligomers. Since this method only considers the number of blinks, it is insensitive to the duration of the off-times. As a consequence, off-time reduction by 488 nm light had no effect on the counting accuracy (**Figure 3.10B** and **Supplementary Figure 2**). However, while this method is insensitive to the off-time duration, it is strongly dependent on accurate determination of the p-value, as we found that a small error in the p-value results in large errors when estimating the size of bigger oligomers (**Figure 3.11A**, **Supplementary Figure 2**). Given that fitting of nBlink histograms is often complicated by a disproportionately large population of molecules that do not blink, possibly due to the existence of multiple FP populations (**Figure 3.11B**), we suspect that off-time based counting is more appropriate than blinking based counting to investigate the stoichiometries of larger complexes.

Altogether, the findings from these simulations motivated us to experimentally investigate the usage of 488 nm light to facilitate molecular counting.

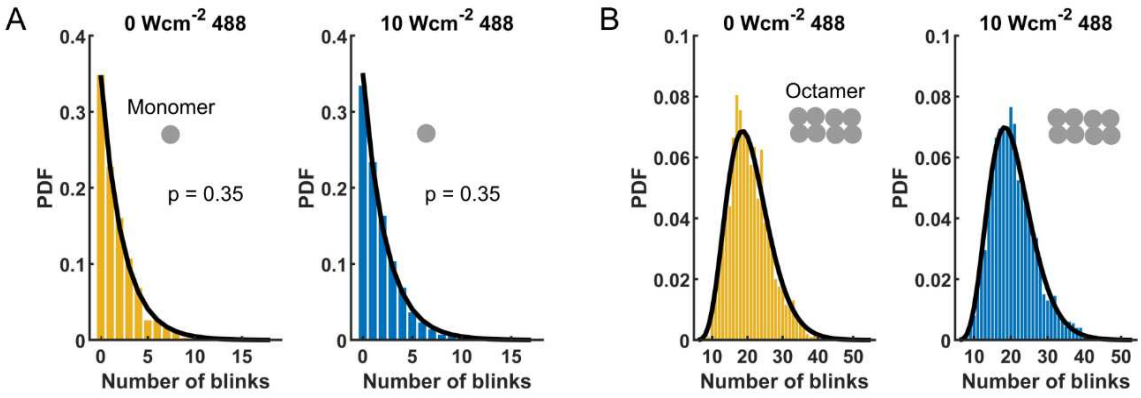

Figure 3.10 Off-time reduction does not facilitate molecular counting based on nBlink histograms. *Molecular counting of simulated oligomers was performed as described by Baldering et al. nBlink histograms of simulated monomers (A) were fitted with a geometric distribution to determine the p-value (solid lines). This p-value was then used to fit the nBlink histograms of simulated octamers unsing a negative binominal distribution (B) to estimate the stoichiometry (n).*

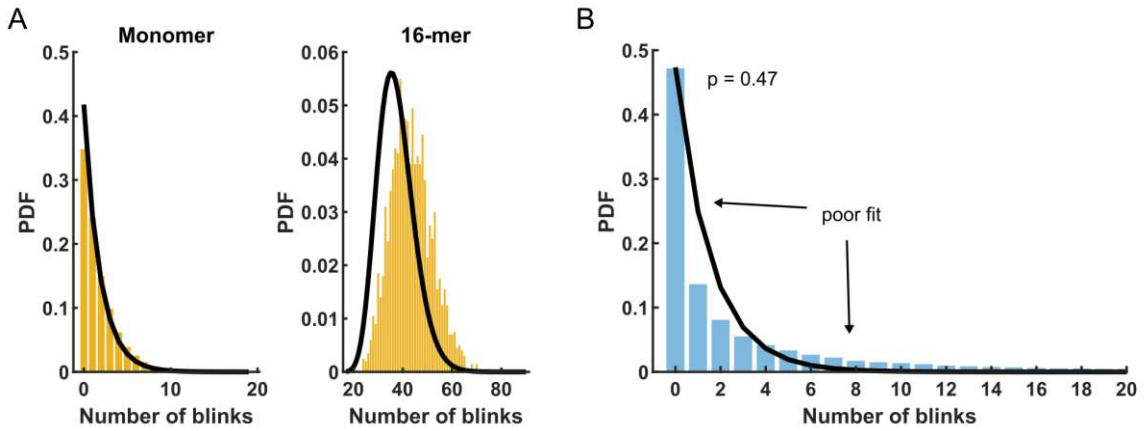

Figure 3.11 Difficulties with counting using nBlink statistics. *A) Counting of simulated data. A 20% error was added to the p-value (p=0.42 instead of p=0.35), resulting in large deviations between the expected nBlink distribution (solid lines) and measured data (yellow histograms). B) Fitting of an nBlink histogram of experimental data (500 W/cm^2 561 nm light and 1 W/cm^2 405 nm light).*

3.1.3.2 Off-time reduction by 405 and 488 nm light is offset by a decreased photoconversion efficiency

To investigate the usability of 488 nm light for counting purposes, we first validated that 488 nm light reduced the duration of the off-times of mEos4b under qPALM imaging conditions. The difference between sptPALM and qPALM imaging is that in sptPALM imaging there is typically minimal, if not zero, 405 nm light to ensure a very low localization density to enable accurate tracking, while for qPALM imaging substantial 405 nm light might be needed to fully exhaust the pool of green molecules to maximize the labeling efficiency. **Figure 3.12A** shows that in qPALM imaging conditions (500 W/cm^2 561 nm and 1 W/cm^2 405 nm light) there is indeed additional off-time reduction by 488 nm light.

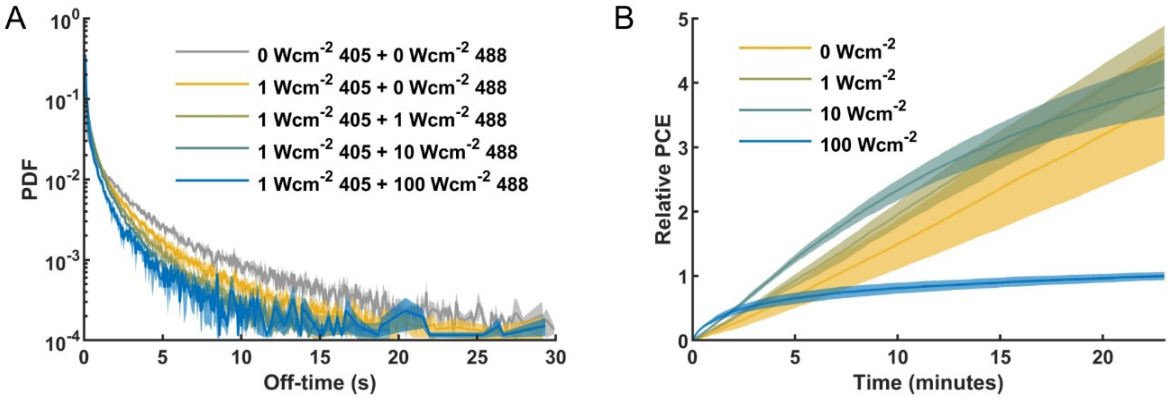

Figure 3.12 A decreased photoconversion efficiency offsets off-time reduction by 488 nm light. *Off-time histograms (A) and the relative PCE (B) of mEos4b embedded in PAA gel at pH 8.5 under alternating excitation with 561 nm (70 ms at 500 W/cm^2), 405 nm (8.2 ms at 1 W/cm^2, unless noted otherwise) and 488 nm (8.2 ms at 0-100 W/cm^2) light. The photoconversion data is normalized to the final number of photoconverted molecules under 100 W/cm^2 488 illumination. Data is shown as mean ± s.d. of ≥ 3 measurements.*

Since a high PCE is critical in counting experiments, we also examined the effect of 488 nm illumination on the PCE of mEos4b. Because we were not able to determine the absolute PCE using our PAA-based samples, we took the normalized number of photoconverted molecules after 23 minutes of imaging as measure for the relative PCE under the different illumination conditions. While

488 nm light slightly increased the photoconversion rate during the first minutes of the measurements, we found that high intensity 488 nm illumination (100 W/cm^2) strongly reduced the final PCE (**Figure 3.12B**). A reduced PCE could be explained by increased bleaching of the red state so that molecules are bleached before they can be detected. However, although 488 nm light does slightly decrease the red state on-times, bleaching-times and photon budget (**Figure 3.13**), the effect does not seem to be large enough to explain the 4x reduced PCE (**Figure 3.12B**), indicating that green state photophysics are most likely at the origin of the decreased PCE.

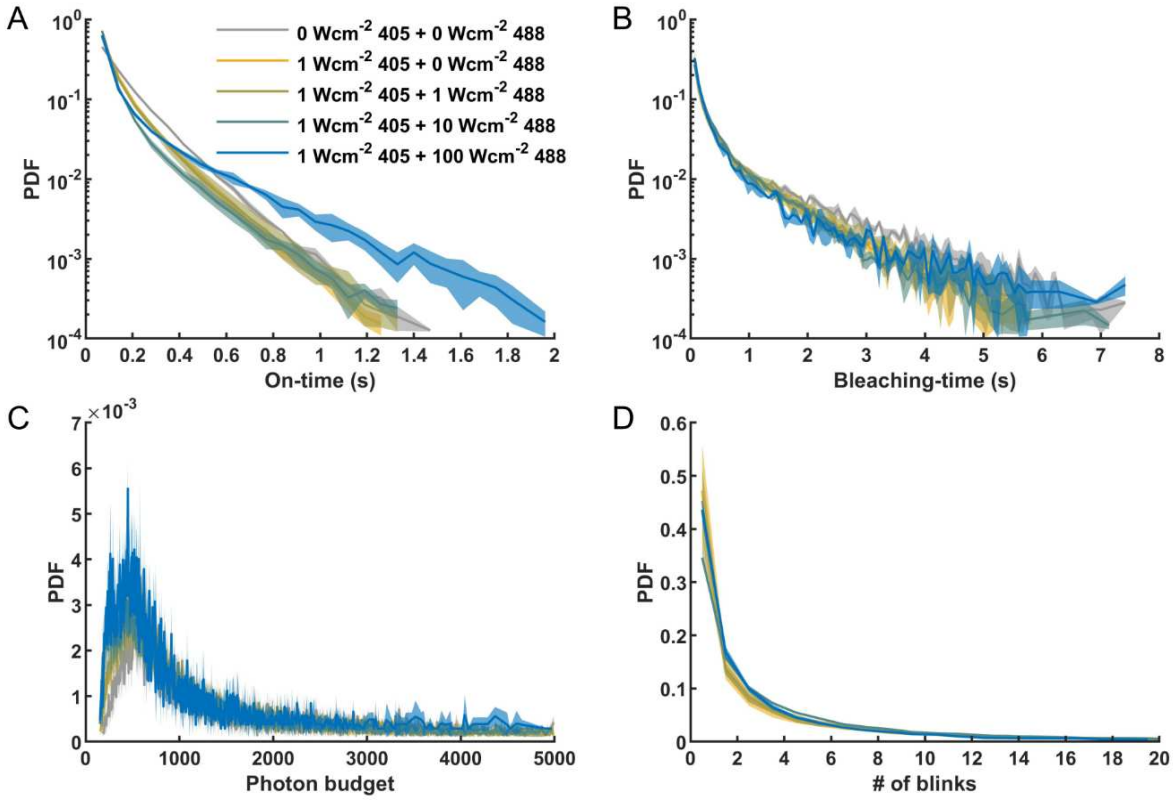

Figure 3.13 Effect of 488 nm light illumination on mEos4b red state photophysics. *On-time histograms (A), Bleaching-time histograms (B), photon budget histograms (C) and histograms of the number of blinks of mEos4b molecules embedded in PAA gel at pH 8.5 under alternating excitation with 561 nm (70 ms at 500 W/cm^2), 405 nm (8.2 ms at 0-1 W/cm^2) and 488 nm (8.2 ms at 0-100 W/cm^2). Data is shown as mean ± s.d. of ≥ 3 measurements.*

Using SMIS simulations, we investigated how 488 nm light reduces the PCE. Photoconversion of mEos4b was simulated using a complete photophysical model of mEos4b (**Table 2.3**) and varying illumination consitions (500 W/cm^2 561 nm, 0 or 1 W/cm2 405 nm, and 0 or 10 W/cm2 488 nm light). The simulations showed that the reduction of the PCE by 488 nm light is readily predicted by the existing photophysical of mEos4b and is caused by increased green state bleaching by the additional 488 nm light (**Figure 3.14B**). Importantly, the simulations also showed that this reduction is only apparent in the presence of 405 nm light. This is because in the absence of 405 nm light, photoconversion is driven, although very ineffectively, by 561 and 488 nm light from the green anionic state, in which case the PCE is determined by the ratio between the bleaching and photoconversion quantum yields, which is independent of the illumination intensity, assuming all processes are single photon (**Figure 3.14A**). In the presence of 405 nm, on the other hand, photoconversion is driven from the green neutral chromophore, which has a much higher photoconversion quantum yield than the green anionic state (in the order of ~10^{-4} vs ~10^{-7}) (**Figure 3.14A**). In this situation, 488 nm light induced bleaching is thus decoupled from the photoconversion

rate, so that increasing the 488 nm intensity increases green state bleaching and thereby decreases the PCE.

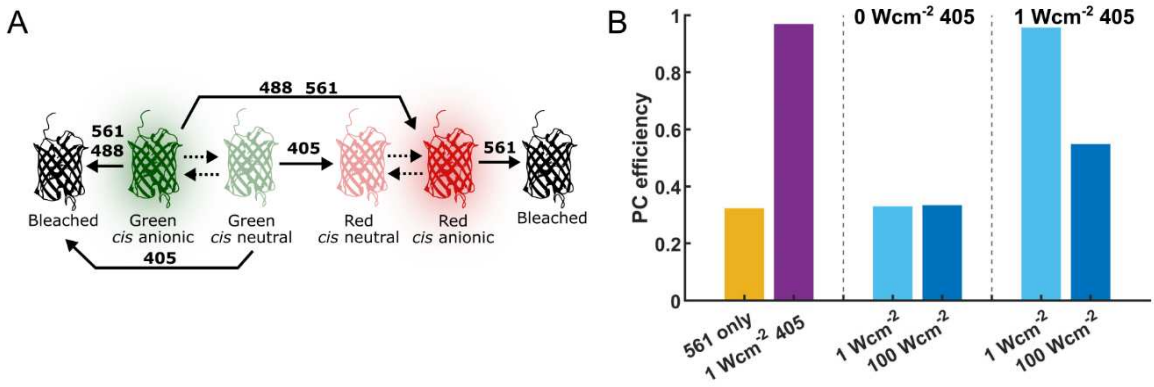

Figure 3.14 Simulations of the PCE of mEos4b under different illumination conditions. *(A) Simplified photophysical model of mEos4b to illustrate the expected effects of 405, 488 and 561 nm light illumination on the PCE of mEos4b. (B) The PCE of mEos4b simulated under different illumination conditions. Left to right: 500 W/cm^2 561 nm light (yellow bar), 500 W/cm^2 561 nm and 1 W/cm2 405 nm light (purple bar), 500 W/cm^2 561 nm light with 1 or 100 W/cm^2 488 nm light (light and dark blue bars), and 500 W/cm^2 561 nm and 1 W/cm^2 405 nm light with 1 or 100 W/cm^2 488 nm light (light and dark blue bars).*

Having established that 488 nm light reduces the PCE in the presence of 405 nm light, we wondered how the 405 nm light intensity by itself affects the PCE. We hypothesized that under typical PALM imaging conditions with high intensity 561 nm light, increasing the 405 intensity would increase the PCE by reducing the acquisition time and thereby limiting the time for the 561 nm light to bleach the green state. Contrary to our expectations, however, we found that high intensity 405 nm light (100 W/cm^2) reduced the PCE of mEos4b (**Figure 3.15B**), although less severely than 488 nm light. Again, red state bleaching appeared minimally affected by the additional laser intensity (**Figure 3.16**), indicating that green state photophysics are also responsible for this effect.

In addition, we plotted the red state off-times as function of the 405 nm light power density and found that 405 nm light alone reduces the off-time durations to a greater extend than 488 nm light at similar power densities (**Figure 3.15A**). This is surprising given that 488 nm light is more effectively absorbed by the *trans* neutral chromophore and was shown to switch on mEos4b at a higher rate than 405 nm light [217]. The reason for this discrepancy remains unknown. One possible explanation is that there are multiple off-states some of which might be sensitive to 405 nm light but not to 488 nm light. This question will be further investigated in section **3.1.4.3**.

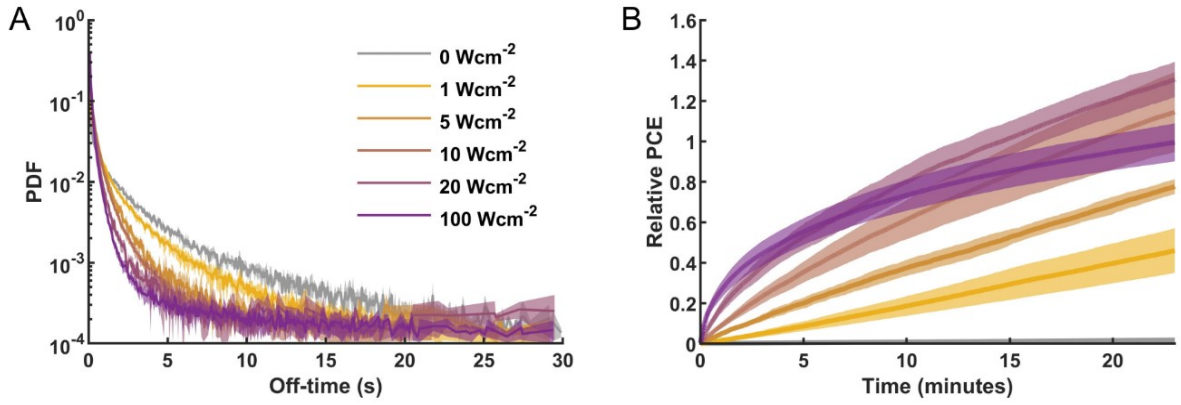

Figure 3.15 A decreased photoconversion efficiency offsets off-time reduction by 405 nm light. *Off-time histograms (A) and the relative PCE (B) of mEos4b molecules embedded in PAA gel at pH 8.5 under alternating*

excitation with 561 nm (70 ms at 500 W/cm^2) and 405 nm (8.2 ms at 0-100 W/cm^2) light. The photoconversion data is normalized to the final number of photoconverted molecules under 100 W/cm^2 405 illumination. Data is shown as mean ± s.d. of ≥ 3 measurements.

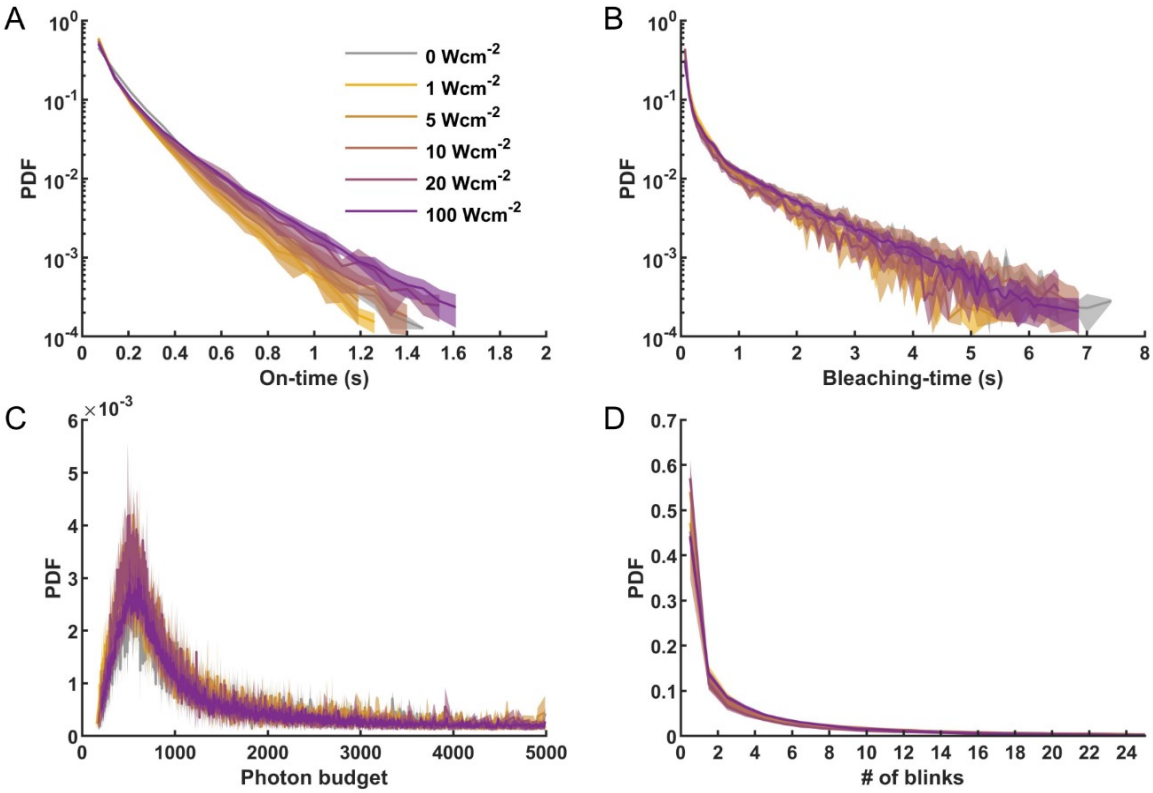

Figure 3.16 Effect of 405 nm light illumination on mEos4b red state photophysics. *On-time histograms (A), bleaching-time histograms (B), photon budget histograms (C) and histograms of the number of blinks of mEos4b molecules embedded in PAA gel at pH 8.5 under alternating excitation with 561 nm (70 ms at 500 W/cm^2) and 405 nm (8.2 ms at 0-100 W/cm^2) light. Data is shown as mean ± s.d. of ≥ 3 measurements.*

3.1.3.3 405 nm light decreases the PCE of mEos4b and other PCFPs in a nonlinear manner

While the existing photophysical model of mEos4b predicts the decrease in PCE by increasing 488 nm illumination, it does not predict the decrease in PCE by increasing 405 nm illumination. Searching for an explanation of the observed effect, we hypothesized that 405 nm light bleaches the green state in a non-linear manner, meaning that, while photoconversion requires a single photon, bleaching requires the absorption of two (or more) photons so that at higher laser intensity the bleaching pathway becomes more important. We investigated this hypothesis by monitoring the PCE of mEos4b under 10 W/cm^2 and 100 W/cm^2 405 nm illumination while keeping the total illumination dose constant by adjusting the exposure time to 82 ms or 8.2 ms, respectively (**Figure 3.17A**). We found that exposure to short pulses of 100 W/cm^2 405 nm light lowered the PCE of mEos4b compared to longer pulses of 10 W/cm^2 light, supporting our hypothesis of a non-linear effect (**Figure 3.17A**). Furthermore, the photophysical behavior of the red state appeared the same under both illumination regimes (**Figure 3.17**), confirming that green state photophysics are most likely responsible for this non-linear effect.

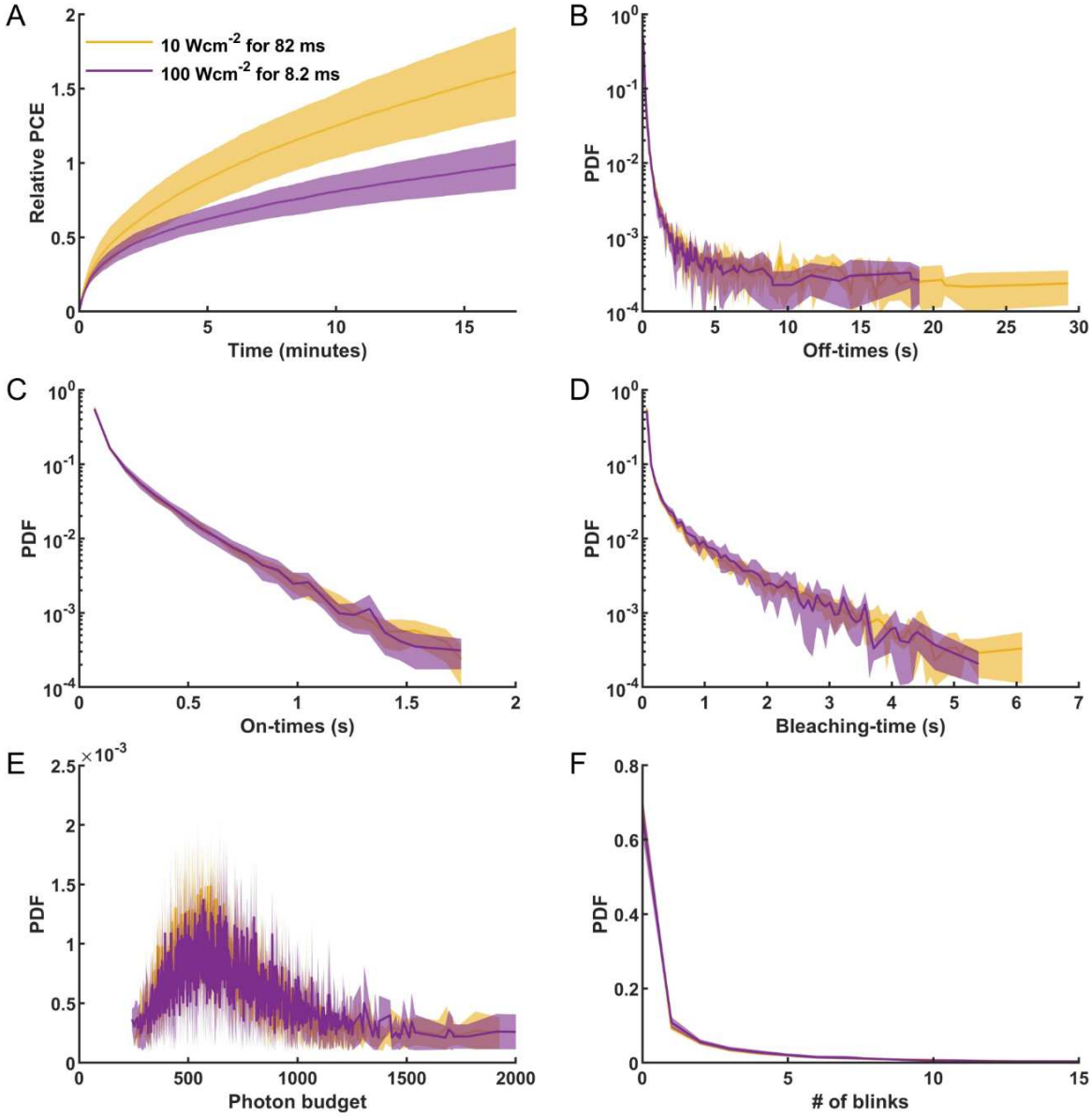

Figure 3.17 405 nm light reduces the PCE of mEos4b in a non-linear manner. *The relative PCE (A), off-time histograms (B), on-time histograms (C), bleaching-time histograms (D), photon budget histograms (E) and histograms of the number of blinks (F) of mEos4b molecules embedded in PAA gel at pH 8.5 under alternating excitation with 561 nm (70 ms at 500 W/cm^2) and 405 nm (82 ms at 10 W/cm^2 or 8.2 ms at 100 W/cm^2) light. The photoconversion data is normalized to the final number of photoconverted molecules under 100 W/cm^2 405 illumination. Data is shown as mean ± s.d. of ≥ 3 measurements.*

Next, we wondered whether the presence of high intensity 561 nm light, as typical in PALM, is necessary for the effect of the 405 nm light intensity on the PCE. This questions was raised by the observation that high intensity 561 nm light populates the green Off state (*trans* neutral chromophore)[204], which strongly absorbs 405 nm light. So, we asked whether this could be the state from which nonlinear bleaching occurs. We addressed this question by ensemble measurements of the photoconversion kinetics of mEos4b to minimize the amount of required 561 nm light to get sufficient signal. PAA samples with mEos4b were exposed to 1, 10 or 100 W/cm^2 405 nm light while the fluorescence of the red state was monitored by application of 8 W/cm^2 561 nm light every 500 ms. In the situation were photoconversion follows a simple three state model (Green -> Red -> Bleached), we would expect that the peak intensity of the red fluorescence increases with increasing 405 intensity because the faster photoconversion kinetics would limit red state bleaching by 561 nm

light. Our data, however, showed a reduced peak height under 100 W/cm^2 illumination compared to 1 and 10 W/cm^2 illumination (**Figure 3.18A**). Furthermore, we compared the PCE at the ensemble level under illumination with 10 W/cm^2 405 nm for 400 ms and 100 W/cm^2 405 nm for 40 ms and found that, again, the PCE was reduced with 100 W/cm^2 405 nm light, even though the integrated dose of illumination was kept constant (**Figure 3.18B**). Together these findings indicate that high intensity 561 nm light is not required for non-linear bleaching of the green state by 405 nm light. These data, however, do not exclude that the green *trans*-state is involved, since the *trans*-state may also be formed from the *cis*-neutral state by absorption of 405 nm light.

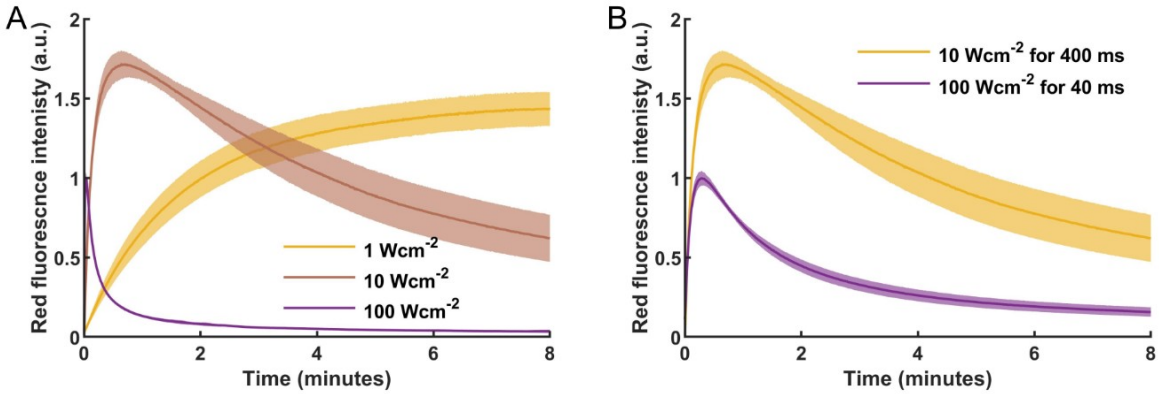

Figure 3.18 High intensity 405 nm light reduces the PCE of mEos4b in the absence of high intensity 561 nm light. *A) Time traces of the ensemble red fluorescent intensity of mEos4b molecules illuminated with 400 ms pulses of 405 nm light at 1-100 W/cm^2 illumination. B) Time traces of the ensemble red fluorescent intensity of mEos4b molecules illuminated with 40 or 400 ms pulses of 405 nm light at 100 or 10 W/cm^2, respectively. The red fluorescent intensity was recorded every 500 ms by excitation with 8 W/cm2 561-nm light for 20 ms. Data is normalized to the maximum red fluorescent intensity under 100 W/cm^2 405 illumination. Data is shown as mean ± s.d. of ≥ 3 measurements.*

It should be noted that the ensemble experiments (**Figure 3.18**) showed that 405 nm light decreases the red fluorescence in a dose dependent manner, while the single molecule experiments indicated that 405 nm light does not significantly increase red state bleaching under PALM imaging conditions (**Figure 3.16**). These seemingly contradicting findings may be explained by strong red-state bleaching by the high intensity 561 nm light used for the PALM experiments, hiding the bleaching (or switching, see **section 3.1.4.3.2**!) induced by the 405 nm laser.

Searching for a solution to the reduced PCE of mEos4b under high intensity 405 nm light, we investigated if other commonly used PCFPs show the same behavior. To this end, we monitored the ensemble photoconversion kinetics of mEos3.2, pcStar and Dendra2, applying the same illumination schemes as in **Figure 3.18**. The results, shown in **Figure 3.19**, reveal that all tested PCFPs exhibit a similar behavior as mEos4b, displaying a reduced PCE under intense 405 nm illumination. We validated these ensemble measurements by PALM imaging of pcStar using 500 W/cm^2 561 nm light and 10 or 100 W/cm^2 405 nm light, similar as in **Figure 3.17**. **Figure 3.20** shows that, similarly as for mEos4b, 100 W/cm^2 405 nm light strongly reduced the PCE of pcStar under PALM imaging conditions. Together these results indicate that nonlinear bleaching of the green state by 405 nm light is a common property of PCFPs.

Looking at the ensemble measurements in **Figure 3.19**, the kinetics of pcStar under 10 W/cm^2 405 nm light are intriguing. The initial increase in red fluorescence, by photoconversion, is followed by a rapid decrease in intensity, presumably by red state bleaching, after which the fluorescence signal stabilizes. To our knowledge, such a behavior has not been reported before. A possible explanation could be the presence of a 405 nm light induced dark state, which recovers in a thermal or light induced manner, resulting in the initial decrease, during which dark state formation dominates,

followed by the plateau phase during which dark state formation and recovery are balanced (see also **section 3.1.4.3**).

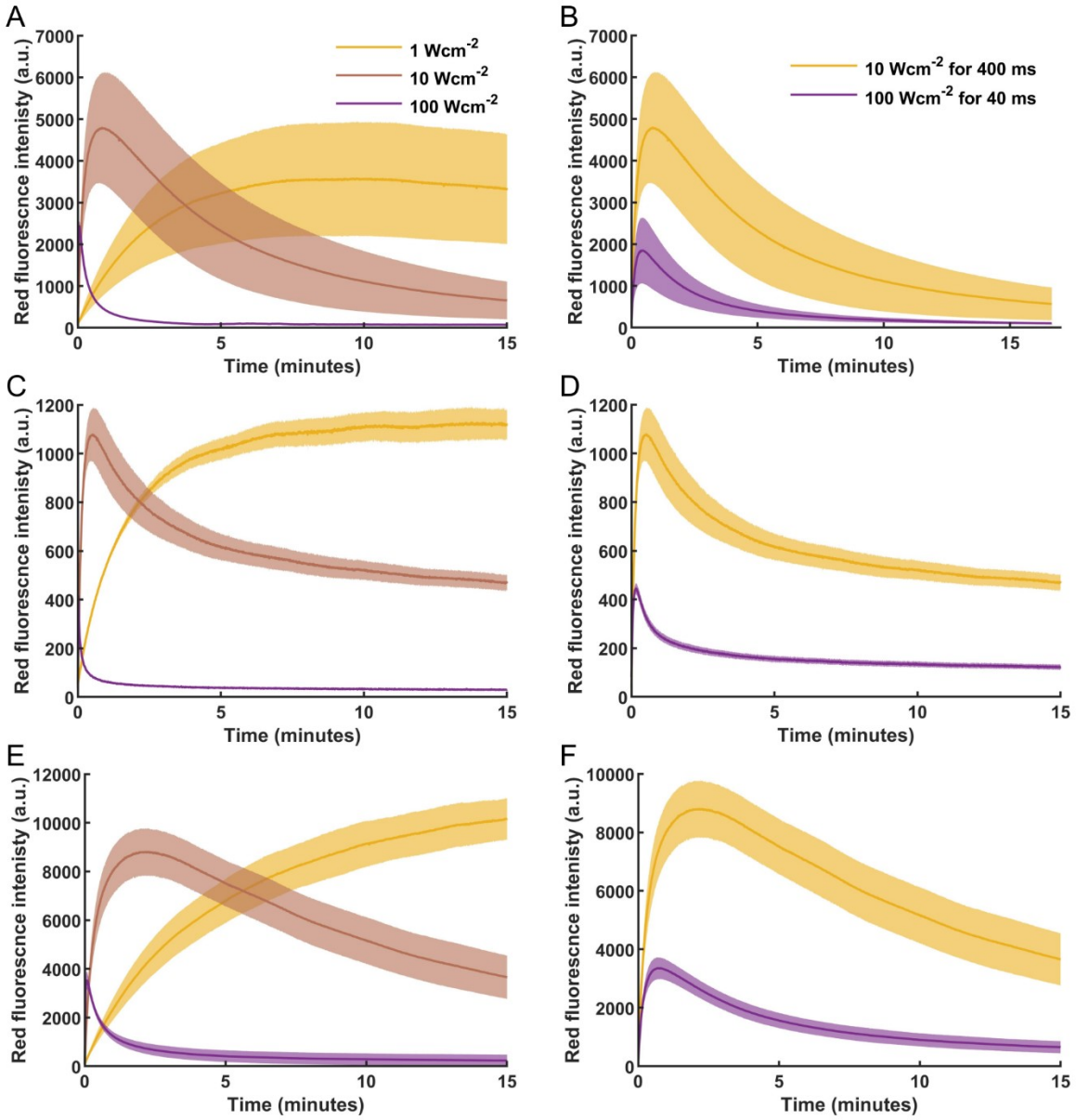

Figure 3.19 High intensity 405 nm light reduces the PCE of commonly used PCFPs. *A) Time traces of the ensemble red fluorescent intensity of mEos3.2 molecules illuminated with 400 ms pulses of 405 nm light at 1, 10 and 100 W/cm^2 illumination. B) Time traces of the ensemble red fluorescent intensity of mEos3.2 molecules illuminated with 40 or 400 ms pulses of 405 nm light at 100 or 10 W/cm^2, respectively. The red fluorescent intensity was recorded every 500 ms by excitation with 8 W/cm^2 561-nm light for 20 ms. Data is normalized to the maximum red fluorescent intensity under 100 W/cm^2 405 illumination. Data is shown as mean ± s.d. of ≥ 3 measurements. C-D and E-F) the same as A and B but with pcStar and Dendra2.*

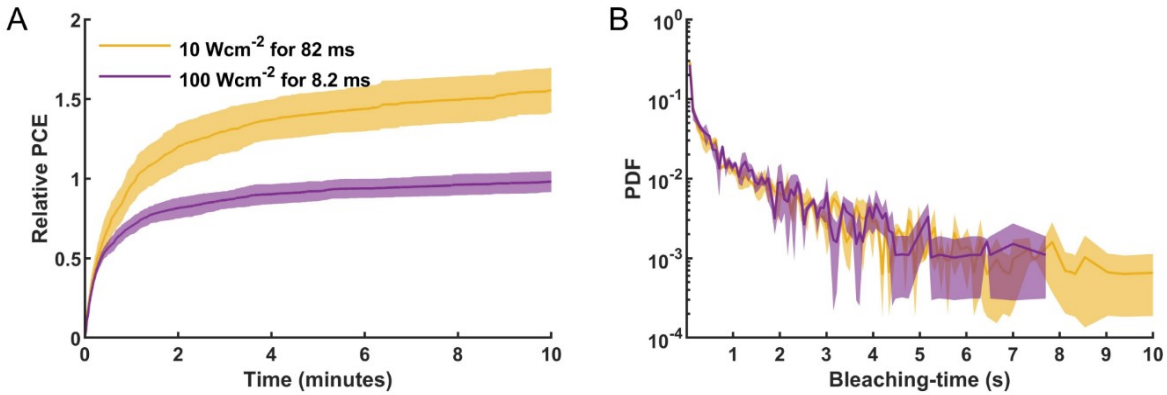

Figure 3.20 High intensity 405 nm light reduces the PCE of pcStar in a non-linear manner under PALM imaging conditions. *The relative PCEs (A) and bleaching-time histograms (B) of pcStar molecules embedded in PAA gel at pH 8.5 under alternating excitation 561 nm (70 ms at 500 W/cm^2) and 405 nm (82 ms at 10 W/cm^2 or 8.2 ms at 100 W/cm^2) light. The photoconversion data is normalized to the final number of photoconverted molecules under 100 W/cm^2 405 illumination. Data is shown as mean ± s.d. of ≥ 3 measurements.*

Having characterized the effect of 405 nm light on the PCE *in vitro*, we sought to confirm this effect under biologically relevant conditions using the Nup96-mEos4b cell line (see **section 3.1.2.2**). For PALM imaging, cells were fixed and images were recorded using 500 W/cm^2 561 nm light and 10 or 100 W/cm^2 405 nm light for 15000 frames. Because of the high local density of the Nup96 molecules in the NPCs, we had to reduce the exposure time of the 405 nm laser, relative to the *in vitro* experiments, to 3.5 and 0.35 ms for 10 and 100 W/cm^2, respectively. Under these imaging conditions, estimation of the effective labeling efficiency (ELE), as proxy for the PCE, did not reveal a significant difference between the data reordered using 10 or 100 W/cm^2 405 nm light (**Figure 3.21**), suggesting that there was no nonlinear bleaching by the 405 nm laser. The absence of nonlinear bleaching might possibly be explained by the reduced illumination period (0.35 ms vs 8.2 ms) not providing enough photons to induce significant bleaching, or by a delay in the formation of the intermediate state (e.g. if it is formed downstream of the triplet state) so that after only 0.35 ms this state is simply not yet present and can thus not absorb a second photon and bleach. Regardless of the exact explanation, this seems to be good news for PALM imaging, as the usage of high intensity 405 nm light for longer periods is typically rare so that nonlinear bleaching of the green state by the 405 nm laser will be minimal. However, care should be taken when gradually increasing the 405 intensity during acquisitions to compensate for the decreasing pool of green molecules and when performing experiments that do require high intensity 405 nm illumination such as high-speed PALM imaging[443].

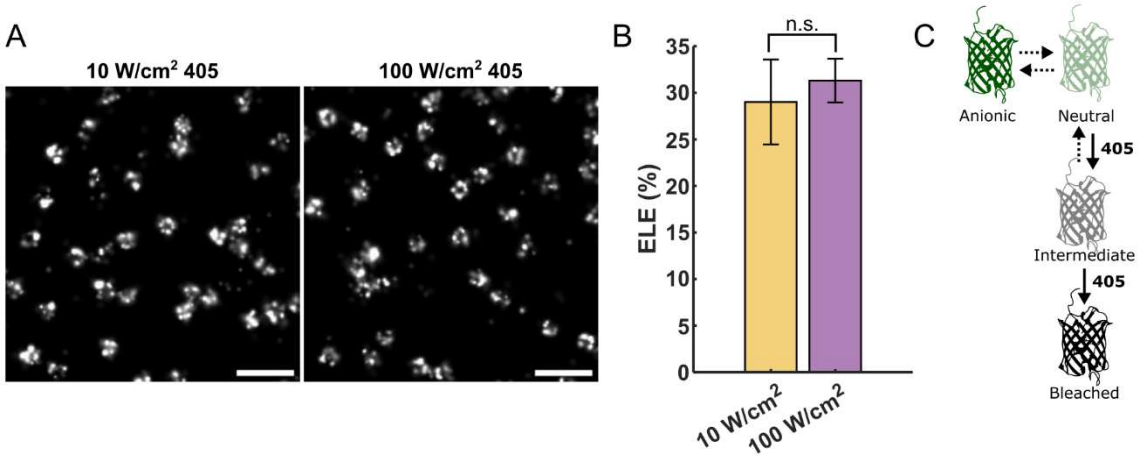

Figure 3.21 Investigation of the effect of 405 nm light on the ELE using the Nup96-mEos4b cell line*. PALM imaging of fixed Nup96-mEos4b cells (pH 8) was performed by alternating excitation with 500 W/cm^2 561 nm*

light (50 ms) and 10 or 100 W/cm^2 405 nm light (3.5 or 0.35 ms). A) Reconstructed PALM images. Scale bar: 500 nm. B) Estimation of the Effective Labelling Efficiency (ELE). N = 2 cells, 400-600 NPCs per cell. C) Proposed photophysical scheme explaining non-linear bleaching of the green state by 405 nm light. Solid lines indicate light induced processes, dotted lines indicate thermal processes.

Although the reduced illumination period provides a logical explanation for the absence of nonlinear bleaching by the 405 nm laser, it cannot be excluded that the different environmental conditions (NPCs vs PAA gel) played a role. The influence of environmental conditions on the effect of 405 nm light on the PCE requires further investigations. This is of interest for the optimization of experimental conditions for qPALM imaging and might also provide insight into the nature of the intermediate state in the bleaching pathway. In particular, it would be interesting to test the usage of reducing thiols, such as BME and MEA, to reduce green state bleaching because these molecules appeared to have a photo-protective effect on the red states of mEos2 and mEos3.2[143,144].

3.1.3.4 A refined model of mEos4b green-state photophysics

Based on the findings presented above we propose an updated photophysical model for the green state of mEos4b (**Figure 3.22**). We propose that excitation of the green neutral chromophore can lead to the formation of an intermediate state, which may thermally relax back or absorb a second 405 nm photon, the latter which may lead to bleaching. The competition between thermal recovery and absorption of a second 405 nm photon gives rise to the nonlinear relationship between bleaching and the intensity of the 405 nm laser.

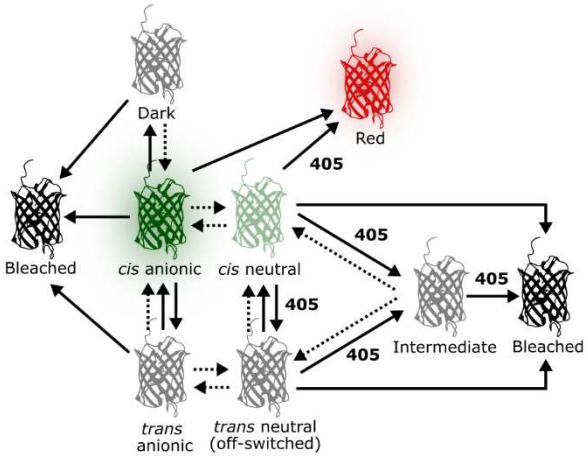

Figure 3.22 Proposed model of mEos4b green state photophysics explaining the reduced PCE under high intensity 405 nm light. *We propose that in addition to photoconversion, absorption of 405 nm light leads to the formation of an intermediate dark state which may thermally relax back or absorb a second 405 nm photon leading to bleaching. The competition between thermal relaxation and absorption of a second 405 nm photon causes the non-linear relationship between bleaching and the 405 nm light intensity. Solid lines indicate light induced processes, dashed lines indicate thermal processes.*

The exact nature of this intermediate state remains to be characterized in future work. One hypothesis to investigate is whether this intermediate could simply be the triplet state, which is known to be relatively long-lived in FPs (~5 ms at RT)[88,97,98,100] and to strongly absorb visible light[88,100]. Alternatively, this intermediate may be a longer-lived dark state down-stream of the triplet state. In light of these hypotheses, it would be interesting to test the effects of triplet state quenchers on the PCE of mEos4b under high intensity 405 nm light.

It should we noted that we previsously estimated the lifetime of the intermediate state at ~15 ms based on an assumed bleaching quantum yield of 10^{-3} and an estimated excitation rate of 7.7×10^4 s^{-1} (lifetime estimated as the time it takes to absorb 10^3 photons), which appeared to match the 8.2 ms

illumination period[444]. The estimation of the excitation rate, however, contained an error leading to a 10-fold overestimation of the rate (should have been k_{ex} = 7.7x10^3 s^{-1}, given a power density of 100 W/cm^2 405 nm light and assuming an extinction coefficient of 10^4 M^{-1}cm^{-1}, see[4]). Given an excitation rate of 7.7x10^3 s^{-1}, the argumentation no longer holds as the expected lifetime would now be ~150 ms, which is in contradiction with the 8.2 ms illumination periods. So, how can 100 W/cm^2 405 nm light still induce nonlinear photobleaching? The answer to this question probably lies in the high formation quantum yield of the intermediate state, presumably the triplet state. In the 'Perspectives' (**section 4**), I propose a refined photophysical model of mEos4b with the triplet state (formation quantum yield = 6.4x10^{-3}, half-life = 5 ms, extinction coefficient = 10^4 M^{-1}cm^{-1} at 405 nm, bleaching quantum yield = 10^{-3}) as intermediate state in the bleaching pathway from the neutral chromophore. Simulations with this model show significant nonlinear bleaching by 100 W/cm^2 405 nm light, eventhough the triplet state only absorbs ~38 photons during its lifetime (7.7x10^3 s^{-1} x 5 ms).

3.1.4 More (dark) secrets of mEos4b

The photophysical behavior of PCFPs is highly complex and many of their properties remain poorly understood. In this section, I report on various unexpected behaviors of mEos4b, which were discovered during characterization of mEos4b by NMR spectroscopy and fluorescence microscopy.

3.1.4.1 Green state heterogeneity modulates photoswitching and photoconversion

Parts of the results of this section are part of a manuscript in preparation:

Arijit Maity, Jip Wulffelé, Isabel Ayala, Adrien Favier, Virgile Adam, Dominique Bourgeois, and Bernhard Brutscher. ***Conformational heterogeneity in the chromophore pocket of mEos4b impacts the observed photoswitching and photoconversion properties.*** *Manuscript in preparation.*

NMR spectroscopy has proven to be a powerful structural tool to interrogate the dynamics of phototransformable FPs[122,302]. To gain a better understanding of the molecular mechanisms underlying green-to-red photoconversion of PCFPs, we studied the structural dynamics and fluorescence properties of mEos4b during photoswitching and photoconversion by NMR spectroscopy and fluorescence microscopy. This work was a collaboration between the teams of Bernhard Brutscher and Dominique Bourgeois. The NMR experimental work was carried out by the group of B. Brutscher, while the microscopy experiments and simulations were carried out by the group of D. Bourgeois. I contributed to this work by discussions and simulations to build a photophysical model explaining the observed photophysical behaviors. The work presented below is a summary of the work submitted for publication, outlining the different properties that were used to develop a refined photophysical model of the green-state of mEos4b.

3.1.4.1.1 NMR spectroscopy reveals two green state populations

To investigate its conformational dynamics, mEos4b was studied by solution NMR spectroscopy. Inspection of the $^{1}H^{15}N$ spectrum of the green-state revealed that mEos4b adopts two conformations (**Figure 3.23A**). These two states were named the A-and B-state (not to be confused with the anionic and neutral states of the chromophore which are also often referred to as A and B!). Not all residues of the protein showed this heterogeneity. The residues that showed distinct A- and B- peaks were mainly located on the β-strands 2,3,11 and 10, facing the histidine and phenol groups of the chromophore, indicating that the chemical/conformational differences are localized to this part of the FP. Similar green state heterogeneity was observed in two other members of the EosFP family, pcStar and mEos4b-V69T, suggesting that this heterogeneity is a common feature of EosFP variants.

Further interrogation of the properties of the A- and B-states showed that the relative occupancies of the two states are dependent on the environmental pH and are sensitive to near-UV illumination. Under standard NMR conditions (35°C, pH 7.5), the A-state had a relative population of ~57%. At lower pH, the relative population of the A-state increased up to ~80% at pH 5, while at higher pH, the population of the A-state decreased down to ~55% at pH 10 (**Figure 3.23B**). Illumination of the protein by 405 nm light decreased the relative amount of the A-state down to ~30% at 25 mW/cm^2 (**Figure 3.23C**). Monitoring of the thermal recovery of the A/B-state equilibrium (57:43) after exposure to 405 nm light enabled determination of the exchange rate of the A- and B-populations (k_{ex} = 2 ± 1 x10^{-2} s^{-1}).

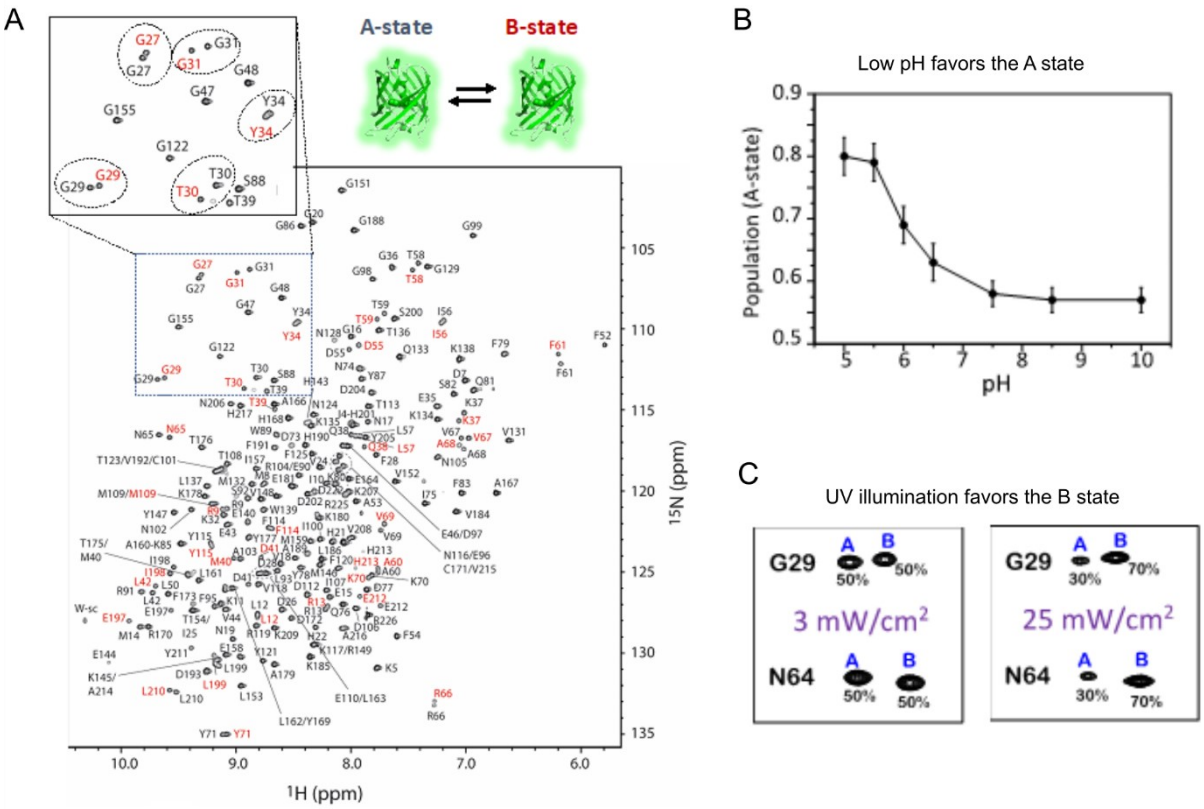

Figure 3.23 NMR reveals green state heterogeneity in mEos4b. *A) ^{1}H-^{15}N correlation spectrum of green-state mEos4b. Peaks correspond to single amino acid residues of the protein as annotated. Peaks that show a different chemical shift in the B-state than in the A-state are shown in red. B) The A-B equilibrium is pH sensitive: at lower pH the A-state becomes more populated. The A-state population was calculated from the relative ^{1}H-^{15}N peak intensities of residues with well-resolved A and B peaks. C) UV illumination shifts the A-B equilibrium towards the B-state. Shown are the ^{1}H-^{15}N cross peaks of two residues (D29 and N64) with distinct A and B peaks under illumination with 3 and 25 mW/cm^2 405 nm light. Data and figures by Bernhard Brutscher and Arijit Maity.*

3.1.4.1.2 Green state heterogeneity affects photoswitching and photoconversion

Having established that the green-state adopts two distinct confirmations, we investigated the consequences of this heterogeneity on the photophysical behaviors of mEos4b.

First, we characterized the off-switching (*cis/trans* isomerization) behavior of mEos4b under illumination with 488 nm light using fluorescence microscopy. We observed that the off-switching rate was faster during the first switching cycle than during following switching cycles (**Figure 3.24A,B**). Interestingly, mEos4b-E212Q and mEos4b-H62L, two mutants that do not show green state heterogeneity, did not show this change in the off-switching rate. Given that illumination with 405 nm, which was used for on-switching, shifts the A/B-equilibrium of WT mEos4b towards the B-state, these findings suggest that a change in the relative populations of the A- and B-states is responsible for the change in the off-switching rate after the first switching cycle and that the A-state switches faster than the B-state.

Next, we investigated whether green-state heterogeneity affects the photoconversion kinetics. To test this, mEos4b was exposed to 405 nm light inside the NMR magnet while spectra were recorded every 10 minutes to monitor green-to-red photoconversion by following the peak intensities of residues that show well-resolved peaks in the green- and red-state (**Figure 3.24D**). 405 nm light was applied in power densities ranging from 2.5 – 25 mW/cm^2, a range over which the relative population

of the A-state is gradually decreased from 57% to 30%. NMR experiments showed that while the photoconversion rate increases with increasing 405 nm intensity, the PCE decreases from maximal ~52% under illumination with 2.5 mW/cm^2 to only 30% under illumination with 25 mW/cm^2 405 nm light. This observation could be explained by photoconversion mainly happening from the A-state while bleaching mainly happening from the B-state so that when the 405 nm light intensity is increased, the B-state is more populated resulting in relatively more bleaching compared to photoconversion, lowering the PCE.

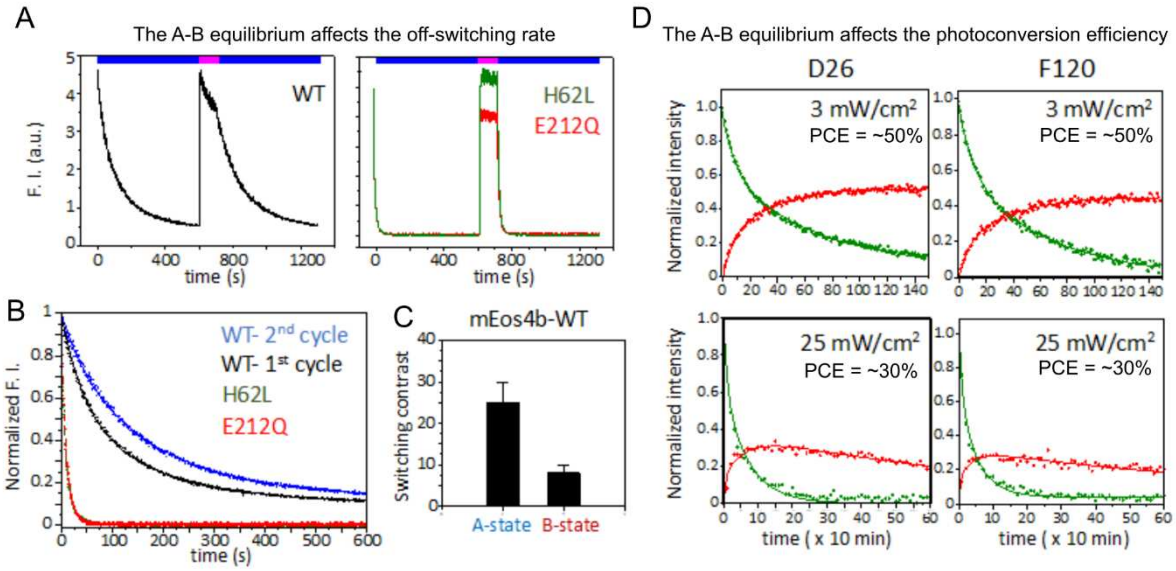

Figure 3.24 Green state heterogeneity affects the off-switching and photoconversion kinetics of mEos4b. *A) Photoswitching curves of WT mEos4b and H62L and E212Q mutants. B) The off-switching rate of WT mEos4b during the first cycle is higher than in following cycles after application of 405 nm light for on-switching. This is expectedly because the B-state, which is increased after exposure to 405 nm light, switches slower than the A-state. C) The switching contrast of the A-and B-state was obtained by fitting of the green fluorescence decay in the first and second switching cycle (B) assuming different A-B populations. D) Green-to-red photoconversion recorded by NMR. Shown are the progressions of the well-resolved green and red state ^{1}H-^{15}N cross peaks corresponding to the residues D26 and F120 under illumination with 3 and 25 mW/cm^2 405 nm light. Data and figures by Bernhard Brutscher and Arijit Maity. Maity et al.*

3.1.4.1.3 Building a photophysical model with support of simulations

Based on the NMR and fluorescence experiments, we developed tentative structural and photophysical models to account for the observed photophysical behaviors (**Figure 3.25**).

The NMR experiments indicated the difference between the A-and B-states is due to a change in the protonation status of residue E212, with E212 being protonated in the A-state but deprotonated in the B-state, and a change in the tautomeric state of H62, the first residue of the chromophore (**Figure 3.25A,B**). Resulting from these differences in protonation, the H-bond networks surrounding and stabilizing the chromophore are different in the A- and B-states (**Figure 3.25A,B**), causing their different photophysical properties.

The photophysical experiments showed that illumination with 405 nm light shifts the A/B-equilibrium towards the B-state, and suggested that the A-state switches faster than the B-state and that while photoconversion mainly happens from the A-state, the B-state is more sensitive to photobleaching (**Figure 3.25C**). To confirm that this tentative model can account for the decrease in PCE when applying more intense 405 nm light, we performed simulations using SMIS.

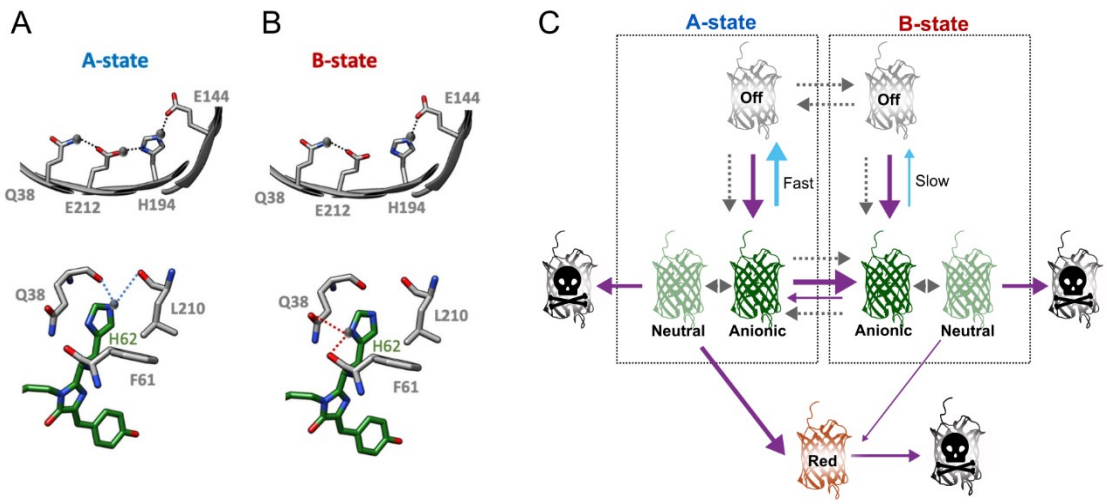

Figure 3.25 Structural and photophysical models explaining green state heterogeneity. *A-B) Tentative structural models of the A-and B-states. In the A-state, E212 is protonated and forms an H-bond network with Q38, H194 and E144. In the B-state, E212 is deprotonated which breaks the H-bond network. In addition, H62, the first residue of the chromophore, is protonated at a different location in the A and B state, changing its H-bonding partners. C) Proposed photophysical model explaining the observed photoswitching and photoconversion behaviors. The A-and B-states are in thermal equilibrium in both the on-and off-states while UV light pushes the protein towards the B-state. The off-switching quantum yield of the A-state is higher than of the B-state, accounting for the change in off-switching rate between sequential switching cycles. Photoconversion mainly happens from the A-state (high PC quantum yield), while the B-state is prone to bleaching, explaining the reduced PCE under higher UV illumination conditions. Figures A and B by Virgile Adams and Bernhard Brutscher.*

Simulations were performed using a simplified version of the model presented in **Figure 3.25C**, omitting green state switching and red state bleaching (**Table 2.4**). Estimation of the thermal exchange rates and phototransformation quantum yields is described in the material and methods. Assuming that photoconversion only occurs from the A-state, we were able to reproduce the co-dependence of the A-state populations and PCE on the applied 405 nm intensity (**Figure 3.26**). Note that we did not attempt to reproduce the time scale and biphasic nature of the photoconversion kinetics observed by NMR because these were likely influenced by inhomogeous illumination of the NMR sample.

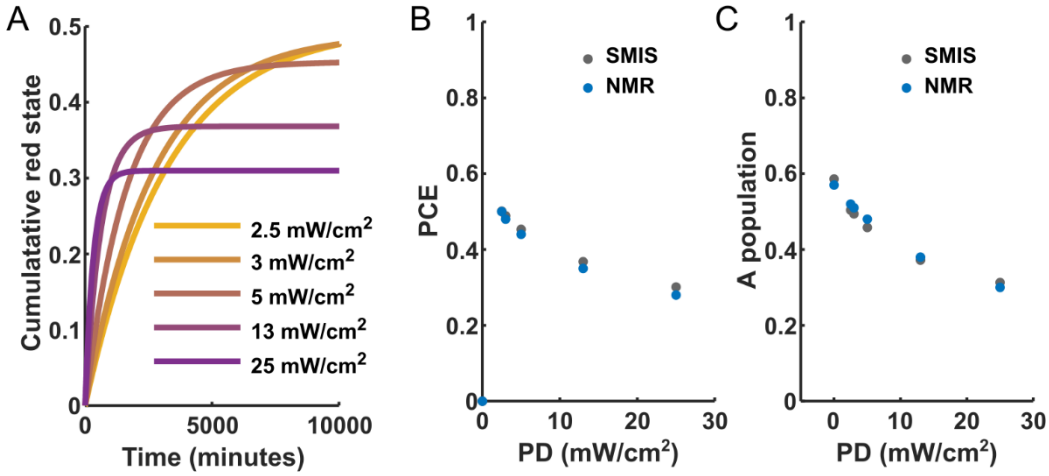

Figure 3.26 Simulations of the effect of green state heterogeneity on the PCE. *A) Simulated red-state build up under illumination with 2.5 – 25 mW/cm^2 405 nm light. Red-state bleaching was omitted from the simulations so that the plateau corresponds to the PCE. B-C) Comparison of the PCE (B) and A-state populations (C) obtained*

by NMR and SMIS simulations, showing that the proposed photophysical model is able to reproduce the photophysical behaviors observed by NMR.

It is not excluded that photoconversion also happens from the B-state. To explore the possibility that photoconversion happens from both the A-and B-state, we performed simulations in which the photoconversion quantum yield of the B state was 10% or 100% of the photoconversion quantum yield of the A-state (**Table 2.5**). These simulations showed that the light dependence of the PCE and A-state population can still be reproduce when there is limited photoconversion (10%) from the B-state (**Figure 3.27A,B**). On the other hand, when we simulated photoconversion assuming equal photoconversion quantum yields of the A-and B-states, the simulations could no longer reproduce the NMR observed trend in PCE (**Figure 3.27C,D**). These simulations support a photophysical model in which photoconversion mainly occurs from the A-state but they also indicate that it is possible that photoconversion also occurs from the B-state with low efficiency.

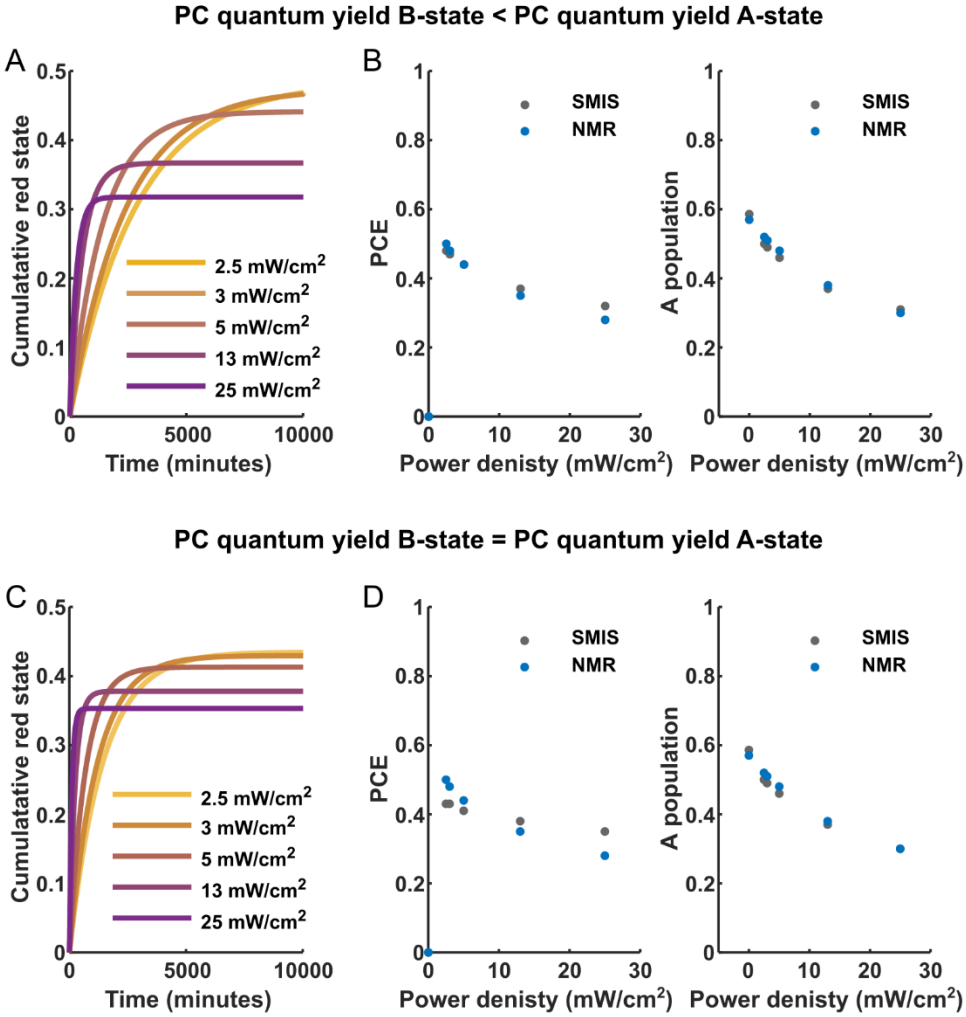

Figure 3.27 Simulations of mEos4b photoconversion assuming photoconversion of both the A-and B-state. *Red-state build up was simulated under illumination with 2.5 – 25 mW/cm^2 405 nm light using a B-state photoconversion quantum yield 10x smaller than the photoconversion quantum yield of the A-state (A and B) or using equal photoconversion quantum yields for the A and B states (C and D). A comparison of the PCE's and A-state populations obtained by simulations and NMR is shown in B and D.*

It is important to note that green-state heterogeneity cannot account for the decreased PCE of mEos4b under illumination with high intensity (100 W/cm^2) 405 nm light, the phenomenon described in **section 3.1.3**. Simulations with the model presented in **Figure 3.25B** show that under conditions with high intensity 405 nm light, the PCE stabilizes around 19% (**Figure 3.28**). This is because at

power densities >>100 mW/cm^2 the thermal A/B exchange rates become negligible compared to the light-induced exchange rates so that the ratio of the light-induced A/B exchange rates determines the A/B equilibrium. Consequently, the A/B equilibrium stabilizes at 18.3% ($qy_{BA}/(qy_{AB} + qy_{BA})$ = 0.0707/(0.315+0.0707) = 18.3) and so the PCE also stabilizes. Although theoretically it is possible that 405 nm light only promotes A-to-B transformation (i.e. qy_{BA}=0), this is unlikely because in this situation the population of the A-state would drop to 0 at higher 405 nm light intenisties and consequently, the PCE would also drop to 0. However, PALM experiments (see for example **Figure 3.21**) show that in conditions with high 405 nm light intensities (>1 W/cm^2) there is still significant photoconversion. Furthermore, NMR experiments show that under illumination with 250 mW/cm^2 405 nm light, the A-state populations remains ~20% (data not shown), suggesting that the A-state population does not decay to 0 but remains significantly populated even under conditions with high intensity 405 nm light.

The other way around, the nonlinear bleaching pathway described in **section 3.1.3** can also not explain the decreased PCE under these low illumination conditions (2.5-25 mW/cm^2) because the excitation rate is too low relative to the estimated lifetime of the tentative intermediate state (~ 5 ms if triplet state) to induce a nonlinear effect. Thus, green-state heterogeneity and high-intensity induced nonlinear bleaching are presumebly two coexisting processes that modulate the PCE of mEos4b under different illumination regimes (**Figure 3.28B**).

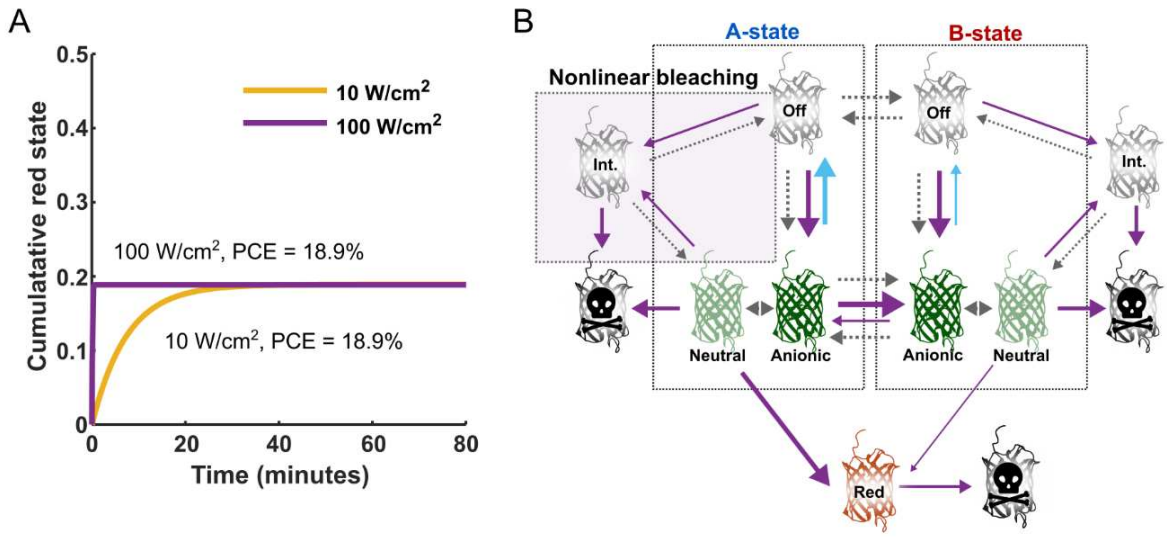

Figure 3.28 Green state heterogeneity cannot account for a reduced PCE under high intensity UV illumination. *A) Simulated red-state build up under illumination with 10 and 100 W/cm^2 405 nm light, showing that in both conditions the same PCE is reached. B) Tentative photophysical model of green state mEos4b accounting for the reduced PCE observed under low (1-100 mW/cm^2) and high (10-100 mW/cm^2) UV illumination conditions.*

3.1.4.1.4 Discussion

NMR spectroscopy revealed that mEos4b adopts two distinct green-state conformations, which modulate photoswitching and photoconversion. With support of simulations, we were able to design a photophysical model to explain the NMR observed dependency of the PCE and A-state population on the 405 nm light intensity. These findings deepen our understanding of the photophysical behavior of PCFPs and could contribute to the development of better performing PCFPs, for example PCFPs that only populate the photostable A-state.

The precise photoconversion pathway of PCFPs remains incompletely understood, but it is clear that E212 plays an essential role. Our data suggest that photoconversion requires E212 to be protonated

(starting from the A-state). Based on this finding, we propose the following photoconversion pathway (**Figure 3.29**), adopted from the pathway proposed by Kim et al[197]: The H-bond between H194 and E212 is weak and fluctuates in a thermal manner. Aditionally, H62 can adopt two rotameric states, sometimes being rotated towards E212. Excitation of the neutral chromophore in this configuration promotes proton transfer from E212 to H62, after which photoconversion proceeds via a concerted β-elimination mechanism. The necessity for H62 to be rotated towards E212 for photoconversion to occur could explain the relatively low photoconversion quantum yield of PCFPs (~10^{-4}), as this rotameric state is expectedly rare, given that it is never observed in crystal strutures of PCFPs. In addition to this proposed main photoconversion pathway starting from the A-state, photoconversion may also occur from the B-state, although expectedly less efficienctly. Photoconversion from the B-state (depronated E212) may follow a similar mechanism as proposed by Fare et al.[195] with E212 acting as a base, or may proceed via the triplet state as proposed by Lelimousin et al.[194], not requiring proton shuttling from E212.

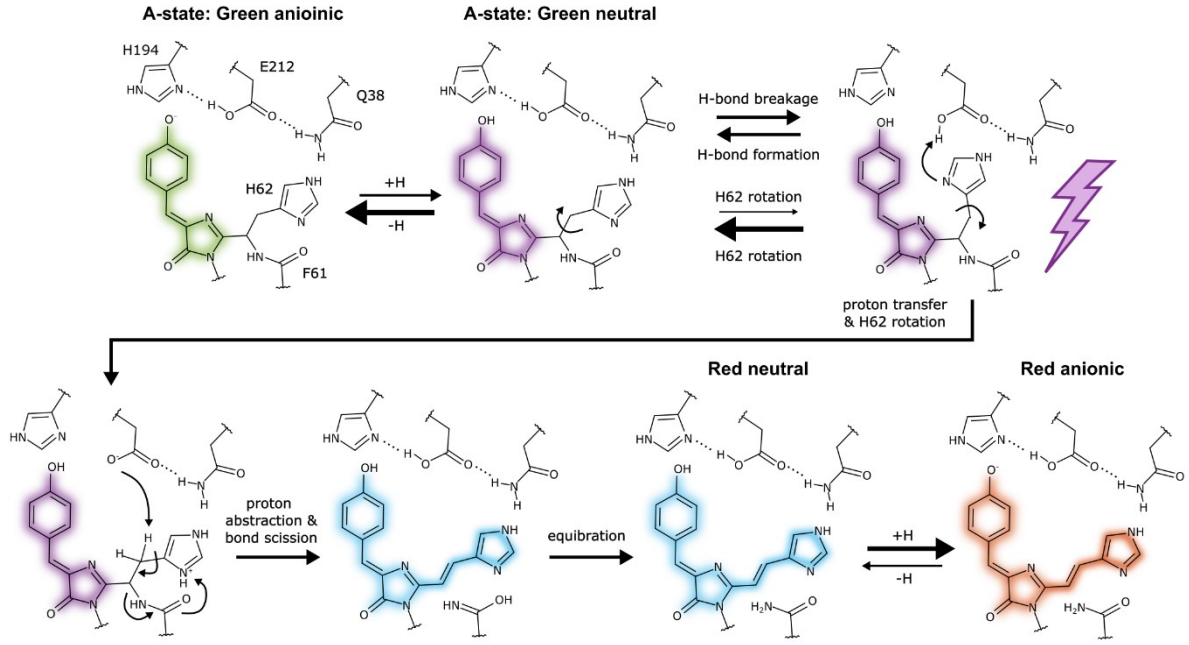

Figure 3.29 Proposed photoconversion mechanism of mEos4b starting from the A-state. *Photoconversion pathway based on the pathway proposed by Kim et al.[197], adjusted to start from the A-state according to the NMR data. See text for details.*

An important question that remains to be addressed is how this green-state heterogeneity affects PALM imaging. In PALM experiments, the 405 nm light intensity is typically between 100 mW/cm^2 and 5 W/cm^2 405, which would restrict the PCE to ~20% at maximum based on the photophysical model presented above. Various studies[144,203,216], however, report photoconversion efficiencies >60% for mEos4b and other EosFP variants, which is in contraction with the NMR observed 20%. A possible explanation for this discrepancy is that the PCE is influenced by yellow light (561 nm), which is used in high intensities in PALM experiments for read out of the red fluorescence. In support of this hypothesis, preliminary NMR data by Bernhard and Arijit show that dual illumination with weak 405 and 561 nm light increases the PCE of mEos4b (see **section 3.1.4.3.3**!). Another possibility is that the PCE extracted from the NMR experiments does not reflect the absolute PCE. In fact, in the NMR experiments, photobleaching is detected as a loss of peak intensities, which is caused by oligomerization/aggregation of the protein. It is unclear, however, how this aggregation relates to actual photobleaching (i.e. irreversible loss of fluorescence). Lastly, differences in environmental conditions (buffer, temperature, pH, etc.) might also have contributed to the differences in reported PCE's.

3.1.4.2 Switching of green state mEos4b: fast fluorescence decay and transient photoactivation?

During the characterization of the off-switching kinetics of mEos4b (**section 3.1.4.1**), Arijit noticed that when green-state mEos4b is continuously exposed to low intensity 488 nm laser light (< 1W/cm^2), the fluorescence signal sharply decays during the first two frames (**Figure 3.30**). Similar behavior was observed for various Hydrozoan green-emitting FPs (data not shown). This curious behavior prompted us to investigate in more detail the photoswitching behavior of mEos4b.

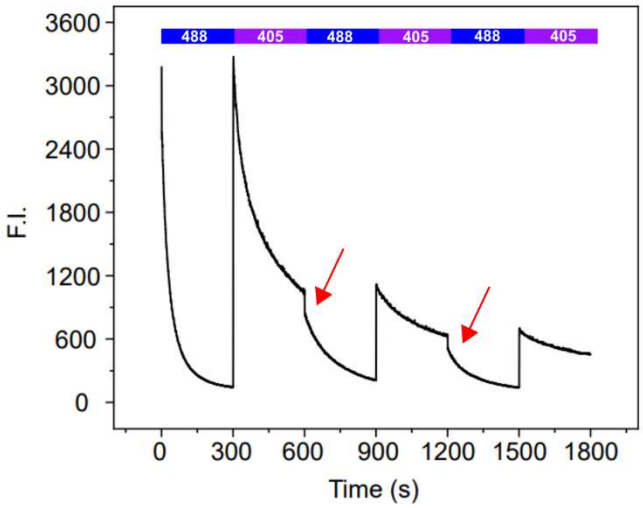

Figure 3.30 Fast fluorescence decay during off-switching of green-state mEos4b. *mEos4b molecules embedded in PAA (pH 7.5) were illuminated with 488 nm light (150 mW/cm^2) to induce off-switching and 405 nm light (260 mW/cm^2) to induce on-switching (signal decays due to photoconversion). The green fluorescence intensity was measured every 100 ms using 150 mW/cm^2 488 nm light. Red arrows highlight the fast fluorescence decay during the first frames of the off-switching period. Note: this decay is also present in the first off-switching phase but it is less visible due to the scaling. Data and figure by Arijit Maity.*

3.1.4.2.1 Characterization of the off-switching kinetics of green state mEos4b

To gain a better understanding of the fast fluorescence decay observed in the photoswitching experiments, we first investigated the contribution of off-switching (*cis/trans* isomerization) to the observed decay. To this end, mEos4b molecules were embedded in PAA gel and illuminated with 280 mW/cm^2 488 nm light, in the presence and absence of 405 nm light (100 mW/cm^2) to prevent accumulation of the Off-state (*trans* neutral chromophore). While in the absence of 405 nm light the fluorescence signal progressively decayed, in the presence of 405 nm light the fluorescence signal stabilized after the initial sharp decay (**Figure 3.31A**), suggesting that, while the gradual decay is due to *cis*-to-*trans* isomerization, the initial decay has another origin.

This photophysical behavior of mEos4b is reminiscent of triplet state saturation seen in rsEGFP2 and EGFP at cryogenic temperature[100]. **Figure 3.31B** shows simulations illustrating the effect of triplet state saturation on the fraction of molecules in the fluorescent state. The formation rate of the triplet state is the product of the population of the fluorescent state, the excitation rate of the fluorescent state (kx_S) and the quantum yield of intersystem crossing (ISC, i.e. triplet state formation, qy_{ISC}). The recovery rate of the triplet state is the sum of the product of the population of the triplet state and the thermal recovery rate (k_{T1S0}), and the rate of light-induced recovery, which is the product of the population of the triplet state, the excitation rate of the triplet state (kx_T) and the quantum yield of reverse inter system crossing (RISK, qy_{RISK}). According to this model, formation of

the triplet state results in a rapid fluorescence decay (rate triplet state formation > triplet state recovery), after which the signal stabilizes when the rate of triplet state formation equals the rate of triplet state recovery:

$$[Fluo] * kx_S * qy_{ISC} = [Triplet] * kx_T * qy_{RISK} + [Triplet] * k_{T1S0}$$

The amplitude of the decay is dependent on the applied laser power density because of the thermal component. However, because triplet state recovery is also light induced, the amplitude stabilizes when the light induced rate is much larger than the thermal rate, at which point the amplitude reflects the ratio between the forward ISC (FISC) and RISC rates.

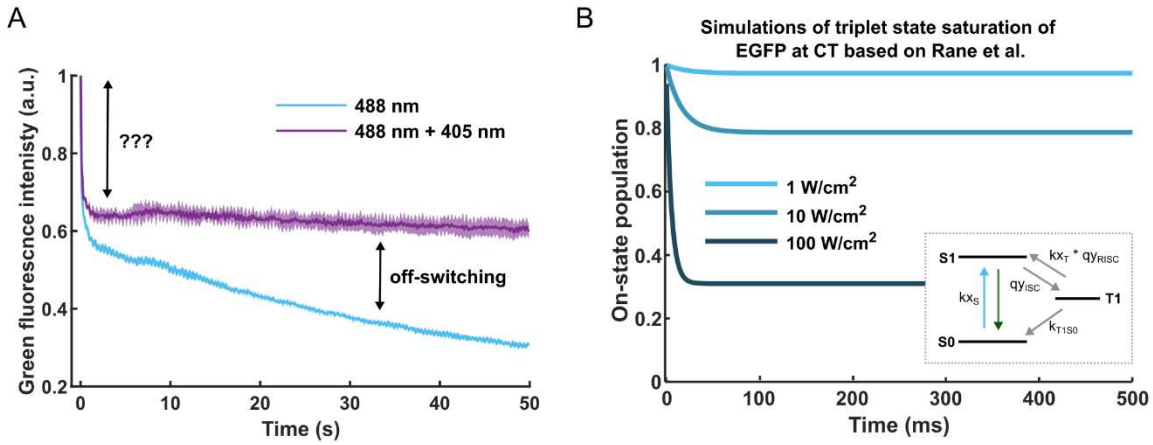

Figure 3.31 Fast fluorescence decay of green state mEos4b is reminiscent of triplet state saturation. *A) mEos4b molecules embedded in PAA gel (pH 8) were exposed to continuous 488 nm light (280 mW/cm^2) with or without additional 405 nm light (100 mW/cm^2) to prevent accumulation of the Off-state (trans neutral chromophore). The green fluorescence intensity was measured every 50 ms using an exposure time of 10 ms. Shown is the mean ± sd of 3 measurements. B) Simulations of triplet state saturation of EGFP at CT based on the model published by Rane et al. Inset shows the photophysical model used for the simulations. Simulation parameters: qy_{ISC} = 0.0032; qy_{RISC} = 0.0012; k_{T1S0} = 46 s^{-1}; EC_{488} S0 = 42400 M^{-1}cm^{-1}; EC_{488} T1 = 10000 M^{-1}cm^{-1} (also see **Figure 1.10**).*

To investigate the nature of the sharp fluorescence decay, we examined the lifetime and the formation quantum yield of the formed non-fluorescent state. To this end, we interleaved illumination periods of 100 ms (280 mW/cm^2 488 nm) with increasing amounts of dark time (0-160 ms), thereby decreasing the amplitude of the sharp decay by allowing thermal recovery (**Figure 3.32A**). Altough the lifetime of the non-fluorescent state cannot be easily extracted from these experiments because it takes more than one frame (i.e. illumination period) to reach the plateau phase, the decreasing amplitude gives an initial idea of the lifetime, which appears relatively long as there remains a significant non-fluorescent population with 160 ms dark time (**Figure 3.32A**). This long lifetime suggests that the non-fluorescent state is not the triplet state, which is expected to live only ~5 ms at RT[88]. The formation quantum yield of the tentative non-fluorescent state appears extremely high (~3.5%, see equation above), assuming that the amplitude under continuous illumination is ~35% (**Figure 3.31A**), that the half-life of the non-fluorescent state is ~100 ms (**Figure 3.32A**), that recovery from the non-fluorescent state is not light-induced and that the excitation rate of the fluorescent state is 111 s^{-1} (EC_{488} = 42214 M^{-1}cm^{-1}). This extremely high formation quantum yield raises the question whether the laser power densities were correctly estimated. Although we measured the laser powers before each experiment, we noticed some instabilities when working at low percentages of the achievable laser power (<1%). This question will be addressed below.

Intrigued by the behavior of the green state of mEos4b, we tested whether similar behavior is shown by the red state of mEos4b. Photoconverted red-state mEos4b molecules were illuminated with 5

W/cm^2 561 nm light (lowest achievable laser power on the set-up without addition of an OD filter) with 0-128 ms dark periods in between illumination periods of 50 ms. Although, a sharp fluorescence decay could not be observed, probably due to the relatively high laser intensity hiding the fast decay whitin the first frame and inducing rapid off-switching, addition of dark time significantly increased the detected fluorescence signal (**Figure 3.32B**). However, the red fluorescence signal did not improve by adding more than 2 ms dark time, suggesting that the implied non-fluorescent state is much shorter lived that the non-fluorescent green state than is observed.

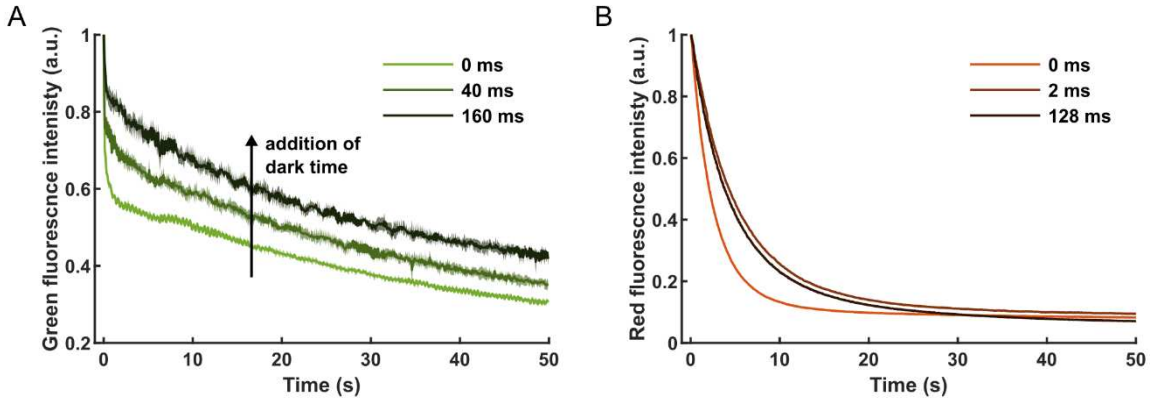

Figure 3.32 Addition of dark time increases the fluorescence signal of green and red state mEos4b. *A) mEos4b molecules embedded in PAA gel (pH 8) were illuminated with 488 nm light (280 mW/cm^2) for periods of 100 ms which were interleaved by 0-160 ms dark time. The green fluorescence intensity was measured at the beginning of each illumination period using an exposure time of 10 ms. B) Photoswitching of red state mEos4 (PAA gel, pH 8) by 561 nm light (5 W/cm^2). Illumination periods (50 ms) were interleaved by 0-128 ms dark time. Shown is the mean ± sd of 3 measurements.*

Knowing that the environmental conditions can be difficult to control in PAA gel and that polymerization of the gel produces reactive oxygen species, we tested whether under other, biologically relevant, conditions this fast fluorescence decay could also be observed. To test this, we used a *D. radiodurans* strain expressing HU-mEos4b (see **section 3.2**). HU-mEos4b is expressed in high levels, allowing ensemble fluorescence measurements (**Figure 3.33**). Cells were manually segmented to extract the fluorescence time-series of mEos4b.

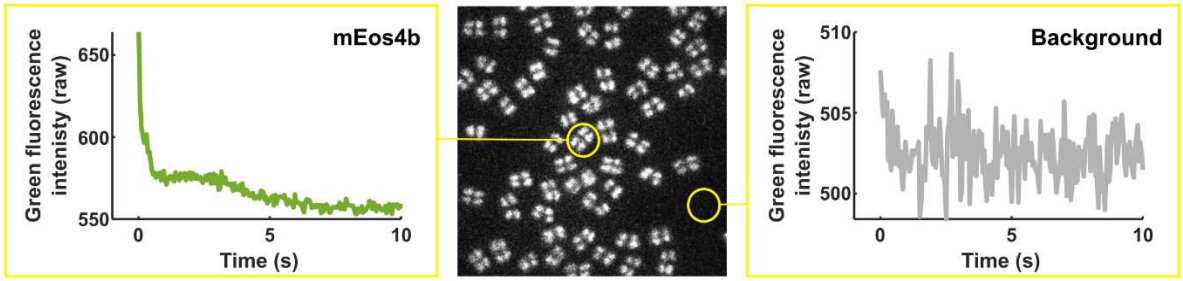

Figure 3.33 Characterization of the photoswitching behavior of mEos4b in D. radiodurans cells. *D. radiodurans cells expressing HU-mEos4b (see **section 3.2**) were illuminated with 488 nm light (250 mW/cm^2) and 405 nm light (100 mW/cm^2). Shown is a fluorescence image (middle) of the cells expressing HU-mEos4b with examples of the fluorescence time series of mEos4b and the background on the left and right, respectively.*

Similar as in PAA gel, the fluorescence intensity of mEos4b molecules expressed in *D. radiodurans* sharply dropped under continuous illumination with 488 and 405 nm light (**Figure 3.34A**). Based on the photophysical model described above, the amplitude of the decay is expected to increase with increasing laser power. However, although the amplitude increased from 100 mW/cm^2 to 250 mW/cm^2, the amplitude decreased under higher illumination intensities (500 and 1000 W/cm^2). This could be explained by fast decay during the camera exposure time reducing the detected signal (discussed in more detail below). Addition of 150 ms dark time in between the frames resulted in

complete removal of the fast decay (**Figure 3.34B**), suggesting that the thermal recovery occurred faster in the *D. radiodurans* cells than in the PAA gel, which could be due to differences in the environment. Lastly, sequential imaging cycles interleaved by 10 s dark periods showed that the fast fluorescence decay is repeatable, providing additional proof that the formed non-fluorescent state is thermally recoverable (**Figure 3.34D**). Altogether, these experiments show that the observed behavior is not an artifact caused by the PAA gel and confirm that the non-fluorescent state is thermally recoverable.

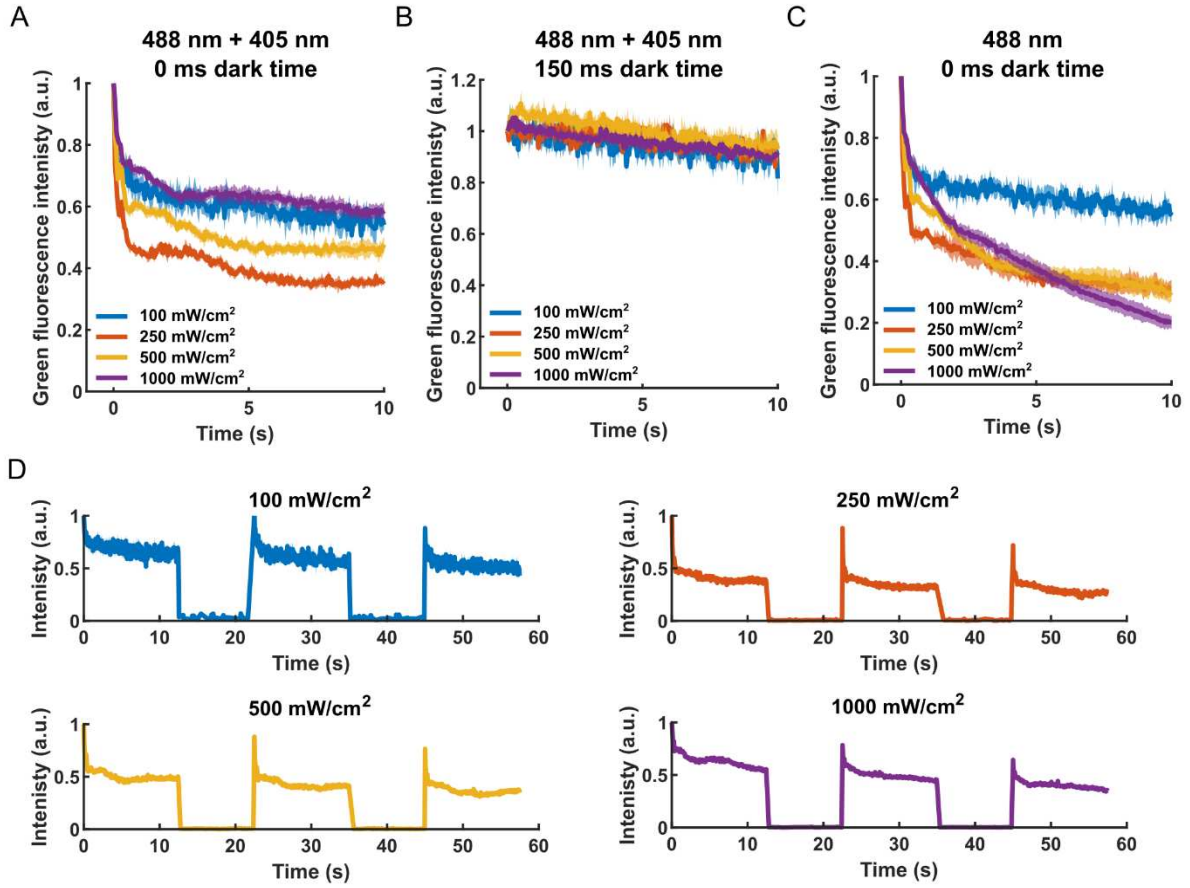

Figure 3.34 Fast fluorescence decay of mEos4b molecules in D. radiodurans cells*. D. radiodurans cells expressing HU-mEos4b were illuminated with 488 nm light (100-1000 mW/cm²) with and without 405 nm light (100 mW/cm²). The green fluorescence intensity was measured every 50 ms using 10 ms exposure time. A) 488 and 405 nm light with no dark time in between illumination periods. B) 488 and 405 nm light with 150 ms dark time in between illumination periods (50 ms). C) 488 nm light with no dark time in between illumination periods. D) Three sequential illumination periods as in A interleaved by 10 s dark time. Shown is the mean ± sd of 2 measurements.*

3.1.4.2.2 A technical artifact?

To investigate in more detail the relation between the light intensity and the amplitude of the fast decay, we repeated the experiments presented above in PAA gel, varying the exposure time from 1 to 50 ms. We expected that when using a short exposure time, the fast kinetics would be better resolved and the amplitude of the decay would be increased, while when using a longer exposure time, the fast kinetics would be hidden in the exposure time, reducing the amplitude of the fast decay. The experiments, however, revealed markedly similar behaviors independently of the exposure time (**Figure 3.35A-C**). However, when using higher light intensities (500-1000 mW/cm²), the fluorescence intensity measured in the first frame was indeed lower than would be expected if the fast fluorescence decay did not affect the measured intensity (**Figure 3.35E-F**). Underestimation

of the initial fluorescence intensity due to fast fluorescence decay could explain why the amplitude of the fast decay appears to decrease with higher 488 nm intensities (**Figure 3.35A-C**).

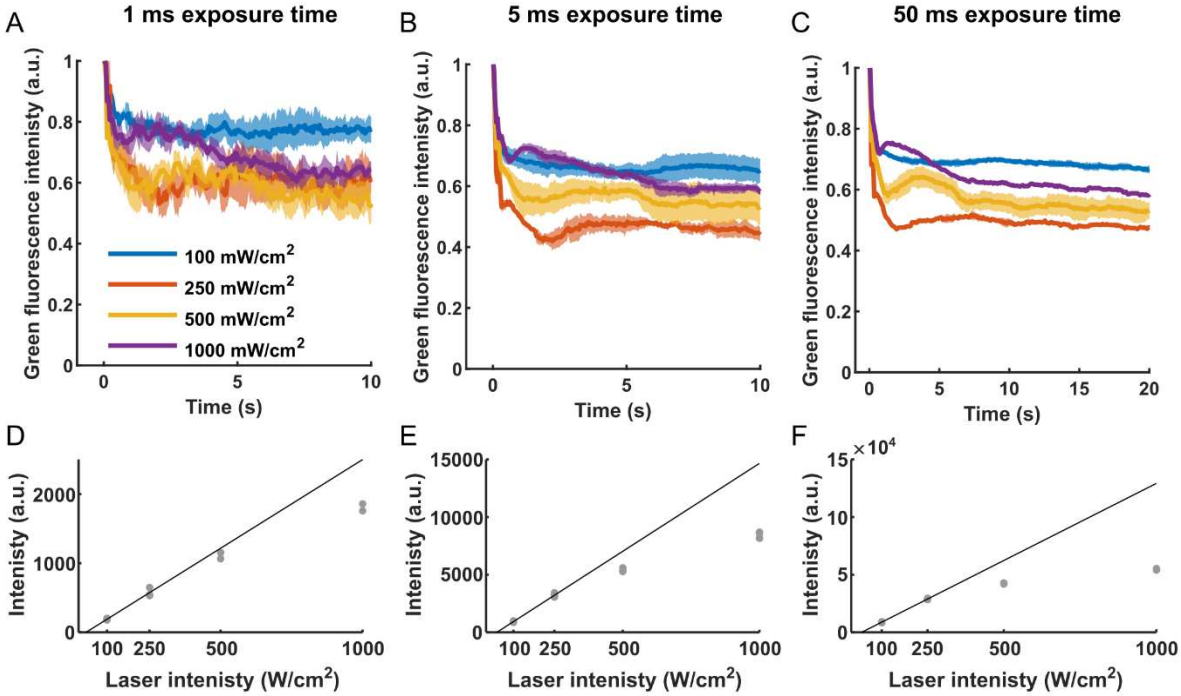

Figure 3.35 Fast decay and transient photoactivation. *mEos4b molecules embedded in PAA gel (pH 8) were illuminated with continuous 488 nm light (100-1000 mW/cm^2) and 405 nm light (100 mW/cm^2). The green fluorescence intensity was measured every 50 (A & B) or 100 (C) ms using an exposure time of 1 ms (A), 5 ms (B) or 50 ms (C). The background-subtracted fluorescence intensities measured in the first frame are plotted as a function of laser intensity using an exposure time of 1 ms (D), 5 ms (E) or 50 ms (F). The black lines show a linear fit through the first 2 sets of data points (100 and 250 W/cm2) to guide the eye. Shown is the mean ± sd of 4 measurements (A-B), or individual data points (E-F).*

As mentioned above, we noticed that the 488 nm laser was unstable at low percentages of its maximal power (<1%). Therefore, to exclude that the observed fast fluorescence decay was caused by an illumination artifact we measured the fluorescence time-series of two other fluorescent materials: ink from a fluorescence marker and a yellow Chroma slide (**Figure 3.36**). We hoped that these materials would give a stable fluorescence signal over time, which would allow us to exclude a technical artifact. However, the fluorescence signal from these materials followed a markedly similar pattern as mEos4b (**Figure 3.36A,B**). This motivated us the measure the laser output directly using a photodiode to exclude that the laser intensity overshoots during the first milliseconds. Although we did not detect an overshoot, we observed that the rise of the laser intensity was relatively slow at low powers (~5 ms) (data not shown). Therefore, we decided to place an OD2 filter in the laser path so that we could work at higher laser powers (25-50%) at which the laser output was more stable over time. Additionally, we used another camera, which was newly installed on the set-up (sCMOS instead of EMCCD), to exclude any problems related to the camera. Using this set-up, the amplitude of the fast decay was overall reduced but increased when the laser intensity was increased from 500 to 1000 mW/cm^2, which was previously not the case (**Figure 3.36C** compare to **Figure 3.35**). This could suggest that we previously underestimated the laser intensity, which could partly explain the extremely high apparent formation quantum yield of the implied non-fluorescent state. Taken altogether, these data suggest that the fast fluorescence decay is not due to an imaging artifact but reflects a real photophysical response. More effort, however, is needed to carefully characterize this behavior.

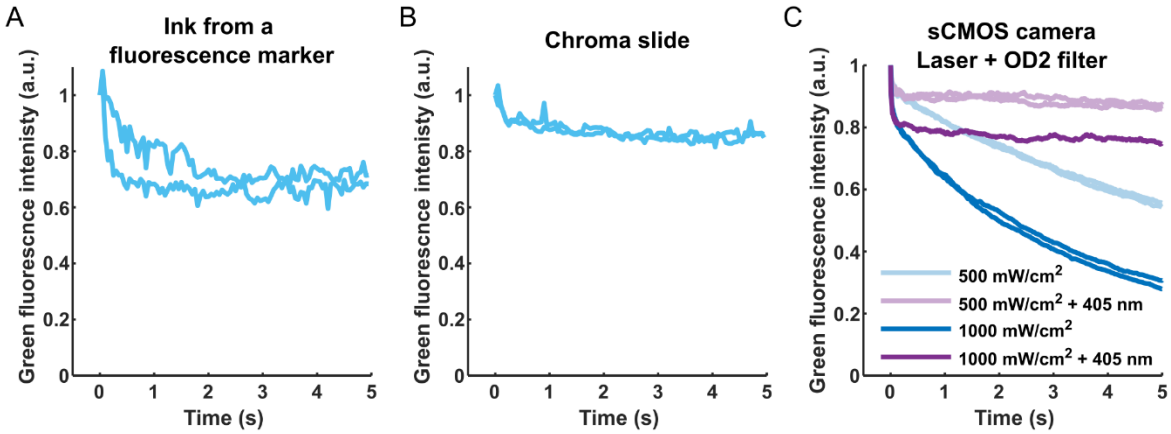

Figure 3.36 Fast fluorescence decay controls. *A) Ink from a fluorescence marker was applied on a cover glass and imaged under continuous illumination with 280 mW/cm^2 488 nm light. The green fluorescence intensity was measured every 50 ms using 5 ms exposure time. B) A yellow Chroma slide imaged under continuous illumination with 2 W/cm^2 488 nm light. The green fluorescence intensity was measured every 50 ms using 5 ms exposure time. C) mEos4b molecules embedded in PAA gel (pH 8) were illuminated with continuous 488 nm light (500 or 1000 mW/cm^2) with or without 405 nm light (100 mW/cm^2) to prevent accumulation of the Off-state. Images were acquired using the new sCMOS camera. Laser light was reduced using an OD2 filter to work in the 25-55% range of the laser power. Shown are the individual traces from 1-2 measurements.*

3.1.4.2.3 Transient photoactivation

In addition to fast fluorescence decay, the data shown in **Figure 3.35** show 2 phases of transient photoactivation (0-2 s and 0-5 s), which is especially visible in the measurements with 50 ms exposure time (**Figure 3.35C**). This behavior can also be observed in the measurements in the DR cells but is less pronounced in these data (**Figure 3.34A**). These transient activations appear to occur earlier when higher 488 nm power densities are used (**Figure 3.35C**), suggesting that they are driven by 488 nm light (and not by 405 nm light). The origin of these behaviors remains to be elucidated.

3.1.4.2.4 Infrared light modulates the bleaching and photoconversion kinetics of mEos4b

The data presented above show that the apparent brightness of mEos4b is strongly reduced by the formation of a short-lived non-fluorescent state. The nature of this non-fluorescent state remains to be elucidated. One hypothesis to address is whether the triplet state is involved in the formation of this state.

Before knowing about the fast fluorescence decay described above, we were already interested in investigating the effect of the triplet state on the apparent brightness and photostability of mEos4b. This interest was driven by the motivation to improve PALM imaging and results from other studies[99,311] showing that reduction of the triplet state lifetime can improve the photostability and apparent brightness of FPs. Therefore, we collaborated with Agathe Espagne and Thomas le Saux (ENS, Paris) to test the effect of infrared light, which is expected to promote RISC, on the apparent brightness and photon budget of mEos4b.

The preliminary findings from this collaboration are shown in **Figure 3.37**. Bleaching of the green state was significantly reduced by the addition of 750 nm light (**Figure 3.37A**), suggesting that, indeed, reducing of the triplet state lifetime improves the photostability of green state mEos4b (assuming the triplet sate absorbs around 750 nm, see[97,98]). Bleaching of the red state, on the other hand, was accelerated by the addition of 750 nm light, although initially the apparent brightness was increased (**Figure 3.37B**). This might have been due to direct excitation of the red state by 750 nm light due to the Urbach tail effect, which would also explain the increased fluorescence signal in the

first few frames. Another possibility could be that bleaching is accelerated due to the formation of a 750 nm sensitive radical state upon excitation of the red state by 561 nm light as was observed in other RFPs[445]. A multiphoton effect, as described in[446], seems unlikely given the relatively low power density of the IR laser (~1-5kW/cm^2). Increasing the IR wavelength from 750 to 800-900 nm prevented accelerated bleaching but did not seem to increase the photostability of the red state (**Figure 3.37C**). It would be interesting to measure the absorption spectrum of the triplet state of the red state of mEos4b to enable optimization of the applied IR wavelength and ensure excitation of the triplet state. Interestingly, we noticed that the photoconversion rate was slightly reduced in the presence of IR light (**Figure 3.37C)**. This observation might be an indication that photoconversion can proceed via the triplet state, as has been proposed by Lelimousin et al.[194]. The minimal effect of IR light, however suggests that the main photoconversion pathway does not involve the triplet state (assuming we effectively excite the triplet state of the neutral chromophore with 750 nm light), which is in line with the photoconversion pathway presented in **Figure 3.29**.

Altogether, these results show that IR light has the potential to modulate the photostability of mEos4b. The increased stability of the green state under IR illumination indicates that the triplet state plays important role in the photostability of the green state. Whether the triplet state plays a role in the fast fluorescence decay described above (see **section 3.1.4.2.1**) remains to be investigated.

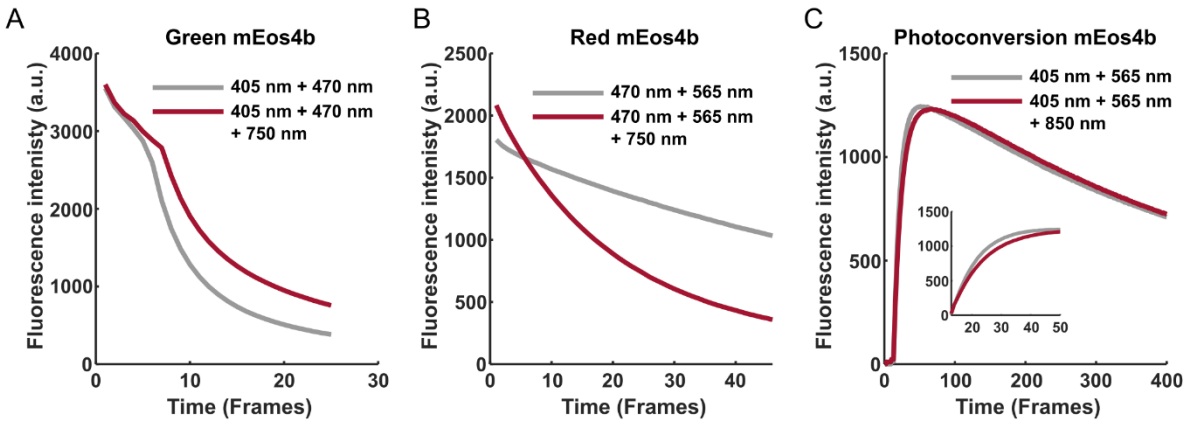

***Figure 3.37 Infrared light modulates the bleaching and photoconversion of mEos4b**. Preliminary results of the effects of IR light on the bleaching and photoconversion of green and red state mEos4b molecules embedded in PAA gel. A) Green mEos4b molecules were illuminated with 405 nm and 470 nm light to induce bleaching, while preventing Off-state accumulation. Addition of 750 nm light (>1 kW/cm^2) slowed down green state bleaching. The strange kinetics in the first 10 frames are due to saturation of the camera. B) Photoconverted red mEos4b molecules were illuminated with 470 nm and 565 nm light to induce bleaching. Addition of 750 nm light (>1 kW/cm^2) accelerated bleaching. C) Photoconversion of mEos4b was induced by illumination with 405 nm light, 565 nm light was used to read out the red fluorescence intensity and induce bleaching. Addition of 850 nm light appeared to slow down the photoconversion rate, while minimally affecting red state bleaching. Inset shows zoom of the first 50 frames. Data acquired in collaboration with Agathe Espagne and Thomas le Saux.*

3.1.4.2.5 Discussion

The photoswitching kinetics of green state mEos4b under low illumination intensities are affected by fast fluorescence decay during the first frames. The data presented above indicate that formation of a short-lived non-fluorescent state is responsible for this fast decay that reduces the fluorescence intensity by up to ~40% depending on the illumination conditions. Recovery from this state is presumably both thermal and light-induced, given that otherwise the fluorescence intensity is expected to drop to zero under higher illumination intensities. The nature of this non-fluorescent state remains to be identified. Preliminary experiments suggest that its lifetime is too long to be the triplet state (**Figure 3.32**), but it could possibly be a longer-lived state down-stream of the triplet

state. To investigate the involvement of the triplet state, it would be interesting to test the effect of IR light on the switching kinetics of mEos4b. In addition to fast fluorescence decay, the switching experiments revealed transient 488 nm light-induced photoactivation (**Figure 3.35**). This activation might be explained by a small fraction of molecules starting in a non-fluorescent state, which is recovered by 488 nm light (possibly the 488 sensitive off-state identified by de Zitter et al.[218]). It is important to note that the experiments presented in this section were carried out using low illumination intensities, revealing these different photophysical behaviors. When using higher illumination intensities, these behaviors are expectedly hidden within the first frame.

Although, we mainly focused on the green state, the red state expectedly suffers from a similar behavior (**Figure 3.32C**). Such a behavior could lead to blinking (if lifetime > frame time) or severely lower the apparent brightness of the red state in PALM experiments (if lifetime < frame time) because the molecules would spend a significant amount of the frame time in a non-fluorescent state. Thus, it would be interesting to quantify this effect and investigate strategies to prevent formation of such a short-lived non-fluorescent state, as this could greatly benefit PALM experiments.

Altogether, the findings presented here open the door for more in depth investigations on dark/off-state formation in mEos4b.

3.1.4.3 A twofold effect of 405/488 nm light on red state mEos4b

During the characterization of the effects of 405 and 488 nm light on the PCE of mEos4b (**section 3.1.3**), we found that 405 nm light reduces the duration of the off-times of mEos4b to a greater extent than 488 nm light (**Figure 3.12** & **Figure 3.13**), which is inconsistent with the higher absorbance of 488 nm light by the red Off state (*trans*-neutral chromophore). This inconsistency motivated us to further investigate the effects of 405 and 488 nm light on the photophysical behavior of mEos4b.

3.1.4.3.1 Switching of red-state mEos4b: 405 vs 488 nm light

To explain the better off-time reduction by 405 nm light, we hypothesized that, in addition to the Off state (*trans*-neutral chromophore), another off-state is formed, which is only sensitive to 405 nm light. To test this hypothesis, we monitored the ensemble red fluorescence intensity during sequential off- and on-switching cycles, using either 405 or 488 nm light. We expected that if there is a second off-state, only sensitive to 405 nm light, the on-switching efficiency would be higher when using 405 nm light than when using 488 nm light.

Interestingly, the switching experiments revealed that the relative effects of 405 and 488 nm light are strongly dependent on the applied power density (**Figure 3.38**). At low power density (0.1 W/cm^2), on-switching with 488 nm light is faster than with 405 nm light but equally effective, which can be explained by the higher absorbance of the Off-state at 488 nm (**Figure 3.38A**). At higher power densities (1 and 10 W/cm^2), the red fluorescent intensity decreased strongly during illumination with 488 nm light but not during illumination with 405 nm light (**Figure 3.38B,C**), suggesting that the protein was bleached by 488 nm light but not by 405 nm light. This observation might be explained by the relatively high absorbance of the red On state at 488 nm, resulting in cycling of the FP between the On and Off state eventually leading to bleaching. This behavior will be further investigated below using simulations. Of note, under these conditions, the on-switching efficiency appeared higher when 405 nm light was used but this is likely explained by the 488 nm induced bleaching lowering the apparent on-switching efficiency rather than by incomplete on-switching. At the highest tested power density (100 W/cm^2, **Figure 3.38D)**, 488 nm light induced a

similar behavior as was seen with 1 and 10 W/cm^2, while 405 nm light seemed to induce strong bleaching. This apparent strong bleaching by 405 nm light is reminiscent of the nonlinear effect of 405 nm light on the PCE, which we ascribed to nonlinear bleaching of the green state (**section 3.1.3**). Although the results presented here suggest that 405 nm light might induce nonlinear bleaching of the red state, it is unlikely that this is responsible for the nonlinear effect of 405 nm light on the PCE because at the single molecule level we found that high intensity 405 nm light does not decrease the photobleaching time because bleaching is dominated by the high intensity 561 nm light used for single molecule imaging. Thus, this finding rather suggests that similar nonlinear bleaching pathways driven by excitation with 405 nm light might be present in both the green and red states of mEos4b. Altogether, these experiments highlighted interesting behaviors of mEos4b but do not provide an obvious explanation for the improved off-time reduction by 405 nm light.

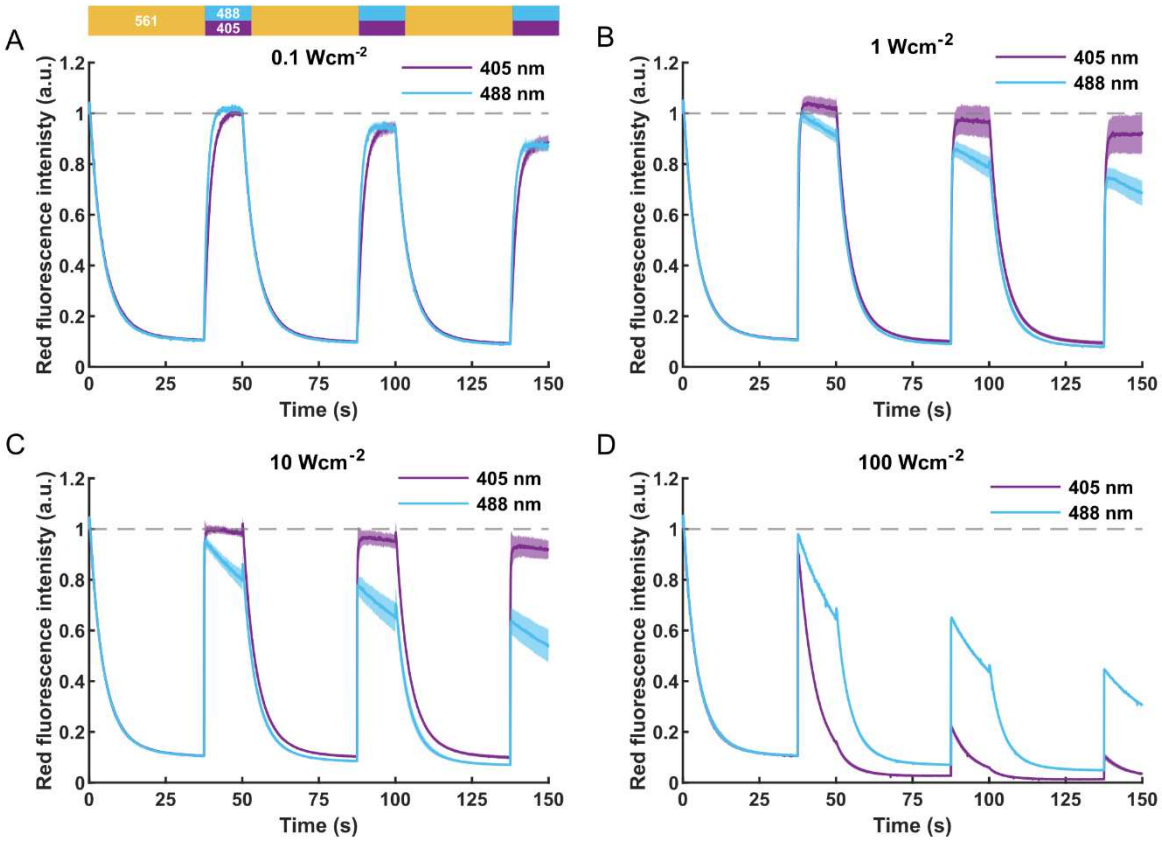

Figure 3.38 Photoswitching of red-state mEos4b with 405 and 488 nm light. *Photoconverted mEos4b molecules embedded in PAA (pH 8) were sequentially illuminated with 10 W/cm^2 561 nm light to induce off-switching and with 0.1 W/cm^2 (A), 1 W/cm^2, (B), 10 W/cm^2 (C) or 100 W/cm^2 405 or 488 nm light to induce on-switching. The red fluorescence intensity was sampled every 50 ms by 5 ms exposure with 10 W/cm^2 561 nm light. Shown is the mean ± sd of >3 measurements.*

Intrigued by the results presented above, we tested whether we could reproduce these switching behaviors by simulations using SMIS. We started with the default mEos4b model provided in SMIS (**Table 2.4**) and simulated off-and on-switching using a similar illumination scheme as in the experiments (**Figure 3.39A**). Using the set-up, the simulated switching behavior deviated from the observed switching behavior at serval points:

- The simulated on-switching efficiency was only 60% due to bleaching of the red On-state during off-switching. This is explained by the used bleaching and off-switching quantum yields (10^{-5} and $1.5x10^{-5}$), resulting in bleaching of 40% of the molecules ($10^{-5}/(10^{-5}+1.5x10^{-5})$) per switching cycle. These quantum yields were based on the quantum yields estimated for photoswitching and bleaching of mEos2 at the single molecule level[147]. Our results, however,

indicate that the bleaching quantum yield of mEos4b is much lower compared to the switching quantum yield (at least when using low laser intensities).

- The simulated on-switching rate was lower than the experimentally observed on-switching rate. This could be explained by either a too low on-switching quantum yield used for the simulations or by underestimation the power density in the experiments.
- The simulated off-switching rate is lower than the experimentally observed off-switching rate. Furthermore, in the simulations the on-state disappears for completely and the fluorescence intensity decays to 0, while in the experiments ~10-15% of the initial fluorescence intensity remains after off-switching. The low off-switching rate in the simulations could again be explained by underestimation of the quantum yield or by underestimation of the applied laser power density. The remaing red fluorescence in the experiments likely reflects the balance between on- and off-switching by 561 nm light, given that the Off state is sensitive to 561 nm light[217]. The Off state absorption spectrum used for the simulations, however, did not have any absorption around 561 nm.
- 100 W/cm^2 405 nm light does not induce strong bleaching, indicating that this pathway is missing from the model.

We attempted to adjust the Off state absorption spectrum and the phototransformation quantum yields of the photophysical model to reproduce better the experimental behaviors (**Table 2.6**). To this end, we estimated the absorption of the Off state at 561 nm to be ~ 0.5 M^{-1}cm^{-1} based on the data provided by de Zitter et al.[217] and adjusted the absoption spectrum accordingly. Furthermore, we increased the on- and off-switching quantum yields, assuming that our estimations of the laser power densities were correct. In addition, we decreased the bleaching quantum yield so that in each switching cycle only ~5% of the molecules was bleached. At this point, we choose to not try to incorporate a nonlinear bleaching pathway driven by 405 nm light to reduce the complexity. The simulated switching curves using this adjusted model are shown in **Figure 3.39B**. Although the simulations still do not fully reproduce the experimentally observed behaviors, they do confirm that 488 nm light cycles the protein between the on-and off-state leading to bleaching, while this is less the case with 405 nm light (see simulations with 100 W/cm^2) (**Figure 3.39C,D**). These simulations indicate that more work is needed to refine the photophysical model of mEos4b.

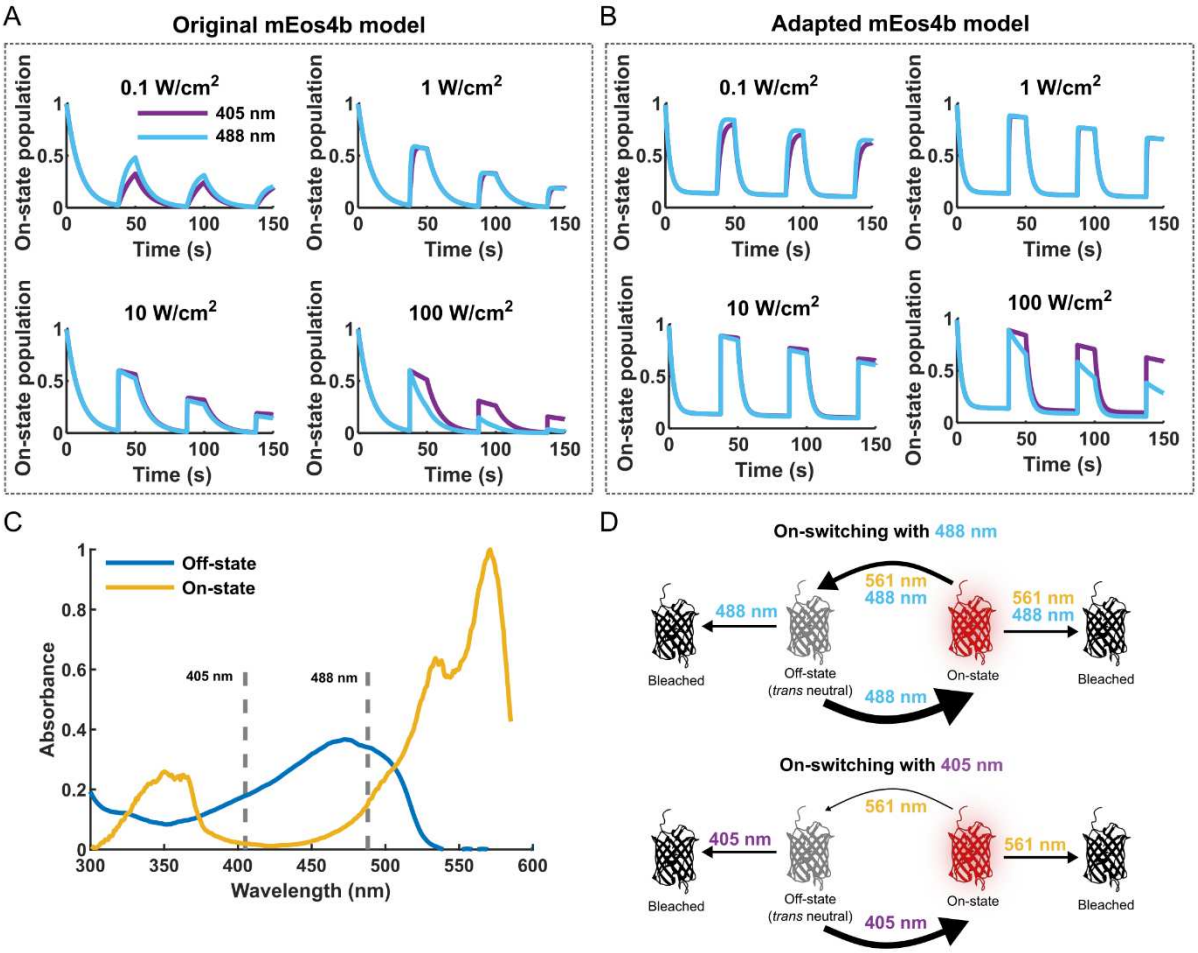

Figure 3.39 Simulations of red-state photoswitching. *Simulations were performed in SMIS using a similar illumination scheme as for the experimental data. Simulations were performed using the original photophysical model of mEos4b (A) and a model with adapted quantum yields to reproduce more closely the experimental data. C) Absorption spectra of the red On- and Off-state. Dashed lines at 405 and 488 nm to guide the eye. D) Photophysical scheme illustrating the 488 nm induced cycling between the On- and Off-states which leads to photobleaching.*

Searching for an alternative explanation for the superior efficiency of 405 nm light in off-time reduction, we hypothesized that it is possible the combination of high intensity 561 nm light and 405 or 488 nm light that makes that 405 nm light appears more efficient. To test this hypothesis, we repeated the switching experiments presented above adding continous illumination with 100 W/cm^2 561 nm light (**Figure 3.40**). Under these conditions, the on-switching effciency was substantially higher when 488 nm light was used (0.1 and 1 W/cm^2), which is logically explained by the higher absorbance of the Off state at 488 nm and competition between on-and off-switching under continous illumination with 100 W/cm^2 561 nm light. In addition, under these conditions, photobleaching appeared to proceed similarly with 405 and 488 nm light, which is likely explained by off-switching being driven by 561 nm light so that in both conditions (405 or 488 nm) the protein is cycled repeatedly between the Off and On state leading to bleaching (compare **Figure 3.40B** with **Figure 3.38B**). At 10 W/cm^2, 405 nm light appeared to induce strong bleaching (**Figure 3.40C**). The fact that in the absence of high intensity 561 nm light, 10 W/cm^2 405 nm light did not induce strong bleaching (**Figure 3.38C**) suggests that there is a combinatorial effect of 405 nm and 561 nm light. This effect does not appear to be induced by the combination of 561 and 488 nm light (**Figure 3.40C**).

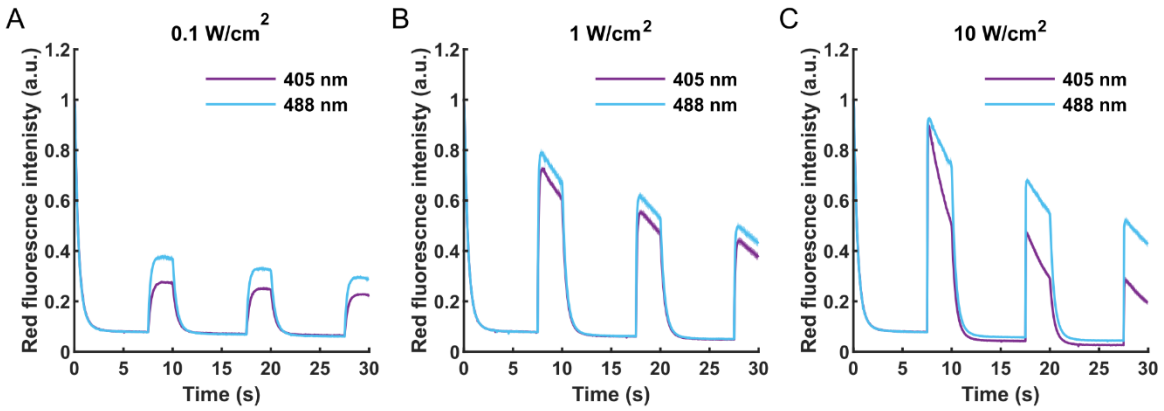

Figure 3.40 Photoswitching of red-state mEos4b under continuous illumination with 100 W/cm² 561 nm light. *Photoconverted mEos4b molecules embedded in PAA (pH 8) were continuously illuminated with 100 W/cm² 561 nm light to induce off-switching. Every 150 frames, on-switching was promoted by application of 0.1 W/cm² (A), 1 W/cm², (B) or 10 W/cm² (C) for 50 frames. The red fluorescence intensity was sampled every 50 ms by 5 ms exposure with 10 W/cm² 561 nm light. Shown is the mean ± sd of >3 measurements.*

Despite our intensive investigations, we did not find an answer to the question why 405 nm light appears to reduce the red-state off-times more efficiently than 488 nm light. In fact, all experiments presented above support the notion that 488 nm light acts more efficiently on the red Off state. Therefore, we decided to have a closer look at the off-time histograms (**Figure 3.41**). When the histograms are plotted in log-scale (**Figure 3.41**A), there appears to be a clear difference in off-time reduction by 405 and 488 nm light. However, the log-scale highlights the long off-times, which occur with a low frequency ($<10^{-2}$). When the histograms are plotted in linear scale (**Figure 3.41B**), on the other hand, there seems to be almost no difference between the 405 and 488 nm light. Although this does not mean that 405 nm light is not more efficient than 488 nm light, it does provide an explanation why we could not observe this effect at the ensemble level. We also had a second look at the on-time and nBlink histograms. The on-time histograms show that 488 nm light increases the fraction of short lived on-times. This was also previously observed by de Zitter et al[217] and might be explained by 488 nm light induced off-switching due to excitation of the anionic chromophore. The nBlink histograms do not reveal any strong difference between 405 and 488 nm light although in the presence of 488 nm light the fraction of molecules that does not blink seems to be increased.

Altogether, these data do not provide a clear indication as to why 405 nm light reduces more efficiently the off-time duration of red-state mEos4b. A possible scenario remains that there is another off-state, which is only sensitive to 405 nm light. It is tempting to speculate that there might be a relation between the better off-time reduction by 405 nm light and the apparent nonlinear bleaching of the red state induced by high intensity 405 nm light because both processes expectedly involve a 405 nm sensitive non-fluorescent state. Whether both processes could actually involve the same state is unclear.

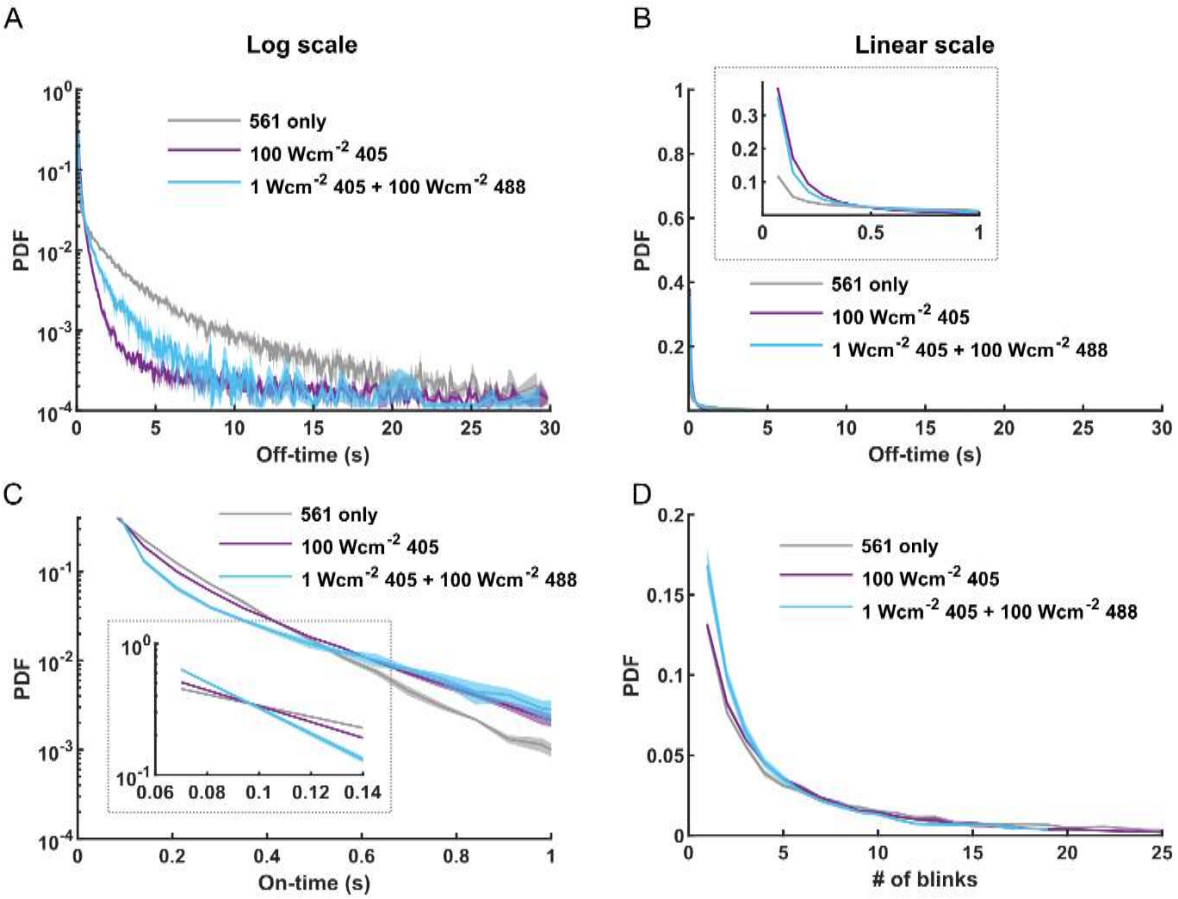

Figure 3.41 Effects of 405 and 488 nm light on the photophysical behavior of mEos4b in PALM conditions. *Figures reproduced from* ***section 3.1.3****. PALM imaging of mEos4b molecules embedded in PAA gel (pH 8.5) was performed using alternating excitation with 561 nm (70 ms at 500 W/cm^2) and 405 nm and/or 488 nm (8.2 ms at 1-100 W/cm^2) light. A) Off-times histogram in log scale. B) Off-time histograms in linear scale. C) On-time histograms. B) nBlink histograms.*

3.1.4.3.2 Identification of a 405/488 nm light induced off-state

During the switching experiments we noticed that the fluorescence intensity transiently increased after the on-switching periods with high intensity 405 and 488 nm light (**Figure 3.39C,D**). This observation is reminiscent of a recent paper published by Sun et al describing a 405 nm light induced off-state sensitive to 561 nm light in mEos3.2[148]. We hypothesized that if this increase is indeed due to recovery of a 405/488 induced off-state, it would likely be stronger at lower pH because this state is probably formed from the neutral chromophore. We tested this idea by repeating the switching experiments at pH 7.4 and pH 6.4 (**Figure 3.42**). In line with our hypothesis, the transient increase in fluorescence after the on-switching periods became more pronounced at lower pH (**Figure 3.42**). Of note, this transient increase was not only present after on-switching but also directly following the photoconversion phase. Although these experiments support the idea that this off-state, which we name $Off_{neutral}$, is formed from the neutral chromophore, they do not provide proof that it is formed from the *cis* neutral chromophore. This is because the excited *cis* neutral chromophore is highly susceptible to isomerization. So, under these conditions of low pH the chromophore is rapidly cycled between the *cis* and *trans* neutral states by illumination with 405 and 488 nm light, so that it remains unknown whether the off-state is formed from the *cis*- or *trans* neutral chromophore.

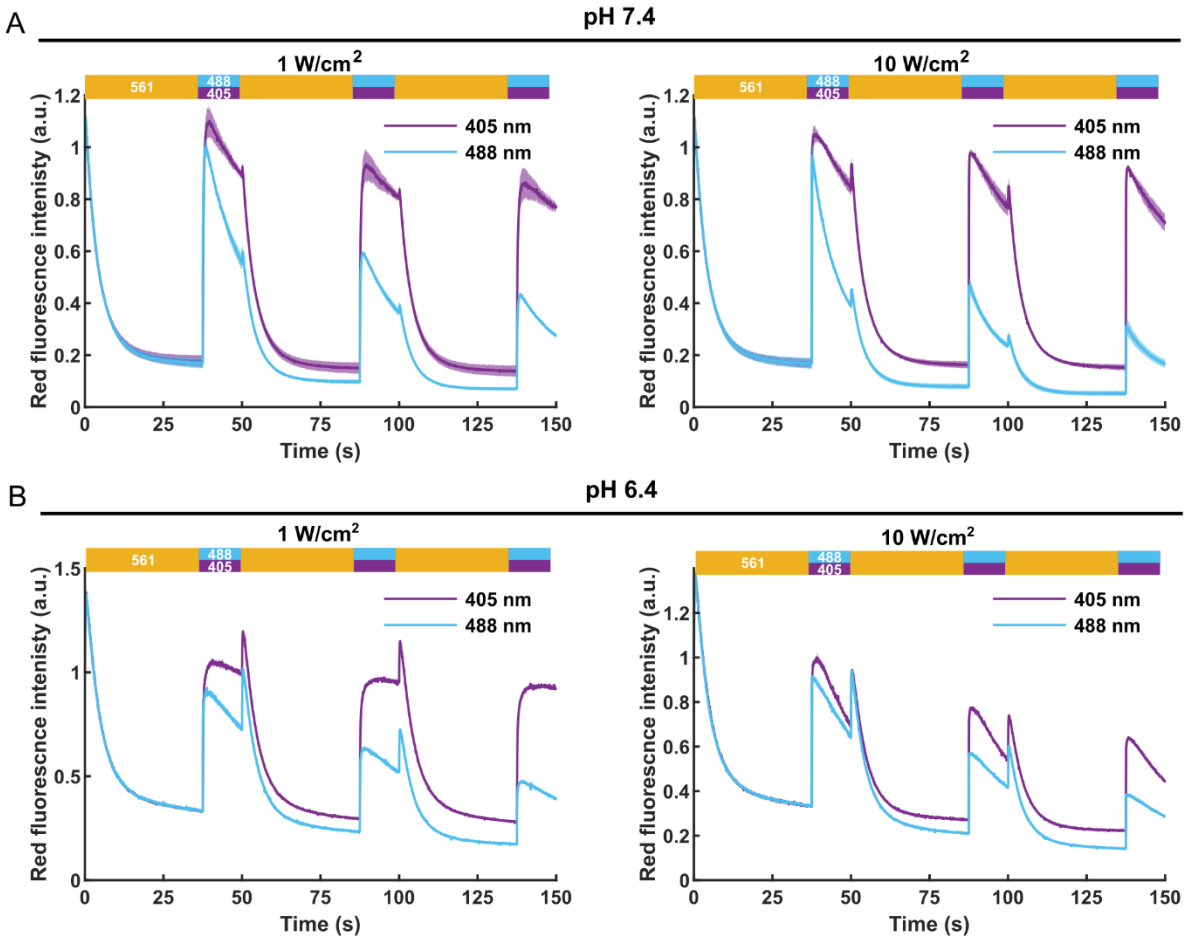

Figure 3.42 The photoswitching behavior of red-state mEos4b is affected by the environmental pH. *Photoconverted mEos4b molecules embedded in PAA at pH 7.4 (A) or pH 6.4 (B) were sequentially illuminated with 10 W/cm^2 561 nm light to induce off-switching, and with 1 W/cm^2 or 10 W/cm^2 405 or 488 nm light to induce on-switching. The red fluorescence intensity was sampled every 50 ms by 5 ms exposure with 10 W/cm^2 561 nm light. Shown is the mean ± sd of >3 measurements.*

Sun et al reported that recovery from this 405-induced off-state in mEos3.2 is promoted by 561 nm light. To test whether this is also the case in mEos4b, we made an experiment at pH 6.4 where we first photoconverted all molecules using 405 nm light after which we applied 561 nm light to induce off-switching as usual or only applied 561 nm to read out the red fluorescence intensity but not in between the frames (**Figure 3.43A**). Indeed, in the absence of additional 561 nm light, off-state recovery was slower (**Figure 3.43A**), indicating that recovery is promoted by 561 nm light.

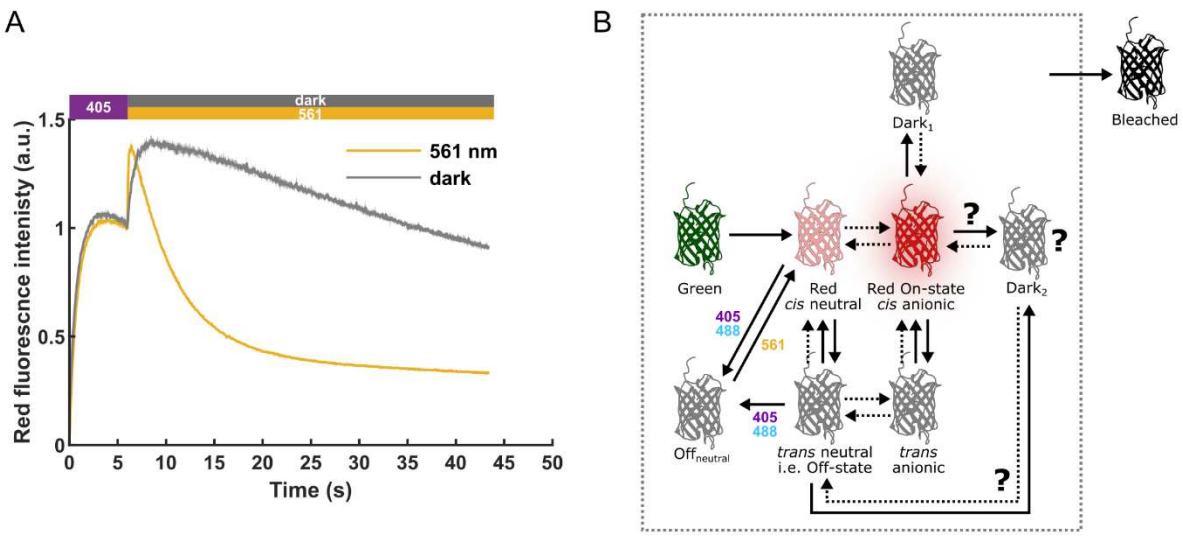

Figure 3.43 561 nm light promotes off-state recovery. *A) mEos4b molecules embedded in PAA gel (pH 6.4) were sequentially illuminated with 405 nm (10 W/cm²) and 561 nm (10 W/cm²) light while the red fluorescence intensity was monitored every 50 ms by 5 ms illumination with 561 nm light. Alternatively, illumination with 561 nm light during the second phase was omitted. B) Tentative photophysical model of red state mEos4b including a 405/488 nm light induced red off-state.*

Given that recovery from $Off_{neutral}$ is promoted by light, we were interested to measure its absorption spectrum. We made a first attempt to do so using a home-built spectrometer (the CAL(AI)^{2}DOSCOPE^{447}). Because all experiments were performed in PAA gel, we first tested whether we could collect absorption spectra from PAA gel samples (**Figure 3.44**). However, although the fluorescence signal followed globally the expected kinetics (**Figure 3.44A-C**), the absorption spectra revealed no differences that could explain the increased fluorescence signal after illumination with 561 nm light (**Figure 3.44D**). Problematically, the absorption spectra were of low quality, which we think is due to scattering of light in the PAA gel, increasing the apparent OD of the sample and thereby lowering the signal-to-noise.

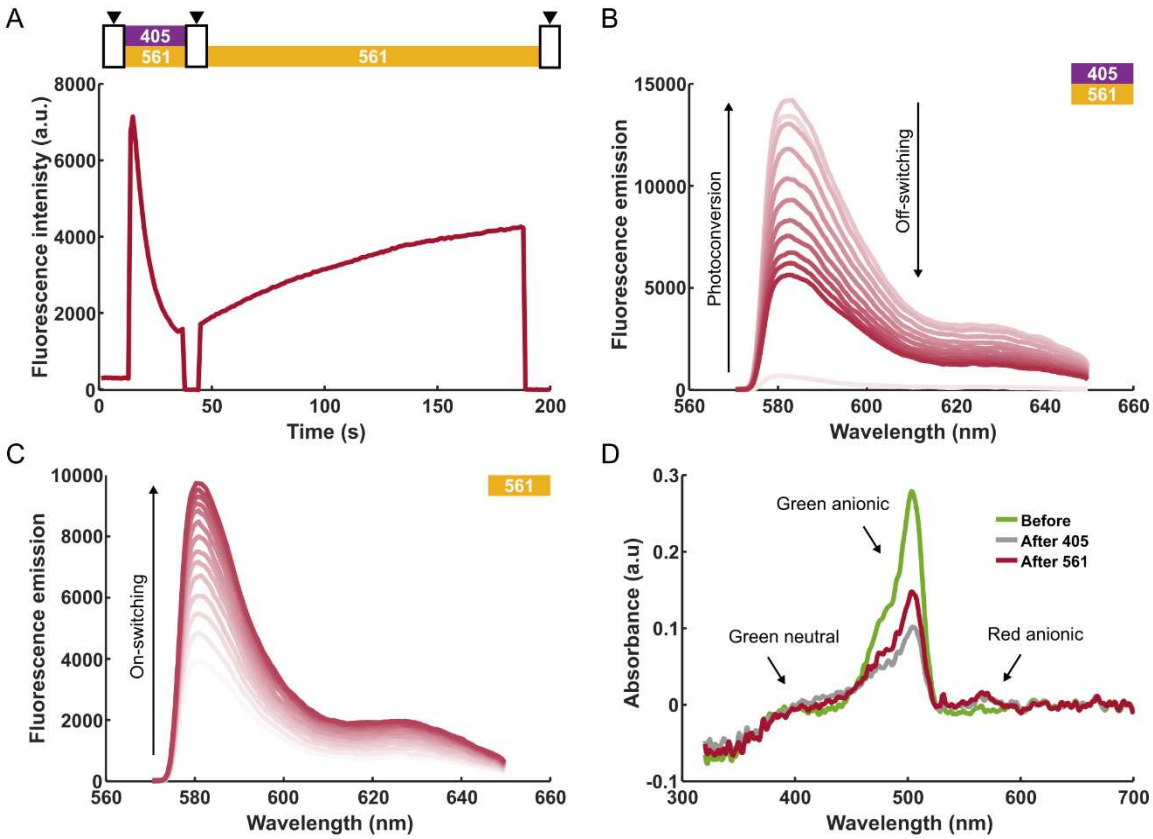

Figure 3.44 Spectroscopic measurements of mEos4b in PAA gel. *mEos4b molecules were embedded in PAA gel (pH 6.4) and fluorescence and emission spectra were recorded before, during and after illumination with 405 nm (8 W/cm^2, 40 ms per cycle) and 561 nm (14 W/cm^2, 40 ms per cycle) light. A) Time-series of the integrated red fluorescence signal (570-640 nm). The illumination scheme is shown above the figure. White boxes indicate physical blockage of the lasers to collect complete absorption spectra (indicated by black triangles). B) Progression (light to dark red) of the fluorescence emission spectra during the first illumination phase (405 + 561 nm) shown in (A). First, the red fluorescence signal increases due to photoconversion, after which it decays due to off-switching and bleaching. C) Progression (light to dark red) of the fluorescence emission spectra during the second illumination phase (561 nm only) shown in (A). D) Absorption spectra collected at the time points indicated in (A). Data collected with the help of Virgile Adams.*

Searching for an alternative to PAA gel to immobilize mEos4b that is compatible with the collection of absorption spectra on the CAL(AI)^{2}DOSCOPE, we tested the usage of glycerol-based samples. mEos4b (30 mg/ml) was mixed with 50% glycerol diluted in MES (final pH 5.2 as deduced from the ratio between the green neutral and anionic peaks) to reduce diffusion, after which the sample was loaded into a capillary. Using these samples, we were able to collect high signal-to-noise absorption spectra (**Figure 3.45**). However, the fluorescence signal did not increase after illumination with 405 nm light was stopped as was the case in the PAA gel sample (**Figure 3.45A**). The absorption spectra, however, did show some interesting properties (**Figure 3.45B**).

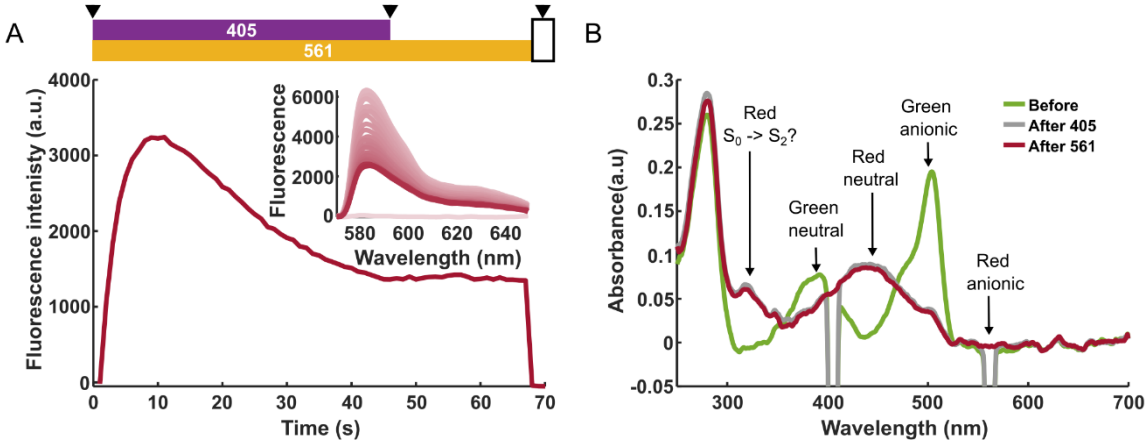

Figure 3.45 Spectroscopic measurements of mEos4b in 50% glycerol. *mEos4b molecules were embedded in % glycerol (pH 6) and fluorescence and emission spectra were recorded before, during and after illumination with 405 nm (8 W/cm^2, 40 ms per cycle) and 561 nm (14 W/cm^2, 40 ms per cycle) light. A) Time-series of the integrated red fluorescence signal (570-640 nm). The illumination scheme is shown above the figure. The white box indicates physical blockage of the lasers. Black triangles indicate the time points at which the absorption spectra shown in (B) were collected. B) Absorption spectra collected at the time points indicated in (A). Data collected with the help of Virgile Adam.*

Firstly, given a pKa of 5.8 and hill coefficient of ~0.75, the anionic fraction of the red state at pH 5.2 is expected to be 27% but the absorption spectra suggest that there is no anionic species while there appears to be substantial red neutral species. Similar behavior has been reported for the PCFP LEA, in which illumination with 400 nm was shown to promote formation of the neutral chromophore at low pH (pH 6.3) but not at high pH (pH 7.9)[199,448]. It seems counter intuitive that 400 nm light promotes the formation of a neutral state. However, the *cis* neutral chromophore, which absorbs strongly around 400 nm, is prone to isomerization[122,181]. So, assuming equal quantum yields for *cis*-to-*trans* and *trans*-to-*cis* isomerization, illumination with 400 nm light will populate the *trans* neutral state and thereby decrease the population of the neutral and anionic *cis* states. Such an effect would be relatively stronger at lower pH because of the already larger neutral population and was also observed in the RSFP rsFolder[122]. This explanation, however, does not explain why, at least in PAA gel, recovery from the 405 nm induced non-fluorescent state appears to be promoted by 561 nm light, while 561 nm light promotes Off state formation and there is no notable absorption around 561 nm (**Figure 3.45B**). It should also be noted that the spectrum expectedly corresponding to the red neutral chromophore in **Figure 3.45B** appears to be blue-shifted compared to the spectrum measured by de Zitter et al.[217] (peaking around 440 nm vs 470 nm), the reason for which being unclear.

A second observation is that, although there is no visible absorption peak corresponding the red anionic state, an absorption band around 320 nm is present after photoconversion (**Figure 3.45B**), which is generally believed to correspond to transitions from S0 to higher electronic states[188]. The same was seen in LEA[448]. Interestingly, after dark recovery of the anionic chromophore following exposure to 400 nm light, this 300-350 nm band of LEA was shown to change and become slightly red shifted[448], suggesting that this band is composed of multiple bands, of which some correspond to the neutral and some to the anionic chromophore. More efforts are required to unravel the different states that are formed in mEos4b under illumination.

3.1.4.3.3 Discussion

We investigated the effects of 405, 488 and 561 nm light on the red state of mEos4b, intrigued by the observation that off-time reduction appears more efficient with 405 nm light than with 488 nm light, despite the higher absorbance of 488 nm light by the red Off state. Although our findings do

not present a clear explanation to this apparent contradiction, a conceivable explanation remains the presence of a second off-state, which is only sensitive to 405 nm light. This off-state, however, is presumably relatively rare, which has as a consequence that it cannot be detected at the ensemble level but only appears in the off-time histograms when plotted in log-scale.

Careful inspection of the switching curves revealed the presence of a 405/488 nm light induced off-state. This off-state, $Off_{neutral}$, is likely formed from the neutral chromophore. Recovery from this state appears to be promoted by 561 nm light. In terms of behavior, this off-state appears similar to the off-state described by Sun et al. in mEos3.2[148]. However, collection of absorption spectra of mEos4b molecules embedded in glycerol after exposure to 405 nm light at low pH (pH 5.2), suggested that 405 nm light promotes population of the neutral chromophore and did not support the finding that 561 nm light promotes recovery. Similar behavior has been previously observed in the PCFP LEA[199,448]. It is unclear whether this 405 induced non-fluorescent state in LEA is related to the 405-induced non-fluorescent state previously described in mEos3.2. Given that recovery from the non-fluorescent state in mEos3.2 is promoted by 561 nm light, while this is unlikely to be the case for the non-fluorescent state in LEA, these are presumably different states. The formation of these different states might be strongly dependent on environmental conditions, explaining why we observed different behaviors depending on whether mEos4b was embedded in PAA gel or in glycerol. More efforts are needed to carefully address these questions.

Assuming that $Off_{neutral}$ is recoverable by 561 nm light and mostly formed at low pH, this state may be expected to have little effect on PALM experiments, which are typically conducted at physiological pH and involve high intensity 561 nm light. However, formation of $Off_{neutral}$, whether recoverable by 561 nm light or not, might have influenced the interpretation of results presented earlier in this manuscript:

- **Section 3.1.3** reports that 405-nm light-induced non-linear bleaching of the green state lowers the PCE of PCFPs based on single molecule and ensemble experiments. Although these experiments were performed at high pH (pH 8), it might be thought that formation of $Off_{neutral}$ could have contributed to the apparent low PCE under high 405 nm light intensities in the ensemble experiments. The single molecule experiments (**Figure 3.17** & **Figure 3.20**) and ensemble experiments using a constant dose of 405 nm light (**Figure 3.18**), however, provide a strong indication that green state bleaching is responsible for the reduced PCE by showing that the red-state on-and bleaching-times are unaffected by increased 405 nm light power densities.

- Of note, **Section 3.1.3** also reports that the photoconversion kinetics of pcStar, and to a lesser extend the other PCFPs, differ from a simple green-to-red-to-bleached model (**Figure 3.19**). As speculated in the corresponding text, the formation of a 405 nm light induced non-fluorescent state could explain this strange kinetics. It remains to be investigated how the 405-induced non-fluorescent state(s) described in this section influence the photoconversion kinetics measured at the ensemble level.

- **Section 3.1.4.1** describes that the PCE of mEos4b decreases with increasing 405 nm light intensities (in the mW/cm^2 range) due to green state heterogeneity, based on NMR experiments. Similar as for the experiments described above, the formation of a 405-nm light induced (non-fluorescent) state could be expected to have affected these measurements, assuming that this state has different chemical shifts than the fluorescent (anionic *cis*) state. To investigate this possibility, NMR experiments were performed by Arijit, in which after photoconversion by 405 nm light, 561 nm light was applied to test the presence of a 405-nm induced state (**Figure 3.46**). Indeed, application of 561 nm light increased the red state population significantly, raising the observed PCE from ~38% to ~58% (4.5 W/cm^2 405 nm,

Figure 3.46A) and providing an explanation for the unexpectedly low PCE's that were observed by NMR (see discussion **Section 3.1.4.1**). However, even after application of 561 nm light, the PCE remained lower when higher 405 nm intensities were used for photoconversion (**Figure 3.46**), supporting our previous conclusions.

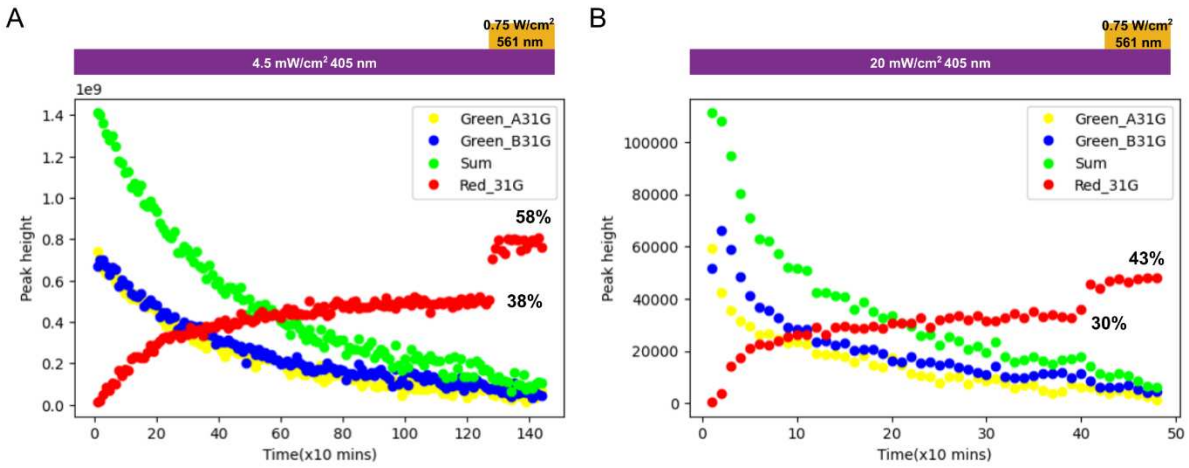

***Figure 3.46 561 nm light increases the observed PCE by NMR**. Photoconversion of mEos4b was monitored by NMR under illumination with by 4.5 (A) or 20 (B) mW/cm^2 405 nm light (shown is the progression of residue 31G). Addition of 561 nm light (0.75 W/cm^2) significantly increased the signal of the red-state thereby increasing the apparent PCE (as noted in the plots). Data and figures by Arijit Maity.*

Taken altogether, the results presented in this section provide new insights into the complex photophysics of mEos4b. Future work in the lab is aimed at elucidating what states are formed under illumination by 405 nm light using a combination of fluorescence microscopy, NMR spectroscopy, and possibly crystallography to gain mechanistic insights. Although such states might be expected to have a minimal impact on PALM experiments (low 405 nm intensity, high 561 nm intensity and physiological pH), they could strongly bias photophysical characterizations if not accounted for, which makes such states of scientific interest (as illustrated by the unexpectedly low PCE's observed by NMR).

3.1.5 Simulating the switching behavior of rsEGFP2 at cryo-temperature

Parts of the results of this section have been published in:

Angela M. R. Mantovanelli, Oleksandr Glushonkov, Virgile Adam, Jip Wulffelé, Daniel Thédié, Martin Byrdin, Ingo Gregor, Oleksii Nevskyi, Jörg Enderlein & Dominique Bourgeois. ***Photophysical studies at cryogenic temperature reveal a novel photoswitching mechanism of rsEGFP2****. Journal of the American Chemical Society. DOI: 10.1021/jacs.3c01500*

One of the main focusses in the lab is the development of improved fluorescent markers for cryoPALM. There is growing interest in cryoPALM imaging because it paves the way for correlative SMLM and cryoEM and because cryofixation can preserve cellular structures that cannot be preserved by classical chemical fixation. One of the challenges for cryoPALM is the lack of fluorescent markers that efficiently activate or blink at cryogenic temperature. Although diverse FPs have been reported to blink at CT, studies report conflicting findings and the molecular mechanisms underlying blinking at CT remain poorly understood.

Recently, rsEGFP2, an efficient negative RSFP at RT, has been identified as a promising candidate for cryoPALM[229]. As part of her PhD work, Angela Mantovanelli tried to unravel the cryo-switching mechanism of rsEGFP2, aiming to improve its switching properties for cryoPALM imaging. Her work resulted in a publication reporting a novel photoswitching mechanism of rsEGFP2 at CT. The experimental work of this project has been mainly carried out by Angela Mantovanelli, Oleksandr Glushonkov and Virgile Adam. I contributed to this work by discussions and simulations to build a photophysical model explaining the observed photophysical behaviors. The experimental work presented below is a summary of the recent publication, outlining the different properties that were used to develop a photophysical model of the photoswitching mechanism of rsEGFP2 at CT.

3.1.5.1 The photoswitching mechanism of rsEGFP2 at CT is different from its mechanism at RT

At RT, photoswitching of rsEGFP2 is mediated by efficient *cis/trans* isomerization of the chromophore. Structural and photophysical characterization, however, revealed that photoswitching of rsEGFP2 at CT proceeds via a different mechanism (**Figure 3.47**). While at RT the Off state chromophore adopts a *trans* conformation, X-ray crystallography showed that at CT the off-state chromophore remains in a *cis* configuration (**Figure 3.47A,B**). Furthermore, microspectrophotometry experiments showed that the absorption spectrum of the off-state at CT is significantly blue-shifted compared to the Off state absorption spectrum at RT (**Figure 3.47C,D**). Together these findings indicate that photoswitching at CT proceeds via a different mechanism than at RT.

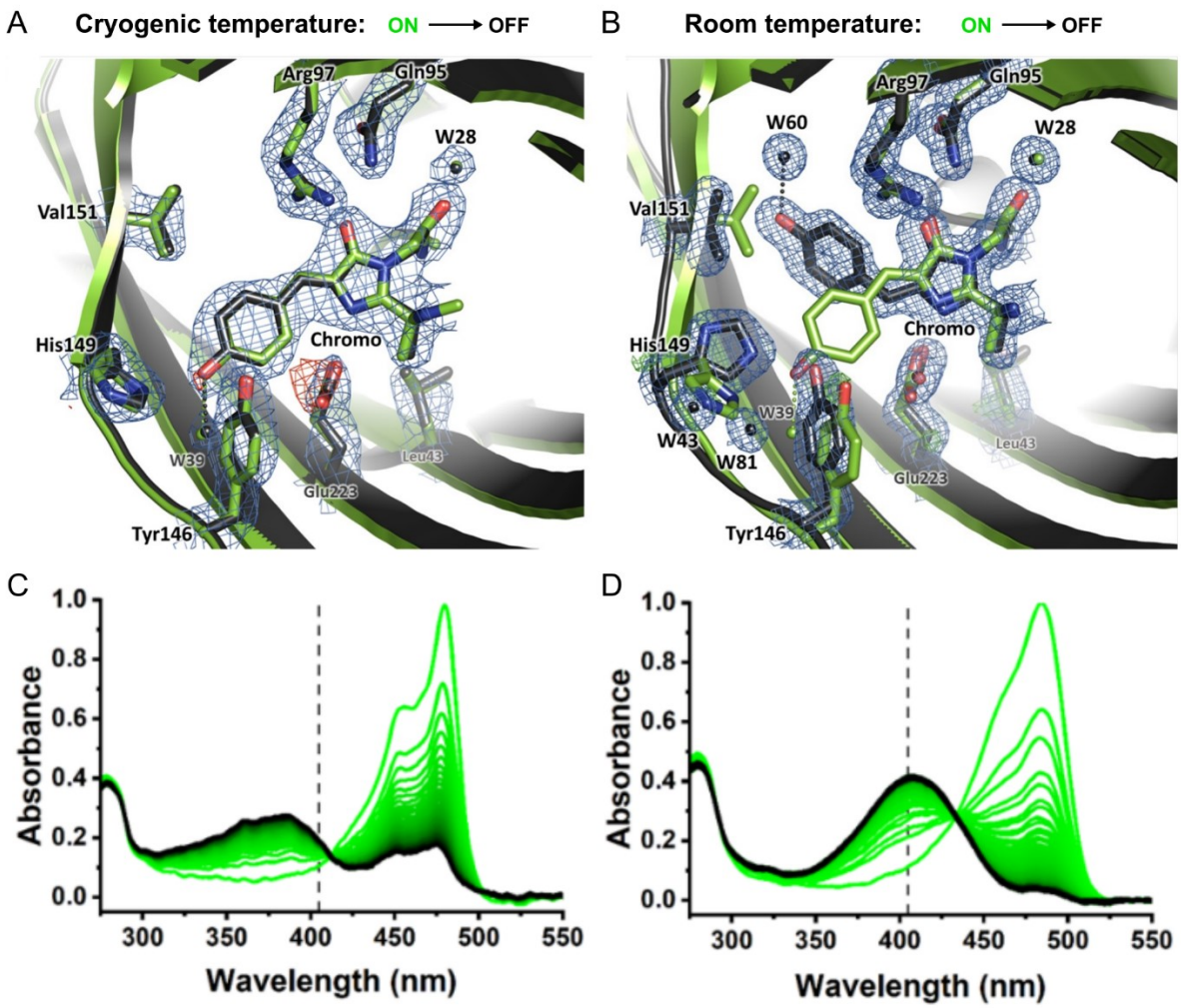

Figure 3.47 Off-switching at CT does not involve cis/trans isomerization. *Crystallographic views of the chromophore pocket of rsEGFP2 in the on-state (green) and off-state (black) at CT (A) and RT (B). Progression of the absorption spectrum of rsEGFP2 during off-switching with 488 nm light at CT (C) and RT (D). Dashed lines at 405 nm to guide the eye. Data and figures by Angela Mantovanelli and Virgile Adam. Figures adopted from Mantovanelli et al. (2023).*

3.1.5.2 355 nm light increases the on-switching efficiency at CT

Reversible photoswitching of rsEGFP2 with 488 and 405 nm light is highly efficient at RT. At CT, however, the on-switching efficiency under illumination with 405 nm light is limited to only ~25% (**Figure 3.48A**). We hypothesized that this limited efficiency could be explained by the blue-shift of the off-state absorption spectrum at CT as shown in **Figure 3.47C**. This motivated us to test the usage of a 355 nm laser, which hits the CT off-state at the left of its peak absorption. Indeed, switching experiments showed that on-switching at CT is more efficient when using 355 nm light (~50% efficiency) (**Figure 3.48A**).

The increased efficiency with 355 nm light, however, is not so easily explained. Although 355 nm light is more efficiently absorbed by the CT off-state than 405 nm light, there is still significant absorption at 405 nm so that on-switching is expected to be slower but equally efficient with 405 nm light. Further investigation of the cryo-switching behavior of rsEGFP2 revealed that sequential application of 405 and 355 nm light results in a stepwise on-switching, reaching about the same efficiency as when using 355 nm light alone (**Figure 3.48B**). On the other hand, when 405 nm light was applied after on-switching by 355 nm light, the on-state population decreased again (**Figure 3.48C**). Careful

inspection of the off-state spectra under the different switching conditions revealed that these observations can be explained by the presence of not one but two off-states (**Figure 3.48D**). While one of the off-states, Off_2, appeared sensitive to both 355 and 405 nm light, the other off-state, Off_1, appeared only sensitive to 355 nm light, explaining the higher on-switching efficiency under illumination with 355 nm light. Still, it remains intriguing that Off_1 is insensitive to 405 nm light while it absorbs significantly at this wavelength. In fact, although Off_2 is sensitive to both 355 and 405 nm light, its sensitivity to 355 nm light appears ~20x higher than its sensitivity to 405 nm light, which can be deduced from the required power densities to reach similar on-switching rates (see **Figure 3.48A**). These observations suggest that the on-switching quantum yields at CT are wavelength dependent. Strong wavelength dependent quantum yields have not been reported before for FPs but have been observed in organic dyes[449]. This phenomenon requires further study.

The presence of two off-states raises the question whether these two states are reached from the same or from different on-states. Based on the data presented in **Figure 3.48** we reasoned that these two off-states are reached from two distinct non-exchanging on-states.

- The first argument was based on the photofatigue experiment with 405 nm light shown in **Figure 3.48A**: While the on-switching efficiency in the first switching cycle is only ~25%, the relative efficiency in the following cycles is much higher (>50%). This would be in line with the presence of two on-states, one of which switches to Off_1 and is not recovered, explaining the low switching efficiency in the first cycle, and one which switches to Off_2 and is subsequently switched back-and-forth with a relatively high efficiency. On the other hand, if there would only be a single on-state, we would expect progressive accumulation of Off_1 and faster photofatigue.
- The second argument comes from the results shown in **Figure 3.48C** and **D**: Application of 405 nm light after on-switching by 355 nm light increase the absorbance at 320 nm, expectedly due to repopulation of Off_1 (**Figure 3.48D**). The increase at 320 nm, however, rapidly plateaus and does not reach the same level as when 488 nm light is applied. If there would be only one on-state (or two exchanging on-states), we would expect that application of 405 nm light would populate Off_1 to the same extend as 488 nm light because moleceules would be expected to cycle between the on-state(s) and Off_2 until they are bleached or switched to Off_1. The data, however, show that the absorbance at 320 nm does not reach the same level under illumination with 405 nm light than with 488 nm light, supporting the hypothesis of two non-exchanging on-states.

Having characterized in detail the switching behavior of rsEGFP2 at the ensemble level, Sasha confirmed that, also at the single molecule level, the usage of 355 nm light boosts the on-switching efficiency of rsEGFP2 (data not shown), which is an important finding for the application of cryoPALM. In addition, the single molecule data revealed that, besides Off_1 and Off_2, rsEGFP2 can enter a short lived-dark state (lifetime ~110 ms), which gives rise to rapid blinking at the single molecule level.

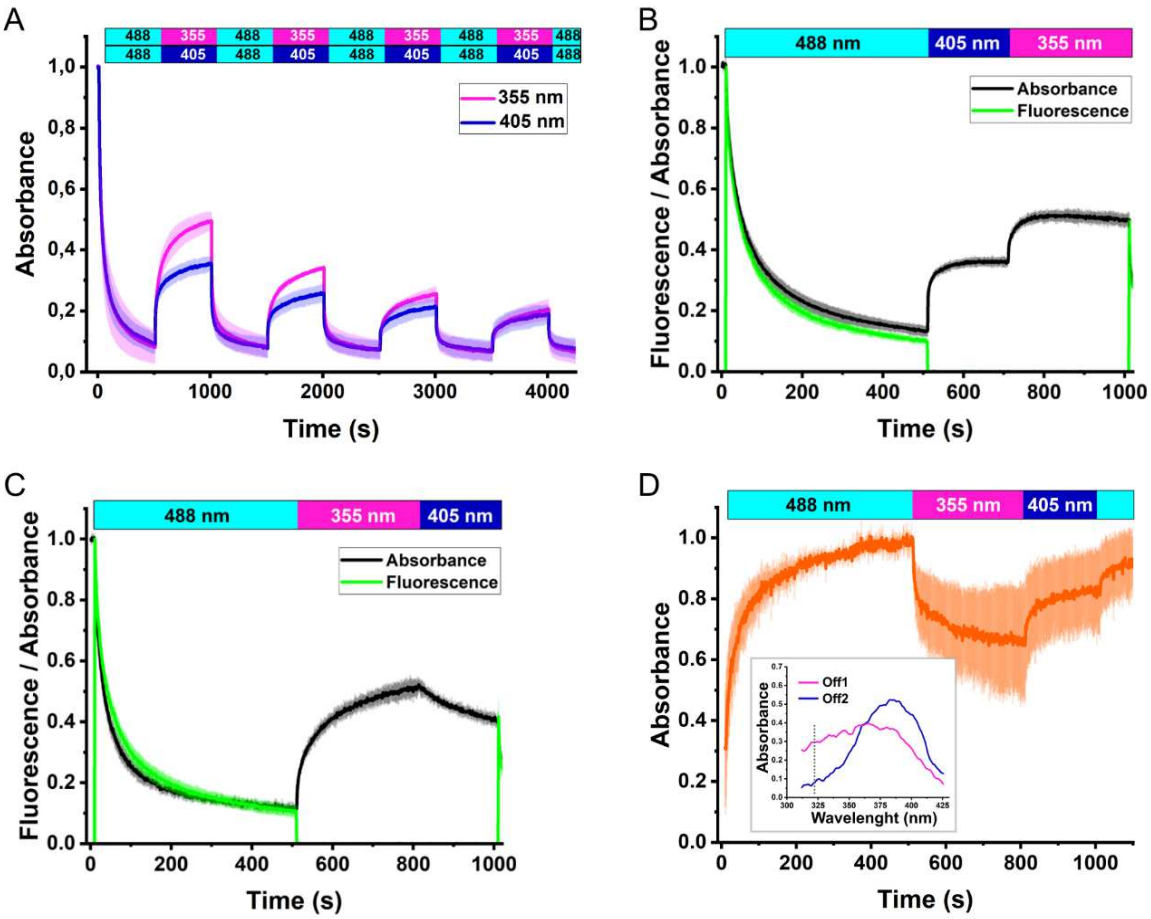

Figure 3.48 Illumination with 355 nm light improves the on-switching efficiency of rsEGFP2 at CT. *Photoswitching of rsEGFP2 at CT was monitored by following its absorbance in the range of 470-500 nm (on-state absorption) (A-C) or at 320 nm (Off1 absorption), and/or by following the fluorescence signal in the range of 495-630 nm. A) Photoswitching was induced alternating illumination with 488 nm (1.0 kW/cm²) for off-switching and 405 nm (0.2 kW/cm², blue) or 355 nm (0.01 kW/cm², magenta) light for on-switching. B) Photoswitching was induced by sequential illumination with 488 nm (0.4 kW/cm²), 405 nm (0.3 kW/cm²) and 355 nm (0.025 kW/cm²) light. C) Photoswitching was induced by sequential illumination with 488 nm (0.4 kW/cm²), 355 nm (0.025 kW/cm²) and 405 nm (0.3 kW/cm²) light. D) Progression of the absorbance at 320 nm (mainly Off1 absorption) under sequential illumination with 488 nm (0.4 kW/cm²), 355 nm (0.025 kW/cm²) and 405 nm (0.3 kW/cm²) light. Inset shows the absorption spectra of Off_1 and Off_2. Dashed line at 320 nm to guide the eye. Data and figures by Angela Mantovanelli. Figures adopted from Mantovanelli et al. (2023)*

3.1.5.3 Building a photophysical model with support of simulations

We hypothesized the following model to explain the observed photoswitching behaviors of rsEGFP2 at CT (**Figure 3.49A**): In the dark, rsEGFP2 molecules reside in two on-states, On_1 or On_2, that do not exchange. Upon excitation by 488 nm light, molecules may enter a short-lived dark state with a lifetime of ~110 ms ($Off_{short\text{-}lived}$) or their respective long-lived off-state (Off_1 or Off_2), with Off_1 being only sensitive to 355 nm light and Off_2 being 20x more sensitive to 355 nm than to 405 nm light. Photobleaching likely happens from all light absorbing states, with the On_1/Off_1 population being more prone to photobleaching than the On_2/Off_2 population as suggested by the photofatigue measurements.

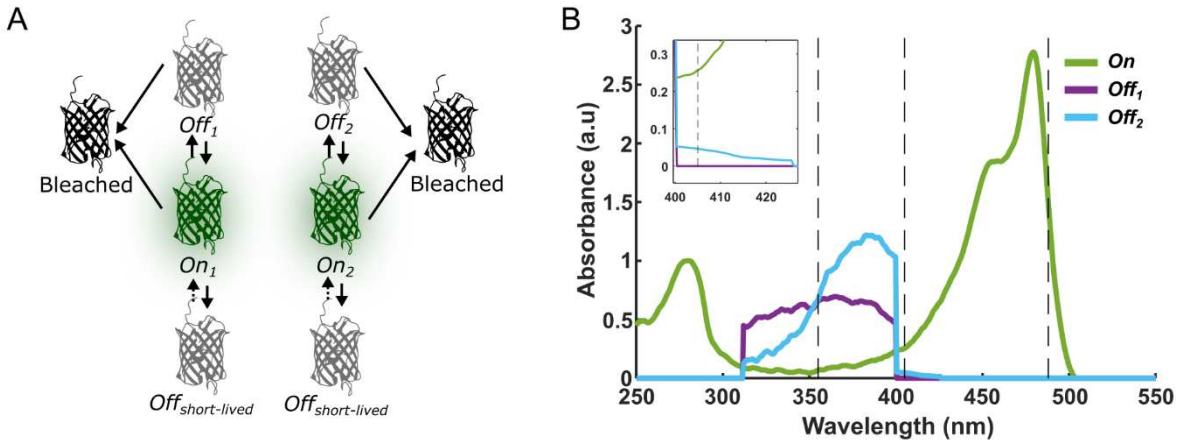

Figure 3.49 photophysical model used for simulations of rsEGFP2 switching at cryogenic temperature. *A) Employed photophysical model including two on-states with corresponding long- and short-lived off states. Solid lines indicate light induced processes; dotted lines indicate thermal processes B) Absorption spectra of the on- and long-lived off states. The raw off-state spectra were scaled according to their relative occupancy. The wavelength dependent quantum yields of on-switching were incorporated into the off-state spectra by scaling down the absorption of Off_2 at wavelengths >400 nm by a factor of twenty while setting the absorption of Off_1 to zero (see inset). Dashed lines indicate 355, 405 and 488 nm to guide the eye.*

To validate that this model can explain the experimentally observed behaviors, we set-up ensemble simulations in SMIS. The switching and bleaching quantum yields were estimated from the experimental switching data (**Table 2.7**). The relative populations of On_1 and On_2 (70% and 30%) were empirically estimated using the photofatigue experiments. Wavelength depended quantum yields cannot be entered in SMIS, so to incorporate this behavior we scaled down the absorption spectra of the off-states at wavelengths >400 nm (**Figure 3.49B**). Using this set-up, we were able to reproduce the experimentally observed photoswitching behaviors of rsEGFP2 *in silico*:

1. The on-switching efficiencies with 355 and 405 nm light are close to ~50% and ~25%, respectively (**Figure 3.50A**).
2. Switching with 355 nm light induces faster photofatigue so that after four switching cycles the apparent difference in switching efficiency between 355 and 405 nm light is minimal (**Figure 3.50B**).
3. Application of 405 nm light after on-switching with 355 nm light decreases the on-state population (**Figure 3.50C**).
4. Application of 355 nm light after on-switching with 405 nm increases the on-state population further to a similar level as when using 355 nm light alone (**Figure 3.50D**).

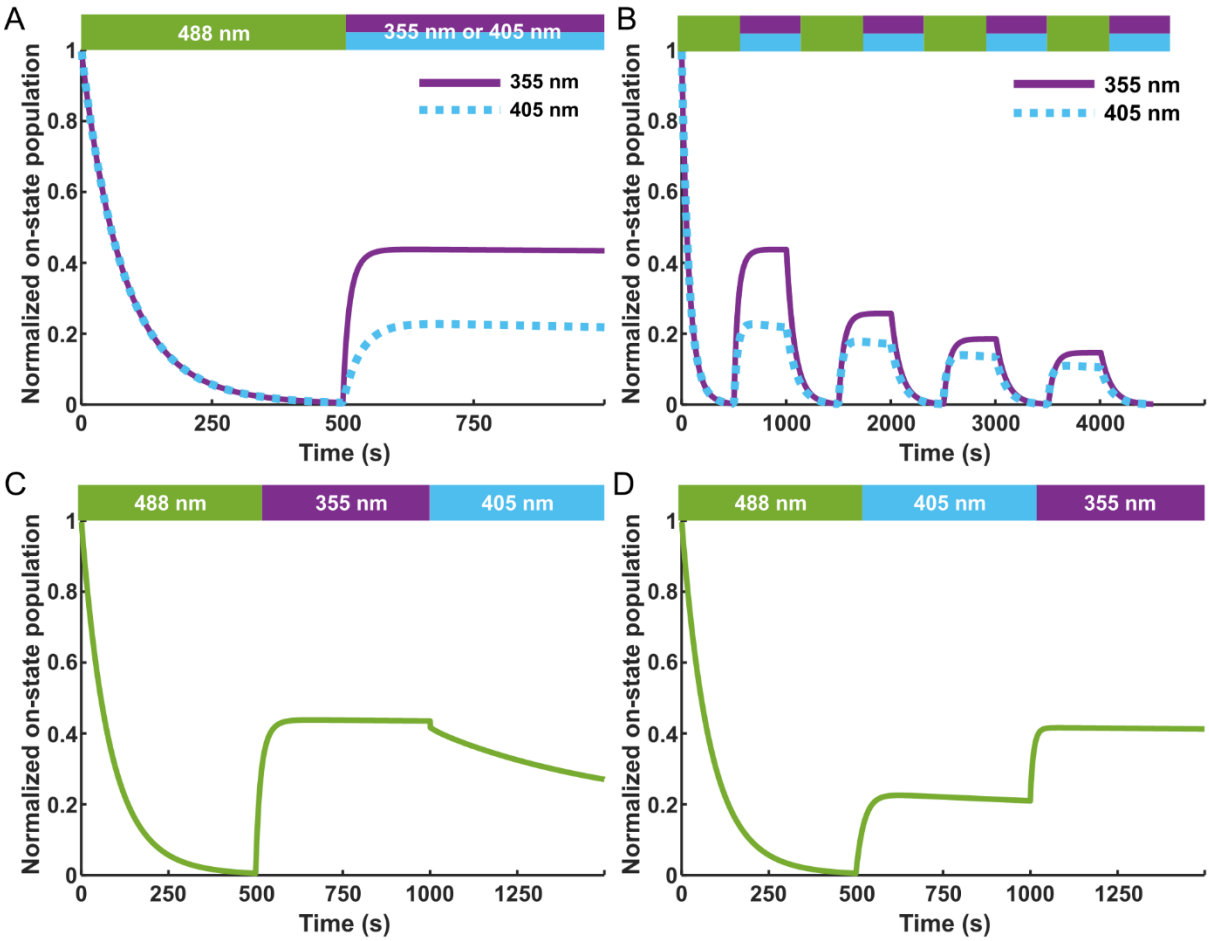

Figure 3.50 Ensemble simulations of rsEGFP2 photoswitching at cryogenic temperature. *A) Off-switching by 400 W/cm^2 488 nm light followed by on-switching by 30 W/cm^2 355 nm light or 200 W/cm^2 488 nm light. B) Repetitive switching cycles (photofatigue experiments) with 1 kW/cm2 488 nm light and 10 W/cm^2 355 nm light or 200 W/cm^2 488 nm light. C) Sequential application of 355 nm (25 W/cm^2) and 405 nm (300 W/cm^2) light after off-switching by 488 nm light. D) Sequential application of 405 nm (300 W/cm^2) and 355 nm (25 W/cm^2) light after off-switching by 488 nm light.*

Next, we used this model to investigate the possibility that both off-states are reached from a single on-state. To simulate photoswitching with a single on-state, without designing a new model, we added fast thermal exchange rates (k_{ex} = 100 s^{-1}) between *On$_1$* and *On$_2$* so that they behaved as a single state (**Figure 3.51A**). First, we re-simulated the photofatigue experiments (**Figure 3.51B**). In agreement with our previous argumentation, 405 nm light induced rapid photofatigue due to accumulation of *Off$_1$* (**Figure 3.51C**). Second, we re-simulated the sequential application of 355 and 405 nm light (**Figure 3.52**). Again, these simulations confirmed our expectations: if there would be only one on-state, photobleaching and accumulation of *Off$_1$* would occur at the same rate and *Off$_1$* would be fully repopulated by 405 nm light alone (**Figure 3.52C,D**). This is in contradiction with the experimental results (**Figure 3.48**), which show that repopulation of *Off$_1$* plateaus rapidly (**Figure 3.48D**). Altogether these simulations support a model in which *Off$_1$* and *Off$_2$* are reached by two distinct non-exchanging on-states (*On$_1$* and *On$_2$*).

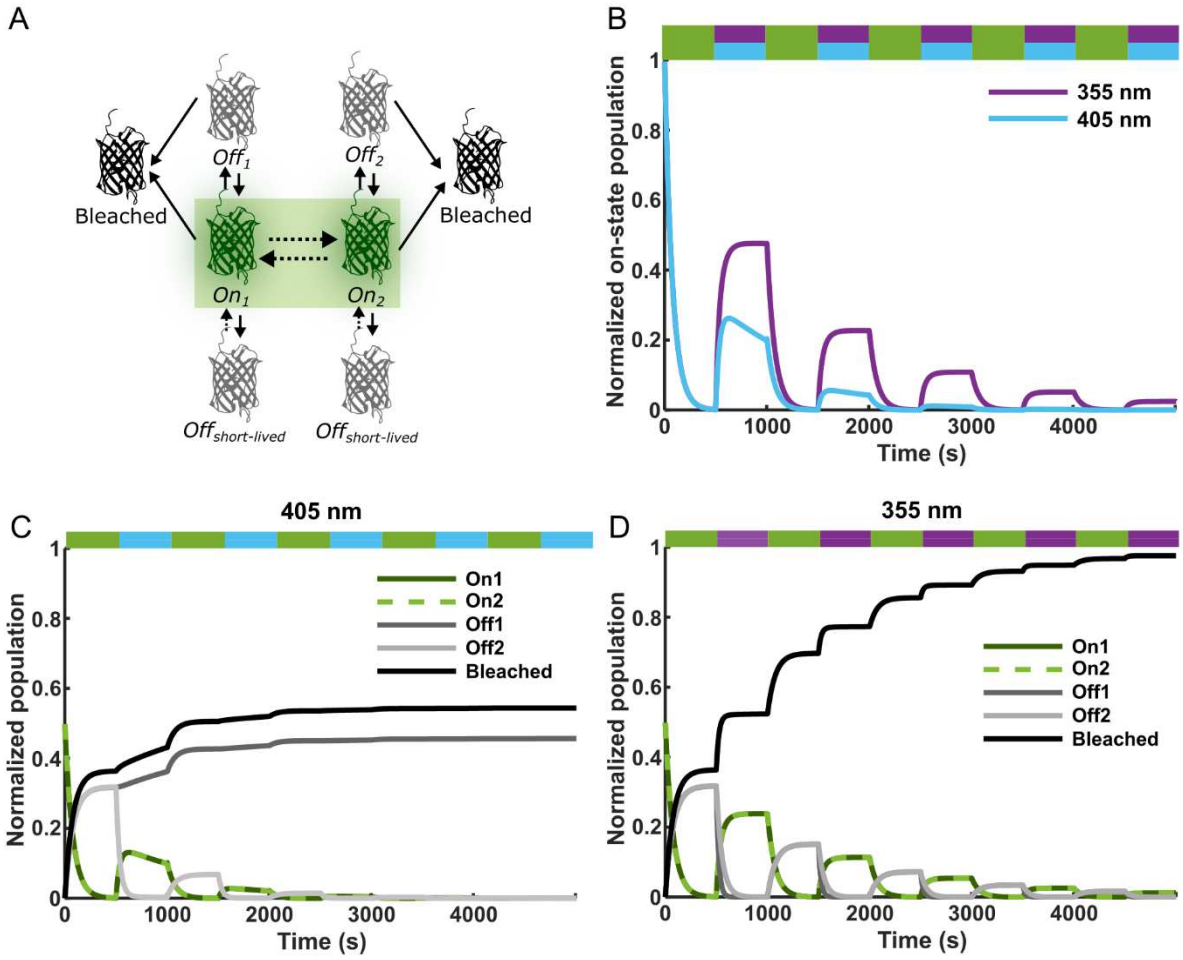

Figure 3.51 Ensemble simulations of rsEGFP2 assuming fast exchange between On1 and On2. *A) Photophysical model of rsEGFP2 cryo-switching with fast exchange between On1 and On2 (k_{ex} = 100 s^{-1}). B) Photofatigue simulations as in* ***Figure 3.50B*** *with alternating illumination with 488 nm and 405 or 355 nm light to induce off- and on-switching, respectively. C-D) Progression of the On1, On2, Off1, Off2 and Bleached populations in the photofatigue simulations when using 405 nm light (C) or 355 nm light (D).*

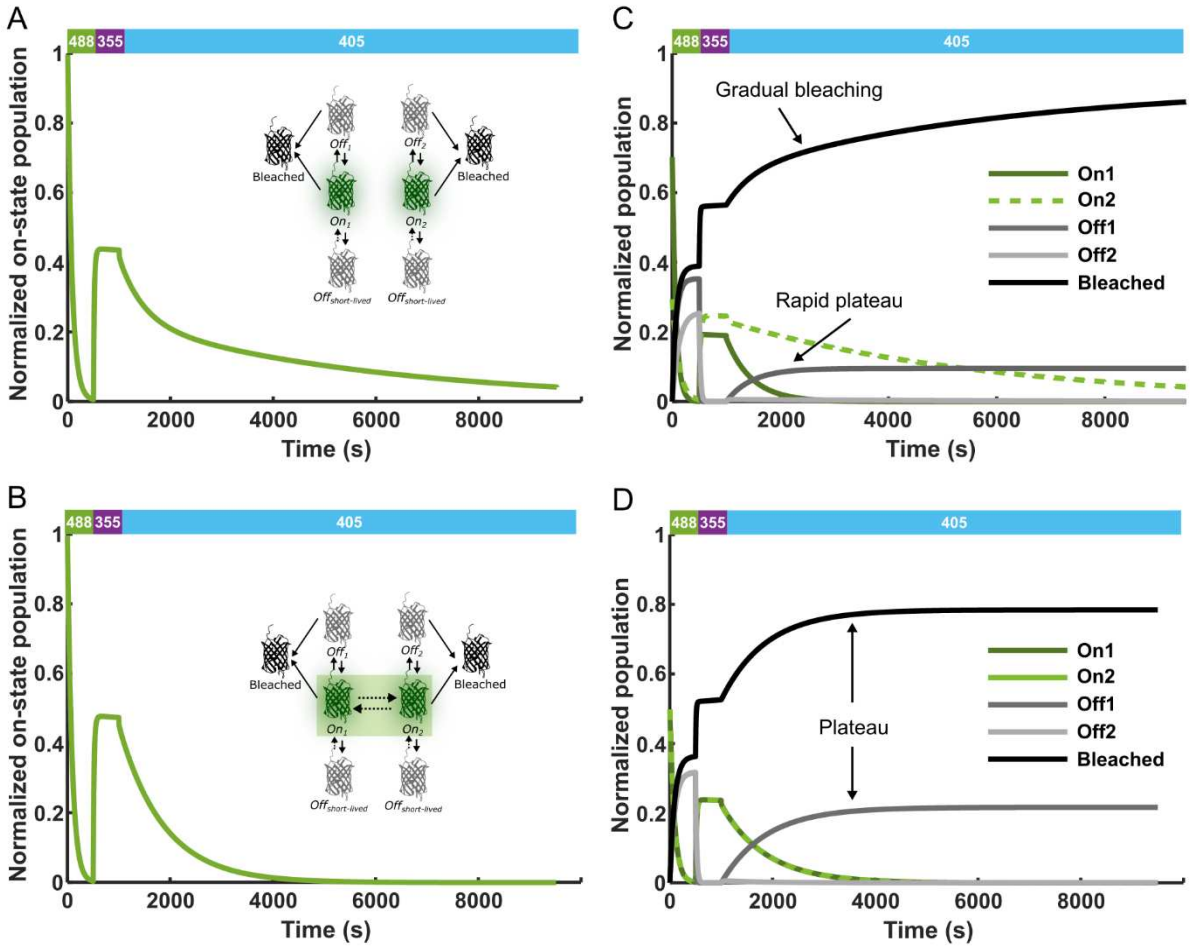

Figure 3.52 Comparison of the switching behavior of rsEGFP2 at CT without and with fast exchange between On1 and On2. *Simulations of rsEGFP2 photoswitching under sequential illumination with 488 nm (400 W/cm^2), 355 nm (25 W/cm^2) and 405 nm (300 W/cm^2) light as in* ***Figure 3.50C****. Switching was simulations assuming no exchange (A and C) or fast exchange (B and D) between On1 and On2. The progression of the total on-state population (On1 + On2) is shown in A and B. C and D show the progressions of the individual states.*

3.1.5.4 Simulations show that 355 nm light has the potential to boost the ELE in cryoPALM

Having established a photophysical model, we used it to interrogate *in silico* the effect of the usage of 355 nm light on the achievable effective labeling efficiency in cryo-SMLM. For single molecule simulations, NPCs were virtually labeled Nup96-rsEGFP2 and blinking was simulated under illumination with 400 W/cm^2 488 nm light and 0.4 W/cm^2 405 nm light or 0.08 W/cm^2 355 nm light. The power densities of the 405 and 355 nm lasers were chosen to ensure single molecule sparsity. The simulated image stacks were processed like normal PALM data using Thunderstorm and SMAP. The reconstructed SMLM images and ELE estimations are shown in **Figure 3.53**. As expected, the ELE was almost twice as high when 355 nm light was used instead of 405 nm light (38±2.5% vs 21±1.0% ELE), reinforcing the potential of 355 nm light to boost SMLM imaging at CT. The slight discrepancies between the ELE estimations and the ensemble on-switching efficiencies are likely due to missed localizations and localizations assigned to wrong corners, and due to imperfections in the model (discussed below).

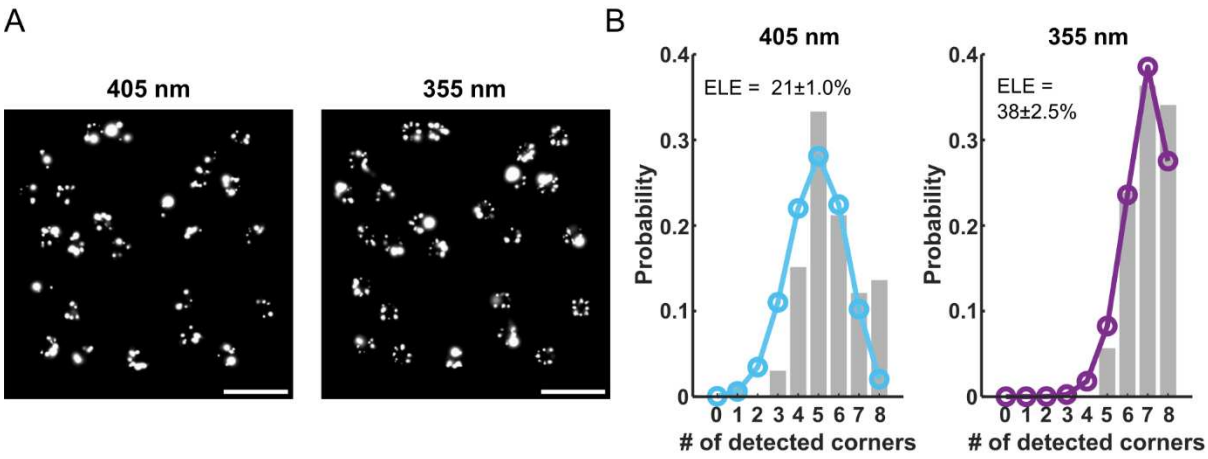

Figure 3.53 On-switching by 355 nm light improves the effective labelling efficiency. *Single molecule simulations of rsEGFP2 at cryogenic temperature tagged to the nucleoporin Nup96. Off-switching and single molecule imaging was achieved by 400 W/cm^2 488 nm light, while on-switching was promoted by 0.04 W/cm^2 355 nm light or 0.8 W/cm^2 405 nm light. A) Reconstructed super resolution images showing individual nuclear pores. Scale bar: 500 nm. B) Estimation of the Effective Labelling Efficiency (ELE) from the analysis of 100 NPCs.*

3.1.5.5 Conclusion

To summarize, characterization of the switching behavior of rsEGFP2 at CT revealed novel switching pathways proceeding via two distinct on-and off-states. We supported our experimental findings by simulations to confirm that the observed switching behaviors could be explained by the proposed model. Furthermore, we performed single molecule simulations to highlight the potential of 355 nm light to enhance cryoPALM imaging.

Despite the intensive investigations, there are still remaining questions concerning the blinking behavior of rsEGFP2 at CT. One of the most important questions is the molecular nature of the two on-state populations. Elucidation of the underlying nature of On_1 and On_2 could inform design of FPs with only the more photostable On_2/Off_2 states. Another question is the nature of the off-states. Future work is needed to address these questions.

Simulations are valuable to test how tentative models behave under specific illumination conditions and can help to refine a photophysical model. Simulations, however, rarely reproduce the exact experimental conditions. One limitation of the simulations presented above is that, in SMIS, ensemble simulations can only be performed assuming tumbling fluorophores, which is obviously not true at CT. A second limitation is that the complex laser sequences that were used in the experiments needed to be simplified to be entered in SMIS. As a consequence of these two limitations, the simulated switching kinetics do not fully match the experimental switching kinetics, and the quantum yields listed in **Table 2.7** should be interpreted as qualitative estimates rather than as absolute values.

In conclusion, better understanding of the photoswitching behavior of FPs at CT is needed to inform the design of FPs with increased switching efficiency and of optimized experimental conditions. Our work on rsEGFP2 provides a first step in this direction, revealing the presence of two off-states, different from the typical *trans* protonated off-state at RT, and demonstrating the advantage of using 355 nm light for cryo-SMLM. In our search to further improve SMLM imaging at CT, simulations provide a powerful strategy to evaluate photophysical models and swiftly test the effect of different imaging schemes.

3.2 sptPALM of histone-like protein HU reveals different modes of nucleoid remodeling in *Deinococcus radiodurans*

Parts of the results of this section are part of a manuscript in preparation:

Pierre Vauclare, Jip Wulffelé, Françoise Lacroix, Pascale Servant, Claire Bouthier de la Tour, Fabrice Confalonieri*, Jean-Philippe Kleman, Dominique Bourgeois and Joanna Timmins.* ***Exposure to stress induces rapid nucleoid remodeling and major changes in HU dynamics in Deinococcus radiodurans.*** *Manuscript in preparation.*

3.2.1 Introduction

Stressed-induced nucleoid remodeling is a wide-spread phenomenon in bacteria, which helps them cope with a variety of stress factors. The molecular mechanisms driving nuclear remodeling under different stress conditions, however, remain incompletely understood.

The objective of this study was to deepen our understanding of this process. To this end we used a combination of confocal microscopy and sptPALM to monitor the overall nucleoid morphology and the dynamics of histone-like protein HU in *D. radiodurans* (DR) during normal growth and in response to UVC irradiation. This work was a collaboration between the PIXEL and GenOM teams, combining our expertise in quantitative super-resolution microscopy, confocal imaging and *D. radiodurans* biology. Characterization of the nucleoid and cell morphologies by confocal microscopy was mainly carried out by Pierre Vauclare and Joanna Timmins. I participated in this work by characterizing the diffusion dynamics of HU by sptPALM. In this section, I will outline the different findings of this collaborative work with a focus on HU.

3.2.2 Nucleoid organization and HU diffusion are growth phase dependent

The nucleoid morphology of *D. radiodurans* during exponential growth conditions was characterized in detail by Floc'h et al., who showed by confocal microscopy that the nucleoid in DR cells is highly dynamic and adopts a variety of shapes in a cell-cycle dependent manner[370]. Confocal imaging of DR cells labeled with Syto9 and Nile red revealed this same diversity of nucleoid shapes in exponentially growing cells (**Figure 3.54A**) but revelaed more compacted and homogenous shapes in early stationary phase cells (24 h of culture). These morphological differences between exponential and stationary phase cells were quantified by measurements of the sphericity and volume of the nucleoid (**Figure 3.54B**), which showed that the average nucleoid in exponentially growing cells is less spherical and ~2 times larger than in early stationary phase cells. Similar observations were made using a DR strain in which nucleoid visualization was enabled by fusion of HU to the FP mCherry (HU-mCherry, data not shown). Assesment of the HU-mCherry expression levels by westernblotting revealed that stationary phase cells express ~5x more HU than exponential phase cells (**Figure 3.54C**).

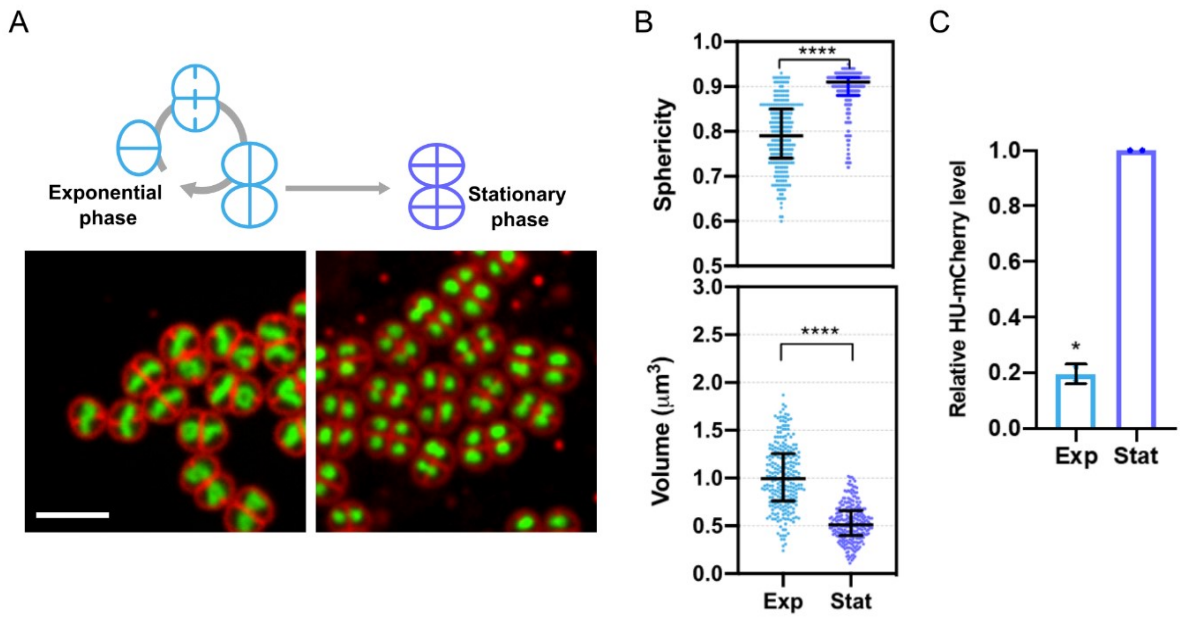

Figure 3.54 Nucleoid morphology is growth phase dependent. *A) Schematics illustrating cell growth and division, and representative confocal images of DR cells in exponential and stationary phase stained with syto9 and Nile red. B) Nucleoid sphericity and volume calculated from syto9 stained nucleoids. C) Assesment of HU-mCherry expression by westernblot in exponential and stationary phase cells.* p<0.05, **** p<0.0001, Mann Whitney U test. Data by Pierre Vauclare and Joanna Timmins.*

To better understand the molecular mechanisms underlying this nucleoid re-organization, we examined the diffusion dynamics of HU by sptPALM. To this end, we used a DR strain genetically engineered to express HU-mEos4b from its native promotor. PALM imaging was performed with a frame time of 10 ms on cells immobilized on M9DR agarose pads to limit autoblinking. Super-resolution images of HU-mEos4b revealed a similar diversity of nucleoid shapes as were observed by syto9 staining of WT cells (**Figure 3.55A**). Calculation of the apparent diffusion coefficients (Dapps) of the HU-mEos4b molecules indicated that HU diffusion is globally decreased in stationary phase cells (**Figure 3.55B**).

Given that the DR nucleoid adopts a variety of shapes in a cell-cycle dependent manner, we wondered whether HU diffusion could be cell-cycle dependent. To investigate this question, we plotted the Dapp distributions of HU per cell (**Figure 3.55C**) and extracted the median HU diffusion coefficient per cell (**Figure 3.55D**). This analysis showed that HU diffusion in exponential and stationary phase cells is rather homogenous on a cell-to-cell basis and confirmed that the apparent diffusion of HU-mEos4b is significantly reduced in stationary phase cells (**Figure 3.55D**). These findings do not exclude that HU diffusion may be to some extent cell-cycle dependent. To really address this question, cells would have to be classified as a function of the stage of the cell cycle. Unfortunately, this analysis is currently not possible because cell-cycle classification is based on progression of the septum, which is revealed by staining the cell membrane with Nile red. Nile red labelling, however, interferes with PALM imaging of mEos4b because both fluorophores emit in the red. A green emitting membrane dye could circumvent this issue, but such a dye is currently not available. An alternative to membrane staining could be to group cells based on their nucleoid morphology (given that nucleoid morphology is cell-cycle dependent), but this is not straightforward because the different nucleoid shapes are less recognizable by sptPALM than by confocal imaging, which might be due to movements of the nucleoids during the relatively long (10 minute) sptPALM data collections.

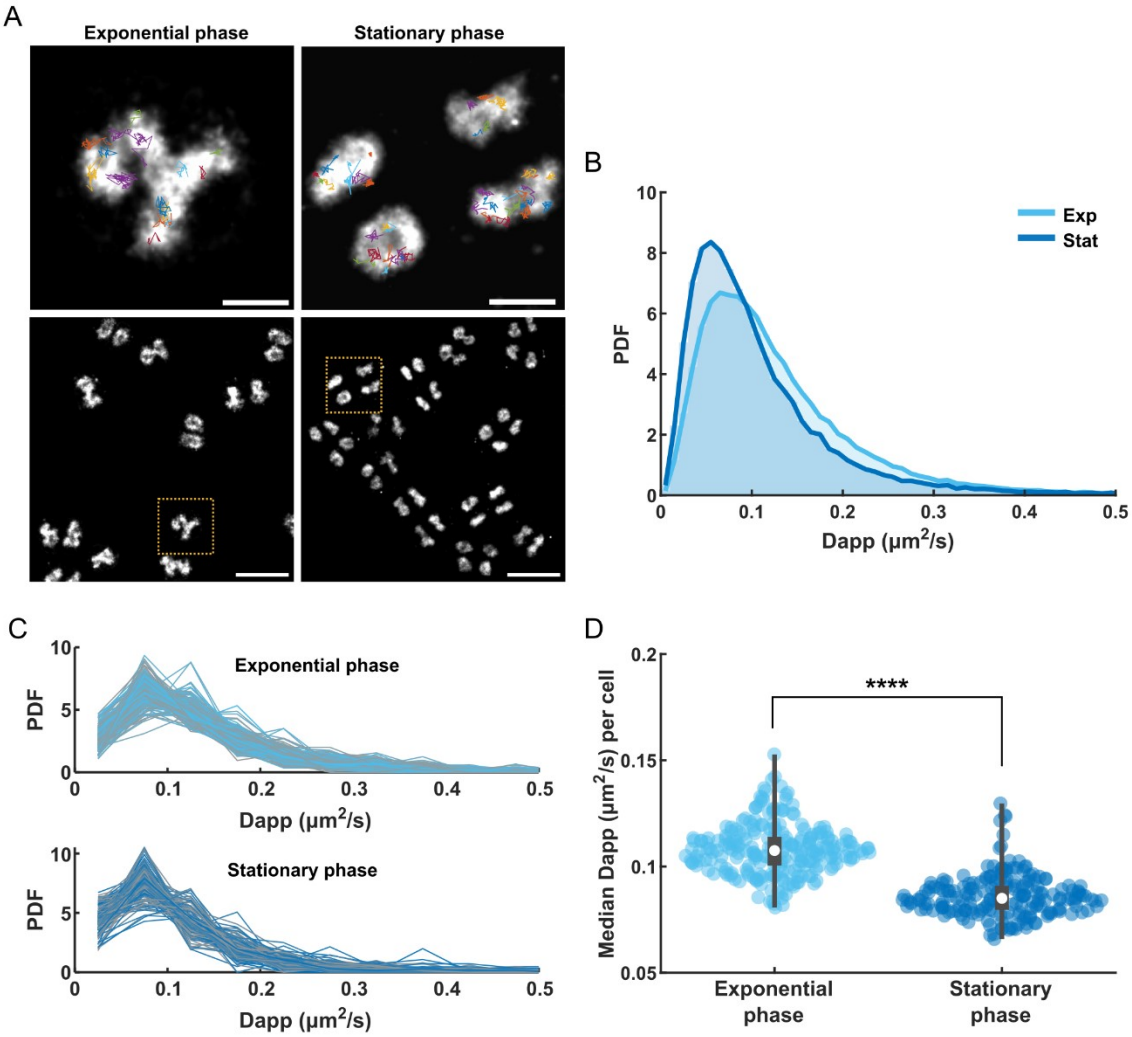

Figure 3.55 HU diffusion is growth phase dependent. *A) Top row: Overlay of tracks and super-resolved images of HU-mEos4b in exponential and stationary phase cells. Bottom row: Representative super-resolved images of HU-mEos4b in exponential and stationary phase cells. B) Histograms of the apparent diffusion coefficient (Dapp) calculated from the 4-step mean square displacement (MSD) in exponential (n = 231, 3 independent experiments) and stationary (n = 196, 4 independent experiments) phase cells. C) Histograms of the Dapp of individual cells in exponential and stationary phase (n = 200-400 tracks per cell). D) Swarm plot of the median Dapp per cell. Box plots indicate the median, the lower and upper quartile, and the min and max. **** p<0.0001, Mann Whitney U test.*

3.2.2.1 Confinement complicates characterization of the diffusion behavior of HU

What is the biological meaning of the decreased HU diffusion in stationary phase cells? HU diffusion is often described by a two-population model consisting of a DNA bound state and a diffusive state, which also interacts with the DNA but in a very transient manner (**Figure 3.56**)[278,279]. The second state, thus, actually consists of two states: a freely diffusive state and a DNA bound state, but because these states rapidly exchange they are detected as a single state by sptPALM. Considering this model, globally decreased HU diffusion could be due to an increase in the fraction of the DNA bound population or due to a decrease in the diffusion coefficients of one or both states. A decreased diffusion coefficient of the DNA bound state could be due to decreased DNA motion, assuming that DNA mobility significantly offsets the apparent diffusion of DNA bound proteins as was shown by Bettridge et al[278]. In fact, Zhu et al. showed that in *E. coli* DNA mobility is decreased in stationary phase cells ($8x10^{-6}$ $\mu m^2/s$ vs $2x10^{-4}$ $\mu m^2/s$)[337]. Decreased diffusion of the diffusive state

could be due to increased interaction with the DNA or again, decreased DNA mobility. To investigate these different possibilities, we analyzed in more detail the Dapp histograms.

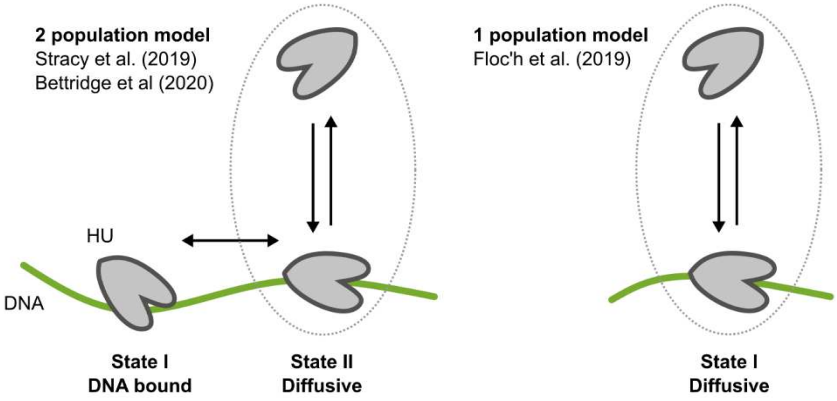

Figure 3.56 Models of HU diffusion. *HU diffusion is typically described by a 1- or 2- population model. The 2-population model consists of 2 states: a state (State I) that is bound to the DNA (for the duration of single particle tracks) and another state (State II) that is diffusive but still transiently interacts with the DNA lowering its apparent diffusion. State II, thus, actually consists of two states: a freely diffusive state and a DNA bound state, but because these states rapidly exchange they are detected as a single state by sptPALM. The 1-population model only consists of the diffusive state.*

Although HU diffusion is often described by a two-population model, Floc'h et al identified only a single diffusive population of HU-PAmCherry in exponential phase *D. radiodurans* cells (Dapp = ~ 0.32 $\mu m^2/s$) (**Figure 3.56**). Therefore, we first tested whether the Dapp histograms of HU-mEos4b could also be described by a single population model (**Figure 3.57A**). However, the histograms of both the exponential and stationary phase cells could not accurately be described by a single population (**Figure 3.57A**). In addition, HU-mEos4b appeared much less diffusive than was reported for HU-PAmCherry (Dapp ~ 0.095 $\mu m^2/s$ vs Dapp ~ 0.32 $\mu m^2/s$). This difference might be partly explained by differences in imaging schemes and sample handling. Notably, we noticed that diffusion of HU-mEos4b increased over time after sample preparation (see **Figure 2.8**), showing that sample handling can affect the observed HU diffusion. Furthermore, the HU-PAmCherry strain was difficult to handle because the PAmCherry signal was very variable and often bleached quickly (J. Timmins, personal communication).

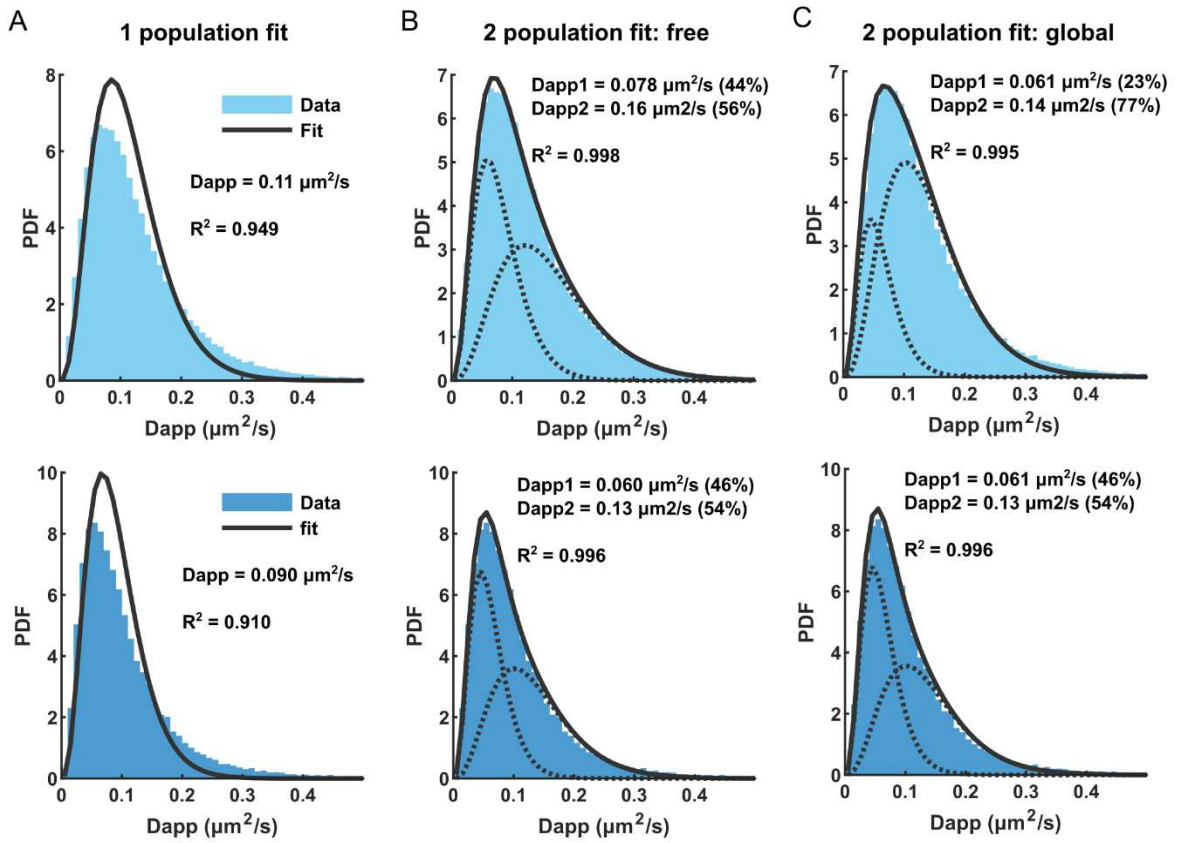

Figure 3.57 Fitting of the Dapp distributions of HU-mEos4b in exponential and stationary phase cells. *Dapp distributions obtained from exponential phase (top row, light blue) and stationary phase (bottom row, dark blue) cells were fitted with a one-population model (A), a free two-population model (B) or a global two-population model in which Dapp1 (corresponding to the DNA-bound population) is shared between exponential and stationary phases.*

Because a 1-population model did not well describe the data, we tested whether we could fit the Dapp histograms with a 2-population model. First, we performed a free fit on both the exponential and stationary phase data. **Figure 3.57B** shows that the Dapp distributions are well described by a 2-population fit. The fits suggest that in stationary phase the diffusion of both HU states is decreased (0.060 vs 0.078 µm^2/s and 0.13 vs 0.16 µm^2/s) but that the relative populations of the two states remain similar in exponential and stationary phases (46%:54% vs 44%:56%).

Decreased diffusion of both states could be caused by decreased DNA mobility as explained above. However, the diffusion coefficients Zhu et al. reported for the DNA in exponential and stationary phase cells (~10^{-4} µm^2/s and ~10^{-6} µm^2/s) are orders of magnitudes lower than the apparent diffusion coefficients of HU in DR. This finding seems in contradiction with the finding of Bettridge et al. that DNA mobility offsets the apparent diffusion of DNA bound HU in *E. coli*[278]. This contradiction may be partly explained by differences in imaging conditions: while Zhu et al. monitored DNA mobility at the second to minute time scale, thus presumably detecting effects from DNA replication and segregation, Bettridge et al. evaluated DNA mobility at the ms timescale, only detecting local wiggling/jiggling of the DNA. It is, however, unclear how both studies dealt with the localization uncertainty, which is known to offset the apparent diffusion of molecules in sptPALM. Especially given the low mobility of the DNA, the localization uncertainty can be expected to significantly contribute to its apparent mobility. In view of this notion, it remains uncertain whether changes in DNA mobility could significantly affect the apparent diffusion of HU in exponential and stationary phase cells. To investigate this question, DNA mobility should be monitored at the ms timescale (similar as the HU-mEos4b experiments) in both exponential and stationary phase cells and carefully

analysed, accounting for the localization precision. Unfortunately, although we have *D. radiodurans* strains with fluorescently labeled *oriC* and *ter* sites, which could be used for this purpose, these strains only show fluorescent foci during exponential phase, making a comparison between exponential and stationary phase impossible. It is unclear why fluorescent foci cannot be distinguished in stationary phase cells.

Although we could not experimentally address the question of DNA mobility, we tested whether the diffusion behavior of HU-mEos4b could be described by a model assuming that changes in DNA mobility do not significantly affect the apparent diffusion of HU in exponential and stationary phase cells. To this end, we fitted the diffusion histograms with a global two-population model, sharing the diffusion coefficient of the supposedly DNA-bound state (Dapp1) (**Figure 3.57B**). Both the histograms of the exponential and stationary phase cells could be well-described by this global fit. The fit suggests that the difference in HU diffusion between exponential and stationary phase could be due to a shift in the relative populations (23%:77% vs 46:54%) rather than due to differences in the apparent diffusion coefficients (Dapp1 = 0.061 $\mu m^2/s$, Dapp2 = 0.14 $\mu m^2/s$ vs 0.13 $\mu m^2/s$).

As an alternative analysis, we also evaluated the diffusion behavior of HU-mEos4b using vbSPT, an analytical tool which can extract the number of diffusive states, the diffusion coefficients and relative populations of those states and the transition rates between the states directly from experimental data[272]. To prevent overfitting, however, we imposed a two-population model. vbSPT identified two populations with diffusion coefficients of 0.080 $\mu m^2/s$ and 0.25 $\mu m^2/s$, and of 0.071 $\mu m^2/s$ and 0.20 $\mu m^2/s$ in exponential and stationary phase cells, respectively (**Figure 3.58**). The relative populations and transitions rates of the identified states were comparable between exponential and stationary phase cells (~ 30%:70% and k_{12}= ~7 s^{-1}, k_{21}= ~20 s^{-1}) (**Figure 3.58**). Transition rates of ~7 and ~20 s^{-1} translate into half-lifes of about ~99 ms and ~35 ms for State I and State II, respectively. A half-life of 35 ms suggests that many of the 5 localization tracks used to compute the Dapp histograms (**Figure 3.57**) contain a state transition. These transitions might not be detected by the tracking software swift because the tracks are relatively short (see **section 2.6.3.1**). Fitting of the Dapp distributions (**Figure 3.57**), however, could be affected by such state transitions. The diffusion coefficients extracted by vbSPT are higher than those estimated from the Dapp distributions but the relative size of the slow population (State I) is estimated to be higher by vbSPT, compensating for the higher diffusion coefficients. Globally, the analysis by vbSPT is in agreement with the MSD analysis presented above, showing that HU diffusion is decreased in stationary phase cells.

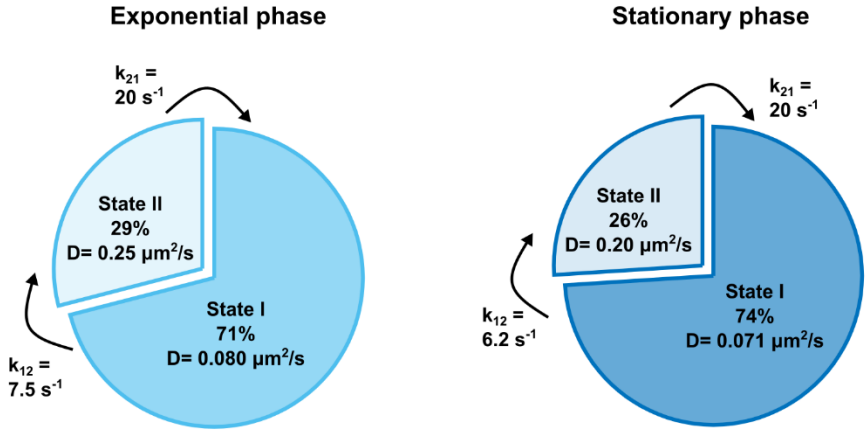

Figure 3.58 Diffusion behavior of HU-mEos4b estimated by vbSPT. *Diffusion coefficients and exchange rates derived from the single particle tracks of HU-mEos4b by vbSPT imposing a two-population model to prevent overfitting.*

So far, our analysis has not accounted for localization uncertainty, temporal averaging, fast state transitions and confinement, all of which are known to affect the observed diffusion in sptPALM

experiments. Consequently, the fitted Dapps and Dapps extracted by vbSPT do not reflect the true diffusing behavior of HU-mEos4b. To uncover the true diffusing behavior of HU-mEos4b in DR, we adopted the strategy recently described by Stracy et al. (2021), which is based on the usage of simulations to estimate unbiased diffusion coefficients.

The localization uncertainty (σ) offsets the measured Dapp by $\sigma^2/\Delta t$, where Δt is the frame time. We evaluated the contribution of the localization uncertainty to the apparent diffusion of HU-mEos4b using fixed cells. Chemical fixation of DR cells disrupts the nucleoid morphology (**Figure 3.59A**) but this should not affect the estimation of the Dapp. The measured Dapp of HU-mEos4b in the fixed cells was 0.050 $\mu m^2/s$ (**Figure 3.59B**), substantially lower than the expected Dapp based on the localization uncertainty estimated by Thunderstorm (~25 nm -> Dapp = 0.063 $\mu m^2/s$, **Figure 3.59C**), in view of the slow diffusion of HU-mEos4b (~Dapp = 0.1 $\mu m^2/s$). This discrepancy raises the question whether Thunderstorm overestimated the localization uncertainty or whether the measured Dapp was underestimated. To address this question, we estimated the average localization uncertainty using the nearest neighbor analysis method described by Endesfelder et al[294]. Using this method, we found an average localization precision of ~20 nm (**Figure 3.59D**), corresponding to a theoretical Dapp of 0.040 $\mu m^2/s$, suggesting that both the uncertainty and Dapp were overestimated. Thunderstorm calculates the localization uncertainty from the intensity of the localizations and user specified camera parameters. Slight deviations between the specified parameters and the actual properties of the camera could be responsible for the overestimation of the localization uncertainty. The measured Dapp, on the other hand, might have been overestimated due to incomplete fixation or tracking mistakes. Although visual inspection of the tracks suggested that almost all molecules were immobile, the fit of the Dapp distribution (**Figure 3.59B**) seemed to be right shifted from the actual peak of the histogram. Therefore, we choose to use the Dapp of 0.040 $\mu m^2/s$, calculated from the nearest neighbor analysis. **Table 3.1** lists the estimated Dapp values of HU-mEos4b corrected for the localization uncertainty. It should be noted that this correction assumes that the offset due to localization uncertainty is independent of the diffusion coefficient of the molecule, which may not be true for fast moving molecules whose detection suffers from motion blur. This could be taken into account by correcting the calculated Dapp on a track-to-track basis using the average localization uncertainty of each track. For HU-mEos4b, however, this seemed unnecessary because its localization uncertainty in living cells was similar as in fixed cells, probably because of its low diffusion coefficient.

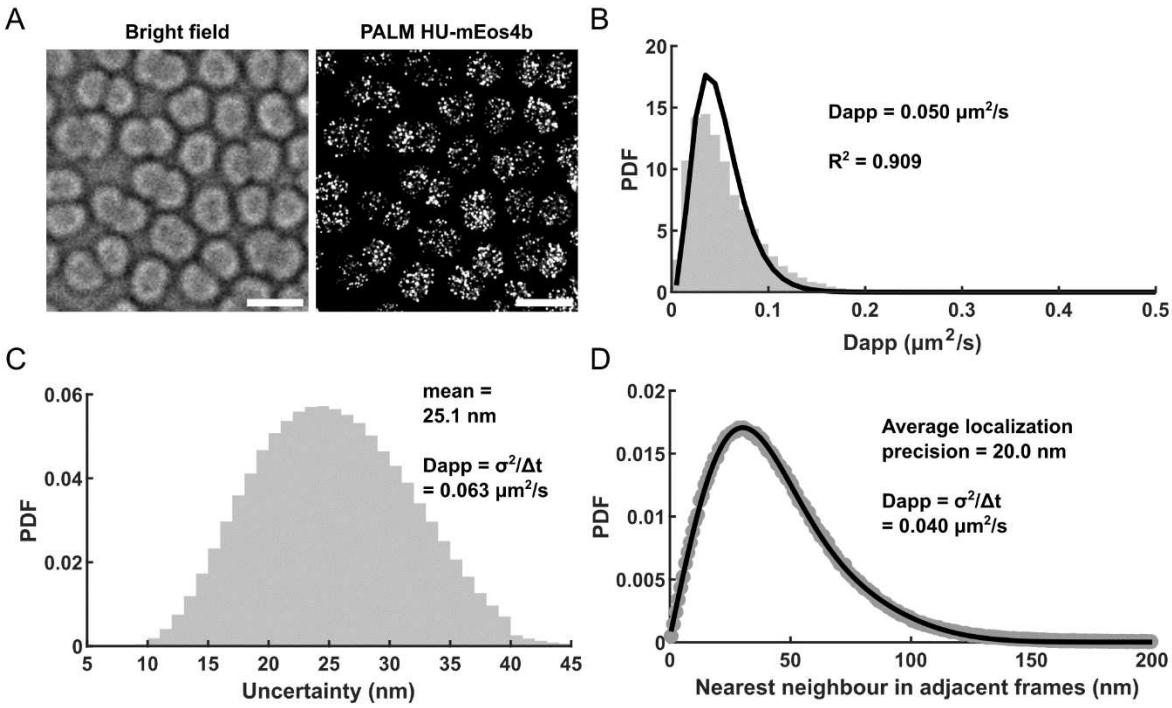

Figure 3.59 Apparent HU diffusion in fixed cells. *A) Representative bright field and super-resolved images of fixed DR cells expressing HU-mEos4b. B) Dapp distribution of HU-mEos4b in fixed cells with a 1-population fit. C) Distribution of the localization uncertainty of HU-mEos4b molecules in fixed cells and estimation of the theoretical offset in apparent diffusion coefficient based on the mean uncertainty. D) Estimation of the average localization precision by nearest neighbor analysis and calculation of the corresponding Dapp. n = 43000 tracks from 2 independent experiments.*

Table 3.1 Dapp values of HU-mEos4b corrected for localization uncertainty. *The Dapp values of HU-mEos4b in exponential and stationary phase cells were estimated using two different methods: a free and global two-population fit of the Dapp distributions. Shown are the estimated Dapp's corrected for the contribution of the localization uncertainty (0.04 µm²/s).*

	Exponential phase		**Stationary phase**	
	State I (µm²/s, %)	**State II (µm²/s, %)**	**State I (µm²/s, %)**	**State II (µm²/s, %)**
Free fit	0.038 (44%)	0.12 (56%)	0.020 (46%)	0.090 (54%)
Global fit	0.021 (23%)	0.10 (77%)	0.021 (46%)	0.090 (54%)

Next, we assessed the effects of confinement and temporal averaging of the apparent diffusion of HU-mEos4b using the simulation software SMIS[266]. To this end, we simulated diffusion of molecules with diffusion coefficients ranging from 0.1 to 10 µm²/s using segmented nucleoids of exponential phase *D. radiodurans* cells as confining volume. Simulated data were analyzed using the same workflow as was used for experimental data to determine the apparent diffusion coefficient (**Figure 3.60**). The simulations revealed that the apparent diffusion coefficient is significantly lower than the underlying true diffusion coefficient. For example, molecules with a true diffusion coefficient of 5 µm²/s had an apparent diffusion coefficient of only ~2 µm²/s (**Figure 3.60A**). From these simulations, we generated a calibration curve by plotting the extracted Dapp against the true D, after subtracting the contribution from the localization uncertainty (10 nm -> 0.01 µm²/s) (**Figure 3.60B**).

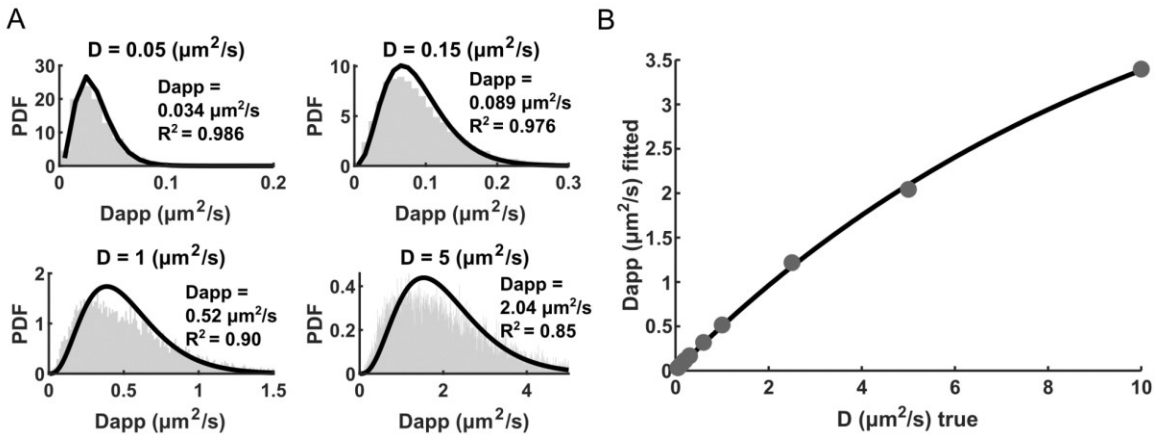

Figure 3.60 Confinement affect the apparent diffusion. *sptPALM simulations were performed in SMIS using 3D segmented DR nucleoids as virtual sample. Simulations were performed with diffusion coefficients ranging from 0.05 μm²/s up to 10 μm²/s. The simulated data were analyzed in the same way as the experimental data using Thunderstorm, SWIFT and MATLAB A) Dapp distributions of four selected simulations with a 1-population fit. B) Calibration curve obtained by plotting the apparent diffusion coefficient (Dapp fitted) against the simulated diffusion coefficient (D true). Data fitted with a mono-exponential model to guide the eye.*

We noticed that, although each simulation only contained a single diffusive population, the Dapp distributions were not well-described by a one-population fit and that the quality of the fits decreased with increasing diffusion coefficients (decreasing R^2, **Figure 3.60A**). Smigiel et al[280] reported that the diffusion of molecules at the border of a confining volume appears slower than in the center of a confining volume due to reflection of the molecules from the border. Such an effect results in the apparent presence of multiple diffusive populations and could explain why the Dapp distribution from the simulated data could not be well-described by a one-population model. To examine whether the simulated data suffered from this 'border effect', we generated heat maps of the average jump distance per pixel. **Figure 3.61** shows the heat maps of simulated molecules with diffusion coefficients of 0.1 μm²/s and 1 μm²/s, revealing that, indeed, diffusion appears to be slower at the borders of the confining volumes and that this effect becomes more pronounced at higher diffusion coefficients.

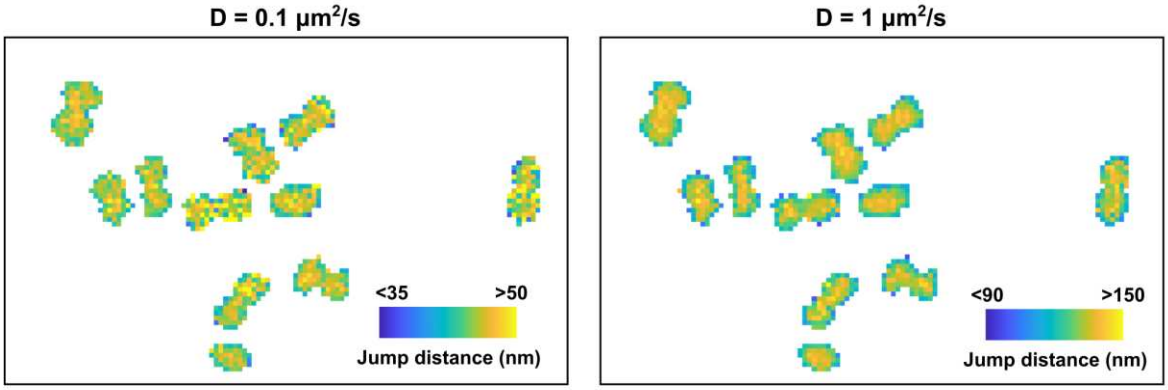

Figure 3.61 The apparent diffusion is decreased at the border of confining volumes. *Diffusion was simulated in SMIS using segmented DR nucleoids as virtual sample. Shown are heat maps of the average jump distance (nm) per pixel of simulations with D = 0.1 μm²/s and D = 1 μm²/s. Pixel size = 200 nm.*

To evaluate whether confinement is sufficient to explain the appearance of multiple populations in the simulated data, we performed simulation in an unconfined volume. The unconfined simulated data could be well-described by a single population model (**Figure 3.62**, right panel), confirming that confinement creates heterogeneity in the apparent diffusion of molecules diffusing with the same

diffusion coefficient. Note, that the Dapp is still underestimated (Dapp = 0.2 µm^2/s vs D_{input} = 0.3 µm^2/s) due to temporal averaging (see **section 1.5.3.1.4**).

Next, to examine whether confinement could be sufficient to explain the appearance of two populations in the experimental data, we compared the Dapp distributions and single population fits obtained with the simulated data (D=0.3 µm^2/s) with those obtained with the experimental data (HU-mEos4b, exponential phase) (**Figure 3.62**). This comparison revealed that the Dapp distribution from the experimental data deviated more from the single population model than the simulated data (lower R^2). This difference became even more pronounced when the Dapp was calculated from 16 instead of 4 displacements per tracks (**Figure 3.62**, bottom row). Here, it should be noted, however, that the segmented nucleoids used for the simulations were of rather low quality (pixel size = 200 nm) and likely overestimated the real nucleoid volume, which could partly explain why the fit on the simulated data was better than on the experimental data. For comparison, we also performed simulations using *E. coli* shaped volumes (rod of 0.5 µm by 2 µm). Compared to the simulations using the segmented DR nucleoids, the simulations using the E.coli shaped volumes were more severely impacted by confinement (lower R^2), which is likely because the *E.coli* shaped volumes were smaller than the segmented DR nucleoids. Lastly, we generated heat maps of the average JD per pixel of HU-mEos4b in exponential and stationary phase cells (**Figure 3.63**). In contrast to the simulated data (**Figure 3.61**), no obvious decrease in diffusion can be observed at the borders of the nucleoids in the experimental data (**Figure 3.63**). Based on these comparisons, it cannot be excluded that there are truly multiple populations present in the experimental data.

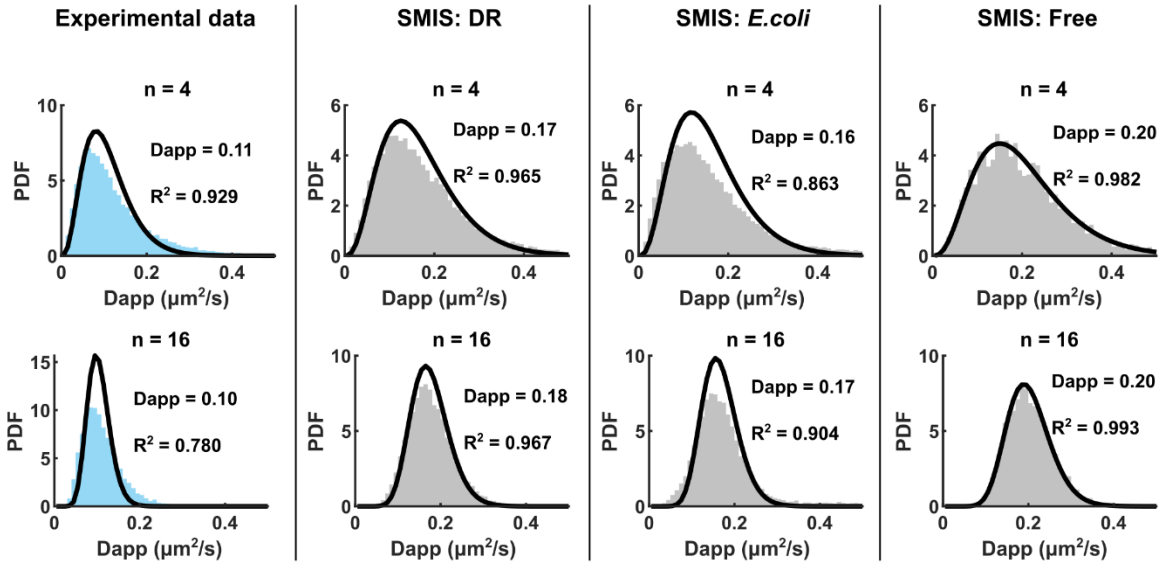

Figure 3.62 Comparison of the Dapp histograms of experimental and simulated data. *Dapp histograms with one-population fits of a subset of exponential phase HU-mEos4b experimental data (left panel) and of SMIS simulations (D = 0.3 µm^2/s). Dapps were calculated from 4 (upper row) or 16 (bottom row) displacements per track. SMIS simulations were performed using virtual samples based on segmented exponential phase DR nucleoids and E.coli shaped volumes (rod of 0.5 µm by 2 µm) to simulate confined diffusion (central panels), or on a large box (67 µm x 67 µm x 3 µm) to simulate unconfined diffusion (right panel).*

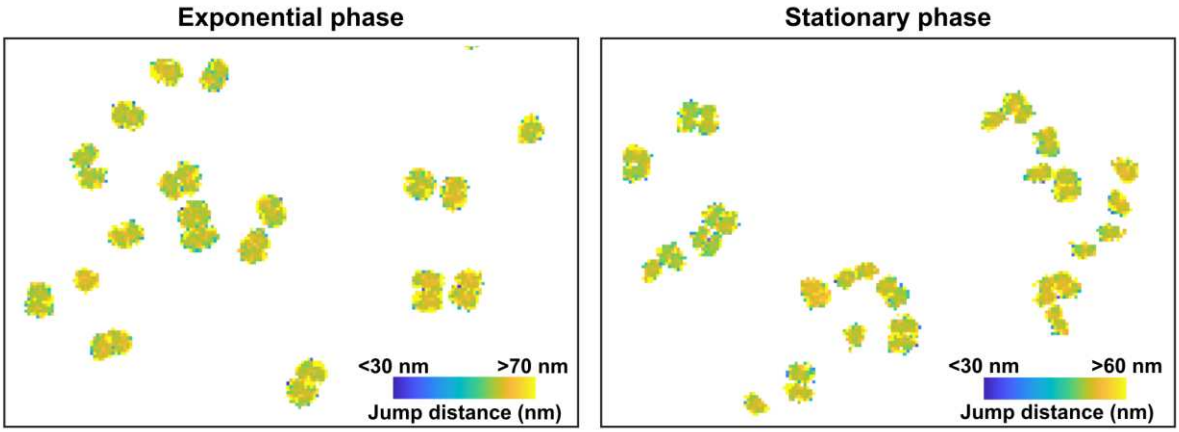

Figure 3.63 Heat maps of HU-mEos4b diffusion in the DR nucleoid. *Shown are representative heat maps of the average jump distance (nm) per pixel of HU-mEos4b in exponential and stationary phase DR cells. Pixel size = 200 nm.*

Although we cannot exclude that there are truly two populations present in the experimental data, their appearance is convoluted by confinement effects. To test whether the diffusion coefficients of multiple populations can still be accurately extracted under such conditions, we performed simulations using the segmented DR nucleoids with two diffusive states with varying diffusion coefficients and relative populations (**Figure 3.64**). We started with a simulation (Default) with two diffusive states with relative populations of 50%:50% and diffusion coefficients of 0.1 $\mu m^2/s$ and 0.2 $\mu m^2/s$. We choose these diffusion coefficients because the resulting apparent diffusion coefficients are comparable to the Dapps extracted from the experimental data. The Dapp distribution from this simulation was best fitted to a two-population model with relative populations of 60% and 40% with diffusion coefficients of 0.063 $\mu m^2/s$ and 0.18 $\mu m^2/s$, respectively. Using the calibration curve presented in **Figure 3.60B** to correct the measured Dapps for confinement and temporal averaging, the true (unbiased) diffusion coefficients were estimated to be 0.10 $\mu m^2/s$ and 0.33 $\mu m^2/s$, respectively (**Table 3.2**). It is interesting to note that while the one-population simulations could not be fitted with a one-population model (**Figure 3.60A**), this two-population simulation is well-described by a two-population model. This is likely because the two simulated populations have largely overlapping Dapp distributions so that the two-population fit can adjust to describe the resulting convolutions from the two populations with the confinement effects. As a consequence, although the fit appears good, the extracted diffusion coefficients and relative populations are not fully accurate. We investigated whether changes in the relative populations or diffusion coefficients could be detected, at least qualitatively (**Figure 3.64**). However, we found that while some changes could be accurately detected, for example increasing Dapp2 from 0.2 $\mu m^2/s$ to 0.5 $\mu m^2/s$, others were not correctly detected, for example changing the relative populations from 50%:50% to 10%:90% (**Figure 3.64**, **Table 3.2**).

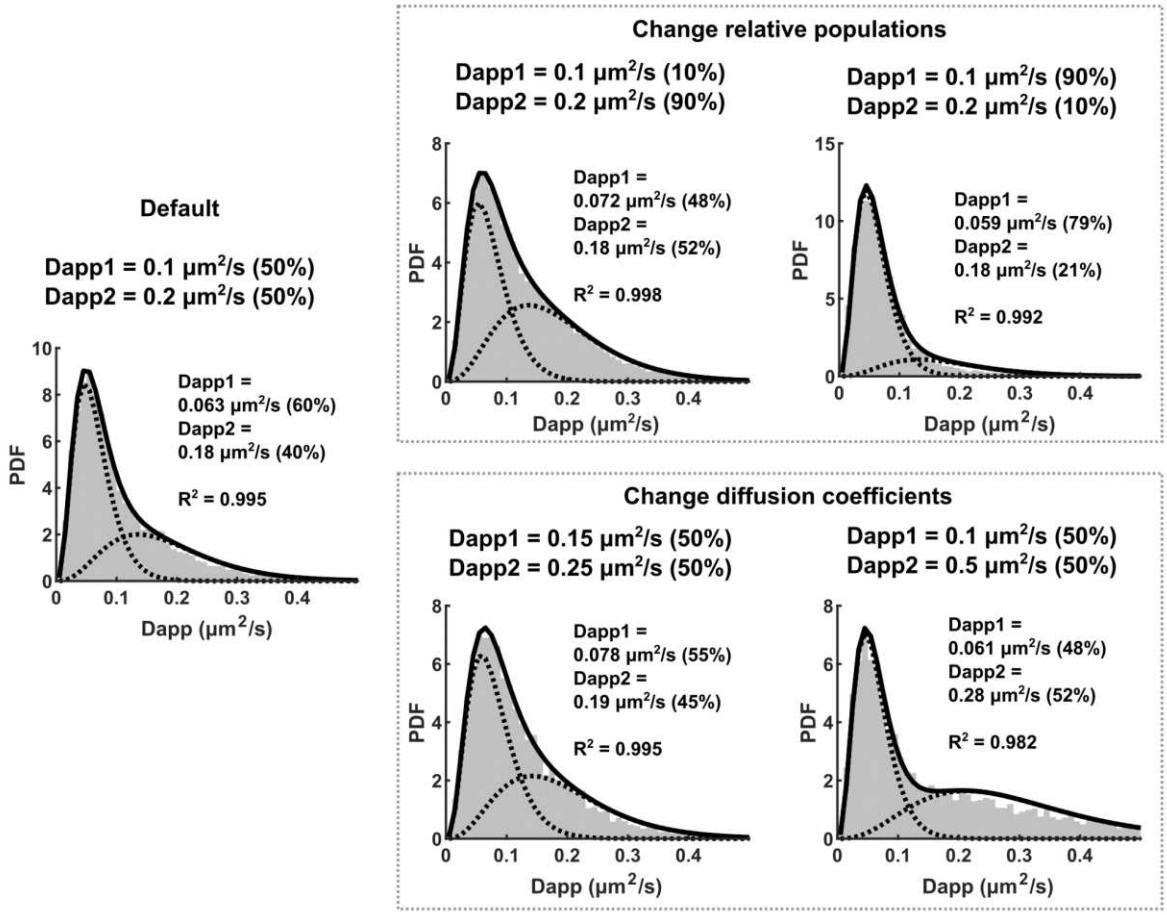

Figure 3.64 Simulations with two diffusive populations. *Simulations with two diffusive populations were performed in SMIS using segmented DR nucleoids as confining volumes. Simulated data were analyzed using Thunderstorm, swift and MATLAB and the Dapp histograms were fitted with a two-population model (fitted values noted in the respective plots). Simulations were performed with varying diffusion coefficients and populations (true simulation parameters are noted above the corresponding plots).*

Pretending that the simulated State I represents molecules bound to the DNA, we tested whether the estimation of the diffusion coefficients and relative populations could be improved by a global fit, in which the diffusion coefficient of State I (Dapp1) would be shared across all simulations (only including the four simulations with Dapp1 = 0.1 μm^2/s) (**Figure 3.65**, **Table 3.2**). Indeed, overall, the global fit improved the estimations. However, Dapp2 was consistently overestimated and the changes in the relative populations remained under estimated (**Table 3.2**).

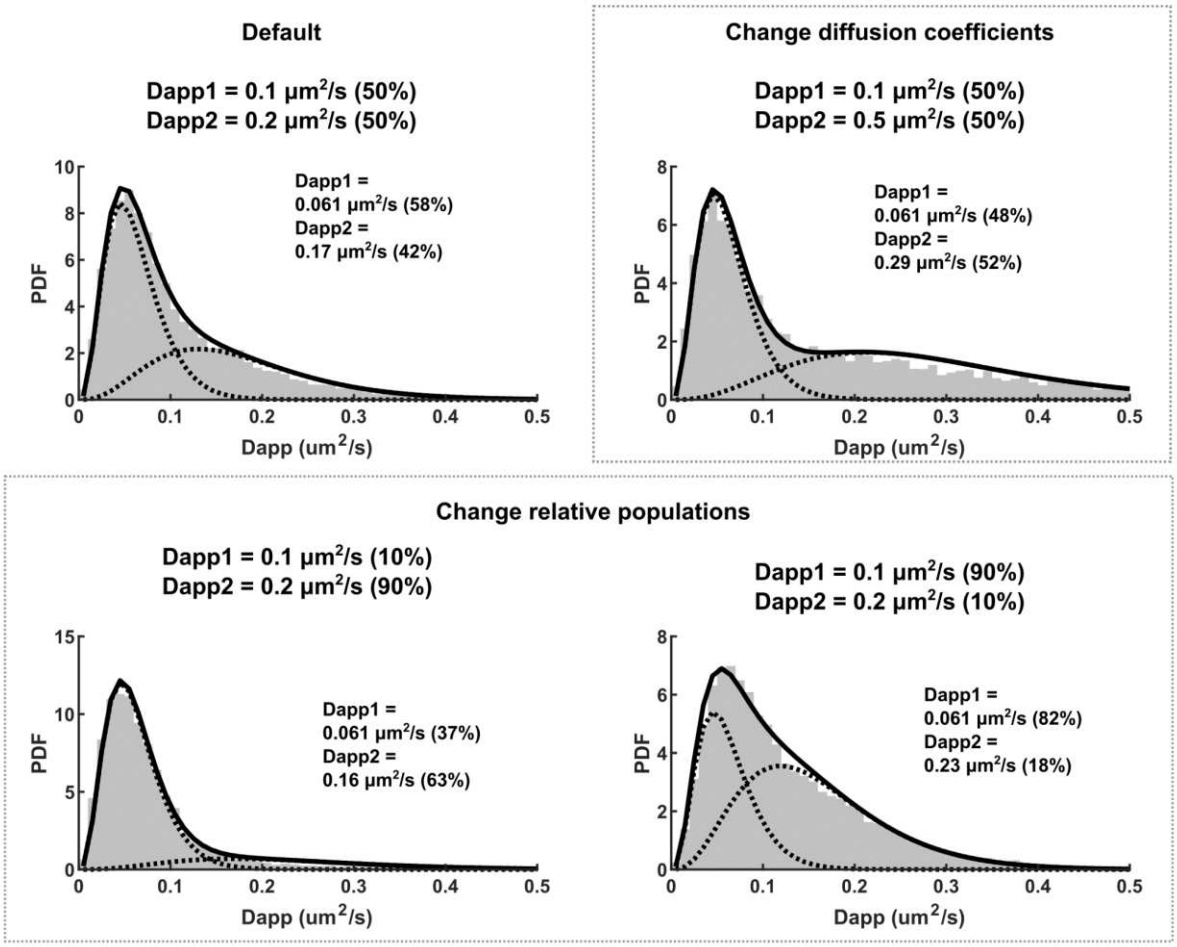

Figure 3.65 Global fitting of simulated two-population sptPALM data. *Simulations with two diffusive populations were performed in SMIS using segmented DR nucleoids as confinement volume. Simulated data were analyzed using thunderstorm, swift and MATLAB and the Dapp histograms were fitted with a global two-population model with Dapp1 as shared parameter (fitted values noted in the respective plots, R^2=0.991). Simulations were performed with varying diffusion coefficients and populations (true simulation parameters are noted above the corresponding plots).*

Table 3.2 Unbiased diffusion coefficients extracted from free and global fits on simulated sptPALM data with two populations. *Unbiased diffusion coefficients were calculated from the fitted diffusion coefficients using the calibration curve presented in* ***Figure 3.60****.*

	Free fit		Global fit	
Ground truth	**Unbiased Dapp1 (μm²/s), occupancy (%)**	**Unbiased Dapp2 (μm²/s), occupancy (%)**	**Unbiased Dapp1 (μm²/s), occupancy (%)**	**Unbiased Dapp2 (μm²/s), occupancy (%)**
Dapp1 = 0.1 (50%) Dapp2 = 0.2 (50%)	0.10 (60%)	0.33 (40%)	0.10 (58%)	0.31 (42%)
Dapp1 = 0.1 (10%) Dapp2 = 0.2 (90%)	0.12 (48%)	0.33 (52%)	0.10 (37%)	0.29 (63%)
Dapp1 = 0.1 (90%) Dapp2 = 0.2 (10%)	0.10 (79%)	0.33 (21 %)	0.10 (82%)	0.42 (18%)
Dapp1 = 0.15 (50%) Dapp2 = 0.25 (50%)	0.13 (55%)	0.34 (45%)	-	-
Dapp1 = 0.1 (50%) Dapp2 = 0.5 (50%)	0.10 (48%)	0.52 (52%)	0.10 (48%)	0.53 (52%)

Altogether, confinement hinders the accurate extraction of diffusion coefficients and relative populations from sptPALM data due to reflection of molecules from the borders of the confining

volume, decreasing their apparent diffusing and creating heterogeneity in the apparent diffusion of the ensemble of molecules, leading to distortion of the Dapp histogram (**Figure 3.61**, **Figure 3.62**). Although the simulations show that relatively big changes can still be extracted from Dapp distributions, at least qualitatively, changes in states with largely overlapping Dapp distributions are not accurately extracted due to convolution with the heterogeneity created by confinement (**Table 3.2**). While we cannot exclude that there are multiple diffusive populations of HU-mEos4b in DR cells, the Dapp distributions of the supposedly different populations are largely overlapping and the difference between exponential and stationary phase cells are relatively small (**Figure 3.57**). In *D. radiodurans* cells this confinement effect may be further complicated by the large variety of nucleoid shapes present in exponentially growing cells, adding extra heterogeneity to the data. Moreover, considering that confinement lowers the apparent diffusion coefficient, it cannot be excluded that the apparent decrease in diffusion of HU-mEos4b in stationary phase DR cells is an artifact from the increased level of confinement in the smaller stationary phase nucleoids. Aditionally, analysis of the tracks by vbSPT revealed that the Dapp histograms of HU-mEos4b might be affected by state transitions within tracks (**Figure 3.58**). Given these complications, we refrain from drawing further conclusion about the diffusion behavior of HU-mEos4b in exponential and stationary phase DR cells.

3.2.3 UVC irradiation elicits acute nucleoid remodeling

Having characterized the DR nucleoid under normal growth conditions, we next investigated how the DR nucleoid respondes to DNA damage induced by UVC irradiation. First, we examined the survival of DR cells after irradiations with increasing doses of UVC. We found that cells in exponential and early stationary phase are equally resistant to UVC irradiation (**Figure 3.66A**), in line with a previous study showing that exponential and early stationary DR cells are equally resistant to gamma-irradiation and heat stress[450]. Characterization of the nucleoids revealed a dose-dependent decrease in nucleoid volume and increase in sphericity in exponential phase cells, while the nucleoid of the early stationary phase cells maintained its already high sphericity and reduced volume (**Figure 3.66B,C**). Based on these findings we selected two UVC doses for more in depth characterizations: 1.9 and 12 KJ/m^2. We selected 1.9 KJ/m^2 as 'sublethal' dose because this dose induced maximal nucleoid compaction in exponential phase cells (**Figure 3.66C**), without severely affecting cell survival (**Figure 3.66A**, between 25 and 50% survival after 48h). We selected 12 KJ/m^2 as 'lethal' dose because it killed most cells (**Figure 3.66A**, < 0.001% survival after 48h).

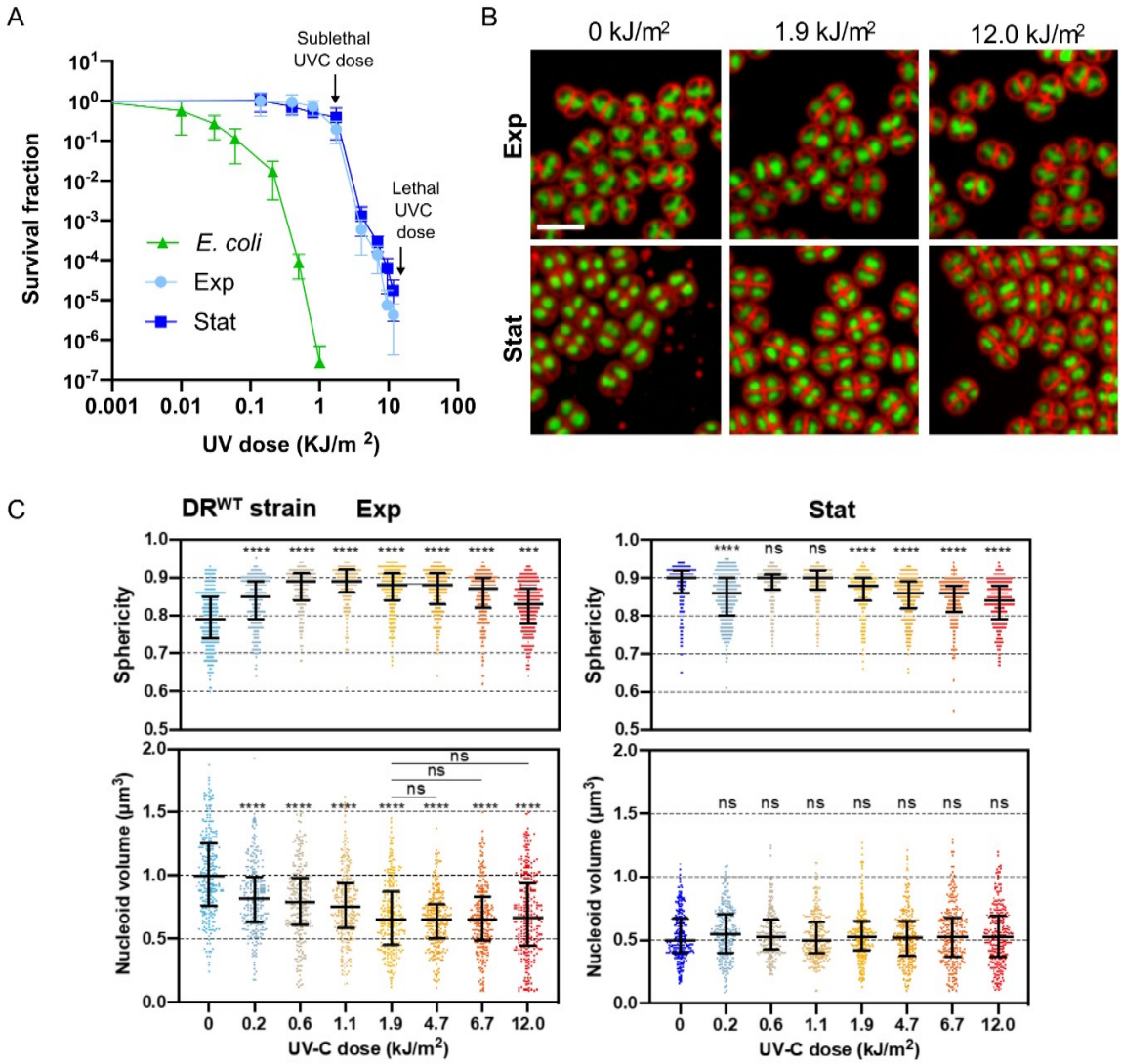

Figure 3.66 UVC irradiation affects DR survival and nucleoid morphology. *A) Survival curves of D. radiodurans cells in exponential and stationary phase, and of E. coli cells in exponential phase after exposure to UVC light. B) Confocal images of non-irradiated and irradiated DR cells labeled with Nile red and Syto9. C) Nucleoid volume and sphericity of exponential and stationary phase cells after UVC irradiation. **** p<0.0001, Kruskal-Wallis test. Data by Pierre Vauclare and Joanna Timmins.*

Next, we assessed whether HU diffusion changes in response to these two doses of UVC irradiation. Given that UVC irradiation elicits similar morphological changes as stationary phase (nucleoid rounding and compaction), we hypothesized that HU diffusion would be decreased after exposure to UVC irradiation. Surprisingly, sptPALM revealed that HU diffusion is increased rather than decreased in irradiated cells (**Figure 3.67**). Given that the nucleoid volumes are decreased after irradiation, this increase in diffusion cannot be ascribed to confinement effects, indicating that this is a real biological response. Increased HU-mEos4b diffusion could be seen in both irradiated exponential and stationary phase cells, suggesting that the acute response to UVC irradiation is independent of the growth phase. Furthermore, HU diffusion was increased in response to both the sublethal and lethal doses of UVC irradiation, suggesting that the initial changes in nucleoid reorganization are independent on whether the cells are able to recover or not.

Careful inspection of the changes in HU diffusion in response to UVC irradiation (**Figure 3.67**), suggests that exponential phase cells respond more strongly than stationary phase cells and that in stationary phase cells the increase in HU diffusion is dose-dependent (median median Dapp per cell:

0.10 µm^2/s after 1.9 KJ/m^2 UVC, 0.11 µm^2/s after 12 KJ/m^2 UVC), while this relation appears absent in exponential phase cells (median median Dapp per cell: 0.21 µm^2/s after 1.9 KJ/m^2 UVC, 0.17 µm^2/s after 12 KJ/m^2 UVC). Although these observations are potentially very interesting, we noted that, overall, the measurements at T0 were more variable than measurements of non-irradiated (NIR) cells and of cells after a certain time of recovery (see below). This is possibly explained by the delay between irradiation and imaging (20 to 30 minutes), related to sample preparation. We cannot exclude that variations in this time delay might have resulted in cells being in slightly different stages of nucleoid remodeling explaining the observed variation in HU diffusion. Such imprecisions in timing could be averaged out by a large number of experiments, but this is challenging with sptPALM because it is a time-consuming technique. Because of these reasons we refrain from drawing more in-depth conclusions from these data.

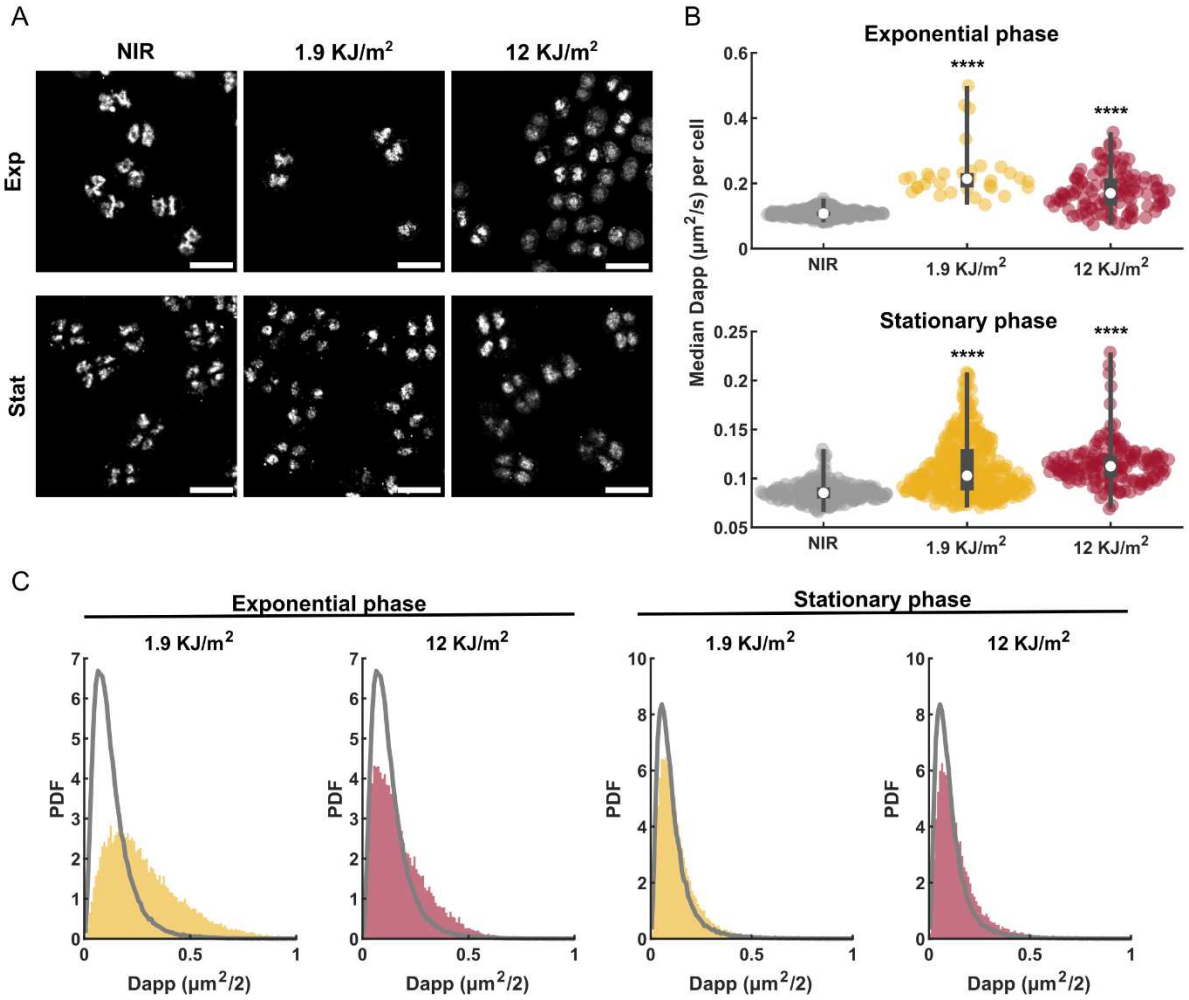

Figure 3.67 HU diffusion changes after exposure to UVC. *A) Representative super-resolved images of exponential and stationary phase DR cells expressing HU-mEos4b before and after irradiation with 1.9 or 12 KJ/m^2 UVC (scale bar = 3 µm). B) Swarm plots of the median Dapp per cell after irradiation with UVC. Box plots indicate the median, the lower and upper quartile and the min and max. C) Histograms of the apparent diffusion coefficients of HU after irradiation. Grey lines show the Dapp histograms previously obtained on NIR exponential or stationary phase cells as a reference. (n = 30-150 cells from 2-3 independent experiments). **** p<0.0001, Kruskal-Wallis test, relative to NIR cells.*

3.2.4 HU diffusion changes progressively after exposure to UVC irradiation

After characterizing the acute changes in nucleoid organization induced by UVC irradiation, we set out to monitor nucleoid remodeling during the recovery from UVC induced damage. To this end, irradiated cells were incubated in fresh 2xTGY medium and allowed to recover at 30°C in a shaking

incubator. Samples were taken at various time points to follow the changes in nucleoid organization by microscopy. Measurements of the cell densities showed that cultures irradiated with a dose of 1.9 KJ/m^2 had a growth delay of ~4 hours compared to non-irradiated cells, while cultures irradiated with a dose of 12 KJ/m^2 showed minimal growth (**Figure 3.68A, Figure 3.69A**).

Characterization of the nucleoid morphology by confocal imaging revealed that after an initial phase of nucleoid compaction (0-2 hours post IR), the nucleoids of the cells irradiated with 1.9 KJ/m^2 expanded and adopted irregular shapes, while the nucleoids of the cells irradiated with 12 KJ/m^2 remained compacted and spherical (**Figure 3.68B-D, Figure 3.69B-D**). In fact, the average volume of the nucleoids of the cells irradiated with 12 KJ/m^2 progressively decreased over 9 hours (**Figure 3.69C**) while there was an increasing number of anucleate cells (**Figure 3.69D**), suggesting that the DNA in these cells was degraded. After 24 hours of recovery, the cells irradiated with the sublethal dose (1.9 KJ/m^2) had reached early stationary phase as judged from their cell shape and nucleoid morphology (**Figure 3.68B**). Although most cells appeared normal, there was still a fraction of cells that had expanded abnormal nucleoids (**Figure 3.68B-D**). Likely, these cells were unable to recover from the UVC induced damage. In addition to the morphological changes of the nucleoid, imaging of cells expressing HU-mCherry showed that HU is transiently upregulated and sequentially downregulated in response to sublethal UVC irradiation (**Figure 3.68E**). Notably, after 24 hours of recovery, when the cells seemed to have reached early stationary phase, HU levels appeared increased compared to NIR exponential phase cells (**Figure 3.68E**), similairly as in NIR stationary phase cells (**Figure 3.54C**). Only a slight increase in HU levels was detected in the cells irradiated with a lethal dose of UVC (**Figure 3.69E**), which is likely due to impairment of the protein synthesis machinery in these heavily damaged cells.

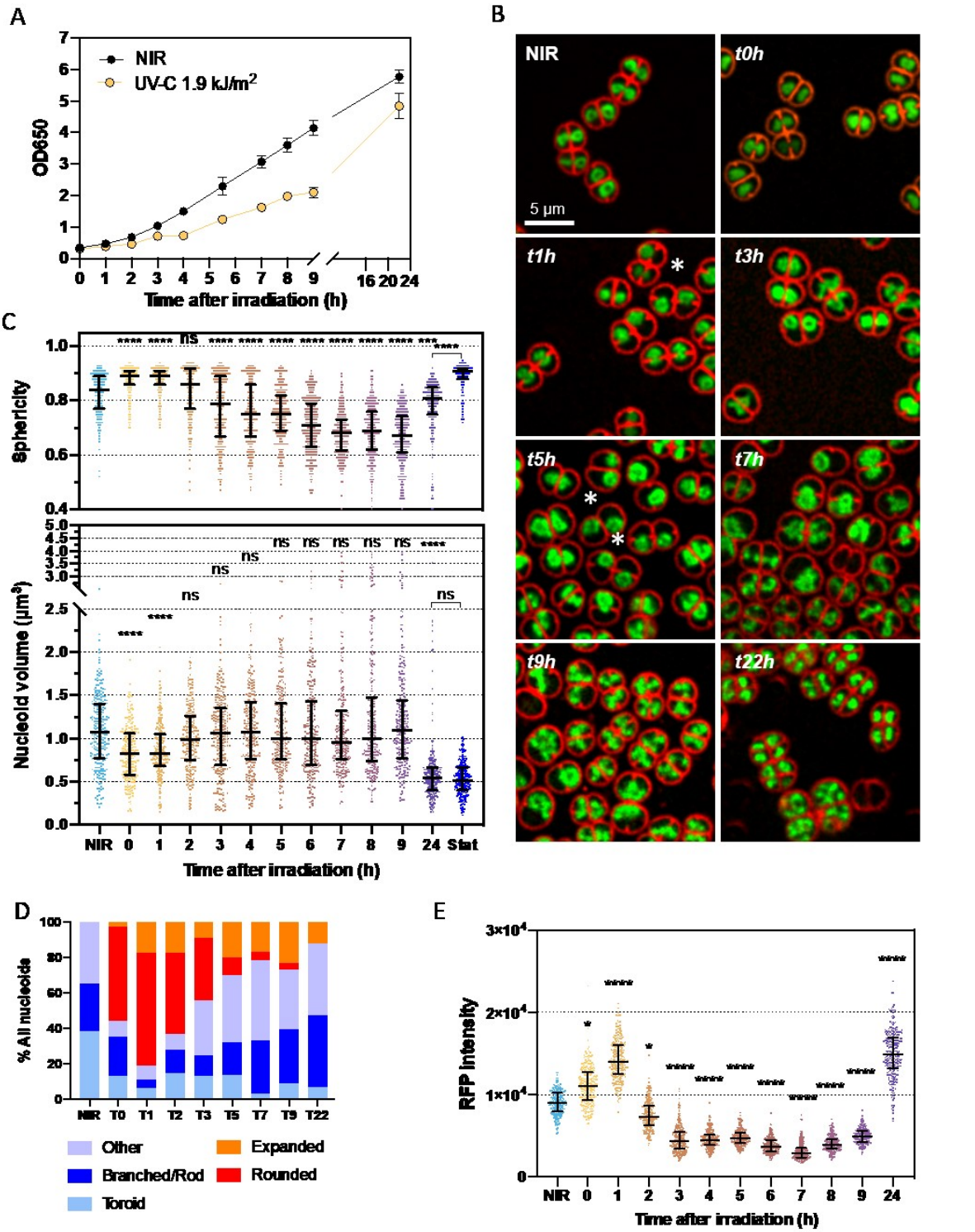

Figure 3.68 Progressive nucleoid remodeling in response to sublethal UVC irradiation. *DR cells (WT and HU-mCherry) in exponential phase were irradiated with 1.9 KJ/m² UVC light and allowed to recover for 0-24 hours before various measurments were taken to follow the recovery process. A) Cell density measurements. B) Representative confocal image of WT cells stained with syto9 and Nile red post-irradiation. C) Nucleoid volume and sphericity 0-24 hours post-irradiation. D) Classification of the nucleoid morphologies 0-22 hours post-irradiation. Blue shades indicate normal nucleoid morphologies, orange/red shades indicate abnormal nucleoid morphologies. E) Mean fluorescence intensity of HU-mCherry per nucleoid 0-24 hours post irradiation. * p<0.05, *** p<0.001, **** p<0.0001, Kruskal-Wallis test, relative to NIR cells. Data by Pierre Vauclare and Joanna Timmins. Figure adopted from Vauclare et al.*

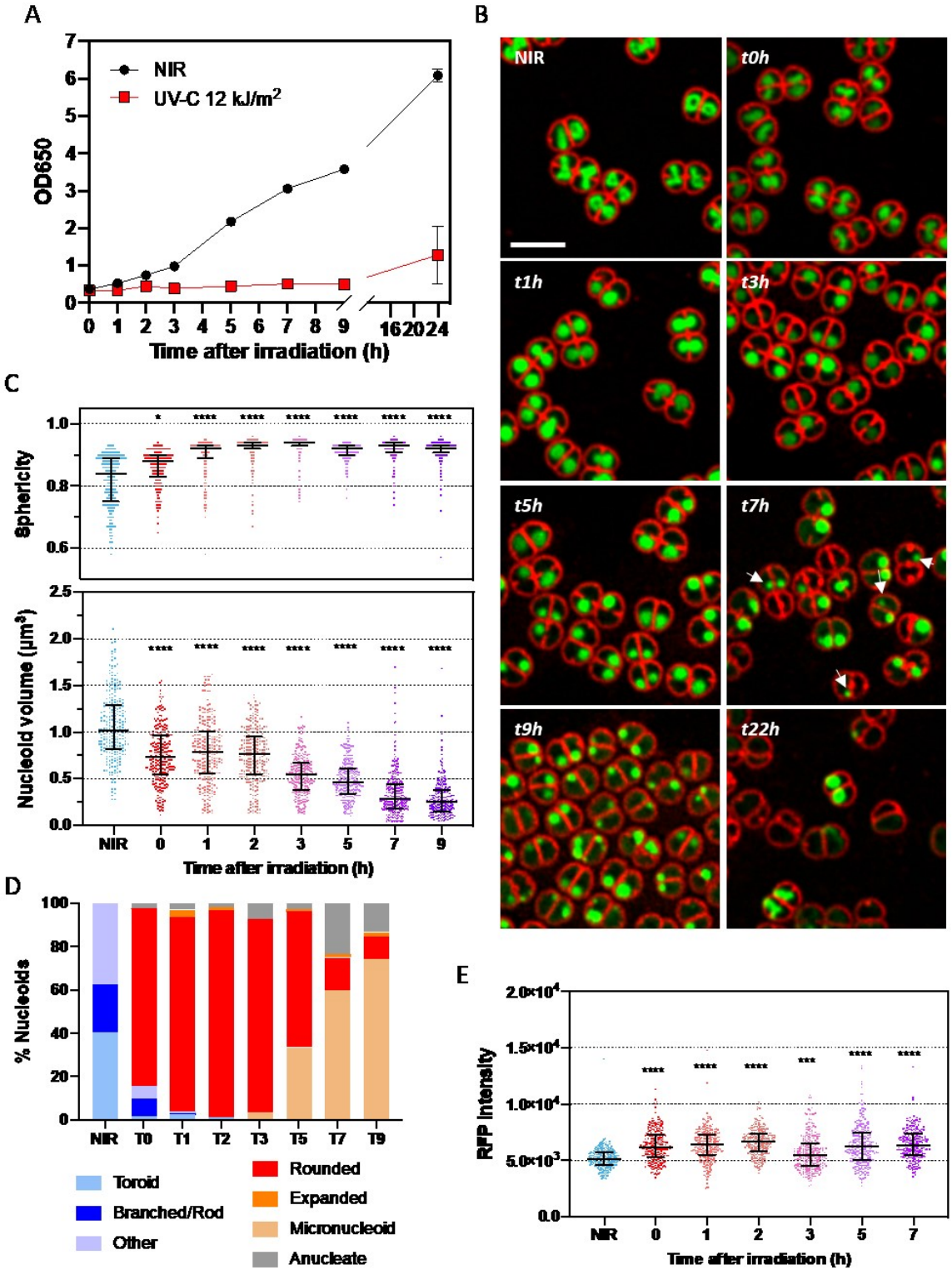

Figure 3.69 Nucleoid remodeling in response to lethal UVC irradiation. *DR cells (WT and HU-mCherry) in exponential phase were irradiated with 12 KJ/m^2 UVC light and allowed to recover for 0-24 hours before various measurments were taken to follow the progression of the cell and nucleoid morphology. A) Cell density measurements. B) Representative confocal image of WT cells stained with syto9 and Nile red post-irradiation. Arrows indicate examples of micronucleoids. C) Nucleoid volume and sphericity 0-9 hours post-irradiation. D) Classification of the nucleoid morphologies 0-9 hours post-irradiation. Blue shades indicate normal nucleoid morphologies, orange/red shades indicate abnormal nucleoid morphologies. E) Mean fluorescence intensity of*

*HU-mCherry per nucleoid 0-7 hours post-irradiation. * p<0.05, *** p<0.001, **** p<0.0001, Kruskal-Wallis test, relative to NIR cells. Data by Pierre Vauclare and Joanna Timmins. Figure adopted from Vauclare et al.*

sptPALM imaging of HU-mEos4b revealed the same diversity in nucleoids shapes as seen by confocal microscopy post-irradiation with 1.9 KJ/m^2. Representative super-resolved images are shown in **Figure 3.70A** with examples or rounded and expanded nucleoids indicated by yellow and orange arrows, respectively. After the initial increase in HU diffusion directly post-irradiation, HU diffusion appeared to decrease progressively until reaching after 24 hours a diffusion that could not be distinguished from that of non-irradiated stationary phase cells (**Figure 3.70B,C**).

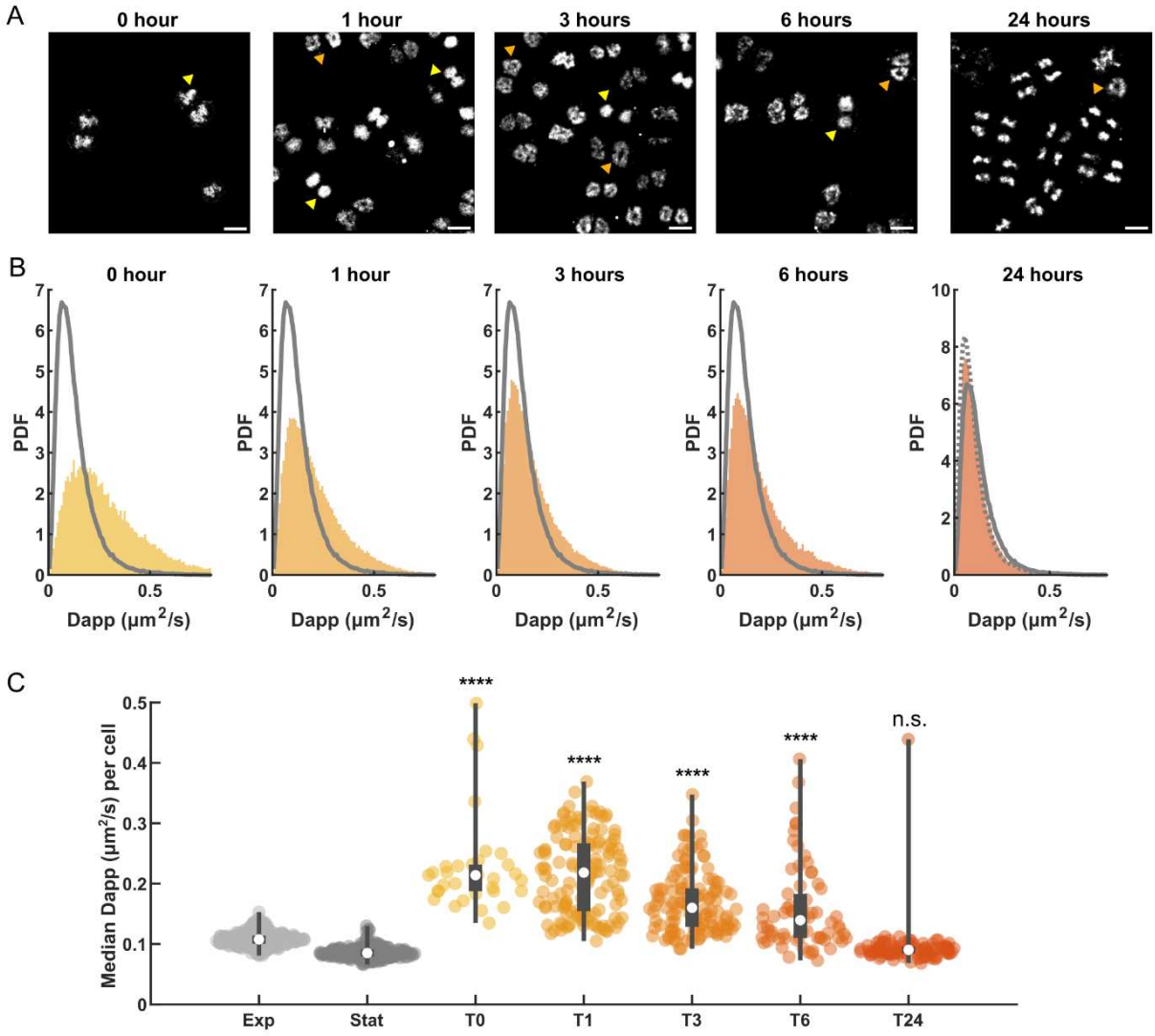

Figure 3.70 HU diffusion during recovery from sublethal UVC irradiation. *DR cells expressing HU-mEos4b were irradiated with 1.9 KJ/m^2 UVC after which they were allowed to recovered in fresh 2xTGY medium at 30°C. HU diffusion was monitored after 0, 1, 3, 6 and 24 hours of recovery by sptPALM. A) Representative super-resolved images of HU-mEos4b. Arrows indicate examples of round (yellow) and expanded (orange) nucleoids. B) Histograms of the apparent diffusion coefficients (Dapp). Grey lines show the diffusion in non-irradiated exponential phase (solid line) or stationary phase (dashed line) cells. C) Swarm plots of the median Dapp per cell after irradiation with UVC. Box plots indicate the median, the lower and upper quartile and the min and max. (n = 30-130 cells from 3-4 independent experiments). **** p<0.0001, Kruskal-Wallis test, relative to NIR exponential (T0-T6) or stationaty (T24) phase cells.*

We noted that post UVC irradiation there was a large cell-to-cell variability in HU diffusion (**Figure 3.70C** and **Figure 3.71A)**. We hypothesized that this variability could be related to the variability in nucleoid morphologies. To investigate this possibility, we visually inspected the tracks belonging to

cells with certain nucleoid morphologies (**Figure 3.71C**). HU diffusion appeared the highest in cells with rounded nucleoids, with HU molecules exploring the entire nucleoid. In expanded nucleoid, on the other hand, HU diffusion seemed more restricted. To quantitatively assess this observation, we classified the cells into 4 categories based on their nucleoid morphology: structured (normal for exponential phase cells), round, expanded and stationary phase like. After classification, we examined again the median Dapp per cell (**Figure 3.71B**). Indeed, after 1 and 3 hours of recovery, HU diffusion appeared the highest in the cells with round nucleoids. After 0 and 6 hours such a relation could not be observed. Furthermore, even after classification of the nucleoid morphologies, HU diffusion appeared highly variable between cells in the same class, suggesting that nucleoid morphology cannot fully predict HU diffusion. It should be noted, however, that the classification from the sptPALM images was challenging; it was especially difficult to distinguish between cells with structured and expanded nucleoids. Possibly, in the future, this analysis could benefit from deep learning programs to classify the cells automatically and in a less biased way (see for example the ZeroCostDL4Mic platform[451,452]).

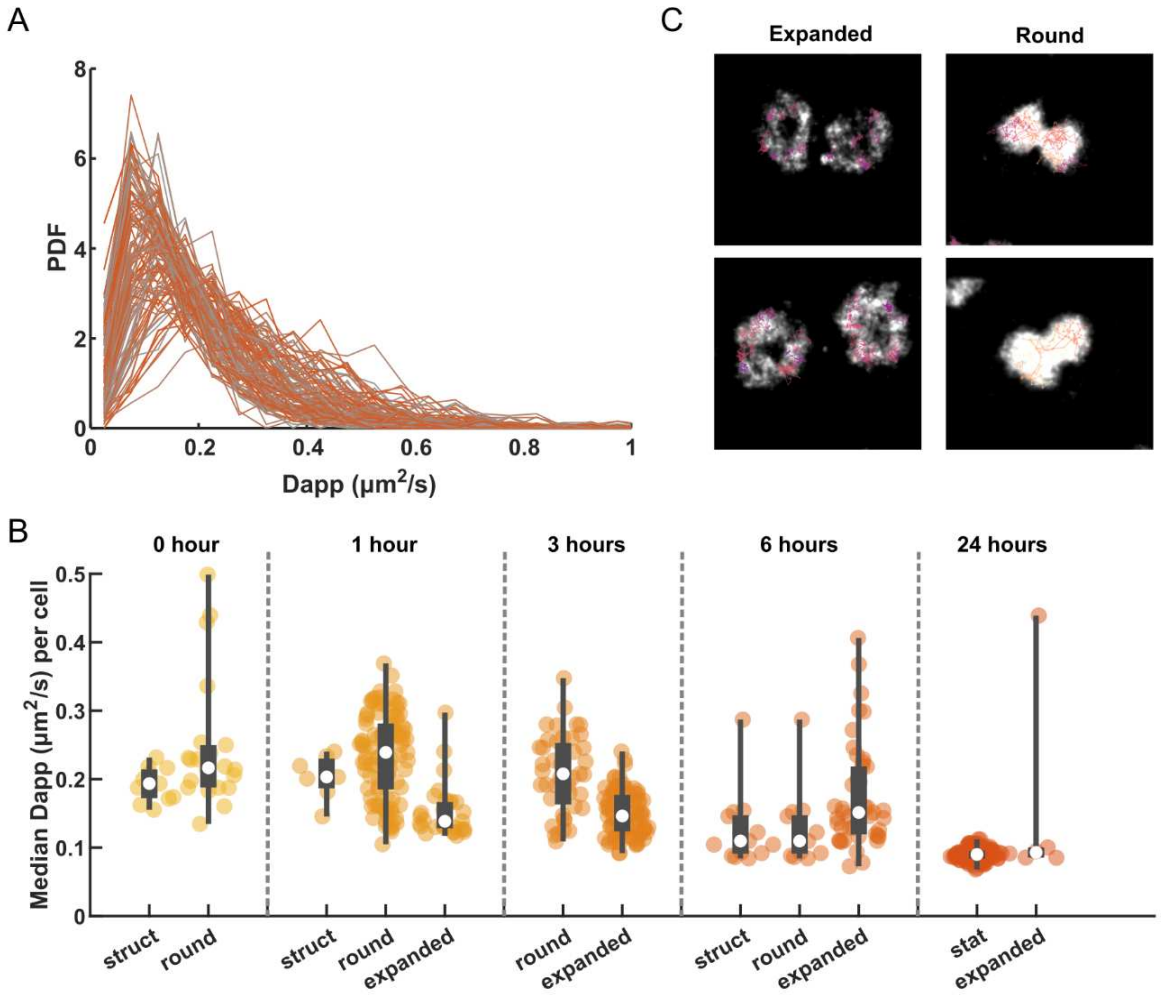

Figure 3.71 Cell-to-cell variability in HU diffusion post UVC irradiation. *A) Dapp histograms of HU-mEos4b of single cells 3 hours post-irradiation with 1.9 KJ/m² UVC. B) HU-mEos4b tracks overlaid with super-resolved images of the corresponding nucleoids. Shown are examples of cells with round and expanded nucleoids 3 hours post irradiation. Tracks are color coded by diffusion coefficient (low-> high = purple-> yellow). C) Swarm plots of the median Dapp per cell after 0-24 hours post irradiation with UVC. Cells were classified into four classes based on their nucleoid morphology: structured (struct, normal for exponential phase cells), round, expanded and stationary phase nucleoid (stat). Box plots indicate the median, the lower and upper quartile and the min and max.*

Next, we assessed HU diffusion in cells irradiated with a lethal dose of UVC irradiation at different time points post-irradiation (**Figure 3.72**). In line with the observations made by confocal microscopy, the nucleoids appeared to stay compacted up to 3-6 hours post irradiation after which they seemed to disintegrate (**Figure 3.72A**). After 24 hours, most cells appeared to be anucleate and HU seemed to be spread throughout the cells (**Figure 3.72A**). sptPALM of HU-mEos4b showed that HU diffusion was increased on average and stayed increased up to 24 hours post-irradiation (**Figure 3.72B,C**). However, there was no clear progression in the changes in HU diffusion. One-hour post irradiation, HU diffusion seemed to peak before it transiently decreased 3- and 6-hours post-irradiation before increasing again 24 hours post irradiation (**Figure 3.72C**). Possibly, this trend could be explained by the progressive shrinkage of the nucleoids seen by confocal microscopy, resulting in increased confinement and consequently decreased apparent HU diffusion 3-6 hours post-irradiation. The increased diffusion after 24 hours could be explained by the absence of a nucleoid in most of the cells, allowing HU to explore the entire cell volume. However, care should be taken not to over-interpret these data considering the large cell-to-cell variability and the limited number of experiments (1-2 depending on the time point). This experiment remains to be repeated before further conclusions can be drawn.

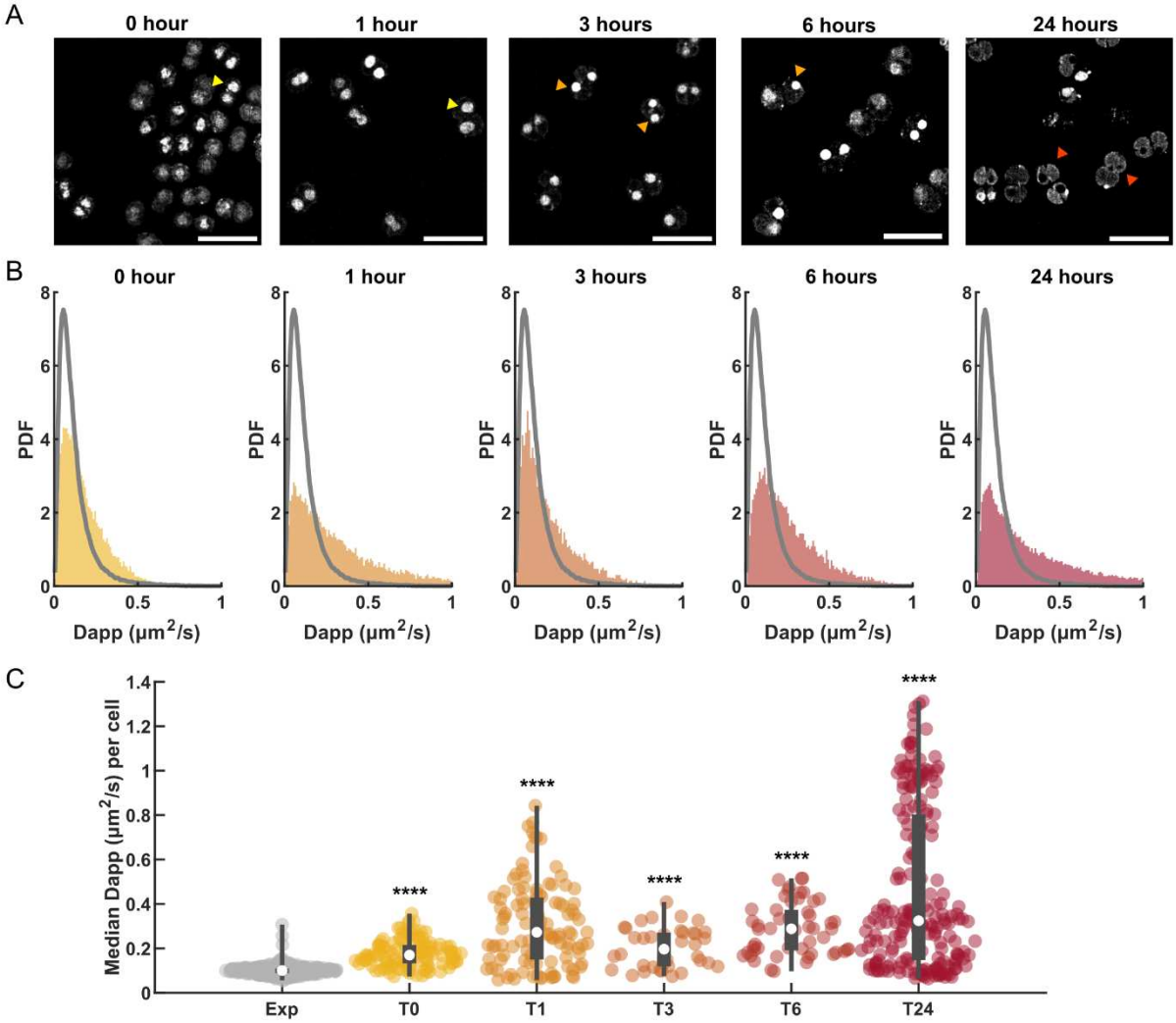

Figure 3.72 HU diffusion stays increased following lethal UVC irradiation. *DR cells expressing HU-mEos4b were irradiated with 12 KJ/m² UVC after which they were allowed to 'recover' in fresh 2xTGY medium at 30°C. HU diffusion was monitored after 0, 1, 3, 6 and 24 hours of recovery by sptPALM. A) Representative super-resolved images of HU-mEos4b. Arrows indicate examples of round (yellow) and micro (orange) nucleoids and anucleate cells (red). B) Histograms of the apparent diffusion coefficients (Dapp). Grey lines show the diffusion in non-*

*irradiated exponential phase cells. C) Swarm plots of the median Dapp per cell after irradiation with UVC. Box plots indicate the median, the lower and upper quartile and the min and max. (n = 38-198 cells from 1-2 independent experiments). **** p<0.0001, Kruskal-Wallis test, relative to NIR exponential phase cells.*

3.2.4.1 DNA mobility in non-irradiated and irradiated cells

The increased mobility of HU-mEos4b after UVC irradiation could be explained by reduced interactions between HU and the DNA and/or by increased mobility of the DNA, increasing the apparent mobility of DNA-bound HU. In fact, DNA mobility has been shown to be increased upon damage in eukaryotic cells, where it has been proposed to facilitate homology search and DNA repair[393,453,454].

To test whether increased mobility of the DNA could be, at least partly, responsible for the increased mobility of HU-mEos4b after UVC irradiation, we monitored the mobility of the DNA in non-irradiated and irradiated DR cells (1.9 KJ/m^2, 1 hour of recovery) with fluorescently labeled *oriC* and *ter* sites (**Figure 3.73**). Fluorescent labeling of the *oriC* and *ter* loci was achieved using the *parS*/ParB system as published previously[370,411]. Fluorescently labeled loci appeared as bright foci which could be localized and tracked like single molecules in sptPALM. Tracking of the *oriC* and *ter* foci was performed using a frame time of 1 s and 10 W/cm^2 488 nm light (100 ms exposure time). Under these conditions, foci could be imaged for approximately 100-200 frames before bleaching. Detection of the foci by Thunderstorm, however, was relatively poor due to a high fluorescence background arising from freely diffusing ParB-GFP molecules, resulting in the recontruction of many short tracks (~15-30 frames). More efforts are required to optimize the sample preparation and analysis pipeline to extract high-quality long tracks or *oriC* and *ter* foci. Cells were co-labeled with HU-mCherry for visualization of the nucleoid.

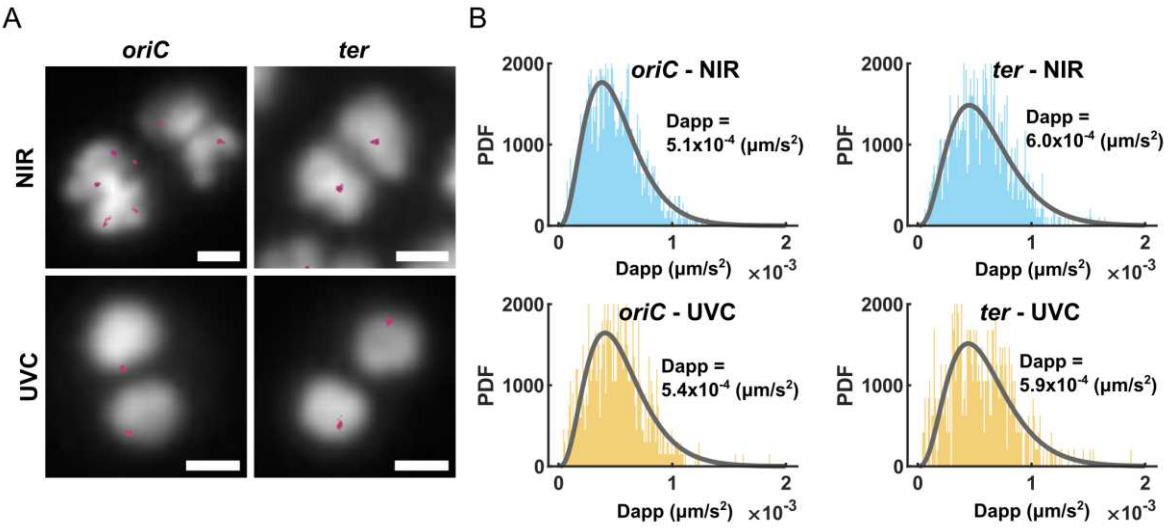

Figure 3.73 DNA mobility in non-irradiated and irradiated DR cells. *A) Representative tracks of the oriC and ter foci (purple) in non-irradiated (NIR) and irradiated (UVC, 1.9 KJ/m^2) cells after 1 hour of recovery. Cells were co-labeled with HU-mCherry for visualization of the nucleoid. B) Dapp distribution of the oriC and ter sites in non-irradiated and irradiated cells after 1 hour of recovery fitted to a one-population model. Scale bar = 500 nm. n=475-1000 tracks (~50-80 foci) from 2 experiments.*

Figure 3.73A shows representative images of tracks from *oriC* and *ter* foci overlayed on fluorescence images of the HU-mCherry labeled nucleoid. In non-irradiated cells, *oriC* foci were spread throughout the nucleoids, while *ter* foci were mostly located in the center of dividing nucleoids, in line with previous observations[370]. After irradiation, nucleoids were rounded and *oriC* and *ter* foci were located at the edge or center of the rounded nucleoids. In both non-irradiated and irradiated cells, the *oriC* and *ter* foci appeared mostly immobile (Dapp = ~5-6x10^{-4} µm^2/s) with no apparent difference

between the non-irradiated and irradiated cells or the *oriC* and *ter* foci. Although these data are not of high enough quality to conclude that there really exists no differences between these conditions, they show that the mobility of the DNA is negligible compared to the increased mobility of HU-mEos4b after irradiation (see the tracks in of HU-mEos4b **Figure 3.72A**), suggesting that the increase in HU-mEos4b mobility is largely due to reduced interactions with the DNA. It should be noted that, here, it is assumed that the diffusion of the *oriC* and *ter* sites is representative for the entire genome, which might not be the case, expecially for the *ter* site, which has been proposed to be anchored to the cell division machinery[345,346]. This assumption could be addressed by tracking of other loci on the genome.

3.2.5 Discussion

Stress-induced nucleoid remodeling in a wide-spread phenomenon in bacteria. Using a combination of confocal imaging and sptPALM, we characterized the morphological changes of the nucleoid and the dynamics of HU in the highly stress-resistant bacterium *D. radiodurans* during stationary phase and in response to UVC-induced DNA damage. Imaging revealed that the nucleoid of *D. radiodurans* adopts a rounded and compacted morphology during stationary phase and in response to UVC induced damage. However, despite the morphological similarities, sptPALM showed that the diffusion dynamics of HU are drastically different: while HU diffusion is decreased during stationary phase, it is increased after exposure to UVC irradiation. Given that we did not detect notable changes in DNA mobility after irradiation, the increased HU diffusion is likely due to reduced interactions with the DNA. During the recovery from sublethal irradiation, HU diffusion gradually decreased until reaching that of non-irradiated stationary phase cells 24 hours post-irradiation. On the other hand, in cells irradiated with a lethal dose of UVC irradiation, HU diffusion remained increased up to 24 hours post-irradiation.

Nucleoid compaction during stationary phase is believed to protect the genomic DNA from damage. In *E.coli*, one of the key regulators of DNA compaction is Dps, which is drastically upregulated during stationary phase[397]. On the other hand, in *D. radiodurans*, which expresses 2 Dps variants, Dps1 is present independent of the growth phase while Dps2 is upregulated in response to oxidative stress[421,424]. It remains, thus, unknown how DNA compaction during stationary phase is regulated in *D. radiodurans*. Our results indicate that, in *D. radiodurans,* HU is upregulated during stationary phase and is tightly associated with the DNA (**Figure 3.54C**, **Figure 3.55**), which could suggest that HU contributes to the increased compaction during stationary phase, possibly by polymerizing on the genomic DNA, causing DNA stiffening and bundling[357–359].

Nucleoid compaction in response to UVC irradiation is thought to stabilize the DNA and facilitate repair. In UVC irradiated *E.coli* cells, the nucleoid has been shown to sequentially compact and expand in a SOS dependent manner before cell division restarts[382,383]. We observed a similar morphological progression in irradiated *D. radiodurans* cells (sublethal dose, **Figure 3.68**). Obsbu and Skarstad proposed that the initial phase of compaction serves to stabilize the DNA and repair double stranded breaks, while repair of other lesions mainly happens during the decompacted stage[383]. This hypothesis is in line with studies in eukaryotic cells showing that the chromatin decondenses in response to DNA damage to facilitate repair[393,455]. Although most cells appeared to recover from 1.9 KJ/m^2 UVC, the nucleoids of a fraction of the *D. radiodurans* cells remained dramatically decompacted up to 24 hours (**Figure 3.68**). These cells were typically larger in size and lacked a septum, suggesting the cell growth was initiated but cell division was blocked. Castro et al. showed that *E. coli* cells that are deficient in DNA repair proteins reach the expanded nucleoid stage but are unable to restart cell division after UVC irradiation, suggesting that DNA repair is required before cell division is restarted[382]. So presumebly, the *D. radiodurans* cells that maintained expanded nucleoids were unable to repair all their DNA damage, prohibiting them from restarting cell division.

Interestingly, acute nucleoid compaction and rounding was also observed in lethally irradiated DR cells (**Figure 3.69**), suggesting that this acute compation is mostly a passive process, assuming that the lethal dose of UVC almost instantly kills the cells. We propose that this passive response is mediated by UVC-induced changes in cell metabolism and/or physico-chemical changes at the protein (notably HU) and/or DNA level. For example, changes in transcription and translation activity might contribute to the remodeling of the nucleoid after exposure to UVC, as arrest of transcription and translation has been shown to have a big influence on the morphology of the bacterial nucleoid[456,457]. Aditionally, damage to the cytoskeleton might also affect the nucleoid organization post-irradiation[456]. Finally, it is tempting to speculate that the reduced interaction post-irradiation between HU and the DNA contributes to the reorganiztaion of the nucleoid (**Figure 3.67**). Notably, Bettridge et al. observed that mutations of HU, which reduce its interaction with the DNA (increased diffusion), can lead to both nucleoid compaction and nucleoid expansion in *E.coli* depending on which residues are mutated[278]. It is important to note that, although the interaction between HU and DNA appears to be reduced after irradiation, HU remains strictly associated with the nucleoid, indicating that the interaction between HU and the DNA is not completely lost. Future work is required to uncover how the interaction between HU and the DNA regulated. Previous studies proposed that the interaction between HU and the DNA is regulated by phosphorylation and acetylation[364,365,367]. While phosphorylation has been shown to enhance DNA binding of HU[365], acetylation is expected to reduce its affinity for DNA[367]. It will be interesting to investigate if HU is modified in response to UVC irradiation, especially considering that the RDR has been reported to include acetyltransferases[430]. In addition to modification of HU, UVC induced modifications of the DNA (i.e. damage) might also influence the interaction between HU and the DNA post-irradiation.

Nucleoid expansion was not observed in the *D. radiodurans* cells irradiated with 12 KJ/m^2 UVC (**Figure 3.69**). Instead, the nucleoids in these cells were often off-center and appeared to become progressively smaller before disappearing completely (**Figure 3.69D**). Using simulation, Joyeux and colleagues showed that the nucleoid preferentially locates at the edge of a bacterial cell, where the curvature of the cell wall is the highest, suggesting that in healthy cells active processes keep the nucleoid centered[322]. In *D. radiodurans,* the *ter* loci of chromosome I has also been shown to be specifically located at the centre of cells at all stages of the cell cycle until the final step of cytokinesis, strongly supporting a model in which the chromosome is actively anchored by a yet uncharacterized process to a specific position of the cell[370]. This active process might be impaired in the strongly irradiated cells, causing the nucleoid to collapse and drift towards the edge of the cell.

In addition to the altered diffusion dynamics of HU, the expression levels of HU also appeared to be changed after UVC irradiation. Imaging of HU-mCherry suggested that in response to sublethal irradiation, HU is transiently upregulated (1 hour post-irradiation) after which it is downregulated (3-9 hours post-irradiation) (**Figure 3.68E**). In eukaryotic cells, DNA damage has been shown to lead to removal and degradation of histones, which has been proposed to enhance DNA mobility and repair[393,458]. Given the histone-like functions of HU, it is conceivable that HU is downregulated for similar reasons. This seems, however, in contradiction with the initial upregulation of HU shortly after irradiation. Possibly, during the first phase of nucleoid compaction, high levels of HU are required to stabilize the severely damaged DNA, while during the second expanded phase, when severe lesions such as double stranded breaks have already been repaired, DNA stabilization is no longer required to the same extend and HU levels are decreased to facilitate the repair of the other lesions.

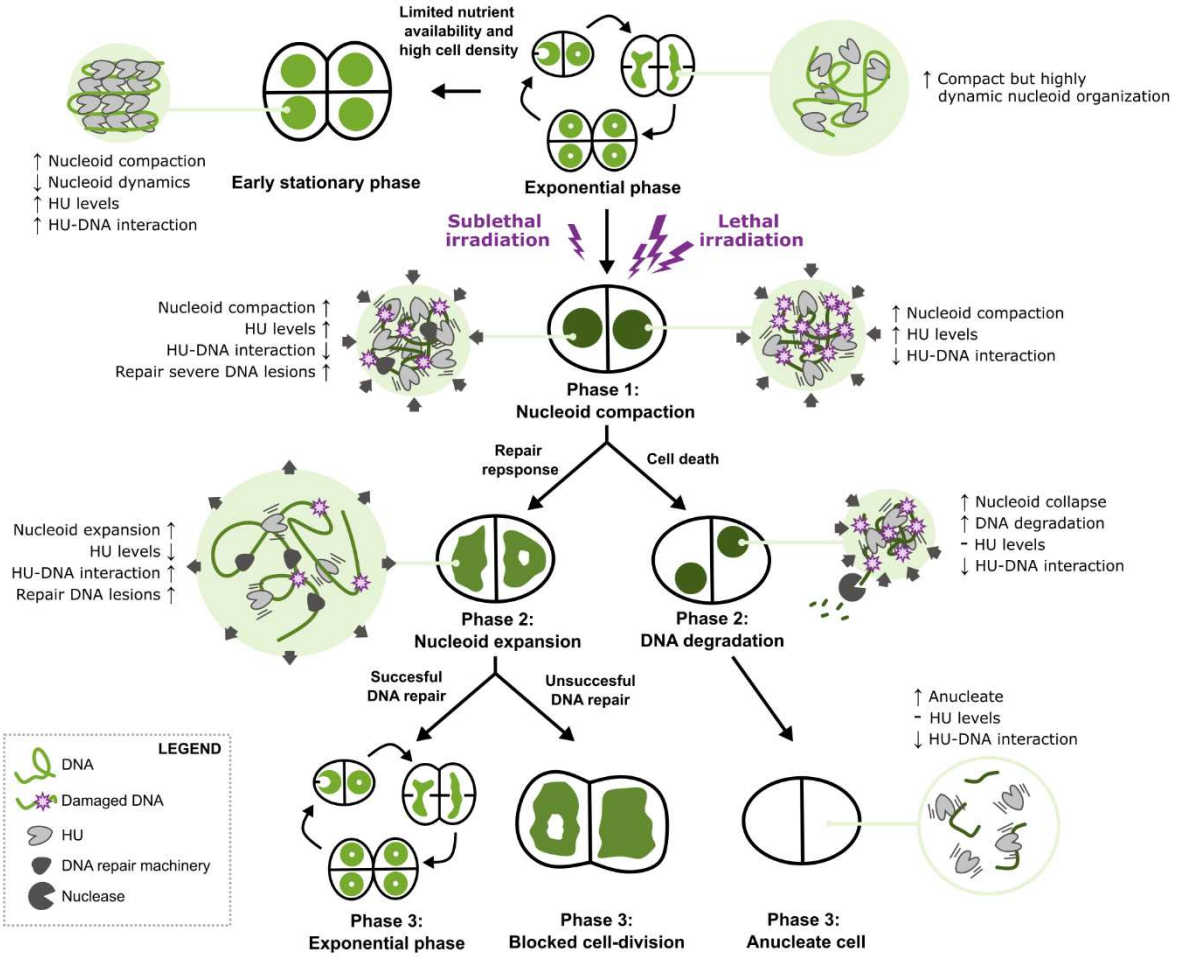

Figure 3.74 Proposed model of stress-induced nucleoid remodeling in D. radiodurans*. Schematics illustrating the main nucleoid morphologies observed by confocal microscopy and the diffusion dynamics of HU as measured by sptPALM in cells entering stationary phase and in response to sublethal and lethal doses of UVC irradiation.*

Besides the biological findings discussed above, this work also pinpointed a challenge for sptPALM studies in bacterial cells, namely that the high level of confinement creates an apparent heterogeneity in the diffusion of the molecules. Although this effect does not prohibit extraction of useful information from sptPALM studies, it is important to be aware of this effect and not over-interpret extracted data. In *D. radiodurans*, this effect might be further aggravated by the diversity of nucleoid shapes.

In conclusion, our data show that, despite the morphological similarities, the mechanisms underlying nucleoid remodeling in response to UVC irradiation and upon transition into stationary phase are distinct. **Figure 3.74** presents a tentative model of the different phases of nucleoid remodeling in D. radiodurans in response to UVC irradiations. Further work is required to unravel the precise roles of HU and investigate the involvement of other NAPs.

4 Perspectives

Quantitative PALM presents a collection of powerful techniques that can provide insights into macromolecular organizations and dynamics at the nanoscale *in cellulo*. Yet, the wide-spread application of quantitative PALM techniques is limited by the complex photophysical behaviors of the employed fluorophores and the need for sophisticated analyses. In this context, the aim of my PhD work was to investigate these challenges, aiming to design strategies to facilitate quantitative PALM experiments. To this end, my thesis consisted of two parts: the photophysical characterization of phototransformable FPs, and the application of sptPALM to study stress-induced nucleoid remodeling in *D. radiodurans*.

In conclusion of this work, **Figure 4.1** shows a schematic of the workflow and requirements for the development of improved PCFPs and experimental designs for quantitative PALM imaging, highlighting current weaknesses and potential solutions. This scheme is further explained in the text below.

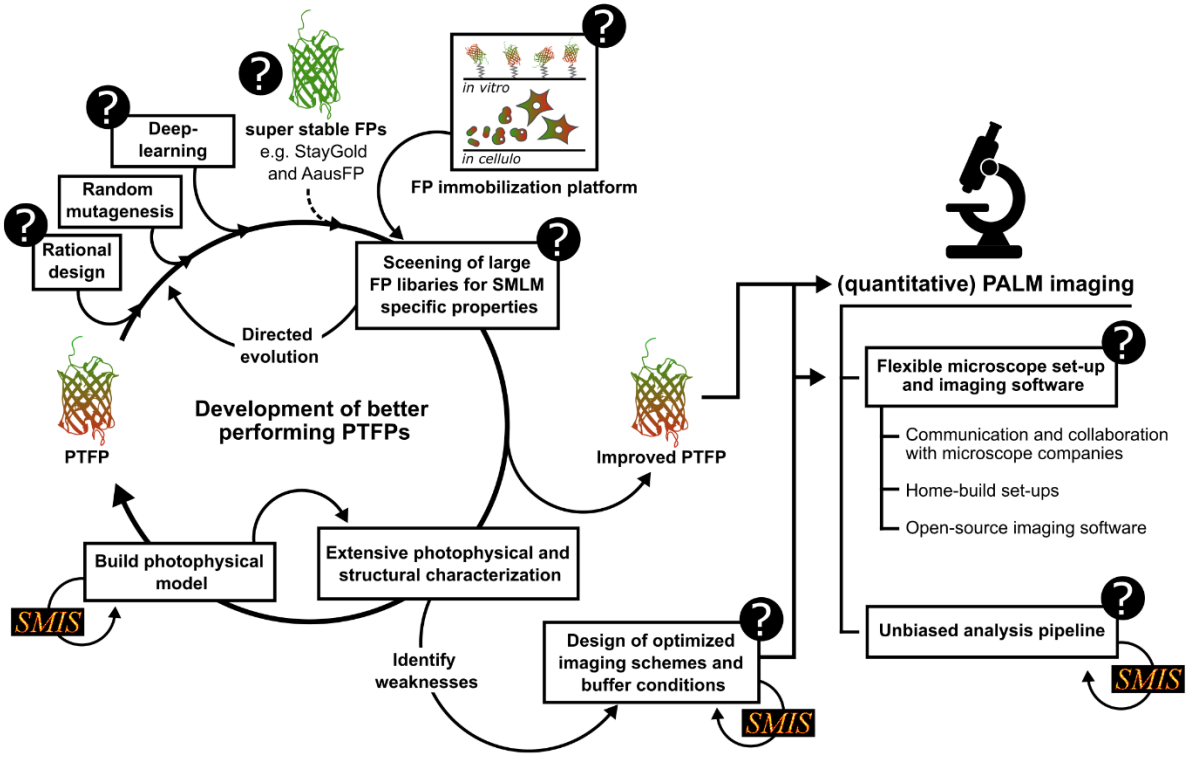

Figure 4.1 Development of improved PTFPs and experimental designs for quantitative PALM. *A better understanding of the photophysics of PTFPs may inform the rational design of better perfoming FPs and of optimized experimental conditions, both of which could greatly benefit the application quantitative PALM. Shown are the different steps and requirements for the development and application of such improved PTFPs and experimental conditions. Questions marks highlight challenging steps/requirements, as also identified in this thesis. Steps in which simulations could contribute are marked by 'SMIS', referring to the simulation software developped in the lab. The different steps/requirements are discussed in more detail in the text below.*

4.1 The complex photophysics of PTFPs hinder PALM experiments

The application of quantitative PALM methods is hindered by suboptimal fluorophore behaviors, including blinking and incomplete photo-activation or -conversion.

We showed that the applied 405 nm light intensity has a strong effect of the PCE of mEos4b, and other PCFPs, due to modulation of green state heterogeneity at low intensities (< 1W/cm^2, **section 3.1.4.1**) and due to nonlinear bleaching, possibly via the triplet state, at high intensities (10-100 W/cm^2, **section 3.1.3**). This reduction of the PCE by 405 nm light is problematic for PALM imaging because it lowers the effective labeling efficiency, lowering the achievable spatial resolution (Nyquist criterion), and complicating counting experiments.

Furthermore, we showed that a short-lived non-fluorescent state lowers the apparent brightness of the green state, and likely also the red state, of mEos4b (**section 3.1.4.2**), and that 405/488 nm light promotes the formation of a non-fluorescent red state (**section 3.1.4.3**). The formation of short-lived non-fluorescent states reduces the detected fluorescence signal in PALM experiments, thereby degrading the localization precision, while the formation of longer-lived non-fluorescent states gives rise to blinking, hindering single molecule counting and tracking.

Lastly, we reported on a novel photoswitching mechanism of rsEGFP2 at CT and showed that the usage of 355 nm light, instead of standard 405 nm light, can improve the effective labeling efficiency when and thereby the achievable spatial resolution in cryoPALM experiments (**section 3.1.5**).

Altogether, the findings from these photophysical studies add to our understanding of FP photophysics and show how complex photophysical behaviors can impact (quantitative) PALM experiments.

4.2 Building a refined photophysical model of mEos4b

Intensive photophysical and structural characterization of mEos4b revealed a variety of behaviors that could not be explained by the existing photophysical model of mEos4b (see **sections 3.1.3** and **3.1.4**). Based on the findings presented in this thesis and existing literature on EosFP variants (and related FPs), I propose an updated photophysical model of mEos4b (**Figure 4.2** and **Supplementary Table 1**).

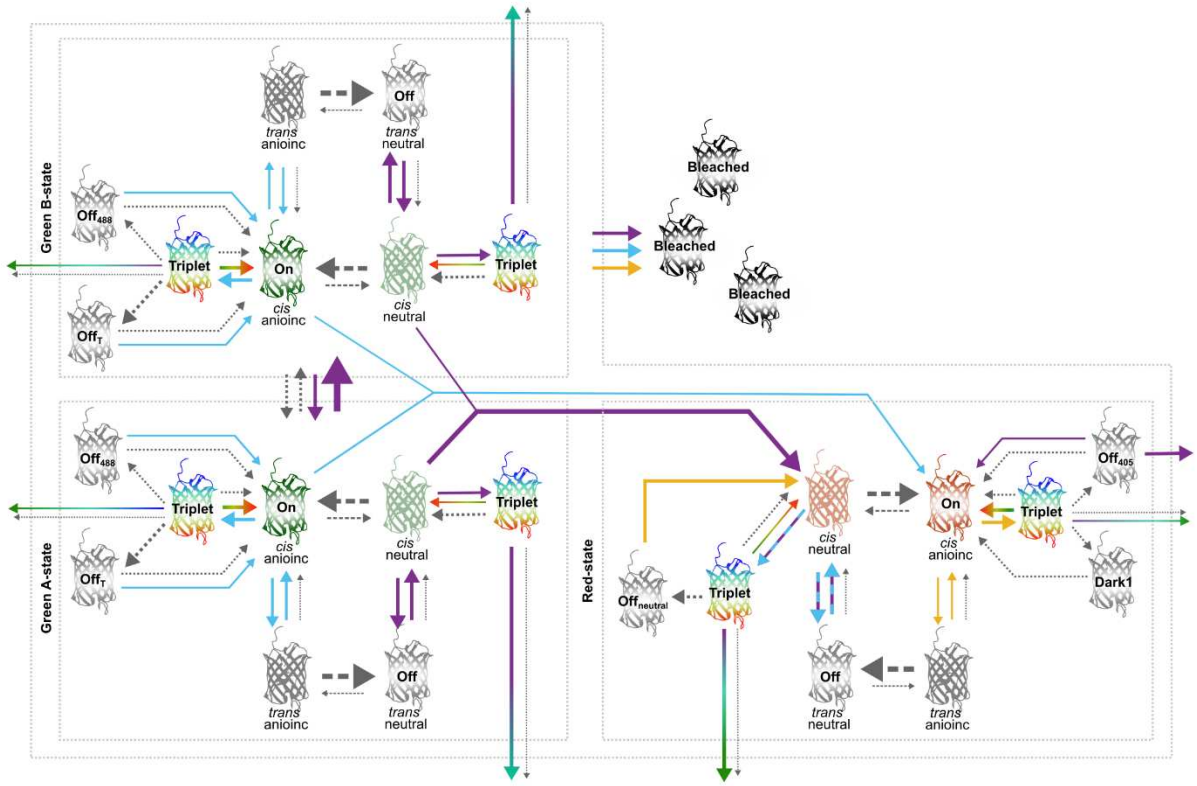

Figure 4.2 Refined photophysical model of mEos4b. *Tentative photophysical model of mEos4b based on results presented in this work and existing literature. See* ***section 6.2.1*** *for an overview of all states. Arrows pointing outside the model indicate bleaching. All light absorbing states can bleach but for simplicity only arrows indicating nonlinear bleaching pathways are shown. The colors of the arrows reflect which commonly used wavelengths induce the transition (purple: 405 nm; cyan: 488 nm; yellow: 561 nm; rainbow: various wavelengths). Dotted arrows indicate thermal transitions. Dashed lines indicate fast equilibria (between anionic and neutral chromophores). The thickness of the arrows reflects the relative rate or quantum yield of certain transitions.*

mEos4b is a green-to-red PCFP, also behaving as a (slow) negative RSFP in both its green and red states. Photoconversion mainly occurs from the neutral green chromophore by excitation with near-UV light. The exact photoconversion mechanism remains elusive, but based on NMR data we propose that photoconversion mainly proceeds as shown in **Figure 3.29**. Residual photoconversion may also occur from the anionic chromophore, possibly involving primed photoconversion as seen in Dendra-like PCFPs[97,98]. The green and red states of mEos4b are both prone to *cis/trans* isomerization, with the *trans* state having a pKa of >>10 (= negative RSFP), affecting the photoconversion kinetics[204] and causing long-lived blinks in single molecule expeirments (see e.g. **Figure 3.12**).

NMR experiments (**section 3.1.4.1**) revealed that the green state of mEos4b is heterogeous and forms two structurally distinct states (A and B), which differ from each other in the protonation status of E212 and the tautomeric state of H62. Detailed characterization revealed that the A/B equilibrium can be modulated by pH and by 405 nm light, and suggested that photoconversion mainly occurs from the A-state, while the B-state is more prone to bleaching. As a consequence of the different photophysical characteristics of the A- and B-states, the PCE of mEos4b decreases with increasing 405 nm light intenisties (mW/cm^2 range) due to increased population of the B-state resulting in increased bleaching. A/B partitioning is not observed in the red state (recent data not shown).

Given its high formation quantum yield (0.1-1%), long lifetime (~5 ms) and high light sensitivity[88,100], the triplet state is expected to play a central role in the photophysical behavior of mEos4b. We found that usage of high intensity 405 nm light (100 W/cm^2) decreases the PCE of mEos4b, which we

proposed is due to nonlinear bleaching involving an intermediate state formed from the neutral chromophore (**section 3.1.3**). This intermediate state is expectedly the triplet state (or a down-stream state). Furthermore, the triplet state of the green anionic chromophore is likely the starting point of the formation of diverse dark/off-states causing blinking (Off_{488})[204] and fast fluorescence decay under continuous illumination (Off_T, **section 3.1.4.2**). Similairly in the red state, the triplet state expectedly presents an entance gate to various dark/off-states, including a 405 nm light sensitive off-state formed from the anionic chromophore (Off_{405}, **section 3.1.4.3.1**) and a 561 nm light sensitive off-state formed from the neutral chromophore ($Off_{neutral}$, **section 3.1.4.3.2**). Of note, every light absorbing state can enter the triplet state, but this is omitted from the model for simplicity.

Implication of the triplet state in the different processes described above raises a question, namely: 'is reexcitation of the triplet state benefical or harmful?' In some situations, reexcitation of the triplet state appears harmful, leading to bleaching[99,313] (in line with the nonlinear bleaching pathway from the green neutral chromophore). In other situation, however, excitation of the triplet state appears beneficial, promoting RISC thereby decreasing the triplet state lifetime and thus increasing the fluorescence signal and reducing the chance of bleaching via biochemical processes[99,100,311] (in line with **Figure 3.37A**). This dual effect of triplet state excitation may be partly explained by the broad absorption spectrum of the triplet state[99]. Assuming that reexcitation of the triplet state can lead to either bleaching or recovery by RISC, the effect of adding additional light depends on the ratio between the bleaching and RISC quantum yields[99]. This ratio is likely dependent on the used excitation wavelength, with higher energy wavelengths (e.g. 405 nm) favoring higher triplet excited states with a higher change of bleaching than lower energy wavelength (e.g. IR light)[99,459]. Additionally, different triplet states may intrinsically have different ratios between RISC and bleaching[99].

To validate that this tentative model can reproduce the diverse photophysical behaviors of mEos4b, I reproduced the model in SMIS and simulated its behavior under the various illumination conditions that were applied in this work. A detailed description of the design of the model can be found in **section 6.2**. Indeed, this model was able to reproduce qualitatively most behaviors. Key figures are shown in **Figure 4.3**, showing the dependence of the PCE on the applied 405 nm light power-density and the superior efficiency of 405 nm light in reducing the red state off-time durations. More simulations can be found in **section 6.2.4**. Altough most behaviors could be reproduced, the simulated data clearly deviate from the experimental data under certain conditions, notably in terms of green and red state bleaching (see **sections 6.2.4.2** and **6.2.4.4**), indicating that the model requires further refinement. In particular, estimation of the FISC ans RISC quantum yields and acquisition of the triplet state absorption spectra could greatly improve the model, as this could shed light on the precise roles of the different triplet states in the various bleaching pathways of mEos4b.

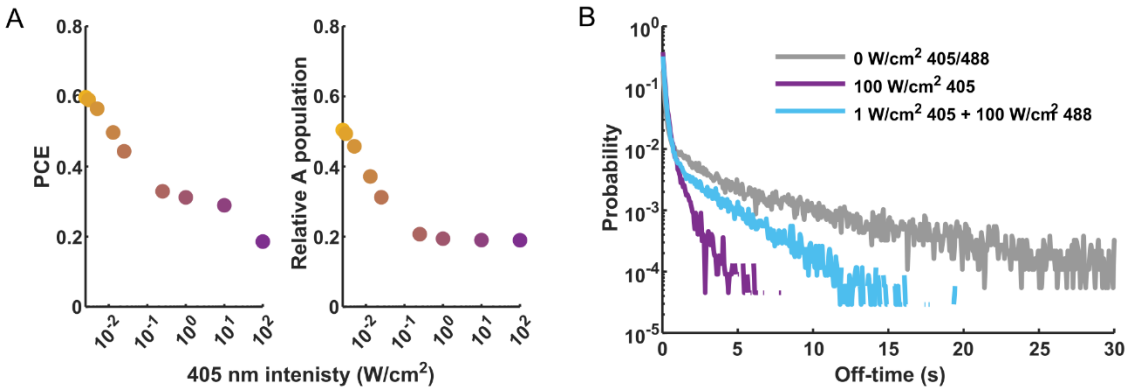

Figure 4.3 The proposed mEos4b model is able to reproduce most experimentally observed behaviors. *Simulations were perfomed in SMIS using the proposed model shown in* ***Figure 4.2*** *(for details see* ***section 6.2****). A) Dependence of the PCE and Green A-state population on the applied 405 nm light power density. Photoconversion was simulated under continous illumination with 405 nm light (2.5 mW/cm² – 100 W/cm²). The PCE is calculated as the cumulatative red state at the end of the simulation. B) Red state off-time reduction by 405 and 488 nm light. Single molecule blinking was simulated under alternating excitation with 500 W/cm² 561 nm light (70 ms) and 0-100 W/cm² 405 and 488 nm light (8 ms).*

To conclude, the photophysical behavior of mEos4b (and likely all other PTFPs) is extremely complicated, with a multitude of states giving rise to a vast variety of behaviors under the influence of the illumination and the environmental conditions. The work presented in this thesis contributes to our understanding of FP photophysics, but the model presented in **Figure 4.2** remains highly speculative. Nevertheless, it is clear that mEos4b is far from the ideal PCFP, displaying supoptimal properties, including green state heterogeneity and nonlinear bleaching. Having identified these unwanted properties, a next step would be to suppress them to boost PALM imaging. But how to do this?

4.3 How to optimize FP performance?

As explained in the introduction (see **section 1.6.4**) there are two strategies to improve the performance of FPs: introduce mutations or tune the experimental conditions. Both strategies have their strengths and drawbacks, and which strategy is most suitable to address a certain behavior depends on a variety of factors.

An unwanted property of both mEos4b and rsEGFP2 is that they display ground-state heterogeneity, with one of the states displaying suboptimal photophysical behavior compared to the other state (see **sections 3.1.4.1** and **3.1.5**). This property could potentially be addressed by mutagenesis, suppressing the suboptimal state. However, (semi-)rational protein design requires information about which residues to target. This presents a first problem, as we do not know (yet) the nature of the heterogeneity present in rsEGFP2. In mEos4b, we know that the protonation status of E212 and the tautomeric state of H62 underly the displayed heterogeinty, but we have no clue as to how to suppress this heterogeneity while preserving photoconversion. Our data show that mutation of either E212 or H62 can suppress the heterogeneity, but both residues are essential for photoconversion, so that this does not present a viable strategy.

The case of mEos4b brings up a fundamental question, namely: 'What is the limit of FP performance?' Recent papers report the discovery and development of super stable and bright FP variants, such as StayGold[35] and AausFP[307], indicating that we have not yet reached the limit of what FPs are capable of. These super FPs could potentially serve as starting point for the development of 'super PTFPs'. But the question remains: 'Can a PTFP be as stable as the most stable non-

transformable FP, or does the capability to undergo photoswitching/conversion inhertently come at the cost of increased flexibility and consequently reduced stability?' Besides the discovery of new FPs, there has been a dramatic progress in the field of deep learning, notably in the field of protein structure prediction with the release of Alphafold[460]. Given the large amount of known FPs with a wide-diversity of properties and the many FP structures that are available, deep learning could possibly make a significant contribution to the design of 'the' optimal PTFP. Of note, protein structure prediction software are already capable of predicting the formation of a chromophore in FPs[461]. Altough existing protein structure prediction software's are limited in their capability to predict the effects of mutations, combining the available FP sequences with their corresponding properties (brightness, stability, monomeric quality etc) and structures could enable to the identification of 'good' and 'bad' FP designs.

A practical concern for the development of new PCFPs is the lack a high-throughput screening platform, which is capable of screening for PTFP specific properties (notably at the single molecule level). The challenges for the development of such a platform are multifold. Firstly, a suitable immobilization platform, which is easily adaptable to different FPs, needs to be identified (see **section 3.1.2**). Collaborators are working on the development of a platform based on the SpyCatcher-SpyTag system, which could provide a suitable platform. Secondly, quantitative assays need to be developed to quantify SMLM specific characteristics, such as the photoconversion efficiency, which is not a straightforward task. Thirdly, the need for a high throughput screening system, such as a high NA microscope which can automatically screen 96-well plates, presents a final challenge.

Given all the difficulties associated with FPs, why not always using organic dyes? Organic dyes typically have a higher photon budget, are more photostable and are available in the far-red. Altough for many years FPs have been the preferred choice for live cell imaging, this trend is now changing with the development of self-labeling tags (e.g. Halo and SNAP) in combination with cell permeable dyes (see e.g.[462–464]). Because of these advances, organic dyes may be expected to replace FPs is more and more experiments. I do not think, however, that organic dyes will completely replace FPs, at least not in the nearby future. The reason for his being that the number of photo-transformable cell-permeable dyes is still limited, and that the usages of organic dyes comes at the cost of unspecific staining and increased sample preparation steps, which may hinder time-course experiments. It is also important to realise that organic dyes, like FPs, can display highly complex photophysical behaviors, which may interfer with imaging (see e.g.[436,465]). Therefore, I think it remains important to invest in the development of better performing FPs.

Besides mutagenesis, the performance of FPs can be optimized by tuning the experimental conditions. As discussed in detail above, the triplet state is expected to play a central role in the different photophysical behaviors of mEos4b, including non-linear bleaching of both the green and red states. Supression of triplet-state formation, or reduction of the triplet-state lifetime, would thus be expected to be of major benefit for PALM imaging. Given that triplet-state formation is an inherent property of fluorophores, this issue can likely not be solved by mutagenesis. Manipulation of the triplet state lifetime by tuning the experimental conditions, on the other hand, is possible and different approaches to do so are described in the literature, including the use of IR light[99,311,312] and triplet state quenchers. But which triplet state to target and how to do this without causing undesired side effects?

Using the proposed model of mEos4b, I investigated the possible effects of IR light on the PCE and red state photon budget of mEos4b. According to the proposed model, the PCE of mEos4b under illumination with high 405 nm light intenisties is limited by nonlinear bleaching via the triplet state of the green neutral chromophore. Simulations showed that, indeed, under such conditions the PCE can be improved by addition of IR light, reducing the lifetime of the involved triplet state (**Figure 4.4A**). It

should be noted, however, that the improvement that can be made by addition of IR light is restricted by the effects of green state heterogeneity. In the red state, triplet state formation lowers the number of detected photons per frame in SMLM and provides a starting point for bleaching. Simulations showed that addition of IR light could greatly improve the fluorescence intensity and photon budget of the red state (**Figure 4.4B**). These simulations provide a promising starting point for future work. To enable precise targeting of the triplet state, it will be important to measure the absorption spectra of the different relevant triplet states that are formed in mEos4b.

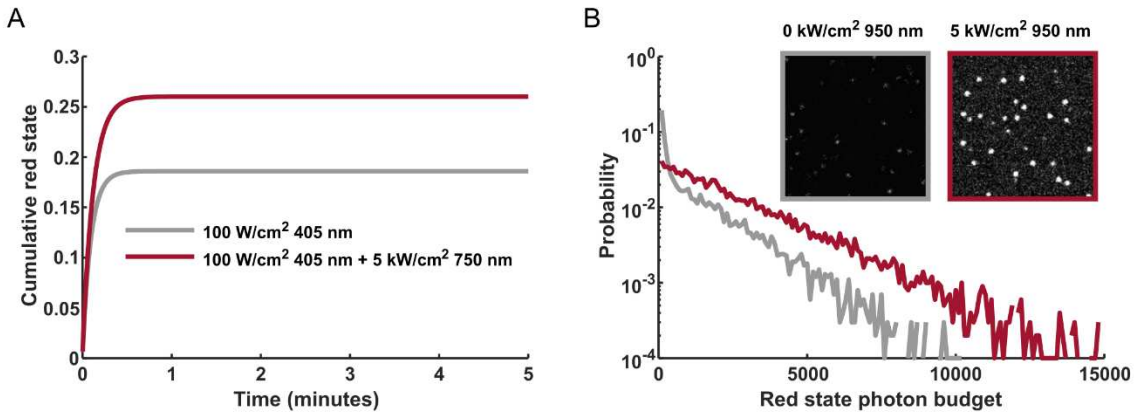

Figure 4.4 Boosting PALM imaging with IR light. *Simulations were performed in SMIS using the proposed photophysical model of mEos4b. A) Photoconversion was simulated under continuous illumination with 405 nm light (100 W/cm^2). Addition of 5 kW/cm^2 750 nm light (red curve) increased the PCE by reducing the lifetime of the triplet state formed from the green neutral chromophore, thereby reducing the change of nonlinear bleaching. B) Red state single molecule blinking was simulated under alternated illumination with 500 W/cm^2 561 nm light (70 ms) and 10 W/cm^2 405 nm light (8 ms). Addition of 5 kW/cm2 950 nm light (red curve) decreased the lifetime of the triplet state formed from the red anionic chromophore and thereby increased the fluorescence signal and the photon budget.*

Rane et al. proposed that the lifetime of the triplet state could be reduced by shifting the primary excitation wavelength to optimize RISC[100]. This strategy requires precise knowledge of the singlet and triplet state absorption spectra. To test the effect of this strategy, I run simulations with the hypothetical fluorophore model shown in **Figure 4.5A** using the experimentally obtained absorption spectra of EGFP[100]. Indeed, the usage of 512 nm light, instead of 488 nm light, enhanced the fluorescent signal, similairly as the addition of IR light (**Figure 4.5B**). Note that this simulation assumes that the ratio between RISC and bleaching is wavelength independent, which might not be true (see[99,459]), is which case this approach could be counterproductive and accerate bleaching. In addition to knowledge of the absorption spectra, this approach is dependent on the availability of high intensity lasers of a given wavelength. Tunable lasers are commercially available but are typically expensive.

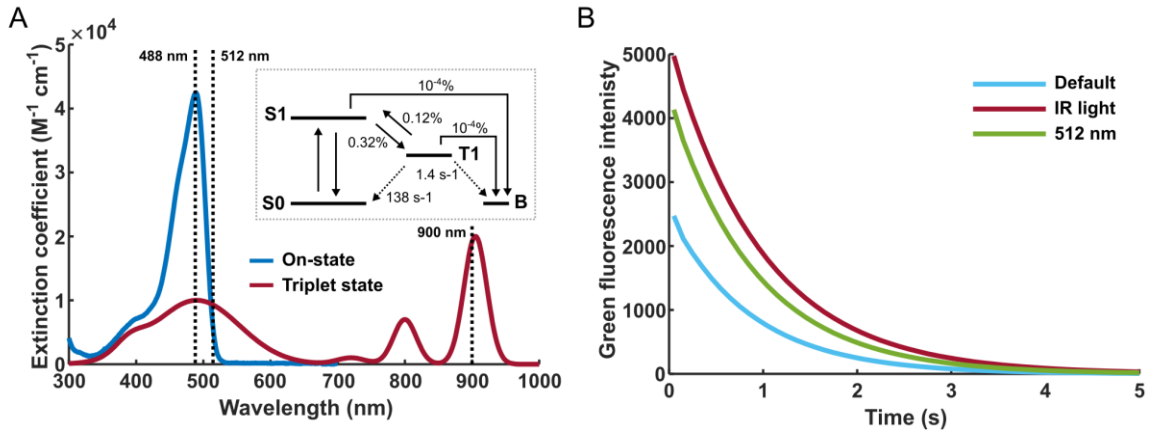

Figure 4.5 Reducing the triplet state life-time by shifting the primary excitation wavelength. *Ensemble simulations were perfomered in SMIS using the photophysical model depicted in A (EGFP based on Rane et al.). Default simulations were perfomed using a 100 ms frame time and 500 W/cm^2 488 nm light (single molceule conditions). To reduce the life-time of the triplet state, IR-light (900 nm at 1 kW/cm^2) was added, or the 488 nm light was replaced by 512 nm light (2444 W/cm^2, compensating for the reduced excitation of S0). A) Absorption spectra and photophysical model used for simulations. Excitation of the On-state (singlet state) can lead to triplet state (T1) formation (FISC, qy=0.32%) or bleaching in a T1 independent manner (qy=10^{-4}%). The triplet state can thermally recover (k=138 s^{-1}) but also has a ~1% chance to bleach in a light independent manner (k=1.4 s^{-1}). Excitation of the triplet state can lead to RISC (qy=0.12%), recovering the fluorescent state, or to bleaching (qy=10^{-4}) in a wavelength independend manner. B) Progression of the green fluorescence intensity.*

Another strategy that has been proposed to increase the fluorescent signal is the usage of pulsed excitation, which should allow thermal relaxation of the triplet state, preventing triplet state saturation and reexcitation[100,313]. SMIS, unfortunately, does not (yet) facilitate incorporation of real ps pulsed excitation so that I could not easily test this strategy. The potential of this approach remains to be tested.

Besides altered illumination schemes, triplet state quenchers could possibly be used to improve the performance of FPs for PALM imaging. Altough the accessibility of the FP chromophore for triplet state quenchers could be questioned because of the surrounding protein barrel, FPs do display a strong sensitivity to their redox environment (see e.g. [112,143–147]), suggesting that addition of triplet state quenchers could exert an effect on the chromophore. A possible strategy could be to attach the quencher directly to the protein barrel as was proposed by Henrikus et al[293], similairly of the design of self-healing organic dyes[466].

To conclude, optimizing the perfomance of FPs is not a straightforward task. Both the development of new PTFPs and the optimization of experimental designs face significant challenges. Progress at the protein level is probably still possible, but likely requires the development of a high troughput screening pipeline. In addition to new FPs, PALM-imaging could benefit from strategies to reduce of the triplet state lifetime, such as the use IR-light or triplet state quenchers. Obtaining the absorption spectra of the different triplet states of mEos4b (or any other relevant PTFPs) should therefore have a high priority in future work. A difficulty that may arise is that the different triplet states might not be effectifely repressed using the same IR-wavelength or the same quencher. In this situation, one would have to choose which triplet state to target, for example the green neutral state to increase the PCE, or the red anionic state to increase the red photon budget. Alternatively, it might be possible to target multple triplet states simultaneously using a combination of quenchers and light. Another potential problem that could arise is that targeting one triplet state might have a negative effect on another state (see **Figure 3.37**). This remains to be investigated.

4.4 A biological application of sptPALM: putting the theory into practice

Remodeling of the nucleoid architecture is a common stress-response in bacteria but the molecular mechanisms driving this reorganization remain incompletely understood. Using a combination of confocal microscopy and sptPALM, we revealed that nucleoid remodeling is differently regulated in cells entering stationary phase than in cells exposed to UVC light (**section 3.2**). In addition to this biological finding, we found that in depth analysis of the sptPALM data was complicated by a high cell-to-cell variability, especially after irradiation, and strong confinement of HU-mEos4b in the nucleoid, hindering the extraction of diffusion coefficients. The challenge presented by the high cell-to-cell variability could probably benefit from recent advances in deep learning to segment and classify the cells based on their cell and nucleoid morphology in an automated way (e.g.[451,452]). By simulations we showed that confinement creates a heterogeneity in the apparent diffusion of molecules, which can bias the estimation of the number of diffusive populations, their relative populations and diffusion coefficients. This finding should not discourage the application of sptPALM in bacteria but should be taken into account in the analysis and interpretation of the spt data.

The aim of the photophysical studies was to inform the design of optimized imaging schemes for quantitative PALM experiments, building on previous work from the lab[217] showing that application of 488 nm light can boost sptPALM imaging. Unfortunately, during my thesis I was not able to apply such optimized imaging schemes, partly due to limited flexibility of the imaging software used to control the microscope and lasers (Abbelight set-up, see **section 2.5.1**). Nevertheless, the photophysical findings presented in the manuscript could maybe be applied in future work to improve sptPALM imaging. In terms of photophysics, sptPALM is mainly limited by poor photostability of the photoconverted state, resulting in short and disrupted tracks. In this work, we showed that the apparent brightness of the green, and likely also the red, state of mEos4b is limited due to the formation of a short-lived dark state (likely the triplet or a down stream state, **section 3.1.4.2**). If formation of the dark state could be suppressed, this would enhance the apparent brightness of mEos4b, which would lower the required laser power and could increase the average track length and reduce potential phototoxic effects.

4.5 What we can and cannot learn from simulations

Both the photophysical and sptPALM studies in this manuscript have been supported by simulations, using a simulation software recently developed in the lab (SMIS)[266]. Simulations provide a valuable addition to experimental work. The high complexity of fluorophore models makes it difficult to predict the behavior of the model without simulating it (see e.g. **sections 3.1.4.1** and **3.1.5**). In this context, simulations enforce the design of precise models and enable the identification of weaknesses and inaccuracies in proposed models. In addition, simulations also present a powerful tool to investigate the effects of photophysics on (quantitative) PALM experiments and to test the accuracy of analysis pipelines. For example, we made use of simulations to investigate the effect of long-lived blinks on molecular counting (**section 3.1.3.1**) and to investigate the effect of confinement on the extraction of diffusion coefficients from spt experiments (**section 3.2.2.1**).

However, it is important to be aware of the limitations of simulations, as simulations rarely truly replicate reality. Differences between simulations and reality might come from limitations of the simulation software, for example SMIS is not able to simulate the ensemble behavior of fluorophores with a fixed dipole orientation and is not always able to implement the highly complex and customized imaging schemes used in experiments (see **section 3.1.5**). In addition, PTFPs are highly sensitive to their environment, which may be difficult or impossible to incorporate into simulations. It is important to know where the weaknesses of a simulation lay because these can provide a misleading view of reality. For example, simulating sptPALM without motion blur ('subframe

diffusion' is 'off' in SMIS) would give the idea that JD analysis is not affected by temporal averaging. Another difficulty of simulating FP photophysics is that all states and transitions have to be quantitatively specified, while the absoption spectra, extinction coefficients, thermal rates and phototransformation quantum yields are often unknown. As a consequence, most simulations contain, at least a few, assumptions and guesses. Therefore, care should be taken when using a photophysical model to predict how a fluorophore would behave under unknown conditions, because a model might correctly reproduce observed behaviors under certain experimental conditions, but incorrectly predict behaviors under other conditions due to imprecisions in the model.

Despite all the limitations, I think that simulations provide a valuable tool in development of photophysical models and the analysis pipelines for quantitative PALM. Altough simulations cannot say whether a model is correct, they allow to narrow down the possibilities and to identify problems in existing models. Recently developed simulation software, such as SMIS, provide an accessible platform for non-simulation-specialist to perform a variety of complex simulations to support experimental work.

4.6 Conclusion

The wide-spread application of quantitative PALM techniques is limited by the complex photophysical behaviors of the employed fluorophores and the need for sophisticated analyses. My PhD work contributes to a more in depth understanding of FP photophysics, which may inform the design of optimized imaging schemes and the development of better performing FPs. Many challenges, however, remain for the progress and implementation of such developments as illustrated in **Figure 4.1**, stressing the need for tight collaborations between molecular and structural biologist, imaging experts and hardware and software engineers. In addition, this thesis highlights the value of sptPALM for the study of bacteria but also identifies weaknesses in current analysis pipelines that may lead to erroneous data interpretation. Finally, the value of simulations for qPALM imaging is highlighted troughout this thesis, showcasing a variety of questions that can be addressed by simulations.

5 Bibliography

(1) Chalfie, M.; Tu, Y.; Euskirchen, G.; Ward, W. W.; Prasher, D. C. Green Fluorescent Protein as a Marker for Gene Expression. *Science* **1994**, *263* (5148), 802–805. https://doi.org/10.1126/science.8303295.
(2) Swaminathan, S. GFP: The Green Revolution. *Nat. Cell Biol.* **2009**, *11* (1), S20–S20. https://doi.org/10.1038/ncb1953.
(3) Myšková, J.; Rybakova, O.; Brynda, J.; Khoroshyy, P.; Bondar, A.; Lazar, J. Directionality of Light Absorption and Emission in Representative Fluorescent Proteins. *Proc. Natl. Acad. Sci.* **2020**, *117* (51), 32395–32401. https://doi.org/10.1073/pnas.2017379117.
(4) Avilov, S.; Berardozzi, R.; Gunewardene, M. S.; Adam, V.; Hess, S. T.; Bourgeois, D. In Cellulo Evaluation of Phototransformation Quantum Yields in Fluorescent Proteins Used As Markers for Single-Molecule Localization Microscopy. *PLoS ONE* **2014**, *9* (6), e98362. https://doi.org/10.1371/journal.pone.0098362.
(5) Acharya, A.; Bogdanov, A. M.; Grigorenko, B. L.; Bravaya, K. B.; Nemukhin, A. V.; Lukyanov, K. A.; Krylov, A. I. Photoinduced Chemistry in Fluorescent Proteins: Curse or Blessing? *Chem. Rev.* **2017**, *117* (2), 758–795. https://doi.org/10.1021/acs.chemrev.6b00238.
(6) Chattoraj, M.; King, B. A.; Bublitz, G. U.; Boxer, S. G. Ultra-Fast Excited State Dynamics in Green Fluorescent Protein: Multiple States and Proton Transfer. *Proc. Natl. Acad. Sci. U. S. A.* **1996**, *93* (16), 8362–8367.
(7) Hou, Y.-N.; Ding, W.-L.; Jiang, X.-X.; Hu, J.-L.; Tan, Z.-Z.; Zhao, K.-H. New Far-Red and Near-Infrared Fluorescent Phycobiliproteins with Excellent Brightness and Photostability. *ChemBioChem* **2022**, *23* (18), e202200267. https://doi.org/10.1002/cbic.202200267.
(8) Hall, C.; von Grabowiecki, Y.; Pearce, S. P.; Dive, C.; Bagley, S.; Muller, P. a. J. IRFP (near-Infrared Fluorescent Protein) Imaging of Subcutaneous and Deep Tissue Tumours in Mice Highlights Differences between Imaging Platforms. *Cancer Cell Int.* **2021**, *21* (1), 247. https://doi.org/10.1186/s12935-021-01918-8.
(9) Matlashov, M. E.; Shcherbakova, D. M.; Alvelid, J.; Baloban, M.; Pennacchietti, F.; Shemetov, A. A.; Testa, I.; Verkhusha, V. V. A Set of Monomeric Near-Infrared Fluorescent Proteins for Multicolor Imaging across Scales. *Nat. Commun.* **2020**, *11* (1), 239. https://doi.org/10.1038/s41467-019-13897-6.
(10) Kwon, J.; Park, J.-S.; Kang, M.; Choi, S.; Park, J.; Kim, G. T.; Lee, C.; Cha, S.; Rhee, H.-W.; Shim, S.-H. Bright Ligand-Activatable Fluorescent Protein for High-Quality Multicolor Live-Cell Super-Resolution Microscopy. *Nat. Commun.* **2020**, *11* (1), 273. https://doi.org/10.1038/s41467-019-14067-4.
(11) Grimm, J. B.; English, B. P.; Choi, H.; Muthusamy, A. K.; Mehl, B. P.; Dong, P.; Brown, T. A.; Lippincott-Schwartz, J.; Liu, Z.; Lionnet, T.; Lavis, L. D. Bright Photoactivatable Fluorophores for Single-Molecule Imaging. *Nat. Methods* **2016**, *13* (12), 985–988. https://doi.org/10.1038/nmeth.4034.
(12) Frei, M. S.; Hoess, P.; Lampe, M.; Nijmeijer, B.; Kueblbeck, M.; Ellenberg, J.; Wadepohl, H.; Ries, J.; Pitsch, S.; Reymond, L.; Johnsson, K. Photoactivation of Silicon Rhodamines via a Light-Induced Protonation. *Nat. Commun.* **2019**, *10* (1), 4580. https://doi.org/10.1038/s41467-019-12480-3.
(13) Hamers-Casterman, C.; Atarhouch, T.; Muyldermans, S.; Robinson, G.; Hammers, C.; Songa, E. B.; Bendahman, N.; Hammers, R. Naturally Occurring Antibodies Devoid of Light Chains. *Nature* **1993**, *363* (6428), 446–448. https://doi.org/10.1038/363446a0.
(14) Woodman, R.; Yeh, J. T.-H.; Laurenson, S.; Ferrigno, P. K. Design and Validation of a Neutral Protein Scaffold for the Presentation of Peptide Aptamers. *J. Mol. Biol.* **2005**, *352* (5), 1118–1133. https://doi.org/10.1016/j.jmb.2005.08.001.
(15) Ellington, A. D.; Szostak, J. W. In Vitro Selection of RNA Molecules That Bind Specific Ligands. *Nature* **1990**, *346* (6287), 818–822. https://doi.org/10.1038/346818a0.

(16) Gautier, A.; Juillerat, A.; Heinis, C.; Corrêa, I. R.; Kindermann, M.; Beaufils, F.; Johnsson, K. An Engineered Protein Tag for Multiprotein Labeling in Living Cells. *Chem. Biol.* **2008**, *15* (2), 128–136. https://doi.org/10.1016/j.chembiol.2008.01.007.
(17) Los, G. V.; Encell, L. P.; McDougall, M. G.; Hartzell, D. D.; Karassina, N.; Zimprich, C.; Wood, M. G.; Learish, R.; Ohana, R. F.; Urh, M.; Simpson, D.; Mendez, J.; Zimmerman, K.; Otto, P.; Vidugiris, G.; Zhu, J.; Darzins, A.; Klaubert, D. H.; Bulleit, R. F.; Wood, K. V. HaloTag: A Novel Protein Labeling Technology for Cell Imaging and Protein Analysis. *ACS Chem. Biol.* **2008**, *3* (6), 373–382. https://doi.org/10.1021/cb800025k.
(18) Grimm, J. B.; English, B. P.; Chen, J.; Slaughter, J. P.; Zhang, Z.; Revyakin, A.; Patel, R.; Macklin, J. J.; Normanno, D.; Singer, R. H.; Lionnet, T.; Lavis, L. D. A General Method to Improve Fluorophores for Live-Cell and Single-Molecule Microscopy. *Nat. Methods* **2015**, *12* (3), 244–250, 3 p following 250. https://doi.org/10.1038/nmeth.3256.
(19) Plass, T.; Milles, S.; Koehler, C.; Schultz, C.; Lemke, E. A. Genetically Encoded Copper-Free Click Chemistry. *Angew. Chem. Int. Ed.* **2011**, *50* (17), 3878–3881. https://doi.org/10.1002/anie.201008178.
(20) Sliogeryte, K.; Thorpe, S. D.; Wang, Z.; Thompson, C. L.; Gavara, N.; Knight, M. M. Differential Effects of LifeAct-GFP and Actin-GFP on Cell Mechanics Assessed Using Micropipette Aspiration. *J. Biomech.* **2016**, *49* (2), 310–317. https://doi.org/10.1016/j.jbiomech.2015.12.034.
(21) Riedl, J.; Crevenna, A. H.; Kessenbrock, K.; Yu, J. H.; Neukirchen, D.; Bista, M.; Bradke, F.; Jenne, D.; Holak, T. A.; Werb, Z.; Sixt, M.; Wedlich-Soldner, R. Lifeact: A Versatile Marker to Visualize F-Actin. *Nat. Methods* **2008**, *5* (7), 605. https://doi.org/10.1038/nmeth.1220.
(22) Resch-Genger, U.; Grabolle, M.; Cavaliere-Jaricot, S.; Nitschke, R.; Nann, T. Quantum Dots versus Organic Dyes as Fluorescent Labels. *Nat. Methods* **2008**, *5* (9), 763–775. https://doi.org/10.1038/nmeth.1248.
(23) Howarth, M.; Liu, W.; Puthenveetil, S.; Zheng, Y.; Marshall, L. F.; Schmidt, M. M.; Wittrup, K. D.; Bawendi, M. G.; Ting, A. Y. Monovalent, Reduced-Size Quantum Dots for Imaging Receptors on Living Cells. *Nat. Methods* **2008**, *5* (5), 397–399. https://doi.org/10.1038/nmeth.1206.
(24) Farlow, J.; Seo, D.; Broaders, K. E.; Taylor, M. J.; Gartner, Z. J.; Jun, Y. Formation of Targeted Monovalent Quantum Dots by Steric Exclusion. *Nat. Methods* **2013**, *10* (12), 1203–1205. https://doi.org/10.1038/nmeth.2682.
(25) Francis, J. E.; Mason, D.; Lévy, R. Evaluation of Quantum Dot Conjugated Antibodies for Immunofluorescent Labelling of Cellular Targets. *Beilstein J. Nanotechnol.* **2017**, *8*, 1238–1249. https://doi.org/10.3762/bjnano.8.125.
(26) Urban, J. M.; Chiang, W.; Hammond, J. W.; Cogan, N. M. B.; Litzburg, A.; Burke, R.; Stern, H. A.; Gelbard, H. A.; Nilsson, B. L.; Krauss, T. D. Quantum Dots for Improved Single-Molecule Localization Microscopy. *J. Phys. Chem. B* **2021**, *125* (10), 2566–2576. https://doi.org/10.1021/acs.jpcb.0c11545.
(27) Liu, H.-Y.; Wang, Z.-G.; Liu, S.-L.; Pang, D.-W. Single-Virus Tracking with Quantum Dots in Live Cells. *Nat. Protoc.* **2023**, *18* (2), 458–489. https://doi.org/10.1038/s41596-022-00775-7.
(28) Bouzigues, C.; Lévi, S.; Triller, A.; Dahan, M. Single Quantum Dot Tracking of Membrane Receptors. *Methods Mol. Biol. Clifton NJ* **2007**, *374*, 81–91. https://doi.org/10.1385/1-59745-369-2:81.
(29) Follenius-Wund, A.; Bourotte, M.; Schmitt, M.; Iyice, F.; Lami, H.; Bourguignon, J.-J.; Haiech, J.; Pigault, C. Fluorescent Derivatives of the GFP Chromophore Give a New Insight into the GFP Fluorescence Process. *Biophys. J.* **2003**, *85* (3), 1839–1850.
(30) Kummer, A. D.; Kompa, C.; Niwa, H.; Hirano, T.; Kojima, S.; Michel-Beyerle, M. E. Viscosity-Dependent Fluorescence Decay of the GFP Chromophore in Solution Due to Fast Internal Conversion. *J. Phys. Chem. B* **2002**, *106* (30), 7554–7559. https://doi.org/10.1021/jp014713v.
(31) Yanushevich, Y. G.; Staroverov, D. B.; Savitsky, A. P.; Fradkov, A. F.; Gurskaya, N. G.; Bulina, M. E.; Lukyanov, K. A.; Lukyanov, S. A. A Strategy for the Generation of Non-Aggregating Mutants of Anthozoa Fluorescent Proteins. *FEBS Lett.* **2002**, *511* (1–3), 11–14. https://doi.org/10.1016/S0014-5793(01)03263-X.

(32) Costantini, L. M.; Fossati, M.; Francolini, M.; Snapp, E. L. Assessing the Tendency of Fluorescent Proteins to Oligomerize under Physiologic Conditions. *Traffic Cph. Den.* **2012**, *13* (5), 643–649. https://doi.org/10.1111/j.1600-0854.2012.01336.x.
(33) Baird, G. S.; Zacharias, D. A.; Tsien, R. Y. Biochemistry, Mutagenesis, and Oligomerization of DsRed, a Red Fluorescent Protein from Coral. *Proc. Natl. Acad. Sci. U. S. A.* **2000**, *97* (22), 11984–11989.
(34) Shaner, N. C.; Campbell, R. E.; Steinbach, P. A.; Giepmans, B. N. G.; Palmer, A. E.; Tsien, R. Y. Improved Monomeric Red, Orange and Yellow Fluorescent Proteins Derived from Discosoma Sp. Red Fluorescent Protein. *Nat. Biotechnol.* **2004**, *22* (12), 1567–1572. https://doi.org/10.1038/nbt1037.
(35) Hirano, M.; Ando, R.; Shimozono, S.; Sugiyama, M.; Takeda, N.; Kurokawa, H.; Deguchi, R.; Endo, K.; Haga, K.; Takai-Todaka, R.; Inaura, S.; Matsumura, Y.; Hama, H.; Okada, Y.; Fujiwara, T.; Morimoto, T.; Katayama, K.; Miyawaki, A. A Highly Photostable and Bright Green Fluorescent Protein. *Nat. Biotechnol.* **2022**, *40* (7), 1132–1142. https://doi.org/10.1038/s41587-022-01278-2.
(36) Nienhaus, G. U.; Nienhaus, K.; Hölzle, A.; Ivanchenko, S.; Renzi, F.; Oswald, F.; Wolff, M.; Schmitt, F.; Röcker, C.; Vallone, B.; Weidemann, W.; Heilker, R.; Nar, H.; Wiedenmann, J. Photoconvertible Fluorescent Protein EosFP: Biophysical Properties and Cell Biology Applications. *Photochem. Photobiol.* **2006**, *82* (2), 351–358. https://doi.org/10.1562/2005-05-19-RA-533.
(37) Kimata, Y.; Iwaki, M.; Lim, C. R.; Kohno, K. A Novel Mutation Which Enhances the Fluorescence of Green Fluorescent Protein at High Temperatures. *Biochem. Biophys. Res. Commun.* **1997**, *232* (1), 69–73. https://doi.org/10.1006/bbrc.1997.6235.
(38) McKinney, S. A.; Murphy, C. S.; Hazelwood, K. L.; Davidson, M. W.; Looger, L. L. A Bright and Photostable Photoconvertible Fluorescent Protein for Fusion Tags. *Nat. Methods* **2009**, *6* (2), 131–133. https://doi.org/10.1038/nmeth.1296.
(39) Costantini, L. M.; Baloban, M.; Markwardt, M. L.; Rizzo, M. A.; Guo, F.; Verkhusha, V. V.; Snapp, E. L. A Palette of Fluorescent Proteins Optimized for Diverse Cellular Environments. *Nat. Commun.* **2015**, *6* (1), 7670. https://doi.org/10.1038/ncomms8670.
(40) El Khatib, M.; Martins, A.; Bourgeois, D.; Colletier, J.-P.; Adam, V. Rational Design of Ultrastable and Reversibly Photoswitchable Fluorescent Proteins for Super-Resolution Imaging of the Bacterial Periplasm. *Sci. Rep.* **2016**, *6*, 18459. https://doi.org/10.1038/srep18459.
(41) Kaberniuk, A. A.; Mohr, M. A.; Verkhusha, V. V.; Snapp, E. L. MoxMaple3: A Photoswitchable Fluorescent Protein for PALM and Protein Highlighting in Oxidizing Cellular Environments. *Sci. Rep.* **2018**, *8* (1), 14738. https://doi.org/10.1038/s41598-018-32955-5.
(42) Kaberniuk, A. A.; Morano, N. C.; Verkhusha, V. V.; Snapp, E. L. MoxDendra2: An Inert Photoswitchable Protein for Oxidizing Environments. *Chem. Commun.* **2017**, *53* (13), 2106–2109. https://doi.org/10.1039/C6CC09997A.
(43) Shaner, N. C.; Lin, M. Z.; McKeown, M. R.; Steinbach, P. A.; Hazelwood, K. L.; Davidson, M. W.; Tsien, R. Y. Improving the Photostability of Bright Monomeric Orange and Red Fluorescent Proteins. *Nat. Methods* **2008**, *5* (6), 545–551. https://doi.org/10.1038/nmeth.1209.
(44) Roldán-Salgado, A.; Muslinkina, L.; Pletnev, S.; Pletneva, N.; Pletnev, V.; Gaytán, P. A Novel Violet Fluorescent Protein Contains a Unique Oxidized Tyrosine as the Simplest Chromophore Ever Reported in Fluorescent Proteins. *Protein Sci. Publ. Protein Soc.* **2022**, *31* (3), 688–700. https://doi.org/10.1002/pro.4265.
(45) Roldán-Salgado, A.; Sánchez-Barreto, C.; Gaytán, P. LanFP10-A, First Functional Fluorescent Protein Whose Chromophore Contains the Elusive Mutation G67A. *Gene* **2016**, *592* (2), 281–290. https://doi.org/10.1016/j.gene.2016.07.026.
(46) Muslinkina, L.; Roldán-Salgado, A.; Gaytán, P.; Juárez-González, V. R.; Rudiño, E.; Pletneva, N.; Pletnev, V.; Dauter, Z.; Pletnev, S. Structural Factors Enabling Successful GFP-Like Proteins with Alanine as the Third Chromophore-Forming Residue. *J. Mol. Biol.* **2019**, *431* (7), 1397–1408. https://doi.org/10.1016/j.jmb.2019.02.013.
(47) Wang, N.; Wang, L. Acid-Brightening Fluorescent Protein (AbFP) for Imaging Acidic Vesicles and Organelles. *Methods Enzymol.* **2020**, *639*, 167–189. https://doi.org/10.1016/bs.mie.2020.04.013.

(48) Auhim, H. S.; Grigorenko, B. L.; Harris, T. K.; Aksakal, O. E.; Polyakov, I. V.; Berry, C.; Gomes, G. dos P.; Alabugin, I. V.; Rizkallah, P. J.; Nemukhin, A. V.; Jones, D. D. Stalling Chromophore Synthesis of the Fluorescent Protein Venus Reveals the Molecular Basis of the Final Oxidation Step. *Chem. Sci.* **2021**, *12* (22), 7735–7745. https://doi.org/10.1039/D0SC06693A.
(49) Rosenow, M. A.; Huffman, H. A.; Phail, M. E.; Wachter, R. M. The Crystal Structure of the Y66L Variant of Green Fluorescent Protein Supports a Cyclization−Oxidation−Dehydration Mechanism for Chromophore Maturation,. *Biochemistry* **2004**, *43* (15), 4464–4472. https://doi.org/10.1021/bi0361315.
(50) Grigorenko, B. L.; Krylov, A. I.; Nemukhin, A. V. Molecular Modeling Clarifies the Mechanism of Chromophore Maturation in the Green Fluorescent Protein. *J. Am. Chem. Soc.* **2017**, *139* (30), 10239–10249. https://doi.org/10.1021/jacs.7b00676.
(51) Sniegowski, J. A.; Lappe, J. W.; Patel, H. N.; Huffman, H. A.; Wachter, R. M. Base Catalysis of Chromophore Formation in Arg96 and Glu222 Variants of Green Fluorescent Protein*. *J. Biol. Chem.* **2005**, *280* (28), 26248–26255. https://doi.org/10.1074/jbc.M412327200.
(52) Strack, R. L.; Strongin, D. E.; Mets, L.; Glick, B. S.; Keenan, R. J. Chromophore Formation in DsRed Occurs by a Branched Pathway. *J. Am. Chem. Soc.* **2010**, *132* (24), 8496–8505. https://doi.org/10.1021/ja1030084.
(53) Zhang, L.; Patel, H. N.; Lappe, J. W.; Wachter, R. M. Reaction Progress of Chromophore Biogenesis in Green Fluorescent Protein. *J. Am. Chem. Soc.* **2006**, *128* (14), 4766–4772. https://doi.org/10.1021/ja0580439.
(54) Stepanenko, O. V.; Verkhusha, V. V.; Shavlovsky, M. M.; Kuznetsova, I. M.; Uversky, V. N.; Turoverov, K. K. Understanding the Role of Arg96 in Structure and Stability of Green Fluorescent Protein. *Proteins* **2008**, *73* (3), 539–551. https://doi.org/10.1002/prot.22089.
(55) Wood, T. I.; Barondeau, D. P.; Hitomi, C.; Kassmann, C. J.; Tainer, J. A.; Getzoff, E. D. Defining the Role of Arginine 96 in Green Fluorescent Protein Fluorophore Biosynthesis. *Biochemistry* **2005**, *44* (49), 16211–16220. https://doi.org/10.1021/bi051388j.
(56) Balleza, E.; Kim, J. M.; Cluzel, P. Systematic Characterization of Maturation Time of Fluorescent Proteins in Living Cells. *Nat. Methods* **2018**, *15* (1), 47–51. https://doi.org/10.1038/nmeth.4509.
(57) Liu, B.; Mavrova, S. N.; van den Berg, J.; Kristensen, S. K.; Mantovanelli, L.; Veenhoff, L. M.; Poolman, B.; Boersma, A. J. Influence of Fluorescent Protein Maturation on FRET Measurements in Living Cells. *ACS Sens.* **2018**, *3* (9), 1735–1742. https://doi.org/10.1021/acssensors.8b00473.
(58) Gadella, T. W. J.; van Weeren, L.; Stouthamer, J.; Hink, M. A.; Wolters, A. H. G.; Giepmans, B. N. G.; Aumonier, S.; Dupuy, J.; Royant, A. MScarlet3: A Brilliant and Fast-Maturing Red Fluorescent Protein. *Nat. Methods* **2023**, *20* (4), 541–545. https://doi.org/10.1038/s41592-023-01809-y.
(59) Muslinkina, L.; Pletnev, V. Z.; Pletneva, N. V.; Ruchkin, D. A.; Kolesov, D. V.; Bogdanov, A. M.; Kost, L. A.; Rakitina, T. V.; Agapova, Y. K.; Shemyakina, I. I.; Chudakov, D. M.; Pletnev, S. Two Independent Routes of Post-Translational Chemistry in Fluorescent Protein FusionRed. *Int. J. Biol. Macromol.* **2020**, *155*, 551–559. https://doi.org/10.1016/j.ijbiomac.2020.03.244.
(60) Subach, O. M.; Vlaskina, A. V.; Agapova, Y. K.; Nikolaeva, A. Y.; Anokhin, K. V.; Piatkevich, K. D.; Patrushev, M. V.; Boyko, K. M.; Subach, F. V. Blue-to-Red TagFT, MTagFT, MTsFT, and Green-to-FarRed MNeptusFT2 Proteins, Genetically Encoded True and Tandem Fluorescent Timers. *Int. J. Mol. Sci.* **2023**, *24* (4), 3279. https://doi.org/10.3390/ijms24043279.
(61) Subach, O. M.; Tashkeev, A.; Vlaskina, A. V.; Petrenko, D. E.; Gaivoronskii, F. A.; Nikolaeva, A. Y.; Ivashkina, O. I.; Anokhin, K. V.; Popov, V. O.; Boyko, K. M.; Subach, F. V. The MRubyFT Protein, Genetically Encoded Blue-to-Red Fluorescent Timer. *Int. J. Mol. Sci.* **2022**, *23* (6), 3208. https://doi.org/10.3390/ijms23063208.
(62) Subach, F. V.; Malashkevich, V. N.; Zencheck, W. D.; Xiao, H.; Filonov, G. S.; Almo, S. C.; Verkhusha, V. V. Photoactivation Mechanism of PAmCherry Based on Crystal Structures of the Protein in the Dark and Fluorescent States. *Proc. Natl. Acad. Sci.* **2009**, *106* (50), 21097–21102. https://doi.org/10.1073/pnas.0909204106.

(63) Petersen, J.; Wilmann, P. G.; Beddoe, T.; Oakley, A. J.; Devenish, R. J.; Prescott, M.; Rossjohn, J. The 2.0-Å Crystal Structure of EqFP611, a Far Red Fluorescent Protein from the Sea Anemone Entacmaea Quadricolor *. *J. Biol. Chem.* **2003**, *278* (45), 44626–44631. https://doi.org/10.1074/jbc.M307896200.
(64) Shinoda, H.; Ma, Y.; Nakashima, R.; Sakurai, K.; Matsuda, T.; Nagai, T. Acid-Tolerant Monomeric GFP from Olindias Formosa. *Cell Chem. Biol.* **2018**, *25* (3), 330-338.e7. https://doi.org/10.1016/j.chembiol.2017.12.005.
(65) Shinoda, H.; Lu, K.; Nakashima, R.; Wazawa, T.; Noguchi, K.; Matsuda, T.; Nagai, T. Acid-Tolerant Reversibly Switchable Green Fluorescent Protein for Super-Resolution Imaging under Acidic Conditions. *Cell Chem. Biol.* **2019**, *26* (10), 1469-1479.e6. https://doi.org/10.1016/j.chembiol.2019.07.012.
(66) Dong, J.; Abulwerdi, F.; Baldridge, A.; Kowalik, J.; Solntsev, K. M.; Tolbert, L. M. Isomerization in Fluorescent Protein Chromophores Involves Addition/Elimination. *J. Am. Chem. Soc.* **2008**, *130* (43), 14096–14098. https://doi.org/10.1021/ja803416h.
(67) Cranfill, P. J.; Sell, B. R.; Baird, M. A.; Allen, J. R.; Lavagnino, Z.; de Gruiter, H. M.; Kremers, G.-J.; Davidson, M. W.; Ustione, A.; Piston, D. W. Quantitative Assessment of Fluorescent Proteins. *Nat. Methods* **2016**, *13* (7), 557–562. https://doi.org/10.1038/nmeth.3891.
(68) Lambert, T. J. FPbase: A Community-Editable Fluorescent Protein Database. *Nat. Methods* **2019**, *16* (4), 277–278. https://doi.org/10.1038/s41592-019-0352-8.
(69) Tomosugi, W.; Matsuda, T.; Tani, T.; Nemoto, T.; Kotera, I.; Saito, K.; Horikawa, K.; Nagai, T. An Ultramarine Fluorescent Protein with Increased Photostability and PH Insensitivity. *Nat. Methods* **2009**, *6* (5), 351–353. https://doi.org/10.1038/nmeth.1317.
(70) Zarowny, L.; Clavel, D.; Johannson, R.; Duarte, K.; Depernet, H.; Dupuy, J.; Baker, H.; Brown, A.; Royant, A.; Campbell, R. E. Cyan Fluorescent Proteins Derived from MNeonGreen. *Protein Eng. Des. Sel. PEDS* **2022**, *35*, gzac004. https://doi.org/10.1093/protein/gzac004.
(71) Sugiura, K.; Nagai, T. Extension of the Short Wavelength Side of Fluorescent Proteins Using Hydrated Chromophores, and Its Application. *Commun. Biol.* **2022**, *5* (1), 1–6. https://doi.org/10.1038/s42003-022-04153-7.
(72) Ai, H.; Shaner, N. C.; Cheng, Z.; Tsien, R. Y.; Campbell, R. E. Exploration of New Chromophore Structures Leads to the Identification of Improved Blue Fluorescent Proteins. *Biochemistry* **2007**, *46* (20), 5904–5910. https://doi.org/10.1021/bi700199g.
(73) Drobizhev, M.; Callis, P. R.; Nifosì, R.; Wicks, G.; Stoltzfus, C.; Barnett, L.; Hughes, T. E.; Sullivan, P.; Rebane, A. Long- and Short-Range Electrostatic Fields in GFP Mutants: Implications for Spectral Tuning. *Sci. Rep.* **2015**, *5* (1), 13223. https://doi.org/10.1038/srep13223.
(74) Drobizhev, M.; Molina, R. S.; Callis, P. R.; Scott, J. N.; Lambert, G. G.; Salih, A.; Shaner, N. C.; Hughes, T. E. Local Electric Field Controls Fluorescence Quantum Yield of Red and Far-Red Fluorescent Proteins. *Front. Mol. Biosci.* **2021**, *8*.
(75) Jung, G.; Brockhinke, A.; Gensch, T.; Hötzer, B.; Schwedler, S.; Veettil, S. K. Fluorescence Lifetime of Fluorescent Proteins. In *Fluorescent Proteins I: From Understanding to Design*; Jung, G., Ed.; Springer Series on Fluorescence; Springer: Berlin, Heidelberg, 2012; pp 69–97. https://doi.org/10.1007/4243_2011_14.
(76) Bindels, D. S.; Haarbosch, L.; van Weeren, L.; Postma, M.; Wiese, K. E.; Mastop, M.; Aumonier, S.; Gotthard, G.; Royant, A.; Hink, M. A.; Gadella, T. W. J. MScarlet: A Bright Monomeric Red Fluorescent Protein for Cellular Imaging. *Nat. Methods* **2017**, *14* (1), 53–56. https://doi.org/10.1038/nmeth.4074.
(77) Mukherjee, S.; Hung, S.-T.; Douglas, N.; Manna, P.; Thomas, C.; Ekrem, A.; Palmer, A. E.; Jimenez, R. Engineering of a Brighter Variant of the FusionRed Fluorescent Protein Using Lifetime Flow Cytometry and Structure-Guided Mutations. *Biochemistry* **2020**, *59* (39), 3669–3682. https://doi.org/10.1021/acs.biochem.0c00484.
(78) Mukherjee, S.; Manna, P.; Hung, S.-T.; Vietmeyer, F.; Friis, P.; Palmer, A. E.; Jimenez, R. Directed Evolution of a Bright Variant of MCherry: Suppression of Nonradiative Decay by

Fluorescence Lifetime Selections. *J. Phys. Chem. B* **2022**, *126* (25), 4659–4668. https://doi.org/10.1021/acs.jpcb.2c01956.
(79) Mukherjee, S.; Jimenez, R. Photophysical Engineering of Fluorescent Proteins: Accomplishments and Challenges of Physical Chemistry Strategies. *J. Phys. Chem. B* **2022**, *126* (4), 735–750. https://doi.org/10.1021/acs.jpcb.1c05629.
(80) Goedhart, J.; von Stetten, D.; Noirclerc-Savoye, M.; Lelimousin, M.; Joosen, L.; Hink, M. A.; van Weeren, L.; Gadella, T. W. J.; Royant, A. Structure-Guided Evolution of Cyan Fluorescent Proteins towards a Quantum Yield of 93%. *Nat. Commun.* **2012**, *3* (1), 751. https://doi.org/10.1038/ncomms1738.
(81) Duwé, S.; De Zitter, E.; Gielen, V.; Moeyaert, B.; Vandenberg, W.; Grotjohann, T.; Clays, K.; Jakobs, S.; Van Meervelt, L.; Dedecker, P. Expression-Enhanced Fluorescent Proteins Based on Enhanced Green Fluorescent Protein for Super-Resolution Microscopy. *ACS Nano* **2015**, *9* (10), 9528–9541. https://doi.org/10.1021/acsnano.5b04129.
(82) Campbell, B.; Nabel, E.; Murdock, M.; Lao-Peregrin, C.; Tsoulfas, P.; Blackmore, M.; Lee, F.; Liston, C.; Morishita, H.; Petsko, G. MGreenLantern: A Bright Monomeric Fluorescent Protein with Rapid Expression and Cell Filling Properties for Neuronal Imaging. *Proc. Natl. Acad. Sci.* **2020**, *117*, 30710–30721. https://doi.org/10.1073/pnas.2000942117.
(83) Botman, D.; de Groot, D. H.; Schmidt, P.; Goedhart, J.; Teusink, B. In Vivo Characterisation of Fluorescent Proteins in Budding Yeast. *Sci. Rep.* **2019**, *9* (1), 2234. https://doi.org/10.1038/s41598-019-38913-z.
(84) Adam, V.; Berardozzi, R.; Byrdin, M.; Bourgeois, D. Phototransformable Fluorescent Proteins: Future Challenges. *Curr. Opin. Chem. Biol.* **2014**, *20*, 92–102. https://doi.org/10.1016/j.cbpa.2014.05.016.
(85) Mueller, F.; Morisaki, T.; Mazza, D.; McNally, J. G. Minimizing the Impact of Photoswitching of Fluorescent Proteins on FRAP Analysis. *Biophys. J.* **2012**, *102* (7), 1656–1665. https://doi.org/10.1016/j.bpj.2012.02.029.
(86) Duwé, S.; Dedecker, P. Optimizing the Fluorescent Protein Toolbox and Its Use. *Curr. Opin. Biotechnol.* **2019**, *58*, 183–191. https://doi.org/10.1016/j.copbio.2019.04.006.
(87) Dean, K. M.; Lubbeck, J. L.; Binder, J. K.; Schwall, L. R.; Jimenez, R.; Palmer, A. E. Analysis of Red-Fluorescent Proteins Provides Insight into Dark-State Conversion and Photodegradation. *Biophys. J.* **2011**, *101* (4), 961–969. https://doi.org/10.1016/j.bpj.2011.06.055.
(88) Byrdin, M.; Duan, C.; Bourgeois, D.; Brettel, K. A Long-Lived Triplet State Is the Entrance Gateway to Oxidative Photochemistry in Green Fluorescent Proteins. *J. Am. Chem. Soc.* **2018**, *140* (8), 2897–2905. https://doi.org/10.1021/jacs.7b12755.
(89) Duan, C.; Adam, V.; Byrdin, M.; Ridard, J.; Kieffer-Jaquinod, S.; Morlot, C.; Arcizet, D.; Demachy, I.; Bourgeois, D. Structural Evidence for a Two-Regime Photobleaching Mechanism in a Reversibly Switchable Fluorescent Protein. *J. Am. Chem. Soc.* **2013**, *135* (42), 15841–15850. https://doi.org/10.1021/ja406860e.
(90) Wang, S.; Chen, X.; Chang, L.; Xue, R.; Duan, H.; Sun, Y. GMars-Q Enables Long-Term Live-Cell Parallelized Reversible Saturable Optical Fluorescence Transitions Nanoscopy. *ACS Nano* **2016**, *10* (10), 9136–9144. https://doi.org/10.1021/acsnano.6b04254.
(91) Strack, R. L.; Hein, B.; Bhattacharyya, D.; Hell, S. W.; Keenan, R. J.; Glick, B. S. A Rapidly Maturing Far-Red Derivative of DsRed-Express2 for Whole-Cell Labeling. *Biochemistry* **2009**, *48* (35), 8279–8281. https://doi.org/10.1021/bi900870u.
(92) Wang, S.; Shuai, Y.; Sun, C.; Xue, B.; Hou, Y.; Su, X.; Sun, Y. Lighting Up Live Cells with Smart Genetically Encoded Fluorescence Probes from GMars Family. *ACS Sens.* **2018**, *3* (11), 2269–2277. https://doi.org/10.1021/acssensors.8b00449.
(93) Nienhaus, K.; Nienhaus, G. U. Photoswitchable Fluorescent Proteins: Do Not Always Look on the Bright Side. *ACS Nano* **2016**, *10* (10), 9104–9108. https://doi.org/10.1021/acsnano.6b06298.
(94) Xu, F.; Shi, D.-Q.; Lau, P.-M.; Lin, M. Z.; Bi, G.-Q. Excitation Wavelength Optimization Improves Photostability of ASAP-Family GEVIs. *Mol. Brain* **2018**, *11* (1), 32. https://doi.org/10.1186/s13041-018-0374-7.

(95) Fredj, A.; Pasquier, H.; Demachy, I.; Jonasson, G.; Levy, B.; Derrien, V.; Bousmah, Y.; Manoussaris, G.; Wien, F.; Ridard, J.; Erard, M.; Merola, F. The Single T65S Mutation Generates Brighter Cyan Fluorescent Proteins with Increased Photostability and PH Insensitivity. *PloS One* **2012**, *7* (11), e49149. https://doi.org/10.1371/journal.pone.0049149.
(96) Roy, A.; Field, M. J.; Adam, V.; Bourgeois, D. The Nature of Transient Dark States in a Photoactivatable Fluorescent Protein. *J. Am. Chem. Soc.* **2011**, *133* (46), 18586–18589. https://doi.org/10.1021/ja2085355.
(97) Mohr, M. A.; Kobitski, A. Yu.; Sabater, L. R.; Nienhaus, K.; Obara, C. J.; Lippincott-Schwartz, J.; Nienhaus, G. U.; Pantazis, P. Rational Engineering of Photoconvertible Fluorescent Proteins for Dual-Color Fluorescence Nanoscopy Enabled by a Triplet-State Mechanism of Primed Conversion. *Angew. Chem. Int. Ed.* **2017**, *56* (38), 11628–11633. https://doi.org/10.1002/anie.201706121.
(98) Turkowyd, B.; Balinovic, A.; Virant, D.; Carnero, H. G. G.; Caldana, F.; Endesfelder, M.; Bourgeois, D.; Endesfelder, U. A General Mechanism of Photoconversion of Green-to-Red Fluorescent Proteins Based on Blue and Infrared Light Reduces Phototoxicity in Live-Cell Single-Molecule Imaging. *Angew. Chem. Int. Ed Engl.* **2017**, *56* (38), 11634–11639. https://doi.org/10.1002/anie.201702870.
(99) Ringemann, C.; Schönle, A.; Giske, A.; von Middendorff, C.; Hell, S. W.; Eggeling, C. Enhancing Fluorescence Brightness: Effect of Reverse Intersystem Crossing Studied by Fluorescence Fluctuation Spectroscopy. *ChemPhysChem* **2008**, *9* (4), 612–624. https://doi.org/10.1002/cphc.200700596.
(100) Rane, L.; Wulffele, J.; Bourgeois, D.; Glushonkov, O.; Mantovanelli, A. M. R.; Zala, N.; Byrdin, M. Light-Induced Forward and Reverse Intersystem Crossing in Green Fluorescent Proteins at Cryogenic Temperatures. *J. Phys. Chem. B* **2023**, *127* (22), 5046–5054. https://doi.org/10.1021/acs.jpcb.3c02971.
(101) Subach, F. V.; Patterson, G. H.; Manley, S.; Gillette, J. M.; Lippincott-Schwartz, J.; Verkhusha, V. V. Photoactivatable MCherry for High-Resolution Two-Color Fluorescence Microscopy. *Nat. Methods* **2009**, *6* (2), 153–159. https://doi.org/10.1038/nmeth.1298.
(102) Patterson, G. H.; Lippincott-Schwartz, J. A Photoactivatable GFP for Selective Photolabeling of Proteins and Cells. *Science* **2002**, *297* (5588), 1873–1877. https://doi.org/10.1126/science.1074952.
(103) Henderson, J. N.; Gepshtein, R.; Heenan, J. R.; Kallio, K.; Huppert, D.; Remington, S. J. Structure and Mechanism of the Photoactivatable Green Fluorescent Protein. *J. Am. Chem. Soc.* **2009**, *131* (12), 4176–4177. https://doi.org/10.1021/ja808851n.
(104) Ren, H.; Yang, B.; Ma, C.; Hu, Y. S.; Wang, P. G.; Wang, L. Cysteine Sulfoxidation Increases the Photostability of Red Fluorescent Proteins. *ACS Chem. Biol.* **2016**, *11* (10), 2679–2684. https://doi.org/10.1021/acschembio.6b00579.
(105) Papadaki, S.; Wang, X.; Wang, Y.; Zhang, H.; Jia, S.; Liu, S.; Yang, M.; Zhang, D.; Jia, J.-M.; Köster, R. W.; Namikawa, K.; Piatkevich, K. D. Dual-Expression System for Blue Fluorescent Protein Optimization. *Sci. Rep.* **2022**, *12* (1), 10190. https://doi.org/10.1038/s41598-022-13214-0.
(106) Subach, O. M.; Patterson, G. H.; Ting, L.-M.; Wang, Y.; Condeelis, J. S.; Verkhusha, V. V. A Photoswitchable Orange-to-Far-Red Fluorescent Protein, PSmOrange. *Nat. Methods* **2011**, *8* (9), 771–777. https://doi.org/10.1038/nmeth.1664.
(107) Makarov, N. S.; Cirloganu, C.; Perry, J. W.; Lukyanov, K. A.; Solntsev, K. M. Steady-State and Time-Resolved Spectroscopic Studies of Green-to-Red Photoconversion of Fluorescent Protein Dendra2. *J. Photochem. Photobiol. Chem.* **2014**, *280*, 5–13. https://doi.org/10.1016/j.jphotochem.2014.02.001.
(108) Chudakov, D. M.; Verkhusha, V. V.; Staroverov, D. B.; Souslova, E. A.; Lukyanov, S.; Lukyanov, K. A. Photoswitchable Cyan Fluorescent Protein for Protein Tracking. *Nat. Biotechnol.* **2004**, *22* (11), 1435–1439. https://doi.org/10.1038/nbt1025.
(109) Chudakov, D. M.; Lukyanov, S.; Lukyanov, K. A. Tracking Intracellular Protein Movements Using Photoswitchable Fluorescent Proteins PS-CFP2 and Dendra2. *Nat. Protoc.* **2007**, *2* (8), 2024–2032. https://doi.org/10.1038/nprot.2007.291.

(110) Kremers, G.-J.; Hazelwood, K. L.; Murphy, C. S.; Davidson, M. W.; Piston, D. W. Photoconversion in Orange and Red Fluorescent Proteins. *Nat. Methods* **2009**, *6* (5), 355–358. https://doi.org/10.1038/nmeth.1319.
(111) Elowitz, M. B.; Surette, M. G.; Wolf, P.-E.; Stock, J.; Leibler, S. Photoactivation Turns Green Fluorescent Protein Red. *Curr. Biol.* **1997**, *7* (10), 809–812. https://doi.org/10.1016/S0960-9822(06)00342-3.
(112) Saha, R.; Verma, P. K.; Rakshit, S.; Saha, S.; Mayor, S.; Pal, S. K. Light Driven Ultrafast Electron Transfer in Oxidative Redding of Green Fluorescent Proteins. *Sci. Rep.* **2013**, *3* (1), 1580. https://doi.org/10.1038/srep01580.
(113) Bogdanov, A. M.; Mishin, A. S.; Yampolsky, I. V.; Belousov, V. V.; Chudakov, D. M.; Subach, F. V.; Verkhusha, V. V.; Lukyanov, S.; Lukyanov, K. A. Green Fluorescent Proteins Are Light-Induced Electron Donors. *Nat. Chem. Biol.* **2009**, *5* (7), 459–461. https://doi.org/10.1038/nchembio.174.
(114) Bidiuk, V. A.; Agaphonov, M. O.; Alexandrov, A. I. Modulation of Green to Red Photoconversion of GFP during Fluorescent Microscopy by Carbon Source and Oxygen Availability. *Yeast* **2021**, *38* (5), 295–301. https://doi.org/10.1002/yea.3543.
(115) Goedhart, J.; Vermeer, J. E. M.; Adjobo-Hermans, M. J. W.; Weeren, L. van; Jr, T. W. J. G. Sensitive Detection of P65 Homodimers Using Red-Shifted and Fluorescent Protein-Based FRET Couples. *PLOS ONE* **2007**, *2* (10), e1011. https://doi.org/10.1371/journal.pone.0001011.
(116) Mastop, M.; Bindels, D. S.; Shaner, N. C.; Postma, M.; Gadella, T. W. J.; Goedhart, J. Characterization of a Spectrally Diverse Set of Fluorescent Proteins as FRET Acceptors for MTurquoise2. *Sci. Rep.* **2017**, *7* (1), 11999. https://doi.org/10.1038/s41598-017-12212-x.
(117) Protasova, E. A.; Mishin, A. S.; Lukyanov, K. A.; Maksimov, E. G.; Bogdanov, A. M. Chromophore Reduction plus Reversible Photobleaching: How the MKate2 “Photoconversion” Works. *Photochem. Photobiol. Sci.* **2021**, *20* (6), 791–803. https://doi.org/10.1007/s43630-021-00060-8.
(118) Pletnev, V. Z.; Pletneva, N. V.; Sarkisyan, K. S.; Mishin, A. S.; Lukyanov, K. A.; Goryacheva, E. A.; Ziganshin, R. H.; Dauter, Z.; Pletnev, S. Structure of the Green Fluorescent Protein NowGFP with an Anionic Tryptophan-Based Chromophore. *Acta Crystallogr. D Biol. Crystallogr.* **2015**, *71* (Pt 8), 1699–1707. https://doi.org/10.1107/S1399004715010159.
(119) Kao, Y.-T.; Zhu, X.; Min, W. Protein-Flexibility Mediated Coupling between Photoswitching Kinetics and Surrounding Viscosity of a Photochromic Fluorescent Protein. *Proc. Natl. Acad. Sci.* **2012**, *109* (9), 3220–3225. https://doi.org/10.1073/pnas.1115311109.
(120) Morikawa, T. J.; Fujita, H.; Kitamura, A.; Horio, T.; Yamamoto, J.; Kinjo, M.; Sasaki, A.; Machiyama, H.; Yoshizawa, K.; Ichimura, T.; Imada, K.; Nagai, T.; Watanabe, T. M. Dependence of Fluorescent Protein Brightness on Protein Concentration in Solution and Enhancement of It. *Sci. Rep.* **2016**, *6* (1), 22342. https://doi.org/10.1038/srep22342.
(121) Pozzi, E. A.; Schwall, L. R.; Jimenez, R.; Weber, J. M. Pressure Induced Changes in the Fluorescence Behavior of Red Fluorescent Proteins. *J. Phys. Chem. B* **2012**, *116* (34), 10311–10316. https://doi.org/10.1021/jp306093h.
(122) Christou, N. E.; Giandoreggio-Barranco, K.; Ayala, I.; Glushonkov, O.; Adam, V.; Bourgeois, D.; Brutscher, B. Disentangling Chromophore States in a Reversibly Switchable Green Fluorescent Protein: Mechanistic Insights from NMR Spectroscopy. *J. Am. Chem. Soc.* **2021**, *143* (19), 7521–7530. https://doi.org/10.1021/jacs.1c02442.
(123) Oltrogge, L. M.; Wang, Q.; Boxer, S. G. Ground-State Proton Transfer Kinetics in Green Fluorescent Protein. *Biochemistry* **2014**, *53* (37), 5947–5957. https://doi.org/10.1021/bi500147n.
(124) Bosisio, C.; Quercioli, V.; Collini, M.; D’Alfonso, L.; Baldini, G.; Bettati, S.; Campanini, B.; Raboni, S.; Chirico, G. Protonation and Conformational Dynamics of GFP Mutants by Two-Photon Excitation Fluorescence Correlation Spectroscopy. *J. Phys. Chem. B* **2008**, *112* (29), 8806–8814. https://doi.org/10.1021/jp801164n.
(125) Haupts, U.; Maiti, S.; Schwille, P.; Webb, W. W. Dynamics of Fluorescence Fluctuations in Green Fluorescent Protein Observed by Fluorescence Correlation Spectroscopy. *Proc. Natl. Acad. Sci.* **1998**, *95* (23), 13573–13578. https://doi.org/10.1073/pnas.95.23.13573.

(126) Markwardt, M. L.; Kremers, G.-J.; Kraft, C. A.; Ray, K.; Cranfill, P. J. C.; Wilson, K. A.; Day, R. N.; Wachter, R. M.; Davidson, M. W.; Rizzo, M. A. An Improved Cerulean Fluorescent Protein with Enhanced Brightness and Reduced Reversible Photoswitching. *PloS One* **2011**, *6* (3), e17896. https://doi.org/10.1371/journal.pone.0017896.
(127) Merzlyak, E. M.; Goedhart, J.; Shcherbo, D.; Bulina, M. E.; Shcheglov, A. S.; Fradkov, A. F.; Gaintzeva, A.; Lukyanov, K. A.; Lukyanov, S.; Gadella, T. W. J.; Chudakov, D. M. Bright Monomeric Red Fluorescent Protein with an Extended Fluorescence Lifetime. *Nat. Methods* **2007**, *4* (7), 555–557. https://doi.org/10.1038/nmeth1062.
(128) Bizzarri, R.; Nifosì, R.; Abbruzzetti, S.; Rocchia, W.; Guidi, S.; Arosio, D.; Garau, G.; Campanini, B.; Grandi, E.; Ricci, F.; Viappiani, C.; Beltram, F. Green Fluorescent Protein Ground States: The Influence of a Second Protonation Site near the Chromophore,. *Biochemistry* **2007**, *46* (18), 5494–5504. https://doi.org/10.1021/bi602646r.
(129) Nienhaus, K.; Renzi, F.; Vallone, B.; Wiedenmann, J.; Nienhaus, G. U. Chromophore-Protein Interactions in the Anthozoan Green Fluorescent Protein AsFP499. *Biophys. J.* **2006**, *91* (11), 4210–4220. https://doi.org/10.1529/biophysj.106.087411.
(130) Gayda, S.; Nienhaus, K.; Nienhaus, G. U. Mechanistic Insights into Reversible Photoactivation in Proteins of the GFP Family. *Biophys. J.* **2012**, *103* (12), 2521–2531. https://doi.org/10.1016/j.bpj.2012.11.011.
(131) Nienhaus, K.; Renzi, F.; Vallone, B.; Wiedenmann, J.; Nienhaus, G. U. Exploring Chromophore−Protein Interactions in Fluorescent Protein CmFP512 from Cerianthus Membranaceus: X-Ray Structure Analysis and Optical Spectroscopy. *Biochemistry* **2006**, *45* (43), 12942–12953. https://doi.org/10.1021/bi060885c.
(132) Konen, T.; Stumpf, D.; Grotjohann, T.; Jansen, I.; Bossi, M.; Weber, M.; Jensen, N.; Hell, S. W.; Jakobs, S. The Positive Switching Fluorescent Protein Padron2 Enables Live-Cell Reversible Saturable Optical Linear Fluorescence Transitions (RESOLFT) Nanoscopy without Sequential Illumination Steps. *ACS Nano* **2021**, *15* (6), 9509–9521. https://doi.org/10.1021/acsnano.0c08207.
(133) Shen, Y.; Rosendale, M.; Campbell, R. E.; Perrais, D. PHuji, a PH-Sensitive Red Fluorescent Protein for Imaging of Exo- and Endocytosis. *J. Cell Biol.* **2014**, *207* (3), 419–432. https://doi.org/10.1083/jcb.201404107.
(134) Violot, S.; Carpentier, P.; Blanchoin, L.; Bourgeois, D. Reverse PH-Dependence of Chromophore Protonation Explains the Large Stokes Shift of the Red Fluorescent Protein MKeima. *J. Am. Chem. Soc.* **2009**, *131* (30), 10356–10357. https://doi.org/10.1021/ja903695n.
(135) Mahon, M. J. PHluorin2: An Enhanced, Ratiometric, PH-Sensitive Green Florescent Protein. *Adv. Biosci. Biotechnol. Print* **2011**, *2* (3), 132–137. https://doi.org/10.4236/abb.2011.23021.
(136) Miesenböck, G.; De Angelis, D. A.; Rothman, J. E. Visualizing Secretion and Synaptic Transmission with PH-Sensitive Green Fluorescent Proteins. *Nature* **1998**, *394* (6689), 192–195. https://doi.org/10.1038/28190.
(137) Kennis, J. T. M.; Larsen, D. S.; van Stokkum, I. H. M.; Vengris, M.; van Thor, J. J.; van Grondelle, R. Uncovering the Hidden Ground State of Green Fluorescent Protein. *Proc. Natl. Acad. Sci.* **2004**, *101* (52), 17988–17993. https://doi.org/10.1073/pnas.0404262102.
(138) Griesbeck, O.; Baird, G. S.; Campbell, R. E.; Zacharias, D. A.; Tsien, R. Y. Reducing the Environmental Sensitivity of Yellow Fluorescent Protein: MECHANISM AND APPLICATIONS*. *J. Biol. Chem.* **2001**, *276* (31), 29188–29194. https://doi.org/10.1074/jbc.M102815200.
(139) Salto, R.; Giron, M. D.; Puente-Muñoz, V.; Vilchez, J. D.; Espinar-Barranco, L.; Valverde-Pozo, J.; Arosio, D.; Paredes, J. M. New Red-Emitting Chloride-Sensitive Fluorescent Protein with Biological Uses. *ACS Sens.* **2021**, *6* (7), 2563–2573. https://doi.org/10.1021/acssensors.1c00094.
(140) Campbell, B. C.; Paez-Segala, M. G.; Looger, L. L.; Petsko, G. A.; Liu, C. F. Chemically Stable Fluorescent Proteins for Advanced Microscopy. *Nat. Methods* **2022**, *19* (12), 1612–1621. https://doi.org/10.1038/s41592-022-01660-7.
(141) Stepanenko, O. V.; Stepanenko, O. V.; Kuznetsova, I. M.; Verkhusha, V. V.; Turoverov, K. K. Sensitivity of Superfolder GFP to Ionic Agents. *PLOS ONE* **2014**, *9* (10), e110750. https://doi.org/10.1371/journal.pone.0110750.

(142) Tutol, J. N.; Kam, H. C.; Dodani, S. C. Identification of MNeonGreen as a PH-Dependent, Turn-On Fluorescent Protein Sensor for Chloride. *ChemBioChem* **2019**, *20* (14), 1759–1765. https://doi.org/10.1002/cbic.201900147.
(143) Endesfelder, U.; Malkusch, S.; Flottmann, B.; Mondry, J.; Liguzinski, P.; Verveer, P.; Heilemann, M. Chemically Induced Photoswitching of Fluorescent Probes-A General Concept for Super-Resolution Microscopy. *Mol. Basel Switz.* **2011**, *16*, 3106–3118. https://doi.org/10.3390/molecules16043106.
(144) Baldering, T. N.; Dietz, M. S.; Gatterdam, K.; Karathanasis, C.; Wieneke, R.; Tampé, R.; Heilemann, M. Synthetic and Genetic Dimers as Quantification Ruler for Single-Molecule Counting with PALM. *Mol. Biol. Cell* **2019**, *30* (12), 1369–1376. https://doi.org/10.1091/mbc.E18-10-0661.
(145) Winterflood, C. M.; Ewers, H. Single-Molecule Localization Microscopy Using MCherry. *ChemPhysChem* **2014**, *15* (16), 3447–3451. https://doi.org/10.1002/cphc.201402423.
(146) Cloin, B. M. C.; De Zitter, E.; Salas, D.; Gielen, V.; Folkers, G. E.; Mikhaylova, M.; Bergeler, M.; Krajnik, B.; Harvey, J.; Hoogenraad, C. C.; Van Meervelt, L.; Dedecker, P.; Kapitein, L. C. Efficient Switching of MCherry Fluorescence Using Chemical Caging. *Proc. Natl. Acad. Sci.* **2017**, *114* (27), 7013–7018. https://doi.org/10.1073/pnas.1617280114.
(147) Berardozzi, R.; Adam, V.; Martins, A.; Bourgeois, D. Arginine 66 Controls Dark-State Formation in Green-to-Red Photoconvertible Fluorescent Proteins. *J. Am. Chem. Soc.* **2016**, *138* (2), 558–565. https://doi.org/10.1021/jacs.5b09923.
(148) Sun, M.; Hu, K.; Bewersdorf, J.; Pollard, T. D. Sample Preparation and Imaging Conditions Affect MEos3.2 Photophysics in Fission Yeast Cells. *Biophys. J.* **2021**, *120* (1), 21–34. https://doi.org/10.1016/j.bpj.2020.11.006.
(149) Fu, Z.; Peng, D.; Zhang, M.; Xue, F.; Zhang, R.; He, W.; Xu, T.; Xu, P. MEosEM Withstands Osmium Staining and Epon Embedding for Super-Resolution CLEM. *Nat. Methods* **2020**, *17* (1), 55–58. https://doi.org/10.1038/s41592-019-0613-6.
(150) Paez Segala, M. G.; Sun, M. G.; Shtengel, G.; Viswanathan, S.; Baird, M. A.; Macklin, J. J.; Patel, R.; Allen, J. R.; Howe, E. S.; Piszczek, G.; Hess, H. F.; Davidson, M. W.; Wang, Y.; Looger, L. L. Fixation-Resistant Photoactivatable Fluorescent Proteins for Correlative Light and Electron Microscopy. *Nat. Methods* **2015**, *12* (3), 215–218. https://doi.org/10.1038/nmeth.3225.
(151) Osuga, M.; Nishimura, T.; Suetsugu, S. Development of a Green Reversibly Photoswitchable Variant of Eos Fluorescent Protein with Fixation Resistance. *Mol. Biol. Cell* **2021**, *32* (21), br7. https://doi.org/10.1091/mbc.E21-01-0044.
(152) Tan, H. L.; Bungert-Plümke, S.; Kortzak, D.; Fahlke, C.; Stölting, G. Determination of Oligomeric States of Proteins via Dual-Color Colocalization with Single Molecule Localization Microscopy. *eLife 11*, e76631. https://doi.org/10.7554/eLife.76631.
(153) Østergaard, H.; Henriksen, A.; Hansen, F. G.; Winther, J. R. Shedding Light on Disulfide Bond Formation: Engineering a Redox Switch in Green Fluorescent Protein. *EMBO J.* **2001**, *20* (21), 5853–5862. https://doi.org/10.1093/emboj/20.21.5853.
(154) Hanson, G. T.; Aggeler, R.; Oglesbee, D.; Cannon, M.; Capaldi, R. A.; Tsien, R. Y.; Remington, S. J. Investigating Mitochondrial Redox Potential with Redox-Sensitive Green Fluorescent Protein Indicators. *J. Biol. Chem.* **2004**, *279* (13), 13044–13053. https://doi.org/10.1074/jbc.M312846200.
(155) Lu, C.; Albano, C. R.; Bentley, W. E.; Rao, G. Quantitative and Kinetic Study of Oxidative Stress Regulons Using Green Fluorescent Protein. *Biotechnol. Bioeng.* **2005**, *89* (5), 574–587. https://doi.org/10.1002/bit.20389.
(156) Ganini, D.; Leinisch, F.; Kumar, A.; Jiang, J.; Tokar, E. J.; Malone, C. C.; Petrovich, R. M.; Mason, R. P. Fluorescent Proteins Such as EGFP Lead to Catalytic Oxidative Stress in Cells. *Redox Biol.* **2017**, *12*, 462–468. https://doi.org/10.1016/j.redox.2017.03.002.
(157) Onukwufor, J. O.; Trewin, A. J.; Baran, T. M.; Almast, A.; Foster, T. H.; Wojtovich, A. P. Quantification of Reactive Oxygen Species Production by the Red Fluorescent Proteins KillerRed, SuperNova and MCherry. *Free Radic. Biol. Med.* **2020**, *147*, 1–7. https://doi.org/10.1016/j.freeradbiomed.2019.12.008.

(158) Takemoto, K.; Matsuda, T.; Sakai, N.; Fu, D.; Noda, M.; Uchiyama, S.; Kotera, I.; Arai, Y.; Horiuchi, M.; Fukui, K.; Ayabe, T.; Inagaki, F.; Suzuki, H.; Nagai, T. SuperNova, a Monomeric Photosensitizing Fluorescent Protein for Chromophore-Assisted Light Inactivation. *Sci. Rep.* **2013**, *3*, 2629. https://doi.org/10.1038/srep02629.
(159) Carpentier, P.; Violot, S.; Blanchoin, L.; Bourgeois, D. Structural Basis for the Phototoxicity of the Fluorescent Protein KillerRed. *FEBS Lett.* **2009**, *583* (17), 2839–2842. https://doi.org/10.1016/j.febslet.2009.07.041.
(160) Pletnev, S.; Gurskaya, N. G.; Pletneva, N. V.; Lukyanov, K. A.; Chudakov, D. M.; Martynov, V. I.; Popov, V. O.; Kovalchuk, M. V.; Wlodawer, A.; Dauter, Z.; Pletnev, V. Structural Basis for Phototoxicity of the Genetically Encoded Photosensitizer KillerRed. *J. Biol. Chem.* **2009**, *284* (46), 32028–32039. https://doi.org/10.1074/jbc.M109.054973.
(161) El Najjar, N.; van Teeseling, M. C. F.; Mayer, B.; Hermann, S.; Thanbichler, M.; Graumann, P. L. Bacterial Cell Growth Is Arrested by Violet and Blue, but Not Yellow Light Excitation during Fluorescence Microscopy. *BMC Mol. Cell Biol.* **2020**, *21* (1), 35. https://doi.org/10.1186/s12860-020-00277-y.
(162) Icha, J.; Weber, M.; Waters, J. C.; Norden, C. Phototoxicity in Live Fluorescence Microscopy, and How to Avoid It. *BioEssays* **2017**, *39* (8), 1700003. https://doi.org/10.1002/bies.201700003.
(163) Vreja, I. C.; Nikić, I.; Göttfert, F.; Bates, M.; Kröhnert, K.; Outeiro, T. F.; Hell, S. W.; Lemke, E. A.; Rizzoli, S. O. Super-Resolution Microscopy of Clickable Amino Acids Reveals the Effects of Fluorescent Protein Tagging on Protein Assemblies. *ACS Nano* **2015**, *9* (11), 11034–11041. https://doi.org/10.1021/acsnano.5b04434.
(164) Wang, S.; Moffitt, J. R.; Dempsey, G. T.; Xie, X. S.; Zhuang, X. Characterization and Development of Photoactivatable Fluorescent Proteins for Single-Molecule–Based Superresolution Imaging. *Proc. Natl. Acad. Sci.* **2014**, *111* (23), 8452–8457. https://doi.org/10.1073/pnas.1406593111.
(165) Ning, L.; Geng, Y.; Lovett-Barron, M.; Niu, X.; Deng, M.; Wang, L.; Ataie, N.; Sens, A.; Ng, H.-L.; Chen, S.; Deisseroth, K.; Lin, M. Z.; Chu, J. A Bright, Nontoxic, and Non-Aggregating Red Fluorescent Protein for Long-Term Labeling of Fine Structures in Neurons. *Front. Cell Dev. Biol.* **2022**, *10*, 893468. https://doi.org/10.3389/fcell.2022.893468.
(166) Schermelleh, L.; Ferrand, A.; Huser, T.; Eggeling, C.; Sauer, M.; Biehlmaier, O.; Drummen, G. P. C. Super-Resolution Microscopy Demystified. *Nat. Cell Biol.* **2019**, *21* (1), 72–84. https://doi.org/10.1038/s41556-018-0251-8.
(167) Heintzmann, R.; Huser, T. Super-Resolution Structured Illumination Microscopy. *Chem. Rev.* **2017**, *117* (23), 13890–13908. https://doi.org/10.1021/acs.chemrev.7b00218.
(168) Jeong, S.; Widengren, J.; Lee, J.-C. Fluorescent Probes for STED Optical Nanoscopy. *Nanomaterials* **2021**, *12* (1), 21. https://doi.org/10.3390/nano12010021.
(169) Hofmann, M.; Eggeling, C.; Jakobs, S.; Hell, S. W. Breaking the Diffraction Barrier in Fluorescence Microscopy at Low Light Intensities by Using Reversibly Photoswitchable Proteins. *Proc. Natl. Acad. Sci.* **2005**, *102* (49), 17565–17569. https://doi.org/10.1073/pnas.0506010102.
(170) Lelek, M.; Gyparaki, M. T.; Beliu, G.; Schueder, F.; Griffié, J.; Manley, S.; Jungmann, R.; Sauer, M.; Lakadamyali, M.; Zimmer, C. Single-Molecule Localization Microscopy. *Nat. Rev. Methods Primer* **2021**, *1* (1), 1–27. https://doi.org/10.1038/s43586-021-00038-x.
(171) Brakemann, T.; Stiel, A. C.; Weber, G.; Andresen, M.; Testa, I.; Grotjohann, T.; Leutenegger, M.; Plessmann, U.; Urlaub, H.; Eggeling, C.; Wahl, M. C.; Hell, S. W.; Jakobs, S. A Reversibly Photoswitchable GFP-like Protein with Fluorescence Excitation Decoupled from Switching. *Nat. Biotechnol.* **2011**, *29* (10), 942–947. https://doi.org/10.1038/nbt.1952.
(172) Flors, C.; Hotta, J.; Uji-i, H.; Dedecker, P.; Ando, R.; Mizuno, H.; Miyawaki, A.; Hofkens, J. A Stroboscopic Approach for Fast Photoactivation−Localization Microscopy with Dronpa Mutants. *J. Am. Chem. Soc.* **2007**, *129* (45), 13970–13977. https://doi.org/10.1021/ja074704l.
(173) Balzarotti, F.; Eilers, Y.; Gwosch, K. C.; Gynnå, A. H.; Westphal, V.; Stefani, F. D.; Elf, J.; Hell, S. W. Nanometer Resolution Imaging and Tracking of Fluorescent Molecules with Minimal Photon Fluxes. *Science* **2017**, *355* (6325), 606–612. https://doi.org/10.1126/science.aak9913.

(174) Dickson, R. M.; Cubitt, A. B.; Tsien, R. Y.; Moerner, W. E. On/off Blinking and Switching Behaviour of Single Molecules of Green Fluorescent Protein. *Nature* **1997**, *388* (6640), 355–358. https://doi.org/10.1038/41048.
(175) Andresen, M.; Stiel, A. C.; Fölling, J.; Wenzel, D.; Schönle, A.; Egner, A.; Eggeling, C.; Hell, S. W.; Jakobs, S. Photoswitchable Fluorescent Proteins Enable Monochromatic Multilabel Imaging and Dual Color Fluorescence Nanoscopy. *Nat. Biotechnol.* **2008**, *26* (9), 1035–1040. https://doi.org/10.1038/nbt.1493.
(176) Brakemann, T.; Weber, G.; Andresen, M.; Groenhof, G.; Stiel, A. C.; Trowitzsch, S.; Eggeling, C.; Grubmüller, H.; Hell, S. W.; Wahl, M. C.; Jakobs, S. Molecular Basis of the Light-Driven Switching of the Photochromic Fluorescent Protein Padron. *J. Biol. Chem.* **2010**, *285* (19), 14603–14609. https://doi.org/10.1074/jbc.M109.086314.
(177) Stiel, A. C.; Andresen, M.; Bock, H.; Hilbert, M.; Schilde, J.; Schönle, A.; Eggeling, C.; Egner, A.; Hell, S. W.; Jakobs, S. Generation of Monomeric Reversibly Switchable Red Fluorescent Proteins for Far-Field Fluorescence Nanoscopy. *Biophys. J.* **2008**, *95* (6), 2989–2997. https://doi.org/10.1529/biophysj.108.130146.
(178) Ando, R.; Mizuno, H.; Miyawaki, A. Regulated Fast Nucleocytoplasmic Shuttling Observed by Reversible Protein Highlighting. *Science* **2004**, *306* (5700), 1370–1373. https://doi.org/10.1126/science.1102506.
(179) Grotjohann, T.; Testa, I.; Leutenegger, M.; Bock, H.; Urban, N. T.; Lavoie-Cardinal, F.; Willig, K. I.; Eggeling, C.; Jakobs, S.; Hell, S. W. Diffraction-Unlimited All-Optical Imaging and Writing with a Photochromic GFP. *Nature* **2011**, *478* (7368), 204–208. https://doi.org/10.1038/nature10497.
(180) Grotjohann, T.; Testa, I.; Reuss, M.; Brakemann, T.; Eggeling, C.; Hell, S. W.; Jakobs, S. RsEGFP2 Enables Fast RESOLFT Nanoscopy of Living Cells. *eLife* **2012**, *1*, e00248. https://doi.org/10.7554/eLife.00248.
(181) Bourges, A. C.; Moeyaert, B.; Bui, T. Y. H.; Bierbuesse, F.; Vandenberg, W.; Dedecker, P. Quantitative Determination of the Full Switching Cycle of Photochromic Fluorescent Proteins. *Chem. Commun.* **2023**. https://doi.org/10.1039/D3CC01617J.
(182) Lacombat, F.; Plaza, P.; Plamont, M.-A.; Espagne, A. Photoinduced Chromophore Hydration in the Fluorescent Protein Dreiklang Is Triggered by Ultrafast Excited-State Proton Transfer Coupled to a Low-Frequency Vibration. *J. Phys. Chem. Lett.* **2017**, *8* (7), 1489–1495. https://doi.org/10.1021/acs.jpclett.7b00348.
(183) Arai, Y.; Takauchi, H.; Ogami, Y.; Fujiwara, S.; Nakano, M.; Matsuda, T.; Nagai, T. Spontaneously Blinking Fluorescent Protein for Simple Single Laser Super-Resolution Live Cell Imaging. *ACS Chem. Biol.* **2018**, *13* (8), 1938–1943. https://doi.org/10.1021/acschembio.8b00200.
(184) Gunewardene, M. S.; Subach, F. V.; Gould, T. J.; Penoncello, G. P.; Gudheti, M. V.; Verkhusha, V. V.; Hess, S. T. Superresolution Imaging of Multiple Fluorescent Proteins with Highly Overlapping Emission Spectra in Living Cells. *Biophys. J.* **2011**, *101* (6), 1522–1528. https://doi.org/10.1016/j.bpj.2011.07.049.
(185) Dahlberg, P. D.; Sartor, A. M.; Wang, J.; Saurabh, S.; Shapiro, L.; Moerner, W. E. Identification of PAmKate as a Red Photoactivatable Fluorescent Protein for Cryogenic Super-Resolution Imaging. *J. Am. Chem. Soc.* **2018**, *140* (39), 12310–12313. https://doi.org/10.1021/jacs.8b05960.
(186) Subach, F. V.; Patterson, G. H.; Renz, M.; Lippincott-Schwartz, J.; Verkhusha, V. V. Bright Monomeric Photoactivatable Red Fluorescent Protein for Two-Color Super-Resolution SptPALM of Live Cells. *J. Am. Chem. Soc.* **2010**, *132* (18), 6481–6491. https://doi.org/10.1021/ja100906g.
(187) Ando, R.; Hama, H.; Yamamoto-Hino, M.; Mizuno, H.; Miyawaki, A. An Optical Marker Based on the UV-Induced Green-to-Red Photoconversion of a Fluorescent Protein. *Proc. Natl. Acad. Sci.* **2002**, *99* (20), 12651–12656. https://doi.org/10.1073/pnas.202320599.
(188) Wiedenmann, J.; Ivanchenko, S.; Oswald, F.; Schmitt, F.; Röcker, C.; Salih, A.; Spindler, K.-D.; Nienhaus, G. U. EosFP, a Fluorescent Marker Protein with UV-Inducible Green-to-Red Fluorescence Conversion. *Proc. Natl. Acad. Sci.* **2004**, *101* (45), 15905–15910. https://doi.org/10.1073/pnas.0403668101.

(189) Bollati, E.; Plimmer, D.; D'Angelo, C.; Wiedenmann, J. FRET-Mediated Long-Range Wavelength Transformation by Photoconvertible Fluorescent Proteins as an Efficient Mechanism to Generate Orange-Red Light in Symbiotic Deep Water Corals. *Int. J. Mol. Sci.* **2017**, *18* (7), 1174. https://doi.org/10.3390/ijms18071174.
(190) Tsutsui, H.; Karasawa, S.; Shimizu, H.; Nukina, N.; Miyawaki, A. Semi-Rational Engineering of a Coral Fluorescent Protein into an Efficient Highlighter. *EMBO Rep.* **2005**, *6* (3), 233–238. https://doi.org/10.1038/sj.embor.7400361.
(191) Hoi, H.; Shaner, N. C.; Davidson, M. W.; Cairo, C. W.; Wang, J.; Campbell, R. E. A Monomeric Photoconvertible Fluorescent Protein for Imaging of Dynamic Protein Localization. *J. Mol. Biol.* **2010**, *401* (5), 776–791. https://doi.org/10.1016/j.jmb.2010.06.056.
(192) Li, X.; Chung, L. W.; Mizuno, H.; Miyawaki, A.; Morokuma, K. Competitive Mechanistic Pathways for Green-to-Red Photoconversion in the Fluorescent Protein Kaede: A Computational Study. *J. Phys. Chem. B* **2010**, *114* (49), 16666–16675. https://doi.org/10.1021/jp1101779.
(193) Tsutsui, H.; Shimizu, H.; Mizuno, H.; Nukina, N.; Furuta, T.; Miyawaki, A. The E1 Mechanism in Photo-Induced Beta-Elimination Reactions for Green-to-Red Conversion of Fluorescent Proteins. *Chem. Biol.* **2009**, *16* (11), 1140–1147. https://doi.org/10.1016/j.chembiol.2009.10.010.
(194) Lelimousin, M.; Adam, V.; Nienhaus, G. U.; Bourgeois, D.; Field, M. J. Photoconversion of the Fluorescent Protein EosFP: A Hybrid Potential Simulation Study Reveals Intersystem Crossings. *J. Am. Chem. Soc.* **2009**, *131* (46), 16814–16823. https://doi.org/10.1021/ja905380y.
(195) Fare, C.; Yuan, L.; Cordon-Preciado, V.; Michels, J. J.; Bearpark, M. J.; Rich, P.; van Thor, J. J. Radical-Triggered Reaction Mechanism of the Green-to-Red Photoconversion of EosFP. *J. Phys. Chem. B* **2020**, *124* (36), 7765–7778. https://doi.org/10.1021/acs.jpcb.0c04587.
(196) Field, S. F.; Matz, M. V. Retracing Evolution of Red Fluorescence in GFP-Like Proteins from Faviina Corals. *Mol. Biol. Evol.* **2010**, *27* (2), 225–233. https://doi.org/10.1093/molbev/msp230.
(197) Kim, H.; Zou, T.; Modi, C.; Dörner, K.; Grunkemeyer, T. J.; Chen, L.; Fromme, R.; Matz, M. V.; Ozkan, S. B.; Wachter, R. M. A Hinge Migration Mechanism Unlocks the Evolution of Green-to-Red Photoconversion in GFP-like Proteins. *Struct. Lond. Engl. 1993* **2015**, *23* (1), 34–43. https://doi.org/10.1016/j.str.2014.11.011.
(198) Kim, H.; Grunkemeyer, T. J.; Modi, C.; Chen, L.; Fromme, R.; Matz, M. V.; Wachter, R. M. Acid–Base Catalysis and Crystal Structures of a Least Evolved Ancestral GFP-like Protein Undergoing Green-to-Red Photoconversion. *Biochemistry* **2013**, *52* (45), 8048–8059. https://doi.org/10.1021/bi401000e.
(199) Krueger, T. D.; Tang, L.; Zhu, L.; Breen, I. L.; Wachter, R. M.; Fang, C. Dual Illumination Enhances Transformation of an Engineered Green-to-Red Photoconvertible Fluorescent Protein. *Angew. Chem. Int. Ed.* **2020**, *59* (4), 1644–1652. https://doi.org/10.1002/anie.201911379.
(200) Krueger, T. D.; Tang, L.; Chen, C.; Zhu, L.; Breen, I. L.; Wachter, R. M.; Fang, C. To Twist or Not to Twist: From Chromophore Structure to Dynamics inside Engineered Photoconvertible and Photoswitchable Fluorescent Proteins. *Protein Sci.* **2023**, *32* (1), e4517. https://doi.org/10.1002/pro.4517.
(201) Adam, V.; Lelimousin, M.; Boehme, S.; Desfonds, G.; Nienhaus, K.; Field, M. J.; Wiedenmann, J.; McSweeney, S.; Nienhaus, G. U.; Bourgeois, D. Structural Characterization of IrisFP, an Optical Highlighter Undergoing Multiple Photo-Induced Transformations. *Proc. Natl. Acad. Sci.* **2008**, *105* (47), 18343–18348. https://doi.org/10.1073/pnas.0805949105.
(202) Habuchi, S.; Tsutsui, H.; Kochaniak, A. B.; Miyawaki, A.; van Oijen, A. M. MKikGR, a Monomeric Photoswitchable Fluorescent Protein. *PLoS ONE* **2008**, *3* (12), e3944. https://doi.org/10.1371/journal.pone.0003944.
(203) Durisic, N.; Laparra-Cuervo, L.; Sandoval-Álvarez, Á.; Borbely, J. S.; Lakadamyali, M. Single-Molecule Evaluation of Fluorescent Protein Photoactivation Efficiency Using an in Vivo Nanotemplate. *Nat. Methods* **2014**, *11* (2), 156–162. https://doi.org/10.1038/nmeth.2784.
(204) Thédié, D.; Berardozzi, R.; Adam, V.; Bourgeois, D. Photoswitching of Green MEos2 by Intense 561 Nm Light Perturbs Efficient Green-to-Red Photoconversion in Localization Microscopy. *J. Phys. Chem. Lett.* **2017**, *8* (18), 4424–4430. https://doi.org/10.1021/acs.jpclett.7b01701.

(205) Puchner, E. M.; Walter, J. M.; Kasper, R.; Huang, B.; Lim, W. A. Counting Molecules in Single Organelles with Superresolution Microscopy Allows Tracking of the Endosome Maturation Trajectory. *Proc. Natl. Acad. Sci.* **2013**, *110* (40), 16015–16020. https://doi.org/10.1073/pnas.1309676110.
(206) Fricke, F.; Beaudouin, J.; Eils, R.; Heilemann, M. One, Two or Three? Probing the Stoichiometry of Membrane Proteins by Single-Molecule Localization Microscopy. *Sci. Rep.* **2015**, *5* (1), 14072. https://doi.org/10.1038/srep14072.
(207) Dempsey, W. P.; Georgieva, L.; Helbling, P. M.; Sonay, A. Y.; Truong, T. V.; Haffner, M.; Pantazis, P. In Vivo Single-Cell Labeling by Confined Primed Conversion. *Nat. Methods* **2015**, *12* (7), 645–648. https://doi.org/10.1038/nmeth.3405.
(208) Virant, D.; Turkowyd, B.; Balinovic, A.; Endesfelder, U. Combining Primed Photoconversion and UV-Photoactivation for Aberration-Free, Live-Cell Compliant Multi-Color Single-Molecule Localization Microscopy Imaging. *Int. J. Mol. Sci.* **2017**, *18* (7), 1524. https://doi.org/10.3390/ijms18071524.
(209) Zhang, M.; Chang, H.; Zhang, Y.; Yu, J.; Wu, L.; Ji, W.; Chen, J.; Liu, B.; Lu, J.; Liu, Y.; Zhang, J.; Xu, P.; Xu, T. Rational Design of True Monomeric and Bright Photoactivatable Fluorescent Proteins. *Nat. Methods* **2012**, *9* (7), 727–729. https://doi.org/10.1038/nmeth.2021.
(210) Zhang, M.; Fu, Z.; Li, C.; Liu, A.; Peng, D.; Xue, F.; He, W.; Gao, S.; Xu, F.; Xu, D.; Yuan, L.; Zhang, F.; Xu, Z.; Xu, T.; Xu, P. Fast Super-Resolution Imaging Technique and Immediate Early Nanostructure Capturing by a Photoconvertible Fluorescent Protein. *Nano Lett.* **2020**, *20* (4), 2197–2208. https://doi.org/10.1021/acs.nanolett.9b02855.
(211) Chang, H.; Zhang, M.; Ji, W.; Chen, J.; Zhang, Y.; Liu, B.; Lu, J.; Zhang, J.; Xu, P.; Xu, T. A Unique Series of Reversibly Switchable Fluorescent Proteins with Beneficial Properties for Various Applications. *Proc. Natl. Acad. Sci.* **2012**, *109* (12), 4455–4460. https://doi.org/10.1073/pnas.1113770109.
(212) Zhang, X.; Zhang, M.; Li, D.; He, W.; Peng, J.; Betzig, E.; Xu, P. Highly Photostable, Reversibly Photoswitchable Fluorescent Protein with High Contrast Ratio for Live-Cell Superresolution Microscopy. *Proc. Natl. Acad. Sci. U. S. A.* **2016**, *113* (37), 10364–10369. https://doi.org/10.1073/pnas.1611038113.
(213) Fuchs, J.; Böhme, S.; Oswald, F.; Hedde, P. N.; Krause, M.; Wiedenmann, J.; Nienhaus, G. U. A Photoactivatable Marker Protein for Pulse-Chase Imaging with Superresolution. *Nat. Methods* **2010**, *7* (8), 627–630. https://doi.org/10.1038/nmeth.1477.
(214) Baxter, J. M.; Hutchison, C. D. M.; Maghlaoui, K.; Cordon-Preciado, V.; Morgan, R. M. L.; Aller, P.; Butryn, A.; Axford, D.; Horrell, S.; Owen, R. L.; Storm, S. L. S.; Devenish, N. E.; van Thor, J. J. Observation of Cation Chromophore Photoisomerization of a Fluorescent Protein Using Millisecond Synchrotron Serial Crystallography and Infrared Vibrational and Visible Spectroscopy. *J. Phys. Chem. B* **2022**, *126* (45), 9288–9296. https://doi.org/10.1021/acs.jpcb.2c06780.
(215) Peng, D.; Li, N.; He, W.; Drasbek, K. R.; Xu, T.; Zhang, M.; Xu, P. Improved Fluorescent Proteins for Dual-Colour Post-Embedding CLEM. *Cells* **2022**, *11* (7), 1077. https://doi.org/10.3390/cells11071077.
(216) Baldering, T. N.; Karathanasis, C.; Harwardt, M.-L. I. E.; Freund, P.; Meurer, M.; Rahm, J. V.; Knop, M.; Dietz, M. S.; Heilemann, M. CRISPR/Cas12a-Mediated Labeling of MET Receptor Enables Quantitative Single-Molecule Imaging of Endogenous Protein Organization and Dynamics. *iScience* **2021**, *24* (1), 101895. https://doi.org/10.1016/j.isci.2020.101895.
(217) De Zitter, E.; Thédié, D.; Mönkemöller, V.; Hugelier, S.; Beaudouin, J.; Adam, V.; Byrdin, M.; Van Meervelt, L.; Dedecker, P.; Bourgeois, D. Mechanistic Investigation of MEos4b Reveals a Strategy to Reduce Track Interruptions in SptPALM. *Nat. Methods* **2019**, *16* (8), 707–710. https://doi.org/10.1038/s41592-019-0462-3.
(218) De Zitter, E.; Ridard, J.; Thédié, D.; Adam, V.; Lévy, B.; Byrdin, M.; Gotthard, G.; Van Meervelt, L.; Dedecker, P.; Demachy, I.; Bourgeois, D. Mechanistic Investigations of Green MEos4b Reveal a Dynamic Long-Lived Dark State. *J. Am. Chem. Soc.* **2020**, *142* (25), 10978–10988. https://doi.org/10.1021/jacs.0c01880.

(219) Urbach, F. The Long-Wavelength Edge of Photographic Sensitivity and of the Electronic Absorption of Solids. *Phys. Rev.* **1953**, *92* (5), 1324–1324. https://doi.org/10.1103/PhysRev.92.1324.
(220) Dahlberg, P. D.; Moerner, W. E. Cryogenic Super-Resolution Fluorescence and Electron Microscopy Correlated at the Nanoscale. *Annu. Rev. Phys. Chem.* **2021**, *72*, 253–278. https://doi.org/10.1146/annurev-physchem-090319-051546.
(221) Whelan, D. R.; Bell, T. D. M. Image Artifacts in Single Molecule Localization Microscopy: Why Optimization of Sample Preparation Protocols Matters. *Sci. Rep.* **2015**, *5* (1), 7924. https://doi.org/10.1038/srep07924.
(222) Korogod, N.; Petersen, C. C.; Knott, G. W. Ultrastructural Analysis of Adult Mouse Neocortex Comparing Aldehyde Perfusion with Cryo Fixation. *eLife 4*, e05793. https://doi.org/10.7554/eLife.05793.
(223) Hoffman, D. P.; Shtengel, G.; Xu, C. S.; Campbell, K. R.; Freeman, M.; Wang, L.; Milkie, D. E.; Pasolli, H. A.; Iyer, N.; Bogovic, J. A.; Stabley, D. R.; Shirinifard, A.; Pang, S.; Peale, D.; Schaefer, K.; Pomp, W.; Chang, C.-L.; Lippincott-Schwartz, J.; Kirchhausen, T.; Solecki, D. J.; Betzig, E.; Hess, H. F. Correlative Three-Dimensional Super-Resolution and Block Face Electron Microscopy of Whole Vitreously Frozen Cells. *Science* **2020**, *367* (6475), eaaz5357. https://doi.org/10.1126/science.aaz5357.
(224) Liu, B.; Xue, Y.; Zhao, W.; Chen, Y.; Fan, C.; Gu, L.; Zhang, Y.; Zhang, X.; Sun, L.; Huang, X.; Ding, W.; Sun, F.; Ji, W.; Xu, T. Three-Dimensional Super-Resolution Protein Localization Correlated with Vitrified Cellular Context. *Sci. Rep.* **2015**, *5*, 13017. https://doi.org/10.1038/srep13017.
(225) Schwartz, C. L.; Sarbash, V. I.; Ataullakhanov, F. I.; Mcintosh, J. R.; Nicastro, D. Cryo-Fluorescence Microscopy Facilitates Correlations between Light and Cryo-Electron Microscopy and Reduces the Rate of Photobleaching. *J. Microsc.* **2007**, *227* (2), 98–109. https://doi.org/10.1111/j.1365-2818.2007.01794.x.
(226) Hulleman, C. N.; Li, W.; Gregor, I.; Rieger, B.; Enderlein, J. Photon Yield Enhancement of Red Fluorophores at Cryogenic Temperatures. *ChemPhysChem* **2018**, *19* (14), 1774–1780. https://doi.org/10.1002/cphc.201800131.
(227) Sartor, A. M.; Dahlberg, P. D.; Perez, D.; Moerner, W. E. Characterization of MApple as a Red Fluorescent Protein for Cryogenic Single-Molecule Imaging with Turn-Off and Turn-On Active Control Mechanisms. *J. Phys. Chem. B* **2023**, *127* (12), 2690–2700. https://doi.org/10.1021/acs.jpcb.2c08995.
(228) Faro, A. R.; Adam, V.; Carpentier, P.; Darnault, C.; Bourgeois, D.; Rosny, E. de. Low-Temperature Switching by Photoinduced Protonation in Photochromic Fluorescent Proteins. *Photochem. Photobiol. Sci.* **2010**, *9* (2), 254–262. https://doi.org/10.1039/B9PP00121B.
(229) Tuijtel, M. W.; Koster, A. J.; Jakobs, S.; Faas, F. G. A.; Sharp, T. H. Correlative Cryo Super-Resolution Light and Electron Microscopy on Mammalian Cells Using Fluorescent Proteins. *Sci. Rep.* **2019**, *9*, 1369. https://doi.org/10.1038/s41598-018-37728-8.
(230) Regis Faro, A.; Carpentier, P.; Jonasson, G.; Pompidor, G.; Arcizet, D.; Demachy, I.; Bourgeois, D. Low-Temperature Chromophore Isomerization Reveals the Photoswitching Mechanism of the Fluorescent Protein Padron. *J. Am. Chem. Soc.* **2011**, *133* (41), 16362–16365. https://doi.org/10.1021/ja207001y.
(231) Chang, Y.-W.; Chen, S.; Tocheva, E. I.; Treuner-Lange, A.; Löbach, S.; Søgaard-Andersen, L.; Jensen, G. J. Correlated Cryogenic Photoactivated Localization Microscopy and Cryo-Electron Tomography. *Nat. Methods* **2014**, *11* (7), 737–739. https://doi.org/10.1038/nmeth.2961.
(232) Kaufmann, R.; Schellenberger, P.; Seiradake, E.; Dobbie, I. M.; Jones, E. Y.; Davis, I.; Hagen, C.; Grünewald, K. Super-Resolution Microscopy Using Standard Fluorescent Proteins in Intact Cells under Cryo-Conditions. *Nano Lett.* **2014**, *14* (7), 4171–4175. https://doi.org/10.1021/nl501870p.
(233) Ovesný, M.; Křížek, P.; Borkovec, J.; Švindrych, Z.; Hagen, G. M. ThunderSTORM: A Comprehensive ImageJ Plug-in for PALM and STORM Data Analysis and Super-Resolution Imaging. *Bioinformatics* **2014**, *30* (16), 2389–2390. https://doi.org/10.1093/bioinformatics/btu202.
(234) Ries, J. SMAP: A Modular Super-Resolution Microscopy Analysis Platform for SMLM Data. *Nat. Methods* **2020**, *17* (9), 870–872. https://doi.org/10.1038/s41592-020-0938-1.

(235) Thompson, R. E.; Larson, D. R.; Webb, W. W. Precise Nanometer Localization Analysis for Individual Fluorescent Probes. *Biophys. J.* **2002**, *82* (5), 2775–2783. https://doi.org/10.1016/S0006-3495(02)75618-X.
(236) Quan, T.; Zeng, S.; Huang, Z.-L. Localization Capability and Limitation of Electron-Multiplying Charge-Coupled, Scientific Complementary Metal-Oxide Semiconductor, and Charge-Coupled Devices for Superresolution Imaging. *J. Biomed. Opt.* **2010**, *15* (6), 066005. https://doi.org/10.1117/1.3505017.
(237) Lampe, A.; Haucke, V.; Sigrist, S. J.; Heilemann, M.; Schmoranzer, J. Multi-Colour Direct STORM with Red Emitting Carbocyanines. *Biol. Cell* **2012**, *104* (4), 229–237. https://doi.org/10.1111/boc.201100011.
(238) Nahidiazar, L.; Agronskaia, A. V.; Broertjes, J.; Broek, B. van den; Jalink, K. Optimizing Imaging Conditions for Demanding Multi-Color Super Resolution Localization Microscopy. *PLOS ONE* **2016**, *11* (7), e0158884. https://doi.org/10.1371/journal.pone.0158884.
(239) Klevanski, M.; Herrmannsdoerfer, F.; Sass, S.; Venkataramani, V.; Heilemann, M.; Kuner, T. Automated Highly Multiplexed Super-Resolution Imaging of Protein Nano-Architecture in Cells and Tissues. *Nat. Commun.* **2020**, *11*, 1552. https://doi.org/10.1038/s41467-020-15362-1.
(240) Sabinina, V. J.; Hossain, M. J.; Hériché, J.-K.; Hoess, P.; Nijmeijer, B.; Mosalaganti, S.; Kueblbeck, M.; Callegari, A.; Szymborska, A.; Beck, M.; Ries, J.; Ellenberg, J. Three-Dimensional Superresolution Fluorescence Microscopy Maps the Variable Molecular Architecture of the Nuclear Pore Complex. *Mol. Biol. Cell* **2021**, *32* (17), 1523–1533. https://doi.org/10.1091/mbc.E20-11-0728.
(241) von Diezmann, L.; Shechtman, Y.; Moerner, W. E. Three-Dimensional Localization of Single Molecules for Super-Resolution Imaging and Single-Particle Tracking. *Chem. Rev.* **2017**, *117* (11), 7244–7275. https://doi.org/10.1021/acs.chemrev.6b00629.
(242) Hulleman, C. N.; Thorsen, R. Ø.; Kim, E.; Dekker, C.; Stallinga, S.; Rieger, B. Simultaneous Orientation and 3D Localization Microscopy with a Vortex Point Spread Function. *Nat. Commun.* **2021**, *12* (1), 5934. https://doi.org/10.1038/s41467-021-26228-5.
(243) Ding, T.; Lew, M. D. Single-Molecule Localization Microscopy of 3D Orientation and Anisotropic Wobble Using a Polarized Vortex Point Spread Function. *J. Phys. Chem. B* **2021**, *125* (46), 12718–12729. https://doi.org/10.1021/acs.jpcb.1c08073.
(244) Thevathasan, J. V.; Kahnwald, M.; Cieśliński, K.; Hoess, P.; Peneti, S. K.; Reitberger, M.; Heid, D.; Kasuba, K. C.; Hoerner, S. J.; Li, Y.; Wu, Y.-L.; Mund, M.; Matti, U.; Pereira, P. M.; Henriques, R.; Nijmeijer, B.; Kueblbeck, M.; Sabinina, V. J.; Ellenberg, J.; Ries, J. Nuclear Pores as Versatile Reference Standards for Quantitative Superresolution Microscopy. *Nat. Methods* **2019**, *16* (10), 1045–1053. https://doi.org/10.1038/s41592-019-0574-9.
(245) Spahn, C. K.; Glaesmann, M.; Grimm, J. B.; Ayala, A. X.; Lavis, L. D.; Heilemann, M. A Toolbox for Multiplexed Super-Resolution Imaging of the E. Coli Nucleoid and Membrane Using Novel PAINT Labels. *Sci. Rep.* **2018**, *8* (1), 14768. https://doi.org/10.1038/s41598-018-33052-3.
(246) Chung, K. K. H.; Zhang, Z.; Kidd, P.; Zhang, Y.; Williams, N. D.; Rollins, B.; Yang, Y.; Lin, C.; Baddeley, D.; Bewersdorf, J. Fluorogenic DNA-PAINT for Faster, Low-Background Super-Resolution Imaging. *Nat. Methods* **2022**, *19* (5), 554–559. https://doi.org/10.1038/s41592-022-01464-9.
(247) Nicovich, P. R.; Owen, D. M.; Gaus, K. Turning Single-Molecule Localization Microscopy into a Quantitative Bioanalytical Tool. *Nat. Protoc.* **2017**, *12* (3), 453–460. https://doi.org/10.1038/nprot.2016.166.
(248) Schodt, D. J.; Lidke, K. A. Spatiotemporal Clustering of Repeated Super-Resolution Localizations via Linear Assignment Problem. *Front. Bioinforma.* **2021**, *1*.
(249) Levet, F.; Hosy, E.; Kechkar, A.; Butler, C.; Beghin, A.; Choquet, D.; Sibarita, J.-B. SR-Tesseler: A Method to Segment and Quantify Localization-Based Super-Resolution Microscopy Data. *Nat. Methods* **2015**, *12* (11), 1065–1071. https://doi.org/10.1038/nmeth.3579.
(250) Fazel, M.; Wester, M. J.; Schodt, D. J.; Cruz, S. R.; Strauss, S.; Schueder, F.; Schlichthaerle, T.; Gillette, J. M.; Lidke, D. S.; Rieger, B.; Jungmann, R.; Lidke, K. A. High-Precision Estimation of Emitter Positions Using Bayesian Grouping of Localizations. *Nat. Commun.* **2022**, *13* (1), 7152. https://doi.org/10.1038/s41467-022-34894-2.

(251) Nieves, D. J.; Pike, J. A.; Levet, F.; Williamson, D. J.; Baragilly, M.; Oloketuyi, S.; de Marco, A.; Griffié, J.; Sage, D.; Cohen, E. A. K.; Sibarita, J.-B.; Heilemann, M.; Owen, D. M. A Framework for Evaluating the Performance of SMLM Cluster Analysis Algorithms. *Nat. Methods* **2023**, *20* (2), 259–267. https://doi.org/10.1038/s41592-022-01750-6.
(252) Hyun, Y.; Kim, D. Recent Development of Computational Cluster Analysis Methods for Single-Molecule Localization Microscopy Images. *Comput. Struct. Biotechnol. J.* **2023**, *21*, 879–888. https://doi.org/10.1016/j.csbj.2023.01.006.
(253) Lee, S.-H.; Shin, J. Y.; Lee, A.; Bustamante, C. Counting Single Photoactivatable Fluorescent Molecules by Photoactivated Localization Microscopy (PALM). *Proc. Natl. Acad. Sci.* **2012**, *109* (43), 17436–17441. https://doi.org/10.1073/pnas.1215175109.
(254) Baldering, T. N.; Bullerjahn, J. T.; Hummer, G.; Heilemann, M.; Malkusch, S. Molecule Counts in Complex Oligomers with Single-Molecule Localization Microscopy. *J. Phys. Appl. Phys.* **2019**, *52* (47), 474002. https://doi.org/10.1088/1361-6463/ab3b65.
(255) Hummer, G.; Fricke, F.; Heilemann, M. Model-Independent Counting of Molecules in Single-Molecule Localization Microscopy. *Mol. Biol. Cell* **2016**, *27* (22), 3637–3644. https://doi.org/10.1091/mbc.E16-07-0525.
(256) Finan, K.; Raulf, A.; Heilemann, M. A Set of Homo-Oligomeric Standards Allows Accurate Protein Counting. *Angew. Chem. Int. Ed.* **2015**, *54* (41), 12049–12052. https://doi.org/10.1002/anie.201505664.
(257) Virant, D.; Vojnovic, I.; Winkelmeier, J.; Endesfelder, M.; Turkowyd, B.; Lando, D.; Endesfelder, U. Unraveling the Kinetochore Nanostructure in Schizosaccharomyces Pombe Using Multi-Color SMLM Imaging. *J. Cell Biol.* **2023**, *222* (4), e202209096. https://doi.org/10.1083/jcb.202209096.
(258) Zanacchi, F. C.; Manzo, C.; Alvarez, A. S.; Derr, N. D.; Garcia-Parajo, M. F.; Lakadamyali, M. A DNA Origami Platform for Quantifying Protein Copy Number in Super-Resolution. *Nat. Methods* **2017**, *14* (8), 789–792. https://doi.org/10.1038/nmeth.4342.
(259) Nino, D. F.; Milstein, J. N. Estimating the Dynamic Range of Quantitative Single-Molecule Localization Microscopy. *Biophys. J.* **2021**, *120* (18), 3901–3910. https://doi.org/10.1016/j.bpj.2021.08.024.
(260) Jungmann, R.; Avendaño, M. S.; Dai, M.; Woehrstein, J. B.; Agasti, S. S.; Feiger, Z.; Rodal, A.; Yin, P. Quantitative Super-Resolution Imaging with QPAINT. *Nat. Methods* **2016**, *13* (5), 439–442. https://doi.org/10.1038/nmeth.3804.
(261) Fischer, L. S.; Klingner, C.; Schlichthaerle, T.; Strauss, M. T.; Böttcher, R.; Fässler, R.; Jungmann, R.; Grashoff, C. Quantitative Single-Protein Imaging Reveals Molecular Complex Formation of Integrin, Talin, and Kindlin during Cell Adhesion. *Nat. Commun.* **2021**, *12* (1), 919. https://doi.org/10.1038/s41467-021-21142-2.
(262) Ulbrich, M. H.; Isacoff, E. Y. Subunit Counting in Membrane-Bound Proteins. *Nat. Methods* **2007**, *4* (4), 319–321. https://doi.org/10.1038/nmeth1024.
(263) Rösch, T. C.; Altenburger, S.; Oviedo-Bocanegra, L.; Pediaditakis, M.; Najjar, N. E.; Fritz, G.; Graumann, P. L. Single Molecule Tracking Reveals Spatio-Temporal Dynamics of Bacterial DNA Repair Centres. *Sci. Rep.* **2018**, *8* (1), 16450. https://doi.org/10.1038/s41598-018-34572-8.
(264) Rahm, J. V.; Malkusch, S.; Endesfelder, U.; Dietz, M. S.; Heilemann, M. Diffusion State Transitions in Single-Particle Trajectories of MET Receptor Tyrosine Kinase Measured in Live Cells. *Front. Comput. Sci.* **2021**, *3*.
(265) Chenouard, N.; Smal, I.; de Chaumont, F.; Maška, M.; Sbalzarini, I. F.; Gong, Y.; Cardinale, J.; Carthel, C.; Coraluppi, S.; Winter, M.; Cohen, A. R.; Godinez, W. J.; Rohr, K.; Kalaidzidis, Y.; Liang, L.; Duncan, J.; Shen, H.; Xu, Y.; Magnusson, K. E. G.; Jaldén, J.; Blau, H. M.; Paul-Gilloteaux, P.; Roudot, P.; Kervrann, C.; Waharte, F.; Tinevez, J.-Y.; Shorte, S. L.; Willemse, J.; Celler, K.; van Wezel, G. P.; Dan, H.-W.; Tsai, Y.-S.; de Solórzano, C. O.; Olivo-Marin, J.-C.; Meijering, E. Objective Comparison of Particle Tracking Methods. *Nat. Methods* **2014**, *11* (3), 281–289. https://doi.org/10.1038/nmeth.2808.

(266) Bourgeois, D. Single Molecule Imaging Simulations with Advanced Fluorophore Photophysics. *Commun. Biol.* **2023**, *6* (1), 1–13. https://doi.org/10.1038/s42003-023-04432-x.
(267) Weimann, L.; Ganzinger, K. A.; McColl, J.; Irvine, K. L.; Davis, S. J.; Gay, N. J.; Bryant, C. E.; Klenerman, D. A Quantitative Comparison of Single-Dye Tracking Analysis Tools Using Monte Carlo Simulations. *PLOS ONE* **2013**, *8* (5), e64287. https://doi.org/10.1371/journal.pone.0064287.
(268) Saxton, M. J. Single-Particle Tracking: The Distribution of Diffusion Coefficients. *Biophys. J.* **1997**, *72* (4), 1744–1753.
(269) Kusumi, A.; Sako, Y.; Yamamoto, M. Confined Lateral Diffusion of Membrane Receptors as Studied by Single Particle Tracking (Nanovid Microscopy). Effects of Calcium-Induced Differentiation in Cultured Epithelial Cells. *Biophys. J.* **1993**, *65* (5), 2021–2040. https://doi.org/10.1016/S0006-3495(93)81253-0.
(270) Vrljic, M.; Nishimura, S. Y.; Brasselet, S.; Moerner, W. E.; McConnell, H. M. Translational Diffusion of Individual Class II MHC Membrane Proteinsin Cells. *Biophys. J.* **2002**, *83* (5), 2681–2692. https://doi.org/10.1016/S0006-3495(02)75277-6.
(271) Martens, K. J. A.; Turkowyd, B.; Endesfelder, U. Raw Data to Results: A Hands-On Introduction and Overview of Computational Analysis for Single-Molecule Localization Microscopy. *Front. Bioinforma.* **2022**, *1*.
(272) Persson, F.; Lindén, M.; Unoson, C.; Elf, J. Extracting Intracellular Diffusive States and Transition Rates from Single-Molecule Tracking Data. *Nat. Methods* **2013**, *10* (3), 265–269. https://doi.org/10.1038/nmeth.2367.
(273) Karslake, J. D.; Donarski, E. D.; Shelby, S. A.; Demey, L. M.; DiRita, V. J.; Veatch, S. L.; Biteen, J. S. SMAUG: Analyzing Single-Molecule Tracks with Nonparametric Bayesian Statistics. *Methods* **2021**, *193*, 16–26. https://doi.org/10.1016/j.ymeth.2020.03.008.
(274) Vink, J. N. A.; Brouns, S. J. J.; Hohlbein, J. Extracting Transition Rates in Particle Tracking Using Analytical Diffusion Distribution Analysis. *Biophys. J.* **2020**, *119* (10), 1970–1983. https://doi.org/10.1016/j.bpj.2020.09.033.
(275) Arts, M.; Smal, I.; Paul, M. W.; Wyman, C.; Meijering, E. Particle Mobility Analysis Using Deep Learning and the Moment Scaling Spectrum. *Sci. Rep.* **2019**, *9* (1), 17160. https://doi.org/10.1038/s41598-019-53663-8.
(276) Kapadia, N.; El-Hajj, Z. W.; Reyes-Lamothe, R. Bound2Learn: A Machine Learning Approach for Classification of DNA-Bound Proteins from Single-Molecule Tracking Experiments. *Nucleic Acids Res.* **2021**, *49* (14), e79. https://doi.org/10.1093/nar/gkab186.
(277) Granik, N.; Weiss, L. E.; Nehme, E.; Levin, M.; Chein, M.; Perlson, E.; Roichman, Y.; Shechtman, Y. Single-Particle Diffusion Characterization by Deep Learning. *Biophys. J.* **2019**, *117* (2), 185–192. https://doi.org/10.1016/j.bpj.2019.06.015.
(278) Bettridge, K.; Verma, S.; Weng, X.; Adhya, S.; Xiao, J. Single-Molecule Tracking Reveals That the Nucleoid-Associated Protein HU Plays a Dual-Role in Maintaining Proper Nucleoid Volume through Differential Interactions with Chromosomal DNA. *Mol. Microbiol.* **2021**, *115* (1), 12–27. https://doi.org/10.1111/mmi.14572.
(279) Stracy, M.; Schweizer, J.; Sherratt, D. J.; Kapanidis, A. N.; Uphoff, S.; Lesterlin, C. Transient Non-Specific DNA Binding Dominates the Target Search of Bacterial DNA-Binding Proteins. *Mol. Cell* **2021**, *81* (7), 1499-1514.e6. https://doi.org/10.1016/j.molcel.2021.01.039.
(280) Śmigiel, W. M.; Mantovanelli, L.; Linnik, D. S.; Punter, M.; Silberberg, J.; Xiang, L.; Xu, K.; Poolman, B. Protein Diffusion in Escherichia Coli Cytoplasm Scales with the Mass of the Complexes and Is Location Dependent. *Sci. Adv.* **2022**, *8* (32), eabo5387. https://doi.org/10.1126/sciadv.abo5387.
(281) Rocha, J.; Corbitt, J.; Yan, T.; Richardson, C.; Gahlmann, A. Resolving Cytosolic Diffusive States in Bacteria by Single-Molecule Tracking. *Biophys. J.* **2019**, *116* (10), 1970–1983. https://doi.org/10.1016/j.bpj.2019.03.039.
(282) Mortensen, K. I.; Flyvbjerg, H.; Pedersen, J. N. Confined Brownian Motion Tracked With Motion Blur: Estimating Diffusion Coefficient and Size of Confining Space. *Front. Phys.* **2021**, *8*.

(283) Adam, V. Phototransformable Fluorescent Proteins: Which One for Which Application? *Histochem. Cell Biol.* **2014**, *142* (1), 19–41. https://doi.org/10.1007/s00418-014-1190-5.
(284) Shannon, C. E. Communication in the Presence of Noise. *Proc. IRE* **1949**, *37* (1), 10–21. https://doi.org/10.1109/JRPROC.1949.232969.
(285) Renz, M.; Wunder, C. Internal Rulers to Assess Fluorescent Protein Photoactivation Efficiency. *Cytometry A* **2018**, *93* (4), 411–419.
(286) Dickson, R. M.; Norris, D. J.; Tzeng, Y.-L.; Moerner, W. E. Three-Dimensional Imaging of Single Molecules Solvated in Pores of Poly(Acrylamide) Gels. *Science* **1996**, *274* (5289), 966–968. https://doi.org/10.1126/science.274.5289.966.
(287) Garcia-Parajo, M. F.; Segers-Nolten, G. M. J.; Veerman, J.-A.; Greve, J.; van Hulst, N. F. Real-Time Light-Driven Dynamics of the Fluorescence Emission in Single Green Fluorescent Protein Molecules. *Proc. Natl. Acad. Sci.* **2000**, *97* (13), 7237–7242. https://doi.org/10.1073/pnas.97.13.7237.
(288) van de Linde, S.; Heilemann, M.; Sauer, M. Live-Cell Super-Resolution Imaging with Synthetic Fluorophores. *Annu. Rev. Phys. Chem.* **2012**, *63*, 519–540. https://doi.org/10.1146/annurev-physchem-032811-112012.
(289) Zondervan, R.; Kulzer, F.; Orlinskii, S. B.; Orrit, M. Photoblinking of Rhodamine 6G in Poly(Vinyl Alcohol): Radical Dark State Formed through the Triplet. *J. Phys. Chem. A* **2003**, *107* (35), 6770–6776. https://doi.org/10.1021/jp034723r.
(290) Piwoński, H.; Sokołowski, A.; Waluk, J. In Search for the Best Environment for Single Molecule Studies: Photostability of Single Terrylenediimide Molecules in Various Polymer Matrices. *J. Phys. Chem. Lett.* **2015**, *6* (13), 2477–2482. https://doi.org/10.1021/acs.jpclett.5b01060.
(291) Mehta, S. B.; McQuilken, M.; La Riviere, P. J.; Occhipinti, P.; Verma, A.; Oldenbourg, R.; Gladfelter, A. S.; Tani, T. Dissection of Molecular Assembly Dynamics by Tracking Orientation and Position of Single Molecules in Live Cells. *Proc. Natl. Acad. Sci.* **2016**, *113* (42), E6352–E6361. https://doi.org/10.1073/pnas.1607674113.
(292) Platzer, R.; Rossboth, B. K.; Schneider, M. C.; Sevcsik, E.; Baumgart, F.; Stockinger, H.; Schütz, G. J.; Huppa, J. B.; Brameshuber, M. Unscrambling Fluorophore Blinking for Comprehensive Cluster Detection via Photoactivated Localization Microscopy. *Nat. Commun.* **2020**, *11* (1), 4993. https://doi.org/10.1038/s41467-020-18726-9.
(293) Henrikus, S. S.; Tassis, K.; Zhang, L.; van der Velde, J. H. M.; Gebhardt, C.; Herrmann, A.; Jung, G.; Cordes, T. Characterization of Fluorescent Proteins with Intramolecular Photostabilization**. *ChemBioChem* **2021**, *22* (23), 3283–3291. https://doi.org/10.1002/cbic.202100276.
(294) Endesfelder, U.; Malkusch, S.; Fricke, F.; Heilemann, M. A Simple Method to Estimate the Average Localization Precision of a Single-Molecule Localization Microscopy Experiment. *Histochem. Cell Biol.* **2014**, *141* (6), 629–638. https://doi.org/10.1007/s00418-014-1192-3.
(295) Jusuk, I.; Vietz, C.; Raab, M.; Dammeyer, T.; Tinnefeld, P. Super-Resolution Imaging Conditions for Enhanced Yellow Fluorescent Protein (EYFP) Demonstrated on DNA Origami Nanorulers. *Sci. Rep.* **2015**, *5* (1), 14075. https://doi.org/10.1038/srep14075.
(296) Golfetto, O.; Wakefield, D. L.; Cacao, E. E.; Avery, K. N.; Kenyon, V.; Jorand, R.; Tobin, S. J.; Biswas, S.; Gutierrez, J.; Clinton, R.; Ma, Y.; Horne, D. A.; Williams, J. C.; Jovanović-Talisman, T. A Platform To Enhance Quantitative Single Molecule Localization Microscopy. *J. Am. Chem. Soc.* **2018**, *140* (40), 12785–12797. https://doi.org/10.1021/jacs.8b04939.
(297) Roebroek, T.; Duwé, S.; Vandenberg, W.; Dedecker, P. Reduced Fluorescent Protein Switching Fatigue by Binding-Induced Emissive State Stabilization. *Int. J. Mol. Sci.* **2017**, *18* (9), 2015. https://doi.org/10.3390/ijms18092015.
(298) Yang, F.; Moss, L. G.; Phillips, G. N. The Molecular Structure of Green Fluorescent Protein. *Nat. Biotechnol.* **1996**, *14* (10), 1246–1251. https://doi.org/10.1038/nbt1096-1246.
(299) Bourgeois, D. Deciphering Structural Photophysics of Fluorescent Proteins by Kinetic Crystallography. *Int. J. Mol. Sci.* **2017**, *18* (6). https://doi.org/10.3390/ijms18061187.
(300) Fromme, P.; Graves, W. S.; Martin-Garcia, J. M. Serial Femtosecond Crystallography: A Decade at the Forefront in Structural Biology. In *Encyclopedia of Life Sciences*; John Wiley & Sons, Ltd, 2020; pp 1–17. https://doi.org/10.1002/9780470015902.a0028964.

(301) Woodhouse, J.; Nass Kovacs, G.; Coquelle, N.; Uriarte, L. M.; Adam, V.; Barends, T. R. M.; Byrdin, M.; de la Mora, E.; Bruce Doak, R.; Feliks, M.; Field, M.; Fieschi, F.; Guillon, V.; Jakobs, S.; Joti, Y.; Macheboeuf, P.; Motomura, K.; Nass, K.; Owada, S.; Roome, C. M.; Ruckebusch, C.; Schirò, G.; Shoeman, R. L.; Thepaut, M.; Togashi, T.; Tono, K.; Yabashi, M.; Cammarata, M.; Foucar, L.; Bourgeois, D.; Sliwa, M.; Colletier, J.-P.; Schlichting, I.; Weik, M. Photoswitching Mechanism of a Fluorescent Protein Revealed by Time-Resolved Crystallography and Transient Absorption Spectroscopy. *Nat. Commun.* **2020**, *11* (1), 741. https://doi.org/10.1038/s41467-020-14537-0.
(302) Christou, N.-E.; Ayala, I.; Giandoreggio-Barranco, K.; Byrdin, M.; Adam, V.; Bourgeois, D.; Brutscher, B. NMR Reveals Light-Induced Changes in the Dynamics of a Photoswitchable Fluorescent Protein. *Biophys. J.* **2019**, *117* (11), 2087–2100. https://doi.org/10.1016/j.bpj.2019.10.035.
(303) Chang, J.; Romei, M. G.; Boxer, S. G. Structural Evidence of Photoisomerization Pathways in Fluorescent Proteins. *J. Am. Chem. Soc.* **2019**, *141* (39), 15504–15508. https://doi.org/10.1021/jacs.9b08356.
(304) De Zitter, E.; Coquelle, N.; Oeser, P.; Barends, T. R. M.; Colletier, J.-P. Xtrapol8 Enables Automatic Elucidation of Low-Occupancy Intermediate-States in Crystallographic Studies. *Commun. Biol.* **2022**, *5*, 640. https://doi.org/10.1038/s42003-022-03575-7.
(305) Dean, K. M.; Davis, L. M.; Lubbeck, J. L.; Manna, P.; Friis, P.; Palmer, A. E.; Jimenez, R. High-Speed Multiparameter Photophysical Analyses of Fluorophore Libraries. *Anal. Chem.* **2015**, *87* (10), 5026–5030. https://doi.org/10.1021/acs.analchem.5b00607.
(306) Wiens, M. D.; Hoffmann, F.; Chen, Y.; Campbell, R. E. Enhancing Fluorescent Protein Photostability through Robot-Assisted Photobleaching. *Integr. Biol. Quant. Biosci. Nano Macro* **2018**, *10* (7), 419–428. https://doi.org/10.1039/c8ib00063h.
(307) Lambert, G. G.; Depernet, H.; Gotthard, G.; Schultz, D. T.; Navizet, I.; Lambert, T.; Adams, S. R.; Torreblanca-Zanca, A.; Chu, M.; Bindels, D. S.; Levesque, V.; Nero Moffatt, J.; Salih, A.; Royant, A.; Shaner, N. C. Aequorea's Secrets Revealed: New Fluorescent Proteins with Unique Properties for Bioimaging and Biosensing. *PLoS Biol.* **2020**, *18* (11), e3000936. https://doi.org/10.1371/journal.pbio.3000936.
(308) Ong, W. Q.; Citron, Y. R.; Schnitzbauer, J.; Kamiyama, D.; Huang, B. Heavy Water: A Simple Solution to Increasing Brightness of Fluorescence Proteins in Super-Resolution Imaging. *Chem. Commun. Camb. Engl.* **2015**, *51* (70), 13451–13453. https://doi.org/10.1039/c5cc04575d.
(309) Maillard, J.; Klehs, K.; Rumble, C.; Vauthey, E.; Heilemann, M.; Fürstenberg, A. Universal Quenching of Common Fluorescent Probes by Water and Alcohols. *Chem. Sci.* **2021**, *12* (4), 1352–1362. https://doi.org/10.1039/D0SC05431C.
(310) Klehs, K.; Spahn, C.; Endesfelder, U.; Lee, S. F.; Fürstenberg, A.; Heilemann, M. Increasing the Brightness of Cyanine Fluorophores for Single-Molecule and Superresolution Imaging. *Chemphyschem Eur. J. Chem. Phys. Phys. Chem.* **2014**, *15* (4), 637–641. https://doi.org/10.1002/cphc.201300874.
(311) Peng, B.; Dikdan, R.; Hill, S. E.; Patterson-Orazem, A. C.; Lieberman, R. L.; Fahrni, C. J.; Dickson, R. M. Optically Modulated and Optically Activated Delayed Fluorescent Proteins through Dark State Engineering. *J. Phys. Chem. B* **2021**, *125* (20), 5200–5209. https://doi.org/10.1021/acs.jpcb.1c00649.
(312) Ludvikova, L.; Simon, E.; Deygas, M.; Panier, T.; Plamont, M.-A.; Ollion, J.; Tebo, A.; Piel, M.; Jullien, L.; Robert, L.; Le Saux, T.; Espagne, A. Near-Infrared Co-Illumination of Fluorescent Proteins Reduces Photobleaching and Phototoxicity. *Nat. Biotechnol.* **2023**, 1–5. https://doi.org/10.1038/s41587-023-01893-7.
(313) Donnert, G.; Eggeling, C.; Hell, S. W. Major Signal Increase in Fluorescence Microscopy through Dark-State Relaxation. *Nat. Methods* **2007**, *4* (1), 81–86. https://doi.org/10.1038/nmeth986.
(314) Glushonkov, O.; Réal, E.; Boutant, E.; Mély, Y.; Didier, P. Optimized Protocol for Combined PALM-DSTORM Imaging. *Sci. Rep.* **2018**, *8* (1), 8749. https://doi.org/10.1038/s41598-018-27059-z.
(315) Diekmann, R.; Kahnwald, M.; Schoenit, A.; Deschamps, J.; Matti, U.; Ries, J. Optimizing Imaging Speed and Excitation Intensity for Single-Molecule Localization Microscopy. *Nat. Methods* **2020**, *17* (9), 909–912. https://doi.org/10.1038/s41592-020-0918-5.

(316) Basu, S.; Needham, L.-M.; Lando, D.; Taylor, E. J. R.; Wohlfahrt, K. J.; Shah, D.; Boucher, W.; Tan, Y. L.; Bates, L. E.; Tkachenko, O.; Cramard, J.; Lagerholm, B. C.; Eggeling, C.; Hendrich, B.; Klenerman, D.; Lee, S. F.; Laue, E. D. FRET-Enhanced Photostability Allows Improved Single-Molecule Tracking of Proteins and Protein Complexes in Live Mammalian Cells. *Nat. Commun.* **2018**, *9*, 2520. https://doi.org/10.1038/s41467-018-04486-0.
(317) Jerkovic´, I.; Cavalli, G. Understanding 3D Genome Organization by Multidisciplinary Methods. *Nat. Rev. Mol. Cell Biol.* **2021**, *22* (8), 511–528. https://doi.org/10.1038/s41580-021-00362-w.
(318) Tolstorukov, M. Y.; Virnik, K.; Zhurkin, V. B.; Adhya, S. Organization of DNA in a Bacterial Nucleoid. *BMC Microbiol.* **2016**, *16* (1), 22. https://doi.org/10.1186/s12866-016-0637-3.
(319) Verma, S. C.; Qian, Z.; Adhya, S. L. Architecture of the Escherichia Coli Nucleoid. *PLOS Genet.* **2019**, *15* (12), e1008456. https://doi.org/10.1371/journal.pgen.1008456.
(320) Birnie, A.; Dekker, C. Genome-in-a-Box: Building a Chromosome from the Bottom Up. *ACS Nano* **2021**, *15* (1), 111–124. https://doi.org/10.1021/acsnano.0c07397.
(321) Dillon, S. C.; Dorman, C. J. Bacterial Nucleoid-Associated Proteins, Nucleoid Structure and Gene Expression. *Nat. Rev. Microbiol.* **2010**, *8* (3), 185–195. https://doi.org/10.1038/nrmicro2261.
(322) Joyeux, M. Preferential Localization of the Bacterial Nucleoid. *Microorganisms* **2019**, *7* (7), 204. https://doi.org/10.3390/microorganisms7070204.
(323) Gupta, A.; Joshi, A.; Arora, K.; Mukhopadhyay, S.; Guptasarma, P. The Bacterial Nucleoid-Associated Proteins, HU, and Dps, Condense DNA into Context-Dependent Biphasic or Multiphasic Complex Coacervates. *J. Biol. Chem.* **2023**, *0* (0). https://doi.org/10.1016/j.jbc.2023.104637.
(324) Feric, M.; Misteli, T. Phase Separation in Genome Organization across Evolution. *Trends Cell Biol.* **2021**, *31* (8), 671–685. https://doi.org/10.1016/j.tcb.2021.03.001.
(325) Lioy, V. S.; Cournac, A.; Marbouty, M.; Duigou, S.; Mozziconacci, J.; Espéli, O.; Boccard, F.; Koszul, R. Multiscale Structuring of the E. Coli Chromosome by Nucleoid-Associated and Condensin Proteins. *Cell* **2018**, *172* (4), 771-783.e18. https://doi.org/10.1016/j.cell.2017.12.027.
(326) Le, T. B. K.; Imakaev, M. V.; Mirny, L. A.; Laub, M. T. High-Resolution Mapping of the Spatial Organization of a Bacterial Chromosome. *Science* **2013**, *342* (6159), 731–734. https://doi.org/10.1126/science.1242059.
(327) Wu, F.; Japaridze, A.; Zheng, X.; Wiktor, J.; Kerssemakers, J. W. J.; Dekker, C. Direct Imaging of the Circular Chromosome in a Live Bacterium. *Nat. Commun.* **2019**, *10* (1), 2194. https://doi.org/10.1038/s41467-019-10221-0.
(328) Mäkelä, J.; Sherratt, D. J. Organization of the Escherichia Coli Chromosome by a MukBEF Axial Core. *Mol. Cell* **2020**, *78* (2), 250-260.e5. https://doi.org/10.1016/j.molcel.2020.02.003.
(329) Japaridze, A.; van Wee, R.; Gogou, C.; Kerssemakers, J. W. J.; van den Berg, D. F.; Dekker, C. MukBEF-Dependent Chromosomal Organization in Widened Escherichia Coli. *Front. Microbiol.* **2023**, *14*.
(330) Badrinarayanan, A.; Le, T. B.; Laub, M. T. Bacterial Chromosome Organization and Segregation. *Annu. Rev. Cell Dev. Biol.* **2015**, *31*, 171–199. https://doi.org/10.1146/annurev-cellbio-100814-125211.
(331) Lal, A.; Dhar, A.; Trostel, A.; Kouzine, F.; Seshasayee, A. S. N.; Adhya, S. Genome Scale Patterns of Supercoiling in a Bacterial Chromosome. *Nat. Commun.* **2016**, *7*, 11055. https://doi.org/10.1038/ncomms11055.
(332) Shen, B. A.; Landick, R. Transcription of Bacterial Chromatin. *J. Mol. Biol.* **2019**, *431* (20), 4040–4066. https://doi.org/10.1016/j.jmb.2019.05.041.
(333) Azaldegui, C. A.; Vecchiarelli, A. G.; Biteen, J. S. The Emergence of Phase Separation as an Organizing Principle in Bacteria. *Biophys. J.* **2021**, *120* (7), 1123–1138. https://doi.org/10.1016/j.bpj.2020.09.023.
(334) Ladouceur, A.-M.; Parmar, B. S.; Biedzinski, S.; Wall, J.; Tope, S. G.; Cohn, D.; Kim, A.; Soubry, N.; Reyes-Lamothe, R.; Weber, S. C. Clusters of Bacterial RNA Polymerase Are Biomolecular Condensates That Assemble through Liquid–Liquid Phase Separation. *Proc. Natl. Acad. Sci.* **2020**, *117* (31), 18540–18549. https://doi.org/10.1073/pnas.2005019117.

(335) Miné-Hattab, J.; Chiolo, I. Complex Chromatin Motions for DNA Repair. *Front. Genet.* **2020**, *11*.
(336) Cass, J. A.; Kuwada, N. J.; Traxler, B.; Wiggins, P. A. Escherichia Coli Chromosomal Loci Segregate from Midcell with Universal Dynamics. *Biophys. J.* **2016**, *110* (12), 2597–2609. https://doi.org/10.1016/j.bpj.2016.04.046.
(337) Zhu, Y.; Mustafi, M.; Weisshaar, J. C. Biophysical Properties of Escherichia Coli Cytoplasm in Stationary Phase by Superresolution Fluorescence Microscopy. *mBio* **2020**, *11* (3), e00143-20. https://doi.org/10.1128/mBio.00143-20.
(338) Zhu, Y.; Mohapatra, S.; Weisshaar, J. C. Rigidification of the Escherichia Coli Cytoplasm by the Human Antimicrobial Peptide LL-37 Revealed by Superresolution Fluorescence Microscopy. *Proc. Natl. Acad. Sci.* **2019**, *116* (3), 1017–1026. https://doi.org/10.1073/pnas.1814924116.
(339) Javer, A.; Long, Z.; Nugent, E.; Grisi, M.; Siriwatwetchakul, K.; Dorfman, K. D.; Cicuta, P.; Cosentino Lagomarsino, M. Short-Time Movement of E. Coli Chromosomal Loci Depends on Coordinate and Subcellular Localization. *Nat. Commun.* **2013**, *4* (1), 3003. https://doi.org/10.1038/ncomms3003.
(340) Elmore, S.; Müller, M.; Vischer, N.; Odijk, T.; Woldringh, C. L. Single-Particle Tracking of OriC-GFP Fluorescent Spots during Chromosome Segregation in Escherichia Coli. *J. Struct. Biol.* **2005**, *151* (3), 275–287. https://doi.org/10.1016/j.jsb.2005.06.004.
(341) Espeli, O.; Mercier, R.; Boccard, F. DNA Dynamics Vary According to Macrodomain Topography in the E. Coli Chromosome. *Mol. Microbiol.* **2008**, *68* (6), 1418–1427. https://doi.org/10.1111/j.1365-2958.2008.06239.x.
(342) Javer, A.; Kuwada, N. J.; Long, Z.; Benza, V. G.; Dorfman, K. D.; Wiggins, P. A.; Cicuta, P.; Lagomarsino, M. C. Persistent Super-Diffusive Motion of Escherichia Coli Chromosomal Loci. *Nat. Commun.* **2014**, *5* (1), 3854. https://doi.org/10.1038/ncomms4854.
(343) Wlodarski, M.; Raciti, B.; Kotar, J.; Cosentino Lagomarsino, M.; Fraser, G. M.; Cicuta, P. Both Genome and Cytosol Dynamics Change in E. Coli Challenged with Sublethal Rifampicin. *Phys. Biol.* **2017**, *14* (1), 015005. https://doi.org/10.1088/1478-3975/aa5b71.
(344) Wlodarski, M.; Mancini, L.; Raciti, B.; Sclavi, B.; Lagomarsino, M. C.; Cicuta, P. Cytosolic Crowding Drives the Dynamics of Both Genome and Cytosol in Escherichia Coli Challenged with Sub-Lethal Antibiotic Treatments. *iScience* **2020**, *23* (10), 101560. https://doi.org/10.1016/j.isci.2020.101560.
(345) Espéli, O.; Borne, R.; Dupaigne, P.; Thiel, A.; Gigant, E.; Mercier, R.; Boccard, F. A MatP-Divisome Interaction Coordinates Chromosome Segregation with Cell Division in E. Coli. *EMBO J.* **2012**, *31* (14), 3198–3211. https://doi.org/10.1038/emboj.2012.128.
(346) Thiel, A.; Valens, M.; Vallet-Gely, I.; Espéli, O.; Boccard, F. Long-Range Chromosome Organization in E. Coli: A Site-Specific System Isolates the Ter Macrodomain. *PLOS Genet.* **2012**, *8* (4), e1002672. https://doi.org/10.1371/journal.pgen.1002672.
(347) Azam, T. A.; Ishihama, A. Twelve Species of the Nucleoid-Associated Protein from Escherichia Coli: SEQUENCE RECOGNITION SPECIFICITY AND DNA BINDING AFFINITY*. *J. Biol. Chem.* **1999**, *274* (46), 33105–33113. https://doi.org/10.1074/jbc.274.46.33105.
(348) Verma, S. C.; Harned, A.; Narayan, K.; Adhya, S. Non-Specific and Specific DNA Binding Modes of Bacterial Histone, HU, Separately Regulate Distinct Physiological Processes through Different Mechanisms. *Mol. Microbiol.* **2023**, *119* (4), 439–455. https://doi.org/10.1111/mmi.15033.
(349) Prieto, A. I.; Kahramanoglou, C.; Ali, R. M.; Fraser, G. M.; Seshasayee, A. S. N.; Luscombe, N. M. Genomic Analysis of DNA Binding and Gene Regulation by Homologous Nucleoid-Associated Proteins IHF and HU in Escherichia Coli K12. *Nucleic Acids Res.* **2012**, *40* (8), 3524–3537. https://doi.org/10.1093/nar/gkr1236.
(350) Oberto, J.; Nabti, S.; Jooste, V.; Mignot, H.; Rouviere-Yaniv, J. The HU Regulon Is Composed of Genes Responding to Anaerobiosis, Acid Stress, High Osmolarity and SOS Induction. *PLoS ONE* **2009**, *4* (2), e4367. https://doi.org/10.1371/journal.pone.0004367.

(351) Berger, M.; Gerganova, V.; Berger, P.; Rapiteanu, R.; Lisicovas, V.; Dobrindt, U. Genes on a Wire: The Nucleoid-Associated Protein HU Insulates Transcription Units in Escherichia Coli. *Sci. Rep.* **2016**, *6* (1), 31512. https://doi.org/10.1038/srep31512.
(352) Miyabe, I.; Zhang, Q. M.; Kano, Y.; Yonei, S. Histone-like Protein HU Is Required for RecA Gene-Dependent DNA Repair and SOS Induction Pathways in UV-Irradiated Escherichia Coli. *Int. J. Radiat. Biol.* **2000**, *76* (1), 43–49. https://doi.org/10.1080/095530000138998.
(353) Thakur, B.; Arora, K.; Gupta, A.; Guptasarma, P. The DNA-Binding Protein HU Is a Molecular Glue That Attaches Bacteria to Extracellular DNA in Biofilms. *J. Biol. Chem.* **2021**, *296*, 100532. https://doi.org/10.1016/j.jbc.2021.100532.
(354) Claret, L.; Rouviere-Yaniv, J. Variation in HU Composition during Growth of Escherichia Coli: The Heterodimer Is Required for Long Term Survival11Edited by M. Gottesman. *J. Mol. Biol.* **1997**, *273* (1), 93–104. https://doi.org/10.1006/jmbi.1997.1310.
(355) Li, S.; Waters, R. Escherichia Coli Strains Lacking Protein HU Are UV Sensitive Due to a Role for HU in Homologous Recombination. *J. Bacteriol.* **1998**, *180* (15), 3750–3756. https://doi.org/10.1128/JB.180.15.3750-3756.1998.
(356) Boubrik, F.; Rouviere-Yaniv, J. Increased Sensitivity to Gamma Irradiation in Bacteria Lacking Protein HU. *Proc. Natl. Acad. Sci. U. S. A.* **1995**, *92* (9), 3958–3962.
(357) Remesh, S. G.; Verma, S. C.; Chen, J.-H.; Ekman, A. A.; Larabell, C. A.; Adhya, S.; Hammel, M. Nucleoid Remodeling during Environmental Adaptation Is Regulated by HU-Dependent DNA Bundling. *Nat. Commun.* **2020**, *11*, 2905. https://doi.org/10.1038/s41467-020-16724-5.
(358) Hammel, M.; Amlanjyoti, D.; Reyes, F. E.; Chen, J.-H.; Parpana, R.; Tang, H. Y. H.; Larabell, C. A.; Tainer, J. A.; Adhya, S. HU Multimerization Shift Controls Nucleoid Compaction. *Sci. Adv.* **2016**, *2* (7), e1600650. https://doi.org/10.1126/sciadv.1600650.
(359) Chen, S. W.; Banneville, A.-S.; Teulon, J.-M.; Timmins, J.; Pellequer, J.-L. Nanoscale Surface Structures of DNA Bound to Deinococcus Radiodurans HU Unveiled by Atomic Force Microscopy. *Nanoscale* **2020**, *12* (44), 22628–22638. https://doi.org/10.1039/D0NR05320A.
(360) van Noort, J.; Verbrugge, S.; Goosen, N.; Dekker, C.; Dame, R. T. Dual Architectural Roles of HU: Formation of Flexible Hinges and Rigid Filaments. *Proc. Natl. Acad. Sci.* **2004**, *101* (18), 6969–6974. https://doi.org/10.1073/pnas.0308230101.
(361) Swinger, K. K.; Lemberg, K. M.; Zhang, Y.; Rice, P. A. Flexible DNA Bending in HU–DNA Cocrystal Structures. *EMBO J.* **2003**, *22* (14), 3749–3760. https://doi.org/10.1093/emboj/cdg351.
(362) Song, H.; Shen, R.; Liu, X.; Yang, X.; Xie, K.; Guo, Z.; Wang, D. Histone Post-Translational Modification and the DNA Damage Response. *Genes Dis.* **2022**. https://doi.org/10.1016/j.gendis.2022.04.002.
(363) Bannister, A. J.; Kouzarides, T. Regulation of Chromatin by Histone Modifications. *Cell Res.* **2011**, *21* (3), 381–395. https://doi.org/10.1038/cr.2011.22.
(364) Barlow, V. L.; Tsai, Y.-H. Acetylation at Lysine 86 of Escherichia Coli HUβ Modulates the DNA-Binding Capability of the Protein. *Front. Microbiol.* **2022**, *12*, 809030. https://doi.org/10.3389/fmicb.2021.809030.
(365) Hou, J.; Dai, J.; Chen, Z.; Wang, Y.; Cao, J.; Hu, J.; Ye, S.; Hua, Y.; Zhao, Y. Phosphorylation Regulation of a Histone-like HU Protein from Deinococcus Radiodurans. *Protein Pept. Lett.* **2022**, *29* (10), 891–899. https://doi.org/10.2174/0929866529666220819121911.
(366) Colak, G.; Xie, Z.; Zhu, A. Y.; Dai, L.; Lu, Z.; Zhang, Y.; Wan, X.; Chen, Y.; Cha, Y. H.; Lin, H.; Zhao, Y.; Tan, M. Identification of Lysine Succinylation Substrates and the Succinylation Regulatory Enzyme CobB in Escherichia Coli*. *Mol. Cell. Proteomics* **2013**, *12* (12), 3509–3520. https://doi.org/10.1074/mcp.M113.031567.
(367) Ghosh, S.; Padmanabhan, B.; Anand, C.; Nagaraja, V. Lysine Acetylation of the Mycobacterium Tuberculosis HU Protein Modulates Its DNA Binding and Genome Organization. *Mol. Microbiol.* **2016**, *100* (4), 577–588. https://doi.org/10.1111/mmi.13339.
(368) Strzałka, A.; Kois-Ostrowska, A.; Kędra, M.; Łebkowski, T.; Bieniarz, G.; Szafran, M. J.; Jakimowicz, D. Enhanced Binding of an HU Homologue under Increased DNA Supercoiling Preserves

Chromosome Organisation and Sustains Streptomyces Hyphal Growth. *Nucleic Acids Res.* **2022**, *50* (21), 12202–12216. https://doi.org/10.1093/nar/gkac1093.
(369) Kamashev, D.; Rouviere-Yaniv, J. The Histone-like Protein HU Binds Specifically to DNA Recombination and Repair Intermediates. *EMBO J.* **2000**, *19* (23), 6527–6535. https://doi.org/10.1093/emboj/19.23.6527.
(370) Floc'h, K.; Lacroix, F.; Servant, P.; Wong, Y.-S.; Kleman, J.-P.; Bourgeois, D.; Timmins, J. Cell Morphology and Nucleoid Dynamics in Dividing Deinococcus Radiodurans. *Nat. Commun.* **2019**, *10* (1), 3815. https://doi.org/10.1038/s41467-019-11725-5.
(371) Kamagata, K.; Itoh, Y.; Tan, C.; Mano, E.; Wu, Y.; Mandali, S.; Takada, S.; Johnson, R. C. Testing Mechanisms of DNA Sliding by Architectural DNA-Binding Proteins: Dynamics of Single Wild-Type and Mutant Protein Molecules in Vitro and in Vivo. *Nucleic Acids Res.* **2021**, *49* (15), 8642–8664. https://doi.org/10.1093/nar/gkab658.
(372) Rösch, T. C.; Oviedo-Bocanegra, L. M.; Fritz, G.; Graumann, P. L. SMTracker: A Tool for Quantitative Analysis, Exploration and Visualization of Single-Molecule Tracking Data Reveals Highly Dynamic Binding of B. Subtilis Global Repressor AbrB throughout the Genome. *Sci. Rep.* **2018**, *8* (1), 15747. https://doi.org/10.1038/s41598-018-33842-9.
(373) Rafiei, N.; Cordova, M.; Navarre, W. W.; Milstein, J. N. Growth Phase-Dependent Chromosome Condensation and Heat-Stable Nucleoid-Structuring Protein Redistribution in Escherichia Coli under Osmotic Stress. *J. Bacteriol.* **2019**, *201* (23), e00469-19. https://doi.org/10.1128/JB.00469-19.
(374) Chawla, M.; Mishra, S.; Anand, K.; Parikh, P.; Mehta, M.; Vij, M.; Verma, T.; Singh, P.; Jakkala, K.; Verma, H. N.; AjitKumar, P.; Ganguli, M.; Narain Seshasayee, A. S.; Singh, A. Redox-Dependent Condensation of the Mycobacterial Nucleoid by WhiB4. *Redox Biol.* **2018**, *19*, 116–133. https://doi.org/10.1016/j.redox.2018.08.006.
(375) Scutigliani, E. M.; Scholl, E. R.; Grootemaat, A. E.; Khanal, S.; Kochan, J. A.; Krawczyk, P. M.; Reits, E. A.; Garzan, A.; Ngo, H. X.; Green, K. D.; Garneau-Tsodikova, S.; Ruijter, J. M.; van Veen, H. A.; van der Wel, N. N. Interfering With DNA Decondensation as a Strategy Against Mycobacteria. *Front. Microbiol.* **2018**, *9*, 2034. https://doi.org/10.3389/fmicb.2018.02034.
(376) Shechter, N.; Zaltzman, L.; Weiner, A.; Brumfeld, V.; Shimoni, E.; Fridmann-Sirkis, Y.; Minsky, A. Stress-Induced Condensation of Bacterial Genomes Results in Re-Pairing of Sister Chromosomes. *J. Biol. Chem.* **2013**, *288* (35), 25659–25667. https://doi.org/10.1074/jbc.M113.473025.
(377) Dwyer, D. J.; Camacho, D. M.; Kohanski, M. A.; Callura, J. M.; Collins, J. J. Antibiotic-Induced Bacterial Cell Death Exhibits Physiological and Biochemical Hallmarks of Apoptosis. *Mol. Cell* **2012**, *46* (5), 561–572. https://doi.org/10.1016/j.molcel.2012.04.027.
(378) Vickridge, E.; Planchenault, C.; Cockram, C.; Junceda, I. G.; Espéli, O. Management of E. Coli Sister Chromatid Cohesion in Response to Genotoxic Stress. *Nat. Commun.* **2017**, *8*, 14618. https://doi.org/10.1038/ncomms14618.
(379) Tour, C. B. de la; Mathieu, M.; Meyer, L.; Dupaigne, P.; Passot, F.; Servant, P.; Sommer, S.; Cam, E. L.; Confalonieri, F. In Vivo and in Vitro Characterization of DdrC, a DNA Damage Response Protein in Deinococcus Radiodurans Bacterium. *PLOS ONE* **2017**, *12* (5), e0177751. https://doi.org/10.1371/journal.pone.0177751.
(380) Odsbu, I.; Morigen; Skarstad, K. A Reduction in Ribonucleotide Reductase Activity Slows Down the Chromosome Replication Fork but Does Not Change Its Localization. *PLoS ONE* **2009**, *4* (10), e7617. https://doi.org/10.1371/journal.pone.0007617.
(381) Smith, B. T.; Grossman, A. D.; Walker, G. C. Localization of UvrA and Effect of DNA Damage on the Chromosome of Bacillus Subtilis. *J. Bacteriol.* **2002**, *184* (2), 488–493. https://doi.org/10.1128/JB.184.2.488-493.2002.
(382) Estévez Castro, C. F.; Serment-Guerrero, J. H.; Fuentes, J. L. Influence of UvrA, RecJ and RecN Gene Mutations on Nucleoid Reorganization in UV-Treated Escherichia Coli Cells. *FEMS Microbiol. Lett.* **2018**, *365* (11), fny110. https://doi.org/10.1093/femsle/fny110.
(383) Odsbu, I.; Skarstad, K. DNA Compaction in the Early Part of the SOS Response Is Dependent on RecN and RecA. *Microbiology* **2014**, *160* (5), 872–882. https://doi.org/10.1099/mic.0.075051-0.

(384) Hołówka, J.; Zakrzewska-Czerwińska, J. Nucleoid Associated Proteins: The Small Organizers That Help to Cope With Stress. *Front. Microbiol.* **2020**, *11*.
(385) Danilowicz, C.; Lee, C. H.; Kim, K.; Hatch, K.; Coljee, V. W.; Kleckner, N.; Prentiss, M. Single Molecule Detection of Direct, Homologous, DNA/DNA Pairing. *Proc. Natl. Acad. Sci.* **2009**, *106* (47), 19824–19829. https://doi.org/10.1073/pnas.0911214106.
(386) Baldwin, G. S.; Brooks, N. J.; Robson, R. E.; Wynveen, A.; Goldar, A.; Leikin, S.; Seddon, J. M.; Kornyshev, A. A. DNA Double Helices Recognize Mutual Sequence Homology in a Protein Free Environment. *J. Phys. Chem. B* **2008**, *112* (4), 1060–1064. https://doi.org/10.1021/jp7112297.
(387) Courcelle, J.; Khodursky, A.; Peter, B.; Brown, P. O.; Hanawalt, P. C. Comparative Gene Expression Profiles Following UV Exposure in Wild-Type and SOS-Deficient Escherichia Coli. *Genetics* **2001**, *158* (1), 41–64.
(388) Maslowska, K. H.; Makiela-Dzbenska, K.; Fijalkowska, I. J. The SOS System: A Complex and Tightly Regulated Response to DNA Damage. *Environ. Mol. Mutagen.* **2019**, *60* (4), 368–384. https://doi.org/10.1002/em.22267.
(389) Reyes, E. D.; Patidar, P. L.; Uranga, L. A.; Bortoletto, A. S.; Lusetti, S. L. RecN Is a Cohesin-like Protein That Stimulates Intermolecular DNA Interactions in Vitro. *J. Biol. Chem.* **2010**, *285* (22), 16521–16529. https://doi.org/10.1074/jbc.M110.119164.
(390) Herbert, S.; Brion, A.; Arbona, J.-M.; Lelek, M.; Veillet, A.; Lelandais, B.; Parmar, J.; Fernández, F. G.; Almayrac, E.; Khalil, Y.; Birgy, E.; Fabre, E.; Zimmer, C. Chromatin Stiffening Underlies Enhanced Locus Mobility after DNA Damage in Budding Yeast. *EMBO J.* **2017**, *36* (17), 2595–2608. https://doi.org/10.15252/embj.201695842.
(391) Paull, T. T.; Rogakou, E. P.; Yamazaki, V.; Kirchgessner, C. U.; Gellert, M.; Bonner, W. M. A Critical Role for Histone H2AX in Recruitment of Repair Factors to Nuclear Foci after DNA Damage. *Curr. Biol. CB* **2000**, *10* (15), 886–895. https://doi.org/10.1016/s0960-9822(00)00610-2.
(392) Rogakou, E. P.; Pilch, D. R.; Orr, A. H.; Ivanova, V. S.; Bonner, W. M. DNA Double-Stranded Breaks Induce Histone H2AX Phosphorylation on Serine 139. *J. Biol. Chem.* **1998**, *273* (10), 5858–5868. https://doi.org/10.1074/jbc.273.10.5858.
(393) Hauer, M. H.; Seeber, A.; Singh, V.; Thierry, R.; Sack, R.; Amitai, A.; Kryzhanovska, M.; Eglinger, J.; Holcman, D.; Owen-Hughes, T.; Gasser, S. M. Histone Degradation in Response to DNA Damage Enhances Chromatin Dynamics and Recombination Rates. *Nat. Struct. Mol. Biol.* **2017**, *24* (2), 99–107. https://doi.org/10.1038/nsmb.3347.
(394) Sakatos, A.; Babunovic, G. H.; Chase, M. R.; Dills, A.; Leszyk, J.; Rosebrock, T.; Bryson, B.; Fortune, S. M. Posttranslational Modification of a Histone-like Protein Regulates Phenotypic Resistance to Isoniazid in Mycobacteria. *Sci. Adv.* **2018**, *4* (5), eaao1478. https://doi.org/10.1126/sciadv.aao1478.
(395) Cesar, S.; Willis, L.; Huang, K. C. Bacterial Respiration during Stationary Phase Induces Intracellular Damage That Leads to Delayed Regrowth. *iScience* **2022**, *25* (3), 103765. https://doi.org/10.1016/j.isci.2022.103765.
(396) Kim, J.; Yoshimura, S.; Hizume, K.; Ohniwa, R.; Ishihama, A.; Takeyasu, K. Fundamental Structural Units of the Escherichia Coli Nucleoid Revealed by Atomic Force Microscopy. *Nucleic Acids Res.* **2004**, *32*, 1982–1992. https://doi.org/10.1093/nar/gkh512.
(397) Janissen, R.; Arens, M. M. A.; Vtyurina, N. N.; Rivai, Z.; Sunday, N. D.; Eslami-Mossallam, B.; Gritsenko, A. A.; Laan, L.; de Ridder, D.; Artsimovitch, I.; Dekker, N. H.; Abbondanzieri, E. A.; Meyer, A. S. Global DNA Compaction in Stationary-Phase Bacteria Does Not Affect Transcription. *Cell* **2018**, *174* (5), 1188-1199.e14. https://doi.org/10.1016/j.cell.2018.06.049.
(398) Karas, V. O.; Westerlaken, I.; Meyer, A. S. The DNA-Binding Protein from Starved Cells (Dps) Utilizes Dual Functions To Defend Cells against Multiple Stresses. *J. Bacteriol.* **2015**, *197* (19), 3206–3215. https://doi.org/10.1128/JB.00475-15.
(399) Nair, S.; Finkel, S. E. Dps Protects Cells against Multiple Stresses during Stationary Phase. *J. Bacteriol.* **2004**, *186* (13), 4192–4198. https://doi.org/10.1128/JB.186.13.4192-4198.2004.

(400) Guo, F.; Adhya, S. Spiral Structure of Escherichia Coli HUalphabeta Provides Foundation for DNA Supercoiling. *Proc. Natl. Acad. Sci. U. S. A.* **2007**, *104* (11), 4309–4314. https://doi.org/10.1073/pnas.0611686104.
(401) Ravanat, J.-L.; Douki, T. UV and Ionizing Radiations Induced DNA Damage, Differences and Similarities. *Radiat. Phys. Chem.* **2016**, *128*, 92–102. https://doi.org/10.1016/j.radphyschem.2016.07.007.
(402) Kuluncsics, Z.; Perdiz, D.; Brulay, E.; Muel, B.; Sage, E. Wavelength Dependence of Ultraviolet-Induced DNA Damage Distribution: Involvement of Direct or Indirect Mechanisms and Possible Artefacts. *J. Photochem. Photobiol. B* **1999**, *49* (1), 71–80. https://doi.org/10.1016/S1011-1344(99)00034-2.
(403) Setlow, R. B.; Carrier, W. L. Pyrimidine Dimers in Ultraviolet-Irradiated DNA's. *J. Mol. Biol.* **1966**, *17* (1), 237–254. https://doi.org/10.1016/S0022-2836(66)80105-5.
(404) Gomes, A. A.; Silva-Júnior, A. C. T.; Oliveira, E. B.; Asad, L. M. B. O.; Reis, N. C. S. C.; Felzenszwalb, I.; Kovary, K.; Asad, N. R. Reactive Oxygen Species Mediate Lethality Induced by Far-UV in *Escherichia Coli* Cells. *Redox Rep.* **2005**, *10* (2), 91–95. https://doi.org/10.1179/135100005X38833.
(405) Silva-Júnior, A. C. T.; Asad, L. M. B. O.; Felzenszwalb, I.; Asad, N. R. Mutagenicity Induced by UVC in Escherichia Coli Cells: Reactive Oxygen Species Involvement. *Redox Rep. Commun. Free Radic. Res.* **2011**, *16* (5), 187–192. https://doi.org/10.1179/1351000211Y.0000000010.
(406) Bradley, M. O.; Taylor, V. I. DNA Double-Strand Breaks Induced in Normal Human Cells during the Repair of Ultraviolet Light Damage. *Proc. Natl. Acad. Sci.* **1981**, *78* (6), 3619–3623. https://doi.org/10.1073/pnas.78.6.3619.
(407) Yajima, H.; Lee, K.-J.; Zhang, S.; Kobayashi, J.; Chen, B. P. C. DNA Double Strand Break Formation upon UV-Induced Replication Stress Activates ATM and DNA-PKcs Kinases. *J. Mol. Biol.* **2009**, *385* (3), 800–810. https://doi.org/10.1016/j.jmb.2008.11.036.
(408) Krisko, A.; Radman, M. Protein Damage and Death by Radiation in Escherichia Coli and Deinococcus Radiodurans. *Proc. Natl. Acad. Sci.* **2010**, *107* (32), 14373–14377. https://doi.org/10.1073/pnas.1009312107.
(409) Anderson, A.; Nordon, H.; Cain, R. F.; Parrish, G.; Duggan, D.; Anderson, A.; Nordan, H.; Parish, G.; Cullum-Dugan, D. Studies on a Radio-Resistant Micrococcus. I. Isolation, Morphology, Cultural Characteristics, and Resistance to Gamma Radiation. *Food Technol.* **1956**.
(410) Mattimore, V.; Battista, J. R. Radioresistance of Deinococcus Radiodurans: Functions Necessary to Survive Ionizing Radiation Are Also Necessary to Survive Prolonged Desiccation. *J. Bacteriol.* **1996**, *178* (3), 633–637. https://doi.org/10.1128/jb.178.3.633-637.1996.
(411) Passot, F. M.; Nguyen, H. H.; Dard-Dascot, C.; Thermes, C.; Servant, P.; Espéli, O.; Sommer, S. Nucleoid Organization in the Radioresistant Bacterium Deinococcus Radiodurans. *Mol. Microbiol.* **2015**, *97* (4), 759–774. https://doi.org/10.1111/mmi.13064.
(412) Harsojo, null; Kitayama, S.; Matsuyama, A. Genome Multiplicity and Radiation Resistance in Micrococcus Radiodurans. *J. Biochem. (Tokyo)* **1981**, *90* (3), 877–880. https://doi.org/10.1093/oxfordjournals.jbchem.a133544.
(413) Englander, J.; Klein, E.; Brumfeld, V.; Sharma, A. K.; Doherty, A. J.; Minsky, A. DNA Toroids: Framework for DNA Repair in Deinococcus Radiodurans and in Germinating Bacterial Spores. *J. Bacteriol.* **2004**, *186* (18), 5973–5977. https://doi.org/10.1128/JB.186.18.5973-5977.2004.
(414) Levin-Zaidman, S.; Englander, J.; Shimoni, E.; Sharma, A. K.; Minton, K. W.; Minsky, A. Ringlike Structure of the Deinococcus Radiodurans Genome: A Key to Radioresistance? *Science* **2003**, *299* (5604), 254–256. https://doi.org/10.1126/science.1077865.
(415) Minton, K. W.; Daly, M. J. A Model for Repair of Radiation-Induced DNA Double-Strand Breaks in the Extreme Radiophile Deinococcus Radiodurans. *BioEssays News Rev. Mol. Cell. Dev. Biol.* **1995**, *17* (5), 457–464. https://doi.org/10.1002/bies.950170514.
(416) Minton, K. W. DNA Repair in the Extremely Radioresistant Bacterium Deinococcus Radiodurans. *Mol. Microbiol.* **1994**, *13* (1), 9–15. https://doi.org/10.1111/j.1365-2958.1994.tb00397.x.

(417) Zimmerman, J. M.; Battista, J. R. A Ring-like Nucleoid Is Not Necessary for Radioresistance in the Deinococcaceae. *BMC Microbiol.* **2005**, *5* (1), 17. https://doi.org/10.1186/1471-2180-5-17.
(418) Toueille, M.; Mirabella, B.; Guérin, P.; Bouthier de la Tour, C.; Boisnard, S.; Nguyen, H. H.; Blanchard, L.; Servant, P.; de Groot, A.; Sommer, S.; Armengaud, J. A Comparative Proteomic Approach to Better Define Deinococcus Nucleoid Specificities. *J. Proteomics* **2012**, *75* (9), 2588–2600. https://doi.org/10.1016/j.jprot.2012.03.002.
(419) Nguyen, H. H.; De La Tour, C. B.; Toueille, M.; Vannier, F.; Sommer, S.; Servant, P. The Essential Histone-like Protein HU Plays a Major Role in Deinococcus Radiodurans Nucleoid Compaction. *Mol. Microbiol.* **2009**, *73* (2), 240–252. https://doi.org/10.1111/j.1365-2958.2009.06766.x.
(420) Kota, S.; Rajpurohit, Y. S.; Charaka, V. K.; Satoh, K.; Narumi, I.; Misra, H. S. DNA Gyrase of Deinococcus Radiodurans Is Characterized as Type II Bacterial Topoisomerase and Its Activity Is Differentially Regulated by PprA in Vitro. *Extremophiles* **2016**, *20* (2), 195–205. https://doi.org/10.1007/s00792-016-0814-1.
(421) Reon, B. J.; Nguyen, K. H.; Bhattacharyya, G.; Grove, A. Functional Comparison of Deinococcus Radiodurans Dps Proteins Suggests Distinct in Vivo Roles. *Biochem. J.* **2012**, *447* (3), 381–391. https://doi.org/10.1042/BJ20120902.
(422) Gao, L.; Zhou, Z.; Chen, X.; Zhang, W.; Lin, M.; Chen, M. Comparative Proteomics Analysis Reveals New Features of the Oxidative Stress Response in the Polyextremophilic Bacterium Deinococcus Radiodurans. *Microorganisms* **2020**, *8* (3), 451. https://doi.org/10.3390/microorganisms8030451.
(423) Santos, S. P.; Yang, Y.; Rosa, M. T. G.; Rodrigues, M. A. A.; De La Tour, C. B.; Sommer, S.; Teixeira, M.; Carrondo, M. A.; Cloetens, P.; Abreu, I. A.; Romão, C. V. The Interplay between Mn and Fe in Deinococcus Radiodurans Triggers Cellular Protection during Paraquat-Induced Oxidative Stress. *Sci. Rep.* **2019**, *9* (1), 17217. https://doi.org/10.1038/s41598-019-53140-2.
(424) Santos, S. P.; Mitchell, E. P.; Franquelim, H. G.; Castanho, M. A. R. B.; Abreu, I. A.; Romão, C. V. Dps from Deinococcus Radiodurans: Oligomeric Forms of Dps1 with Distinct Cellular Functions and Dps2 Involved in Metal Storage. *FEBS J.* **2015**, *282* (22), 4307–4327. https://doi.org/10.1111/febs.13420.
(425) Ott, E.; Kawaguchi, Y.; Kölbl, D.; Rabbow, E.; Rettberg, P.; Mora, M.; Moissl-Eichinger, C.; Weckwerth, W.; Yamagishi, A.; Milojevic, T. Molecular Repertoire of Deinococcus Radiodurans after 1 Year of Exposure Outside the International Space Station within the Tanpopo Mission. *Microbiome* **2020**, *8* (1), 150. https://doi.org/10.1186/s40168-020-00927-5.
(426) Magerand, R.; Rey, P.; Blanchard, L.; de Groot, A. Redox Signaling through Zinc Activates the Radiation Response in Deinococcus Bacteria. *Sci. Rep.* **2021**, *11* (1), 4528. https://doi.org/10.1038/s41598-021-84026-x.
(427) Narumi, I.; Satoh, K.; Kikuchi, M.; Funayama, T.; Yanagisawa, T.; Kobayashi, Y.; Watanabe, H.; Yamamoto, K. The LexA Protein from Deinococcus Radiodurans Is Not Involved in RecA Induction Following γ Irradiation. *J. Bacteriol.* **2001**, *183* (23), 6951–6956. https://doi.org/10.1128/JB.183.23.6951-6956.2001.
(428) Blanchard, L.; de Groot, A. Coexistence of SOS-Dependent and SOS-Independent Regulation of DNA Repair Genes in Radiation-Resistant Deinococcus Bacteria. *Cells* **2021**, *10* (4), 924. https://doi.org/10.3390/cells10040924.
(429) Blanchard, L.; Guérin, P.; Roche, D.; Cruveiller, S.; Pignol, D.; Vallenet, D.; Armengaud, J.; de Groot, A. Conservation and Diversity of the IrrE/DdrO-Controlled Radiation Response in Radiation-Resistant Deinococcus Bacteria. *MicrobiologyOpen* **2017**, *6* (4), e00477. https://doi.org/10.1002/mbo3.477.
(430) Eugénie, N.; Zivanovic, Y.; Lelandais, G.; Coste, G.; Bouthier de la Tour, C.; Bentchikou, E.; Servant, P.; Confalonieri, F. Characterization of the Radiation Desiccation Response Regulon of the Radioresistant Bacterium Deinococcus Radiodurans by Integrative Genomic Analyses. *Cells* **2021**, *10* (10), 2536. https://doi.org/10.3390/cells10102536.

(431) Rajpurohit, Y. S.; Sharma, D. K.; Misra, H. S. PprA Protein Inhibits DNA Strand Exchange and ATP Hydrolysis of Deinococcus RecA and Regulates the Recombination in Gamma-Irradiated Cells. *Front. Cell Dev. Biol.* **2021**, *9*.
(432) Kota, S.; Charaka, V. K.; Ringgaard, S.; Waldor, M. K.; Misra, H. S. PprA Contributes to Deinococcus Radiodurans Resistance to Nalidixic Acid, Genome Maintenance after DNA Damage and Interacts with Deinococcal Topoisomerases. *PLOS ONE* **2014**, *9* (1), e85288. https://doi.org/10.1371/journal.pone.0085288.
(433) Banneville, A.-S.; Bouthier de la Tour, C.; De Bonis, S.; Hognon, C.; Colletier, J.-P.; Teulon, J.-M.; Le Roy, A.; Pellequer, J.-L.; Monari, A.; Dehez, F.; Confalonieri, F.; Servant, P.; Timmins, J. Structural and Functional Characterization of DdrC, a Novel DNA Damage-Induced Nucleoid Associated Protein Involved in DNA Compaction. *Nucleic Acids Res.* **2022**, *50* (13), 7680–7696. https://doi.org/10.1093/nar/gkac563.
(434) Devigne, A.; Ithurbide, S.; Bouthier de la Tour, C.; Passot, F.; Mathieu, M.; Sommer, S.; Servant, P. DdrO Is an Essential Protein That Regulates the Radiation Desiccation Response and the Apoptotic-like Cell Death in the Radioresistant Deinococcus Radiodurans Bacterium. *Mol. Microbiol.* **2015**, *96* (5), 1069–1084. https://doi.org/10.1111/mmi.12991.
(435) Dey, S.; Fan, C.; Gothelf, K. V.; Li, J.; Lin, C.; Liu, L.; Liu, N.; Nijenhuis, M. A. D.; Saccà, B.; Simmel, F. C.; Yan, H.; Zhan, P. DNA Origami. *Nat. Rev. Methods Primer* **2021**, *1* (1), 1–24. https://doi.org/10.1038/s43586-020-00009-8.
(436) Helmerich, D. A.; Beliu, G.; Matikonda, S. S.; Schnermann, M. J.; Sauer, M. Photoblueing of Organic Dyes Can Cause Artifacts in Super-Resolution Microscopy. *Nat. Methods* **2021**, *18* (3), 253–257. https://doi.org/10.1038/s41592-021-01061-2.
(437) Floc'h, K.; Lacroix, F.; Barbieri, L.; Servant, P.; Galland, R.; Butler, C.; Sibarita, J.-B.; Bourgeois, D.; Timmins, J. Bacterial Cell Wall Nanoimaging by Autoblinking Microscopy. *Sci. Rep.* **2018**, *8* (1), 14038. https://doi.org/10.1038/s41598-018-32335-z.
(438) Mau, A.; Friedl, K.; Leterrier, C.; Bourg, N.; Lévêque-Fort, S. Fast Widefield Scan Provides Tunable and Uniform Illumination Optimizing Super-Resolution Microscopy on Large Fields. *Nat. Commun.* **2021**, *12* (1), 3077. https://doi.org/10.1038/s41467-021-23405-4.
(439) McEvoy, A. L.; Hoi, H.; Bates, M.; Platonova, E.; Cranfill, P. J.; Baird, M. A.; Davidson, M. W.; Ewers, H.; Liphardt, J.; Campbell, R. E. MMaple: A Photoconvertible Fluorescent Protein for Use in Multiple Imaging Modalities. *PLOS ONE* **2012**, *7* (12), e51314. https://doi.org/10.1371/journal.pone.0051314.
(440) Rothemund, P. W. K. Folding DNA to Create Nanoscale Shapes and Patterns. *Nature* **2006**, *440* (7082), 297–302. https://doi.org/10.1038/nature04586.
(441) Cho, Y.; An, H. J.; Kim, T.; Lee, C.; Lee, N. K. Mechanism of Cyanine5 to Cyanine3 Photoconversion and Its Application for High-Density Single-Particle Tracking in a Living Cell. *J. Am. Chem. Soc.* **2021**, *143* (35), 14125–14135. https://doi.org/10.1021/jacs.1c04178.
(442) Zakeri, B.; Fierer, J. O.; Celik, E.; Chittock, E. C.; Schwarz-Linek, U.; Moy, V. T.; Howarth, M. Peptide Tag Forming a Rapid Covalent Bond to a Protein, through Engineering a Bacterial Adhesin. *Proc. Natl. Acad. Sci.* **2012**, *109* (12), E690–E697. https://doi.org/10.1073/pnas.1115485109.
(443) Fujiwara, T.; Takeuchi, S.; Kalay, Z.; Nagai, Y.; Tsunoyama, T.-A.; Kalkbrenner, T.; Iwasawa, K.; Ritchie, K.; Suzuki, K.; Kusumi, A. *Development of Ultrafast Camera-Based Imaging of Single Fluorescent Molecules and Live-Cell PALM*; 2021. https://doi.org/10.1101/2021.10.26.465864.
(444) Wulffele, J.; Thédié, D.; Glushonkov, O.; Bourgeois, D. MEos4b Photoconversion Efficiency Depends on Laser Illumination Conditions Used in PALM. *J. Phys. Chem. Lett.* **2022**, 5075–5080. https://doi.org/10.1021/acs.jpclett.2c00933.
(445) Vegh, R. B.; Bravaya, K. B.; Bloch, D. A.; Bommarius, A. S.; Tolbert, L. M.; Verkhovsky, M.; Krylov, A. I.; Solntsev, K. M. Chromophore Photoreduction in Red Fluorescent Proteins Is Responsible for Bleaching and Phototoxicity. *J. Phys. Chem. B* **2014**, *118* (17), 4527–4534. https://doi.org/10.1021/jp500919a.
(446) Drobizhev, M.; Molina, R. S.; Franklin, J. Multiphoton Bleaching of Red Fluorescent Proteins and the Ways to Reduce It. *Int. J. Mol. Sci.* **2022**, *23* (2), 770. https://doi.org/10.3390/ijms23020770.

(447) Byrdin, M.; Bourgeois, D. The CAL(AI)2DOSCOPE: A Microspectrophotometer for Accurate Recording of Correlated Absorbance and Fluorescence Emission Spectra. *Spectrosc. Eur.* **2016**, *28* (6), 14.
(448) Wachter, R. M. Photoconvertible Fluorescent Proteins and the Role of Dynamics in Protein Evolution. *Int. J. Mol. Sci.* **2017**, *18* (8), 1792. https://doi.org/10.3390/ijms18081792.
(449) Sotome, H.; Une, K.; Nagasaka, T.; Kobatake, S.; Irie, M.; Miyasaka, H. A Dominant Factor of the Cycloreversion Reactivity of Diarylethene Derivatives as Revealed by Femtosecond Time-Resolved Absorption Spectroscopy. *J. Chem. Phys.* **2020**, *152* (3), 034301. https://doi.org/10.1063/1.5134552.
(450) Sukhi, S. S.; Shashidhar, R.; Kumar, S. A.; Bandekar, J. R. Radiation Resistance of Deinococcus Radiodurans R1 with Respect to Growth Phase. *FEMS Microbiol. Lett.* **2009**, *297* (1), 49–53. https://doi.org/10.1111/j.1574-6968.2009.01652.x.
(451) von Chamier, L.; Laine, R. F.; Jukkala, J.; Spahn, C.; Krentzel, D.; Nehme, E.; Lerche, M.; Hernández-Pérez, S.; Mattila, P. K.; Karinou, E.; Holden, S.; Solak, A. C.; Krull, A.; Buchholz, T.-O.; Jones, M. L.; Royer, L. A.; Leterrier, C.; Shechtman, Y.; Jug, F.; Heilemann, M.; Jacquemet, G.; Henriques, R. Democratising Deep Learning for Microscopy with ZeroCostDL4Mic. *Nat. Commun.* **2021**, *12* (1), 2276. https://doi.org/10.1038/s41467-021-22518-0.
(452) Spahn, C.; Gómez-de-Mariscal, E.; Laine, R. F.; Pereira, P. M.; von Chamier, L.; Conduit, M.; Pinho, M. G.; Jacquemet, G.; Holden, S.; Heilemann, M.; Henriques, R. DeepBacs for Multi-Task Bacterial Image Analysis Using Open-Source Deep Learning Approaches. *Commun. Biol.* **2022**, *5* (1), 1–18. https://doi.org/10.1038/s42003-022-03634-z.
(453) Hauer, M.; Gasser, S. Chromatin and Nucleosome Dynamics in DNA Damage and Repair. *Genes Dev.* **2017**, *31*, 2204–2221. https://doi.org/10.1101/gad.307702.117.
(454) Oshidari, R.; Mekhail, K.; Seeber, A. Mobility and Repair of Damaged DNA: Random or Directed? *Trends Cell Biol.* **2020**, *30* (2), 144–156. https://doi.org/10.1016/j.tcb.2019.11.003.
(455) dos Santos, Á.; Cook, A. W.; Gough, R. E.; Schilling, M.; Olszok, N. A.; Brown, I.; Wang, L.; Aaron, J.; Martin-Fernandez, M. L.; Rehfeldt, F.; Toseland, C. P. DNA Damage Alters Nuclear Mechanics through Chromatin Reorganization. *Nucleic Acids Res.* **2020**, *49* (1), 340–353. https://doi.org/10.1093/nar/gkaa1202.
(456) Chai, Q.; Singh, B.; Peisker, K.; Metzendorf, N.; Ge, X.; Dasgupta, S.; Sanyal, S. Organization of Ribosomes and Nucleoids in Escherichia Coli Cells during Growth and in Quiescence. *J. Biol. Chem.* **2014**, *289* (16), 11342–11352. https://doi.org/10.1074/jbc.M114.557348.
(457) Bakshi, S.; Choi, H.; Mondal, J.; Weisshaar, J. C. Time-Dependent Effects of Transcription- and Translation-Halting Drugs on the Spatial Distributions of the E. Coli Chromosome and Ribosomes. *Mol. Microbiol.* **2014**, *94* (4), 871–887. https://doi.org/10.1111/mmi.12805.
(458) Cheblal, A.; Challa, K.; Seeber, A.; Shimada, K.; Yoshida, H.; Ferreira, H. C.; Amitai, A.; Gasser, S. M. DNA Damage-Induced Nucleosome Depletion Enhances Homology Search Independently of Local Break Movement. *Mol. Cell* **2020**, *80* (2), 311-326.e4. https://doi.org/10.1016/j.molcel.2020.09.002.
(459) Marian, C. M.; Etinski, M.; Rai-Constapel, V. Reverse Intersystem Crossing in Rhodamines by Near-Infrared Laser Excitation. *J. Phys. Chem. A* **2014**, *118* (34), 6985–6990. https://doi.org/10.1021/jp506904v.
(460) Jumper, J.; Evans, R.; Pritzel, A.; Green, T.; Figurnov, M.; Ronneberger, O.; Tunyasuvunakool, K.; Bates, R.; Žídek, A.; Potapenko, A.; Bridgland, A.; Meyer, C.; Kohl, S. A. A.; Ballard, A. J.; Cowie, A.; Romera-Paredes, B.; Nikolov, S.; Jain, R.; Adler, J.; Back, T.; Petersen, S.; Reiman, D.; Clancy, E.; Zielinski, M.; Steinegger, M.; Pacholska, M.; Berghammer, T.; Bodenstein, S.; Silver, D.; Vinyals, O.; Senior, A. W.; Kavukcuoglu, K.; Kohli, P.; Hassabis, D. Highly Accurate Protein Structure Prediction with AlphaFold. *Nature* **2021**, *596* (7873), 583–589. https://doi.org/10.1038/s41586-021-03819-2.
(461) Hartley, S. M.; Tiernan, K. A.; Ahmetaj, G.; Cretu, A.; Zhuang, Y.; Zimmer, M. AlphaFold2 and RoseTTAFold Predict Posttranslational Modifications. Chromophore Formation in GFP-like Proteins. *PLOS ONE* **2022**, *17* (6), e0267560. https://doi.org/10.1371/journal.pone.0267560.

(462) Banaz, N.; Mäkelä, J.; Uphoff, S. Choosing the Right Label for Single-Molecule Tracking in Live Bacteria: Side-by-Side Comparison of Photoactivatable Fluorescent Protein and Halo Tag Dyes. *J. Phys. Appl. Phys.* **2018**, *52* (6), 064002. https://doi.org/10.1088/1361-6463/aaf255.
(463) Erdmann, R. S.; Baguley, S. W.; Richens, J. H.; Wissner, R. F.; Xi, Z.; Allgeyer, E. S.; Zhong, S.; Thompson, A. D.; Lowe, N.; Butler, R.; Bewersdorf, J.; Rothman, J. E.; St Johnston, D.; Schepartz, A.; Toomre, D. Labeling Strategies Matter for Super-Resolution Microscopy: A Comparison between HaloTags and SNAP-Tags. *Cell Chem. Biol.* **2019**, *26* (4), 584-592.e6. https://doi.org/10.1016/j.chembiol.2019.01.003.
(464) Barlag, B.; Beutel, O.; Janning, D.; Czarniak, F.; Richter, C. P.; Kommnick, C.; Göser, V.; Kurre, R.; Fabiani, F.; Erhardt, M.; Piehler, J.; Hensel, M. Single Molecule Super-Resolution Imaging of Proteins in Living Salmonella Enterica Using Self-Labelling Enzymes. *Sci. Rep.* **2016**, *6* (1), 31601. https://doi.org/10.1038/srep31601.
(465) Baibakov, M.; Wenger, J. Laser-Induced Fluorescence Quenching of Red Fluorescent Dyes with Green Excitation: Avoiding Artifacts in PIE-FRET and FCCS Analysis. *Chem. Phys. Lett.* **2018**, *706*, 669–674. https://doi.org/10.1016/j.cplett.2018.06.057.
(466) Isselstein, M.; Zhang, L.; Glembockyte, V.; Brix, O.; Cosa, G.; Tinnefeld, P.; Cordes, T. Self-Healing Dyes—Keeping the Promise? *J. Phys. Chem. Lett.* **2020**, *11* (11), 4462–4480. https://doi.org/10.1021/acs.jpclett.9b03833.
(467) Adam, V.; Carpentier, P.; Violot, S.; Lelimousin, M.; Darnault, C.; Nienhaus, G. U.; Bourgeois, D. Structural Basis of X-Ray-Induced Transient Photobleaching in a Photoactivatable Green Fluorescent Protein. *J. Am. Chem. Soc.* **2009**, *131* (50), 18063–18065. https://doi.org/10.1021/ja907296v.
(468) Adam, V.; Nienhaus, K.; Bourgeois, D.; Nienhaus, G. U. Structural Basis of Enhanced Photoconversion Yield in Green Fluorescent Protein-like Protein Dendra2. *Biochemistry* **2009**, *48* (22), 4905–4915. https://doi.org/10.1021/bi900383a.
(469) Nienhaus, K.; Ulrich Nienhaus, G. Fluorescent Proteins of the EosFP Clade: Intriguing Marker Tools with Multiple Photoactivation Modes for Advanced Microscopy. *RSC Chem. Biol.* **2021**, *2* (3), 796–814. https://doi.org/10.1039/D1CB00014D.

6 Appendices

6.1 Supplementary figures

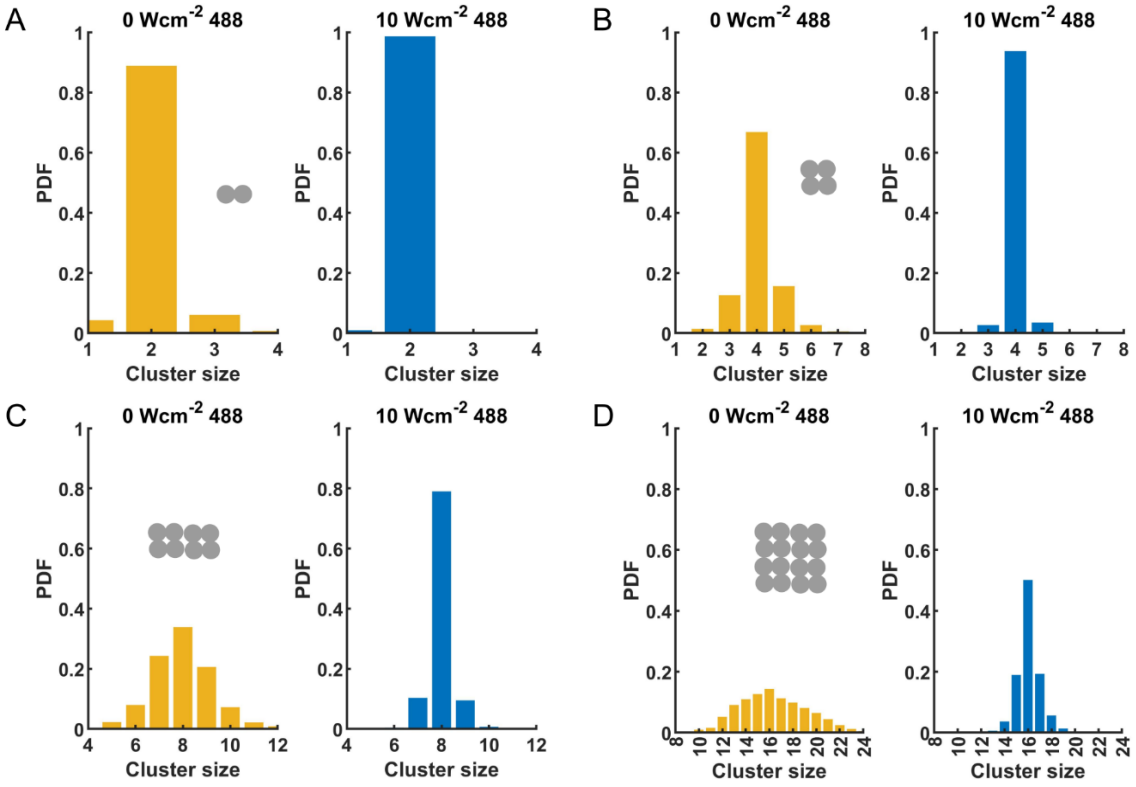

Supplementary Figure 1 Reduction of long-lived blinks facilitates molecule counting by off-time thresholding. *Molecular counting of simulated oligomers was performed as described by Lee et al. Simulations were performed with (blue histograms) and without (yellow histograms) 10 W/cm² 488 nm light to reduce the live-time of long-lived blinks. Counted were oligomers of various stoichiometries: dimers (A), tetramers (B), octamers (C) and 16-mers (D).*

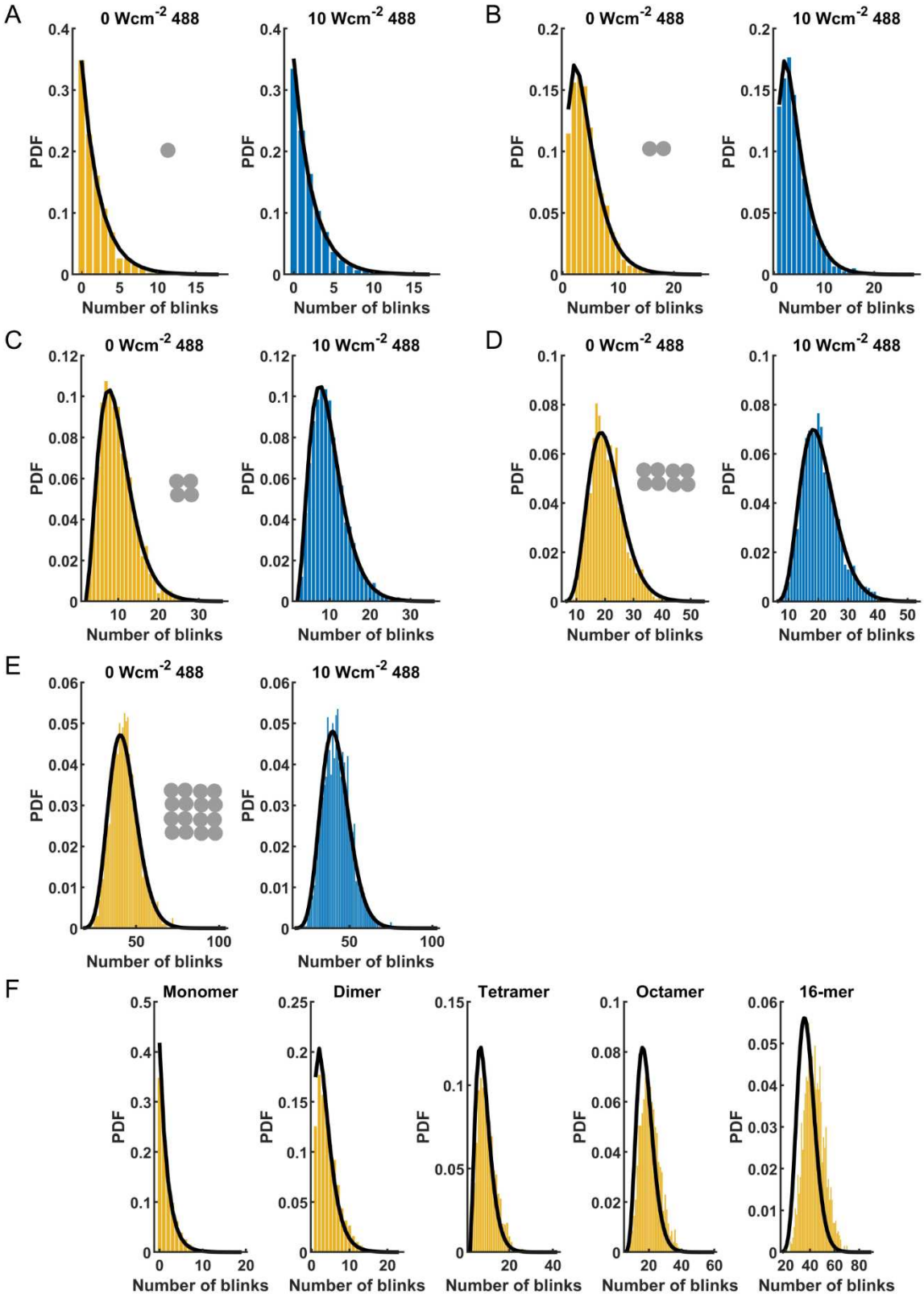

Supplementary Figure 2 Off-time reduction does not facilitate counting by blinking statistics. *Molecular counting of simulated oligomers was performed as described by XXX. Simulations were performed with (blue histograms) and without (yellow histograms) 10 W/cm^2 488 nm light to reduce the live-time of long-lived blinks. Monomers (A), dimers (B), tetramers (C), octamers (D) and 16-mers (E) were reconstituted with a labeling efficiency of 1 and histograms of the number of blinks (nBlink) were plotted. Solid lines show fits of the p-value (A) or fits of negative binomial distributions (B-E) according to ref 8, assuming a labeling efficiency of 1. F) A*

20% error was added to the p-value (p=0.42 instead of p=0.35), resulting in large deviations between the expected nBlink distribution (solid lines) and measured data (yellow histograms) at high stoichiometries.

6.2 Building a refined model of mEos4b in SMIS

6.2.1 Model design

The design of the proposed photophysical model of mEos4b is shown in **Figure 4.2** and **Supplementary Table 1** provides an overview of all the tentative states.

Supplementary Table 1 List of the tentative states of mEos4b. *Note that listed halflifes and rates might depend on environmental factors, such as pH, redox environment and temperature.*

Group	**State**	**Characteristics**	**References**
Green A-state	On, *cis* anionic	• Fluorescent state, *cis* anionic chromophore • Referred to as the 'On-state' • Ex = 505 nm, Em = 516 • In fast equilibrium with the *cis* neutral state (pKa = 5.5, h = ~0.75) • Inefficient 'readout' photoconversion might occur from this state (primed photoconversion?)	[150,204]
	On, *cis* neutral	• Non-fluorescent state, *cis* neutral chromophore • Absorption around 400 nm • Photoconversion predominantly occurs from this state • Very prone to isomerization	
	Off, *trans* anionic	• Non-fluorescent state, *trans* anionic chromophore • Ex = 505 nm • In fast equilibrium with the *trans* neutral state (pKa>> 10) • Typically, undetectable because of its high pKa	
	Off, *trans* neutral	• Non-fluorescent state, *trans* neutral chromophore • Referred to as the classical 'Off-state' • Absorption around 400 nm • Thermal relaxation to the *cis* state, half-life of ~2.8 hours	[218]
	Triplet state – *cis* anionic chromophore	• Phosphorescent state formed from the On-state • High formation quantum yield (0.1-1%) • Expected life time ~ 5 ms • Expectedly a broad absorption spectrum • Gateway to diverse dark/off-states and bleached states	
	Off_{488}	• Non-fluorescent state, expectedly down-stream of the triplet state (radical state?) • Half-life ~400 ms • Absorbs around 488 nm • Could Off_{488} and Off_T be the same state?	[204,218] see **section 1.3.3.1**
	Off_T	• Short-lived non-fluorescent state, expectedly down-stream of the triplet state • Responsible for fast fluorescence decay under low illumination intensities • Presumably light sensitive	**Section 3.1.4.2**

		• Half-life >100 ms? • Could Off_{488} and Off_T be the same state?	
	Triplet state – *cis* neutral chromophore	• Phosphorescent state formed from the neutral chromophore • Expected life time ~ 5ms • Intermediate state presenting a gateway to nonlinear bleaching under high 405 nm light intensities (10-100 W/cm^2) resulting in a reduced PCE	**Section 3.1.3**
Green B-state		• Differs from the green A-state in the H-bonding network around the chromophore • Expectedly contains the same states as the green A-state • In thermal exchange with the A-state (k = 2e-2 s^{-1}, at 35°C) • A/B equilibrium is pH dependent: lower pH more A state • 405 nm light favors the B-state • The B-state is prone to bleaching and has a low photoconversion quantum yield • A/B heterogeneity is responsible for the dependence of the PCE on the 405 nm light power density under low illumination intensities (< 1W/cm^2) • A/B heterogeneity contributes to the multiphasic character of off-switching (*cis*/*trans* isomerization)	**Section 3.1.4.1**
Red-state	On, *cis* anionic	• Fluorescent state, *cis* anionic chromophore • Referred to as the 'On-state' • Ex = 570 nm, Em = 580 • In fast equilibrium with the cis neutral state (pKa = 5.8, h = ~0.75)	[150]
	On, *cis* neutral	• Non-fluorescent state, *cis* neutral chromophore • Absorption around 400/488 nm • Very prone to isomerization: likely explains population of the neutral state by excitation with 405 nm light at low pH	[199] **Section 3.1.4.3.2**
	Off, *trans* anionic	• Non-fluorescent state, *trans* anionic chromophore • Ex = 570 nm • In fast equilibrium with the *trans* neutral state (pKa >> 10) • Typically undetectable because of its high pKa	
	Off, *trans* neutral	• Non-fluorescent state, *trans* neutral chromophore • Referred to as the classical 'Off-state' • Absorption around 400/488 nm • Thermal relaxation to the *cis* state, half-life of ~2 hours	[217]
	Triplet state – *cis* anionic chromophore	• Phosphorescent state formed from the On-state • High formation quantum yield (0.1-1%) • Expected life time ~ 5ms • Expectedly a broad absorption spectrum	

		• Gateway to diverse dark/off-states and bleached states	
	Off_{405}	• Non-fluorescent state, expectedly down-stream of the triplet state • Sensitive to 405 nm light • Expectedly explains the better off-time reduction by 405 nm light than by 488 nm light • Possibly involved in nonlinear bleaching promoted by 405 nm light (combined effect of 561 and 405 nm light?)	[217] **Section 3.1.3** **Section 3.1.4.3.1**
	$Dark_1$	• Short-lived non-fluorescent state, expectedly down-stream of the triplet state • Non-absorbing • Proposed to be a radical state • Responsible for short-lived blinks in PALM experiments	[217]
	Triplet state – *cis* neutral chromophore	• Non-fluorescent state formed from the neutral chromophore • Expected life time ~ 5ms • Expectedly a broad absorption spectrum • Gateway to diverse dark/off-states and bleached states • Possibly the intermediate state presenting a gateway to nonlinear bleaching under high 405 nm light intensities, similairly as in the green state	
	$Off_{neutral}$	• Non-fluorescent state, expectedly down-stream of the triplet state (neutral chromophore) • Sensitive to 561 nm light • Its formation can affect estimation of the PCE in ensemble measurements	[148] **Section 3.1.4.3.2**
Red XX-state		• NMR data suggests that, in contrast to the green state, the red ground-state of mEos4b is homogenous (no A/B–like partitioning). This may be explained by the involvement of H62 in the A/B heterogeneity (different tautomeric states), which may no longer be possible when H62 is incorporated into the chromophore.	Data not shown
Bleached	Bleached	• Irreversible non-fluorescent state due to destruction of the chromophore or chromophore environment • Bleaching may occur from every light-absorbing state • There exists a variety of bleaching pathways and thus expectedly a variety of bleached states • Illumination conditions (wavelength and intensity) and environmental conditions (pH, redox…) determine the dominant bleaching pathway(s)	[89]

6.2.2 Absorption and emission spectra spectra

All absorption and emission spectra are shown in **Supplementary Figure 3**. **Supplementary Table 2** lists the extinction coefficients of all states.

The absorption and emission spectra of the green and red anionic states were taken from FPbase[68]. The absorption spectra of the green and red neutral states were available in the lab[217,218]. The experimental absorption spectrum of the red neutral state was modified to introduce weak absorption around 561 nm light (as was observed in[217]). The absorption spectra of the other states are unknown and were approximated based on their known, or expected, light sensitivity. The short-lived green off-states (Off_{488} and Off_{T}) are sensitive to 488 nm light (but likely not to 561 nm light, see[204,218]), so there absorption spectra were approximated by a narrow Gaussian function peaking at 488 nm. The absorption spectrum of the red off-state Off_{405} was approximated by a narrow Gaussian function peaking at 405 nm, allowing only minimal absorption at 488 nm. The absorption spectrum of the red off-state $Off_{neutral}$ was approximated by a Gaussian function peaking at 561 nm.

The design of the triplet state absorption spectra was based on the experimentally measured triplet state spectra of EGFP and rsEGFP2[100], showing a broad absorption in both the visible spectrum as well as in the NIR. Thus, the absorption spectra of the triplet states were approximated by two broad Gaussian functions: one peaking around the excitation peak of the corresponding singlet state and another peaking 350-400 nm red-shifted from the excitation peak of the corresponding singlet state. Only the absorption spectrum of the triplet state of the red neutral chromophore was modified to absorb around 405 nm (instead of 488 nm), to introduce nonlinear bleaching of the red state by 405 nm light, via a similair pathway as in the green state (see **Figure 3.38**). The phototransformation yields of the triplet state are expected to be wavelength dependent, with higher energy wavelengths favoring bleaching and lower energy wavelengths favoring RISC[99]. SMIS does not enable direct simulation of wavelength length dependent quantum yields. Therefore, each triplet state was split into two states, with one state ($Triplet_{visible}$) absorbing around the excitation peak of the corresponding singlet state and the other state ($Triplet_{NIR}$) absorbing around 350-400 nm red-shifted from the excitation peak of the corresponding singlet state. Fast exchange between $Triplet_{visible}$ and $Triplet_{NIR}$ was introduced to make the two states effectively behave as a single state. This way, different phototransformation quantum yields could be assigned to the two triplet 'substates', incorporating wavelength dependent effects.

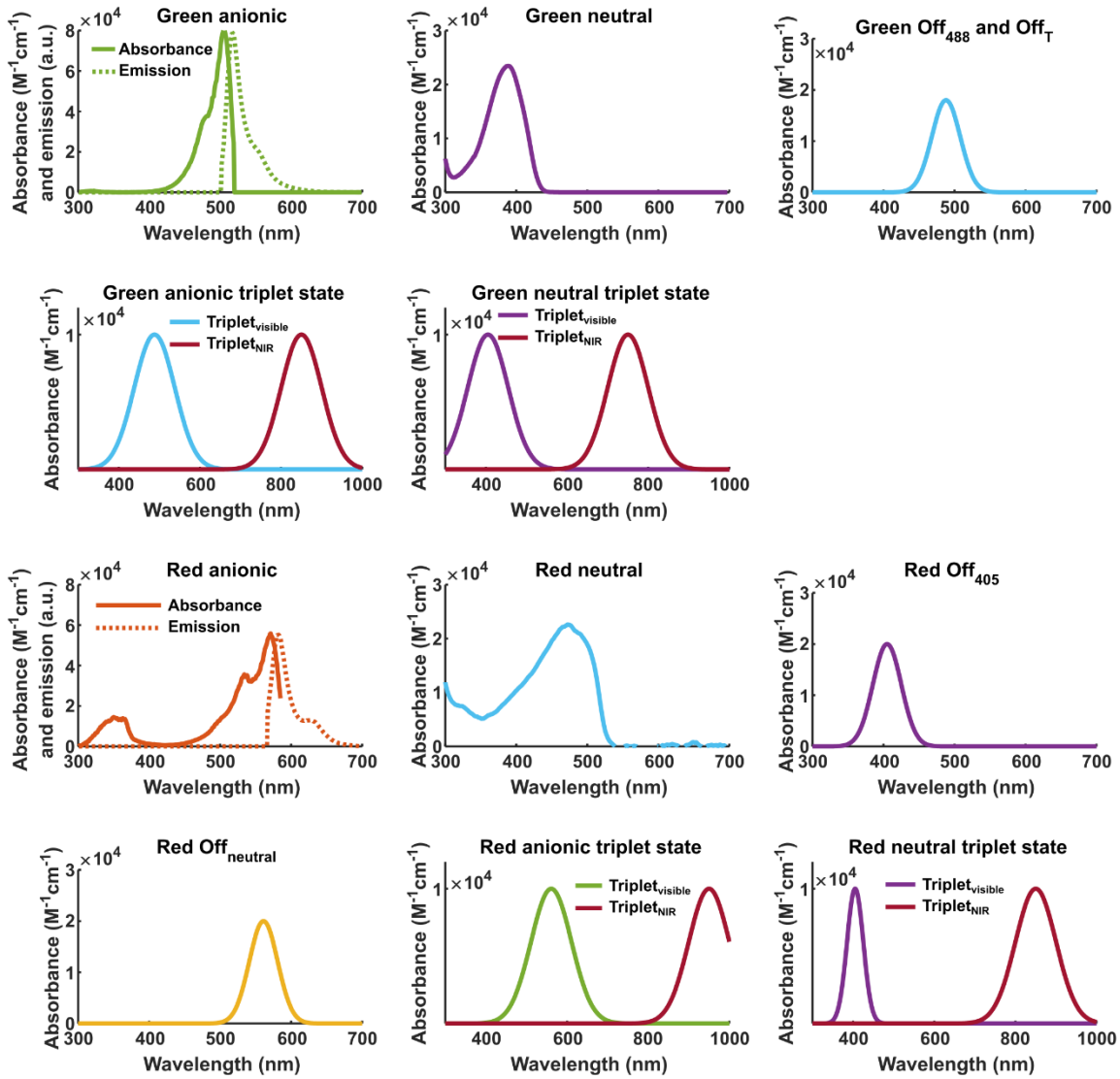

Supplementary Figure 3. Tentative absorption and emission spectra.

Supplementary Table 2. Tentative extinction coefficients.

State	Sub-state	EC ($M^{-1}cm^{-1}$)	Wavelength (nm)	Notes
Green *cis*/ *trans* anionic		7.8952e4	507	FPbase[68] The cis and anionic states are assigned the same absorption spectra and EC's
Green *cis*/ *trans* neutral		1.8e4	405	The cis and anionic states are assigned the same absorption spectra and EC's
Green Off_{488} and Off_T		1e4	488	Based on the weak light sensitivity of short-lived off-states (expectedly radical states) observed is previous work[218,467].
Green anionic triplet	$Triplet_{visible}$	1e4	488	Based on the EC of the triplet state of EGFP and rsEGFP2 as reported in[100]
	$Triplet_{NIR}$	1e4	850	Based on the EC of the triplet state of EGFP and rsEGFP2 as reported in[100]
Green neutral triplet	$Triplet_{visible}$	1e4	405	Based on the EC of the triplet state of EGFP and rsEGFP2 as reported in[100]

	$Triplet_{NIR}$	1e4	750	Based on the EC of the triplet state of EGFP and rsEGFP2 as reported in[100]
Red *cis/trans* anionic		5.55e4	570	FPbase[68] The cis and anionic states are assigned the same absorption spectra and EC's
Red *cis/trans* neutral		2.1e4	488	Based on the absorption spectra shown in **Figure 3.45** and published absorption spectra of Dendra2[468] and EosFP *thermo*[469]
Red Off_{405}		2e4	405	Based on the apparent high light sensitivity of this state (**Figure 3.42**).
Red $Off_{neutral}$		2e4	561	Based on the apparent high light sensitivity of this state (**Figure 3.43** and **Figure 3.46**).
Red anionic triplet	$Triplet_{visible}$	1e4	561	Based on the EC of the triplet state of EGFP and rsEGFP2 as reported in[100]
	$Triplet_{NIR}$	1e4	950	Based on the EC of the triplet state of EGFP and rsEGFP2 as reported in[100]
Red neutral triplet	$Triplet_{visible}$	1e4	405	Based on the EC of the triplet state of EGFP and rsEGFP2 as reported in[100]
	$Triplet_{NIR}$	1e4	850	Based on the EC of the triplet state of EGFP and rsEGFP2 as reported in[100]

6.2.3 Estimation of the phototransformation quantum yields and thermal rates

The phototransformation quantum yields and thermal rates were estimated using the experimental data shown in this work.

Firstly, *cis/trans* isomerization and A/B partitioning of the green state were incorporated into the model, using the observed green state photoswitching kinetics (see **Figure 3.24**) and the dependence of the PCE and A-state population on the applied 405 nm light intenisty (see **Figure 3.26**) as reference. Secondly, the triplet states of the anioic and neutral green chromophores were introduced, provinding a pathway for 405 nm light induced nonlinear bleaching (see **Figure 3.17**) and a mechanism for fast fluorescence decay under continuous illumination with 488 nm light (see **Figure 3.31**). Thirdly, *cis/trans* isomerization of the red state was added to reproduce the photoswitching kinetics of mEos4b under low illumination intenisties (see **Figure 3.38A-B**), after which the triplet state of the neutral chromophore and $Off_{neutral}$ were added to to provide a pathway for nonlinear bleaching under high 405 nm light intenisties (see **Figure 3.38D**) and a mechanism of the formation of a nonfluorescent state by 405/488 nm light at low pH (see **Figure 3.42**). Finally, the triplet state of the *cis* anionic chromophore and the downstream non-fluorescent states Dark1 and Off_{405} were added to the model to tune the blinking kinetics of the red state (see **section 3.1.3**).

The model was refined in an empirical and iterative manner, aiming to, at least qualitatively, reproduce all the different photophysical behaviors of mEos4b that were observed in this work. Of course, this is not the ideal approach. A better strategy would be to fit the quantum yields and rates of the model to the experimental data, which could be done in a global manner. However, given the high complexity of the model, the unknown absoprtion spectra, the often inhomogeous illumination conditions (especially in the NMR) and the differences in pH and temperature (NMR vs PALM), this was not feasible in the short time that was available.

The final phototransformation quantum yields and thermal rates are listed in **Supplementary Table 3**, **Supplementary Table 4**, **Supplementary Table 5** and **Supplementary Table 6**.

Supplementary Table 3. Phototransformation quantum yields of the green states. *Tn= triplet state from the neutral chromophore; Ta = triplet state from the anionic chromophore*

	Green A cis anionic	Green A cis neutral	Green A trans anionic	Green A trans neutral	Green A Tn visible	Green A Tn NIR	Green A Ta visible	Green A Ta NIR	Green A Off_T	Green A Off_{488}	Green B cis anionic	Green B cis neutral	Green B trans anionic	Green B trans neutral	Green B Tn visible	Green B Tn NIR	Green B Ta visible	Green B Ta NIR	Green B Off_T	Green B Off_{488}	Red cis anionic	Red cis neutral	Bleached Green
Green A cis anionic	0	0	2e-4	0	0	0	6.4e-3	0	0	0	0	0	0	0	0	0	0	0	0	0	1e-7	0	2.5e-6
Green A cis neutral	0	0	0	0.02	0	6.4e-3	0	0	0	0	0	0.302	0	0	0	0	0	0	0	0	0	5.1e-4	1e-4
Green A trans anionic	4e-4	0	0	0	0	0	0	0	0	0	0	0	0	0	0	0	0	0	0	0	0	0	2.5e-6
Green A trans neutral	0	0.05	0	0	0	0	0	0	0	0	0	0	0	0.302	0	0	0	0	0	0	0	0	2.5e-6
Green A Tn visible	0	1.2e-3	0	0	0	0	0	0	0	0	0	0	0	0	0	0	0	0	0	0	0	0	1.2e-3
Green A Tn NIR	0	1.2e-3	0	0	0	0	0	0	0	0	0	0	0	0	0	0	0	0	0	0	0	0	1e-6
Green A Ta visible	2.4e-3	0	0	0	0	0	0	0	0	0	0	0	0	0	0	0	0	0	0	0	0	0	1.5e-4
Green A Ta NIR	2.4e-3	0	0	0	0	0	0	0	0	0	0	0	0	0	0	0	0	0	0	0	0	0	1e-6
Green A Off_T	0.049	0	0	0	0	0	0	0	0	0	0	0	0	0	0	0	0	0	0	0	0	0	1e-6
Green A Off_{488}	1e-3	0	0	0	0	0	0	0	0	0	0	0	0	0	0	0	0	0	0	0	0	0	1e-6
Green B cis anionic	0	0	0	0	0	0	0	0	0	0	0	0	5e-5	0	0	0	6.4e-3	0	0	0	1e-7	0	2.5e-6
Green B cis neutral	0	7.1e-2	0	0	0	0	0	0	0	0	0	0	0	0.02	6.4e-3	0	0	0	0	0	0	0	2.4e-4
Green B trans anionic	0	0	0	0	0	0	0	0	0	0	1e-4	0	0	0	0	0	0	0	0	0	0	0	2.5e-6

Green B trans neutral	0	0	0	7.1e-2	0	0	0	0	0	0	0	0.05	0	0	0	0	0	0	0	0	0	2.5e-6
Green B Tn visible	0	0	0	0	0	0	0	0	0	0	0	1.2e-3	0	0	0	0	0	0	0	0	0	1.2e-3
Green B Tn NIR	0	0	0	0	0	0	0	0	0	0	0	1.2e-3	0	0	0	0	0	0	0	0	0	1e-6
Green B Ta visible	0	0	0	0	0	0	0	0	0	0	2.4e-3	0	0	0	0	0	0	0	0	0	0	1.5e-4
Green B Ta NIR	0	0	0	0	0	0	0	0	0	0	2.4e-3	0	0	0	0	0	0	0	0	0	0	1e-6
Green B Off_T	0	0	0	0	0	0	0	0	0	0	4.9e-2	0	0	0	0	0	0	0	0	0	0	1e-6
Green B Off_{488}	0	0	0	0	0	0	0	0	0	0	1e-3	0	0	0	0	0	0	0	0	0	0	1e-6

Supplementary Table 4. Phototransformation quantum yields of the red states. *Tn= triplet state from the neutral chromophore; Ta = triplet state from the anionic chromophore*

	Red cis anionic	**Red cis neutral**	**Red trans anionic**	**Red trans neutral**	**Red Tn visible**	**Red Tn NIR**	**Red $Off_{neutral}$**	**Red Ta visible**	**Red Ta NIR**	**Red Off_{405}**	**Red Dark1**	**Bleached Red**
Red cis anionic	0	0	3.2e-5	0	0	0	0	3.2e-3	0	0	0	2.2e-7
Red cis neutral	0	0	0	3.37e-2	6.4e-3	0	0	0	0	0	0	1e-5
Red trans anionic	3.2e-5	0	0	0	0	0	0	0	0	0	0	1e-6
Red trans neutral	0	0.17	0	0	0	0	0	0	0	0	0	5e-5
Red Tn visible	0	2.4e-3	0	0	0	0	0	0	0	0	0	2.4e-3
Red Tn NIR	0	2.4e-3	0	0	0	0	0	0	0	0	0	1e-6
Red $Off_{neutral}$	0	3.3e-3	0	0	0	0	0	0	0	0	0	1e-6
Red Ta visible	3.2e-3	0	0	0	0	0	0	0	0	0	0	1.5e-4
Red Ta NIR	3.2e-3	0	0	0	0	0	0	0	0	0	0	1e-7
Red Off_{405}	1.386e-2	0	0	0	0	0	0	0	0	0	0	1.386

Red Dark1	0	0	0	0	0	0	0	0	0	0	0	0	0	0	0	0	0	0	0	0	0

Supplementary Table 5. Thermal rates (s^{-1}) of the green states. *Tn= triplet state from the neutral chromophore; Ta = triplet state from the anionic chromophore*

	Green A cis anionic	**Green A cis neutral**	**Green A trans anionic**	**Green A trans neutral**	**Green A Tn visible**	**Green A Tn NIR**	**Green A Ta visible**	**Green A Ta NIR**	**Green A Off_T**	**Green A Off_{488}**	**Green B cis anionic**	**Green B cis neutral**	**Green B trans anionic**	**Green B trans neutral**	**Green B Tn visible**	**Green B Tn NIR**	**Green B Ta visible**	**Green B Ta NIR**	**Green B Off_T**	**Green B Off_{488}**	**Bleached Green**
Green A cis anionic	0	0	0	0	0	0	0	0	0	0	0.0086	0	0	0	0	0	0	0	0	0	0
Green A cis neutral	0	0	0	0	0	0	0	0	0	0	0	0.0086	0	0	0	0	0	0	0	0	0
Green A trans anionic	6.9e-5	0	0	0	0	0	0	0	0	0	0	0	0.011	0	0	0	0	0	0	0	0
Green A trans neutral	0	6.9e-5	0	0	0	0	0	0	0	0	0	0	0	0.011	0	0	0	0	0	0	0
Green A Tn visible	0	138	0	0	0	0	0	0	0	0	0	0	0	0	0	0	0	0	0	0	0.01
Green A Tn NIR	0	138	0	0	0	0	0	0	0	0	0	0	0	0	0	0	0	0	0	0	1e-2
Green A Ta visible	66	0	0	0	0	0	0	0	66	6.9	0	0	0	0	0	0	0	0	0	0	0.001
Green A Ta NIR	66	0	0	0	0	0	0	0	66	6.9	0	0	0	0	0	0	0	0	0	0	1e-3
Green A Off_T	6.9	0	0	0	0	0	0	0	0	0	0	0	0	0	0	0	0	0	0	0	0
Green A Off_{488}	1.7	0	0	0	0	0	0	0	0	0	0	0	0	0	0	0	0	0	0	0	0
Green B cis anionic	0.0114	0	0	0	0	0	0	0	0	0	0	0	0	0	0	0	0	0	0	0	0
Green B cis neutral	0	0.0114	0	0	0	0	0	0	0	0	0	0	0	0	0	0	0	0	0	0	0

Green B trans anionic	0	0	0.009	0	0	0	0	0	0	0	6.9e-5	0	0	0	0	0	0	0	0	0	0
Green B trans neutral	0	0	0	0.009	0	0	0	0	0	0	0	6.9e-5	0	0	0	0	0	0	0	0	0
Green B Tn visible	0	0	0	0	0	0	0	0	0	0	0	138	0	0	0	0	0	0	0	0	0.01
Green B Tn NIR	0	0	0	0	0	0	0	0	0	0	0	138	0	0	0	0	0	0	0	0	1e-2
Green B Ta visible	0	0	0	0	0	0	0	0	0	0	66	0	0	0	0	0	0	0	66	6.9	0.001
Green B Ta NIR	0	0	0	0	0	0	0	0	0	0	66	0	0	0	0	0	0	0	66	6.9	1e-3
Green B Off_T	0	0	0	0	0	0	0	0	0	0	6.9	0	0	0	0	0	0	0	0	0	0
Green B Off_{488}	0	0	0	0	0	0	0	0	0	0	1.7	0	0	0	0	0	0	0	0	0	0

Supplementary Table 6. Thermal rates (s^{-1}) of the red states. *Tn= triplet state from the neutral chromophore; Ta = triplet state from the anionic chromophore*

	Red cis anionic	**Red cis neutral**	**Red trans anionic**	**Red trans neutral**	**Red Tn visible**	**Red Tn NIR**	**Red $Off_{neutral}$**	**Red Ta visible**	**Red Ta NIR**	**Red Off_{405}**	**Red Dark1**	**Bleached Green**	**Bleached Red**
Red cis anionic	0	0	0	0	0	0	0	0	0	0	0	0	0
Red cis neutral	0	0	0	0	0	0	0	0	0	0	0	0	0
Red trans anionic	9.6e-5	0	0	0	0	0	0	0	0	0	0	0	0
Red trans neutral	0	9.6e-5	0	0	0	0	0	0	0	0	0	0	0
Red Tn visible	0	130	0	0	0	0	8	0	0	0	0	0	0.01
Red Tn NIR	0	130	0	0	0	0	8	0	0	0	0	0	0.01
Red $Off_{neutral}$	0	1.16e-4	0	0	0	0	0	0	0	0	0	0	0
Red Ta visible	138	0	0	0	0	0	0	0	0	0.5	1	0	0.001
Red Ta NIR	138	0	0	0	0	0	0	0	0	0.5	1	0	0.001
Red Off_{405}	0.2773	0	0	0	0	0	0	0	0	0	0	0	0
Red Dark1	6.9	0	0	0	0	0	0	0	0	0	0	0	0

6.2.4 Simulation results

This section discusses the behavior of the proposed mEos4b model compared to the experimentally data obtained in this work.

6.2.4.1 Simulation of the green state switching kinetics

NMR experiments and ensemble fluorescence measurments revelaed that A/B partitioning of the green state affects the photoswitching kinetics of mEos4b (**Figure 3.24**): after exposure to 405 nm light (second switching cycle) the A/B equilibrium is shifted towards the B-state resulting in slower off-switching kinetics. This behavior could be reproduced by the proposed model (**Supplementary Figure 4**), altough the effect appears less strongly as in the experimental data. This difference might be partly explained by the temperature difference between the PALM-microscope (27°C) and the NMR-setup (35°C). The A/B-exchange rates used in the model are based on NMR-data but these rates are expectedly lower on the PALM-setup due to the lower temperature. Consequently, the simulations are probably more affected by A/B-reequilibration during the second switing cycle (see **Supplementary Figure 4A**) than the experimentally obtained data.

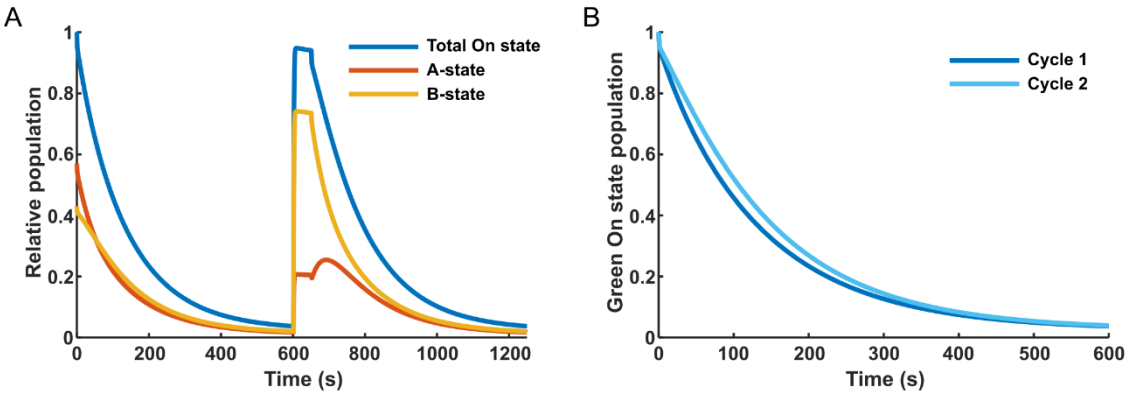

Supplementary Figure 4. A/B partitioning affects green state photoswitching. *Green state photoswitching was simulated under illumination with 300 mW/cm² 488 nm light and 300 mW/cm² 405 nm light for off- and on-switching, respectively. Illumination periods (500 ms) were alternated with dark periods (500 ms) to allow recovery of short lived non-fluorescent states. A) Progressions of the total on-state population (A + B) and the A- and B-states individually. B) Comparison of the first and second off-switching cycles.*

Ensemble fluorescence measurments showed that the fluorescence signal of the green state rapidly decays under continuous illumination with low intensity 488 nm light (**Figure 3.31**) and that the amplitude of this decay can be decreased by addition of dark time in between frames (**Figure 3.32**). This behavior could be reproduced by the designed model (**Supplementary Figure 5A**). **Supplementary Figure 5B** shows that, according to the proposed model, multiple non-fluorescent states contribute to this fast decay: Off_T, Off_{488}, the triplet state and the Off state (*trans* neutral chromophore).

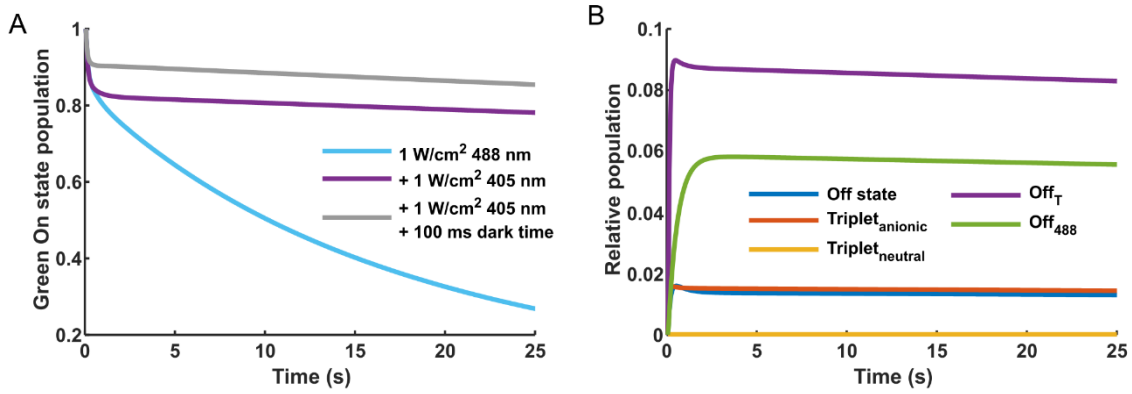

Supplementary Figure 5. Rapid fluorescence decay under continous illumination. *Green state decay was simulated under continous illumination with 1W/cm² 488 nm light in the absence and presence of 1 W/cm² 405 nm light to prevent accumulation of the Off state. 100 ms dark time (grey curve in A) was added in between frames (50 ms) to allow recovery of short-lived non-fluorescent states. A) Progressions of the green on-state (sum of the A- and B-states) under the different illumination conditions. B) Relative occupancies of the non-fluorescent states formed under continuous illumination with 1W/cm² 488 and 405 nm light (purple curve in A).*

6.2.4.2 Simulation of the photoconversion kinetics on various illumination conditions

PALM and NMR experiments revealed that the PCE of mEos4b is strongly dependend on the applied 405 nm light intenisty, with the PCE decreasing with increasing light intensities (**Figure 3.17** and **Figure 3.24**). We proposed that this is due to modulation of the A/B equilibrium at low 405 nm light power denisties (<1 W/cm^2) and due nonlinear bleaching via a short-lived intermediate state (the triplet state of the neutral chromophore?) at high 405 nm light power denisties (>10 W/cm^2). **Supplementary Figure 6** shows that this trend is well reproduced by the proposed model. In the range of 0-250 mW/cm^2 405 nm light, the PCE and the relative A-state population decrease together, while at higher power denisties, the A-state population stabilizes while the PCE keeps decreasing (**Supplementary Figure 6B**). Note that the estimation of the PCE's in the design of the model was corrected for the formation of Off$_{neutral}$ (see **Figure 3.46**) and that the PCE's are thus higher than reported before based on the NMR data alone (see **Figure 3.26**).

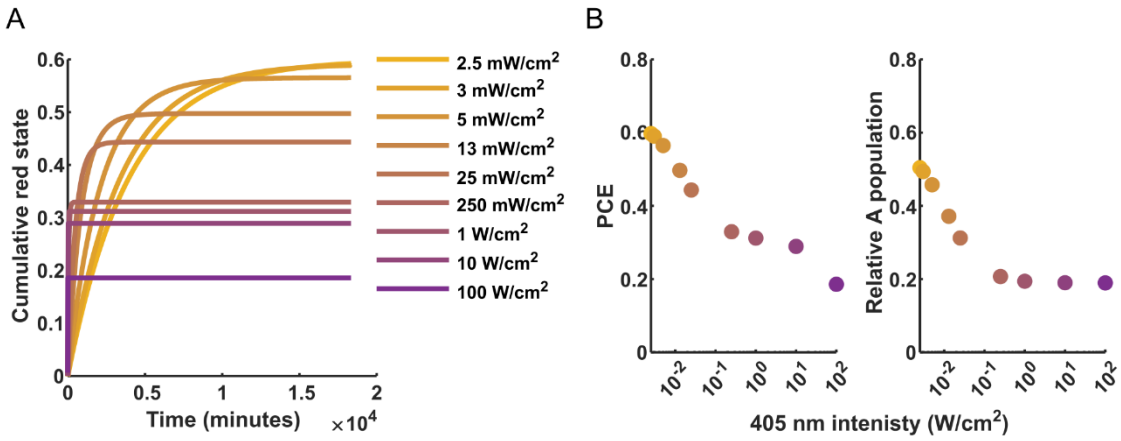

Supplementary Figure 6. Dependence of the PCE on the applied 405 nm light power density. *Photoconversion was simulated under continous illumination with 405 nm light (2.5 mW/cm² – 100 W/cm²). A) Cumulative red state. B) Dependence of the PCE and the relative A-state population on the applied power denisty.*

The formation and accumulation of Off$_{neutral}$ could be observed in the simulations (**Supplementary Figure 7**) and was especially pronounced at higher 405 nm light intensities. Compared to **Figure 3.46**, the accumulation of Off$_{neutral}$ appears less strong in the simulations than in the experimental data,

which is probably due to imprecisions in the model (too short halflife? too low formation quantum yield?). Nevertheless, the model appears to behave qualitatively correct.

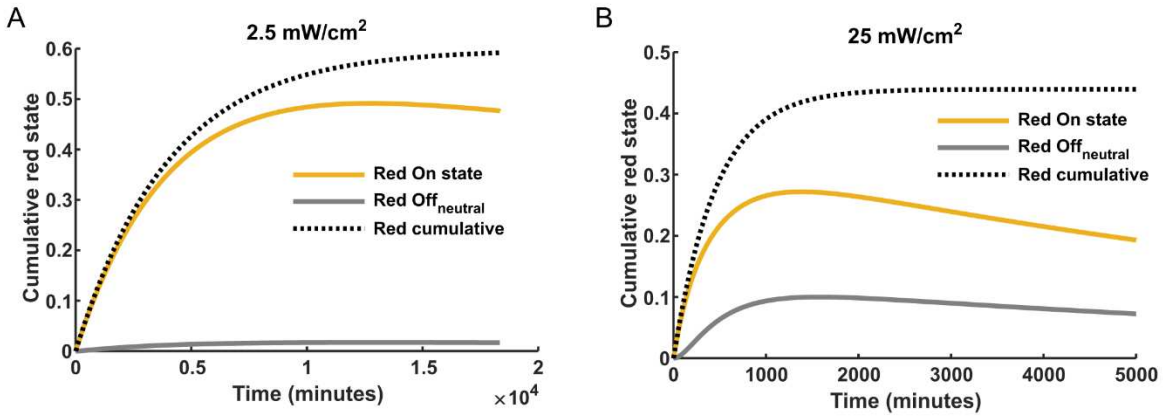

Supplementary Figure 7. Formation of $Off_{neutral}$ affects estimation of the PCE. *Photoconversion was simulated under continous illumination with 405 nm light at 2.5 mW/cm² (A) and 25 mW/cm² (B). Shown are the progressions of the cumulative red state (black dotted curves), the red On state (yellow curves) and the $Off_{neutral}$ state (grey curves).*

In ensemble fluorescence experiments, the FPs are not only exposed to 405 nm light (as in the NMR experiments) but also to low doses of 561 nm light to follow the progression of the red state. To test how this low dose of 561 nm light affects the appearance of the photoconversion kinetics, I simulated photoconversion under alternating illumination with 561 nm light (10 W/cm² for 10 ms) and 405 nm light (1-100 W/cm² for 100 ms). Under these conditions, the peak red fluorescence intensity appears lower with 1 W/cm² 405 nm light than with 10 Wcm² 405 nm light (**Supplementary Figure 8A**), while the PCE is higher with 1 W/cm² light. This can also be seen in the experimental data (**Figure 3.18**), and is explained by bleaching of the red state by the 561 nm light. The nonlinear effect of high 405 nm light intenisties (**Figure 3.18B**) could also be nicely reproduced under these conditions (**Supplementary Figure 8B**).

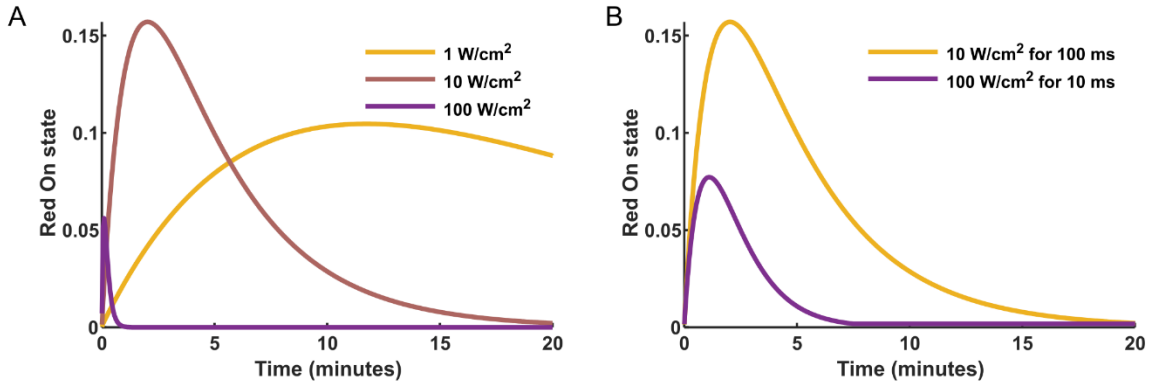

Supplementary Figure 8. Low intenisty 561 nm light affects the appearance of the photoconversion kinetics. *Photoconversion was simulated under alternating illumination with 561 nm light (10 W/cm² for 10 ms) and 405 nm light (1-100 W/cm² for 100 ms (or 10 ms in B)), mimicking the imaging scheme applied on the PALM set-up (see **Figure 3.18**). A) Progression of the red On state (100 ms 405 nm illumination periods). B) Progression of the red On state under illumination with 10 W/cm² for 100 ms (same as in A) compared to 100 W/cm² for 10 ms.*

Lastly, I simulated the photoconversion kinetics of mEos4b under SMLM imaging conditions (500 W/cm² 561 nm and 1-100 W/cm² 405 nm). The simulations again revelaed a lower PCE with 100 W/cm² 405 nm light than with 10 W/cm² (**Supplementary Figure 9A**), similairly as the experimental data (**Figure 3.15**). However, it be noted that the overall photoconversion kinetics appear differently:

while in the experimental data the cumulatative number of converted molecules keeps increasing for more than 20 minutes (100 W/cm^2), the cumulative red state in the simulations sharply plateaus after ~8 minutes. This difference is not simply because the photoconversion rate in the simulations is too fast (compare **Supplementary Figure 8** with **Figure 3.18**). One explanation for this difference could be that proposed photophysical model is incomplete. Alternatively, the steady increase in the experimental data might be an artifact caused by the detection of fluorescence impurties or by the detection of diffusing molecules. This requires further investigation. In addition to 405 nm light, 488 nm light was also shown to decrease the PCE of mEos4b due to bleaching of the green state (**Figure 3.12**). This effect was also appearent in the simulations (**Supplementary Figure 9B**). Compared to the experimental data (**Figure 3.12**), green state bleaching appears too strongly in the simulations (**Supplementary Figure 9B**), indicating that the proposed model requires further refinement.

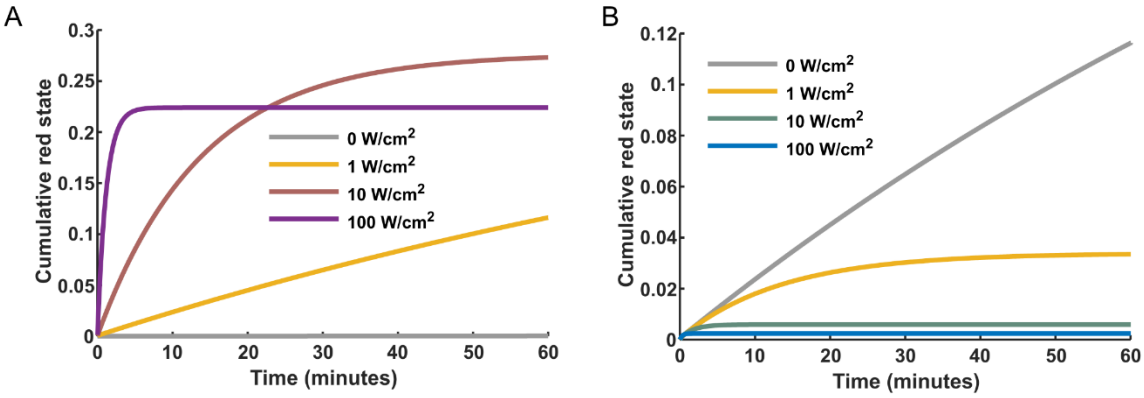

Supplementary Figure 9. The photoconversion kinetics under SMLM-imaging conditions. *Photoconversion was simulated under alternating illumination with 561 nm light (500 W/cm2 for 70 ms) and 405 nm light (0-100 W/cm^2 for 8 ms) in A, or 1 W/cm^2 405 nm light and 0-100 W/cm^2 488 nm light for 8 ms in B, mimicking SMLM imaging conditions (see **Figure 3.12** and **Figure 3.15**).*

6.2.4.3 Simulation of Red state photoswitching

Ensemble fluorescence measurments showed that the photoswitching behavior of the red state is highly dependent on the wavelength used for on-switching (405 or 488 nm), on the applied power density and on the environmental pH (**Figure 3.38** and **Figure 3.42**). The model was able to reproduce most experimentally observed trends (**Supplementary Figure 10** and **Supplementary Figure 11**). On-switching with 488 nm light is faster than with 405 nm light because the Off state (*trans* neutral chromophore) absorbs 488 nm light more efficiently (**Supplementary Figure 10A**). At high power densities, 488 nm light induces rapid cycling between the On and Off states, leading to bleaching (**Supplementary Figure 10D**). On/Off cycling is less efficient with 405 nm light because the On state absorbs very little at 405 nm. However, at high intenisties, 405 nm light causes bleaching via the triplet state of the neutral chromophore, similairly as in the green state (**Supplementary Figure 10D**). These different mechanisms by which 488 and 405 nm light cause bleaching can be easily distinguished when the simulation is performed using a model in which there is no bleaching from the triplet state (**Supplementary Figure 11C**).

In the switching simulations with 100 W/cm^2 488 nm light (**Supplementary Figure 10D**), the formation of $Off_{neutral}$ can be observed as little spikes in the On state population at the beginning of the off-switching periods. In agreement with the experimental data, population of $Off_{neutral}$ became more pronounced at pH 6 (**Supplementary Figure 11A**).

In the experiments, I used the addition of 100 W/cm^2 561 nm light to confirm that 488 nm light acts more efficienctly on the Off state (**Figure 3.40**). When high intensity 561 nm light was added to the simulations, however, this led to rapid bleaching (**Supplementary Figure 11A**), which was not

observed in the experiments. This bleaching is due reexcitation of the triplet state of the anionic chromophore (which does not occur when using only 10 W/cm2 561 nm as in **Supplementary Figure 10**). Altough the experimental data in **Figure 3.40** suggest that 100 W/cm^2 561 nm light causes minimal nonlinear bleaching, the relatively short on- and bleaching-times observed in the single molecule experiments indicate that at 500 W/cm^2 561 nm light there is strong bleaching (**Figure 3.16**). In fact, with the current model, the simulated on- and bleaching times are too long compared to the experimental data (compare **Supplementary Figure 13** and **Figure 3.16**). This mismatch between the simulations and the experimental data might me partly explained by the way the single molecule simulations were processed (discussed below) but also shows that the bleaching of the red state complex and requires further refinement.

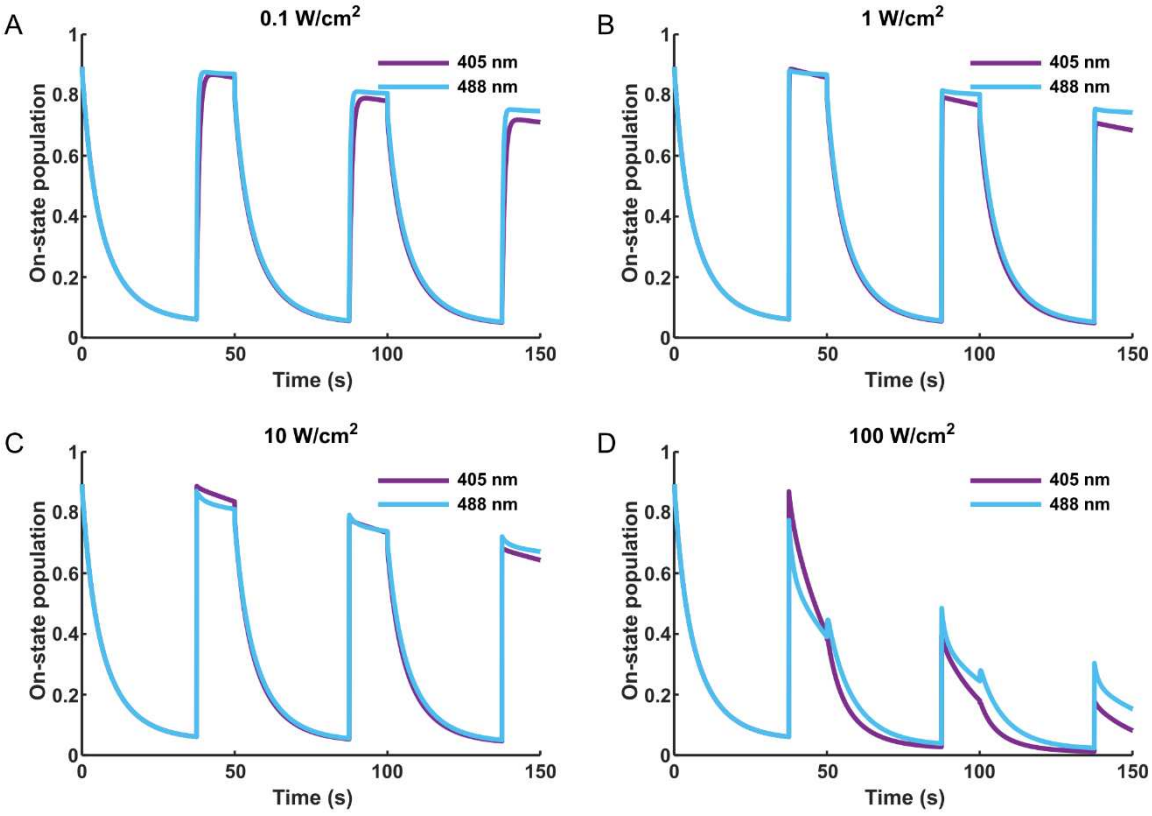

Supplementary Figure 10. Effects of the applied 405 and 488 nm light intenisties on the switching kinetics of the Red state*. Red state photoswitching was simulated under alternating illumination with 561 nm light (10 W/cm^2), and 405 or 488 nm light (0.1 – 100 W/cm^2) for off- and on-switching, respectively. The red state fluorescence was recorded every 40 ms by illumination with 10 W/cm^2 561 nm light. Simulation were performed assuming a pH of 8.*

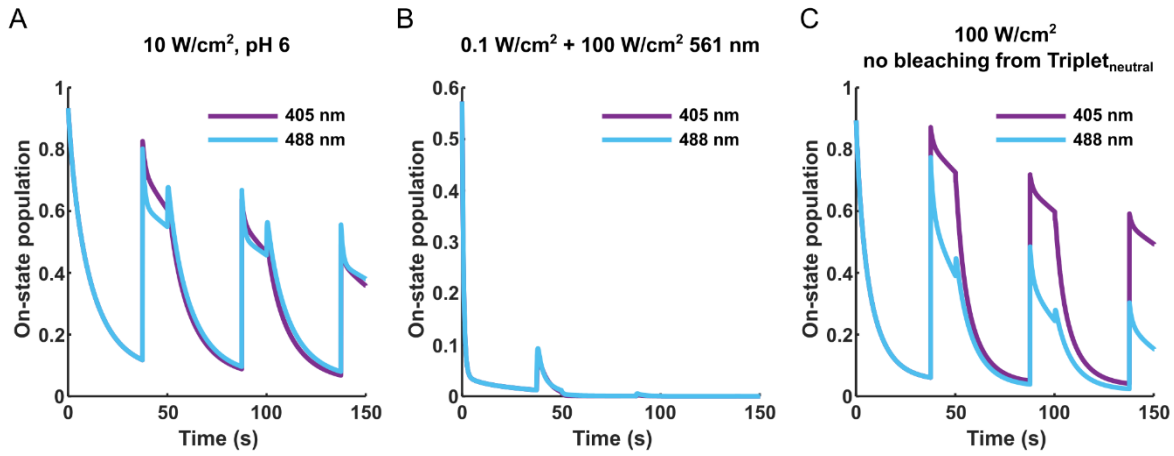

Supplementary Figure 11. The complex switching behavior of the red state. *Red state photoswitching was simulated as in* ***Supplementary Figure 10*** *except for the changes noted below. The applied 405 and 488 nm light intensties are noted above the plots. A) Switching at pH 6 instead of pH 8. B) Switching in the presence of 100 W/cm² 561 nm light. C) Switching using a modified fluorophore model not exhibiting bleaching from the triplet state of the neutral chromophore.*

6.2.4.4 Simulation of Red state blinking

Lastly, I simulated the single molecule blinking kinetics of the red state. The simulations were performed assuming a fixed dipole orientation of the FPs, as appeared to be the case in PAA gel (**Figure 3.1**). The blinking statistics were extracted from the groundtruth data provided by SMIS, which allowed to perform the simulations at high protein densities and starting from the red state, which made the simulations much faster. Ideally, for a fair comparison, the simulated data should be processed similairly as the experimental data but this was not feasible in the limited time.

PALM experiments revealed that off-time reduction is more efficient with 405 than with 488 nm light (**Figure 3.42**). Given that 488 nm light excites the Off state (*trans* neutral chromophore) more efficiently, we ascribed this effect to the formation of an off-state only sensitive to 405 nm light. We incorporated this off-state into the model as Off_{405}, an off-state formed downstream of the triplet state of the anioinic chromophore. In line with the experimental data, the simulations showed more efficient off-stime reduction by 405 nm light (**Supplementary Figure 12**), while this higher efficiency was not apparent in the ensemble simulations (**Supplementary Figure 10**). Curiously, the off-time reduction appeared slightly less efficient with higher 488 nm ligh intenisties (100 W/cm² vs 1 W/cm², **Supplementary Figure 12B**). This was not seen in the experimental data (**Figure 3.12**) and the origin of this effect in the simulations is unclear.

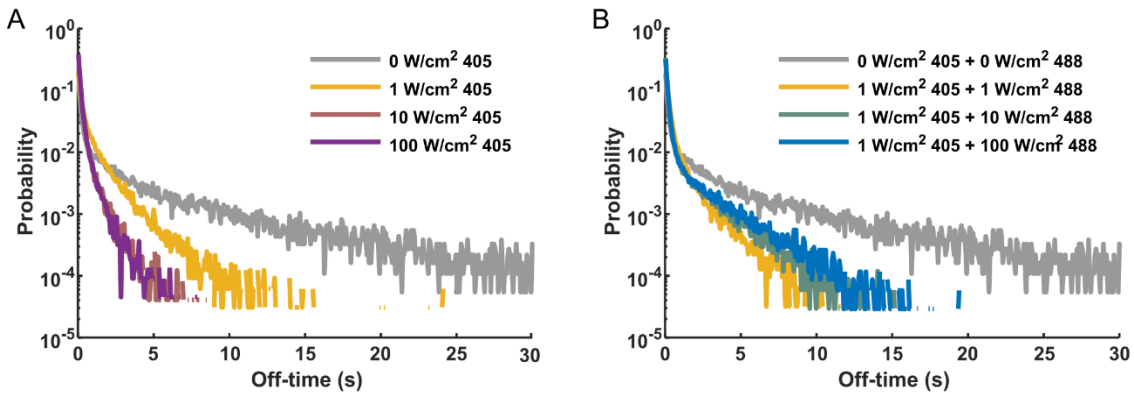

Supplementary Figure 12. Red state off-time reduction by 405 and 488 nm light. *Red state blinking was simulated under alternating illumination with 561 nm light (500 W/cm² for 70 ms) and 405 nm light (0-100 W/cm² for 8 ms) in A or 1 W/cm² 405 nm light and 1-100 W/cm² 488 nm light (8 ms) in B. The off-time durations were extracted from the ground-thruth data provided by SMIS.*

In addition to the off-times, we also extracted the on-times, the bleaching-times and the number of blinks per molecule from the simulated data (**Supplementary Figure 13**). The on- and bleaching-times extracted from the simulations are much longer than the experimentally measured on- and bleaching-times (**Supplementary Figure 13** vs **Figure 3.16**). This might be due to the different ways the simulated data and experimental data were processed. Of note, the apparent brightness of the simulated molecules was much lower than the apparent brightness of the experimental data (**Supplementary Figure 14A**). If these simulated data would be processed similairly as the experimental data, many of the localizations would likely be missed. The low apparent brightness of the simulated molecules is possibly due to too much triplet state formation or a too long triplet state lifetime. Reduction of the triplet state lifetime (triplet state of the red anionic chromophore) by addition of 950 nm light, significantly increased the apparent brightness of the simulated molecules, confirming that the triplet state contributed to the low apparent brightness (**Supplementary Figure 14B,D**). In depth characterization of triplet state formation in mEos4b should help to further refine the proposed photophysical model.

While the nBlink distributions of the experimental data were minimally affected by addition of 488 of 405 nm light (**Figure 3.13** and **Figure 3.16**), the simulated molecules blink less in the prescence of high intensity 405 or 488 nm light (**Supplementary Figure 13A,B**). This is likely explained by too efficient off-time reduction, causing on-times to merge and thereby reducing the number of blinks. This effect can also be seen in the on-time histograms: the on-times are longer in the prescence of 405/488 nm light (**Supplementary Figure 13A,B**).

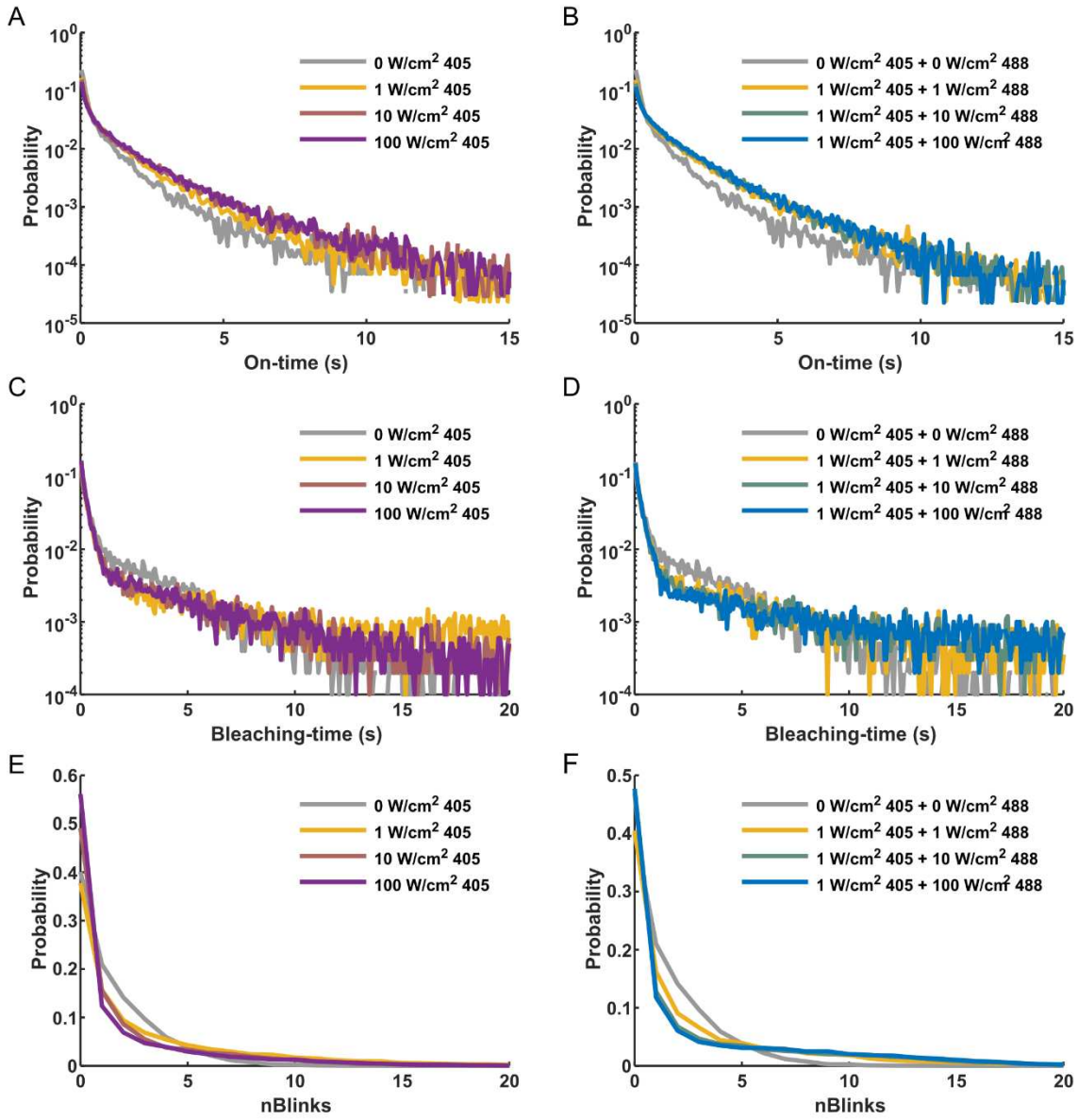

Supplementary Figure 13. Effects of 405 and 488 nm light on red state blinking. *Red state blinking was simulated under alternating illumination with 561 nm light (500 W/cm² for 70 ms) and 405 nm light (0-100 W/cm² for 8 ms) in A, C and E, or 1 W/cm² 405 nm light and 1-100 W/cm² 488 nm light (8 ms) in B, D and F. The on-time and bleaching-time durations and the number of blinks were extracted from the ground-thruth data provided by SMIS.*

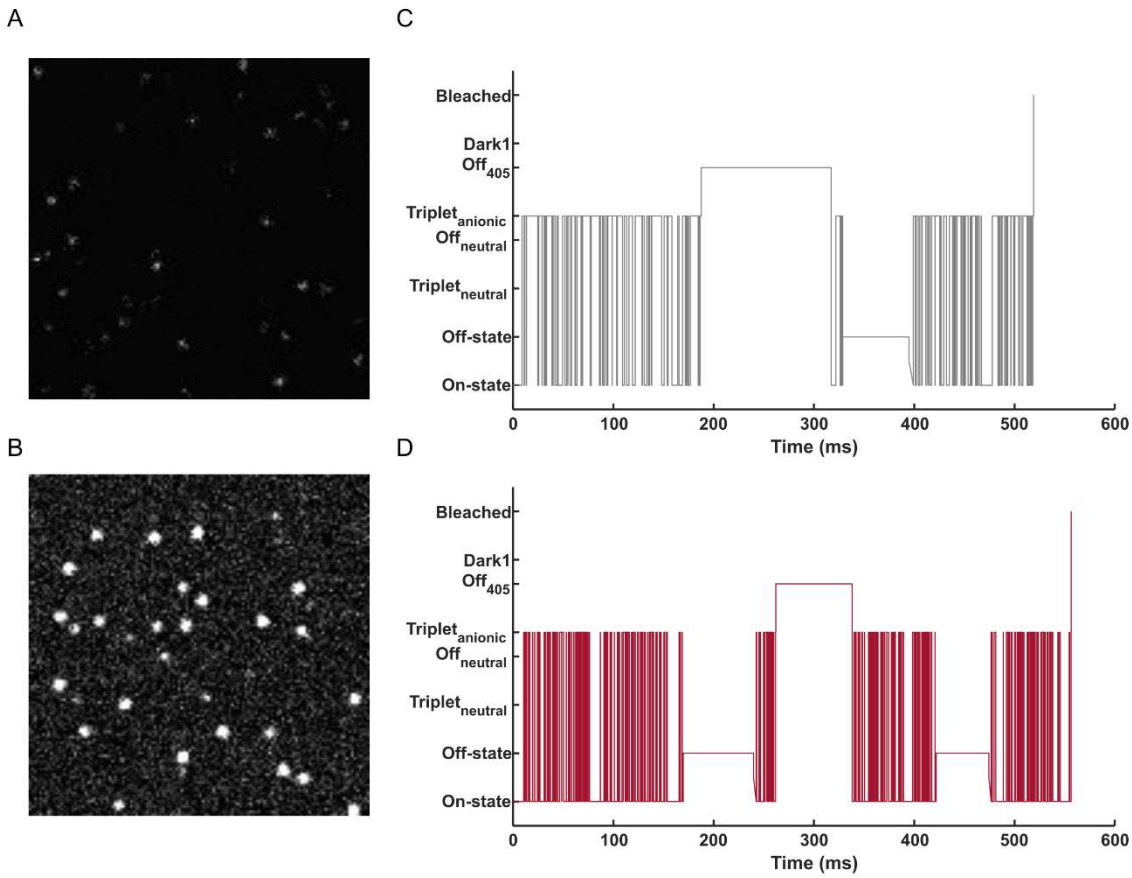

Supplementary Figure 14. Triplet state formation reduces the apparent brightness of mEos4b*. Single molecule blinking of the Red state was simulated under alternating illumination with 561 nm light (500 W/cm^2 for 70 ms) and 405 nm light (10 W/cm^2 for 8 ms). Continous illumination with 5 kW/cm^2 950 nm light was added (B and D) to redcue the lifetime of the triplet state of the anionic chromophore. A and B) Simulated single molecule image (same contrast in A and B). C and D) Example state traces of single fluorophores.*

6.2.4.5 Discussion

In conclusion, the proposed photophysical model of mEos4b can reproduce most experimentally observed behaviors and thus presents a good starting point for further refinement. To further refine this model, in depth characterization of the different triplet states (as in[100]) is essential since these are expected to play a central role in the different photophysical behaviors of mEos4b. In the current model, all quantum yields, rates and absorption spectra related to the triplet states are based on assumptions, adding a lot of uncertainty to the model. Characterization of the triplet state is challenging because of the short time-scale and the prescence of many other photo-induced transformations that may interfer with triplet state characterization. However, assuming that the characteristics of the triplet state are simulair at CT as at RT, perfoming the characterizations at CT could provide a solution as photoconversion and *cis/trans* isomerization are presumably blocked at this temperature.

6.3 Summaries translated in French

6.3.1 Introduction

La microscopie à super résolution (SRM) permet d'observer des structures biologiques au-delà de la limite de diffraction de la lumière. Avant l'avènement de la SRM, l'imagerie optique était limitée par la diffraction de la lumière à des résolutions correspondant à environ la moitié de la longueur d'onde de la lumière. Par conséquent, les détails inférieurs à ~250 nm ne pouvaient pas être résolus. Aujourd'hui, des résolutions de 10 à 30 nm sont couramment atteintes par les techniques de SRM, ce qui permet de découvrir des structures biologiques qui étaient auparavant cachées. Le développement de la SMR a été récompensé en 2014 par le prix Nobel de chimie décerné à Eric Betzig, Stefan Hell et William Moerner. Mais le succès de la SRM ne serait pas aussi grand qu'il l'est aujourd'hui sans la découverte des protéines fluorescentes (PF).

La protéine fluorescente verte (GFP) a été découverte par Shimomura et ses collègues en 1962 dans la méduse *Aequora Victoria*. Ce n'est toutefois qu'en 1994 que Chalfie et al. ont démontré que la GFP pouvait être génétiquement fusionnée à n'importe quelle protéine d'intérêt et utilisée comme marqueur protéique fluorescent pour l'imagerie des cellules vivantes, ce qui a véritablement lancé la "révolution verte" de la microscopie à fluorescence. La découverte et le développement de la GFP en tant que marqueur protéique fluorescent ont été récompensés en 2008 par le prix Nobel de chimie décerné à Osamu Shimomura, Martin Chalfie et Roger Tsien.

La SRM est réalisée à l'aide de différents types de fluorophores, mais le fait que les protéines fluorescentes soient codées génétiquement offre des avantages spécifiques pour l'imagerie des cellules vivantes et les applications quantitatives. La SRM se transforme de plus en plus en une technique quantitative grâce aux progrès réalisés dans le domaine des fluorophores, de l'instrumentation et des logiciels. La SRM quantitative peut être utilisée pour évaluer le regroupement et l'oligomérisation de la protéine d'intérêt, ou pour suivre sa dynamique de diffusion dans son environnement cellulaire. Ces applications quantitatives sont principalement basées sur la microscopie de localisation à molécule unique (Single Molecule Localization Microscopy - SMLM), une variante de la SRM, qui repose sur le comportement photophysique "intelligent" des fluorophores utilisés. Cependant, l'application à grande échelle de la SRM quantitative est actuellement limitée par les comportements sous-optimaux des fluorophores et la nécessité d’utiliser des outils d'analyse sophistiqués.

6.3.2 Objectifs de la these

Une grande partie de mes travaux s’est concentrée sur la populaire PCFP mEos4b. Ce travail s'appuie sur des résultats antérieurs du laboratoire montrant que la lumière de 488 nm peut être utilisée pour supprimer les clignotements de longue durée et stimuler sptPALM, ce qui a inspiré l'idée que la lumière de 488 nm pourrait également bénéficier au PALM quantitatif ou qPALM (dans la continuité des travaux de thèse de Daniel Thédié). Cette idée nous a incité à étudier de façon plus approfondie les effets de la lumière à 405 et 488 nm sur le comportement de clignotement et l'efficacité de photoconversion de mEos4b. En outre, l'équipe dirigée par Bernhard Brutscher de l’IBS a découvert par spectroscopie RMN que l'état fondamental de la mEos4b à l'état vert est hétérogène, ce qui a motivé l'étude des effets de cette hétérogénéité sur le comportement photophysique de la mEos4b.

En plus de mEos4b, une partie de ma thèse est consacrée à l'étude du RSFP rsEGFP2, qui a été identifié comme un candidat prometteur pour le cryoPALM. L'étude du comportement de commutation de rsEGFP2 à température cryogénique (CT) était le travail de thèse d'Angela

Mantovanelli, qui a soutenu sa thèse en mars 2023. Ses travaux, ainsi que ceux d'Oleksandr Glushonkov et de Virgile Adam, ont révélé des comportements de commutation intrigants qui ne pouvaient pas être expliqués par les modèles photophysiques existants. Parallèlement à ce projet, des travaux menés par Martin Byrdin ont révélé que la luminosité apparente d'EGFP et de rsEGFP2 à CT est fortement affectée par la formation d'états triplets. J'ai contribué au développement d'un nouveau modèle photophysique de rsEGFP2 en discutant et en utilisant des simulations pour examiner quels modèles pourraient expliquer les comportements observés.

En soutien à ces études photophysiques, ma thèse commence par la discussion des forces et des inconvénients des différentes stratégies d'immobilisation qui peuvent être utilisées pour étudier la photophysique des PF. Ce travail a bénéficié d'une collaboration avec le laboratoire Tinnefeld (LMU, Munich), pour explorer l'utilisation de l'ADN-origami pour la caractérisation photophysique de mEos4b.

En résumé, les objectifs de cette partie sont les suivants :

1. Comparer différentes plateformes d'immobilisation pour la caractérisation photophysique des PF
2. Caractériser les effets de différentes conditions d'illumination sur le comportement de clignotement et l'efficacité de photoconversion de mEos4b afin de construire un modèle photophysique affiné
3. Développer un modèle photophysique expliquant le comportement photophysique de rsEGFP2 à température cryogénique à l'aide de simulations.

Outre les études photophysiques, ma thèse comprend l'application de sptPALM à l'étude du remodelage des nucléoïdes induit par le stress chez *D. radiodurans*. L'élucidation des mécanismes moléculaires qui régissent l'organisation des nucléoïdes en réponse aux lésions de l'ADN est l'un des thèmes centraux du laboratoire. Ce travail est principalement mené par Pierre Vauclare et Joanna Timmins, qui ont caractérisé en détail les changements morphologiques du nucléoïde de *Deinococcus radiodurans* en réponse au rayonnement ultra-violet C (UVC). Ce travail s'appuie également sur les travaux antérieurs du laboratoire de Kevin Floc'h et Françoise Lacroix qui ont caractérisé la morphologie des cellules et du nucléoïde de *D. radiodurans* dans des conditions de croissance normales.

Bien que ce projet soit motivé par une question biologique, à savoir comment le remodelage des nucléoïdes est orchestré en réponse au stress, mon travail s’est principalement axé sur l'analyse et l'interprétation des données sptPALM.

Les objectifs de cette partie sont donc les suivants :

4. Trouver les méthodes les plus appropriées pour collecter et analyser les données spt chez *D. radiodurans*
5. Caractériser la dynamique de diffusion de HU dans des conditions de croissance normales (phase exponentielle et stationnaire) et en réponse à une irradiation aux UVC

6.3.3 Résultats et discussion

Les techniques de qPALM comprennent un ensemble de techniques puissantes qui peuvent donner un aperçu des organisations et des dynamiques macromoléculaires à l'échelle nanométrique in cellulo. Cependant, l'application à grande échelle des techniques qPALM est limitée par les comportements photophysiques complexes des fluorophores utilisés et la nécessité d’effectuer des

analyses sophistiquées. Dans ce contexte, l'objectif de mon travail était de mieux comprendre le comportement photophysique de plusieurs PF phototransformables, de concevoir des stratégies pour faciliter les expériences de qPALM et ainsi contribuer au développement du qPALM en tant que méthode standard de biologie cellulaire. À cette fin, ma thèse comportait deux parties : la caractérisation photophysique des PF phototransformables et l'application de sptPALM pour étudier le remodelage des nucléoïdes induit par le stress chez *Deinococcus radiodurans*.

L'application des méthodes de qPALM est entravée par des comportements sous-optimaux des fluorophores, notamment le clignotement et une photo-activation ou une conversion incomplète. Nous avons montré que l'intensité lumineuse du laser à 405 nm appliquée a un effet important sur l'ECP de mEos4b, et probablement d'autres PCFP, en raison de la modulation de l'hétérogénéité de l'état vert à de faibles intensités (< 1W/cm^2) et du blanchiment non linéaire à des intensités élevées (10-100W/cm^2). En outre, nous avons montré qu'un état non fluorescent de courte durée diminue la luminosité apparente de l'état vert, et probablement aussi de l'état rouge, de mEos4b, et que la lumière à 405/488 nm favorise la formation d'un état rouge non fluorescent dans mEos4b, vraisemblablement par excitation du chromophore neutre. Enfin, nous avons rapporté un nouveau mécanisme de photoswitching de rsEGFP2 à température cryogénique et montré que l'utilisation d'une lumière à 355 nm, au lieu de la lumière standard à 405 nm, peut améliorer l'efficacité du marquage dans les expériences cryoPALM. Dans l'ensemble, les résultats de ces caractérisations photophysiques nous permettent de mieux comprendre la photophysique des PF, nous aident à concevoir des schémas d'imagerie optimisés et pourraient guider le développement de PF plus performants.

Le remodelage de l'architecture du nucléoïde est une réponse commune au stress chez les bactéries, mais les mécanismes moléculaires à l'origine de cette réorganisation restent incomplètement compris. En utilisant une combinaison de microscopie confocale et de sptPALM, nous avons révélé que le remodelage du nucléoïde est régulé différemment dans les cellules entrant en phase stationnaire et dans les cellules exposées à la lumière UVC. Outre cette découverte biologique, nous avons constaté que l'analyse approfondie des données sptPALM était compliquée par une forte variabilité d'une cellule à l'autre, en particulier après l'irradiation, et par un fort confinement des molécules dans le nucléoïde qui entrave l'extraction des coefficients de diffusion. Le défi posé par la grande variabilité entre les cellules pourrait probablement bénéficier des récentes avancées en matière d'apprentissage profond pour segmenter et classer les cellules sur la base de leur morphologie et de celle du nucléoïde de manière automatisée. Par des simulations, nous montrons que le confinement crée une hétérogénéité dans la diffusion apparente des molécules, ce qui peut fausser l'estimation du nombre de populations diffusives, de leurs populations relatives et des coefficients de diffusion. Cette constatation ne doit pas décourager l'application de sptPALM dans les bactéries, mais doit être prise en compte dans l'analyse et l'interprétation des données spt.

L'objectif des études photophysiques était de permettre la conception de schémas d'imagerie optimisés pour les expériences PALM quantitatives, en s'appuyant sur des travaux antérieurs du laboratoire montrant que l'application d'une lumière à 488 nm peut améliorer l'imagerie sptPALM. Malheureusement, au cours de ma thèse, je n'ai pas été en mesure d'appliquer ces schémas d'imagerie optimisés, en partie à cause de la flexibilité limitée du logiciel d'imagerie utilisé pour contrôler le microscope et les lasers. Néanmoins, les résultats photophysiques présentés dans le manuscrit pourraient être appliqués dans des travaux futurs pour améliorer l'imagerie sptPALM. En termes de photophysique, le sptPALM est principalement limité par une faible photostabilité, ce qui se traduit par des pistes courtes et interrompues. Dans ce travail, nous avons montré que la luminosité apparente de l'état vert, et probablement aussi de l'état rouge, de mEos4b est limitée par la formation d'un état sombre de courte durée. Si la formation de l'état sombre pouvait être supprimée, cela augmenterait la luminosité apparente de mEos4b, ce qui réduirait la puissance laser

nécessaire et pourrait augmenter la longueur moyenne de la piste et réduire les effets phototoxiques potentiels.

Les études photophysiques et sptPALM présentées dans ce manuscrit ont été étayées par des simulations réalisées à l'aide du logiciel SMIS récemment mis au point. Les simulations constituent un complément précieux au travail expérimental. La grande complexité des modèles de fluorophores impliquant une multitude d'états fait qu'il est difficile de prédire le comportement du modèle sans le simuler. Dans ce contexte, les simulations renforcent la conception de modèles précis et permettent d'identifier les faiblesses et les imprécisions des modèles proposés. En outre, les simulations constituent également un outil puissant pour étudier les effets de la photophysique sur les expériences PALM (quantitatives) et pour tester la précision des pipelines d'analyse. Par exemple, nous avons utilisé des simulations pour étudier l'effet des clignotements à longue durée de vie sur le comptage moléculaire et pour étudier l'effet du confinement sur l'extraction des coefficients de diffusion à partir d'expériences spt.

L'application à grande échelle des techniques PALM quantitatives est limitée par les comportements photophysiques complexes des fluorophores utilisés et la nécessité d'analyses sophistiquées. Mon travail de doctorat contribue à une compréhension plus approfondie de la photophysique des fluorophores, ce qui peut contribuer à la conception de schémas d'imagerie optimisés et au développement de fluorophores plus performants. En outre, cette thèse met en évidence la valeur de sptPALM pour l'étude des bactéries, mais identifie également les faiblesses des pipelines d'analyse actuels qui peuvent conduire à une interprétation erronée des données. L'ensemble de ce travail contribue à l'amélioration des techniques quantitatives PALM.

6.4 Publications and manuscripts in preparation

Jip Wulffelé, Daniel Thédié, Oleksandr Glushonkov, and Dominique Bourgeois. **mEos4b Photoconversion Efficiency Depends on Laser Illumination Conditions Used in PALM**. The Journal of Physical Chemistry Letters 2022 13 (22), 5075-5080. DOI: 10.1021/acs.jpclett.2c00933

Lukas Rane, Jip Wulffelé, Dominique Bourgeois, Oleksandr Glushonkov, Angela M. R. Mantovanelli, Ninon Zala, and Martin Byrdin. **Light-Induced Forward and Reverse Intersystem Crossing in Green Fluorescent Proteins at Cryogenic Temperatures**. The Journal of Physical Chemistry B 2023 127 (22), 5046-5054. DOI: 10.1021/acs.jpcb.3c02971

Angela M. R. Mantovanelli, Oleksandr Glushonkov, Virgile Adam, Jip Wulffelé, Daniel Thédié, Martin Byrdin, Ingo Gregor, Oleksii Nevskyi, Jörg Enderlein & Dominique Bourgeois. **Photophysical studies at cryogenic temperature reveal a novel photoswitching mechanism of rsEGFP2**. *Journal of the American Chemical Society. DOI: 10.1021/jacs.3c01500*

A. Maity, J. Wulffelé, I. Ayala, A. Favier, V. Adam, D. Bourgeois, B. Brutscher. **Structural Heterogeneity in a Phototransformable Fluorescent Protein Impacts its Photochemical Properties**. Adv. Sci. 2023, 2306272. https://doi.org/10.1002/advs.202306272

Pierre Vauclare*, Jip Wulffelé*, Françoise Lacroix, Pascale Servant, Claire Bouthier de la Tour, Fabrice Confalonieri, Jean-Philippe Kleman, Dominique Bourgeois and Joanna Timmins. **Stress-induced nucleoid remodeling in Deinococcus radiodurans is associated with major changes in HU abundance and dynamics.** bioRxiv 2023.10.18.562934; doi: https://doi.org/10.1101/2023.10.18.562934
** Equal contribution*

Jip Wulffelé and Dominique Bourgeois. **Fluorophores & Labeling Methods for Fluorescence Microscopy**. Manuscript in preparation.

THE JOURNAL OF PHYSICAL CHEMISTRY LETTERS
A JOURNAL OF THE AMERICAN CHEMICAL SOCIETY

pubs.acs.org/JPCL Letter

mEos4b Photoconversion Efficiency Depends on Laser Illumination Conditions Used in PALM

Jip Wulffele, Daniel Thédié, Oleksandr Glushonkov, and Dominique Bourgeois*

Cite This: J. Phys. Chem. Lett. 2022, 13, 5075−5080 Read Online

ACCESS | Metrics & More | Article Recommendations | Supporting Information

ABSTRACT: Green-to-red photoconvertible fluorescent proteins (PCFPs) are widely employed as markers in photoactivated localization microscopy (PALM). However, their highly complex photophysical behavior complicates their usage. The fact that only a limited fraction of a PCFP ensemble can form the photoconverted state upon near-UV light illumination, termed photoconversion efficiency (PCE), lowers the achievable spatial resolution in PALM and creates undercounting errors in quantitative counting applications. Here, we show that the PCE of mEos4b is not a fixed property of this PCFP but strongly depends on illumination conditions. Attempts to reduce long-lived blinking in red mEos4b by application of 488 nm light lead to a reduction of the PCE. Furthermore, the PCE of mEos4b strongly depends on the applied 405 nm power density. A refined photophysical model of mEos4b accounts for the observed effects, involving nonlinear green-state photobleaching upon violet light illumination favored by photon absorption by a putative radical dark state.

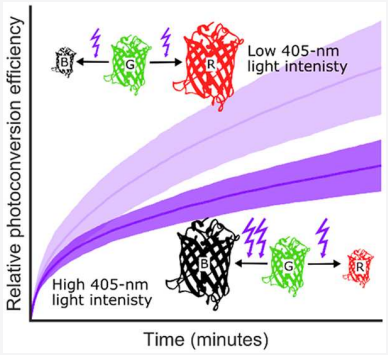

For now more than a decade, super-resolution microscopy has provided unprecedented insights into biological processes.[1] Photoactivation localization microscopy (PALM) is a single-molecule-based localization technique that typically takes advantage of so-called phototransformable fluorescent proteins (PTFPs).[2] Major advantages of using PTFPs are the possibility to work on living cells, the ideal specificity of labeling, and the option to label endogenous targets of interest with genome editing techniques.[2] Green-to-red photoconvertible fluorescent proteins (PCFPs) of the mEos family are often used as PTFP markers in PALM because of their relatively high brightness as well as high monomeric character and also because successfully labeled samples can be easily detected by monitoring green-state fluorescence prior to PALM data collection.[3] However, a disadvantage of mEos-based PCFPs is their highly complex photophysical behavior (Figure S1).[4−7]

One property essential to the success of PALM experiments using PCFPs is the so-called photoconversion efficiency (PCE),[8,9] sometimes also termed signaling efficiency.[10] Typically, upon prolonged violet light illumination, green-to-red photoconversion remains incomplete, meaning that from a pool of PCFPs, only a limited fraction can ever be imaged in the red channel of the microscope.[4,9,11,12] In addition to unsuccessful protein folding or chromophore maturation, incomplete PCE's can be attributed to possible subpopulations within the PCFP pool unable to photoconvert, rapid photobleaching in the red state before detection can be made, or premature photobleaching in the green state before photoconversion occurs.[4,9,11,12] In general, green-to-red photoconversion, the mechanism of which remains incompletely understood,[3] is in competition with other photophysical pathways that upon absorption of a violet photon may lead to reversible dark-state formation or photobleaching.[9]

A limited PCE is highly detrimental to PALM experiments. First, it limits the achievable spatial resolution of nanoscopy images due to a reduced apparent labeling efficiency, compromising the high labeling density necessary to satisfy the Nyquist criterium.[8] Second, it complicates counting by quantitative PALM (qPALM).[12] In this technique the stoichiometry of protein complexes, typically nonresolvable spatially, can in principle be determined by counting fluorescence bursts from each complex.[12−16] However, a limited PCE results in severe undercounting errors. Such errors can in theory be corrected for based on the expected binomial distribution of measured stoichiometries, but this comes at the cost of increased uncertainty of the extracted values, notably when a distribution of stoichiometries is inherently present in the sample.[12,16]

PCEs of various PCFPs have been reported in several papers,[9,10,12,13,17,18] usually relying on the use of biological templates.[14] The measured values, however, tend to differ widely for a single PCFP, e.g., from ∼1%[10] to ∼90%[17] for mEos2. One hypothesis to account for such variability could be

Received: March 31, 2022
Accepted: May 27, 2022
Published: June 2, 2022

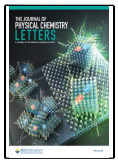

https://doi.org/10.1021/acs.jpclett.2c00933
J. Phys. Chem. Lett. 2022, 13, 5075−5080

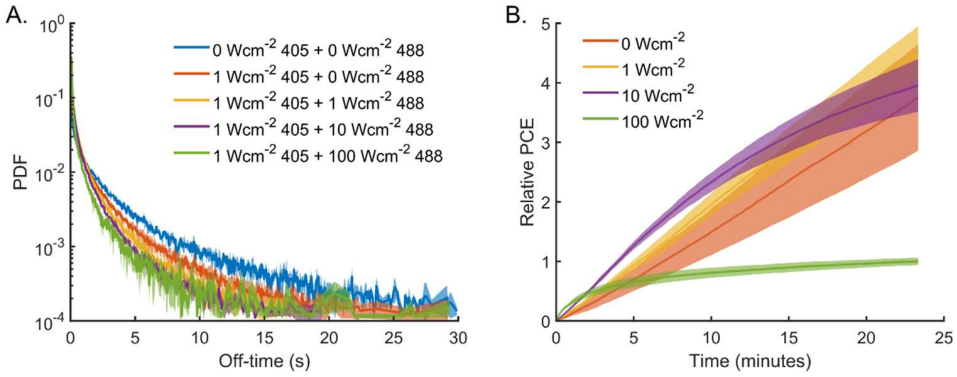

Figure 1. Off-time reduction by 488 nm light is offset by a reduced photoconversion efficiency. Off-time histograms (A) and the relative PCE (B) of mEos4b molecules embedded in PAA under alternating illumination with 500 W/cm^2 561 nm light (70 ms) and 1 W/cm^2 405 nm light plus 0−100 W/cm^2 488 nm light (8.2 ms). Data are normalized to the final number of photoconverted molecules under 100 W/cm^2 488 illumination. Data represent mean ± s.d. of ≥3 measurements.

that the employed templates might induce biases due to factors such as template heterogeneity, reduced tumbling of the labels in fixed samples or uncontrolled energy transfer mechanisms between neighboring PCFPs.[11−13] However, the possibility that PCEs may depend on the employed illumination conditions, notably the applied power densities, has not been put forward. Here, we investigate the effects of 405 and 488 nm light illumination on the PCE of mEos4b, a now popular mEos variant initially designed to withstand chemical fixation.[19]

The study was initially stimulated by the prospect of extending to qPALM applications a blinking reduction strategy that we recently introduced in the context of single-particle-tracking PALM (sptPALM).[5] In this technique, 488 nm light is used in addition to readout (561 nm) and very weak activating (405 nm, of the order of mW/cm^2) light to increase the length of single-molecule tracks through a reduction of fluorescence intermittencies in red mEos4b molecules.[5] The mechanistic interpretation of the effect is that long off-times in mEos-based PCFPs originate at least in part from 561 nm induced *cis*−*trans* isomerization of the chromophore and that back-isomerization to the fluorescent *cis* state is efficiently promoted by 488 nm light.[5] Thus, we wondered whether the same strategy could be used to improve counting accuracy with qPALM by reducing long-lived blinking expected to be at the origin of overcounting errors.

We first performed simulations to check whether long-lived off-time reduction effectively improves counting, deliberately ignoring the rich photophysics of mEos4b in its green state.[4,6] The qPALM data were simulated by using the photophysical model depicted in Figure S2A and Table S1, in the absence or the presence of additional 488 nm light. Then, keeping in mind that widely different strategies have been proposed to process qPALM data,[20] we analyzed the data using either the off-times thresholding method of Lee et al.[15] or the blinking statistics method of Heilemann et al.[13,16,17,21] The results shown in Figures S3 and S4 revealed that whereas the accuracy of stoichiometry retrieval by off times thresholding benefited from long-lived dark-state reduction, this was not observed in the case of blinking statistics analysis (Supporting Information, Note 1). However, importantly, we noticed that slight measurement errors in the blinking propensity (*p*-value) of mEos4b measured in the monomeric state propagated to very large errors when evaluating complexes of high stoichiometries (Figure S4F). Overall, the performed simulations encouraged us to experimentally test the potential benefit of additional 488 nm light for counting purposes.

mEos4b proteins were immobilized in polyacrylamide (PAA) gel, and fluorescence traces of photoconverted molecules were recorded by using 500 W/cm^2 561 nm light under increasing 488 nm light intensities with wide-field illumination. First, we validated that 488 nm illumination reduces the off-time duration of red mEos4b in the presence of weak 405 nm laser light (1 W/cm^2, which can be taken as representative for qPALM experiments)[22] (Figure 1A). We noticed, however, that the reduction in off-times was not as pronounced as with 405 nm light alone when using similar intensities (Figure S5). The mechanism behind this experimental observation remains to be deciphered, but it could result from the presence of one or several long-lived dark states, in addition to the switched-off protonated *trans* chromophore, which would be reactive to 405 nm but insensitive to 488 nm light.

Next, we assessed the effect of 488 nm illumination on the PC rate and efficiency. Although absolute PCEs could not be reliably extracted using our experimental setup (Supporting Information, Note 4), we could compare relative values over time at different illumination intensities. We thus measured the numbers of photoconverted molecules at the end of experiments by using 405, 488, and 561 nm light illumination and compared them with those using only 405 and 561 nm light. Figure 1B shows that although low 488 nm light intensity (1 W/cm^2) had a minimal effect on the PC kinetics within the time window of the experiment, high 488 nm light intensity (100 W/cm^2) drastically decreased the PCE. Because the bleaching time and photon budget of photoconverted red molecules were not reduced by 488 nm illumination (Figure S6), green-state photophysics is likely at the origin of the decrease in PCE. Using simulations with the current model of mEos4b photophysics,[4] we found that the decrease can be explained by green-state bleaching by the 488 nm light (Figure S7). Importantly, the dependence of the PCE on 488 nm light is only observed in the presence of significant 405 nm light (∼1 W/cm^2) (Figure S7). This is explained by the fact that in such case photoconversion (mostly driven by 405 nm light) and green-state photobleaching (driven by all lasers) become strongly decoupled. Thus, under very weak 405 nm light (≪1 W/cm^2) often used in sptPALM to achieve strong single-molecule sparsity,[5] the PCE is low[4] but there is little additional penalty in using 488 nm light to reduce red-state

https://doi.org/10.1021/acs.jpclett.2c00933
J. Phys. Chem. Lett. 2022, 13, 5075−5080

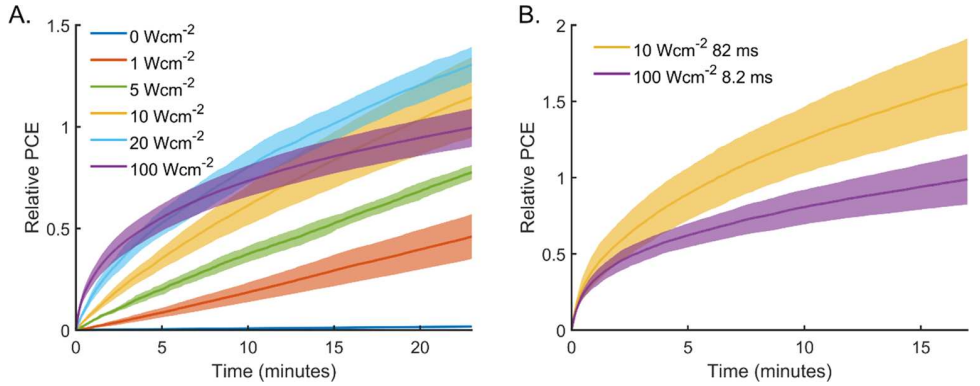

Figure 2. High 405 nm illumination intensities reduce the photoconversion efficiency of mEos4b under PALM imaging conditions. (A) Relative PCE of mEos4b molecules embedded in PAA under alternating illumination with 500 W/cm^2 561 nm light (70 ms) and 1−100 W/cm^2 405 nm light (8.2 ms). (B) Relative PCE of mEos4b molecules embedded in PAA under alternating illumination with 500 W/cm^2 561 nm light (70 ms) and 10 or 100 W/cm^2 405 nm light for 82 and 8.2 ms, respectively. Data are normalized to the final number of photoconverted molecules under 100 W/cm^2 405 nm illumination. Data represent mean ± s.d. of ≥3 measurements.

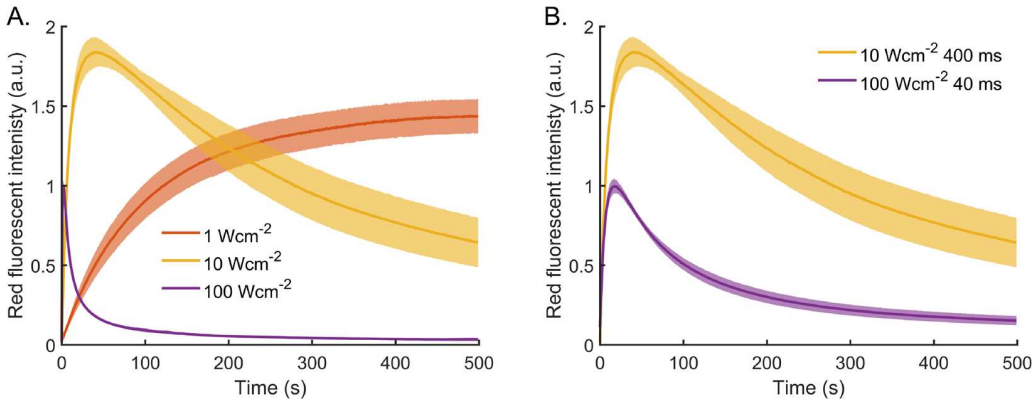

Figure 3. High 405 nm light illumination intensities reduce the photoconversion efficiency of mEos4b in the absence of 561 nm light illumination. Ensemble fluorescence time traces of mEos4b molecules embedded in PAA. The red fluorescent intensity was measured every 500 ms by illumination with 8 W/cm^2 561 nm light for 20 ms. (A) Samples were exposed to 400 ms pulses of 405 nm light (1−100 W/cm^2). (B) Samples were exposed to 40 and 400 ms pulses of 100 and 10 W/cm^2 405 nm, respectively. Data represent mean ± s.d. of ≥3 measurements.

intermittencies. Overall, these results show that 488 nm light illumination is not beneficial in qPALM measurements with mEos4b, as the gain in red-state off-time reduction is relatively limited and the PCE becomes compromised in the presence of >∼1 W/cm^2 405 nm light.

Intrigued by the finding that 488 nm light drastically reduces the mEos4b PCE in the presence of 405 nm light, we set out to investigate how the intensity of the 405 nm light itself affects the PCE in the absence of 488 nm light. We first hypothesized that the PCE could increase with increasing 405 nm light because 405 nm induced photoconversion and photobleaching rates would evolve in proportion if based on single-photon mechanisms while bleaching of green molecules by the 561 nm laser[4] would be reduced due to shorter acquisition times. To test this, we acquired single-molecule data at varying 405 nm power densities, similar to the 488 nm illumination experiments described above. Whereas low levels of 405 nm light (1 W/cm^2) increased the PCE as compared to readout photoconversion only, in line with our previous findings,[4] we found that high 405 nm intensities (100 W/cm^2) substantially decreased the PCE despite a higher initial photoconversion rate (Figure 2A). Ensemble measurements where we monitored the cumulative fluorescence of the mEos4b red state under identical light illumination conditions as in the single-molecule case revealed a similar relation between the 405 nm light intensity and the PCE (Figure S8). To evaluate whether the decrease in PCE at high 405 nm light intensity could be due to increased bleaching of red molecules, we examined the single-molecule bleaching time and photon budget histograms of the red state (Figure S9). These histograms reveal that red-state bleaching was not significantly increased when raising the 405 nm light power density, suggesting that, again, green-state photophysics are at the origin of the decreased PCE under increased 405 nm light intensities.

In contrast to the case of 488 nm light, the dependence of the mEos4b PCE on 405 nm light cannot be explained by the current photophysical model of this PCFP (Figure S7).[4] To explain the decrease of the PCE at high 405 nm light intensity, 405 nm photons must bleach the green state in a nonlinear manner; that is, bleaching must require the subsequent absorption of two (or more) photons. To verify this hypothesis, we compared the PCEs under 10 and 100 W/cm^2 405 nm light while keeping the integrated illumination dose constant by adjusting the exposure time (82 ms for 10 W/cm^2 and 8.2 ms for 100 W/cm^2). As expected, application of short exposures of 100 W/cm^2 405 nm light decreased the mEos4b PCE as compared to longer exposures to 10 W/cm^2,

https://doi.org/10.1021/acs.jpclett.2c00933
J. Phys. Chem. Lett. 2022, 13, 5075−5080

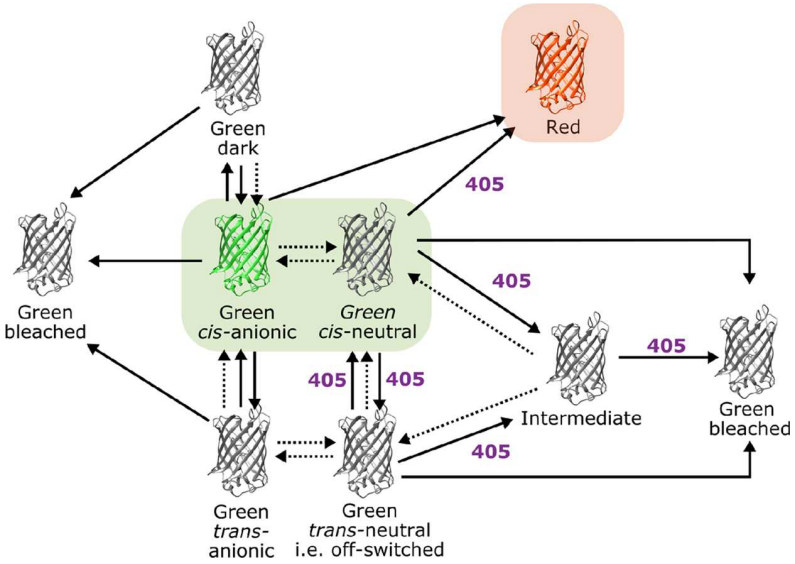

Figure 4. Tentative updated model of mEos4b green-state photophysics. An intermediate state, downstream of the neutral green chromophore, thermally recovers or absorbs a second 405 nm photon leading to nonlinear bleaching at high 405 nm power densities. Single-photon bleaching may occur from every light-absorbing state. Solid arrows indicate photoinduced transitions; dotted arrows indicate thermal transitions or pH-dependent equilibria.

while this did not affect the red-state photophysics (Figure 2B and Figure S10).

Next, we aimed to identify the photophysical state(s) of green mEos4b involved in nonlinear bleaching by 405 nm light. Violet light is predominantly absorbed by the protonated states of the green chromophore,[6] which makes the *cis*-protonated and *trans*-protonated (i.e., off-switched) states likely starting points for the mechanism at play. The *trans*-protonated state can be populated by intense 561 nm illumination,[4] as used in PALM measurements to reach single-molecule sensitivity, which made us wonder whether 405 nm light also induced nonlinear bleaching in the absence of 561 nm light. To test this, we monitored the progression of ensemble mEos4b red fluorescence under 1, 10, and 100 W/cm^2 405 nm illumination and weak exposure to 561 nm light (8 W/cm^2) (Figure 3A). Sun et al.[7] reported that the ensemble red fluorescence intensity of mEos3.2 under constant 405 and 561 nm illumination follows a three-state model: green → red → bleached. Such a model implies that the level of the maximum recorded red fluorescence increases with the applied 405 nm light intensity as bleaching by the 561 nm laser lowers the peak height at low 405 nm intensities. However, the experimentally measured maximum intensity under 100 W/cm^2 405 nm light reached a significantly lower value as compared to illumination with 1 and 10 W/cm^2 405 nm light (Figure 3A and Supporting Information, Note 3), suggesting that the model of Sun et al. is insufficient to account for our data. To further validate this finding, we monitored the ensemble red-state fluorescence under illumination with either 10 or 100 W/cm^2 405 nm light while keeping the integrated dose of 405 nm light constant. The data again revealed that high-intensity 405 nm light decreased the red fluorescence maximum intensity (Figure 3B). Altogether, these ensemble measurements are consistent with the notion that 405 nm light induces nonlinear photobleaching of the mEos4b green state independently of the presence of additional 561 nm light. We speculate that, upon absorption of a 405 nm photon in either the *cis*-neutral or *trans*-neutral chromophore state, an intermediate state forms with a minimum lifetime in the tens of milliseconds range (Figure 4 and Supporting Information, Note 5). Such a lifetime appears too long to attribute the intermediate to the triplet state.[23] However, a radical state, similar to the one that we pinpointed in an earlier X-ray-based study of IrisFP (a PCFP derived from EosFP), could be invoked.[24] This intermediate would thermally relax to the fluorescence state or lead to photobleaching upon absorption of violet light. The precise mechanism of nonlinear bleaching of PCFPs by 405 nm light will now need further dedicated studies. A possible scenario is decarboxylation of Glu212,[25] a fully conserved residue in fluorescent proteins of the GFP family, that was found critical for successful photoconversion in PCFPs,[26] in line with our previous structural studies of photobleaching in green IrisFP.[27] An updated model of mEos4b photophysics is presented in Figure 4, of use for the future design of optimized illumination schemes.

We also observed nonlinear photobleaching by 405 nm light in mEos3.2, pcStar, and Dendra2 (Figure S11), and we anticipate that the described mechanism applies to most commonly used PCFPs of anthozoan origin. Moreover, Renz and Wunder[28] reported that the photoactivation efficiency of the photoactivatable FPs PA-GFP and PA-mCherry is reduced by high-intensity 405 nm illumination, which suggests that 405 nm light-induced nonlinear bleaching could be a feature shared by many phototransformable FPs. In the future, it will be interesting to investigate the effects of pH, oxygen removal, and the addition of triplet-state quenchers, reducers, or oxidizers on the nonlinear photobleaching phenomenon.[29,30] Of particular interest would be the investigation of the effects of reducing thiols, which have been shown to significantly increase red-state blinking in mEos2[31] and mEos3.2,[13] possibly resulting from a photoprotective effect that might be beneficial for increasing PCE at high violet light intensities. More generally, how our findings made *in vitro* using PAA gel immobilization can be altered in the many different cellular nanoenvironments encountered in biological samples will need

https://doi.org/10.1021/acs.jpclett.2c00933
J. Phys. Chem. Lett. 2022, 13, 5075−5080

to be investigated in detail, for example, by using specific nanotemplates.[14,32]

In conclusion, our results demonstrate that the photoconversion efficiency of mEos4b and other PCFPs strongly depends on the employed illumination conditions. In the presence of 405 nm light the PCE of mEos4b decreases with increasing 488 nm illumination because 488 nm light significantly increases the overall green-state bleaching rate while the overall photoconversion rate remains governed by the applied 405 nm light. Most importantly, high 405 nm light intensities decrease the PCE of mEos4b due to nonlinear bleaching of the green state, possibly through subsequent photon absorptions by a neutral state of mEos4b and a short-lived radical state.

A high PCE is essential to ensure sufficient labeling density in PALM and accurate molecular counting in qPALM. Whereas the use of very low 405 nm light ($\ll$1 W/cm^2) should be avoided whenever possible (depending on single-molecule sparsity) due to accumulating green-state photobleaching by readout 561 nm light, high 405 nm light is expected to also yield suboptimal results in the following circumstances: (i) in high-speed PALM,[33] (ii) whenever the photoconversion light is progressively ramped-up in PALM or qPALM, or (iii) whenever short and intense photoconversion light pulses (e.g., in between recorded frames) are used instead of longer and weaker pulses. Finally, this work highlights the complexity and, yet, key importance of green-state photophysics in photoconvertible fluorescent proteins.

■ ASSOCIATED CONTENT

Supporting Information

The Supporting Information is available free of charge at https://pubs.acs.org/doi/10.1021/acs.jpclett.2c00933.

Materials and methods, detailed notes on the experimental setup and data analysis, and supporting figures (PDF)

Transparent Peer Review report available (PDF)

■ AUTHOR INFORMATION

Corresponding Author

Dominique Bourgeois − *Institut de Biologie Structurale, Univ. Grenoble Alpes, CNRS, CEA, F-38044 Grenoble, France;* orcid.org/0000-0002-1862-7712; Phone: + 33 4 57 42 86 44; Email: dominique.bourgeois@ibs.fr

Authors

Jip Wulffele − *Institut de Biologie Structurale, Univ. Grenoble Alpes, CNRS, CEA, F-38044 Grenoble, France*

Daniel Thédié − *Institut de Biologie Structurale, Univ. Grenoble Alpes, CNRS, CEA, F-38044 Grenoble, France; University of Edinburgh, EH9 3FF Edinburgh, United Kingdom*

Oleksandr Glushonkov − *Institut de Biologie Structurale, Univ. Grenoble Alpes, CNRS, CEA, F-38044 Grenoble, France*

Complete contact information is available at: https://pubs.acs.org/10.1021/acs.jpclett.2c00933

Author Contributions

J.W. and D.B. conceived of the project; J.W. and D.T. performed experiments and data analysis; J.W. and D.B. performed simulations; O.G. and D.T. developed data acquisition schemes; J.W. and D.B. wrote the paper with contributions from all authors.

Notes

The authors declare no competing financial interest.

■ ACKNOWLEDGMENTS

We thank Ninon Zala, Virgile Adam, Joanna Timmins, Salvatore De Bonis, and Isabel Ayala for PCFP's production and purification and Jean-Philippe Kleman for assistance with the M4D imaging platform. This work was supported by the Agence Nationale de la Recherche (Grants ANR-17-CE11-0047-01 and ANR-20-CE11-0013-01 to D.B. and ANR-16-CE11-0016-01) and used the M4D imaging platform of the Grenoble Instruct-ERIC Center (ISBG: UMS 3518 CNRS-CEA-UGA-EMBL) with support from FRISBI (Grant ANR-10-INBS-05-02) and GRAL, a project of the Université Grenoble Alpes graduate school (Ecoles Universitaires de Recherche) CBH-EUR-GS (ANR-17-EURE-0003) within the Grenoble Partnership for Structural Biology (PSB). J.W. acknowledges funding by the GRAL Labex.

■ REFERENCES

(1) Lelek, M.; Gyparaki, M. T.; Beliu, G.; Schueder, F.; Griffié, J.; Manley, S.; Jungmann, R.; Sauer, M.; Lakadamyali, M.; Zimmer, C. Single-Molecule Localization Microscopy. *Nat. Rev. Methods Primer* **2021**, *1* (1), 1−27.

(2) Shcherbakova, D. M.; Sengupta, P.; Lippincott-Schwartz, J.; Verkhusha, V. V. Photocontrollable Fluorescent Proteins for Superresolution Imaging. *Annu. Rev. Biophys.* **2014**, *43*, 303−329.

(3) Nienhaus, K.; Nienhaus, G. U. Fluorescent Proteins of the EosFP Clade: Intriguing Marker Tools with Multiple Photoactivation Modes for Advanced Microscopy. *RSC Chem. Biol.* **2021**, *2* (3), 796−814.

(4) Thédié, D.; Berardozzi, R.; Adam, V.; Bourgeois, D. Photoswitching of Green MEos2 by Intense 561 Nm Light Perturbs Efficient Green-to-Red Photoconversion in Localization Microscopy. *J. Phys. Chem. Lett.* **2017**, *8* (18), 4424−4430.

(5) De Zitter, E.; Thédié, D.; Mönkemöller, V.; Hugelier, S.; Beaudouin, J.; Adam, V.; Byrdin, M.; Van Meervelt, L.; Dedecker, P.; Bourgeois, D. Mechanistic Investigation of MEos4b Reveals a Strategy to Reduce Track Interruptions in SptPALM. *Nat. Methods* **2019**, *16* (8), 707−710.

(6) De Zitter, E.; Ridard, J.; Thédié, D.; Adam, V.; Lévy, B.; Byrdin, M.; Gotthard, G.; Van Meervelt, L.; Dedecker, P.; Demachy, I.; Bourgeois, D. Mechanistic Investigations of Green MEos4b Reveal a Dynamic Long-Lived Dark State. *J. Am. Chem. Soc.* **2020**, *142* (25), 10978−10988.

(7) Sun, M.; Hu, K.; Bewersdorf, J.; Pollard, T. D. Sample Preparation and Imaging Conditions Affect MEos3.2 Photophysics in Fission Yeast Cells. *Biophys. J.* **2021**, *120* (1), 21−34.

(8) Diekmann, R.; Kahnwald, M.; Schoenit, A.; Deschamps, J.; Matti, U.; Ries, J. Optimizing Imaging Speed and Excitation Intensity for Single-Molecule Localization Microscopy. *Nat. Methods* **2020**, *17* (9), 909−912.

(9) Durisic, N.; Laparra-Cuervo, L.; Sandoval-Álvarez, Á.; Borbely, J. S.; Lakadamyali, M. Single-Molecule Evaluation of Fluorescent Protein Photoactivation Efficiency Using an in Vivo Nanotemplate. *Nat. Methods* **2014**, *11* (2), 156−162.

(10) Wang, S.; Moffitt, J. R.; Dempsey, G. T.; Xie, X. S.; Zhuang, X. Characterization and Development of Photoactivatable Fluorescent Proteins for Single-Molecule−Based Superresolution Imaging. *Proc. Natl. Acad. Sci. U. S. A.* **2014**, *111* (23), 8452−8457.

(11) Tao, A.; Zhang, R.; Yuan, J. Characterization of Photophysical Properties of Photoactivatable Fluorescent Proteins for Super-Resolution Microscopy. *J. Phys. Chem. B* **2020**, *124* (10), 1892−1897.

(12) Puchner, E. M.; Walter, J. M.; Kasper, R.; Huang, B.; Lim, W. A. Counting Molecules in Single Organelles with Superresolution Microscopy Allows Tracking of the Endosome Maturation Trajectory. *Proc. Natl. Acad. Sci. U. S. A.* **2013**, *110* (40), 16015−16020.
(13) Baldering, T. N.; Dietz, M. S.; Gatterdam, K.; Karathanasis, C.; Wieneke, R.; Tampé, R.; Heilemann, M. Synthetic and Genetic Dimers as Quantification Ruler for Single-Molecule Counting with PALM. *Mol. Biol. Cell* **2019**, *30* (12), 1369−1376.
(14) Finan, K.; Raulf, A.; Heilemann, M. A Set of Homo-Oligomeric Standards Allows Accurate Protein Counting. *Angew. Chem., Int. Ed.* **2015**, *54* (41), 12049−12052.
(15) Lee, S.-H.; Shin, J. Y.; Lee, A.; Bustamante, C. Counting Single Photoactivatable Fluorescent Molecules by Photoactivated Localization Microscopy (PALM). *Proc. Natl. Acad. Sci. U. S. A.* **2012**, *109* (43), 17436−17441.
(16) Baldering, T. N.; Bullerjahn, J. T.; Hummer, G.; Heilemann, M.; Malkusch, S. Molecule Counts in Complex Oligomers with Single-Molecule Localization Microscopy. *J. Phys. Appl. Phys.* **2019**, *52* (47), 474002.
(17) Fricke, F.; Beaudouin, J.; Eils, R.; Heilemann, M. One, Two or Three? Probing the Stoichiometry of Membrane Proteins by Single-Molecule Localization Microscopy. *Sci. Rep.* **2015**, *5* (1), 14072.
(18) Nan, X.; Collisson, E. A.; Lewis, S.; Huang, J.; Tamgüney, T. M.; Liphardt, J. T.; McCormick, F.; Gray, J. W.; Chu, S. Single-Molecule Superresolution Imaging Allows Quantitative Analysis of RAF Multimer Formation and Signaling. *Proc. Natl. Acad. Sci. U. S. A.* **2013**, *110* (46), 18519−18524.
(19) Paez Segala, M. G.; Sun, M. G.; Shtengel, G.; Viswanathan, S.; Baird, M. A.; Macklin, J. J.; Patel, R.; Allen, J. R.; Howe, E. S.; Piszczek, G.; Hess, H. F.; Davidson, M. W.; Wang, Y.; Looger, L. L. Fixation-Resistant Photoactivatable Fluorescent Proteins for Correlative Light and Electron Microscopy. *Nat. Methods* **2015**, *12* (3), 215−218.
(20) Khater, I. M.; Nabi, I. R.; Hamarneh, G. A Review of Super-Resolution Single-Molecule Localization Microscopy Cluster Analysis and Quantification Methods. *Patterns* **2020**, *1* (3), 100038.
(21) Baldering, T. N.; Karathanasis, C.; Harwardt, M.-L. I. E.; Freund, P.; Meurer, M.; Rahm, J. V.; Knop, M.; Dietz, M. S.; Heilemann, M. CRISPR/Cas12a-Mediated Labeling of MET Receptor Enables Quantitative Single-Molecule Imaging of Endogenous Protein Organization and Dynamics. *iScience* **2021**, *24* (1), 101895.
(22) Fricke, F.; Beaudouin, J.; Malkusch, S.; Eils, R.; Heilemann, M. Quantitative Single-Molecule Localization Microscopy (QSMLM) of Membrane Proteins Based on Kinetic Analysis of Fluorophore Blinking Cycles. In *Super-Resolution Microscopy: Methods and Protocols*; Erfle, H., Ed.; Methods in Molecular Biology; Springer: New York, 2017; pp 115−126.
(23) Byrdin, M.; Duan, C.; Bourgeois, D.; Brettel, K. A Long-Lived Triplet State Is the Entrance Gateway to Oxidative Photochemistry in Green Fluorescent Proteins. *J. Am. Chem. Soc.* **2018**, *140* (8), 2897−2905.
(24) Roy, A.; Field, M. J.; Adam, V.; Bourgeois, D. The Nature of Transient Dark States in a Photoactivatable Fluorescent Protein. *J. Am. Chem. Soc.* **2011**, *133* (46), 18586−18589.
(25) van Thor, J. J.; Gensch, T.; Hellingwerf, K. J.; Johnson, L. N. Phototransformation of Green Fluorescent Protein with UV and Visible Light Leads to Decarboxylation of Glutamate 222. *Nat. Struct. Biol.* **2002**, *9* (1), 37−41.
(26) Wachter, R. M. Photoconvertible Fluorescent Proteins and the Role of Dynamics in Protein Evolution. *Int. J. Mol. Sci.* **2017**, *18* (8), 1792.
(27) Duan, C.; Adam, V.; Byrdin, M.; Ridard, J.; Kieffer-Jaquinod, S.; Morlot, C.; Arcizet, D.; Demachy, I.; Bourgeois, D. Structural Evidence for a Two-Regime Photobleaching Mechanism in a Reversibly Switchable Fluorescent Protein. *J. Am. Chem. Soc.* **2013**, *135* (42), 15841−15850.
(28) Renz, M.; Wunder, C. Internal Rulers to Assess Fluorescent Protein Photoactivation Efficiency. *Cytometry A* **2018**, *93* (4), 411−419.
(29) Henrikus, S. S.; Tassis, K.; Zhang, L.; Velde, J. H. M.; Gebhardt, C.; Herrmann, A.; Jung, G.; Cordes, T. Characterization of Fluorescent Proteins with Intramolecular Photostabilization. *ChemBioChem* **2021**, *22* (23), 3283−3291.
(30) Jusuk, I.; Vietz, C.; Raab, M.; Dammeyer, T.; Tinnefeld, P. Super-Resolution Imaging Conditions for Enhanced Yellow Fluorescent Protein (EYFP) Demonstrated on DNA Origami Nanorulers. *Sci. Rep.* **2015**, *5* (1), 14075.
(31) Endesfelder, U.; Malkusch, S.; Flottmann, B.; Mondry, J.; Liguzinski, P.; Verveer, P.; Heilemann, M. Chemically Induced Photoswitching of Fluorescent Probes-A General Concept for Super-Resolution Microscopy. *Mol. Basel Switz.* **2011**, *16*, 3106−3118.
(32) Thevathasan, J. V.; Kahnwald, M.; Cieśliński, K.; Hoess, P.; Peneti, S. K.; Reitberger, M.; Heid, D.; Kasuba, K. C.; Hoerner, S. J.; Li, Y.; Wu, Y.-L.; Mund, M.; Matti, U.; Pereira, P. M.; Henriques, R.; Nijmeijer, B.; Kueblbeck, M.; Sabinina, V. J.; Ellenberg, J.; Ries, J. Nuclear Pores as Versatile Reference Standards for Quantitative Superresolution Microscopy. *Nat. Methods* **2019**, *16* (10), 1045−1053.
(33) Development of ultrafast camera-based imaging of single fluorescent molecules and live-cell PALM. bioRxiv https://www.biorxiv.org/content/10.1101/2021.10.26.465864v2 (accessed 2022-02-22).

https://doi.org/10.1021/acs.jpclett.2c00933
J. Phys. Chem. Lett. 2022, 13, 5075−5080

THE JOURNAL OF PHYSICAL CHEMISTRY B
A JOURNAL OF THE AMERICAN CHEMICAL SOCIETY

pubs.acs.org/JPCB Article

Light-Induced Forward and Reverse Intersystem Crossing in Green Fluorescent Proteins at Cryogenic Temperatures

Lukas Rane, Jip Wulffele, Dominique Bourgeois, Oleksandr Glushonkov, Angela M. R. Mantovanelli, Ninon Zala, and Martin Byrdin*

Cite This: J. Phys. Chem. B 2023, 127, 5046−5054

ABSTRACT: Combining fluorescence and phosphorescence kinetics, we characterize forward and reverse intersystem crossing (FISC and RISC, respectively) between the singlet and triplet manifolds S ↔ T in photoswitchable (rsEGFP2) and non-photoswitchable (EGFP) green fluorescent proteins upon continuous 488 nm laser excitation at cryogenic temperatures (CTs). Both proteins behave very similarly, with T_1 absorption spectra showing a visible peak at 490 nm (10 mM^{-1} cm^{-1}) and a vibrational progression in the near-infrared (720 to 905 nm). The dark lifetime of T_1 is 21−24 ms at 100 K and very weakly temperature-dependent up to 180 K. Above 180 K, T_1 lifetimes reduce rapidly to few milliseconds as found at room temperature (RT). FISC and RISC quantum yields are 0.3 and 0.1%, respectively, for both proteins. The light-induced RISC channel becomes faster than the dark reversal at power densities as low as 20 W cm^{-2}. We discuss implications for fluorescence (super resolution-) microscopy at CT and RT.

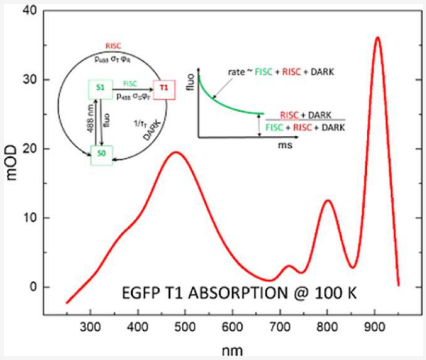

INTRODUCTION

Cryogenic light microscopy has become increasingly popular in biology mainly for two reasons: less harsh sample preservation conditions than those resulting from chemical fixation and increased resistance of the employed fluorescent markers to photobleaching.[1,2] Especially in the context of rapidly developing CLEM (correlated light and electron microscopy), where the light microscope serves to identify those sample portions that deserve to be further investigated by electron microscopy (EM), a sufficiently resolved fluorescence image under cryo-EM conditions is desirable.[3,4] The resulting efforts to develop cryo-super-resolution microscopy are accompanied by the search for suitable fluorescent markers that can be photoswitched at cryogenic temperatures (CTs).[5−9]

The uncontestable observation of longer resistance to photobleaching both for fluorescent proteins (FPs) in whole cells[1] and for organic dyes in buffer solution[2] could be explained either by the lack of some ingredients necessary for photobleaching processes due to diffusion slowed by CT or by the temperature-induced slowing of some intramolecular processes involved in photobleaching.[10] As to the latter, we recently proposed for some green fluorescent protein (GFP)-type proteins an entrance gateway to photochemical bleaching via the triplet state.[11] Intriguingly, we also observed that the decay of that triplet state accelerates about twice upon heating from 10 to 40 °C. From this effect, we concluded that the decay pathway proceeds via an uphill step with an apparent activation barrier of 0.26 ± 0.02 eV. Based on this finding, at CTs, a substantially longer triplet lifetime and, as a consequence of high reactivity of the triplet state, also an increased propensity for some bleaching pathways could be expected. In order to illuminate this discrepancy, we seek to experimentally establish values for triplet state lifetime and formation quantum yield of some popular GFPs at CTs.

Historically, the FP triplet state was believed to be microsecond-lived at ambient conditions. This assumption was based on the analogy to the typical behavior of organic dyes and on the observation of microsecond-lived reversible dark states in fluorescence correlation spectroscopy measurements.[12] The true nature of these microsecond-lived reversible dark states remains to be finally clarified; most probably, they are linked to changes in the isomerization and/or protonation state of the GFP chromophore.[13] Regardless of their chemical identity, the D-Rex concept (dark state relaxation), using microsecond-interleaved illumination schemes that allow relaxation of these dark states to the ground state, afforded a more than tenfold signal increase in stimulated emission depletion (STED)-type measurements with MHz excitation.[14]

Received: May 5, 2023
Revised: May 12, 2023
Published: May 26, 2023

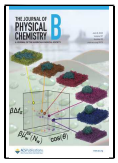

https://doi.org/10.1021/acs.jpcb.3c02971
J. Phys. Chem. B 2023, 127, 5046−5054

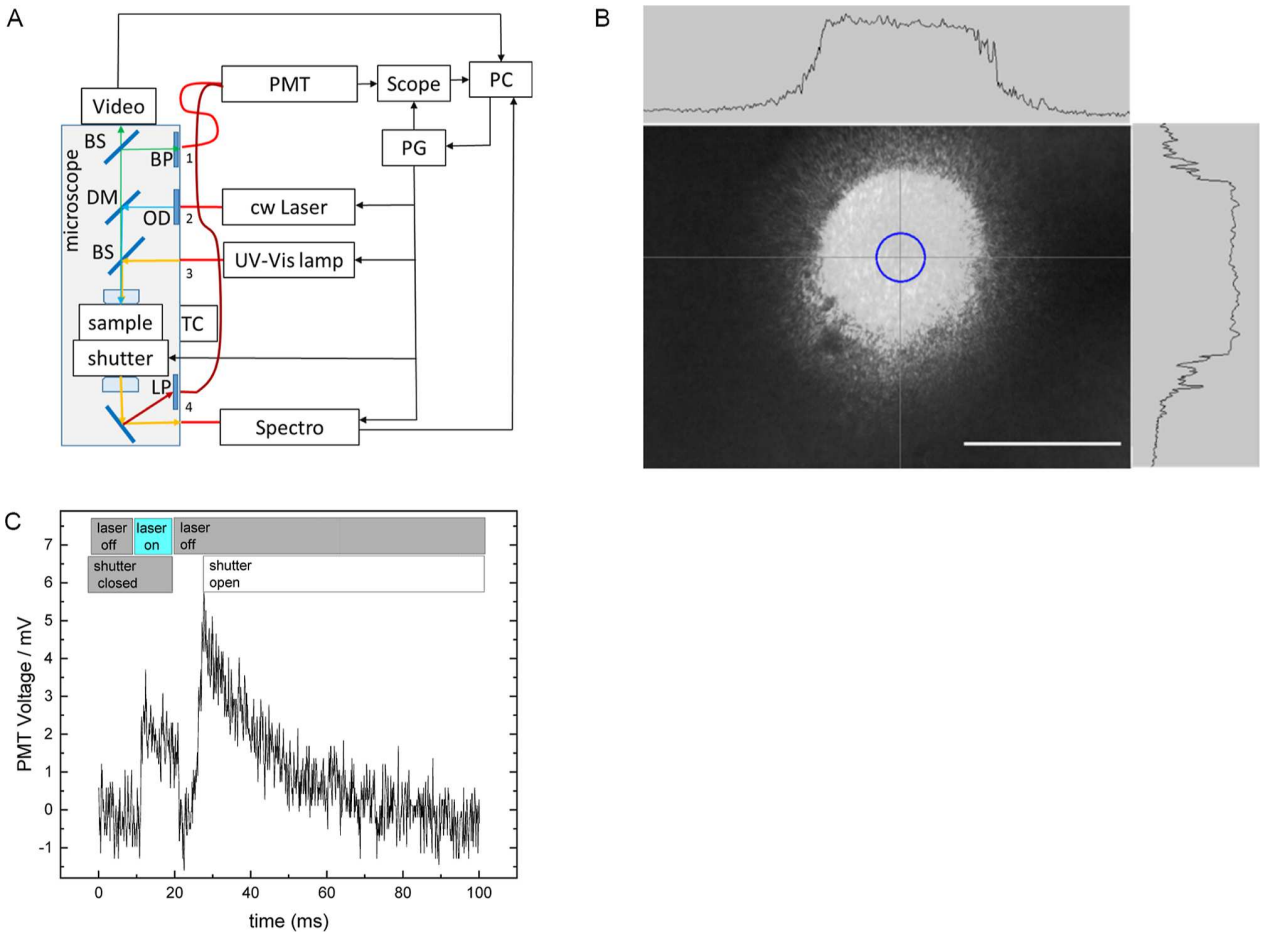

Figure 1. Opto-mechanico-electrical setup for submillisecond-resolved detection of absorption/emission of microscopic samples at CTs (CAL(AI)^{2}DOSCOPE). (A) Scheme of the setup. Black lines represent electrical connections; red lines, optical fibers; and all other colors, open air light path. BS: beam splitter, BP: bandpass filter, DM: dichroic mirror, LP: longpass filter >650 nm, OD: neutral density filter, PC: personal computer, PG: pulse generator, PMT: photomultiplier tube, and TC: temperature control. The dark red fiber is used for phosphorescence detection via channel 4 instead of fluorescence detection via channel 1. (B) Excitation beam profile. The diameter at half height is 120 μm. The blue circle in the center (30 μm diameter) is the spot illuminated for the absorption measurement (200 μm fiber diameter); the fluorescence detection spot is half that size (100 μm fiber, 15 μm spot). Scale bar: 100 μm. (C) Pulsing scheme and time trace for phosphorescence detection. The 2 mV signal from 11 to 21 ms is diffused laser light reaching the detector regardless of closed shutter and notch filter. The period from 21 to 28 ms is the time it takes the shutter to open completely. Therefore, the initial part of the phosphorescence decay is not detected.

Unequivocal identification of the enhanced GFP (EGFP) triplet state by observation of millisecond-lived phosphorescence revealed that its actual lifetime is three orders longer than previously anticipated, in hindsight not completely unexpected due to the shielded position of the GFP chromophore inside the tight protein barrel.[11] Such long-lived dark states were bound to escape confocal detection, whose accessible time window is limited by diffusion to microseconds. Wide-field detection can overcome this limitation but the observed kinetics will still result from a superposition of intrinsic chromophore photophysics and diffusional exchange at the borders of the illuminated area. This exchange could be prevented by immobilization via embedding in gels, e.g., polyvinyl alcohol or polyacrylamide, but these procedures may still perturb observations of the desired states. Luckily, at cryo-temperatures, this exchange is slowed or completely stalled, so that millisecond photophysics should become directly observable in a wide-field setting. This perspective motivated us to improve the time resolution of our cryo-microspectrophotometer (CAL(AI)^{2}DOSCOPE[15]) by introducing modalities for both faster excitation-laser switching and fluorescence detection. As a consequence, we can now reliably resolve kinetics in the low millisecond time range, also relevant for an electron multiplying charge-coupled device or a scientific complementary metal-oxide semiconductor (sCMOS) camera acquisition exposure times. In this contribution, we follow the kinetic evolution of the fluorescence intensity level of two specific GFP-type fluorescent marker proteins during the first few milliseconds: EGFP and its reversibly switchable analogue rsEGFP2. The former is the one that served to establish room-temperature triplet state characteristics;[11] the latter has recently been proposed as a suitable candidate for cryoactivation-based microscopy.[5] Both prototypical FPs serve as benchmarks for the performance characterization of a steady stream of newly developed FPs of various colors and enhanced properties.[16,17] Here, we provide insight into two processes that decisively determine the performances of EGFP and rsEGFP2: light-induced formation and decay of the first excited triplet state T_1 (forward and reverse intersystem crossing, denoted FISC and

https://doi.org/10.1021/acs.jpcb.3c02971
J. Phys. Chem. B 2023, 127, 5046−5054

RISC, respectively).[18−21] Strategies to enhance photostability by RISC enhancement have been proposed.[20] In EGFP, T_1 has been shown to live few milliseconds at room temperature (RT), and a T_1 absorption spectrum at RT has been measured,[11] but the dominant contribution of ground-state bleaching prevented the determination of the T_1 absorption coefficient at the popular excitation wavelength 488 nm.[11] Here, we make use of the cooling-induced lifetime prolongation of T_1 to measure its complete NUV−vis−NIR absorption spectrum at CT, immediately after a saturating pulse of 488 nm laser excitation. Moreover, we report the decay kinetics of the accompanying phosphorescence.

MATERIALS AND METHODS

Sample Preparation. Proteins were overexpressed and purified as previously described.[22] A tiny fraction of a 2 μL drop of a 1:1 mixture of a 2 mg/mL (ca. 0.1 mM) protein solution (50 mM HEPES, pH 7.5) with glycerol (final glycerol concentration estimated to 50%) was placed in a crystallographic loop and mounted on the magnetic sample holder of our cryo-microspectrophotometer CAL(AI)^{2}DOSCOPE.[15]

Apparatuses. Our cryogenic micro-spectrophotometer CAL(AI)^{2}DOSCOPE allows for simultaneous sample illumination/observation via a video camera (ueye, IDS Obersulm, Germany) and four separate optical channels (see Figure 1A for a schematic presentation of the setup). Here, we make use of channels 2 and 1 for laser excitation and fluorescence observation, respectively. A dichroic mirror (Di02-R488, Semrock) serves to separate the two: light from a fiber coupled (Avantes 0.6 mm Ø) Oxxius 488 nm laser (LBX-488-200) and fluorescence emission from the sample. Kinetic traces of fluorescence intensity upon laser exposure were recorded via a 512/25 bandpass filter (Semrock) and an additional notch filter (NF03-488E-25, Semrock). For this, the microscope output was fiber-coupled (Avantes 0.1 mm diameter) to a photomultiplier tube (PMT, Hamamatsu H13543-20) which in turn was coupled via a 100 kΩ load resistance to a LeCroy Wavejet 334A oscilloscope (DC—100 MHz bandpass). Laser exposition was controlled by a digital delay-pulse generator (9518, Quantum Composer) and had a rise time of 100 μs. For each condition (temperature, power density), a total of 64 illumination sequences were averaged at a frequency of 1 Hz and with durations varying from 4 to 16 ms laser exposition, followed by dark time. The initial signal amplitude did not decrease between subsequent illumination pulses of the acquisition series, indicating that photobleaching during averaging was negligible and dark recovery was completed. Sample temperature was controlled by an Oxford Cryosystems 600 gaseous nitrogen cryostat to a precision of ±0.1 K.

The remaining channels 3 and 4 serve for simultaneous white light illumination (Avantes) and absorption detection, respectively. The absorption spectrometer (Avantes) is additionally protected from laser illumination and sample fluorescence by a mechanical shutter (Thorlabs SH05R with driver SC10) that was also synchronized by the pulse generator.

To compensate for temporal drift and optical aberration at wavelengths >500 nm, these spectra were measured interleaved: alternatively, with laser on and with laser off. Three spectra of 7 ms exposure time each with laser off were followed accordingly by three spectra with laser on at 10, 17, and 24 ms after laser off-switching. From these latter three spectra, exponential extrapolation to time zero (moment of off-switching) allowed to reconstruct the T_1-S_0 difference absorption spectrum. For these experiments, we used the maximal obtainable protein stock concentration of 30 mg/mL.

For phosphorescence detection, the setup was modified as follows (Figure 1C): Instead of to channel 1, the PMT input was coupled via a 650 nm longpass filter to the output of channel 4 (dark red in Figure 1A), and the PMT output was coupled to the oscilloscope entrance set to 1 MΩ. With this setup, opening the shutter immediately after a saturating 10 ms laser pulse, allowed for the direct registration of the time course of phosphorescence decay. 256 single traces were averaged. The signal vanished when the longpass filter was replaced by the 512/25 nm bandpass filter thus excluding the possibility of delayed fluorescence.

Data Treatment. For the determination of excitation rates, excitation power for an illuminated sample spot of 120 μm diameter (Figure 1B) was measured at the sample position using a PM100D power meter with an S120C measuring head (Thorlabs). The excitation rate kX is the product of excitation photon flux density p_{488} and chromophore absorption cross section σ_S. For the proteins used here, the extinction coefficient at 488 nm is temperature dependent because upon cooling both absorption and fluorescence spectra are narrowed and blue-shifted (see Figure 2). Consequently, we used for epsilon 80% of the peak value reported for RT, i.e., 41.9 and 48.8 mM^{-1} cm^{-1} for EGFP and rsEGFP2, respectively.

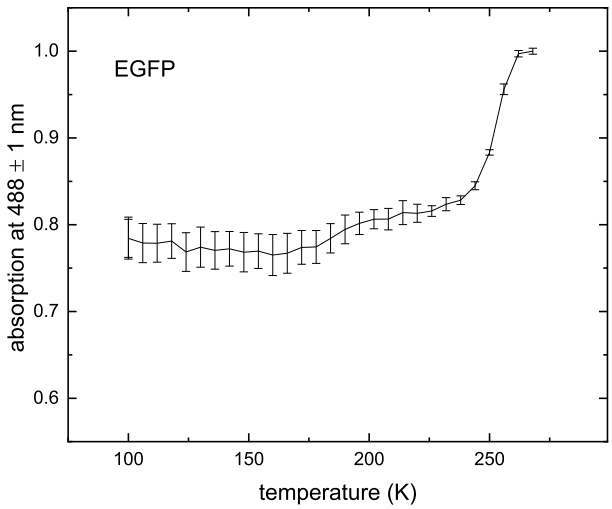

Figure 2. Absorption shift of EGFP upon cooling to 100 K. Error bars are s.d. from averaging over 487 to 489 nm. They are smaller above 240 K (peak) than below (flank).

For amplitude normalization, all experimental fluorescence decay curves at a given temperature were first fitted with an (exponential rise + exponential decay + offset)-model where all parameters are free except the time constant of the rise term that was shared among all curves. Subsequently, curves were normalized to the sum of decay phase amplitude and offset, thus assuring unity amplitude for full fluorescence onset and correcting for slight amplitude loss due to shutter opening kinetics (100 μs).

The thus-normalized curve families were fitted using a model consisting of a rise term with fixed amplitude (−1) and lifetime (100 μs) and a model of eq 4 in the Results section.

https://doi.org/10.1021/acs.jpcb.3c02971
J. Phys. Chem. B 2023, 127, 5046−5054

RESULTS

We first determined the absorption spectrum of the reversibly populated triplet state. For this, we illuminated a protein sample at 100 K until saturation (20 ms), then stopped the laser and opened the shutter. At this moment, the sample contains a mixture of S_0 and T_1 state molecules.

Figure 3 shows the raw absorption spectra without any 488 nm laser illumination and immediately after its stopping, together with their difference (Figure 3B).

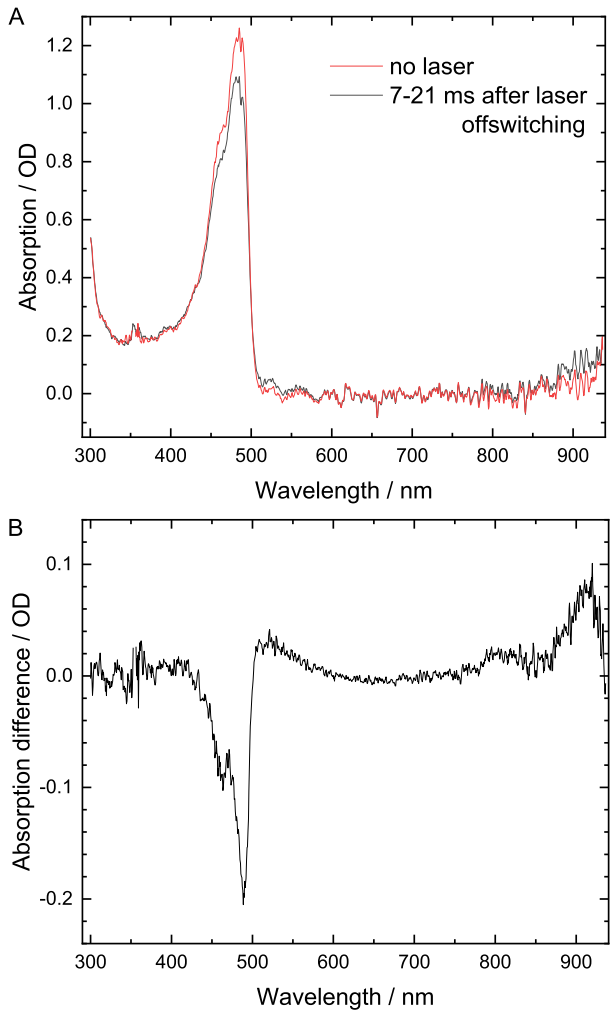

Figure 3. Absorption spectrum of EGFP at 100 K. Spectra were acquired alternatively with laser off (A, red) and laser on, rapidly after laser off-switching (A, black). The difference spectrum (B) is obtained by subtraction of the spectrum without illumination (A, red) from the first dark spectrum after laser off-switching (A, black). It contains ground-state bleaching (negative feature around 490 nm) and excited-state absorption (positive features to the left and right immediately around the ground-state bleach and in the near infrared above 700 nm).

Subtraction of an appropriate fraction (i.e., eliminating the 488 nm centered dip and reconstituting a positive Gaussian shape to the resulting band) of the ground-state absorption (Figure 3A, red) from the difference spectrum (Figure 3B) yielded the pure triplet state absorption spectrum (Figure 4A) that could be satisfactorily fitted by a sum of five Gaussians with peaks at 390, 490, 720, 800, and 905 nm. Fitting parameters are listed in Table 1.

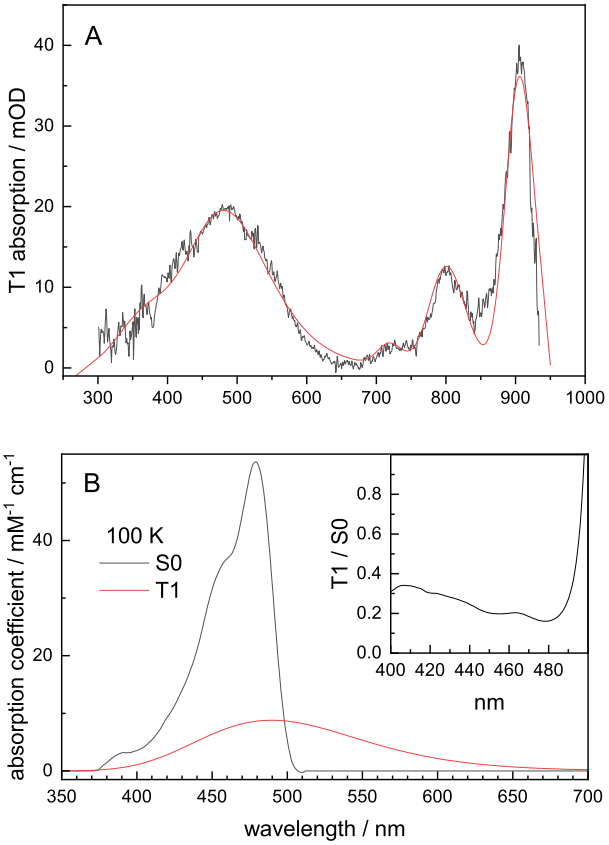

Figure 4. Absorption spectra of rsEGFP2 at 100 K. (A) Light minus dark difference spectrum at 20 ms after 488 nm illumination, corrected for the weighted contribution of ground-state (S_0) bleaching (black); fit with 5 Gaussians (red, see also Table 1); (B) S_0 spectrum and the 490 nm centered band of the T_1 spectrum scaled to an epsilon scale using normalization at 278 nm. (inset) Ratio of the values in the main panel.

Table 1. Parameters of Fitting Five Symmetric (on an Energy Scale) Gaussians to the T_1 Absorption Spectrum in Figure 4A

peak position in nm	peak position in cm^{-1}	peak fwhm in cm^{-1}
390	25,621.65238	9337.55145
490	20,423.13753	5270.20272
720	13,895.34884	824.18702
800	12,486.32011	941.92802
905	11,036.25171	588.70501

Figure 4A shows the T_1 absorption spectrum of rsEGFP2 at 100 K. The spectrum of EGFP is indistinguishable from that of rsEGFP2 within our signal-to-noise ratio.

The T_1 absorption spectrum shows a hitherto not resolved vibronic progression in the near infrared, with an inter-sideband spacing of 1440 cm^{-1}, in good agreement with the 1340 cm^{-1} previously reported for the singlet chromophore absorption at 77 K.[23] In the visible, the spectrum is dominated by a large band, peaking at 490 nm and stretching from 400 to 600 nm, thus covering the whole of the S_0 absorption band as well. This overlap previously prevented the unequivocal

https://doi.org/10.1021/acs.jpcb.3c02971
J. Phys. Chem. B 2023, 127, 5046−5054

determination of the shape and amplitude of the T_1 visible absorption band but has also an important consequence: light of any wavelength that is used to excite green fluorescence does not only pump a fraction of the singlet population into T_1 (FISC) but, at the same time, also pumps backward from there into the singlet manifold (RISC). The backward/forward RISC/FISC efficiency ratio is given by the ratio of the absorption coefficients of T_1 and S_0 at the excitation wavelength (Figure 4B, with the ratio as shown in the inset) and the FISC and RISC quantum yields φ_F and φ_R. Moreover, under a continuous incident photon flux with density p_{488}, the amount of T_1 population that is formed depends on the intrinsic triplet state lifetime τ_T. In the following, we describe an approach to extract simultaneously φ_F, φ_R, and τ_T, based on the measurement of millisecond fluorescence kinetics. We make use of our microspectrophotometer CAL-(AI)^{2}DOSCOPE[15] together with protein immobilization by low-temperature vitrification and a continuous 488 nm laser that can be switched at kHz frequency with a rise time of 100 μs, i.e., sufficiently fast to be separated from the ISC processes we strive to observe (see Materials and Methods section for details).

Scheme 1 shows the relevant photophysical processes for a FP under monochromatic illumination. Under conditions of fast equilibrium between S_0 and S_1, we need to consider only their (normalized) sum S. Fluorescence is a measure of the temporal evolution of this singlet-state population and is given by eq 1 (scheme 1A).

$$S(t) = 1 - A(1 - \exp(-kt)) \quad (1)$$

Scheme 1. Photophysics of GFP-type Proteins. (A) Simplified Two State Model; (B) Photophysical Parameters Affecting the Rate Constants for the Three Processes Constituting $k1$ (FISC) and $k2$ (RISC and DARK). Under Continuous Illumination, at Steady State, the T_1 State has Population and Absorption Comparable to Those of S_0. However, in View of Its Much Longer Lifetime and Higher Reactivity, it is the Most Probable Gateway to All Kinds of Photochemistry Including Slow Blinking, Switching, Bleaching Phenomena. Therefore, in Addition to the Two Arrows Leading Back to S_0, an Additional (mostly) Irreversible Decay Pathway k_{PC} is Shown. The Arrow is Dotted Because the Total Photochemistry Yield is Small in Comparison with the Former Two Channels

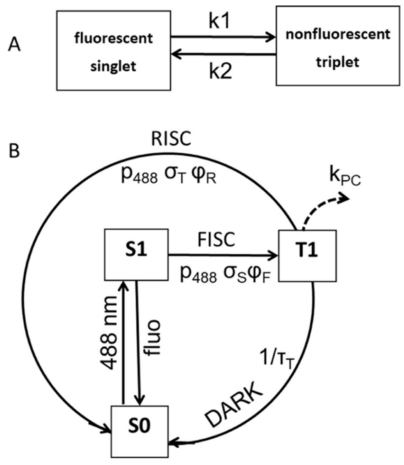

with (see scheme 1B)

$$[S](t = 0) = 1,\ k = (k1 + k2),\ A = k1/(k1 + k2) \quad (2)$$

At steady state (i.e., after having reached the kinetic plateau), we have $S = k2/(k1 + k2)$. Here, σ_S and σ_T are the absorption cross sections (in cm^2) of the singlet and triplet states, respectively, and relate to ε_S and ε_T (in M^{-1} cm^{-1}) by $\sigma_S = 1000 \ln 10\ \varepsilon_S/N_A$ and $\sigma_T = 1000 \ln 10\ \varepsilon_T/N_A$, where N_A is the Avogadro number.

Substituting

$$k1 = p_{488}\sigma_S\varphi_F,\ k2 = k_{RISC} + k_{DARK} = p_{488}\sigma_T\varphi_R + 1/\tau_T \quad (3)$$

into eq 2 and then eq 2 into eq 1, we obtain eq 4 that describes the fluorescence decay as a function of the rates of the FISC, RISC, and DARK processes (scheme 1B).

The resulting final fitting function has the form

$$S = 1 - \exp(-t/0.1) - 1/(1 + phiR \times \mathrm{eps} + 1/(kX \times tauT \times phiF/100))$$
$$x(1 - \exp(-(kX \times phiF/100 \times (1 + phiR \times \mathrm{eps} + 1/(tauT \times phiF/100 \times kX)) \times t))) \quad (4)$$

where $\mathrm{eps} = \sigma_S/\sigma_T$ is the ratio of the absorption cross sections of S_0 and T_1 at 488 nm, $kX = p_{488}$, σ_S is the excitation rate in kHz of the singlet ground state S_0, and the factor 100 converts the forward and reverse ISC quantum yields *phiF* and *phiR* to percent units.

Equation 4 thus provides an expression for fitting simultaneously φ_F, φ_R, and τ_T, knowing p_{488} from independent power measurements and both σ_S and σ_T values from Figure 4B. We then perform global fitting over data collected at various temperatures and excitation power densities. Preliminary "free" fits (no parameter sharing among datasets) indicated that upon temperature variation, *phiF* and *phiR* tended to be constant, whereas *tauT* varied systematically. Therefore, in the following, simultaneous fits at various temperatures were performed, where of the three free parameters *tauT*, *phiF*, and *phiR*, *phiF* and *phiR* were shared across temperatures and energies, whereas *tauT* was allowed to vary as a function of temperature (but not power density), yielding robust results.

Figures 5 and 6 show such fits for rsEGFP2 (Figure 5) and EGFP (Figure 6). The fitted parameters for both proteins are very similar and are given in Table 2, together with the EGFP literature values at RT for comparison.

Figure 7 shows the temperature dependence for τ_T for both proteins (solid symbols). The approach to assign the temperature dependence to the dark lifetime rather than to the forward and reverse quantum yield is justified, and the found values confirmed by comparison to the fitted lifetimes of phosphorescence decay kinetics for rsEGFP2 (open symbols in Figure 7) that do not depend on any assumptions.

DISCUSSION

We observed a rapidly reversible dark state and measured its lifetime and absorption spectrum. The identical decay times observed directly via phosphorescence and indirectly via fluorescence quenching kinetics indicate that in both cases the observed dark state is T_1 and that the spectra in Figure 4 and parameters in Tables 1 and 2 apply indeed to the first

https://doi.org/10.1021/acs.jpcb.3c02971
J. Phys. Chem. B 2023, 127, 5046−5054

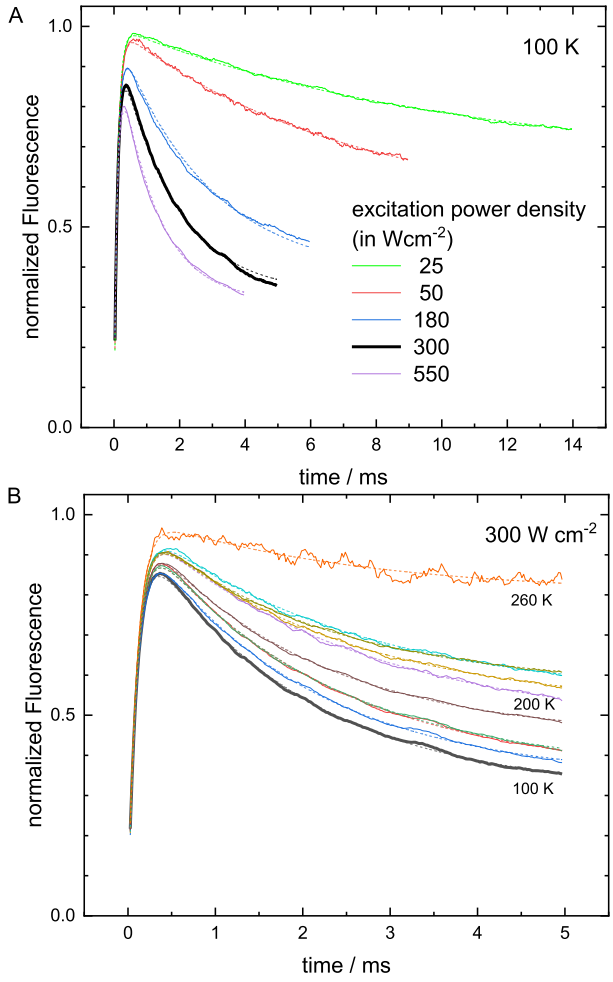

Figure 5. Time traces of the first milliseconds of fluorescence of dark-adapted rsEGFP2. (A) Various 488 nm excitation power densities at 100 K. (B) Various temperatures (increasing in 20 K steps) at 300 W cm^{-2} excitation power density. The thick black curves in panels A and B are the same. Dashed lines are fits using eq 4 and parameters as indicated in Table 1, last line.

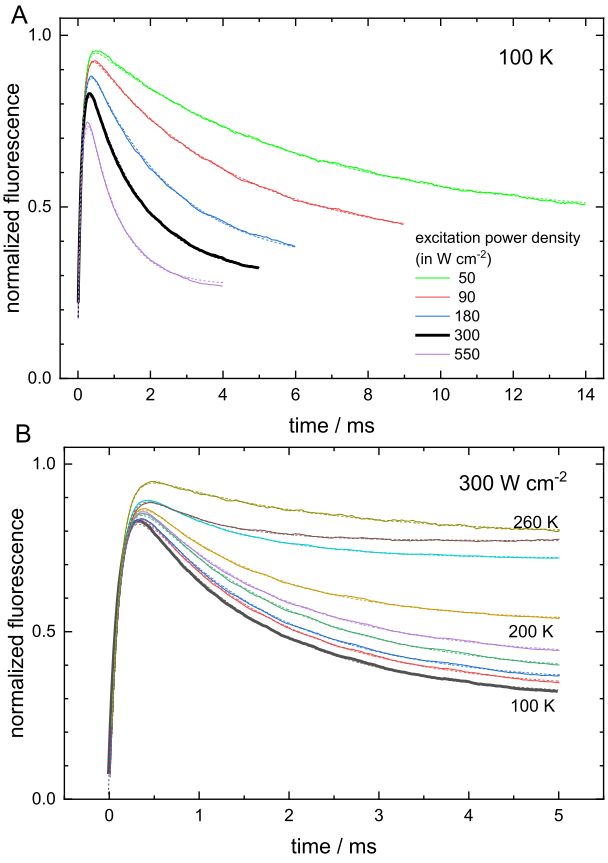

Figure 6. Time traces of the first milliseconds of EGFP fluorescence of a dark-adapted sample. (A) Various excitation power densities at 100 K. (B) Various temperatures (increasing in 20 K steps) at 300 W cm^{-2} excitation power density. The thick black curves in panels A and B are the same. Dashed lines are fits using eq 4 and parameters as indicated in Table 1, line 2.

excited triplet state. Although rsEGFP2 is known to cis/trans isomerize at RT, we argue that in the states we observe in this work the chromophore is always in its anionic cis conformation. T_1 is formed from its precursor S_1 that in turn is formed from S_0. The only form of the chromophore that contributes to fluorescence is the anionic cis conformation. Full recovery during the 1 s dark period testifies against accumulation of slowly switched species in appreciable amount. If any, these cannot correspond to isomerized or protonated states but would be radical states building up from intramolecular electron transfer as described in detail by Mantovanelli et al. (no diffusion, pH dependence, or structural changes observable at CT).[5]

It appears that the intrinsic triplet lifetimes of EGFP and rsEGFP2 are only slightly temperature-dependent between 100 and 180 K, i.e., up to the glass transition temperature (T_g) of our 50% glycerol/water mixture.[24] Above 180 K, the lifetimes decrease rapidly by a factor of about 3 down to the RT values (see Figure 7B for an Arrhenius presentation of the data in Figure 7A). The absence of a clear Arrhenius-type behavior over the whole temperature range suggests that below T_g, a deactivation channel present above T_g is shut off. The remaining channel is most likely intramolecular as it should not be diffusion dependent. This channel remains probably available above T_g, but its lifetime is too long to outcompete the diffusion-limited oxygen-related intermolecular pathway that likely dominates at high temperatures. Importantly, the 20 ms-pathway prevailing below T_g limits triplet-state saturation and the accumulation of long-lived dark states, which would otherwise offset the observed increased photostability at CTs.[1,2] This temperature- and power-dependent change in triplet quenching pathways is reminiscent of the earlier described power-dependent change between dominant bleaching mechanisms at RT in the EosFP-derivated marker IrisFP.[25] Interestingly, a comparable dark state with a formation yield of 0.3% and a lifetime of 25 ms has been recently reported by Peng et al. for a YFP mutant at RT.[26] They ascribed their observation to a further downstream, possibly radical, state but the similar parameters suggest that it might have T_1 character as well.

We have found that in both non-switchable and reversibly switchable GFPs at CTs upon continuous laser illumination, a significant fraction of the potentially fluorescing chromophores rapidly enters the dark T_1 state with a lifetime that is comparable to typical exposure times of CCD or sCMOS cameras used in fluorescence microscopy of biological samples. Both amount and formation rate of this fraction increase with excitation power density and, for 488 nm excitation, become

https://doi.org/10.1021/acs.jpcb.3c02971
J. Phys. Chem. B 2023, 127, 5046−5054

Table 2. Photophysical Parameters for RT (Literature) and CT (Our Fits) of Forward and Reverse ISC

protein and condition	singlet ground state S_0		first excited triplet state T_1		
	absorption coefficient at 488 nm ε_S in mM^{-1} cm^{-1}	forward ISC quantum yield φ_F in %	absorption coefficient at 488 nm ε_T in $mM^{-1}cm^{-1}$	reverse ISC quantum yield φ_R in %	dark lifetime τ_T in ms
EGFP RT	53[b]	1.0 ± 0.5[c]	10 ± 5[c]	n.d.[a]	5.6[c,g]
EGFP 100 K	41.9[d]	0.32 ± 0.04[d,e]	10 ± 2[d,f]	0.12 ± 0.02[d,e]	21 ± 2[d]
rsEGFP2 100 K	48.8[d]	0.27 ± 0.04[d,e]	10 ± 2[d,f]	0.12 ± 0.02[d,e]	24 ± 6[d]

[a]n.d. Not determined. [b]From ref 16 [c]From ref 11 [d]This work. [e]Mean ± S.D. from $n \geq 6$ datasets. [f]Range estimated from uncertainty in ε_S contribution. [g]Value in the absence of oxygen.

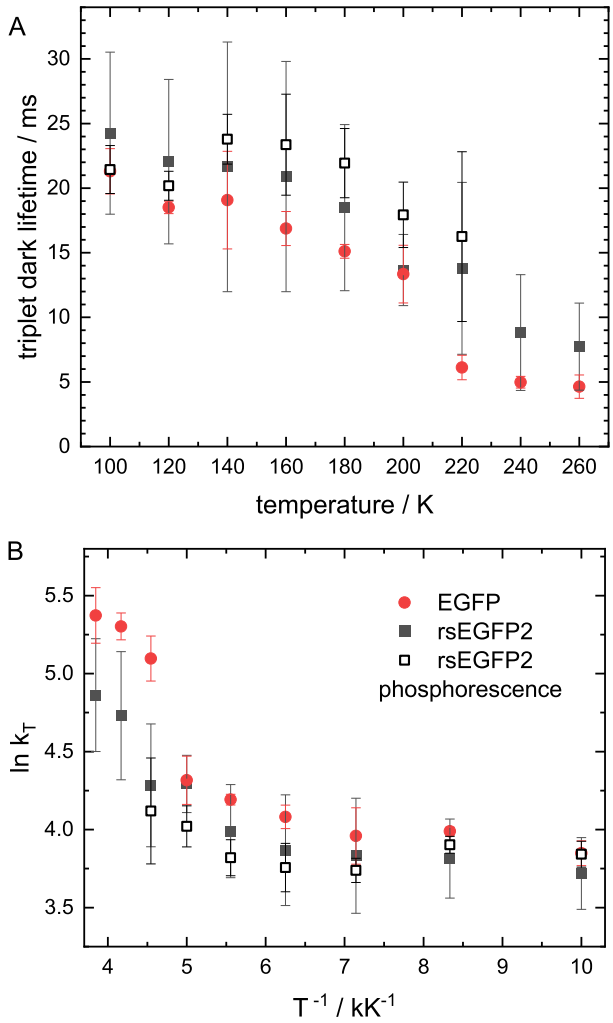

Figure 7. Temperature dependence of intrinsic triplet state lifetime for EGFP and rsEGFP2. Solid symbol data are mean ± SD from $n = 2$ datasets from fits to curves as in Figures 5 and 6; empty symbols are fits to phosphorescence decays as in Figure 1C. For $T > 220$ K, these curves are too noisy to extract meaningful lifetimes. (A) Linear presentation lifetime vs temperature. (B) Arrhenius presentation ln(1/lifetime) vs 1000/temperature of the same data (note that temperature increases from right to left in this presentation). The slope on the steep left half is four times smaller than at RT, on the flat right half 120 times, formally corresponding to activation barriers of 65 and 2.2 meV.

>50% and faster than 0.2 ms^{-1} at power densities as moderate as 100 W cm^{-2}. Triplet state saturation thus leads to a considerable loss of detectable fluorescence intensity already at very moderate illumination levels. This loss, however, can be recovered within relatively short dark periods as also routinely applied in microscopy, e.g., for camera readout. The fact that both dark state formation and recovery happen on the same time scale as image acquisition by the camera provides an extraordinary sensitivity of observable photon count rates on camera and laser parameters as a consequence. Thus, in addition to standardized sample preparation and illumination schemes, a "standardized" acquisition timing is also important.

CONCLUSIONS

Combining fluorescence and phosphorescence kinetics, we have determined the spectrum and yields for light-induced formation and decay of the first excited triplet state of two GFPs upon continuous 488 nm laser excitation at CTs. Knowing these parameters, we can conclude on the importance of FISC and RISC between the singlet and triplet manifolds S ↔ T in photoswitchable (rsEGFP2) and non-photoswitchable (EGFP) GFPs for their population dependence on excitation energy flux, also at RT.

The concept of pulsed illumination to allow for T_1 relaxation (T-Rex), as proposed earlier for MHz excitation,[14] should be applicable in the millisecond illumination regime such as used in PALM-type super-resolution imaging as well.[27] By allowing for complete triplet state relaxation between subsequent excitation pulses (i.e., few ms at RT and few tens of ms at CT), the singlet-state population may be more than doubled, and this could provide hope for corresponding signal enhancement. This possibility is supported by the published reports of reduced bleaching at RT using pulsed illumination.[28] In the picture drawn here at CT, the triplet state T_1 acts, by analogy to what has been found at RT,[11] as the entrance gateway to further absorption and photochemistry. Then, the similarity of the parameters obtained for EGFP and rsEGFP2 suggests that a certain cryo switchability could also be expected for EGFP.[3,5,29] The similarity of the T_1 absorption spectrum at CT found here to that at RT introduced earlier[11] makes it a useful tool for performance optimization attempts such as tuning the excitation wavelength to maximize back-pumping from T_1 or additionally using specific infrared wavelengths. For GFP-type proteins at RT, the T_1 dark lifetime is shorter, but this is partly compensated for by the shift of the absorbance peak closer to the pump laser wavelength (488 nm), making light pumping non-negligible for even lower energy densities.

As the technique could also be applied to other FPs, knowledge of their T_1 spectrum would be very useful, e.g., primed photoconversion, RISC optimization, or the like.

https://doi.org/10.1021/acs.jpcb.3c02971
J. Phys. Chem. B 2023, 127, 5046−5054

AUTHOR INFORMATION

Corresponding Author

Martin Byrdin − *Institut de Biologie Structurale, CNRS, Université Grenoble Alpes, CEA, IBS, 38044 Grenoble, France;* orcid.org/0000-0002-6389-8714; Email: martin.byrdin@ibs.fr

Authors

Lukas Rane − *Institut de Biologie Structurale, CNRS, Université Grenoble Alpes, CEA, IBS, 38044 Grenoble, France;* orcid.org/0000-0003-4609-2265

Jip Wulffele − *Institut de Biologie Structurale, CNRS, Université Grenoble Alpes, CEA, IBS, 38044 Grenoble, France*

Dominique Bourgeois − *Institut de Biologie Structurale, CNRS, Université Grenoble Alpes, CEA, IBS, 38044 Grenoble, France;* orcid.org/0000-0002-1862-7712

Oleksandr Glushonkov − *Institut de Biologie Structurale, CNRS, Université Grenoble Alpes, CEA, IBS, 38044 Grenoble, France*

Angela M. R. Mantovanelli − *Institut de Biologie Structurale, CNRS, Université Grenoble Alpes, CEA, IBS, 38044 Grenoble, France*

Ninon Zala − *Institut de Biologie Structurale, CNRS, Université Grenoble Alpes, CEA, IBS, 38044 Grenoble, France*

Complete contact information is available at: https://pubs.acs.org/10.1021/acs.jpcb.3c02971

Notes

The authors declare no competing financial interest.

ACKNOWLEDGMENTS

M.B. thanks Klaus Brettel, Saclay, for fruitful discussions. Virgile Adam and Arijit Maity (both Grenoble) are acknowledged for critical comments. This work was supported by ANR-17-CE11-0047-01 and an Impulsion grant by the French Commissariat for atomic and renewable energies. The IBS acknowledges integration into the Interdisciplinary Research Institute of Grenoble (IRIG, CEA).

REFERENCES

(1) Schwartz, C. L.; Sarbash, V. I.; Ataullakhanov, F. I.; McIntosh, J. R.; Nicastro, D. Cryo-Fluorescence Microscopy Facilitates Correlations between Light and Cryo-Electron Microscopy and Reduces the Rate of Photobleaching. *J. Microsc.* **2007**, *227*, 98−109.

(2) Hulleman, C. N.; Li, W.; Gregor, I.; Rieger, B.; Enderlein, J. Photon Yield Enhancement of Red Fluorophores at Cryogenic Temperatures. *ChemPhysChem* **2018**, *19*, 1774−1780.

(3) Tuijtel, M. W.; Koster, A. J.; Jakobs, S.; Faas, F. G. A.; Sharp, T. H. Correlative Cryo Super-Resolution Light and Electron Microscopy on Mammalian Cells Using Fluorescent Proteins. *Sci. Rep.* **2019**, *9*, 1369.

(4) Hoffman, D. P.; Shtengel, G.; Xu, C. S.; Campbell, K. R.; Freeman, M.; Wang, L.; Milkie, D. E.; Pasolli, H. A.; Iyer, N.; Bogovic, J. A.; Stabley, D. R.; Shirinifard, A.; Pang, S.; Peale, D.; Schaefer, K.; Pomp, W.; Chang, C.-L.; Lippincott-Schwartz, J.; Kirchhausen, T.; Solecki, D. J.; Betzig, E.; Hess, H. F. Correlative Three-Dimensional Super-Resolution and Block-Face Electron Microscopy of Whole Vitreously Frozen Cells. *Science* **2020**, *367*, No. eaaz5357.

(5) Mantovanelli, A. M. R.; Glushonkov, O.; Adam, V.; Wulffele, J.; Thédié, D.; Byrdin, M.; Gregor, I.; Nevskyi, O.; Enderlein, J.; Bourgeois, D. Photophysical Studies at Cryogenic Temperature Reveal a Novel Photoswitching Mechanism of RsEGFP2. *bioRxiv* **2022**, 504779 Posted August 22, 2022.

(6) Dahlberg, P. D.; Sartor, A. M.; Wang, J.; Saurabh, S.; Shapiro, L.; Moerner, W. E. Identification of PAmKate as a Red Photoactivatable Fluorescent Protein for Cryogenic Super-Resolution Imaging. *J. Am. Chem. Soc.* **2018**, *140*, 12310−12313.

(7) Regis Faro, A.; Carpentier, P.; Jonasson, G.; Pompidor, G.; Arcizet, D.; Demachy, I.; Bourgeois, D. Low-Temperature Chromophore Isomerization Reveals the Photoswitching Mechanism of the Fluorescent Protein Padron. *J. Am. Chem. Soc.* **2011**, *133*, 16362−16365.

(8) Dahlberg, P. D.; Moerner, W. E. Cryogenic Super-Resolution Fluorescence and Electron Microscopy Correlated at the Nanoscale. *Annu. Rev. Phys. Chem.* **2021**, *72*, 253−278.

(9) DeRosier, D. J. Where in the Cell Is My Protein? *Q. Rev. Biophys.* **2021**, *54*, No. e9.

(10) Orrit, M.; Bernard, J. Single Pentacene Molecules Detected by Fluorescence Excitation in a *p* -Terphenyl Crystal. *Phys. Rev. Lett.* **1990**, *65*, 2716−2719.

(11) Byrdin, M.; Duan, C.; Bourgeois, D.; Brettel, K. A Long-Lived Triplet State Is the Entrance Gateway to Oxidative Photochemistry in Green Fluorescent Proteins. *J. Am. Chem. Soc.* **2018**, *140*, 2897−2905.

(12) Widengren, J.; Mets, Ü.; Rigler, R. Photodynamic Properties of Green Fluorescent Proteins Investigated by Fluorescence Correlation Spectroscopy. *Chem. Phys.* **1999**, *250*, 171−186.

(13) Coquelle, N.; Sliwa, M.; Woodhouse, J.; Schirò, G.; Adam, V.; Aquila, A.; Barends, T. R. M.; Boutet, S.; Byrdin, M.; Carbajo, S.; et al. Chromophore Twisting in the Excited State of a Photoswitchable Fluorescent Protein Captured by Time-Resolved Serial Femtosecond Crystallography. *Nat. Chem.* **2018**, *10*, 31−37.

(14) Donnert, G.; Eggeling, C.; Hell, S. W. Major Signal Increase in Fluorescence Microscopy through Dark-State Relaxation. *Nat. Methods* **2007**, *4*, 81−86.

(15) Byrdin, M.; Bourgeois, D. The CAL(AI)2DOSCOPE: A Microspectrophotometer for Accurate Recording of Correlated Absorbance and Fluorescence Emission Spectra. *Spectrosc. Eur.* **2016**, *28*, 14−17.

(16) Patterson, G. H.; Knobel, S. M.; Sharif, W. D.; Kain, S. R.; Piston, D. W. Use of the Green Fluorescent Protein and Its Mutants in Quantitative Fluorescence Microscopy. *Biophys. J.* **1997**, *73*, 2782−2790.

(17) Grotjohann, T.; Testa, I.; Reuss, M.; Brakemann, T.; Eggeling, C.; Hell, S. W.; Jakobs, S. RsEGFP2 Enables Fast RESOLFT Nanoscopy of Living Cells. *eLife* **2012**, *1*, No. e00248.

(18) Keller, R. A. Excited Triplet — Singlet Intersystem Crossing. *Chem. Phys. Lett.* **1969**, *3*, 27−29.

(19) Ringemann, C.; Schonle, A.; Giske, A.; von Middendorff, C.; Hell, S. W.; Eggeling, C. Enhancing Fluorescence Brightness: Effect of Reverse Intersystem Crossing Studied by Fluorescence Fluctuation Spectroscopy. *Chemphyschem* **2008**, *9*, 612−624.

(20) Smit, R.; Ristanović, Z.; Kozankiewicz, B.; Orrit, M. Reverse Intersystem Crossing of Single Deuterated Perylene Molecules in a Dibenzothiophene Matrix. *ChemPhysChem* **2021**, *23*, No. e202100679.

(21) Mukherjee, S.; Jimenez, R. Photophysical Engineering of Fluorescent Proteins: Accomplishments and Challenges of Physical Chemistry Strategies. *J. Phys. Chem. B* **2022**, *126*, 735−750.

(22) Adam, V.; Hadjidemetriou, K.; Jensen, N.; Shoeman, R. L.; Woodhouse, J.; Aquila, A.; Banneville, A.; Barends, T. R. M.; Bezchastnov, V.; Boutet, S.; et al. Rational Control of Off-State Heterogeneity in a Photoswitchable Fluorescent Protein Provides Switching Contrast Enhancement. *ChemPhysChem* **2022**, *23*, No. e202200192.

(23) Lin, C.-Y.; Romei, M. G.; Oltrogge, L. M.; Mathews, I. I.; Boxer, S. G. Unified Model for Photophysical and Electro-Optical Properties of Green Fluorescent Proteins. *J. Am. Chem. Soc.* **2019**, *141*, 15250−15265.

(24) Weik, M.; Vernede, X.; Royant, A.; Bourgeois, D. Temperature Derivative Fluorescence Spectroscopy as a Tool to Study Dynamical Changes in Protein Crystals. *Biophys. J.* **2004**, *86*, 3176−3185.
(25) Duan, C.; Adam, V.; Byrdin, M.; Ridard, J.; Kieffer-Jaquinod, S.; Morlot, C.; Arcizet, D.; Demachy, I.; Bourgeois, D. Structural Evidence for a Two-Regime Photobleaching Mechanism in a Reversibly Switchable Fluorescent Protein. *J. Am. Chem. Soc.* **2013**, *135*, 15841−15850.
(26) Peng, B.; Dikdan, R.; Hill, S. E.; Patterson-Orazem, A. C.; Lieberman, R. L.; Fahrni, C. J.; Dickson, R. M. Optically Modulated and Optically Activated Delayed Fluorescent Proteins through Dark State Engineering. *J. Phys. Chem. B* **2021**, *125*, 5200−5209.
(27) Hess, S. T.; Girirajan, T. P. K.; Mason, M. D. Ultra-High Resolution Imaging by Fluorescence Photoactivation Localization Microscopy. *Biophys. J.* **2006**, *91*, 4258−4272.
(28) Shaner, N. C.; Lin, M. Z.; McKeown, M. R.; Steinbach, P. A.; Hazelwood, K. L.; Davidson, M. W.; Tsien, R. Y. Improving the Photostability of Bright Monomeric Orange and Red Fluorescent Proteins. *Nat. Methods* **2008**, *5*, 545−551.
(29) Kaufmann, R.; Schellenberger, P.; Seiradake, E.; Dobbie, I. M.; Jones, E. Y.; Davis, I.; Hagen, C.; Grünewald, K. Super-Resolution Microscopy Using Standard Fluorescent Proteins in Intact Cells under Cryo-Conditions. *Nano Lett.* **2014**, *14*, 4171−4175.

https://doi.org/10.1021/acs.jpcb.3c02971
J. Phys. Chem. B 2023, 127, 5046−5054

JACS
JOURNAL OF THE AMERICAN CHEMICAL SOCIETY

pubs.acs.org/JACS

Article

Photophysical Studies at Cryogenic Temperature Reveal a Novel Photoswitching Mechanism of rsEGFP2

Angela M. R. Mantovanelli,[§] Oleksandr Glushonkov,[§] Virgile Adam,[§] Jip Wulffelé, Daniel Thédié, Martin Byrdin, Ingo Gregor, Oleksii Nevskyi, Jörg Enderlein, and Dominique Bourgeois*

Cite This: *J. Am. Chem. Soc.* 2023, 145, 14636−14646

Read Online

ACCESS | Metrics & More | Article Recommendations | Supporting Information

ABSTRACT: Single-molecule localization microscopy (SMLM) at cryogenic temperature opens new avenues to investigate intact biological samples at the nanoscale and perform cryo-correlative studies. Genetically encoded fluorescent proteins (FPs) are markers of choice for cryo-SMLM, but their reduced conformational flexibility below the glass-transition temperature hampers efficient cryo-photoswitching. We investigated cryo-switching of rsEGFP2, one of the most efficient reversibly switchable fluorescent proteins at ambient temperature due to facile *cis*−*trans* isomerization of the chromophore. UV−visible microspectrophotometry and X-ray crystallography revealed a completely different switching mechanism at ∼110 K. At this cryogenic temperature, on−off photoswitching involves the formation of two off-states in *cis* conformation with blue-shifted absorption relative to that of the *trans* protonated chromophore populated at ambient temperature. Only one of these off-states can be switched back to the fluorescent on-state by 405 nm light, while both of them are sensitive to UV light at 355 nm. Superior recovery to the fluorescent on-state by 355 nm light was confirmed at the single-molecule level. This suggests, as also shown by simulations, that employing 355 nm light in cryo-SMLM experiments using rsEGFP2 and possibly other FPs could improve the effective labeling efficiency achievable with this technique. The rsEGFP2 photoswitching mechanism discovered in this work adds to the panoply of known switching mechanisms in fluorescent proteins.

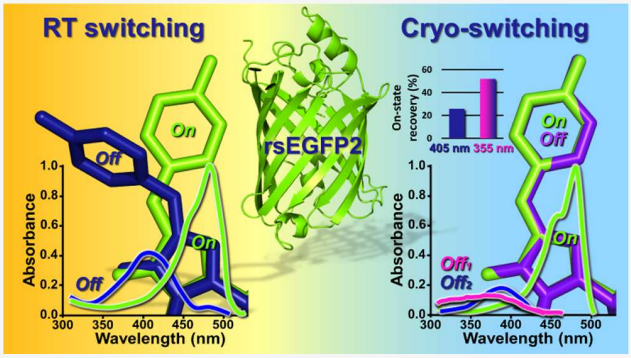

INTRODUCTION

Super-resolution fluorescence microscopy has revolutionized our ability to investigate life at the nanoscale.[1] Yet, to prevent motion artifacts and facilitate labeling, many nanoscopy studies are still based on chemically fixed cells. Chemical fixation of membrane proteins remains challenging, and a number of artifacts may result from fixation that become even more detrimental as the quest for high-resolution increases.[2−4] One strategy to better preserve the fine morphological details of biological samples is to image flash-frozen cells at cryogenic temperature (CT).[5−14] Furthermore, performing super-resolution microscopy at CT opens the door to cryo-correlative (CLEM) studies with cryo-electron microscopy.[6,10,15] In addition, CT fluorescence imaging offers other benefits such as improved fluorescence quantum yield and reduced photobleaching of the fluorescent markers, as well as narrowing of fluorescence emission bands, potentially facilitating multicolor data acquisition schemes.[6,11,16−18] Yet, although impressive progress has been achieved recently,[14,19,20] cryo-nanoscopy faces significant challenges. One of those concerns the development of user-friendly instrumentation compatible with high numerical aperture objectives and long data acquisition time with low sample drift.[11,21−24] A more fundamental issue concerns the development of fluorescent markers with favorable photoswitching properties at CT.[7,13,17,25−27]

Fluorescent proteins (FPs) are arguably the most appropriate markers for super-resolution microscopy at CT, as they are genetically encoded and thus do not require fixation and permeabilization for labeling. In contrast, many organic dyes do not cross membranes naturally. Furthermore, organic dyes typically used in single-molecule localization techniques such as stochastic optical reconstruction microscopy ((d)STORM) or point accumulation in nanoscale topography (PAINT) cannot be used at CT because their efficient blinking relies on the diffusion of buffer molecules or of the fluorophores themselves, which is arrested in a frozen solvent. A number of fluorescent proteins have been tested for their ability to switch at CT.[7−9,11,13,14,25,27] While phototransformable FPs[28,29] have

Received: February 9, 2023
Published: June 30, 2023

https://doi.org/10.1021/jacs.3c01500
J. Am. Chem. Soc. 2023, 145, 14636−14646

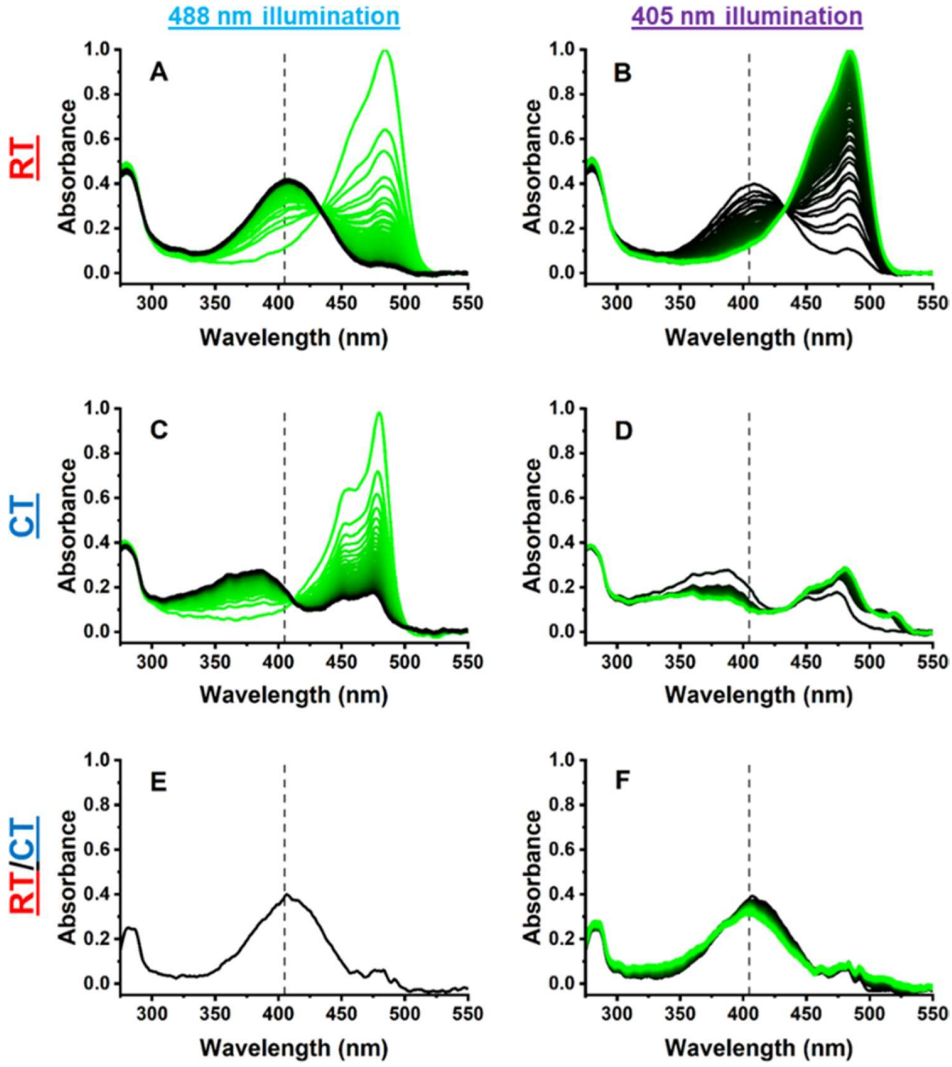

Figure 1. Photoswitching of rsEGFP2 monitored by absorption microspectrophotometry. (A) On-to-off switching at RT with 488 nm laser light (80 W/cm^2). (B) Off-to-on switching at RT with 405 nm laser light (4 W/cm^2). (C) On-to-off switching at 110 K with 488 nm laser light (0.4 kW/cm^2). (D) Off-to-on switching at CT with 405 nm laser light (0.2 kW/cm^2). (E) On-to-off switching at RT followed by flash cooling and spectral recording at CT, in contrast to (A) where spectra were recorded at RT. (F) Same as (E) followed by illumination at CT with 405 nm laser light (0.1 kW/cm^2). Spectral series evolve from green to black during off-switching (A, C) or from black to green during on-switching (B, D, F). Absorbance spectra in (A, B) and (C, D) were normalized at the anionic chromophore peak of the first spectrum in (A) and (C), respectively. Spectra in (E) and (F) were normalized to match the height of the protonated peak of the last spectrum in (A). Representative spectral series are shown from $n \geq 3$ measurements. Dashed vertical lines are positioned at 405 nm to guide the eye.

been mostly investigated,[7,8,11,25−27] other more standard FPs have also been shown to undergo cryo-switching.[8,9,14,26] Conflicting results have sometimes been reported, notably concerning reversibly switchable FPs (RSFPs). For example, Dronpa has been shown to not switch at CT, due to restricted structural dynamics,[7,30] to cryo-switch moderately[26] or quite efficiently.[8,13] While the positively photoswitchable FP Padron was reported to maintain *trans* to *cis* isomerization at 100 K,[7] negative photoswitching at 77 K was also observed.[13] Overall, mechanistic knowledge about the photoswitching mechanisms adopted by FPs at CT remains scarce, although some hypotheses have been put forward such as the possible involvement of the triplet state in the case of mEmerald[14] or of Kolbe-driven photo-decarboxylation of the conserved Glu222 (GFP amino-acid numbering) in PA-GFP or PA-mKate.[25,31] In this work, employing a combination of UV−visible microspectrophotometry, X-ray crystallography, and single-molecule studies, we focused on the cryo-switching mechanism of rsEGFP2, a well-known RSFP[32] for which extended knowledge has been gathered in the case of room-temperature (RT) switching.[33−37] We show that switching of rsEGFP2 at ∼110 K proceeds via a completely different pathway than at RT, which does not involve chromophore isomerization but instead populates two main dark states in the *cis* conformation of the chromophore. Based on ensemble and single-molecule data backed up by simulations, we show that the use of 355 nm laser light is expected to enhance the effective rsEGFP2 labeling efficiency in cryo-PALM experiments.

RESULTS

Stimulated by our recent structural investigations of rsEGFP2 at RT,[33−36] and by the fact that this RSFP was recently shown to maintain efficient switching at 77 K,[13] we were interested to know whether cryo-switching proceeds by the same *cis*−*trans*

https://doi.org/10.1021/jacs.3c01500
J. Am. Chem. Soc. 2023, 145, 14636−14646

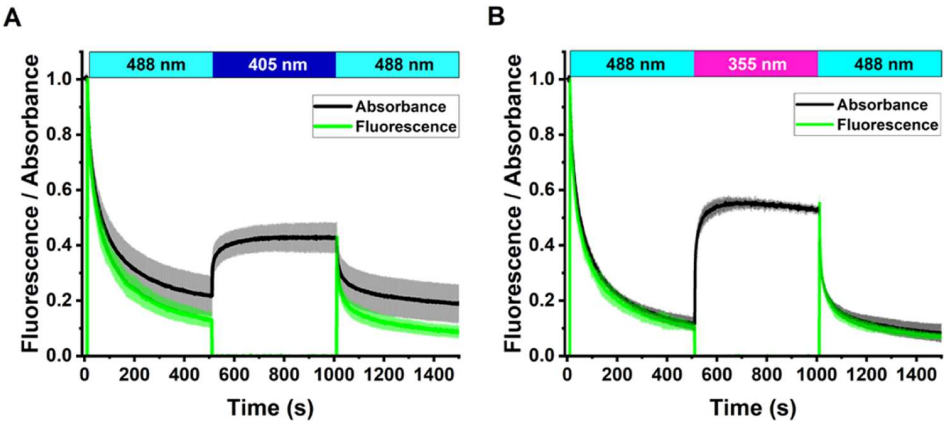

Figure 2. On-state recovery of switched-off rsEGFP2 at cryogenic temperature. Absorbance and fluorescence levels are calculated by integration of the absorption and fluorescence emission spectra in 470−500 and 495−630 nm spectral ranges, respectively. (A) Recovery by 405 nm light. (B) Recovery by 355 nm light. Absorbance (gray) and fluorescence (green) switching kinetics are measured at 110 K by alternate illumination at 488 nm (0.4 kW/cm^2) and either 405 nm (0.2 kW/cm^2) or 355 nm (0.03 kW/cm^2), as indicated in the upper bars. Absorbance and fluorescence are normalized to 1 at start of acquisition. Fluorescence is only measured in the presence of 488 nm light. The mean ± s.d. of n = 3 measurements is shown.

isomerization mechanism as observed at RT. In view of the very efficient switching of rsEGFP2 observed at 300 K, we initially assumed that sufficient conformational flexibility could be maintained at CT to enable chromophore isomerization. UV−visible microspectrophotometry experiments using a dedicated instrument[38] were first performed on flash-cooled samples of purified rsEGFP2 mixed with glycerol which were held in micro capillaries (Supporting Methods). In comparison with RT switching, a considerably reduced rate of switching upon illumination with 488 nm laser light was observed at ∼110 K (Figures S1 and S2). Furthermore, in contrast to the off-state reached at RT (absorption peak maximum at 411 nm) (Figure 1A), the absorption peak for the cryo-switched off-state (Figure 1C) was largely blue-shifted (peak maximum at 385 nm) and more structured. The blue shift was not an effect of the temperature at which spectra were recorded, as the absorption of a sample switched at RT followed by flash cooling was only blue-shifted to a minor extent (peak maximum at 406 nm) (Figure 1E). Although back switching by typical 405 nm laser light was nearly complete at RT (Figure 1B), only partial recovery was obtained at CT after extensive illumination (Figures 1D and S1). A significant fraction of rsEGFP2 molecules appeared to be trapped in the off-state, and a minor red-shifted absorbance peak was also observed to grow at 520 nm. Interestingly, if rsEGFP2 was off-switched at RT and then flash-cooled to CT (Figure 1E), little back switching could be observed by 405 nm illumination, populating mostly the red-shifted absorbance peak (Figure 1F). This suggests that below the glass-transition temperature, the protonated *trans* chromophore (the off-switched state at RT) is unable to efficiently undergo *trans* to *cis* back-isomerization followed by deprotonation to the canonical anionic fluorescent state absorbing at 479 nm. Taken together, these data suggest that the off-state reached upon 488 nm illumination at CT differs from that populated at RT.

Titration experiments as a function of the employed laser power density and fitting of the observed cryo-switching rates indicate that off-switching by 488 nm light as well as on-switching by 405 nm light are (at least) biphasic (Figure S3). The multiphasic nature of photoswitching curves in rsEGFP2 has already been noticed at CT[13] and RT[36] and could result from heterogeneous FP populations or from the transient built up of short-lived dark states.[36] It also follows from the fact that at CT the protein molecules cannot tumble in the vitreous solvent and thus switch at different rates depending on their dipole orientation. The fitted rates varied linearly as a function of the applied laser power density, suggesting that both off-switching and on-switching at 110 K proceed via single-photon absorption mechanisms (Figure S3).

In line with the absorbance data, off-switching at CT of rsEGFP2 by 488 nm light and subsequent on-switching by 405 nm light only allowed the recovery of ∼25% of the fluorescence (Figure 2A). Such a low recovery level is problematic for cryo-PALM applications, as only a minor fraction of the fluorescently labeled biological targets would then be detectable, giving rise to a low effective labeling efficiency (ELE). In comparison, in standard RT PALM using green-to-red photoconvertible FPs, typically 60−70% of the labels can be imaged under favorable illumination conditions.[39,40]

Photobleaching during off-switching by 488 nm light or on-switching by 405 nm light at CT can be invoked to explain the low recovery level to the fluorescent state. In particular, increasing the 405 nm light power density resulted in faster recovery that was nevertheless followed by a progressive decay of the on-state absorbance (Figure S4A), suggesting a balance between back switching and photobleaching mechanisms. Yet, the fraction of recovered on-state absorbance was independent of the applied 488 or 405 nm power density, suggesting that nonlinear bleaching mechanisms are not predominant in the investigated range (Figure S4B).

In addition to photobleaching, two other mechanisms may contribute to the limited recovery of the fluorescent on state. The first mechanism is similar to that limiting the photoswitching contrast in e.g., RESOLFT experiments at RT[36] and involves residual off-switching by 405 nm light. However, calculations that assume a wavelength-independent off-switching quantum yield (Supporting Methods) suggest that the ratio of on-switching and off-switching rates by the 405 nm light amounts to ∼900. Therefore, off-switching by 405 nm light is not expected to contribute to the limited recovery level.

https://doi.org/10.1021/jacs.3c01500
J. Am. Chem. Soc. 2023, 145, 14636−14646

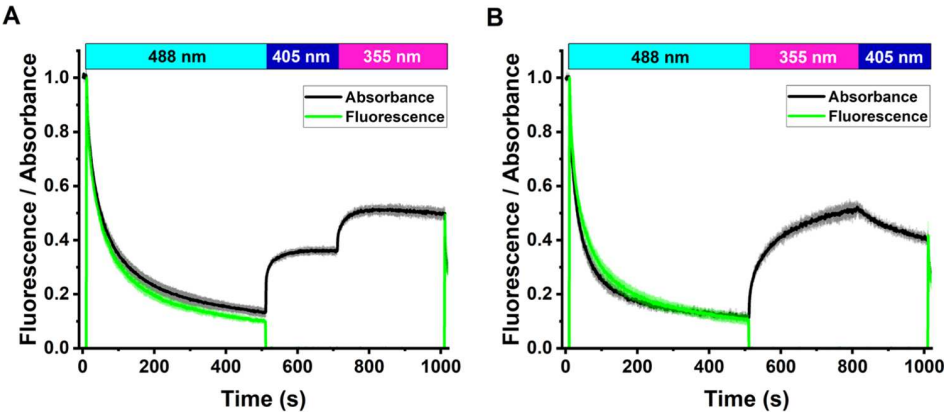

Figure 3. Recovery of rsEGFP2 on-state by subsequent illumination with 405 and 355 nm light. Absorbance and fluorescence levels are calculated by integration of the absorption and fluorescence emission spectra in 470−500 and 495−630 nm spectral ranges, respectively. (A) Recovery by 405 nm light followed by 355 nm light. (B) Recovery by 355 nm light followed by 405 nm light. Absorbance (gray) and fluorescence (green) evolutions are measured at 110 K by illumination at 488 (0.4 kW/cm^2), 405 (0.3 kW/cm^2), and 355 nm (0.025 kW/cm^2), according to the schemes indicated in the upper bars. Absorbance and fluorescence are normalized to 1 at start of acquisition. Fluorescence was only measured in the presence of 488 nm light. The mean ± s.d. of n = 3 measurements is shown.

The second mechanism involves dark state trapping and would be in line with the residual off-state absorption observed in the spectra of Figure 1D. In fact, although 405 nm light is nearly centered on the absorption band of the off-switched rsEGFP2 chromophore at RT, it sits on the red edge of the CT off-switched absorption band, possibly limiting on-state recovery. Thus, we replaced the 405 nm laser by a 355 nm laser. This wavelength sits on the blue edge of the absorption band, and the higher-energy photons may thus interact more efficiently with the CT off-switched chromophore. 355 nm light effectively enhanced the rsEGFP2 recovery level to ∼50% (Figure 2B), in line with near-complete disappearance of the off-state absorption band after illumination (Figure S5).

To further confirm the different on-switching efficiencies of 405 and 355 nm light, we sequentially applied both lasers (Figure 3). Application of 355 nm light after 405 nm light increased the recovery level to ∼45%, close to the level observed with 355 nm light only (Figure 3A). Application of 405 nm light after 355 nm light substantially decreased the recovery level (Figure 3B). Those data suggest that 355 nm light is able to pump back to the on-state a fraction of rsEGFP2 molecules residing in an off-state that does not respond to 405 nm light (Off_1), while another fraction of molecules appears to reside in a second off-state (Off_2) sensitive to both 405 and 355 nm light. Upon off-switching at CT by 488 nm light, Off_1 and Off_2 are populated and do not exchange significantly. Application of 405 nm light after 355 nm light repopulates Off_1 due to residual off-switching at this wavelength while the Off_2 steady-state level is maintained. This mechanism is clearly visible upon monitoring the absorbance at 320 nm (Figure S6). The observation of Off_1 and Off_2 is reminiscent of the two off states recently observed spectroscopically and structurally in rsEGFP2 at RT.[35,36]

Interestingly, we also observed that ∼9% of the off-switched molecules recovered to the fluorescent on-state at 110 K in the dark. The thermal recovery data were best fitted using a power law model (Figure S7). Inspection of the absorbance spectral change during thermal recovery suggested that both Off_1 and Off_2 were able to partially relax (Figure S7B,C).

The 355 nm laser we used was a nanosecond YAG laser pulsed at 3.3 kHz so that we wondered whether pulsing played a role in the improved recovery level. The temporal profile of laser illumination could act on the recovery level in case of a mechanism involving two photons or more. Yet, titration of the on-switching rate as a function of the employed 355 nm laser power density suggested, as for 488 and 405 nm lasers, a single-photon mechanism (Figure S8A). In addition, varying the intensity of the 355 nm illumination also did not have a significant effect on the recovery level (Figure S8B). These data indicate that the enhanced recovery of the rsEGFP2 on-state relative to that observed by 405 nm illumination is mostly due to the blue-shifted wavelength and not to the pulsed pattern of the employed 355 nm laser.

Strikingly, we also observed that, to achieve on-switching at similar rates, the needed 355 nm average power density was ∼20 times lower than that required using 405 nm light. The photoswitching efficiency depends on the product of the extinction coefficient by the switching quantum yield at the used wavelength. Attempts to obtain pure absorption spectra of Off_1 and Off_2 by computing difference spectra (Figure S9) indicated that, for both off states, differences in extinction coefficients at the two illumination wavelengths are unlikely to explain the drastic changes in switching efficiency. This suggests that, at CT, the on-switching quantum yield at the lower-energy 405 nm wavelength is significantly lower (× ∼0.05) than at 355 nm for Off_2, and practically zero for Off_1. This wavelength-dependence of a reaction quantum yield[41] will require further investigations, but could possibly be exacerbated at CT due to slowdown of vibrational relaxation to a point where photoswitching pathways efficiently compete with relaxation.

Off switching of RSFPs at RT typically involves protonation of the chromophore at the hydroxybenzylidene ring. To evaluate the possible involvement of proton transfer during off-switching at CT, we measured the switching rate in flash-cooled solution samples at various pHs (Figure S10). No significant pH dependence was observed.

Finally, we recorded multiswitching absorbance and fluorescence curves with on-switching either induced by 405 or 355 nm light (Figures 4 and S11). Photofatigue at CT was much higher than that measured at RT.[32] This observation is in line with the incomplete recovery observed in Figure 2A,B

https://doi.org/10.1021/jacs.3c01500
J. Am. Chem. Soc. 2023, 145, 14636−14646

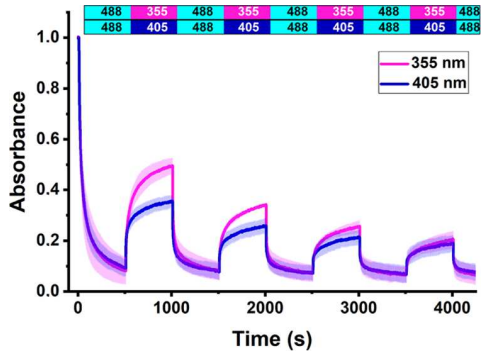

Figure 4. Absorbance photofatigue switching curves of rsEGFP2 at CT. The absorbance signal was calculated by integration of the absorption spectra in the 470−500 nm spectral range. rsEGFP2 was switched back and forth with 488 nm (1.0 kW/cm^2) and either 405 nm (0.2 kW/cm^2, blue) or 355 nm (0.01 kW/cm^2, magenta) laser light, according to the illumination schemes shown in the upper bars. The mean ± s.d. of n = 3 measurements is shown.

attributed in part to photobleaching by 488, 405, and 355 nm light. Of note, photofatigue developed faster when 355 nm light was employed. Reducing the UV-illumination time by a factor of 10 to only record the fast-recovery phase produced similar photofatigue profiles (Figure S11) although the differential photobleaching between 405 and 355 nm light was attenuated. These data show that the advantage of a higher on-state recovery using 355 nm light is progressively offset by faster photobleaching upon repeated switching. This might result from the Off_1 dark state being more prone to photobleaching than Off_2, but may also relate to enhanced photodamage by UV light compared to 405 nm light on biological material, including at CT.[42]

In order to investigate the structural signature of the rsEGFP2 cryo off-switched states, we illuminated rsEGFP2 crystals maintained in the ∼110 K nitrogen gas stream of our microspectrophotometer with 488 nm light. We verified by absorption microspectrophotometry that the same off states were produced as in solution samples (Figure S12) and that they did not significantly relax to the on-state in the dark after many hours (Figure S13). We then collected cryo-crystallographic data after transfer to a synchrotron beamline. Likely due to the prolonged illumination required at CT to achieve photoswitching, only moderate resolution (2.4 Å, Supporting Table 1) could be obtained, as opposed to control measurements where crystals were illuminated at RT (1.5 Å, Supporting Table 2).

In contrast to RT, electron density maps do not show *cis*−*trans* isomerization of the chromophore at CT (Figure 5). Possible conformational differences between Off_1 and Off_2 could also not be distinguished. Residual negative electron density at the level of the conserved Glu223 (rsEGFP2 amino-acid numbering) suggested partial decarboxylation of this residue at CT. Decarboxylation through electron transfer via a Kolbe mechanism has previously been observed in fluorescent proteins to induce photoactivation[31] or photobleaching,[43] including at CT.[44] We assign the decarboxylation observed here to photobleaching. Overall, the crystallographic data are consistent with the notion that the rsEGFP2 cryo off-states are predominantly *cis* states.

We also observed that rsEGFP2 chromophores switched off at RT by 488 nm laser light and then irradiated at CT with 405 nm laser light essentially stayed in the *trans*-conformation (Figure S14, Supporting Table 3). This is in line with the observation by spectroscopy that on-switching at CT of the RT-off-switched chromophore is limited to weak recovery of a red-shifted on-state (Figure 1D). The data are in fact consistent with a scenario in which this residual red-shifted on-state would originate from anionic chromophores in the *trans* configuration. Of note, a significant negative difference in electron density is visible on Glu223 as well as on the hydroxybenzylidene moiety of the chromophore. Decarboxylation of Glu223 in the *trans* isomer form of the chromophore might induce chromophore destabilization, a signature for photobleaching that might have resulted from the extensive 405 nm illumination employed in this experiment.

Next, we wondered whether the results obtained by microspectrophotometry could be reproduced at both the ensemble and single-molecule level using a PALM microscope operating at CT (110 K). To that aim, we equipped a home-built cryo-PALM set up with a 355 nm laser (Supporting

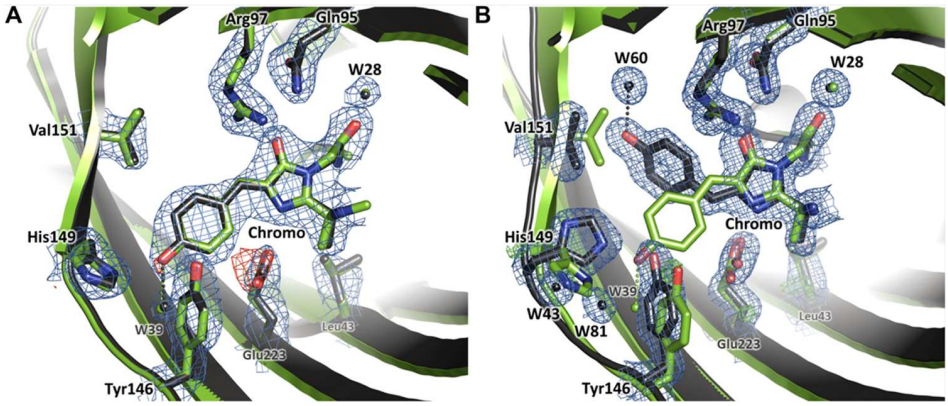

Figure 5. Crystallographic views of rsEGFP2 switching at CT and RT. (A) Refined models of the chromophore and surrounding residues of rsEGFP2 are shown in the *cis* on-state and in the cryo-switched *cis* off-state (PDB code 8AHA), switched with 488 nm laser light for 700 s (0.05 kW/cm^2). (B) Refined models of the chromophore and surrounding residues of rsEGFP2 are shown in the *cis* on-state and in the room-temperature-switched *trans* off-state upon switching with 488 nm laser light for ∼45 s (15 mW/cm^2). For both panels, on-states are shown with green carbons and water molecules, off-states are shown with dark gray carbons and water molecules, $2F_{obs}-F_{calc}$ electron density maps are contoured at 1σ (blue) and $F_{obs}-F_{calc}$ difference electron density maps are contoured at ± 3 σ (red: negative, green: positive). W: water molecules.

https://doi.org/10.1021/jacs.3c01500
J. Am. Chem. Soc. 2023, 145, 14636−14646

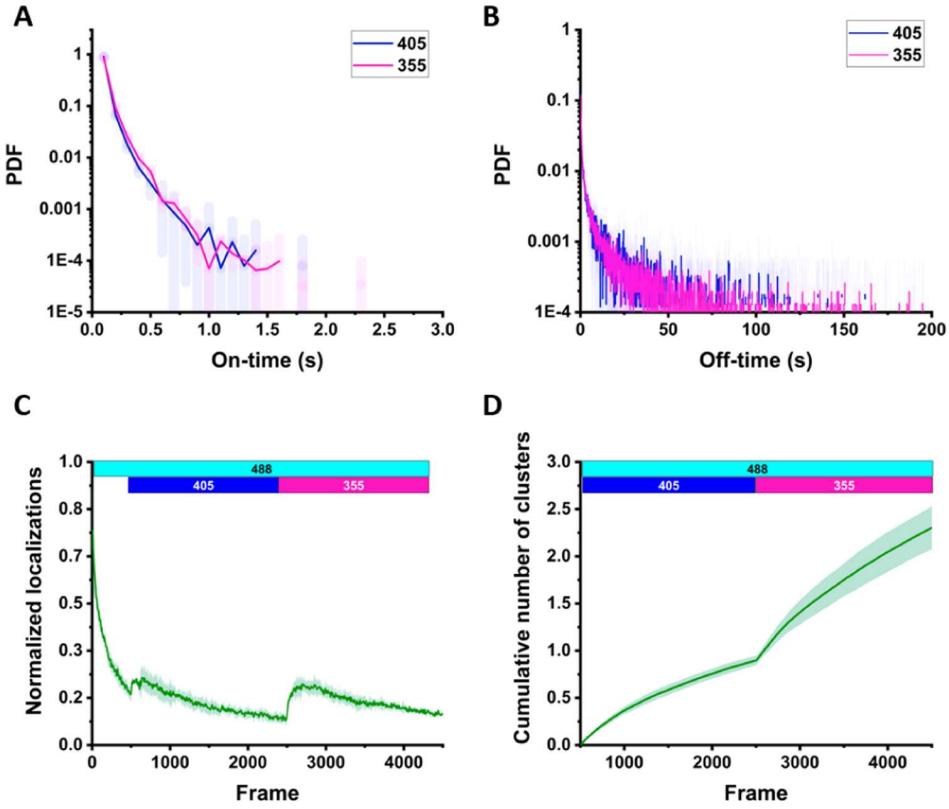

Figure 6. Single-molecule behavior of rsEGFP2 at CT under 405 and 355 nm illumination. (A) On-time and (B) Off-time histograms. (C) Number of localizations per frame (normalized to the value at the beginning of data acquisition) during cryo-PALM acquisition. (D) Cumulative number of photoactivated molecules after grouping localizations (normalized to the value reached at the end of the 405 nm illumination phase). The upper bars show applied lasers. The mean ± s.d. of $n \geq 3$ measurements is shown. PDF: probability density function.

Methods).[21] Fluorescence data were collected from thin layers of purified rsEGFP2 molecules flash-frozen on coverslips.

At the ensemble level, when rsEGFP2 was mixed with 25% glycerol to achieve flash cooling (as for all microspectrophotometry experiments described above), superior recovery by 355 nm light was confirmed (Figure S15, Supporting Note 1).

Single-molecule data were then recorded from flash-frozen samples prepared similarly. rsEGFP2 was initially off-switched by 488 nm light, and 405 and 355 nm lights were then added sequentially to elicit activation. A representative single-molecule pattern and a single-molecule trace are shown in Figure S16. Analysis of the data allowed generating histograms revealing the rsEGFP2 single-molecule photophysical behavior at CT under 405 or 355 nm illumination (Figures 6 and S17).

The on-time and off-time histograms did not seem to depend on the employed UV activation wavelength and are clearly multiphasic. The fast phases in both histograms suggest that the rsEGFP2 molecules rapidly toggle between the on-state and one (or several) short-lived dark state(s). Blinking at the single-molecule level could be linked to triplet-state relaxation and/or the partial thermal recovery from Off_1 and Off_2 observed to follow a power law at the ensemble level. The slow phase of the on-time histogram is also attributed to the fixed dipole orientation of the fluorescent proteins at CT, generating an anisotropic response to illumination (as for the kinetic traces measured at the ensemble level). The slow phase of the off-time histogram is attributed to the longer-lived Off_1 and Off_2 states, with lifetimes being primarily dependent on slower thermal recovery pathways at the applied 405 or 355 nm laser power densities. Of note, the median number of detected photons per localization (214 ± 16 ph, Figure S17) is lower than typical values recorded from SMLM datasets collected at RT with green-to-red photoconvertible fluorescent proteins (PCFPs) such as mEos4b (365 ± 42 ph), using similar acquisition parameters (Supporting Methods). We attribute this mostly to significant triplet state blinking and to the reduced photon detection efficiency at CT due to the employed low-NA air objective, those factors being only partly compensated by the increased fluorescence quantum yield of rsEGFP2 at CT. The median localization precision is thus only 44 ± 3 nm (Figure S17), substantially lower than that at RT with PCFPs (24 ± 3.5 nm), which also results from the low-NA objective and thus larger point spread function of the cryo-microscope. This highlights the importance of using long frame times and/or advanced localization merging procedures[14] to obtain FP-based cryo-SMLM images of superior quality compared to SMLM images collected at RT.

To verify that an increased rsEGFP2 recovery level by 355 nm light could also be achieved at the single-molecule level, we switched off a sample by 488 nm light, and then sequentially applied 405 and 355 nm light, similarly to the illumination scheme employed in Figure 3A. Monitoring the number of localizations per frame, a first boost of localizations appeared upon 405 nm illumination, followed by a second more pronounced boost upon subsequent application of 355 nm illumination (Figure 6C). Computing the cumulative number of photoactivated molecules after grouping localizations provided final evidence for the beneficial effect of applying 355 nm light instead or in addition to 405 nm light (Figure 6D).

https://doi.org/10.1021/jacs.3c01500
J. Am. Chem. Soc. 2023, 145, 14636−14646

DISCUSSION

Combining the ensemble and single-molecule data presented above allows drawing a consistent model of the cryo-photophysical behavior of rsEGFP2 (Figure 7). We propose

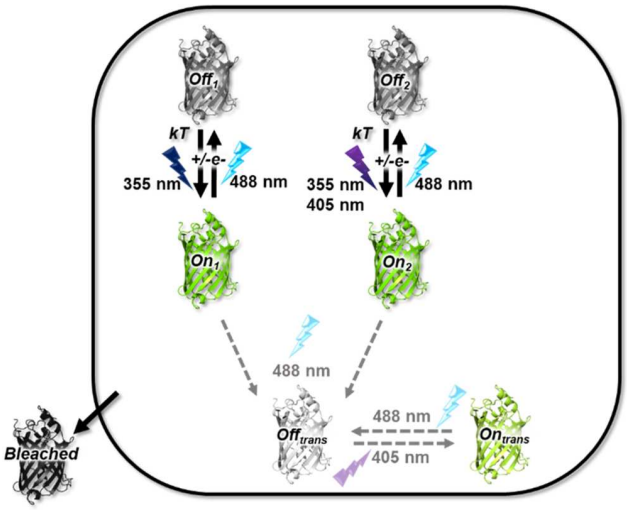

Figure 7. Proposed model of rsEGFP2 photophysics at CT. Sensitivity to light at defined wavelengths is indicated. kT: thermal activation. Dashed lines indicate residual involvement of *trans* chromophore states in CT-photoswitching.

that rsEGFP2 in its thermally relaxed on-state adopts two conformations (On_1 and On_2) that are in rapid exchange at RT, but that do not exchange significantly at CT. These two populations may differ by e.g., different H-bonding patterns around the chromophore. On_1, upon illumination by 488 nm light at CT, produces the nonfluorescent state Off_1, while On_2 switches to Off_2. Upon illumination with 405 nm light, Off_2 is able to switch back to On_2, while Off_1 remains essentially unresponsive. Upon illumination with 355 nm light, both Off_1 and Off_2 are able to switch back to their respective fluorescent on-states, causing more extensive recovery than with 405 nm illumination. The two populations of rsEGFP2 molecules do not photobleach at the same rate, with On_1/Off_1 being more prone to photodestruction. Off_1 and Off_2 partially relax to their respective on-states in the absence of light. Such relaxation occurs at multiple rates, which might result from heterogeneity in the chromophore environment at CT. Short-lived blinking observed at the single-molecule level might be associated with fast thermal recovery from Off_1 and Off_2 or from the triplet state, the lifetime of which was recently measured to be ~20 ms at CT.[45]

The existence of two rsEGFP2 on-states that would not exchange at CT is supported by the data presented in Figures 3B and 4, as detailed in Supporting Note 2. The presence of several on-states could relate to the multiple switching pathways that have also been identified at RT.[36,37] In the future, it could be interesting to investigate the cryo-switching mechanisms of the rsEGFP2 V151A and V151L mutants, which have been shown to abrogate off-state heterogeneity at RT.[36]

Radical species are known to form in FPs and are typically short-lived at RT.[44,46,47] We propose that Off_1 and Off_2 be anionic or cationic radicals formed from the triplet state via photoinduced electron transfer. This hypothesis is in line with our observations that (*i*) the absorption spectra of Off_1 and Off_2 are blue-shifted relative to spectra of switched-off protonated states typically observed at RT, (ii) no *cis*−*trans* isomerization occurs upon photoswitching at CT, and (iii) the cryo off-photoswitching rate is independent on pH, in agreement with reduced H^+ diffusion below the glass-transition temperature.[48]

Yet, the exact natures of Off_1 and Off_2 remain to be determined. To confirm that they are radical species, electron paramagnetic resonance (EPR) experiments could be attempted if cryo-switching of sufficient sample quantities could be achieved. To study the dependence of Off_1 and/or Off_2 on the addition of triplet-state quenchers, oxidizing or reducing agents, attaching such molecules directly to rsEGFP2 could be an alternative strategy.[49]

Based on a comparison between the absorption spectra measured upon on-state recovery at CT following off-switching at either RT or CT (Figure 1D,F), we propose that, in addition to Off_1 and Off_2, a residual fraction of the on-state rsEGFP2 molecules may still be able to photo-isomerize at CT to a protonated *trans* configuration similar to that populated at RT. This RT-like off-state would be able to deprotonate upon absorption of a 405 nm photon, producing a fluorescent *trans* state with red-shifted absorption and fluorescence emission. This mechanism may explain why, in cryo-PALM imaging, prior illumination of the sample at RT followed by flash cooling and single-molecule data collection at CT still elicits single-molecule blinking.[13] However, in view of the low signal recovered in such case (Figure 1E), this procedure likely results in unfavorable ELE and is not recommended. The RT-like off-state, with its absorption band peaking at around 400 nm, is only weakly sensitive to 355 nm light, in contrast to 405 nm light. Thus, less red-shifted fluorescent molecules are produced upon 355 nm light illumination.

Sample devitrification is an important concern in cryo-SMLM experiments, and it has been suggested that when carbon-coated EM grids are used, a laser power density as low as ~30 W/cm^2 may induce devitrification.[50] In the course of this study, 488 nm laser power densities were typically of the order of 0.4 kW/cm^2, a value similar to those used in several previous cryo-SMLM reports.[15] Such power density, at least with rsEGFP2, appears to be required to achieve sufficient localization precision. In our case, sample devitrification was not an issue, as we used nonabsorbing glass capillaries or fused silica coverslips instead of EM grids (Supporting Note 3). In the future, it will be key to use weakly absorbing sample holders[8] for cryo-CLEM compatible with power densities required to ensure sufficient single-molecule localization precision.

To evaluate the potential gain in using 355 nm rather than 405 nm light in cryo-SMLM experiments, we performed simulations using the recently developed SMIS software.[51] Our main goal was to evaluate whether the more efficient on-switching provided by 355 nm illumination could improve the effective labeling efficiency of rsEGFP2 despite more pronounced photobleaching. The ensemble switching behavior was first reproduced by implementing the rsEGFP2 photophysical model described above (Supporting Materials and Methods, Supporting Table 4, Figures S18 and S19). The model was then used in virtual cryo-SMLM experiments aimed at quantitative imaging of the Nup96 nucleoporin within nuclear pore complexes (NPCs).[52] The results, presented in Figure 8, suggest that the ELE can be raised from ~21 to

https://doi.org/10.1021/jacs.3c01500
J. Am. Chem. Soc. 2023, 145, 14636−14646

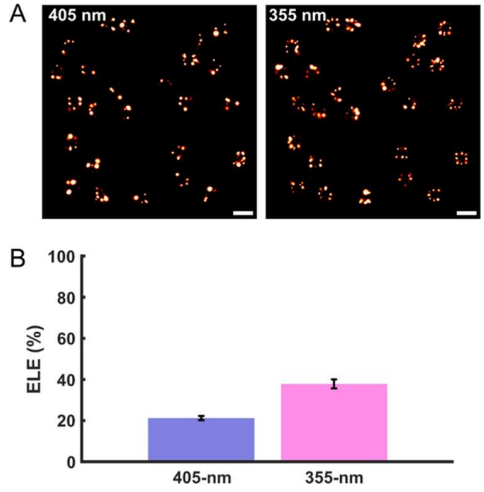

Figure 8. Simulated cryo-SMLM of rsEGFP2-labeled Nup96 in NPCs. (A) Reconstructed images using 355 or 405 nm illumination. (B) Effective labeling efficiency (ELE) using 355 nm or 405 nm illumination. ELE was extracted from the analysis of 100 NPCs (Figure S19), and error bars were derived by bootstrapping. Scale bar: 0.5 μm.

~38% (Supporting Note 4). Thus, based on our rsEGFP2 photophysical model, we conclude that the more efficient recovery level offered by the 355 nm laser prevails over the more stringent photobleaching induced by this laser. This finding will now need to be confirmed in genuine experimental conditions.

It will be interesting in the future to evaluate whether the results reported here can be generalized to other FPs such as EGFP, EYFP,[26] mEmerald,[14] PA-GFP,[53] or PA-mKate.[25] As the cryo-switching mechanism of rsEGFP2 does not seem to relate to the *cis*−*trans* isomerization-based mechanism adopted at RT, we anticipate that FPs that are not necessarily phototransformable or adopt different phototransformation mechanisms at RT may share the described behavior and, in particular, be sensitive to enhanced reactivation by 355 nm light. In fact, the various FPs studied by Tuijtel et al.[13] show relatively similar behaviors, including EGFP, PA-GFP, and Padron. In the case of PA-GFP, the observed reversible photoswitching behavior at CT[13] suggests that reversible radical formation may follow activation through nonreversible photoinduced decarboxylation of the conserved Glu222 through a Kolbe-type mechanism. Thus, in photoactivatable FPs such as PA-GFP or PA-mKate, multiple routes for photoactivation at CT may coexist. Yet, it is difficult to evaluate whether these FPs would provide superior ELEs in cryo-PALM experiments compared to rsEGFP2. Although the ELEs of both PA-GFP and PA-mKate were reported to be similar at CT and RT,[25] the ELE of PA-GFP was reported to be only ~28% at RT.[54] Thus, we deem unlikely that the achieved ELE with these proteins be superior to the one achieved in this work with rsEGFP2, but a more precise answer will need to await quantitative cryo-PALM experiments employing e.g., biological templates with known stoichiometries. Finally, it is remarkable to note that, in the case of Padron, both negative and positive photoswitching at CT have been described.[13,27] Similarly to PA-GFP, it is likely that this FP can sustain two different mechanisms: *trans* to *cis* isomerization at CT (positive switching) and reversible radical formation via the same mechanism as in rsEGFP2 (negative switching).

CONCLUSIONS

This work presents the first in-depth investigation of the cryo-switching mechanism of a fluorescent protein. We have shown that rsEGFP2, an efficient RSFP that switches at ambient temperature through coupled *cis*−*trans* isomerization and protonation of its chromophore, adopts a different switching mechanism at cryogenic temperature. Because of the lack of conformational freedom below the glass-transition temperature (~180 K), isomerization of the rsEGFP2 chromophore is largely hindered at ~110 K. In contrast, this FP populates two off-switched states adopting *cis* configurations and displaying absorption bands largely blue-shifted relative to that of the *trans* protonated off-state reached at RT. These off-switched states are likely to be radical states, and rsEGFP2 may be functioning at CT like some organic dyes under dSTORM conditions at RT. Indeed, at CT, oxygen scavenging is mimicked by the lack of oxygen diffusion and, while traditional phototransformation routes are blocked, intra- or intermolecular electron transfer pathways remain open to form stable radicals from the triplet state. A key finding of our work is that a 405 nm laser classically used in RT-SMLM switches back only one of the off-states, whereas a 355 nm laser applied at very low power is able to efficiently reactivate both off-states and thus a larger fraction of the molecules. Single-molecule data collection *in vitro* and cryo-SMLM simulations on the nuclear pore complex suggest that, as a consequence, there would be a net gain in using such a laser for real studies thanks to an increased effective labeling efficiency. Yet, cellular damage induced by 355 nm light, although likely limited at cryogenic temperature, would need to be evaluated. The present study highlights that population heterogeneity is a major hallmark of fluorescent protein photophysical behavior. Removing this heterogeneity in favor of only the more photostable On_2 population would be an even more attractive option than using 355 nm light for efficient activation of rsEGFP2 at CT. In conclusion, the present study opens the door to FP engineering and optimization of illumination conditions to improve cryo-photoswitching in cryo-SMLM.

ASSOCIATED CONTENT

Supporting Information

The Supporting Information is available free of charge at https://pubs.acs.org/doi/10.1021/jacs.3c01500.

Sample preparation, microspectrophotometry, X-ray crystallography, single-molecule imaging, and simulations (Materials and Methods); switching rates, on-state populations, sample heating, and labeling efficiencies (Notes S1−S4); additional spectroscopic, crystallographic, and single-molecule data, and setup description (Figures S1−S25); and crystallographic statistics and photophysical parameters from simulations (Tables S1−S4) (PDF)

AUTHOR INFORMATION

Corresponding Author

Dominique Bourgeois − *Institut de Biologie Structurale, CNRS, Université Grenoble Alpes, CEA, IBS, 38044 Grenoble, France;* orcid.org/0000-0002-1862-7712; Email: dominique.bourgeois@ibs.fr

Authors

Angela M. R. Mantovanelli − *Institut de Biologie Structurale, CNRS, Université Grenoble Alpes, CEA, IBS, 38044 Grenoble, France*

Oleksandr Glushonkov − *Institut de Biologie Structurale, CNRS, Université Grenoble Alpes, CEA, IBS, 38044 Grenoble, France*

Virgile Adam − *Institut de Biologie Structurale, CNRS, Université Grenoble Alpes, CEA, IBS, 38044 Grenoble, France;* orcid.org/0000-0003-2209-7846

Jip Wulffelé − *Institut de Biologie Structurale, CNRS, Université Grenoble Alpes, CEA, IBS, 38044 Grenoble, France*

Daniel Thédié − *Institut de Biologie Structurale, CNRS, Université Grenoble Alpes, CEA, IBS, 38044 Grenoble, France;* Present Address: Institute of Cell Biology and SynthSys, University of Edinburgh, EH9 3FF Edinburgh, UK

Martin Byrdin − *Institut de Biologie Structurale, CNRS, Université Grenoble Alpes, CEA, IBS, 38044 Grenoble, France;* orcid.org/0000-0002-6389-8714

Ingo Gregor − *Institute of Physics−Biophysics, Georg August University, 37077 Göttingen, Germany;* orcid.org/0000-0002-1775-2159

Oleksii Nevskyi − *Institute of Physics−Biophysics, Georg August University, 37077 Göttingen, Germany;* orcid.org/0000-0003-2893-481X

Jörg Enderlein − *Institute of Physics−Biophysics, Georg August University, 37077 Göttingen, Germany;* orcid.org/0000-0001-5091-7157

Complete contact information is available at: https://pubs.acs.org/10.1021/jacs.3c01500

Author Contributions

[§]A.M.R.M., O.G., and V.A. contributed equally to this work.

Funding

This work was supported by the Agence Nationale de la Recherche (grant nos. ANR-17-CE11-0047-01 and ANR-20-CE11-0013-01) and used the M4D imaging platform of the Grenoble Instruct-ERIC Center (ISBG: UMS 3518 CNRS-CEA-UGA-EMBL) with support from FRISBI (grant no. ANR-10-INBS-05-02) and GRAL, a project of the Université Grenoble Alpes graduate school (Ecoles Universitaires de Recherche) CBH-EUR-GS (ANR-17-EURE-0003) within the Grenoble Partnership for Structural Biology (PSB). A.M. acknowledges funding by the CEA. J.W. acknowledges funding by the GRAL Labex.

Notes

The authors declare no competing financial interest.

■ ACKNOWLEDGMENTS

The authors thank Antoine Royant for the loan of the 355 nm laser and Ninon Zala for rsEGFP2 protein production. Michel Sliwa is acknowledged for providing insight into wavelength-dependent phototransformation quantum yields. The authors thank the staff of the MX beamlines from the ESRF, Grenoble, France.

■ ABBREVIATIONS

SMLM	single-molecule localization microscopy
(d)STORM	stochastic optical reconstruction microscopy
PAINT	point accumulation in nanoscale topography
PALM	photoactivation localization microscopy
RT	room temperature
CT	cryogenic temperature
FPs	fluorescent proteins
RSFPs	reversibly switchable fluorescent proteins
PCFPs	photoconvertible fluorescent proteins
CLEM	correlative light and electron microscopy
EPR	electron paramagnetic resonance
NPC	nuclear pore complex

■ REFERENCES

(1) Liu, S.; Hoess, P.; Ries, J. Super-Resolution Microscopy for Structural Cell Biology. *Annu. Rev. Biophys.* **2022**, *51*, 301−326.

(2) Schnell, U.; Dijk, F.; Sjollema, K. A.; Giepmans, B. N. G. Immunolabeling Artifacts and the Need for Live-Cell Imaging. *Nat. Methods* **2012**, *9*, 152−158.

(3) Whelan, D. R.; Bell, T. D. M. Image Artifacts in Single Molecule Localization Microscopy: Why Optimization of Sample Preparation Protocols Matters. *Sci. Rep.* **2015**, *5*, No. 7924.

(4) Tanaka, K. A. K.; Suzuki, K. G. N.; Shirai, Y. M.; Shibutani, S. T.; Miyahara, M. S. H.; Tsuboi, H.; Yahara, M.; Yoshimura, A.; Mayor, S.; Fujiwara, T. K.; Kusumi, A. Membrane Molecules Mobile Even after Chemical Fixation. *Nat. Methods* **2010**, *7*, 865−866.

(5) Sartori, A.; Gatz, R.; Beck, F.; Rigort, A.; Baumeister, W.; Plitzko, J. M. Correlative Microscopy: Bridging the Gap between Fluorescence Light Microscopy and Cryo-Electron Tomography. *J. Struct. Biol.* **2007**, *160*, 135−145.

(6) Schwartz, C. L.; Sarbash, V. I.; Ataullakhanov, F. I.; McIntosh, J. R.; Nicastro, D. Cryo-Fluorescence Microscopy Facilitates Correlations between Light and Cryo-Electron Microscopy and Reduces the Rate of Photobleaching. *J. Microsc.* **2007**, *227*, 98−109.

(7) Chang, Y.-W.; Chen, S.; Tocheva, E. I.; Treuner-Lange, A.; Löbach, S.; Søgaard-Andersen, L.; Jensen, G. J. Correlated Cryogenic Photoactivated Localization Microscopy and Cryo-Electron Tomography. *Nat. Methods* **2014**, *11*, 737−739.

(8) Liu, B.; Xue, Y.; Zhao, W.; Chen, Y.; Fan, C.; Gu, L.; Zhang, Y.; Zhang, X.; Sun, L.; Huang, X.; Ding, W.; Sun, F.; Ji, W.; Xu, T. Three-Dimensional Super-Resolution Protein Localization Correlated with Vitrified Cellular Context. *Sci. Rep.* **2015**, *5*, No. 13017.

(9) Kaufmann, R.; Schellenberger, P.; Seiradake, E.; Dobbie, I. M.; Jones, E. Y.; Davis, I.; Hagen, C.; Grünewald, K. Super-Resolution Microscopy Using Standard Fluorescent Proteins in Intact Cells under Cryo-Conditions. *Nano Lett.* **2014**, *14*, 4171−4175.

(10) Wolff, G.; Hagen, C.; Grünewald, K.; Kaufmann, R. Towards Correlative Super-Resolution Fluorescence and Electron Cryo-Microscopy. *Biol. Cell* **2016**, *108*, 245−258.

(11) Nahmani, M.; Lanahan, C.; DeRosier, D.; Turrigiano, G. G. High-Numerical-Aperture Cryogenic Light Microscopy for Increased Precision of Superresolution Reconstructions. *Proc. Natl. Acad. Sci. U.S.A.* **2017**, *114*, 3832−3836.

(12) Dahlberg, P. D.; Saurabh, S.; Sartor, A. M.; Wang, J.; Mitchell, P. G.; Chiu, W.; Shapiro, L.; Moerner, W. E. Cryogenic Single-Molecule Fluorescence Annotations for Electron Tomography Reveal in Situ Organization of Key Proteins in Caulobacter. *Proc. Natl. Acad. Sci. U.S.A.* **2020**, *117*, 13937−13944.

(13) Tuijtel, M. W.; Koster, A. J.; Jakobs, S.; Faas, F. G. A.; Sharp, T. H. Correlative Cryo Super-Resolution Light and Electron Microscopy on Mammalian Cells Using Fluorescent Proteins. *Sci. Rep.* **2019**, *9*, No. 1369.

(14) Hoffman, D. P.; Shtengel, G.; Xu, C. S.; Campbell, K. R.; Freeman, M.; Wang, L.; Milkie, D. E.; Pasolli, H. A.; Iyer, N.; Bogovic, J. A.; Stabley, D. R.; Shirinifard, A.; Pang, S.; Peale, D.; Schaefer, K.; Pomp, W.; Chang, C.-L.; Lippincott-Schwartz, J.; Kirchhausen, T.; Solecki, D. J.; Betzig, E.; Hess, H. F. Correlative Three-Dimensional Super-Resolution and Block-Face Electron Microscopy of Whole Vitreously Frozen Cells. *Science* **2020**, *367*, No. eaaz5357.

(15) Dahlberg, P. D.; Moerner, W. E. Cryogenic Super-Resolution Fluorescence and Electron Microscopy Correlated at the Nanoscale. *Annu. Rev. Phys. Chem.* **2021**, *72*, 253−278.
(16) Moerner, W. E.; Orrit, M. Illuminating Single Molecules in Condensed Matter. *Science* **1999**, *283*, 1670−1676.
(17) Hulleman, C. N.; Li, W.; Gregor, I.; Rieger, B.; Enderlein, J. Photon Yield Enhancement of Red Fluorophores at Cryogenic Temperatures. *Chemphyschem* **2018**, *19*, 1774−1780.
(18) Weisenburger, S.; Jing, B.; Hänni, D.; Reymond, L.; Schuler, B.; Renn, A.; Sandoghdar, V. Cryogenic Colocalization Microscopy for Nanometer-Distance Measurements. *ChemPhysChem* **2014**, *15*, 763−770.
(19) Weisenburger, S.; Boening, D.; Schomburg, B.; Giller, K.; Becker, S.; Griesinger, C.; Sandoghdar, V. Cryogenic Optical Localization Provides 3D Protein Structure Data with Angstrom Resolution. *Nat. Methods* **2017**, *14*, 141−144.
(20) Mazal, H.; Wieser, F.-F.; Sandoghdar, V. Deciphering a Hexameric Protein Complex with Angstrom Optical Resolution. *eLife* **2022**, *11*, No. e76308.
(21) Li, W.; Stein, S. C.; Gregor, I.; Enderlein, J. Ultra-Stable and Versatile Widefield Cryo-Fluorescence Microscope for Single-Molecule Localization with Sub-Nanometer Accuracy. *Opt. Express* **2015**, *23*, 3770−3783.
(22) Faoro, R.; Bassu, M.; Mejia, Y. X.; Stephan, T.; Dudani, N.; Boeker, C.; Jakobs, S.; Burg, T. P. Aberration-Corrected Cryoimmersion Light Microscopy. *Proc. Natl. Acad. Sci. U.S.A.* **2018**, *115*, 1204−1209.
(23) Xu, X.; Xue, Y.; Tian, B.; Feng, F.; Gu, L.; Li, W.; Ji, W.; Xu, T. Ultra-Stable Super-Resolution Fluorescence Cryo-Microscopy for Correlative Light and Electron Cryo-Microscopy. *Sci. China Life Sci.* **2018**, *61*, 1312−1319.
(24) Wang, L.; Bateman, B.; Zanetti-Domingues, L. C.; Moores, A. N.; Astbury, S.; Spindloe, C.; Darrow, M. C.; Romano, M.; Needham, S. R.; Beis, K.; Rolfe, D. J.; Clarke, D. T.; Martin-Fernandez, M. L. Solid Immersion Microscopy Images Cells under Cryogenic Conditions with 12 Nm Resolution. *Commun. Biol.* **2019**, *2*, 74.
(25) Dahlberg, P. D.; Sartor, A. M.; Wang, J.; Saurabh, S.; Shapiro, L.; Moerner, W. E. Identification of PAmKate as a Red Photoactivatable Fluorescent Protein for Cryogenic Super-Resolution Imaging. *J. Am. Chem. Soc.* **2018**, *140*, 12310−12313.
(26) Faro, A. R.; Adam, V.; Carpentier, P.; Darnault, C.; Bourgeois, D.; Rosny, E. de. Low-Temperature Switching by Photoinduced Protonation in Photochromic Fluorescent Proteins. *Photochem. Photobiol. Sci.* **2010**, *9*, 254−262.
(27) Regis Faro, A.; Carpentier, P.; Jonasson, G.; Pompidor, G.; Arcizet, D.; Demachy, I.; Bourgeois, D. Low-Temperature Chromophore Isomerization Reveals the Photoswitching Mechanism of the Fluorescent Protein Padron. *J. Am. Chem. Soc.* **2011**, *133*, 16362−16365.
(28) Shcherbakova, D. M.; Sengupta, P.; Lippincott-Schwartz, J.; Verkhusha, V. V. Photocontrollable Fluorescent Proteins for Superresolution Imaging. *Annu. Rev. Biophys.* **2014**, *43*, 303−329.
(29) Adam, V.; Berardozzi, R.; Byrdin, M.; Bourgeois, D. Phototransformable Fluorescent Proteins: Future Challenges. *Curr. Opin. Chem. Biol.* **2014**, *20*, 92−102.
(30) Mizuno, H.; Mal, T. K.; Wälchli, M.; Kikuchi, A.; Fukano, T.; Ando, R.; Jeyakanthan, J.; Taka, J.; Shiro, Y.; Ikura, M.; Miyawaki, A. Light-Dependent Regulation of Structural Flexibility in a Photochromic Fluorescent Protein. *Proc. Natl. Acad. Sci. U.S.A.* **2008**, *105*, 9227−9232.
(31) van Thor, J. J.; Gensch, T.; Hellingwerf, K. J.; Johnson, L. N. Phototransformation of Green Fluorescent Protein with UV and Visible Light Leads to Decarboxylation of Glutamate 222. *Nat. Struct. Biol.* **2002**, *9*, 37−41.
(32) Grotjohann, T.; Testa, I.; Reuss, M.; Brakemann, T.; Eggeling, C.; Hell, S. W.; Jakobs, S. RsEGFP2 Enables Fast RESOLFT Nanoscopy of Living Cells. *eLife* **2012**, *1*, No. e00248.
(33) El Khatib, M.; Martins, A.; Bourgeois, D.; Colletier, J.-P.; Adam, V. Rational Design of Ultrastable and Reversibly Photoswitchable Fluorescent Proteins for Super-Resolution Imaging of the Bacterial Periplasm. *Sci. Rep.* **2016**, *6*, No. 18459.
(34) Coquelle, N.; Sliwa, M.; Woodhouse, J.; Schirò, G.; Adam, V.; Aquila, A.; Barends, T. R. M.; Boutet, S.; Byrdin, M.; Carbajo, S.; De la Mora, E.; Doak, R. B.; Feliks, M.; Fieschi, F.; Foucar, L.; Guillon, V.; Hilpert, M.; Hunter, M. S.; Jakobs, S.; Koglin, J. E.; Kovacsova, G.; Lane, T. J.; Lévy, B.; Liang, M.; Nass, K.; Ridard, J.; Robinson, J. S.; Roome, C. M.; Ruckebusch, C.; Seaberg, M.; Thepaut, M.; Cammarata, M.; Demachy, I.; Field, M.; Shoeman, R. L.; Bourgeois, D.; Colletier, J.-P.; Schlichting, I.; Weik, M. Chromophore Twisting in the Excited State of a Photoswitchable Fluorescent Protein Captured by Time-Resolved Serial Femtosecond Crystallography. *Nat. Chem.* **2018**, *10*, 31−37.
(35) Woodhouse, J.; Nass Kovacs, G.; Coquelle, N.; Uriarte, L. M.; Adam, V.; Barends, T. R. M.; Byrdin, M.; de la Mora, E.; Bruce Doak, R.; Feliks, M.; Field, M.; Fieschi, F.; Guillon, V.; Jakobs, S.; Joti, Y.; Macheboeuf, P.; Motomura, K.; Nass, K.; Owada, S.; Roome, C. M.; Ruckebusch, C.; Schirò, G.; Shoeman, R. L.; Thepaut, M.; Togashi, T.; Tono, K.; Yabashi, M.; Cammarata, M.; Foucar, L.; Bourgeois, D.; Sliwa, M.; Colletier, J.-P.; Schlichting, I.; Weik, M. Photoswitching Mechanism of a Fluorescent Protein Revealed by Time-Resolved Crystallography and Transient Absorption Spectroscopy. *Nat. Commun.* **2020**, *11*, No. 741.
(36) Adam, V.; Hadjidemetriou, K.; Jensen, N.; Shoeman, R. L.; Woodhouse, J.; Aquila, A.; Banneville, A.-S.; Barends, T. R. M.; Bezchastnov, V.; Boutet, S.; Byrdin, M.; Cammarata, M.; Carbajo, S.; Eleni Christou, N.; Coquelle, N.; De la Mora, E.; El Khatib, M.; Moreno Chicano, T.; Bruce Doak, R.; Fieschi, F.; Foucar, L.; Glushonkov, O.; Gorel, A.; Grünbein, M. L.; Hilpert, M.; Hunter, M.; Kloos, M.; Koglin, J. E.; Lane, T. J.; Liang, M.; Mantovanelli, A.; Nass, K.; Nass Kovacs, G.; Owada, S.; Roome, C. M.; Schirò, G.; Seaberg, M.; Stricker, M.; Thépaut, M.; Tono, K.; Ueda, K.; Uriarte, L. M.; You, D.; Zala, N.; Domratcheva, T.; Jakobs, S.; Sliwa, M.; Schlichting, I.; Colletier, J.-P.; Bourgeois, D.; Weik, M. Rational Control of Off-State Heterogeneity in a Photoswitchable Fluorescent Protein Provides Switching Contrast Enhancement**. *ChemPhysChem* **2022**, *23*, No. e202200192.
(37) Chang, J.; Romei, M. G.; Boxer, S. G. Structural Evidence of Photoisomerization Pathways in Fluorescent Proteins. *J. Am. Chem. Soc.* **2019**, *141*, 15504−15508.
(38) Byrdin, M.; Bourgeois, D. The CAL(AI)2DOSCOPE: A Microspectrophotometer for Accurate Recording of Correlated Absorbance and Fluorescence Emission Spectra. *Spectrosc. Eur.* **2016**, *28*, 14−17.
(39) Durisic, N.; Laparra-Cuervo, L.; Sandoval-Álvarez, Á.; Borbely, J. S.; Lakadamyali, M. Single-Molecule Evaluation of Fluorescent Protein Photoactivation Efficiency Using an in Vivo Nanotemplate. *Nat. Methods* **2014**, *11*, 156−162.
(40) Wulffele, J.; Thédié, D.; Glushonkov, O.; Bourgeois, D. MEos4b Photoconversion Efficiency Depends on Laser Illumination Conditions Used in PALM. *J. Phys. Chem. Lett.* **2022**, *13*, 5075−5080.
(41) Sotome, H.; Une, K.; Nagasaka, T.; Kobatake, S.; Irie, M.; Miyasaka, H. A Dominant Factor of the Cycloreversion Reactivity of Diarylethene Derivatives as Revealed by Femtosecond Time-Resolved Absorption Spectroscopy. *J. Chem. Phys.* **2020**, *152*, No. 034301.
(42) Vernede, X.; Lavault, B.; Ohana, J.; Nurizzo, D.; Joly, J.; Jacquamet, L.; Felisaz, F.; Cipriani, F.; Bourgeois, D. UV Laser-Excited Fluorescence as a Tool for the Visualization of Protein Crystals Mounted in Loops. *Acta Crystallogr., Sect. D: Biol. Crystallogr.* **2006**, *62*, 253−261.
(43) Duan, C.; Adam, V.; Byrdin, M.; Ridard, J.; Kieffer-Jaquinod, S.; Morlot, C.; Arcizet, D.; Demachy, I.; Bourgeois, D. Structural Evidence for a Two-Regime Photobleaching Mechanism in a Reversibly Switchable Fluorescent Protein. *J. Am. Chem. Soc.* **2013**, *135*, 15841−15850.
(44) Adam, V.; Carpentier, P.; Violot, S.; Lelimousin, M.; Darnault, C.; Nienhaus, G. U.; Bourgeois, D. Structural Basis of X-Ray-Induced Transient Photobleaching in a Photoactivatable Green Fluorescent Protein. *J. Am. Chem. Soc.* **2009**, *131*, 18063−18065.

https://doi.org/10.1021/jacs.3c01500
J. Am. Chem. Soc. 2023, 145, 14636−14646

(45) Rane, L.; Wulffele, J.; Bourgeois, D.; Glushonkov, O.; Mantovanelli, A. M. R. A.; Zala, N.; Byrdin, M. Light Induced Forward and Reverse Intersystem Crossing in Green Fluorescent Proteins at Cryogenic Temperatures. *J. Phys. Chem. B* **2023**, *127*, 5046−5054.
(46) Roy, A.; Field, M. J.; Adam, V.; Bourgeois, D. The Nature of Transient Dark States in a Photoactivatable Fluorescent Protein. *J. Am. Chem. Soc.* **2011**, *133*, 18586−18589.
(47) Vegh, R. B.; Bravaya, K. B.; Bloch, D. A.; Bommarius, A. S.; Tolbert, L. M.; Verkhovsky, M.; Krylov, A. I.; Solntsev, K. M. Chromophore Photoreduction in Red Fluorescent Proteins Is Responsible for Bleaching and Phototoxicity. *J. Phys. Chem. B* **2014**, *118*, 4527−4534.
(48) Fisher, M.; Devlin, J. P. Defect Activity in Amorphous Ice from Isotopic Exchange Data: Insight into the Glass Transition. *J. Phys. Chem. A* **1995**, *99*, 11584−11590.
(49) Henrikus, S. S.; Tassis, K.; Zhang, L.; van der Velde, J. H. M.; Gebhardt, C.; Herrmann, A.; Jung, G.; Cordes, T. Characterization of Fluorescent Proteins with Intramolecular Photostabilization. *ChemBioChem* **2021**, *22*, 3283−3291.
(50) Tuijtel, M. W.; Koster, A. J.; Jakobs, S.; Faas, F. G. A.; Sharp, T. H. Author Correction: Correlative Cryo Super-Resolution Light and Electron Microscopy on Mammalian Cells Using Fluorescent Proteins. *Sci. Rep.* **2022**, *12*, No. 10897.
(51) Bourgeois, D. Single Molecule Imaging Simulations with Advanced Fluorophore Photophysics. *Commun. Biol.* **2023**, *6*, 1−13.
(52) Thevathasan, J. V.; Kahnwald, M.; Cieśliński, K.; Hoess, P.; Peneti, S. K.; Reitberger, M.; Heid, D.; Kasuba, K. C.; Hoerner, S. J.; Li, Y.; Wu, Y.-L.; Mund, M.; Matti, U.; Pereira, P. M.; Henriques, R.; Nijmeijer, B.; Kueblbeck, M.; Sabinina, V. J.; Ellenberg, J.; Ries, J. Nuclear Pores as Versatile Reference Standards for Quantitative Superresolution Microscopy. *Nat. Methods* **2019**, *16*, 1045−1053.
(53) Patterson, G. H.; Lippincott-Schwartz, J. A Photoactivatable GFP for Selective Photolabeling of Proteins and Cells. *Science* **2002**, *297*, 1873−1877.
(54) Renz, M.; Wunder, C. Internal Rulers to Assess Fluorescent Protein Photoactivation Efficiency. *Cytometry, Part A* **2018**, *93*, 411−419.

https://doi.org/10.1021/jacs.3c01500
J. Am. Chem. Soc. 2023, 145, 14636−14646

ADVANCED SCIENCE Open Access
www.advancedscience.com

Structural Heterogeneity in a Phototransformable Fluorescent Protein Impacts its Photochemical Properties

Arijit Maity, Jip Wulffelé, Isabel Ayala, Adrien Favier, Virgile Adam, Dominique Bourgeois, and Bernhard Brutscher**

Photoconvertible fluorescent proteins (PCFP) are important cellular markers in advanced imaging modalities such as photoactivatable localization microscopy (PALM). However, their complex photophysical and photochemical behavior hampers applications such as quantitative and single-particle-tracking PALM. This work employs multidimensional NMR combined with ensemble fluorescence measurements to show that the popular mEos4b in its Green state populates two conformations (A and B), differing in side-chain protonation of the conserved residues E212 and H62, altering the hydrogen-bond network in the chromophore pocket. The interconversion (protonation/deprotonation) between these two states, which occurs on the minutes time scale in the dark, becomes strongly accelerated in the presence of UV light, leading to a population shift. This work shows that the reversible photoswitching and Green-to-Red photoconversion properties differ between the A and B states. The chromophore in the A-state photoswitches more efficiently and is proposed to be more prone to photoconversion, while the B-state shows a higher level of photobleaching. Altogether, this data highlights the central role of conformational heterogeneity in fluorescent protein photochemistry.

1. Introduction

Green-to-red photoconvertible fluorescent proteins (PCFPs) play a central role in advanced fluorescence microscopy approaches such as single molecule localization microscopy (SMLM).[1] A number of such PCFPs have been derived from the tetrameric *Lobophyllia hemprichii* EosFP coral protein,[2] such as the popular mEos3.2, mEos4b, PCStar, and mEosEM.[3–6] The mEos4b and mEosEM variants are particularly resistant to fixation conditions, including the conditions required for correlative light and electron microscopy.[4,6] mEos4b, like other PCFPs of anthozoan origin, bears a histidine as the first amino acid of the chromophore triad (His-Tyr-Gly) that autocatalytically maturates into a p-HBI (4-(p-hydroxybenzylidine)−5-imidazolinone) chromophore (Green-state). Green-to-Red photoconversion then proceeds through absorption of a violet photon by the protonated neutral p-HBI chromophore (**Figure 1**). Photoconversion leads to backbone breakage at the CA atom linking residues F61 and H62 (mEos4b notation), resulting in increased chromophore electron conjugation and bathochromic shifts of the excitation and emission wavelengths.[7] The Green-state of mEos4b also shows substantial photochromism (Figure 1).[8] Upon illumination with cyan light (488-nm), mEos4b switches to a non-fluorescent Off-state, involving *cis-to-trans* isomerization and protonation of the chromophore. Contrary to photoconversion, on-to-off switching can be reversed by applying UV light (405 nm).

The photoconversion mechanism of Eos-like PCFPs has been intensely discussed in the literature, but remains incompletely understood.[7,9–14] Deciphering this mechanism is of key importance to better understand photoconversion kinetics and efficiency.[15–17] A number of scenarios have been proposed, involving β-elimination of type I or II,[7,10–13] histidine rotamer adjustment,[13] intersystem crossing to the triplet state,[11] radical formation,[14] and quadrupolar electrostatic coupling between neighboring residues.[18] A consensus between these mechanisms is that the fully conserved E212 plays an essential role. Mutation of E212 to glutamine is known to abolish photoconversion.[7,19] However, the exact role of E212 along the photoconversion pathway remains questioned.

In all known anthozoan PCFPs, E212 is part of a conserved Q38-E212-H194-E144 amino-acid motif, located directly beneath the chromophore (**Figure 2C**). Residues in this motif form a hydrogen-bond network that contributes to stabilize the chromophore in the protein scaffold. Intriguingly, E212 is observed to adopt an ill-defined conformation in crystallographic structures of some PCFPs,[3,20–22] and in some cases, ensemble refinement procedures suggest a large set of conformations.[8] This local

A. Maity, J. Wulffelé, I. Ayala, A. Favier, V. Adam, D. Bourgeois, B. Brutscher
CEA
CNRS
Institut de Biologie Structurale (IBS)
Université Grenoble Alpes
71 avenue des Martyrs, Cedex 9, Grenoble 38044, France
E-mail: dominique.bourgeois@ibs.fr; bernhard.brutscher@ibs.fr

The ORCID identification number(s) for the author(s) of this article can be found under https://doi.org/10.1002/advs.202306272

DOI: 10.1002/advs.202306272

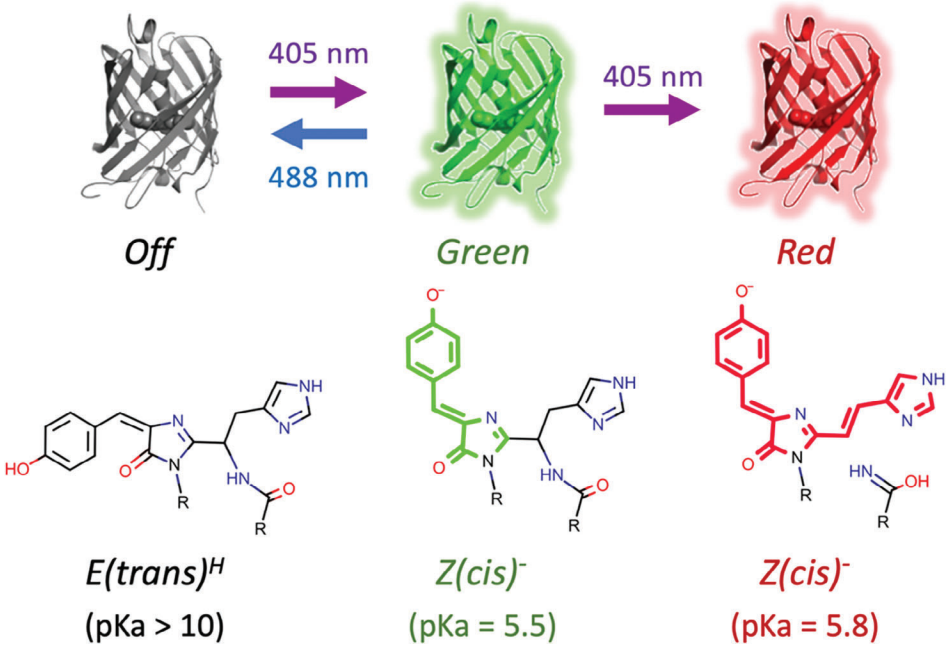

Figure 1. Phototransformations of Green mEos4b and corresponding chromophore structure and isomeric states. The relative population of protonated neutral and deprotonated anionic chromophore species can be derived from the chromophore pKa values given for each state.

heterogeneity of E212 might be fundamentally related to the enhanced flexibility of the chromophore pocket that seems to be necessary to catalyze photoconversion in PCFPs.[23]

Recently, solution NMR spectroscopy has demonstrated its potential for investigating the conformational dynamics of reversibly switchable fluorescent proteins,[24–26] providing crucial information on the conformation and protonation states of the chromophore moiety and neighboring amino acid side chains.[26] Here, we investigate by solution NMR and fluorescence approaches the conformational dynamics of mEos4b. We find that this PCFP exhibits two well-defined conformational Green states that differ in terms of protonation and H-bonding patterns of amino-acid side chains in the chromophore pocket. We also study the exchange kinetics and thermodynamics of the two Green states in the dark and under UV illumination. Moreover, we discuss differences in the reversible photoswitching of both states, and conformational heterogeneities in the photoswitched Off-state. Finally, we perform in situ NMR photoconversion experiments at different illumination power levels, which allow us to propose a photophysical model that accounts for the observed photoconversion kinetics.

2. Results and Discussion

2.1. Conformational Green-State Heterogeneity of mEos4b

Despite the fact that X-ray diffraction data of mEos4b crystals at cryogenic temperatures could be well fitted to a single protein conformation,[27] solution NMR data showed a pronounced conformational heterogeneity of mEos4b in its Green state (Figure 2A). Sequential backbone NMR assignments revealed the presence of two distinct conformations, in the following termed A- and B-states, that coexist with relative populations of 57 ± 2% (A-state) and 43 ± 2% (B-state) under the chosen experimental conditions. Interestingly, similar NMR spectral features are also observed for two other variants of the mEos family, PCStar, and the Dendra-like[22] mEos4b-V69T mutant (Figure S1, Supporting Information), suggesting that the observed conformational Green-state heterogeneity is a general feature of EosFP-derived PCFPs.

Mapping the observed ^{1}H, ^{15}N chemical shift variations between the A- and B-states on the structure of mEos4b (Figure 2B and Figure S2, Supporting Information) reveals the largest differences for residues in β-strands β3, β10 and β11 facing the histidine and phenol moieties of the chromophore, and harboring the first 3 amino-acid residues of the highly conserved and functionally important Q38-E212-H194-E144 motif. Distinct CD_1-H and CD_2-H (as well as CE_1-H and CE_2-H) correlation peaks could be detected for the symmetry-related C-H sites of the chromophore's phenol moiety (Figure S3, Supporting Information), indicative of slow ring-flip dynamics. Interestingly, only the ^{13}C-^{1}H groups on one side of the phenol are sensitive to the A/B-state heterogeneity, resulting in slightly different NMR signals that we could unambiguously assign to the phenol side pointing toward the side chain of E212 (Figure 2C and Figure S4A, Supporting Information). The A/B exchange kinetics is slow ($k_{ex} < 1\ s^{-1}$) at 35 °C as deduced from the observation of distinct NMR signals for A and B, and the absence of cross peaks detected in EXSY spectra.[28]

2.2. Coupled Protonation/Deprotonation Events in the Chromophore Pocket of mEos4b

In view of these initial NMR observations, and the fact that E212 is often not well defined in crystal structures of Eos-like

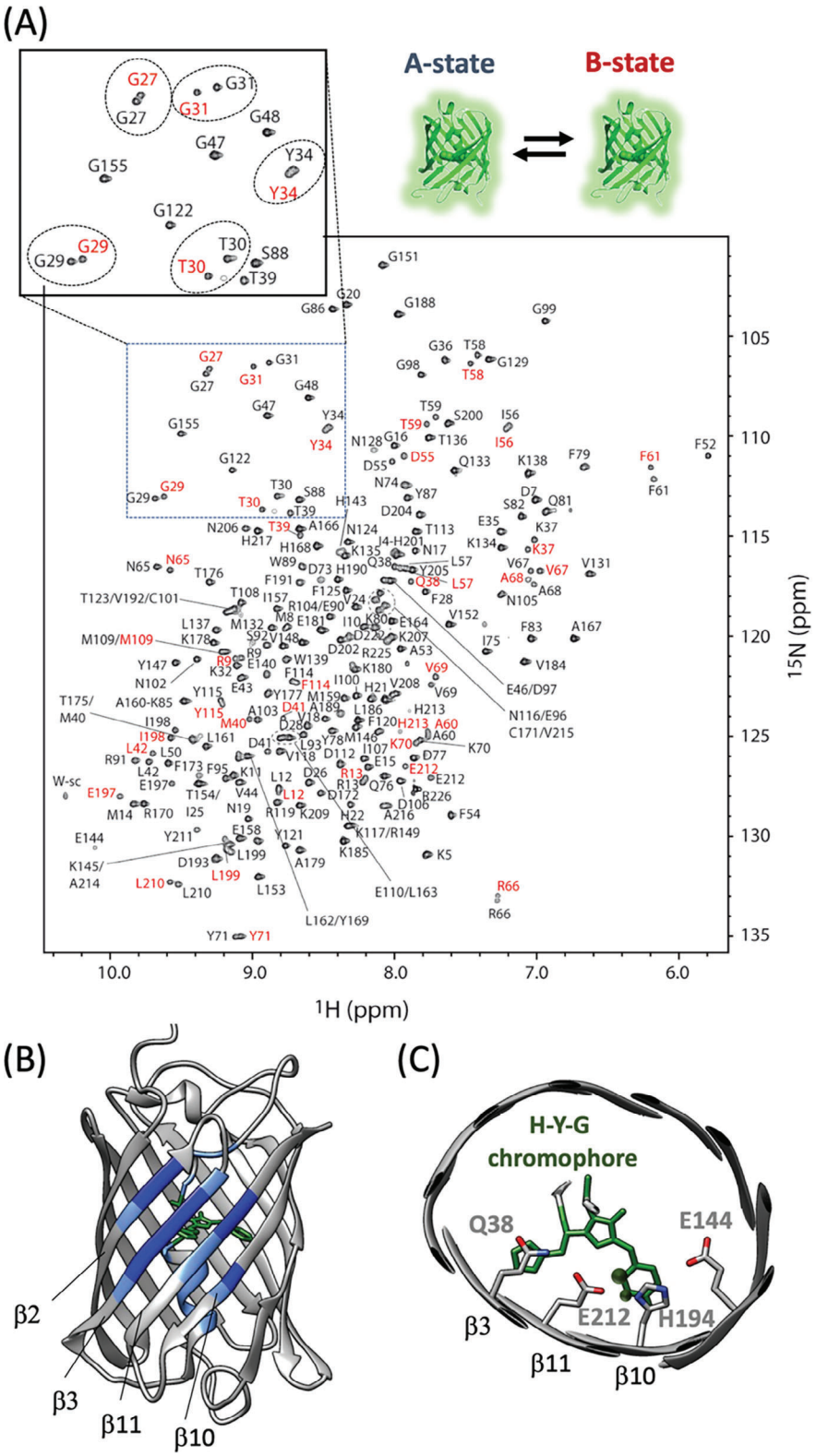

Figure 2. mEos4b Green-state heterogeneity. A) ^{1}H-^{15}N correlation spectrum recorded at 35 °C and pH 7.5. Cross peaks are annotated by their residue type and number. Well resolved B-state peaks are highlighted in red. B) Large chemical shift changes between the A- and B-states are color-coded (dark blue: $\Delta\delta_{HN} > 1.0$ ppm; light blue: 0.5 ppm $< \Delta\delta_{HN} < 1.0$ ppm) on the crystal structure of mEos4b Green-state (PDB 6GOY). C) Structural view of the chromophore in the mEos4b β-barrel, and the Q38-E212-H194-E144 motif. Chromophore ^{1}H-^{13}C moieties that show NMR peak doubling are indicated by black balls.

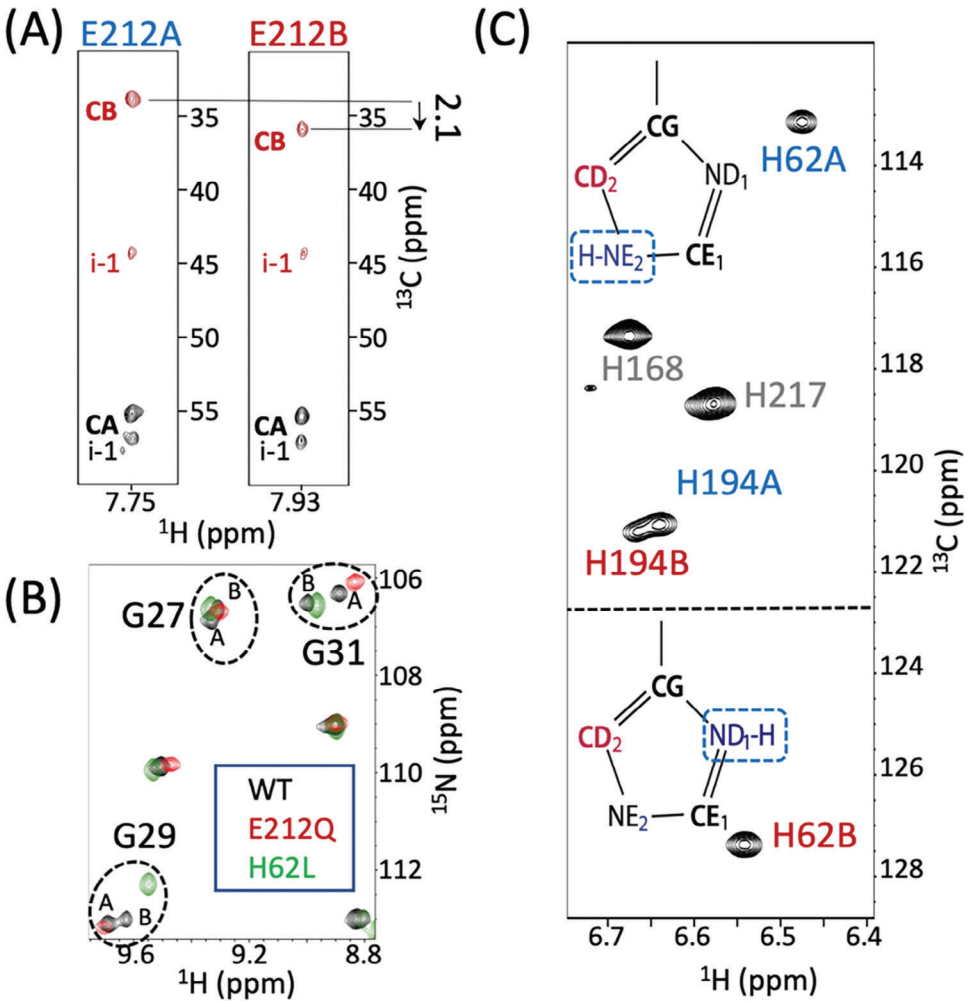

Figure 3. Protonation/deprotonation equilibria in Green mEos4b. A) Strips from a 3D Best-TROSY HNCACB correlation spectrum,[30] extracted at the ^{15}N frequencies of E212 in the A- and B-states. B) Spectral overlay (glycine region) of mEos4b WT (black), E212Q (red), and H62L (green) mutants. C) Tautomeric states of H62 and H194 side chains in the A- and B-states, deduced from characteristic ^{13}C chemical shifts at CD2 position.

PCFPs,[21,22] we hypothesized that E212 protonation at its carboxylic side-chain could be involved in the observed conformational heterogeneity. We therefore measured the ^{13}CB chemical shifts of E212 in the A- and B-states (**Figure 3**A) as a reporter of its side chain protonation. The measured chemical shift difference of +2.1 ppm is in good agreement with reported values for glutamate deprotonation.[28] In order to further validate the implication of E212 in the observed Green-state heterogeneity, we performed additional NMR experiments on a mEos4b E212Q mutant that cannot undergo deprotonation at its side chain. Indeed, the recorded NMR spectra (Figure 3B) are in agreement with the presence of a single conformation, and ^{13}C chemical shifts that closely match those of the wild-type (WT) A-state (Figure S5, Supporting Information). Therefore, we can conclude that the A-state corresponds to a conformation with a protonated E212 (E212^{OH}), while the B-state is characterized by a negatively charged E212 (E212^{O-}).

A-B state heterogeneity was also detected for two histidine side chains, H194 that is part of the Q38-E212-H194-E144 motif, as well as H62, the first residue of the chromophore-forming tripeptide (Figure 3C). While only small chemical shift differences are detected for the ^{13}CD$_2$-^{1}H spin pair of H194, a 14-ppm chemical shift difference is detected for the ^{13}CD$_2$ of H62 between the A- and B-states. The ^{13}C chemical shift of CD$_2$ is particularly sensitive to the tautomeric state of the imidazole,[28,29] and the observed chemical shift values imply that H62 mainly populates the NE$_2$-H tautomer in the A-state, while the ND$_1$-H tautomer is stabilized in the B-state.

In order to investigate whether the presence of the H62 side chain is required for the observed partitioning of the E212 side-chain protonation state, we prepared a mEos4b-H62L mutant. No peak doubling, and thus no conformational heterogeneity, was observed in the NMR spectra of this Skylan-NS like[31] mutant (Figure 3B). Our NMR data thus point toward a coupled mechanism at the origin of the Green-state heterogeneity, where the protonation/deprotonation of the E212 side chain carboxylate is accompanied by a tautomeric state change of the imidazole ring of H62, and vice versa. The protonation patterns can thus be described as E212^{OH}-H62^{E2H} (A-state) and E212^{O-}-H62^{D1H} (B-state).

2.3. Green mEos4b A- and B-State Conformation and Dynamics

The chromophore's hydroxyphenyl moiety is deprotonated at ≈97% at pH ≥ 7.5, as deduced from the reported pKa and Hill coefficient,[4] and confirmed by the absence of a pronounced absorbance band at 400 nm (Figure S6A, Supporting Information), and characteristic ^{13}C chemical shifts of the hydroxyphenyl ring carbon CZ (Figure S4A, Supporting Information). NMR also provides information about chromophore rigidity, and in particular ring-flip rates about the phenoxy bond of the chromophore's methine bridge.[26] Such ring-flip measurements for mEos4b at pH 8.5 and 35 °C reveal that the chromophore is structurally well stabilized in both A- and B-state conformations, with ring-flip rates $k_{RF} < 1\ s^{-1}$ (Figure S4B, Supporting Information).

Additional structural information about the involvement of histidine side chains in hydrogen-bond interactions is obtained from histidine ^{1}H-^{15}N correlation spectra.[32] At neutral pH, the labile nitrogen-bound imidazole hydrogens only become NMR observable if they are protected from chemical exchange with the solvent by hydrogen bonding. For mEos4b, a total of 5 imidazole ^{1}H-^{15}N correlation peaks could be detected (**Figure 4A**) and unambiguously assigned to H62, H194, as well as His190 (Figure S7A, Supporting Information). Again, H62 and H194 give rise to distinct correlation peaks for the A- and B-state conformations, revealing their engagement in hydrogen bonding interactions in both states.

The imidazole ^{1}H-^{15}N correlation peaks detected for H62 and H194 show a distinctive temperature dependence. For H194, the weak peaks detected at 35 °C become significantly enhanced at 15 °C (Figure 4A). This suggests that H194 hydrogen-bonding is stabilized at low temperature in both the A- and B-states. The crystallographic structure indicates a H-bond-compatible short interatomic distance between the protonated imidazole nitrogen (NE_2) of H194 and the carboxylic side chain group of E144 ($R_{O\text{-}N}$ = 2.8 Å). The most likely H-bonding networks in this important Q38-E212-H194-E144 motif are depicted in Figure 4B (and Figure S8A, Supporting Information), 4C (and Figure S8B, Supporting Information) for the A- and B-states, respectively. Our NMR data, however, highlight that the H-bond formed between E144 and H194 is highly dynamic at elevated temperature (35 °C). The presence of milliseconds time-scale motions in the chromophore pocket of mEos4b is confirmed by extensive exchange line broadening observed for NMR signals of backbone amides located on strands β7 (142-144), β10 (212-213), and β11 (194-196) comprising E144, H194, and E212. The situation is strikingly different for H62. In the A-state, the ^{1}H-^{15}N correlation peak detected at 35 °C (and 700 MHz ^{1}H frequency) is about a factor of 3 weaker than the corresponding signal observed for the B-state, despite the slightly higher A-state population. The NMR intensity becomes further reduced at lower temperature, and the peak completely disappears (intensity below noise threshold) at T ≤ 15 °C. The magnetic field dependence of the NMR peak intensities (Figure S7B, Supporting Information) indicates an exchange process in the A-state that is fast on the NMR chemical shift time scale $k_{ex} \gtrsim 100\ s^{-1}$ ($\nu_A - \nu_{A'}$). Exchange line broadening is also observed for the two ^{1}H-^{13}C spin pairs in the imidazole ring of the H62 A-state with a similar temperature and magnetic field dependence (Figure S7C, Supporting Information). Our NMR data are thus in agreement with a model where H62 in the A-state exchanges between two (or more) H-bonded conformations, while in the B-state, hydrogen-bonding of H62 is only little temperature dependent, indicative of a strongly H-bonded conformation.

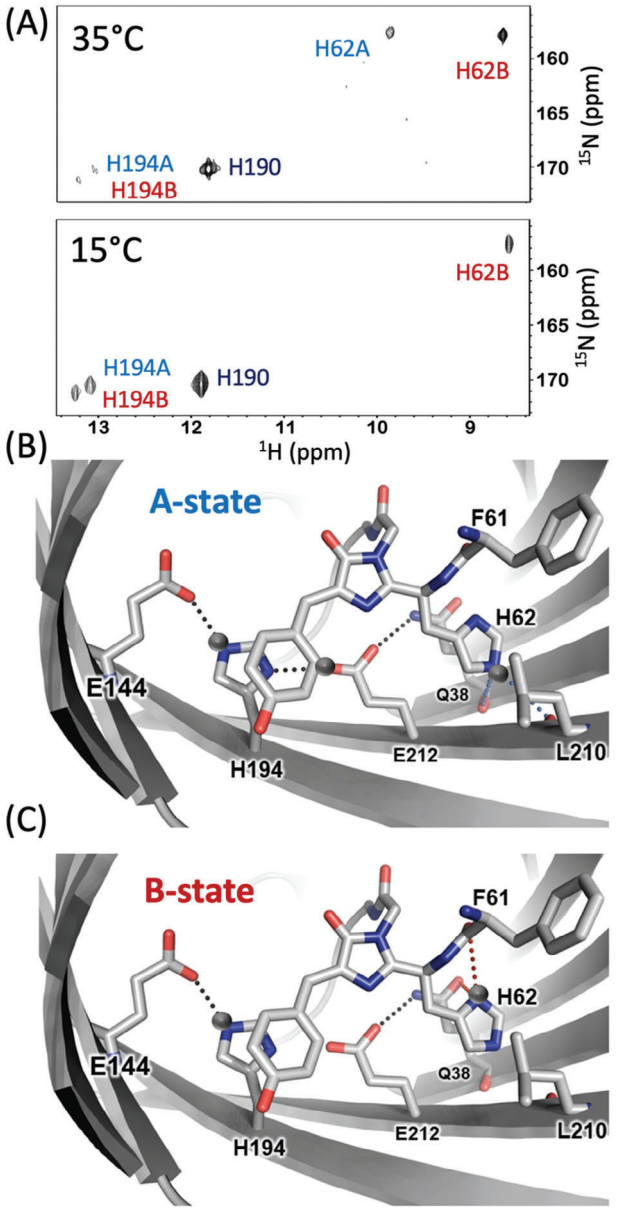

Figure 4. Hydrogen bonding patterns in Green mEos4b A- and B-states plotted on the crystal structure (PDB 6GOY). A) ^{1}H-^{15}N histidine SOFAST-HMQC[33] spectra of mEos4b recorded at 700 MHz and 15 °C (left), 35 °C (right). B,C) Potential H-bonds (dashed lines) involving the Q38-E212-H194-E144 motif and the H62 side chain in the A- and B-states as inferred from the crystal structure and the NMR data. Protonation of the H62, H194, and E212 side chains is indicated by grey balls. A different view of these conformational states is provided in Figure S9, Supporting Information.

In the crystallographic structure, neither H62 NE_2 (A-state) nor ND_1 (B-state) is found at H-bond-compatible short interatomic distance to potential hydrogen acceptors. Thus, the low-temperature X-ray structure does not reflect the conformational

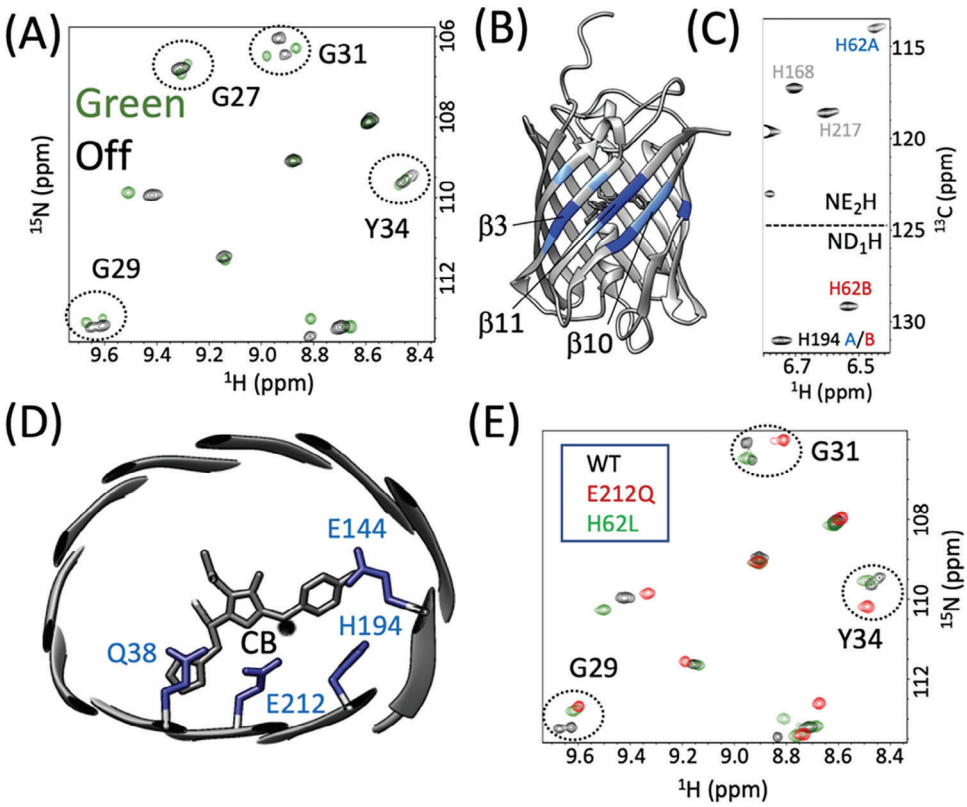

Figure 5. Off-state conformational heterogeneity. A) Spectral overlay (glycine region) of mEos4b Green- (green) and Off-state (black) ^{1}H-^{15}N spectra (35 °C, pH 7.5). B) Large chemical shift differences between the A- and B-states are color-coded on the crystal structure of mEos4b Off-state (PDB: 6GOZ). C) Tautomeric states of H62 and H194 side chains in the Off A- and B-states, deduced from characteristic $^{13}CD_2$ chemical shifts. D) Structural view of the E(trans) chromophore and Q38-E212-H194-E144 motif in the Off-state (left). The ^{13}CB-1H moiety (blue ball) of the chromophore shows peak doubling. E) Off-state ^{1}H-^{15}N spectra of mEos4b WT (black), E212Q (red), and H62L (green) mutants. The peak doubling observed for residues G29, G31, and Y34 in the WT is not observed in the two mutants.

side-chain arrangements in the chromophore pocket of either the A- or B-states, but rather some population-weighted average. Figure 4B (and Figure S8A, Supporting Information), 4C (and Figure S8B, Supporting Information) show the most likely H-bond patterns of H62 in the A- and B-states, according to the crystal structure ($R_{O\text{-}N}$ distances ranging between 3.3 and 3.7 Å).

2.4. Conserved A/B-State Heterogeneity in Photoswitched Off-State

Photoswitching of mEos4b involves a *Z(cis)* to *E(trans)* isomerization of the chromophore accompanied by protonation of the chromophore's tyrosine moiety (Figure 1).[27] We therefore questioned whether the conformational Green-state heterogeneity is conserved in the photoswitched Off-state. NMR experiments of mEos4b under continuous 488-nm illumination revealed the presence of two major conformational Off-states (**Figure 5**A). We could quantify the relative Off-state populations to 45 ± 3% A and 55 ± 3% B. Plotting the observed amide ^{1}H-^{15}N chemical shift differences between the Off-A and Off-B states points again to the β-barrel region covering strands β3, β10, and β11 (Figure 5B and Figure S9, Supporting Information).

At the chromophore level, peak doubling is now observed for the ^{1}H-^{13}C pair of the methine bridge CB-site that in the crystal structure of the Off-state is located close to the carboxylic side chain of E212 (Figure 5D and Figure S3, Supporting Information). A ^{13}CB chemical shift difference of 1.3 ppm between the Off-A and Off-B states again suggests a change in protonation state of the E212 side chain. Also the tautomeric state difference of H62 between A and B is conserved in the Off-state, while the imidazole side chain of H194 switches from a (NE_2-H)-tautomer in the Green-state to a (ND_1-H)-tautomer in the Off-state (Figure 5C). Similarly to our observations for the Green-state, mutating either H62 or E212 removes this Off-state conformational heterogeneity (Figure 5E).

2.5. UV Light Dependence of Green A/B-State Equilibrium

Photoconversion of mEos4b from a Green to a Red fluorescent state requires UV light (Figure 1). We thus investigated the effect of UV illumination on the Green A- and B-state populations. Under weak illumination conditions, where photoconversion kinetics are slow, we observed a partial conversion from the A- to the B-state (**Figure 6**A). At a power density of ≈25 mW cm^{-2} the equilibrium B-state population has increased from 43% (in the

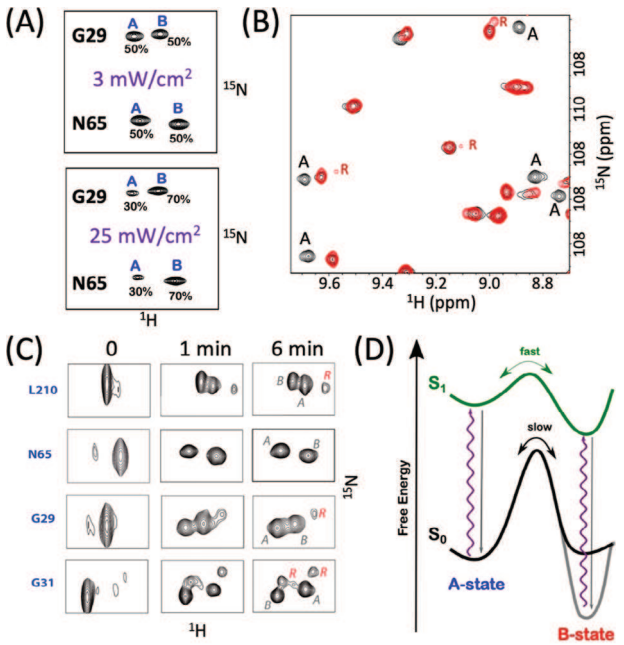

Figure 6. Free energy landscape of Green mEos4b. A/B-state equilibrium at A) low-power and B) high-power (≈250 mW cm^{-2}) UV (405 nm) illumination (red contours). C) A-B exchange kinetics as experienced by 4 amide backbone sites in mEos4b after short (a few seconds) high power UV illumination. The first time point (0) has been recorded in a short acquisition time (1 min) resulting in apparent broader lines in the ^{15}N dimension. Red-state peaks that appear as a result of photoconversion under UV illumination are annotated ("R"). D) Schematic energy landscape of Green mEos4b in the ground (S_0) and electronically excited (S_1) states. The black and grey lines correspond to dark and UV-light conditions, respectively.

dark) to about 70%. Increasing the UV power density by another order of magnitude (≈250 mW cm^{-2}) results in only a slight further shift of the A/B-state equilibrium to ≈80% B-state (Figure 6B and Figure S10, Supporting Information). This finding suggests that even at the high power levels used in SMLM modalities, the A-state remains populated to a significant extent.

This UV-induced population shift allowed unambiguous identification of A- and B-state peaks. Furthermore, it provided an opportunity to quantify the slow A/B exchange kinetics in the dark by off-equilibrium real-time 2D NMR. Figure 6C shows the thermal recovery of the A/B state population equilibrium at pH 7.5 and 35 °C after a short high-power UV light pulse. These data fit to an A-B exchange with a rate constant $k_{ex} = 2 \pm 1\ 10^{-2}\ s^{-1}$. Our observations imply that in the electronically excited S_1 state, the B-state conformation is energetically favored with respect to the A-state. UV power densities of a few mW cm^{-2} are sufficient to create conditions where mEos4b molecules are efficiently shuffled from the A- to the B-state (Figure 6D).

2.6. Green-to-Off Photoswitching

The ability to change the relative A/B-state population ratio by UV light enabled us to investigate how the conformational heterogeneity influences the photophysics of mEos4b. Ensemble fluorescence measurements using an alternation of cyan (488 nm) and violet (405 nm) light was used to check for differences in photoswitching kinetics and contrast between the A- and B-states (**Figure** 7A). The first switching cycle starts from thermodynamic equilibrium, with an A/B state population ratio (≈57%/43%), while subsequent cycles are representative of the switching behavior of an A/B-state population ratio (≈30%/70%). The UV power was adjusted to allow a significant A-to-B population shift and effective off-to-on back switching, but limited Green-to-Red photoconversion. Interestingly, faster fluorescence intensity decay is observed for the first cycle compared to cycles recorded after an UV light pulse (Figure 7B). Adding a thermal relaxation delay makes the system again behave similar to the first cycle (Figure S11, Supporting Information). We ascribe this different switching behavior to the UV-induced change in A/B population ratio. Fitting our kinetic data to a bi-exponential model, accounting for 2 independently switching states (A and B) with different kinetics and switching contrast, revealed that photoswitching in the A-state is about four times faster than in the B-state (Figure 7D). We also measured photo-switching kinetics for the mEos4b E212Q and H62L mutants that both populate a unique conformation which, in the case of E212Q, resembles the WT A-state (Figure 7A,B). In both cases, photoswitching is 4–5 times faster than the A-state of mEos4b-WT, and no difference between switching cycles is observed in agreement with our assumption that this difference is mainly caused by the UV light-induced changes of the A/B-state equilibrium.

Our data fitting also provides a measure of the apparent switching contrast for the A- and B-states. The faster switching A-state shows a higher apparent switching contrast (lower residual Off-state fluorescence) than the slower switching B-state (Figure 7C). The correlation between faster switching kinetics and higher contrast, previously observed in several RSFPs,[8,34,35] also holds true for the two mEos4b mutants E212Q and H62L that both have an apparent switching contrast of more than 200. Our observation of a moderate switching contrast (< 30) of both the A- and B-states of mEos4b, as deduced from fluorescence measurements, is not fully in line with the residual Green-state population detected in the Off-state NMR spectra recorded under 448-nm illumination (Figure 7E). An apparent NMR switching contrast of 65 ± 15 is obtained from the average (and standard deviation) of intensity ratios measured for 30 well resolved Green-state signals that do not overlap with any Off-state peak. This value is more than a factor of 2 higher than the switching contrast derived from fluorescence measurements (Figure 7C). Residual Off-state fluorescence is generally ascribed to an incomplete conformational transition from a fluorescent *Z(cis)*$^-$ to a non-fluorescent *E(trans)*^{H} chromophore configuration due to residual on-switching by the off-switching cyan light. Moreover, fluorescence measurements revealed a *E(trans)* chromophore pKa > 10 in mEos4b (Figure S12, Supporting Information), in line with previous reports,[36] suggesting an insignificant amount of fluorescent anionic *E(trans)* chromophores at pH 7.5. Our NMR data thus show that additional factors influence the observed switching contrast in fluorescence measurements.

2.7. Green-to-Red Photoconversion

We further investigated by NMR Green-to-Red photoconversion at low UV illumination power (≈2.5 to 25 mW cm^{-2}). Under

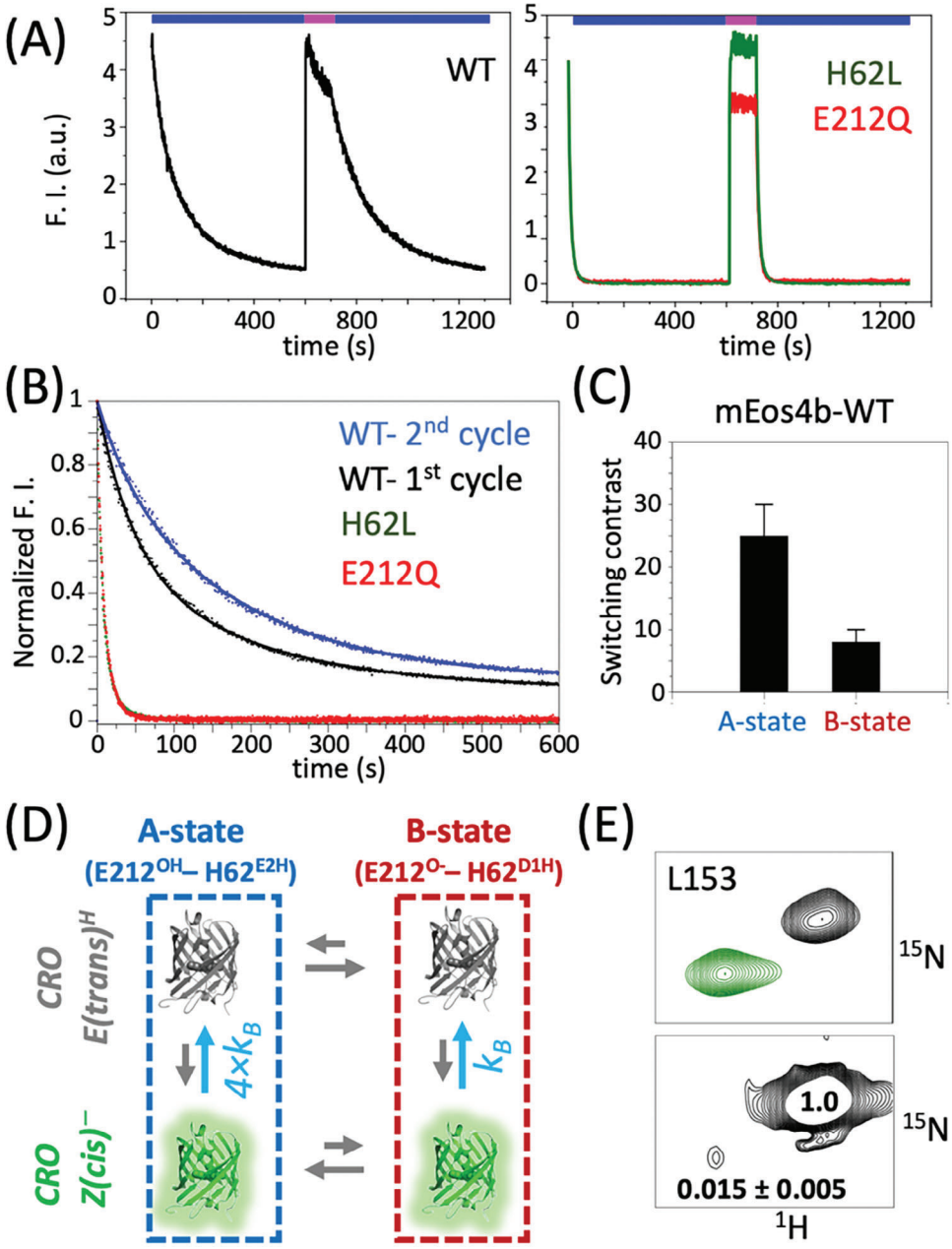

Figure 7. Photoswitching properties of mEos4b under 488-nm illumination. A) Fluorescence intensity of mEos4b-WT, E212Q and H62L mutants measured by applying a UV-cyan light illumination scheme (indicated on top) B) Superposition of different switching cycles: WT first cycle (black), second cycle (blue); for E212Q (red) and H62L (green), the first 2 switching cycles are superposed. C) Apparent fluorescence switching contrast of WT A- and B-states, obtained by global fitting the Green-state decay (first and second) cycle assuming different A- and B-state populations. D) On-to-off photoswitching model for mEos4b. E) NMR derived switching contrast, exemplified for the amide spin pair of residue L153. The upper spectrum shows a superposition of the Green- (green) and Off-state (black) spectra, while the lower graph shows the same Off-state spectrum plotted at low contour levels in order to observe the residual Green-state peak.

these conditions the A/B state population ratio can be tuned by the applied UV power as demonstrated above (Figure 6A), and photoconversion occurs on timescales of minutes to hours, that are compatible with real-time 2D NMR data acquisition.

Many residues in mEos4b experience distinct ^{1}H-^{15}N chemical shifts in the Green- and Red-states (Figure S13, Supporting Information) thus allowing to follow NMR peak intensity changes simultaneously for the Green- and Red-states during photoconversion. **Figure** 8A shows Green-state decay and Red-state build-up curves for selected ^{1}H-^{15}N pairs that show no peak doubling and give rise to well-resolved ^{1}H-^{15}N correlation peaks in both the Green- and Red-state NMR spectra. The plotted data have been recorded with UV power densities of 3 (top panel) and 25 mW cm^{-2} (bottom panel), measured at the sample top. The

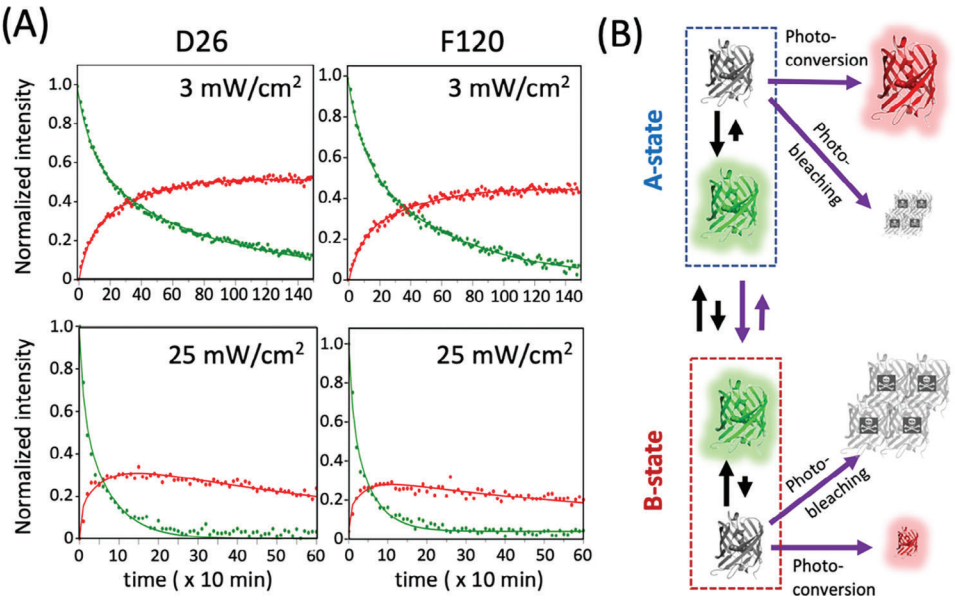

Figure 8. mEos4b Green-to-Red photoconversion. A) NMR real time data recorded under continuous UV (405-nm) illumination at different light power densities. Green state decay and Red-state build-up curves are plotted for residues D26 and F120. The NMR-derived photoconversion efficiencies are ≈50% at 3 mW cm^{-2} and ≈30% at 25 mW cm^{-2}. B) Simple photoconversion model that accounts for the NMR kinetics data.

kinetic data extracted for a total of 6 mEos4b residues, comprising sites with distinct Green A- and B-state signatures, are well fitted to a biphasic kinetic model, assuming identical rate constants for Green-state decay and Red-state build-up, and relative amplitudes of 0.35 ± 0.05 for the fast phase and 0.65 ± 0.05 for the slow phase (Figure S14, Supporting Information). Undistinguishable Green-state decay kinetics are observed for the A- and B-states, in agreement with fast A-B exchange kinetics compared to the photoconversion time scale. Both (fast and slow) kinetic rates increase linearly with the applied UV power density, indicating that the involved photochemical transformations are single-photon processes.

Apparent photoconversion efficiencies are obtained from the ratio between the maximal Red-state peak intensity reached during the kinetics and the initial Green-state intensity. As can be appreciated from Figure 8A, the photoconversion efficiency reaches up to ≈50% at very low UV power density (3 mW cm^{-2}), but decreases to ≤30% at 25 mW cm^{-2}. Assuming that Red-state photobleaching is also a single-photon process (in agreement with our NMR data), this observation suggests that the difference in the Green A/B-state population equilibrium may be at the origin of the observed drop in photoconversion efficiency with increasing UV power density. The observation that a higher A-state population correlates with an improved photoconversion efficiency suggests a photophysical model where photoconversion takes place predominantly in the A state, while Green-state photobleaching is more pronounced in the B state (Figure 8B). This simple model allows to reproduce the main features of our NMR data using SMIS[37] simulations (Figure S15 and Table S1, Supporting Information),

The NMR-derived photoconversion efficiencies of mEos4b are lower than what has been reported in the literature based on measurements at the single-molecule level.[38] This discrepancy may possibly be explained by the presence of strong additional illumination at 561 nm in optical microscopy experiments, resulting in enhanced photoconversion efficiencies.[39] We thus cannot exclude that photoconversion of mEos4b is based on a more complex scenario than the simple model proposed in Figure 8B, involving additional photo-induced transformations and states. Future NMR experiments in the presence of both illumination lasers will allow to address this issue.

2.8. Implications for the Photoconversion Mechanism(s) of mEos4b

Several mechanistic scenarios proposed in the literature assume as the starting point for photoconversion a conformation with H194 in an imidazolium cationic form.[11–13,18] Our NMR data clearly show that H194 adopts a neutral tautomeric form in the Green-state, strongly suggesting that photoconversion to the Red-state occurs in this form. Previous work by the Watcher group on the Least Evolved Ancestor (LEA) PCFP[18] emphasizes that a flexible chromophore environment is required for photoconversion, particularly at the level of H62 which likely needs to undergo conformational changes during the photoconversion process. Our data are fully consistent with this notion of a high conformational plasticity of the chromophore environment in the Green A state. Although NMR does not provide direct evidence of the photochemical mechanism at play, a photoconversion model similar to the one introduced by Kim et al.[13] and starting from the Green A-state, is in good agreement with our NMR data (Figure S16, Supporting Information).[13] This model proposes an excited state proton transfer (ESPT) from the protonated E212 to H62-ND_1 after transient rotamer adjustment of H62 bringing the E212 carboxylate and H62 imidazole in close proximity. Photoconversion then proceeds via concerted β-elimination involving backward proton shuttling from H62-CB to E212.

If photoconversion also occurs from the Green B-state, different scenarios are possible. First, a mechanism similar to that proposed by Fare et al.,[14] requiring E212 to act as a base and involving rapid formation of the ethylenic CA=CB bond on H62 followed by slow decay of a cationic imidazole radical, could constitute a plausible scenario. In the B-state, H62 is singly protonated at its ND_1 and is thus poised for excited state proton transfer to F61. Hence, the mechanism proposed by Lelimousin et al.[11] may also be possible, involving the triplet state and not requiring any proton shuttling from E212. Such a mechanism could in fact relate to so-called primed photoconversion in Dendra2 variants,[40,41] in which E212 maintains a salt bridge with R66 and may thus be predominantly deprotonated as observed for the B state.

3. Conclusion

PCFPs are an essential tool for super-resolution fluorescence microscopy. A better understanding of the photophysical and photochemical pathways underlying photoconversion and photoswitching is essential for future efforts aiming at engineering improved PCFP variants for particular applications. Most of the mechanistic knowledge reported in the literature has been derived from crystallographic structures and quantum-chemical calculations. Here, we have demonstrated that solution NMR spectroscopy provides critical additional information on conformational dynamics and structural heterogeneity in the chromophore pocket of PCFPs from the Eos family. Two conformations of similar free energy coexist in solution, and their populations (free energies) and exchange kinetics (free energy barriers) are modulated by UV light. Furthermore, we could establish that the two NMR-observed Green states correspond to different local hydrogen-bond networks caused by a concerted change in the protonation state at the side chains of H62 and E212. Finally, combining NMR and fluorescence data we could show how these two states differ in terms of their photoswitching and photoconversion behavior, and shed some new light on the underlying mechanisms.

The faster photoswitching kinetics of the Green A-state relative to the B-state should be taken into account when EosFP-derived RSFPs are employed in applications exploiting photoswitching rates quantitatively.[42] In PALM applications, our hypothesis that photoconversion is more efficient starting from the Green A-state would suggest the use of low-UV illumination schemes to minimize B-state occupancy and maximize photoconversion efficiency. However, such a strategy might be challenged by practical considerations (e.g., PALM data collection time) and additional complexity in PCFP's photophysics such as photobleaching by readout light.[43] The possibility to engineer mEos4b variants experiencing a population shift toward the Green A-state offers an interesting perspective. However, the fundamental question of whether photoconversion capability and A/B-state heterogeneity are intimately coupled should be addressed first.

In summary, we have shown that adding solution NMR spectroscopy with in situ sample illumination capabilities to the panoply of biophysical techniques used for the characterization of fluorescent protein markers improves our understanding of their photophysical and photochemical properties, as required for rational design and engineering of improved fluorescent protein variants.

Supporting Information

Supporting Information is available from the Wiley Online Library or from the author.

Acknowledgements

Financial support from iNEXT-Discovery (871037) funded by the Horizon 2020 program of the European Commission, and the Agence Nationale de la Recherche (grants no. ANR-20-CE11-0013-01 and ANR-22-CE11-0011-01) is acknowledged. This work used the platforms of the Grenoble Instruct-ERIC centre (ISBG; UAR 3518 CNRS-CEA-UGA-EMBL) within the Grenoble Partnership for Structural Biology (PSB), supported by FRISBI (ANR-10-INBS-0005-02) and GRAL, financed within the University Grenoble Alpes graduate school (Ecoles Universitaires de Recherche) CBH-EUR-GS (ANR-17-EURE-0003). IBS acknowledges integration into the Interdisciplinary Research Institute of Grenoble (IRIG, CEA).

Conflict of Interest

The authors declare no conflict of interest.

Data Availability Statement

The data that support the findings of this study are available from the corresponding author upon reasonable request.

Keywords

fluorescence, PCFP, protein, solution NMR, super-resolution microscopy

Received: September 1, 2023
Revised: November 29, 2023
Published online:

[1] D. M. Shcherbakova, P. Sengupta, J. Lippincott-Schwartz, V. V. Verkhusha, *Annu. Rev. Biophys.* **2014**, *43*, 303.
[2] J. Wiedenmann, S. Ivanchenko, F. Oswald, F. Schmitt, C. Röcker, A. Salih, K.-D. Spindler, G. U. Nienhaus, *Proc. Natl. Acad. Sci. USA* **2004**, *101*, 15905.
[3] M. Zhang, H. Chang, Y. Zhang, J. Yu, L. Wu, W. Ji, J. Chen, B. Liu, J. Lu, Y. Liu, J. Zhang, P. Xu, T. Xu, *Nat. Methods* **2012**, *9*, 727.
[4] M. G. Paez-Segala, M. G. Sun, G. Shtengel, S. Viswanathan, M. A. Baird, J. J. Macklin, R. Patel, J. R. Allen, E. S. Howe, G. Piszczek, H. F. Hess, M. W. Davidson, Y. Wang, L. L. Looger, *Nat. Methods* **2015**, *12*, 215.
[5] M. Zhang, Z. Fu, C. Li, A. Liu, D. Peng, F. Xue, W. He, S. Gao, F. Xu, D. Xu, L. Yuan, F. Zhang, Z. Xu, T. Xu, P. Xu, *Nano Lett.* **2020**, *20*, 2197.
[6] Z. Fu, D. Peng, M. Zhang, F. Xue, R. Zhang, W. He, T. Xu, P. Xu, *Nat. Methods* **2020**, *17*, 55.
[7] K. Nienhaus, G. U. Nienhaus, J. Wiedenmann, H. Nar, *Proc. Natl. Acad. Sci. USA* **2005**, *102*, 9156.
[8] E. De Zitter, J. Ridard, D. Thédié, V. Adam, B. Lévy, M. Byrdin, G. Gotthard, L. Van Meervelt, P. Dedecker, I. Demachy, D. Bourgeois, *J. Am. Chem. Soc.* **2020**, *142*, 10978.

[9] H. Mizuno, T. K. Mal, K. I. Tong, R. Ando, T. Furuta, M. Ikura, A. Miyawaki, *Mol. Cell* **2003**, *12*, 1051.
[10] H. Tsutsui, H. Shimizu, H. Mizuno, N. Nukina, T. Furuta, A. Miyawaki, *Chem. Biol.* **2009**, *16*, 1140.
[11] M. Lelimousin, V. Adam, G. U. Nienhaus, D. Bourgeois, M. J. Field, *J. Am. Chem. Soc.* **2009**, *131*, 16814.
[12] X. Li, L. W. Chung, H. Mizuno, A. Miyawaki, K. Morokuma, *J. Phys. Chem. B* **2010**, *114*, 16666.
[13] H. Kim, T. Zou, C. Modi, K. Dörner, T. J. Grunkemeyer, L. Chen, R. Fromme, M. V. Matz, S. B. Ozkan, R. M. Wachter, *Structure* **2015**, *23*, 34.
[14] C. Fare, L. Yuan, V. Cordon-Preciado, J. J. Michels, M. J. Bearpark, P. Rich, J. J. Van Thor, *J. Phys. Chem. B* **2020**, *124*, 7765.
[15] S. Wang, J. R. Moffitt, G. T. Dempsey, X. S. Xie, X. Zhuang, *Proc. Natl. Acad. Sci. USA* **2014**, *111*, 8452.
[16] D. Thédié, R. Berardozzi, V. Adam, D. Bourgeois, *J. Phys. Chem. Lett.* **2017**, *8*, 4424.
[17] J. Wulffele, D. Thédié, O. Glushonkov, D. Bourgeois, *J. Phys. Chem. Lett.* **2022**, *13*, 5075.
[18] H. Kim, T. J. Grunkemeyer, C. Modi, L. Chen, R. Fromme, M. V. Matz, R. M. Wachter, *Biochemistry* **2013**, *52*, 8048.
[19] G. U. Nienhaus, K. Nienhaus, A. Hölzle, S. Ivanchenko, F. Renzi, F. Oswald, M. Wolff, F. Schmitt, C. Röcker, B. Vallone, W. Weidemann, R. Heilker, H. Nar, J. Wiedenmann, *Photochem. Photobiol.* **2006**, *82*, 351.
[20] V. Adam, K. Nienhaus, D. Bourgeois, G. U. Nienhaus, *Biochemistry* **2009**, *48*, 4905.
[21] J.-P. Colletier, M. Sliwa, F.-X. Gallat, M. Sugahara, V. Guillon, G. Schirò, N. Coquelle, J. Woodhouse, L. Roux, G. Gotthard, A. Royant, L. M. Uriarte, C. Ruckebusch, Y. Joti, M. Byrdin, E. Mizohata, E. Nango, T. Tanaka, K. Tono, M. Yabashi, V. Adam, M. Cammarata, I. Schlichting, D. Bourgeois, M. Weik, *J. Phys. Chem. Lett.* **2016**, *7*, 882.
[22] R. Berardozzi, V. Adam, A. Martins, D. Bourgeois, *J. Am. Chem. Soc.* **2016**, *138*, 558.
[23] R. Wachter, *Mol. Sci.* **2017**, *18*, 1792.
[24] H. Mizuno, T. K. Mal, M. Wälchli, A. Kikuchi, T. Fukano, R. Ando, J. Jeyakanthan, J. Taka, Y. Shiro, M. Ikura, A. Miyawaki, *Proc. Natl. Acad. Sci. USA* **2008**, *105*, 9227.
[25] N.-E. Christou, I. Ayala, K. Giandoreggio-Barranco, M. Byrdin, V. Adam, D. Bourgeois, B. Brutscher, *Biophys. J.* **2019**, *117*, 2087.
[26] N. E. Christou, K. Giandoreggio-Barranco, I. Ayala, O. Glushonkov, V. Adam, D. Bourgeois, B. Brutscher, *J. Am. Chem. Soc.* **2021**, *143*, 7521.
[27] E. De Zitter, D. Thédié, V. Mönkemöller, S. Hugelier, J. Beaudouin, V. Adam, M. Byrdin, L. Van Meervelt, P. Dedecker, D. Bourgeois, *Nat. Methods* **2019**, *16*, 707.
[28] G. Platzer, M. Okon, L. P. Mcintosh, *J. Biomol. NMR* **2014**, *60*, 109.
[29] J. A. Vila, Y. A. Arnautova, Y. Vorobjev, H. A. Scheraga, *Proc. Natl. Acad. Sci. USA* **2011**, *108*, 5602.
[30] Z. Solyom, M. Schwarten, L. Geist, R. Konrat, D. Willbold, B. Brutscher, *J. Biomol. NMR* **2013**, *55*, 311.
[31] X. Zhang, M. Zhang, D. Li, W. He, J. Peng, E. Betzig, P. Xu, *Proc. Natl. Acad. Sci. USA* **2016**, *113*, 10364.
[32] N. E. Christou, B. Brutscher, *J. Biomol. NMR* **2018**, *72*, 115.
[33] P. Schanda, B. Brutscher, *J. Am. Chem. Soc.* **2005**, *127*, 8014.
[34] V. Adam, K. Hadjidemetriou, N. Jensen, R. L. Shoeman, J. Woodhouse, A. Aquila, A.-S. Banneville, T. R. M. Barends, V. Bezchastnov, S. Boutet, M. Byrdin, M. Cammarata, S. Carbajo, N. E. Christou, N. Coquelle, E. De La Mora, M. El Khatib, T. M. Chicano, R. B. Doak, F. Fieschi, L. Foucar, O. Glushonkov, A. Gorel, M. L. Grünbein, M. Hilpert, M. Hunter, M. Kloos, J. E. Koglin, T. J. Lane, M. Liang, et al., *ChemPhysChem* **2022**, *23*, 202200192.
[35] S. Duwe, E. De Zitter, V. Gielen, B. Moeyaert, W. Vandenberg, T. Grotjohann, K. Clays, S. Jakobs, L. Van Meervelt, P. Dedecker, *ACS Nano* **2015**, *9*, 9528.
[36] S. Gayda, K. Nienhaus, G. U. Nienhaus, *Biophys. J.* **2012**, *103*, 2521.
[37] D. Bourgeois, *Commun. Biol.* **2023**, *6*, 53.
[38] N. Durisic, L. Laparra-Cuervo, Á. Sandoval-Álvarez, J. S. Borbely, M. Lakadamyali, *Nat. Methods* **2014**, *11*, 156.
[39] M. Sun, K. Hu, J. Bewersdorf, T. D. Pollard, *Biophys. J.* **2021**, *120*, 21.
[40] M. A. Mohr, A. Y. Kobitski, L. R. Sabater, K. Nienhaus, C. J. Obara, J. Lippincott-Schwartz, G. U. Nienhaus, P. Pantazis, *Angew. Chem., Int. Ed.* **2017**, *56*, 11628.
[41] B. Turkowyd, A. Balinovic, D. Virant, H. G. G. Carnero, F. Caldana, M. Endesfelder, D. Bourgeois, U. Endesfelder, *Angew. Chem., Int. Ed.* **2017**, *56*, 11634.
[42] R. Chouket, A. Pellissier-Tanon, A. Lahlou, R. Zhang, D. Kim, M.-A. Plamont, M. Zhang, X. Zhang, P. Xu, N. Desprat, D. Bourgeois, A. Espagne, A. Lemarchand, T. L. Saux, L. Jullien, *Nat. Commun.* **2022**, *13*, 1482.
[43] A. Acharya, A. M. Bogdanov, B. L. Grigorenko, K. B. Bravaya, A. V. Nemukhin, K. A. Lukyanov, A. I. Krylov, *Chem. Rev.* **2016**, *117*, 758.

Stress-induced nucleoid remodeling in *Deinococcus radiodurans* is associated with major changes in HU abundance and dynamics

Pierre Vauclare[1†], Jip Wulffelé[1†], Françoise Lacroix[1], Pascale Servant[2], Fabrice Confalonieri[2], Jean-Philippe Kleman[1], Dominique Bourgeois[1*] and Joanna Timmins[1*].

[1]Univ. Grenoble Alpes, CNRS, CEA, IBS, F-38000 Grenoble, France

[2]Université Paris-Saclay, CEA, CNRS, Institute for Integrative Biology of the Cell (I2BC), 91198, Gif-sur-Yvette, France

* Corresponding authors

† These authors contributed equally to this work

ABSTRACT

Bacteria have developed a wide range of strategies to respond to stress, one of which is the rapid large-scale reorganization of their nucleoid, which is often associated with a major reprogramming of the gene expression profile. Nucleoid associated proteins (NAPs) are believed to be major actors in this process, but the molecular mechanisms underlying stress-induced nucleoid remodeling remain poorly understood. Here, using the radiation resistant bacterium, *D. radiodurans*, as a model, and advanced fluorescence microscopy approaches, we examined the changes in nucleoid morphology and compaction induced by either entry into stationary phase or exposure to UV-C light, and characterized the associated changes in abundance and dynamics of the major NAP in *D. radiodurans*, the heat-unstable (HU) protein. While both types of stress induced a similar macroscopic rearrangement of the nucleoid into a more compact structure, HU diffusion was significantly reduced in stationary phase cells, but was instead dramatically increased following exposure to UV-C, suggesting that the underlying mechanisms of remodeling are distinct. Furthermore, a detailed comparison of the cellular response to sublethal and lethal doses of UV-C light revealed that UV-induced nucleoid remodeling involves a rapid nucleoid condensation step associated with increased HU diffusion and abundance, followed by a slower decompaction phase to restore normal nucleoid morphology and HU dynamics, before cell growth and division can resume. Together, these findings shed light on the diversity and complexity of stressed-induced nucleoid remodeling processes in bacteria.

INTRODUCTION

An organism's capacity to survive depends largely on its ability to sense and respond to changes in its environment. This is particularly true for bacteria that are constantly exposed to adverse environmental conditions, affecting their physiology, growth and survival. To respond to such stress, bacteria have developed a wide range of strategies. Among these, large-scale reorganization of the overall architecture of the genome appears to be one of the most rapid and effective strategies, especially in response to sudden stress (Dame *et al.*, 2020; Hołówka and Zakrzewska-Czerwińska, 2020), and is generally associated with temporal changes in the gene expression profile of the bacterium (Steil *et al.*, 2005; Kar *et al.*, 2005; Mitosch *et al.*, 2019; Remesh *et al.*, 2020). Stress-induced nucleoid remodeling is a widespread mechanism shared across many bacterial species including human pathogens and often results in a more compact nucleoid. It typically occurs in bacteria entering stationary phase or undergoing sporulation (Meyer and Grainger, 2013; Floc'h *et al.*, 2019; Dame *et al.*, 2020; Szafran *et al.*, 2020), states in which bacteria can withstand major changes in their environment, such as reduced nutrient availability (Piggot and Hilbert, 2004; Hengge, 2011). Nucleoid remodeling has also been reported in bacteria exposed to antibiotics, low pH, or oxidative stress (Chawla *et al.*, 2018; Morikawa *et al.*, 2019; Hołówka and Zakrzewska-Czerwińska, 2020; Remesh *et al.*, 2020). Nucleoid condensation has been proposed to insulate genomic DNA from its environment by creating a physical barrier between the genome and the stress factors (Shechter *et al.*, 2013; Hołówka and Zakrzewska-Czerwińska, 2020), and to facilitate DNA repair by limiting the diffusion of broken chromosomes (Zimmerman and Battista, 2005). Despite the well-recognized importance of nucleoid remodeling as a major response to stress, the molecular mechanisms underlying this reorganization remain poorly understood.

The bacterial nucleoid displays a highly hierarchical organization, composed of macro- and micro-domains that play key roles in genome maintenance and regulation of gene expression (Dame *et al.*, 2020; Szafran *et al.*, 2020). This packaging of the genome is achieved by several factors, including DNA supercoiling, molecular crowding and the abundant nucleoid-associated proteins (NAPs). NAPs are small positively charged proteins that interact with the genomic DNA to define the architecture of the nucleoid. NAPs preferentially bind to DNA in a non-specific manner and control DNA packaging through DNA bending, wrapping or bridging distant strands. However, they have also been reported to bind specifically to DNA motifs thereby contributing to regulating processes such as gene-specific transcription, replication, recombination and repair (Dillon and Dorman, 2010; Verma *et al.*, 2019; Dame *et al.*, 2020). A large number of genes involved in bacterial viability, metabolism and stress response are thus directly or indirectly regulated by NAPs (Azam and Ishihama, 1999; Macvanin and Adhya, 2012; Remesh *et al.*, 2020). Environmental changes have been shown to affect the expression level and/or DNA binding properties of

NAPs, notably through post-translational modifications such as phosphorylation, acetylation, methylation, succinylation, oxidation and deamination, in turn affecting the DNA topological organization (Gupta *et al.*, 2014; Ghosh *et al.*, 2016; Okanishi *et al.*, 2017; Dilweg and Dame, 2018). In many bacteria, NAPs and in particular Dps (DNA-binding protein from starved cells) proteins have been shown to contribute to nucleoid condensation and DNA protection, notably in stationary phase (Nair and Finkel, 2004; Haikarainen and Papageorgiou, 2010; Sato *et al.*, 2013; Karas *et al.*, 2015). NAPs are thus likely to be key players in stress-induced nucleoid remodeling (Boor, 2006; Boutte and Crosson, 2013).

Most of our current knowledge on nucleoid organization comes from the study of rod-shaped bacteria like *E. coli*, while studies on cocci are still sparse. A fascinating model is the well-known *Deinococcus radiodurans,* a non-pathogenic gram-positive coccus (Makarova *et al.*, 2001; Cox and Battista, 2005). The exceptional resistance of *D. radiodurans* to a wide range of genotoxic stresses including desiccation, oxidizing agents, and ionizing and UV radiation, has been attributed to its effective anti-oxidant and reactive oxygen species (ROS)-scavenging strategies combined with a highly efficient DNA repair machinery (Krisko and Radman, 2013; Timmins and Moe, 2016). *D. radiodurans* possesses a complex multipartite and multicopy genome arranged into a condensed nucleoid (Zimmerman and Battista, 2005; Floc'h *et al.*, 2019). Interestingly, it was shown that *D. radiodurans* nucleoids remain nonetheless highly dynamic, capable of adopting multiple distinct structures in exponential phase as cells progress through their cell cycle (Floc'h *et al.*, 2019). Strikingly, in comparison with radiosensitive bacteria (Azam and Ishihama, 1999), the high level of chromosome compaction in *D. radiodurans* is managed by a small number of versatile NAPs (Bouthier de la Tour *et al.*, 2013; Chen *et al.*, 2020). Indeed, amongst the five most abundant NAPs found in *E. coli* (HU, IHF, H-NS, Fis and Dps), only two of them, HU and two Dps variants (Dps1 and Dps2), are present in *D. radiodurans* (Makarova *et al.*, 2001; Romao *et al.*, 2006; Cuypers *et al.*, 2007). These two Dps proteins, however, do not appear to play a major role in nucleoid organization and condensation as observed in *E. coli*, but have instead been shown to contribute to protection against oxidative stress by regulating the availability of manganese and iron in the cell (Nguyen *et al.*, 2009; Santos *et al.*, 2015; Santos *et al.*, 2019).

The ubiquitous histone-like HU protein is the most widespread and abundant NAP in bacteria (Stojkova *et al.*, 2019). Extensive studies have shown that HU is a dimeric protein that exists mostly as a homodimer, but also as a heterodimer in enterobacteria such as *E. coli*, where it can form either homo- (HUα-HUα) or heterodimers (HUα/Huβ) (Nguyen *et al.*, 2009; Grove, 2011; Hammel *et al.*, 2016). Its role in nucleoid compaction appears multifold. Recent single-particle tracking experiments have suggested that HU mainly contributes to nucleoid organization via transient non-specific interactions (Bettridge *et al.*, 2021; Stracy *et al.*, 2021). At the same time, *in vitro* studies have shown that HU exhibits both non-specific binding to unstructured DNA and higher affinity specific binding to distorted DNA structures (Kamashev and Rouviere-Yaniv, 2000; Ghosh and Grove, 2004; Verma *et al.*, 2023). HU is also able to multimerize on DNA, leading to DNA stiffening or compaction depending on its concentration (Hammel *et al.*, 2016; Remesh *et*

al., 2020; Chen *et al.*, 2020). HU-DNA interactions have indeed been proposed to be affected by the local HU concentration, but also by post-translational modifications, in particular phosphorylation and acetylation, which contribute to the fine tuning of the global architecture of the nucleoid (Gupta *et al.*, 2014; Ghosh *et al.*, 2016; Dilweg and Dame, 2018; Hou *et al.*, 2022). Beyond its role in nucleoid organization, HU, like other NAPs, has been reported to play a role in transcriptional regulation, DNA replication and DNA repair (Aki, 1997; Oberto *et al.*, 2009; Hammel *et al.*, 2016; Li and Waters, 1998; Kamashev and Rouviere-Yaniv, 2000). HU-deficient *E. coli* cells remain viable with a modest change in phenotype, but have been found to be more sensitive to UV irradiation (Huisman *et al.*, 1989), suggesting a role for HU in bacterial stress-response.

In *D. radiodurans*, unlike in *E. coli*, the *hbs* gene encoding HU is essential for cell viability, and the progressive depletion of *D. radiodurans* HU (DrHU) using a thermosensitive plasmid leads to nucleoid decondensation, fractionation and eventually cell lysis (Nguyen *et al.*, 2009). Together with the DNA gyrase that modulates the topology of the genomic DNA, DrHU thus appears to be the primary structuring protein orchestrating nucleoid organization in *D. radiodurans* (Bouthier De La Tour *et al.*, 2015). Interestingly, DrHU harbors an additional 30 amino acid long N-terminal lysine-rich extension, that is reminiscent of the C-terminal domain of eukaryotic histone H1, which is also involved in DNA compaction (Ghosh and Grove, 2006; Bouthier De La Tour *et al.*, 2015).

In this work, using notably a combination of 3D spinning-disk microscopy and single-particle tracking experiments, we have performed an in-depth study of nucleoid remodeling in *D. radiodurans* and its associated changes in HU abundance and dynamics, induced by two types of stress: (i) entry into stationary phase, a stress that occurs frequently in the natural environment, during which bacteria are faced with resource-limited conditions preventing any further growth (Gefen *et al.*, 2014; Dworkin and Harwood, 2022), and (ii) exposure to intense UV-C light that produces extensive DNA damage, and notably the formation of pyrimidine photoproducts, but also ROS (Richa *et al.*, 2015). The data reveal that the nucleoid adopts a compacted and spherical morphology both in stationary phase and immediately after exposure to UV-C radiation. However, strikingly, single-particle tracking of HU revealed that while HU diffusion decreases during stationary phase, it dramatically increases following exposure to UV-C, suggesting that the underlying mechanisms are distinct. Furthermore, by comparing the cellular response of *D. radiodurans* to sublethal and lethal doses of UV-C light, we determined that the nucleoid remodeling process starts with a rapid nucleoid condensation step associated with increased HU abundance and diffusion, which is then followed by a slower decompaction phase, seen only in surviving cells, during which genome integrity and nucleoid organization are restored before DNA replication and cell growth can resume. Together, these findings highlight the key role of HU in stress-induced nucleoid remodelling, but also the complexity of this phenomenon in bacteria.

RESULTS

Entry into stationary phase induces nucleoid compaction associated with decreased HU dynamics

In our previous work, we characterized the size and morphology of *D. radiodurans* nucleoids, revealing a great diversity of nucleoid shapes in exponential growth phase and more condensed and homogeneous nucleoids in stationary phase (Floc'h et al., 2019). We confirmed these findings by 3D confocal imaging of membrane (Nile Red)- and DNA (Syto9)-stained wild-type D. radiodurans (DR^{WT}) cells and of a genetically engineered strain of *D. radiodurans* expressing HU-mCherry from its endogenous locus (DR^{HUmCh}) (SI Fig. S1A). Imaging was performed on bacteria in both exponential and early stationary growth phases (Fig. 1A and SI Fig. S2A-B). In DR^{HUmCh}, HU-mCherry covers the genomic DNA and serves as a proxy to follow changes in the organization of the nucleoid (SI Fig. S1A). As reported previously, the mean volume of DR^{HUmCh} nucleoids is slightly higher than that of DR^{WT}, possibly as a result of steric hindrance caused by the mCherry label (Floc'h *et al.*, 2019). For both strains, we evaluated the fraction of rounded nucleoids, and determined the volume and sphericity of individually segmented nucleoids, so as to perform a thorough statistical comparison of exponential versus stationary phase cells. We found that in stationary phase, almost 90% of cells exhibited a rounded nucleoid (SI Fig. S2B) and the mean nucleoid volume was decreased by almost 50% compared to that in exponential phase, going from 1.01 ± 0.34 μm^3 to 0.53 ± 0.19 μm^3 (Fig. 1B). The sphericity, in contrast, increased significantly (+12%) and displayed a markedly reduced distribution in stationary phase (Fig. 1B), confirming that the nucleoid morphology is indeed much more homogeneous in this growth phase. Similar observations were made on the DR^{HUmCh} strain with a 40% drop in the nucleoid volume and a significant increase in the sphericity (Fig. 1B). Western blot detection of HU-mCherry in cell extracts of DR^{HUmCh} revealed that HU levels were significantly higher (3-fold) in stationary phase cells compared to exponential phase cells (Fig. 1C and SI Fig. S2C).

Next, we compared the dynamics of HU in exponential and stationary phase cells by single-particle tracking (spt; SI Fig. S3A). For this, we constructed a *D. radiodurans* strain expressing HU fused to mEos4b (De Zitter *et al.*, 2019), DR^{HUmEos} (SI Fig. S1A), enabling an in-depth characterization of HU dynamics (Fig. 1D-F). PALM imaging of this strain revealed the same variety of nucleoid shapes as seen by confocal microscopy in exponential phase and a similar change in nucleoid morphology upon entering stationary phase (Fig. 1F). We plotted the apparent diffusion coefficient (D_{app}) values calculated from the mean square jump distance of 4 displacements per track in exponential and stationary phase cells (Fig. 1D), and extracted the median D_{app} per cell (Fig. 1E). We observed that nucleoid rounding and compaction upon entry into stationary phase was accompanied by a marked reduction in the dynamics of HU, with an almost 20% lower D_{app} than that observed in exponential phase cells, suggesting a major reorganization of the HU-DNA assembly in these highly condensed nucleoids. We chose not to fit the spt data to distinct populations of molecules as reported in several earlier studies (Kapanidis *et al.*, 2018; Bettridge *et al.*, 2021; Stracy *et al.*, 2021), since simulations revealed that such an analysis would likely be biased by the strong and heterogeneous confinement encountered by HU molecules in the various nucleoid morphologies observed in *D. radiodurans.* A detailed discussion of this issue is provided in the supplementary data (SI discussion).

UV-C light elicits a rapid dose-dependent compaction of the nucleoid

D. radiodurans is known to exhibit an outstanding resistance to UV light (Harsojo *et al.*, 1981; Battista, 1997; Slade and Radman, 2011). We exposed exponential and stationary phase DR^{WT} cultures to a range of UV-C doses. Up to 1.9 kJ/m^2, the survival of *D. radiodurans* was largely unaffected, but rapidly dropped beyond this dose, regardless of whether cells were in exponential or stationary phase (Fig. 2A). In contrast, survival of *E. coli* under the same experimental conditions was severely impacted already at a dose of 0.2 kJ/m^2. The UV resistance of DR^{HUmCh} and DR^{HUmEos} strains was similar to that of DR^{WT}, with between 30 and 50% cell survival at the sublethal dose of 1.9 kJ/m^2 and less than 0.01% survival at the lethal dose of 12.0 kJ/m^2 (SI Fig. S1B).

UV-C-induced changes in nucleoid volume and morphology were then evaluated by 3D spinning-disk microscopy, as described above, after irradiation of *D. radiodurans*. Due to the time needed for sample preparation, confocal images were typically acquired 30 minutes after irradiation (cf. Materials and Methods). A dose-dependent compaction of the nucleoid of exponentially growing DR^{WT} and DR^{HUmCh} was observed up to 1.9 kJ/m^2 (Fig. 2B-C and SI Fig. S4 and S5) reaching a minimal volume of 0.65 µm^3 for DR^{WT} and 1.11 µm^3 for DR^{HUmCh}, corresponding to respectively a 35% and 18% decrease in the mean nucleoid volume. As in the case of stationary phase cells, this nucleoid compaction was accompanied by an increased sphericity and a marked reduction in the spread of the sphericity values, suggesting the formation of more compact and homogeneous nucleoids in the cell population (Fig. 2B-C and SI Fig. S4 and S5). Of note, in DR^{WT}, beyond the sublethal dose of 1.9 kJ/m^2, the nucleoid volume remained constant at its minimal value, whereas the mean sphericity seemed less affected by the higher UV-C doses, suggesting that nucleoid rounding might be partly impaired at these highly cytotoxic UV-C doses (Fig. 2B-C and SI Fig. S4 and S5). The same experiments were then performed on stationary DR^{WT} and DR^{HUmCh} cultures. While no further nucleoid compaction was observed for DR^{WT} stationary phase nucleoids following exposure to UV-C light (Fig. 2B-C and SI Fig. S4A and S5A), the volume of stationary phase DR^{HUmCh} nucleoids did show a significant dose-dependent reduction going from 0.74 µm^3 in non-irradiated samples to 0.39 µm^3 in response to 12.0 kJ/m^2 (SI Fig. S4B and S5B). This difference may be explained by the different levels of compaction of stationary phase nucleoids in the two strains before irradiation.

Having established the global changes in nucleoid shape and size following exposure to UV-C light, we next examined the effects of sublethal (1.9 kJ/m^2) and lethal (12.0 kJ/m^2) doses of UV-C radiation on HU dynamics using the DR^{HUmEos} strain. We first ensured that UV-C illumination does not change the fluorescence properties of mEos4b (SI Fig. S1A and Fig. S3B). We then observed that, although UV-C induced a clear compaction of the nucleoid as in cells entering stationary phase (SI Fig. S6), UV-C also led to a significant increase in the apparent diffusion coefficient (D_{app}) of HU in irradiated cells (at both sublethal

and lethal doses) in both exponentially and stationary phase cells (Fig. 2D-E). In exponential cells, the median D_{app} of HU-mEos4b in irradiated cells was approximately twice that measured in non-irradiated samples, while in stationary phase cells, HU diffusion was ~30% higher after irradiation. The more compact structure of stationary phase nucleoids may be more restrictive for HU diffusion.

To determine whether the increased HU diffusion coefficient observed after exposure to UV-C light could be due to increased mobility of the genomic DNA as a result of UV-induced DNA damage, we probed the dynamics of the *OriC* and *Ter* loci of chromosome 1 (the largest chromosome of *D. radiodurans*, corresponding to ~80% of the genome) by spt using a heterologous *parS*-ParB system (SI Fig. S7A-B) previously used to track these loci in *D. radiodurans* cells (Passot *et al.*, 2015; Floc'h *et al.*, 2019). Exponentially growing *D. radiodurans* strains in which either *OriC* or *Ter* were labelled with ParB-GFP were thus irradiated with a sublethal dose of UV-C light and imaged after 1 hour of recovery. No noticeable changes in the mobility of chromosome 1 loci were observed after exposure to UV-C light (SI Fig. S7C-D), suggesting that changes in HU dynamics probably reflect altered HU-DNA interactions and not increased mobility of the damaged DNA.

Cell and nucleoid recovery after a sublethal dose of UV-C light involves three distinct stages

To decipher the different stages of UV-C-induced nucleoid remodeling, we carried out a detailed analysis of the response of exponentially growing *D. radiodurans* cells to a sublethal dose of UV-C light up to 24h following irradiation (Fig. 3 and 4, and SI Fig. S8 and S9). For this purpose, irradiated cells (DR^{WT}, DR^{HUmCh} and DR^{HUmEos}) were transferred back into fresh medium immediately after irradiation and samples were then collected at different timepoints and subjected to a variety of measurements: (i) optical density measurements to determine growth curves after irradiation, (ii) 3D confocal microscopy on DR^{WT} and DR^{HUmCh} to assess cell growth and division, changes in size and morphology of the nucleoids, (iii) western blot analysis of DR^{HUmCh} cell extracts and 3D confocal microscopy on DR^{HUmCh} to follow the abundance of HU, and (iv) spt experiments on DR^{HUmEos} cells to probe the dynamics of HU. Before carrying out these analyses, we confirmed that the three strains of *D. radiodurans* respond in a similar way to exposure to UV-C light by establishing their growth curves and determining the size and morphology of their nucleoids at selected timepoints after irradiation (SI Fig. S8).

The recovery of *D. radiodurans* bacteria exposed to a sublethal (SL) UV-C dose can be divided into three main stages: stage 1^{SL} (t_0 to t_{1h} post-irradiation) during which cell growth and division are arrested and the nucleoids become round and more condensed, stage 2^{SL} (t_{1h} to t_{7h} post-irradiation) corresponding to nucleoid decompaction and a progressive recovery of cellular activity, and stage 3^{SL} (t_{7h} to t_{24h} post-irradiation) in which most cells have recovered native nucleoid and cell morphologies (Table S1). Optical density measurements performed on DR^{WT}, DR^{HUmCh} and DR^{HUmEos} strains exposed to a sublethal dose of UV-

C light showed a clear arrest of their cell cycle immediately after irradiation causing a 2 to 3 hour delay in their growth curve (Fig. 3A and SI Fig. S8B), which is in good agreement with the time estimated in earlier studies to allow cells to repair the heavy radiation-induced DNA damage (Zahradka *et al.*, 2006). We indeed observed that in DR^{WT} both septation and cell growth were rapidly blocked after irradiation and throughout stage 1^{SL} of recovery. As a result, transition from phase 3 to phase 4 of the cell cycle, corresponding to the onset of septation, was impaired, leading to an increased fraction of phase 3 cells in the population at the end of stage 1^{SL} (t_{1h}; SI Fig. S9A-C). Interestingly, the splitting of tetrads into diads (transition from phase 6 to phase 1; SI Fig. S9A) did not appear to be affected by the irradiation, as evidenced by a significant reduction in the proportion of phase 6 cells during stage 1^{SL} (SI Fig. S9B). No obvious defects in cell morphology or plasma membrane integrity were seen in this first stage (Fig. 3B).

Arrest of the cell cycle immediately after irradiation was accompanied by a marked reduction in the size of the nucleoid, constituting the first step in the nucleoid remodeling process (Fig. 3B-D for DR^{WT} and SI Fig. S8C for $DR^{HU\text{-}mCh}$). The minimal nucleoid volume was reached already at t_0 (Fig. 3C and SI Fig. S8C), while the change in nucleoid morphology was found to progress more slowly throughout stage 1^{SL} to reach its maximum at t_{1h} with the highest median sphericity value (0.91) and near 80% of cells exhibiting abnormal nucleoid morphologies, of which 75% were rounded (Fig. 3B-D and SI Fig. S10A). Interestingly, the nucleoids of phase 5 cells (last phase before cytokinesis) responded differently to those of other cells, with almost 50% of phase 5 cells maintaining a structured, elongated nucleoid at t_{1h} (SI Fig. S10B), suggesting that nucleoid compaction may be less efficient in cells in which chromosome segregation is already well advanced. Nucleoid rounding resulted in different nucleoid morphologies depending on the phase of the cell cycle the cells were in when exposed to UV-C light (Fig. 3E, SI Fig. S10C). A majority of cells in early phases of the cell cycle (phases 1-3) bearing mostly crescent-shaped and ring-shaped nucleoids exhibited ball-like nucleoids after irradiation, whereas cells at later stages of the cell cycle (phases 4-5) in which active chromosome segregation was taking place, exhibited bilobed or pear-shaped nucleoids after irradiation (Fig. 3E and SI Fig. S10C). Moreover, irrespective of their phase of the cell cycle, over 30% of cells exhibited off-center nucleoids at the end of stage 1^{SL} (Fig. 3B and SI Fig. S10D), in contrast with healthy *D. radiodurans* cells in which the nucleoid is always located in the center of the cell, except immediately after chromosome segregation in phases 5 and 6 (Floc'h *et al.*, 2019). Analysis of the HU protein revealed that its dynamics (Fig. 4A-C) and abundance (Fig. 4D and SI Fig. S11A-B) also rapidly increased after irradiation, reaching a maximum at the end of stage 1 (t_{1h}; Fig. 4A-D).

In stage 2^{SL} (t_{1h} to t_{7h} post-irradiation; Table S1), HU dynamics and levels were found to progressively decrease again (Fig. 4C-D). This coincided with the start of the reversal of the nucleoid compaction process. As with compaction, the first step in nucleoid decompaction was the recovery of a 'normal' nucleoid volume as early as t_{2h} (Fig. 3C and SI Fig. S8C), whereas full recovery of the diverse nucleoid shapes typical of exponentially growing *D. radiodurans* cells took several hours and most of stage

2^{SL} (Fig. 3D and SI Fig. S10A and D). Nucleoid decompaction was also accompanied by a progressive decrease in the median sphericity of nucleoids and a marked increase in the spread of the sphericity values, reflecting the great diversity of nucleoid shapes observed during the recovery stage, most likely resulting from active DNA repair and cell recovery processes (Fig. 3C and SI Fig. S8C).

Cell growth and division were also largely recovered during stage 2^{SL} as illustrated by the increased optical density of DR^{WT}, DR^{HUmCh} and DR^{HUmEos} cultures (Fig. 3A and SI Fig. S8B) and a restored distribution of cells within the different phases of the cell cycle (SI Fig. S9B). A slow increase in the mean cell size was nonetheless observed between t_{1h} and t_{3h}, which may have resulted from a slight delay between the recovery of cell growth and that of cell division (SI Fig. S9B-C). Beyond t_{3h}, most cells appeared to have recovered their ability to grow and divide and the mean cell size decreased progressively as the cell density increased and the bacterial population moved towards stationary phase. However, we also observed during this period the accumulation of a small fraction (<5%) of anucleate cells (*i.e.* no Syto9 staining; Fig. 3B and E and SI Fig. S10D) that typically also exhibited a damaged cell membrane, and a significant number (~10% cells) of abnormally large cells in which cell division appeared to be impaired or blocked (Fig. 3B and E and SI Fig. S10E). Many of these enlarged cells also exhibited abnormally large nucleoids that were either spread out throughout the cell and exhibited significantly increased volumes or forming very large rings with a largely unchanged nucleoid volume (Fig. 3C-E and SI Fig. 10F). These cells were likely more severely damaged, causing a delay or even an arrest in the nucleoid remodeling process.

In stage 3^{SL} of the recovery from a sublethal dose of UV-C light (t_{7h} to t_{24h} post-irradiation; Table S1), a vast majority of cells had fully recovered and exhibited normal growth and division as evidenced by the rapid increase in the optical densities of the cultures (Fig. 3A and SI Fig. S8B) and the changes in cell phase distribution as the cells shifted from exponential to stationary phase (Fig. 3A-C and SI Fig. S9B). Indeed, at t_{24h} post-irradiation, these cultures had reached early stationary phase as seen by the accumulation of phase 6-8 cells (Fig. 3B and SI Fig. S9B). Most cells (80-90%) now exhibited normal, structured and centered nucleoids (Fig. 3D and SI Fig. S10D). After a slight reduction of HU abundance during stage 2^{SL}, HU levels stabilised in stage 3 at ~2-fold higher level than in non-irradiated exponential phase samples (Fig. 4D). This increased level may result from the cells reaching stationary phase, which we showed in Fig. 1B is associated with a ~3-fold increase in HU levels. During stage 3^{SL}, HU diffusion also continued its recovery to reach values under 0.1 μm^2/sec as obtained in non-irradiated stationary phase cells (Fig. 4B-C and Fig. 1E). Surprisingly, however, at the end of stage 3^{SL}, around 10% of cells still exhibited major defects (large cells with impaired septation, expanded nucleoids and high HU diffusion), suggesting that these large, abnormal cells appeared to still arise at late stages of recovery, likely as a result of unrepaired DNA damage leading to cell dysfunctions (Fig. 3B-E, Fig. 4B-C, and SI Fig. S10).

A lethal dose of UV-C light induces a progressive loss of nucleoid structure and cellular functions

We then subjected our three exponentially growing *D. radiodurans* strains (DR^{WT}, $DR^{HU\text{-}mCh}$ and $DR^{HU\text{-}mEos}$) to a lethal dose of UV-C light and followed the effects of this high dose on the cells and their nucleoids in the hours following irradiation (Fig. 5 and 6 and SI Fig. S12). As with the sublethal dose, all three strains responded in a similar manner (SI Fig. S12A-B) and the recovery could also be divided into three stages, but the nature and duration of these stages differed from those observed after exposure to sublethal UV-C. After a lethal UV-C dose, rapid nucleoid rounding and condensation were also observed in stage 1^L (t_0 to t_{2h} post-irradiation; Table S1), but this process lasted longer than after the sublethal dose. Indeed, while a reversal of nucleoid compaction was observed at t_{1h} (corresponding to the onset of stage 2^{SL}) after a sublethal dose, here, instead, we noted that after the rapid condensation of the nucleoids immediately after irradiation, the mean nucleoid volume (~0.75 μm^3) then remained constant for the rest of stage 1^L until t_{2h} (Fig. 5B-C and SI Fig. S12A and Fig. S13A). The change in nucleoid morphology was also more progressive with the highest sphericity (>0.9) reached at t_{2h} (Fig. 5B-C). With this higher dose of UV-C, 100% of cells exhibited abnormal nucleoids with ~95% of cells exhibiting rounded nucleoids and 50% of cells having off-center nucleoids at t_{2h} (Fig. 5B-D and SI Fig. S13B). These values are considerably higher than those determined for cells exposed to the sublethal dose (Fig. 3D and SI Fig. S10D). During stage 1^L, the levels of HU-mCherry were found to increase immediately after irradiation (t_0) as in response to a sublethal dose of UV-C (Fig. 6A-B) and HU-mEos4b dynamics were also strongly increased, beyond the value obtained for the sublethal dose with a very large cell-to-cell variation observed at t_{1h} (Fig. 6C-E). As expected, cell growth and division were rapidly arrested after this acute UV-C dose as evidenced by the flat growth curve of DR^{WT}, DR^{HUmCh} and DR^{HUmEos} cultures (Fig. 5A and and SI Fig. S12B) and the stable cell size during stage 1^L (SI Fig. S12C).

Whereas nucleoid compaction was reversed in stage 2^{SL} after the sublethal dose, no such reversal was seen after the lethal dose. Instead, during stage 2^L (t_{2h} to t_{9h} post-irradiation; Table S1), evidence for severe cellular dysfunction was observed: (i) lack of cell growth (SI Fig. S12C), (ii) increased fraction of cells exhibiting off-center nucleoids (Fig. 5B and SI Fig. S13B), (iii) accumulation of anucleate cells with reduced size due to a damaged cell wall (up to ~25% of cells at t_{7h}; Fig. 5B and D), (iv) stable HU levels exhibiting high HU diffusion (Fig. 6A and D), and (v) progressive reduction in the size of rounded nucleoids leading to the accumulation of micro-nucleoids with a mean volume of 0.27 μm^3 corresponding to a 75% reduction in the nucleoid volume compared to non-irradiated samples (Fig. 5E).

In stage 3^L (t_{9h} to t_{24h} post-irradiation; Table S1), there is a marked accumulation of cells exhibiting either no or diffuse staining of the DNA, suggesting that for a vast majority of cells, the integrity of the nucleoid was severely affected and genomic DNA was being heavily degraded (Fig. 5B-D and SI Fig. S13B). Indeed, at t_{24h}, 95% of cells showed either no Syto9-DNA staining (40% of anucleate cells) or diffuse Syto9-DNA staining throughout the cytosol (55%). In accordance with this, HU diffusion remained at a high level

throughout stages 2^L and 3^L, with many cells showing D_{app} values close or above 1 $\mu m^2/s$, confirming the probable release of HU from the degraded genomic DNA in these cells (Fig. 6D-E). Strikingly, there were also many cells in which HU diffusion was very low (D_{app} < 0.1 $\mu m^2/s$), possibly as a result of protein aggregation. Extensive DNA degradation was also evidenced in Syto9-stained DR^{HUmCh} cells, where an increasing number of HU-mCherry positive and Syto9 negative nucleoids were seen to accumulate during stage 3^L (SI Fig. S14).

DISCUSSION

In this study, we have investigated nucleoid remodeling in *D. radiodurans* in response to two different types of stress: (i) entry into stationary phase, which is associated with nutritional stress and (ii) exposure to UV-C light, which is known to cause severe DNA damage. A comparison of the response to these two types of stress (Fig. 7) provides important insight into the mechanisms underlying bacterial nucleoid remodeling.

In both cases, nucleoids rapidly became more compact and changed their morphology to adopt a more rounded shape, and this phenomenon was associated with increased levels of the HU protein, in agreement with earlier work that showed that conversely HU depletion leads to nucleoid expansion (Nguyen *et al.*, 2009). Upon entry into stationary phase, however, this nucleoid compaction was accompanied by a significant decrease in HU diffusion (Fig. 7), suggesting that HU is binding more tightly, and perhaps in a different configuration, to the genomic DNA compared to exponentially growing cells. The increased HU levels in stationary phase cells combined with the markedly reduced volumes of stationary phase nucleoids is likely to result in a strongly increased local concentration of HU in such cells. This may indeed modify the DNA binding properties of HU and favor the formation of HU-DNA assemblies in which HU polymerizes along the genomic DNA, thereby stiffening and bundling the genomic DNA (Fig. 7). A similar model was recently proposed by Hammel and colleagues for *E. coli* HU in stationary phase (Hammel *et al.*, 2016; Remesh *et al.*, 2020). This model is also supported by *in vitro* atomic force microscopy studies of DrHU-plasmid DNA assemblies, in which stiffening and bridging of plasmid DNA by DrHU were observed at high HU:DNA ratios only (Chen *et al.*, 2020) and would explain the reduced apparent diffusion of HU observed in the highly condensed stationary phase *D. radiodurans* nucleoids. By maintaining this condensed genomic configuration in stationary phase, HU also likely serves as a global transcriptional regulator, facilitating the transcription of stationary phase specific genes required for survival under resource-limited growth conditions as has been reported in *E. coli* (Hengge, 2011; Sobetzko *et al.*, 2012; Lal *et al.*, 2016).

As in stationary phase cells, exposure of *D. radiodurans* cells to UV-C light rapidly induced nucleoid compaction, although to a lesser extent, and this phenomenon was again associated with an increase in HU

levels regardless of the UV dose. HU thus appears to be a key player in the process of stress-induced nucleoid condensation and regulated *de novo* synthesis of HU during the very early stage of nucleoid remodeling may contribute to maintaining the integrity of the nucleoid by providing functional HU protein (Fig. 7). However, while HU diffusion was decreased in stationary phase cells, it was significantly increased in response to UV-C light. The structure of condensed stationary phase nucleoids is thus distinct from that of UV-C-irradiated nucleoids, although in both cases, HU-DNA interactions are likely playing an important role in the underlying organization. Increased mobility of the irradiated genomic DNA due to DNA damage could have been one of the causes of the observed increased HU dynamics, but the tracking of the *oriC* and *ter* loci of the major chromosome of *D. radiodurans* showed no evidence for a substantial change in DNA mobility after exposure to UV-C light. The increased HU diffusion thus most likely results from weakened HU-DNA interactions. These may be induced by either post-translational modifications and/or physico-chemical changes occurring at the level of HU and/or the genomic DNA, directly induced by the high-intensity UV-C light and the overproduction of ROS (Kehrer, 2000; Díaz-Riaño *et al.*, 2019).

A major consequence of HU release from the genomic DNA as a result of weakened HU-DNA interactions could be compaction or collapse of the nucleoid (Fig. 7), although additional factors are likely also involved in this process. UV-induced arrest (or partial arrest) of cellular processes, including cell growth and division, but also DNA replication and transcription or protein translation, which are known to induce changes in nucleoid organization (Woldringh *et al.*, 1995; Miangolarra *et al.*, 2021), is likely to also contribute to this rapid stress-induced nucleoid condensation. Similarly, reduced transcription and translation as well as severe damage to the bacterial cytoskeleton network may be responsible for the subsequent drift of nucleoids off-center, that was particularly striking in cells exposed to lethal UV-C light (Fig. 7). Using theoretical approaches, Marc Joyeux showed that bacterial nucleoids preferentially locate to the edges of the cell, where the curvature of the cell wall is the highest (Joyeux, 2019), suggesting that in healthy cells active cellular processes, including transcription and translation (Miangolarra *et al.*, 2021), are indeed responsible for maintaining the nucleoid in a central position. These processes are likely impaired in the strongly irradiated cells, causing the nucleoid to lose its structure and drift to the edge of the cell.

A major difference in the response of *D. radiodurans* to sublethal versus lethal UV-C doses was the reversibility of the process. In *D. radiodurans* cells exposed to sublethal UV-C light, the rapid initial nucleoid compaction stage (stage 1^{SL}) was followed by a slower decompaction phase (stage 2^{SL}) during which the nucleoids progressively recovered their well-structured states and cells recovered their ability to grow and divide. HU is likely to play an important role in this recovery stage (Fig. 7). We, indeed, observed that the kinetics of recovery of nucleoid morphology after exposure to sublethal UV-C light coincided with that of recovery of HU dynamics, suggesting that progressive re-assembly of HU on the genomic DNA is an important determinant of nucleoid organization and may be critical for regulating access of DNA repair enzymes to the genomic DNA. On the contrary, in stage 2^{L}, a lethal dose of UV-C light lead to progressive

loss of nucleoid structure, heavy degradation of the genomic DNA, full arrest of cell growth and division, and eventually to the accumulation of damaged and anucleate cells in stage 3^{L}. In such cells, HU diffusion was found to be either very high, indicating that HU-DNA interactions were largely disrupted, or instead very low, possibly as a result of HU aggregation in the absence of genomic DNA on which to assemble.

Cell survival is thus essential to restore nucleoid organization following exposure to UV-C light and in contrast to nucleoid condensation which may be a mostly passive process, nucleoid decompaction, and more generally cell recovery, largely relies on active cellular processes (Fig. 7). In particular, active checkpoint control factors must be functional to rapidly coordinate the arrest of the cell cycle and chromosome segregation with the intervention of the DNA repair machinery to restore the integrity of the genome. A similar sequential compaction and expansion of nucleoids was reported in UV-C irradiated *E. coli* cells before cell division could restart (Odsbu and Skarstad, 2014; Estévez Castro *et al.*, 2018). Obsbu and Skarstad proposed that the initial phase of compaction serves to stabilize the DNA and repair DNA double-strand breaks, while repair of other lesions takes place largely during the decompaction stage (Odsbu and Skarstad, 2014). In *D. radiodurans*, nucleoid condensation appears to occur regardless of the nature of the stress and its intensity, suggesting that it may constitute an early stress response mechanism, which could act mostly as a protective measure to minimize dispersion of the damaged genome. Earlier studies have shown that activation of the DNA repair machinery occurs 30 to 60 minutes after exposure to radiation (Liu *et al.*, 2003; Basu and Apte, 2012), suggesting that most of the repair process would therefore take place during the decompaction stage. This hypothesis is in line with studies in eukaryotic cells showing that the chromatin decondenses in response to DNA damage to facilitate repair (Hauer *et al.*, 2017; dos Santos *et al.*, 2020). The 2-3h delay in the growth of *D. radiodurans* after exposure to UV-C is also in good agreement with this hypothesis and the estimated time needed to allow cells to repair heavy radiation-induced DNA damage (Zahradka *et al.*, 2006).

In *D. radiodurans,* although many cells recovered well from exposure to the sublethal UV-C dose and started to grow and divide again during stage 2^{SL} of the recovery phase, a fraction of cells exhibited highly expanded nucleoids. These cells were typically larger in size and lacking a division septum, suggesting that they had recovered their ability to grow, but not to divide. Castro *et al.* showed that *E. coli* cells that are deficient in DNA repair proteins reach the expanded nucleoid stage, but are unable to restart cell division after UV-C irradiation, suggesting that DNA repair is required before cell division can restart (Estévez Castro *et al.*, 2018). *D. radiodurans* cells exhibiting highly expanded nucleoids were thus probably either failing to repair their DNA damage or delayed in their repair process, leading to arrested cell division and partial loss of their nucleoid organization. A fraction of such cells may eventually recover and start dividing again after completion of the repair process. Interestingly, such cells arose progressively during the recovery, suggesting that cells that initially appeared to have recovered subsequently developed cellular defects probably as a consequence of accumulated DNA damage.

In conclusion, this study highlights the key role of HU and the versatility of its interactions with genomic DNA in the nucleoid remodeling process in *D. radiodurans* and the survival strategy of this remarkable organism. However, besides HU, additional factors, such as DdrC, a *Deinococcus*-specific NAP that is strongly up-regulated in response to irradiation (Bouthier de la Tour *et al.*, 2017; Banneville *et al.*, 2022), the partitioning factors (ParA/ParB) or the DNA gyrase, all of which are found in nucleoids after irradiation (Bouthier de la Tour *et al.*, 2013), may also contribute to varying extent to this nucleoid remodeling process. Further work will be needed to explore these different avenues. Moreover, a number of recent studies have revealed the importance of post-translational modifications of NAPs for regulating the activities and DNA-binding properties of these small basic proteins, so in the future, establishing the post-translational modification profiles of key NAPs, and notably of HU, at different stages of the nucleoid remodeling process will certainly shed new light on the underlying mechanisms.

MATERIALS AND METHODS

Bacterial cultures

Bacterial strains used in this study are listed in Table S2. All *D. radiodurans* strains were derivatives of the wild-type strain R1 ATCC 13939 (DR^{WT}). The genetically engineered strain of *D. radiodurans* expressing HU fused to mEos4b (GY16993; DR^{HUmEos}) was obtained by the tripartite ligation method (Mennecier *et al.*, 2004). For this, a codon-optimized gene encoding mEos4b to which we added the 9 N-terminal residues of mCherry was synthesized and subloned into plasmid pEX-128 by Eurofins MWG Biotech (SI Fig. S15). Obtaining a viable and functional strain of *D. radiodurans* expressing HU fused to a fluorescent protein is not trivial. Since we knew that mCherry fusions were functional, we decided to add the extra N-terminal residues of mCherry to the N-terminus of mEos4b. We inserted a hygromycin resistance (*hph*) cassette into the AgeI/XbaI sites of pEX-128 downstream of the mEos4b gene, then amplified the mEos4bΩ*hph* cassette and the regions flanking the insertion site (3' end of *hu* gene, DR_A0065) by PCR using oligonucleotides listed in Table S3, and after restriction digestion the three fragments were ligated together. *D. radiodurans* cells were then transformed by the ligation product and plated on selective medium containing 50 µg/ml hygromycin, leading to allelic replacement on one genome copy. Because *D. radiodurans* is multigenomic, the transformant colonies were further streaked three times successively on selective medium to ensure that all copies of the genome had incorporated the foreign DNA. This was then confirmed by PCR analysis and DNA sequencing, which also revealed a point mutation in mEos4b (Ala^{112} to Val^{112}). *D. radiodurans* cells were grown aerobically at 30°C in a shaking incubator (160 rpm) in TGY2X medium (Bonacossa *et al.*, 2002). The medium was supplemented with the appropriate antibiotics: 3.4 µg/ml chloramphenicol for DR^{HUmCh} GY15743 strain and *oriC/ter* labelled strains GY15787 and GY15800, and 50 µg/ml hygromycin for DR^{HUmEos} GY16993. Typically for microscopy experiments, *D. radiodurans* cells were pre-grown the day before and

then diluted for an overnight growth until reaching exponential (OD_{650} ~0.3-0.5) or early stationary phase (OD_{650} >3) the next morning. *oriC/ter* labelled strains GY15787 and GY15800 were grown overnight and were diluted 60X the next morning in TGY2X and grown for a further 5h until reaching an OD_{650} between 0.3 and 0.5. *Escherichia coli* strain DH5α was grown at 37°C in LB medium. Optical density measurements were made on a Clariostar (BMG Labtech) plate reader.

UV irradiation and survival curve

Before irradiation, cells were washed two times with minimal medium M9DR (45.5 mM Na_2HPO_4, 22 mM KH_2PO_4 and 15.1 mM $(NH_4)_2SO_4$, pH7.3) to eliminate the strongly UV-absorbing TGY2X medium. Cells were finally resuspended in M9DR medium at an OD_{650} between 0.3 and 0.5 and transferred to a 6-well plate (1 ml per well). Cells were irradiated at a low cell density and in a minimal volume to ensure a homogeneous exposure of the cells. UV-C (254nm) irradiation was performed using a Stratalinker oven equipped with germicide UV-C lamps producing a continuous dose of ~30J/m^2/sec. Cells were typically irradiated between 0.5 and 5 minutes. The exact dose received by the cells was determined using a UV-C light monitor placed next to the 6-well plate in the UV oven. Exposure to UV-C irradiation did not affect the fluorescence of the fluorescent proteins (SI Fig. S3B). After irradiation, cells were centrifuged and resuspended in fresh TGY2X medium. For the recovery experiments, these cultures were returned to the 30°C shaking incubator. Samples were collected immediately after resuspending cells in TGY2X medium (t_0) and then 1, 2, 3, 5, 7, 9 and 24 hours post-irradiation (for the confocal analysis) or 1, 3, 6 and 24 hours post-irradiation (for the spt analysis). OD_{650} measurements were made every hour on three independent cultures for 9h post-irradiation and then the following day (t_{24h}). Full UV-C survival curves were performed for *E. coli* DH5α and exponential and stationary phase DR^{WT} by serially diluting non-irradiated and irradiated cultures (exposed to 0 to 12 kJ/m^2 for DR^{WT} or 0 to 0.95 kJ/m^2 for *E. coli*) and spotting 8 µl of each dilution on TGY1X or LB (for *E. coli*) agar plates. After 48h incubation of the plates at 37°C, individual colonies were counted and the surviving fraction was determined using non-irradiated cells as a reference. A similar procedure was used to determine the survival fraction of $DR^{HU\text{-}mCh}$ and $DR^{HU\text{-}mEos}$ strains after exposure to 1.9 and 12.0 kJ/m^2.

Sample preparation for confocal microscopy and sptPALM

For confocal microscopy analysis, DR^{WT} cells were stained with Nile Red (30 µM) and Syto9 (200 nM) for 10 min at room temperature, to visualize the cell membrane and nucleoid, respectively, while $DR^{HU\text{-}mCh}$ cells were only stained with syto9 (200 nM). The cells were then harvested by centrifugation and resuspended in 10 µl TGY2X. 0.5 µl of this cell suspension was then placed on a 1.5% (w/v) low melting agarose (LMA; Bio-Rad) TGY2X pad prepared on a cover glass using a gene frame (Thermo Scientific). A 2 mm-wide band of LMA was cut out to provide oxygen. A glass slide was then placed on top of the pad and the sample was sealed with picodent twinsil. Sample preparation for microscopy typically took approximately 30 min, so cells were usually imaged 30 min after the designated timepoint. The samples were maintained at 30°C during image acquisition. For spt analysis, cells were washed 3 times in M9DR medium to limit autoblinking,

as described previously (Floc'h *et al.*, 2018), and were finally resuspended in 20-100 µl M9DR medium, depending on the size of the pellet. 10 µl of this cell suspension was then placed on a coverslip cleaned with an ozone cleaner device (UVOCS) and the cells were left to sediment for 2 minutes, after which the excess liquid was removed. After a further 2-4 minute of air-drying, 10 µl 1.5% (w/v) LMA in M9DR was poured over the cells and a glass slide was placed on top to evenly distribute the LMA. Samples were sealed with picodent Twinsil® and imaged within 20 minutes.

Confocal data acquisition

Spinning-disk confocal microscopy was performed using an Olympus IX81 inverted microscope equipped with a Yokogawa CSU-X1 confocal head. The excitation laser beam (Ilas2 laser bench, GATACA systems) was focused to the back focal plane of a 100X 1.49-numerical-aperture (NA) oil immersion apochromatic objective. For cell and nucleoid analyses, series of Z-planes were acquired every 100 nm using a PRIOR N400 piezo stage. Fluorescence excitation was performed at 488 nm for Syto 9 and 561 nm for Nile Red or mCherry. Fluorescence emission was collected with an Andor iXon Ultra EMCCD camera through a quad-band Semrock™ Di01-T405/488/568/647 dichroic mirror and single-band emission filters adapted to each fluorophore used: 520 nm for Syto9 (FF02-520/28 Semrock™), and 600 nm for mCherry or Nile Red (ET600/50m Chroma™). Data acquisition was performed using Metamorph 7.10 (Molecular devices).

SptPALM data acquisition and tracking of *oriC/ter* loci

SptPALM acquisitions on the DR^{HUmEos} strain were acquired on a SAFE 360 (Abbelight) SMLM set up. Data was acquired at 27°C under continuous illumination with 400 W/cm² 561 nm light and a frame time of 10 ms. The intensity of the 405 nm laser was manually increased during acquisition to maintain approximately constant localization density. 40,000 – 60,000 frames were acquired per dataset. A transmission light image was acquired prior to sptPALM acquisition for segmentation of the cells. *oriC* and *ter* labeled strains of *D. radiodurans* were imaged on a home-built PALM set-up. First, a bright field image and an image of HU-mCherry were collected (100 ms exposure time, 10 W/cm^2 561 nm light). Second, the *oriC* or *ter* sites labelled with ParB-GFP were imaged every second using an exposure time of 100 ms and 10 W/cm^2 488 nm light, until all sites had bleached (~100-500 frames).

Confocal data analysis

3D nucleoids were segmented by automatic thresholding of the Syto9 or mCherry fluorescence signal using the 'surface' procedure of the Imaris software (Oxford instruments) after parameter optimization (surface smoothing detail = 0.1 µm and background subtraction = 0.2 µm). The volume, sphericity and mean channel intensities (in the two channels) of the segmented nucleoids were then extracted for further analysis. After exposure to sublethal and lethal doses of UV-C light, 450-550 individual cells from each timepoint (t_0 to t_{24h}) were classified in terms of phase of the cell cycle (phase P1 to P6 for exponentially growing cells and phases P1 to P8 for stationary cells), cell perimeter, cell integrity, nucleoid volume,

nucleoid morphology and nucleoid position (centered or off-center). Cell perimeters were obtained by automatic segmentation of cells using Cellpose (Stringer *et al.*, 2021) and conversion of the obtained masks into ROIs in Fiji (Schneider *et al.*, 2012), which could be used to extract the perimeter of the segmented cells. Phase 5 cells, in particular, but also some distorted cells were poorly segmented by Cellpose. In these cases, segmentation was performed manually in ImageJ.

sptPALM and *oriC/ter* tracking data analysis

Nucleoids were manually segmented from an overlay of the bright field and super-resolved images of HU-mEos4b. A small fraction of cells with poorly defined nucleoids were excluded from further analysis. Despite the washing steps, occasionally a fraction of cells still showed strong autoblinking (Floc'h *et al.*, 2018); these cells were also discarded from the analysis. Single molecules were localized using the Thunderstorm plugin in ImageJ (Ovesný *et al.*, 2014). Trajectories of single molecules were obtained using the tracking software Swift (Endesfelder *et al.* in prep), using the following tracking parameters: 'exp_displacement = 60 nm', 'p_bleach = 0.1', 'p_blink = 0.2', 'p_reappear = 0.5', 'precision = 22 nm', 'max_displacement = 250 nm', 'max_displacement_pp = 250 nm' and 'max_blinking_duration = 2 frames'. Default values were used for the other parameters. Swift splits tracks, which contain motion changes (i.e. immobile -> diffusive), into segments containing unique behaviors. These segments were considered as trajectories for further analysis. Of note, only a small fraction of the tracks of HU-mEos4b contained multiple segments (~1-2%) suggesting that the time HU-mEos4b spends in a given state is relatively long compared to the average track length.

Trajectories were further analyzed in MATLAB to assign them to specific nucleoid morphologies based on the applied segmentation and to calculate the apparent diffusion coefficients. Apparent diffusion coefficients of single trajectories (Di*) were calculated from the 1-step mean squared jump distance (MJD) as described by Stracy et al. (Stracy *et al.*, 2021) using:

$$D_i^* = \frac{1}{4n\Delta t}\sum_{i=1}^{n}[x(i\Delta t) - x(i\Delta t + \Delta t)]^2 + [y(i\Delta t) - y(i\Delta t + \Delta t)]^2$$

where n is the number of displacements over which the 1-step MSD is calculated, $x(t)$ and $y(t)$ are the coordinates of the molecule at time t and Δt is the frametime. In this work, 4 displacements per track (made of at least 5 measurements) were taken into account (n = 4).

OriC and *ter* loci were localized using Thunderstorm (Ovesný *et al.*, 2014). Trajectories were obtained using Swift (Endesfelder *et al.* in prep) with the following tracking parameters: 'exp_displacement = 50 nm', 'p_bleach = 0.001 ', 'precision = 50 nm', 'max_displacement = 250 nm', 'max_displacement_pp = 250 nm'. Default values were used for the other parameters. Trajectories were further analyzed in MATLAB to calculate the apparent diffusion coefficients. Only trajectories with >10 localizations were considered.

Western blot analysis

10 ml samples of DR^{HUmCh} cultures were collected immediately after resuspending cells in TGY2X medium (t_0) and then 1, 2 (for sublethal dose only), 3, 6 and 24 hours post-irradiation with either sublethal (1.9 kJ/m^2) or lethal (12.0 kJ/m^2) UV-C dose. Similarly, non-irradiated samples of exponentially and stationary phase cells were also processed alongside these irradiated samples. Each culture was resuspended in 0.2 ml PBS supplemented with protease inhibitors (Roche), DNaseI (Roche) and lysozyme (Roche). Cell suspensions were lysed by two 10-sec sonications with a microtip followed by 45 min mechanical shaking with 100 µl glass beads (Macherey Nagel) at 4°C. Cell debris were eliminated by centrifugation at 14,000 rpm for 10 min and the soluble fraction was recovered. 7 µg of each cell extract was loaded on a 12% stain-free SDS-PAGE gel (BioRad) and separated by gel electrophoresis at 175 V for 45 min, before transferring the bands to a nitrocellulose membrane using the BioRad transblot system. A stain-free image of the blot was acquired at this point for normalization of the lanes before blocking the membrane with 5% milk in PBS for 30 min. The membrane was then incubated overnight at 4°C with a mouse monoclonal anti-mCherry antibody (Origene; 1:1500) diluted in 5% milk in PBS. After three washes with PBS supplemented with 0.02% Tween20 (PBS-Tween), the membrane was further incubated 1 hour at 25°C with a second antibody (anti-mouse HRP conjugated antibody; Sigma) diluted 1:10,000 in PBS-Tween. After three additional washes with PBS-Tween, the bands were revealed by electrochemiluminescence (ECL) using Clarity Western substrate (BioRad) on a Chemidoc MP imager (BioRad). Using ImageLab (BioRad), bands corresponding to HU-mCherry were quantified relative to the non-irradiated sample loaded on the same gel after normalization of the lanes using the stain-free image. Blots were performed in triplicate and the mean and standard deviation of the obtained values were plotted in GraphPad Prism 8. Statistical differences were determined using a one-way ANOVA (Holm Sidak) multiple comparisons test.

Statistical analysis

Unless otherwise stated, non-parametric Kruskal-Wallis statistical tests were performed with GraphPad Prism 8 in order to assess the significance of the data. Two-tailed p values below 0.05 were considered as significant and were indicated with asterisks: ns: non-significant, * $p \leq 0.05$, ** $p \leq 0.01$, *** $p \leq 0.001$, **** $p \leq 0.0001$.

ACKNOWLEDGEMENTS

We thank Claire Bouthier de la Tour for help in the preparation of the genetically engineered strain of *D. radiodurans*. This work was supported by the CEA Radiobiology program. JW's PhD position was funded by GRAL, a project of the University Grenoble Alpes graduate school (Ecoles Universitaires de Recherche) CBH-EUR-GS (ANR-17-EURE-0003). This work was supported by the Agence Nationale de la Recherche (grants no. ANR-20-CE11-0013-01 and ANR-22-CE11-0029-01) and used the M4D imaging platform of the Grenoble

Instruct-ERIC Center (ISBG : UMS 3518 CNRS-CEA-UGA-EMBL) within the Grenoble Partnership for Structural Biology (PSB), supported by FRISBI (ANR-10-INBS-05-02) and GRAL (ANR-10-LABX-49-01), financed within the University Grenoble Alpes graduate school (Ecoles Universitaires de Recherche) CBH-EUR-GS (ANR-17-EURE-0003). IBS acknowledges integration into the Interdisciplinary Research Institute of Grenoble (IRIG, CEA).

COMPETING INTERESTS

The authors declare no competing interests.

AUTHOR CONTRIBUTIONS

PV, JW, JPK, DB and JT designed the research. PV, JW, FL and JPK performed the microscopy experiments. PS prepared the genetically modified strains of *D. radiodurans*. PV, JW, JPK, FC, DB and JT analyzed the data. PV, JW, DB and JT wrote the manuscript and all authors discussed the results and approved the manuscript.

REFERENCES

Aki, T. (1997) Repressor induced site-specific binding of HU for transcriptional regulation. *The EMBO Journal* **16**: 3666–3674.

Azam, T.A., and Ishihama, A. (1999) Twelve Species of the Nucleoid-associated Protein from *Escherichia coli*. *Journal of Biological Chemistry* **274**: 33105–33113.

Banneville, A.-S., Bouthier de la Tour, C., De Bonis, S., Hognon, C., Colletier, J.-P., Teulon, J.-M., *et al.* (2022) Structural and functional characterization of DdrC, a novel DNA damage-induced nucleoid associated protein involved in DNA compaction. *Nucleic Acids Research* **50**: 7680–7696 https://doi.org/10.1093/nar/gkac563. Accessed August 16, 2022.

Basu, B., and Apte, S.K. (2012) Gamma radiation-induced proteome of *Deinococcus radiodurans* primarily targets DNA repair and oxidative stress alleviation. *Mol Cell Proteomics* **11**: M111.011734.

Battista, J.R. (1997) Against all odds: the survival strategies of *Deinococcus radiodurans*. *Annu Rev Microbiol* **51**: 203–24.

Bettridge, K., Verma, S., Weng, X., Adhya, S., and Xiao, J. (2021) Single-molecule tracking reveals that the nucleoid-associated protein HU plays a dual role in maintaining proper nucleoid volume through differential interactions with chromosomal DNA. *Molecular Microbiology* **115**: 12–27 https://doi.org/10.1111/mmi.14572. Accessed June 20, 2023.

Boor, K.J. (2006) Bacterial Stress Responses: What Doesn't Kill Them Can Make Them Stronger. *PLoS Biol* **4**: e23.

Bouthier De La Tour, C., Armengaud, J., Dulermo, R., Blanchard, L., Devigne, A., De Groot, A., *et al.* (2015) The abundant and essential HU proteins in *Deinococcus deserti* and *Deinococcus radiodurans* are translated from leaderless mRNA. *Microbiology* **161**: 2410–2422.

Bouthier de la Tour, C., Mathieu, M., Meyer, L., Dupaigne, P., Passot, F., Servant, P., *et al.* (2017) In vivo and in vitro characterization of DdrC, a DNA damage response protein in *Deinococcus radiodurans* bacterium. *PLoS One* **12**: e0177751.

Bouthier de la Tour, C., Passot, F.M., Toueille, M., Mirabella, B., Guerin, P., Blanchard, L., *et al.* (2013) Comparative proteomics reveals key proteins recruited at the nucleoid of *Deinococcus* after irradiation-induced DNA damage. *Proteomics* **13**: 3457–69.

Boutte, C.C., and Crosson, S. (2013) Bacterial lifestyle shapes stringent response activation. *Trends in Microbiology* **21**: 174–180.

Chawla, M., Mishra, S., Anand, K., Parikh, P., Mehta, M., Vij, M., *et al.* (2018) Redox-dependent condensation of the mycobacterial nucleoid by WhiB4. *Redox Biology* **19**: 116–133.

Chen, S.W.W., Banneville, A.S., Teulon, J.M., Timmins, J., and Pellequer, J.L. (2020) Nanoscale surface structures of DNA bound to *Deinococcus radiodurans* HU unveiled by atomic force microscopy. *Nanoscale* **12**: 22628–22638.

Cox, M.M., and Battista, J.R. (2005) *Deinococcus radiodurans* - The consummate survivor. *Nature Reviews Microbiology* **3**: 882–892.

Cuypers, M.G., Mitchell, E.P., Romao, C.V., and McSweeney, S.M. (2007) The crystal structure of the Dps2 from *Deinococcus radiodurans* reveals an unusual pore profile with a non-specific metal binding site. *J Mol Biol* **371**: 787–99.

Dame, R.T., Rashid, F.-Z.M., and Grainger, D.C. (2020) Chromosome organization in bacteria: mechanistic insights into genome structure and function. *Nature Reviews Genetics* **21**: 227–242 https://doi.org/10.1038/s41576-019-0185-4.

De Zitter, E., Thédié, D., Mönkemöller, V., Hugelier, S., Beaudouin, J., Adam, V., *et al.* (2019) Mechanistic investigation of mEos4b reveals a strategy to reduce track interruptions in sptPALM. *Nature Methods* **16**: 707–710 https://doi.org/10.1038/s41592-019-0462-3.

Díaz-Riaño, J., Posada, L., Acosta, I.C., Ruíz-Pérez, C., García-Castillo, C., Reyes, A., and Zambrano, M.M. (2019) Computational search for UV radiation resistance strategies in *Deinococcus swuensis* isolated from Paramo ecosystems. *PLoS ONE* **14**.

Dillon, S.C., and Dorman, C.J. (2010) Bacterial nucleoid-associated proteins, nucleoid structure and gene expression. *Nat Rev Microbiol* **8**: 185–195.

Dilweg, I.W., and Dame, R.T. (2018) Post-translational modification of nucleoid-associated proteins: an extra layer of functional modulation in bacteria? *Biochemical Society Transactions* **46**: 1381–1392 https://doi.org/10.1042/BST20180488. Accessed March 3, 2022.

dos Santos, Á., Cook, A.W., Gough, R.E., Schilling, M., Olszok, N.A., Brown, I., *et al.* (2020) DNA damage alters nuclear mechanics through chromatin reorganization. *Nucleic Acids Res* **49**: 340–353.

Dworkin, J., and Harwood, C.S. (2022) Metabolic Reprogramming and Longevity in Quiescence. *Annu Rev Microbiol* **76**: 91–111.

Endesfelder, M., Schließl, C., Turkowyd, B., Lechner, T., and Endesfelder, U. swift – fast, probabilistic tracking for dense, highly dynamic single-molecule data. **Manuscript in prep.**

Estévez Castro, C.F., Serment-Guerrero, J.H., and Fuentes, J.L. (2018) Influence of uvrA, recJ and recN gene mutations on nucleoid reorganization in UV-treated *Escherichia coli* cells. *FEMS Microbiology Letters* **365**: fny110 https://doi.org/10.1093/femsle/fny110. Accessed August 16, 2023.

Floc'h, K., Lacroix, F., Barbieri, L., Servant, P., Galland, R., Butler, C., *et al.* (2018) Bacterial cell wall nanoimaging by autoblinking microscopy. *Sci Rep* **8**: 14038 http://www.nature.com/articles/s41598-018-32335-z. Accessed October 19, 2019.

Floc'h, K., Lacroix, F., Servant, P., Wong, Y.-S., Kleman, J.-P., Bourgeois, D., and Timmins, J. (2019) Cell morphology and nucleoid dynamics in dividing *Deinococcus radiodurans*. *Nature Communications* **10**: 3815 https://doi.org/10.1038/s41467-019-11725-5.

Gefen, O., Fridman, O., Ronin, I., and Balaban, N.Q. (2014) Direct observation of single stationary-phase bacteria reveals a surprisingly long period of constant protein production activity. *Proc Natl Acad Sci USA* **111**: 556–561.

Ghosh, S., and Grove, A. (2004) Histone-like protein HU from *Deinococcus radiodurans* binds preferentially to four-way DNA junctions. *J Mol Biol* **337**: 561–71.

Ghosh, S., and Grove, A. (2006) The *Deinococcus radiodurans* -Encoded HU Protein Has Two DNA-Binding Domains. *Biochemistry* **45**: 1723–1733.

Ghosh, S., Padmanabhan, B., Anand, C., and Nagaraja, V. (2016) Lysine acetylation of the *Mycobacterium tuberculosis* HU protein modulates its DNA binding and genome organization. *Molecular Microbiology* **100**: 577–588.

Grove, A. (2011) Functional evolution of bacterial histone-like HU proteins. *Curr Issues Mol Biol* **13**: 1–12.

Gupta, M., Sajid, A., Sharma, K., Ghosh, S., Arora, G., Singh, R., *et al.* (2014) HupB, a Nucleoid-Associated Protein of *Mycobacterium tuberculosis,* Is Modified by Serine/Threonine Protein Kinases *In Vivo*. *J Bacteriol* **196**: 2646–2657.

Haikarainen, T., and Papageorgiou, A.C. (2010) Dps-like proteins: structural and functional insights into a versatile protein family. *Cell Mol Life Sci* **67**: 341–351.

Hammel, M., Amlanjyoti, D., Reyes, F.E., Chen, J.H., Parpana, R., Tang, H.Y.H., *et al.* (2016) HU multimerization shift controls nucleoid compaction. *Science Advances* **2**.

Harsojo, Kitayama, S., and Matsuyama, A. (1981) Genome multiplicity and radiation resistance in *Micrococcus radiodurans*. *J Biochem* **90**: 877–80.

Hauer, M.H., Seeber, A., Singh, V., Thierry, R., Sack, R., Amitai, A., *et al.* (2017) Histone degradation in response to DNA damage enhances chromatin dynamics and recombination rates. *Nat Struct Mol Biol* **24**: 99–107.

Hengge, R. (2011) Stationary-Phase Gene Regulation in *Escherichia coli*. *EcoSal Plus* **4**: ecosalplus.5.6.3.

Hołówka, J., and Zakrzewska-Czerwińska, J. (2020) Nucleoid Associated Proteins: The Small Organizers That Help to Cope With Stress. *Front Microbiol* **11**: 590.

Hou, J., Dai, J., Chen, Z., Wang, Y., Cao, J., Hu, J., *et al.* (2022) Phosphorylation Regulation of a Histone-like HU Protein from *Deinococcus radiodurans*. *Protein & Peptide Letters* **29**: 891–899 http://www.eurekaselect.com/article/125634.

Huisman, O., Faelen, M., Girard, D., Jaffé, A., Toussaint, A., and Rouvière-Yaniv, J. (1989) Multiple defects in Escherichia coli mutants lacking HU protein. *J Bacteriol* **171**: 3704–3712.

Joyeux, M. (2019) Preferential Localization of the Bacterial Nucleoid. *Microorganisms* **7**.

Kamashev, D., and Rouviere-Yaniv, J. (2000) The histone-like protein HU binds specifically to DNA recombination and repair intermediates. *The EMBO Journal* **19**: 6527–6535 https://doi.org/10.1093/emboj/19.23.6527. Accessed June 20, 2023.

Kapanidis, A.N., Uphoff, S., and Stracy, M. (2018) Understanding Protein Mobility in Bacteria by Tracking Single Molecules. *J Mol Biol* **430**: 4443–4455.

Kar, S., Edgar, R., and Adhya, S. (2005) Nucleoid remodeling by an altered HU protein: Reorganization of the transcription program. *Proceedings of the National Academy of Sciences* **102**: 16397–16402 https://doi.org/10.1073/pnas.0508032102. Accessed July 12, 2023.

Karas, V.O., Westerlaken, I., and Meyer, A.S. (2015) The DNA-Binding Protein from Starved Cells (Dps) Utilizes Dual Functions To Defend Cells against Multiple Stresses. *Journal of Bacteriology* **197**: 3206–3215 http://www.ncbi.nlm.nih.gov/pmc/articles/PMC4560292/.

Kehrer, J.P. (2000) The Haber–Weiss reaction and mechanisms of toxicity. *Toxicology* **149**: 43–50.

Krisko, A., and Radman, M. (2013) Biology of extreme radiation resistance: the way of *Deinococcus radiodurans*. *Cold Spring Harbor perspectives in biology* **5**.

Lal, A., Dhar, A., Trostel, A., Kouzine, F., Seshasayee, A.S.N., and Adhya, S. (2016) Genome scale patterns of supercoiling in a bacterial chromosome. *Nat Commun* **7**: 11055.

Li, S., and Waters, R. (1998) *Escherichia coli* Strains Lacking Protein HU Are UV Sensitive due to a Role for HU in Homologous Recombination. *J Bacteriol* **180**: 3750–3756.

Liu, Y., Zhou, J., Omelchenko, M.V., Beliaev, A.S., Venkateswaran, A., Stair, J., *et al.* (2003) Transcriptome dynamics of *Deinococcus radiodurans* recovering from ionizing radiation. *Proc Natl Acad Sci U S A* **100**: 4191–6. Epub 2003 Mar 21.

Macvanin, M., and Adhya, S. (2012) Architectural organization in *E. coli* nucleoid. *Biochimica et Biophysica Acta (BBA) - Gene Regulatory Mechanisms* **1819**: 830–835.

Makarova, K.S., Aravind, L., Wolf, Y.I., Tatusov, R.L., Minton, K.W., Koonin, E.V., and Daly, M.J. (2001) Genome of the extremely radiation-resistant bacterium *Deinococcus radiodurans* viewed from the perspective of comparative genomics. *Microbiol Mol Biol Rev* **65**: 44-79.

Mennecier, S., Coste, G., Servant, P., Bailone, A., and Sommer, S. (2004) Mismatch repair ensures fidelity of replication and recombination in the radioresistant organism *Deinococcus radiodurans*. *Mol Genet Genomics* **272**: 460–9.

Meyer, A.S., and Grainger, D.C. (2013) The *Escherichia coli* Nucleoid in Stationary Phase. In *Advances in Applied Microbiology*. Elsevier, pp. 69–86 https://linkinghub.elsevier.com/retrieve/pii/B9780124076785000027. Accessed September 2, 2022.

Miangolarra, A.M., Li, S.H.-J., Joanny, J.-F., Wingreen, N.S., and Castellana, M. (2021) Steric interactions and out-of-equilibrium processes control the internal organization of bacteria. *Proceedings of the National Academy of Sciences* **118**: e2106014118 https://doi.org/10.1073/pnas.2106014118. Accessed July 13, 2023.

Mitosch, K., Rieckh, G., and Bollenbach, T. (2019) Temporal order and precision of complex stress responses in individual bacteria. *Molecular Systems Biology* **15**: e8470 https://doi.org/10.15252/msb.20188470. Accessed July 12, 2023.

Morikawa, K., Ushijima, Y., Ohniwa, R.L., Miyakoshi, M., and Takeyasu, K. (2019) What Happens in the Staphylococcal Nucleoid under Oxidative Stress? *Microorganisms* **7**: 631.

Nair, S., and Finkel, S.E. (2004) Dps protects cells against multiple stresses during stationary phase. *J Bacteriol* **186**: 4192–4198.

Nguyen, H.H., Tour, C.B. de la, Toueille, M., Vannier, F., Sommer, S., and Servant, P. (2009) The essential histone-like protein HU plays a major role in *Deinococcus radiodurans* nucleoid compaction. *Molecular Microbiology* **73**: 240–52.

Oberto, J., Nabti, S., Jooste, V., Mignot, H., and Rouviere-Yaniv, J. (2009) The HU Regulon Is Composed of Genes Responding to Anaerobiosis, Acid Stress, High Osmolarity and SOS Induction. *PLoS ONE* **4**: e4367.

Odsbu, I., and Skarstad, K. (2014) DNA compaction in the early part of the SOS response is dependent on RecN and RecA. *Microbiology* **160**: 872–882.

Okanishi, H., Kim, K., Fukui, K., Yano, T., Kuramitsu, S., and Masui, R. (2017) Proteome-wide identification of lysine succinylation in thermophilic and mesophilic bacteria. *Biochimica et Biophysica Acta (BBA) - Proteins and Proteomics* **1865**: 232–242.

Ovesný, M., Křížek, P., Borkovec, J., Švindrych, Z., and Hagen, G.M. (2014) ThunderSTORM: a comprehensive ImageJ plug-in for PALM and STORM data analysis and super-resolution imaging. *Bioinformatics* **30**: 2389–2390 https://doi.org/10.1093/bioinformatics/btu202. Accessed June 30, 2023.

Passot, F.M., Nguyen, H.H., Dard-Dascot, C., Thermes, C., Servant, P., Espeli, O., and Sommer, S. (2015) Nucleoid organization in the radioresistant bacterium *Deinococcus radiodurans*. *Mol Microbiol* **97**: 759–74.

Piggot, P.J., and Hilbert, D.W. (2004) Sporulation of *Bacillus subtilis*. *Curr Opin Microbiol* **7**: 579–586.

Remesh, S.G., Verma, S.C., Chen, J.-H., Ekman, A.A., Larabell, C.A., Adhya, S., and Hammel, M. (2020) Nucleoid remodeling during environmental adaptation is regulated by HU-dependent DNA bundling. *Nature Communications* **11**: 2905 https://doi.org/10.1038/s41467-020-16724-5.

Richa, Sinha, R.P., and H Ä Der, D.P. (2015) Physiological aspects of UV-excitation of DNA. *Topics in Current Chemistry* **356**: 203–248.

Romao, C.V., Mitchell, E.P., and McSweeney, S. (2006) The crystal structure of *Deinococcus radiodurans* Dps protein (DR2263) reveals the presence of a novel metal centre in the N terminus. *J Biol Inorg Chem* **11**: 891–902.

Santos, S.P., Mitchell, E.P., Franquelim, H.G., Castanho, M.A., Abreu, I.A., and Romao, C.V. (2015) Dps from *Deinococcus radiodurans*: oligomeric forms of Dps1 with distinct cellular functions and Dps2 involved in metal storage. *Febs J* **282**: 4307–27.

Santos, S.P., Yang, Y., Rosa, M.T.G., Rodrigues, M.A.A., De La Tour, C.B., Sommer, S., *et al.* (2019) The interplay between Mn and Fe in *Deinococcus radiodurans* triggers cellular protection during paraquat-induced oxidative stress. *Sci Rep* **9**: 17217.

Sato, Y.T., Watanabe, S., Kenmotsu, T., Ichikawa, M., Yoshikawa, Y., Teramoto, J., *et al.* (2013) Structural Change of DNA Induced by Nucleoid Proteins: Growth Phase-Specific Fis and Stationary Phase-Specific Dps. *Biophysical Journal* **105**: 1037–1044 https://doi.org/10.1016/j.bpj.2013.07.025. Accessed March 3, 2022.

Schneider, C.A., Rasband, W.S., and Eliceiri, K.W. (2012) NIH Image to ImageJ: 25 years of image analysis. *Nature Methods* **9**: 671–675 https://doi.org/10.1038/nmeth.2089.

Shechter, N., Zaltzman, L., Weiner, A., Brumfeld, V., Shimoni, E., Fridmann-Sirkis, Y., and Minsky, A. (2013) Stress-induced Condensation of Bacterial Genomes Results in Re-pairing of Sister Chromosomes. *Journal of Biological Chemistry* **288**: 25659–25667.

Slade, D., and Radman, M. (2011) Oxidative stress resistance in *Deinococcus radiodurans*. *Microbiol Mol Biol Rev* **75**: 133–91.

Sobetzko, P., Travers, A., and Muskhelishvili, G. (2012) Gene order and chromosome dynamics coordinate spatiotemporal gene expression during the bacterial growth cycle. *Proc Natl Acad Sci USA* **109** https://pnas.org/doi/full/10.1073/pnas.1108229109. Accessed September 12, 2023.

Steil, L., Serrano, M., Henriques, A.O., and Völker, U. (2005) Genome-wide analysis of temporally regulated and compartment-specific gene expression in sporulating cells of *Bacillus subtilis*. *Microbiology (Reading)* **151**: 399–420.

Stojkova, P., Spidlova, P., and Stulik, J. (2019) Nucleoid-Associated Protein HU: A Lilliputian in Gene Regulation of Bacterial Virulence. *Frontiers in Cellular and Infection Microbiology* **9** https://www.frontiersin.org/articles/10.3389/fcimb.2019.00159.

Stracy, M., Schweizer, J., Sherratt, D.J., Kapanidis, A.N., Uphoff, S., and Lesterlin, C. (2021) Transient non-specific DNA binding dominates the target search of bacterial DNA-binding proteins. *Molecular Cell* **81**: 1499-1514.e6 https://doi.org/10.1016/j.molcel.2021.01.039. Accessed June 20, 2023.

Stringer, C., Wang, T., Michaelos, M., and Pachitariu, M. (2021) Cellpose: a generalist algorithm for cellular segmentation. *Nature Methods* **18**: 100–106 https://app.readcube.com/library/undefined/item/5d567c6e-6e34-47aa-965f-65f37acff83e.

Szafran, M.J., Jakimowicz, D., and Elliot, M.A. (2020) Compaction and control—the role of chromosome-organizing proteins in *Streptomyces*. *FEMS Microbiology Reviews* **44**: 725–739.

Timmins, J., and Moe, E. (2016) A decade of biochemical and structural studies of the DNA repair machinery of *Deinococcus radiodurans*. *Computational and Structural Biotechnology Journal* **14**: 168–176.

Verma, S.C., Harned, A., Narayan, K., and Adhya, S. (2023) Non-specific and specific DNA binding modes of bacterial histone, HU, separately regulate distinct physiological processes through different mechanisms. *Molecular Microbiology* **119**: 439–455 https://doi.org/10.1111/mmi.15033. Accessed June 20, 2023.

Verma, S.C., Qian, Z., and Adhya, S.L. (2019) Architecture of the *Escherichia coli* nucleoid. *PLoS Genet* **15**: e1008456.

Woldringh, C.L., Jensen, P.R., and Westerhoff, H.V. (1995) Structure and partitioning of bacterial DNA: determined by a balance of compaction and expansion forces? *FEMS Microbiol Lett* **131**: 235–242.

Zahradka, K., Slade, D., Bailone, A., Sommer, S., Averbeck, D., Petranovic, M., *et al.* (2006) Reassembly of shattered chromosomes in *Deinococcus radiodurans*. *Nature* **443**: 569–73.

Zimmerman, J.M., and Battista, R.J. (2005) A ring-like nucleoid is not necessary for radioresistance in the *Deinococcaceae*. *BMC Microbiology* **5**.

FIGURE LEGENDS

Figure 1: Growth phase-dependent nucleoid remodeling and associated changes in HU dynamics. (A) Representative images of DR^{WT} cells (upper panels) stained with Syto 9 and Nile Red and DR^{HUmCh} (lower panels) in exponential (left) and stationary (right) phase. Scale bar: 5 µm. (B) Nucleoid volume and sphericity of DR^{WT} (blue) and DR^{HUmCh} (red) strains in exponential (light color) and stationary phase (dark color) cells (n=250). Error bars represent the median and interquartile range. **** p<0.0001, Kruskal-Wallis statistical test performed in GraphPad Prism 8. (C) Expression levels of HU-mCherry in exponential and stationary phase (n=3). (D) Histogram distribution of the apparent diffusion coefficient (D_{app}) of HU-mEos4b in exponential (light blue; n=231) and stationary (dark blue; n=196) phase DR^{HUmEos} cells. PDF: Probability density function. (E) Median D_{app} of HU-mEos4b per cell in exponential (light blue; n=231) and stationary phase (dark blue; n=196) cells. Error bars represent the median and interquartile range. **** p<0.0001, Kruskal-Wallis statistical test performed in GraphPad Prism 8. (F) Representative images of exponential (left) and stationary (right) phase $DR^{HU\text{-}mEos}$ nucleoids. The right panel is a close up view of the boxed cells in the left panel and individual HU-mEos4b tracks are overlayed on the epi-fluorescence image. Scale bar upper panel: 0.5 µm. Scale bar lower panel: 3 µm.

Figure 2: Dose-dependent effects of UV-C light on nucleoid organization. (A) Survival curves of exponential (light blue) and stationary (dark blue) DR^{WT} and *E. coli* (green) at different UV doses. The sublethal (1.9 kJ/m^2) and lethal (12.0 kJ/m^2) doses used for the subsequent studies are indicated with arrows. Data represent the mean and standard deviation of at least 3 independent experiments. (B) Representative images of exponential (top panel) and stationary phase (lower panel) DR^{WT} cells stained with Syto9 and Nile Red before (0 kJ/m^2; left) and after exposure to 1.9 (middle) or 12.0 kJ/m^2 UV-C light. Scale bar: 2.5 µm. (C) Nucleoid volume and sphericity of exponential (left) and stationary (right) DR^{WT} cells before (0 kJ/m^2; blue) and after exposure to 1.9 (orange) or 12.0 kJ/m^2 (red) UV-C light cells (n=250). Error bars represent the median and interquartile range. ns: non-significant, **** p<0.0001, Kruskal-Wallis statistical test performed in GraphPad Prism 8. (D-E) Histogram distribution of the apparent diffusion coefficient (D_{app}) of HU-mEos4b (left) and median D_{app} of HU-mEos4b per cell (right) in exponential (top panel) and stationary (lower panel) DR^{HUmEos} before (blue; n=231 for exp and 196 for stat) and after exposure to 1.9 (orange; n=32 for exp and 356 for stat) or 12.0 kJ/m^2 (red; n=114 for exp and 152 for stat)

UV-C light. PDF: Probability density function. Error bars represent the median and interquartile range. **** p<0.0001, Kruskal-Wallis statistical test performed in GraphPad Prism 8.

Figure 3: Effects of sublethal UV-C exposure on nucleoid organization and morphology. (A) Growth curves of non-irradiated (NIR; full line) and irradiated DR^{WT} (1.9 kJ/m^2; dashed line). Data represent the mean and standard deviation of at least 3 independent experiments. (B) Representative images of DR^{WT} cells stained with Syto9 and Nile Red at different timepoints after exposure to 1.9 kJ/m^2 UV-C light. White and yellow arrows indicate cells with off-center nucleoids and anucleate cells respectively. Scale bar: 5 µm. (C) Nucleoid volume and sphericity of DR^{WT} cells at different timepoints after exposure to 1.9 kJ/m^2 UV-C light (n=250). Error bars represent the median and interquartile range. ns: non-significant, **** p<0.0001, Kruskal-Wallis statistical test performed in GraphPad Prism 8. (D) Evolution of nucleoid morphologies during the recovery from exposure to 1.9 kJ/m^2 UV-C light (n>450). (C)-(D) The three different stages of the recovery phase are indicated above the plots. (E) Examples of the most common UV-C-induced nucleoid and cell morphologies observed by confocal microscopy of Syto9 and Nile Red stained DRWT cells before and after exposure to 1.9 kJ/m^2 UV-C light. In (D), rounded nucleoids correspond to ball-like, bilobed and pear-shaped nucleoids, while expanded nucleoids refer to both expanded and large toroids as depicted in (E).

Figure 4: Effects of sublethal UV-C exposure on the dynamics and abundance of HU. (A) Representative images of DR^{HUmEos} nucleoids at different timepoints after exposure to 1.9 kJ/m^2 UV-C light. Yellow and red arrows indicate rounded and expanded nucleoids respectively. Scale bar: 2 µm. (B) Histogram distribution of the apparent diffusion coefficient (D_{app}) of HU-mEos4b in non-irradiated stationary DR^{HUmEos} (dashed blue line) cells and at different timepoints after exposure to 1.9 kJ/m^2 UV-C light (orange to purple; n>30). PDF: Probability density function. (C) Median D_{app} of HU-mEos4b per cell in non-irradiated exponential (light blue) and stationary (dark blue) DR^{HUmEos} cells and at different timepoints after exposure to 1.9 kJ/m^2 UV-C light (orange to purple; n>30). Error bars represent the median and interquartile range. ns: non-significant, **** p<0.0001, Kruskal-Wallis statistical test performed in GraphPad Prism 8. (D) Relative HU-mCherry levels determined by Western blot analysis at different timepoints after exposure to 1.9 kJ/m^2 UV-C light (orange to purple; n=3). The intensity of NIR samples was set to 1. Error bars represent the standard deviation. * p<0.05, ** p<0.01, **** p<0.0001, unpaired t-test performed in GraphPad

Prism 8. (C)-(D) The three different stages of the recovery phase are indicated above the plots. (E) Representative images of DR^{HUmCh} at different timepoints after exposure to 1.9 kJ/m^2 UV-C light. Yellow arrows indicate cells with diffuse HU-mCherry staining. Scale bar: 5 µm.

Figure 5: Effects of lethal UV-C exposure on nucleoid organization and morphology. (A) Growth curves of non-irradiated (NIR; full line) and irradiated DR^{WT} (12.0 kJ/m^2; dashed line). Data represent the mean and standard deviation of at least 3 independent experiments. (B) Representative images of DR^{WT} cells stained with Syto9 and Nile Red at different timepoints after exposure to 12.0 kJ/m^2 UV-C light. White and yellow arrows indicate cells with micro-nucleoids and anucleate cells respectively. Scale bar: 5 µm. (C) Nucleoid volume and sphericity of DR^{WT} cells at different timepoints after exposure to 12.0 kJ/m^2 UV-C light (n=250). Error bars represent the median and interquartile range. * p<0.05, **** p<0.0001, Kruskal-Wallis statistical test performed in GraphPad Prism 8. (D) Evolution of nucleoid morphologies during the recovery from exposure to 12.0 kJ/m^2 UV-C light (n>450). (C)-(D) The three different stages of the response phase are indicated above the plots. (E) Nucleoid volumes associated with different nucleoid morphologies (n>400). **** p<0.0001, Kruskal-Wallis statistical test performed in GraphPad Prism 8.

Figure 6: Effects of lethal UV-C exposure on the dynamics and abundance of HU. (A) Relative HU-mCherry levels determined by Western blot analysis at different timepoints after exposure to 12.0 kJ/m^2 UV-C light (red to purple; n=3). The intensity of NIR samples was set to 1. Error bars represent the standard deviation. ns: non-significant, * p<0.05, *** p<0.001, **** p<0.0001, unpaired t-test performed in GraphPad Prism 8. (B) Representative images of DR^{HUmCh} at different timepoints after exposure to 12.0 kJ/m^2 UV-C light. Micronucleoids are indicated with white arrows, while yellow arrows indicate cells with diffuse HU-mCherry staining. Scale bar: 5 µm. (C) Representative images of DR^{HUmEos} nucleoids at different timepoints after exposure to 12.0 kJ/m^2 UV-C light. Yellow and red arrows indicate micronucleoids and diffuse nucleoids respectively. Scale bar: 5 µm. (D) Histograms of the apparent diffusion coefficient (D_{app}) of HU-mEos4b in non-irradiated exponential DR^{HUmEos} (dashed blue line) cells and at different timepoints after exposure to 12.0 kJ/m^2 UV-C light (red to purple; n>37). (E) Median D_{app} of HU-mEos4b per cell in non-irradiated exponential (light blue) $DR^{HU\text{-}mEos}$ cells and at different timepoints after exposure to 12.0 kJ/m^2 UV-C light (red to purple; n>37). Error bars represent the median and interquartile range. **** p<0.0001, Kruskal-Wallis statistical test performed in GraphPad Prism 8. (A)-(E) The three

different stages of the response phase are indicated above the plots.

Figure 7: Model of stress-induced nucleoid remodeling in *D. radiodurans*. Schematic diagram summarizing the main stages of nucleoid remodeling in *D. radiodurans* induced by either entry into stationary phase (top right) or by exposure to either sublethal (lower left) or lethal (lower right) doses of UV-C irradiation. Changes in nucleoid size and shape are accompanied by significant variations in the level and dynamics of the HU protein, likely reflecting altered HU-DNA interactions. Nucleoid remodeling is also tightly coordinated with cell growth and division.

Figure 1

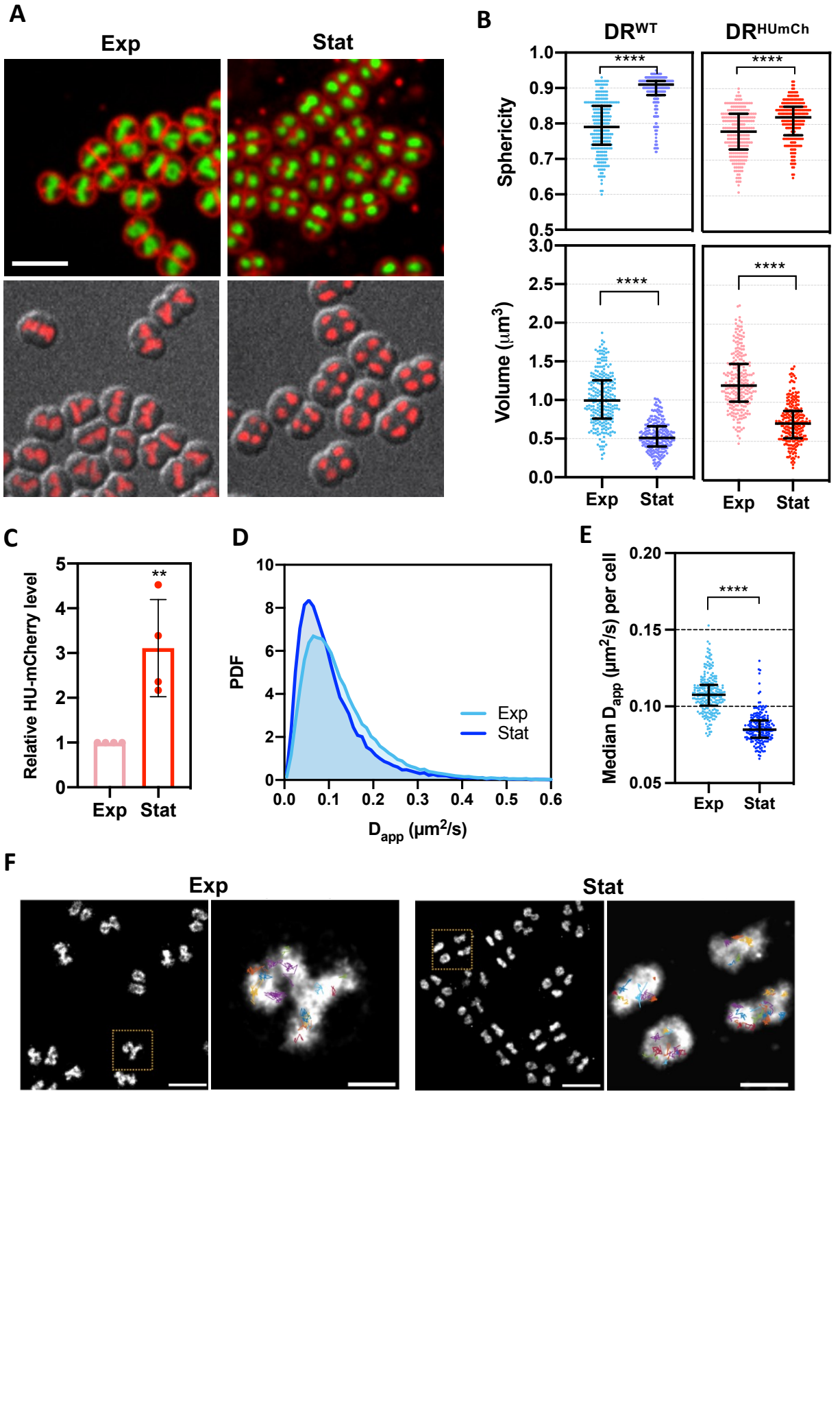

Figure 2

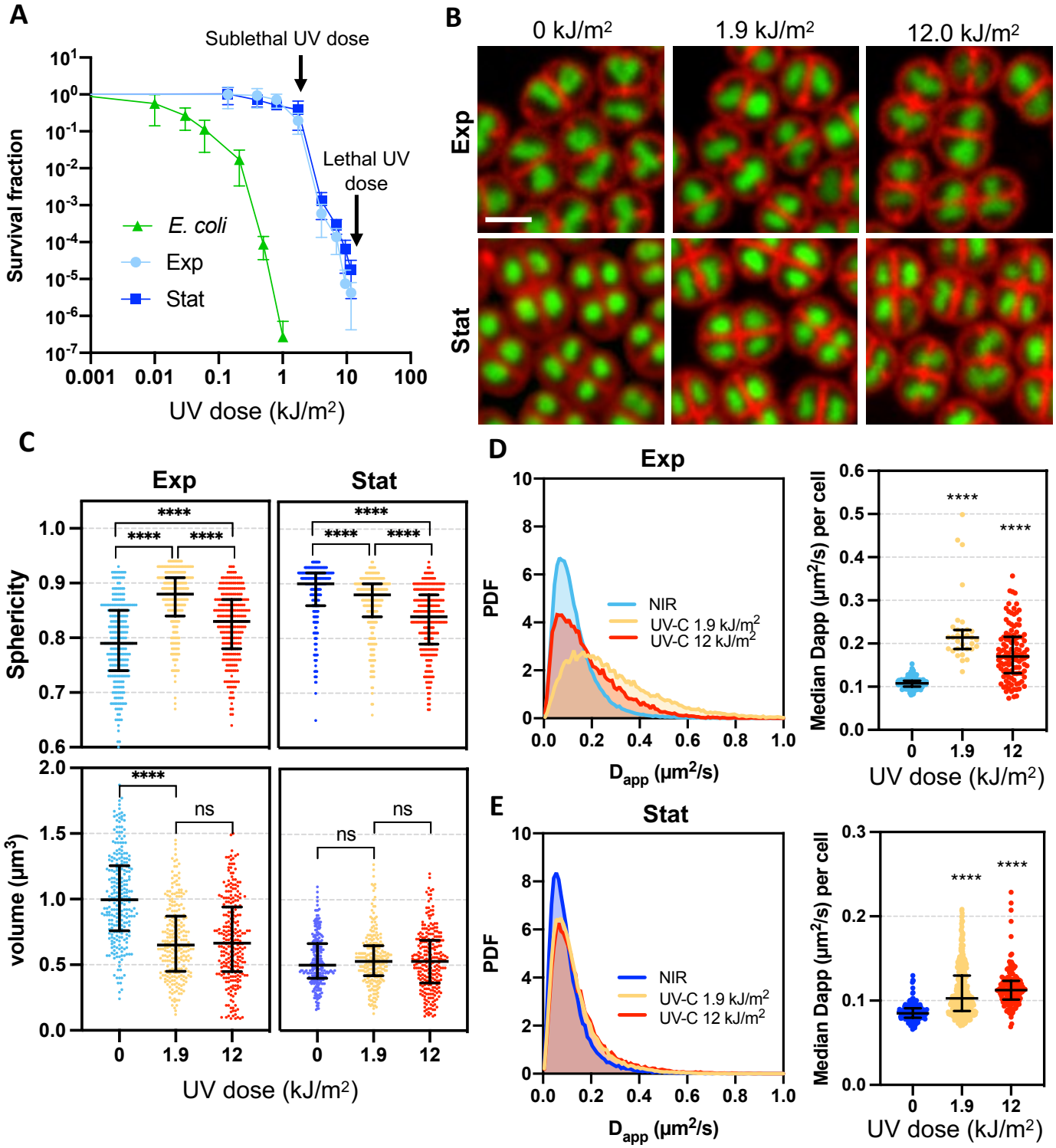

Figure 3

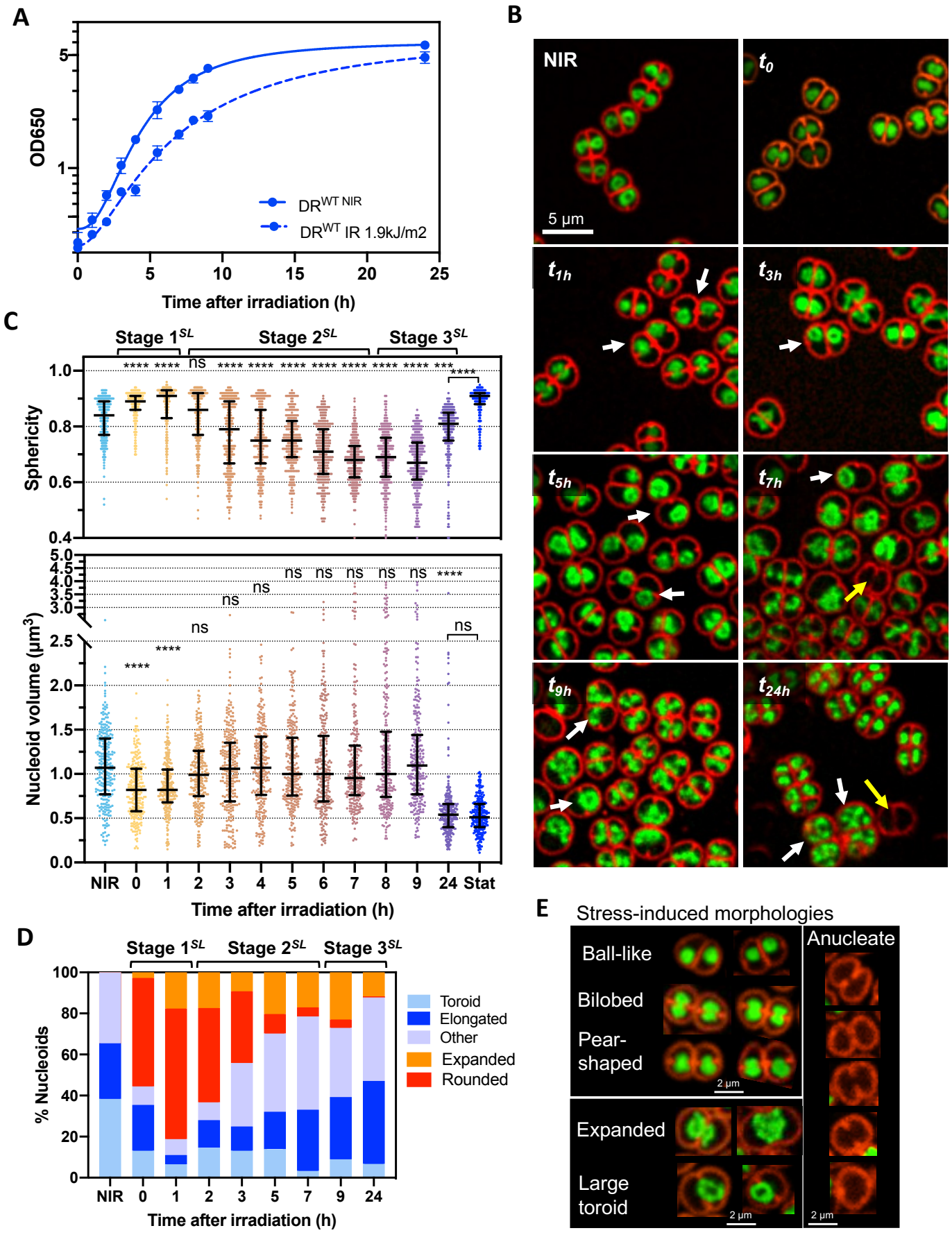

Figure 4

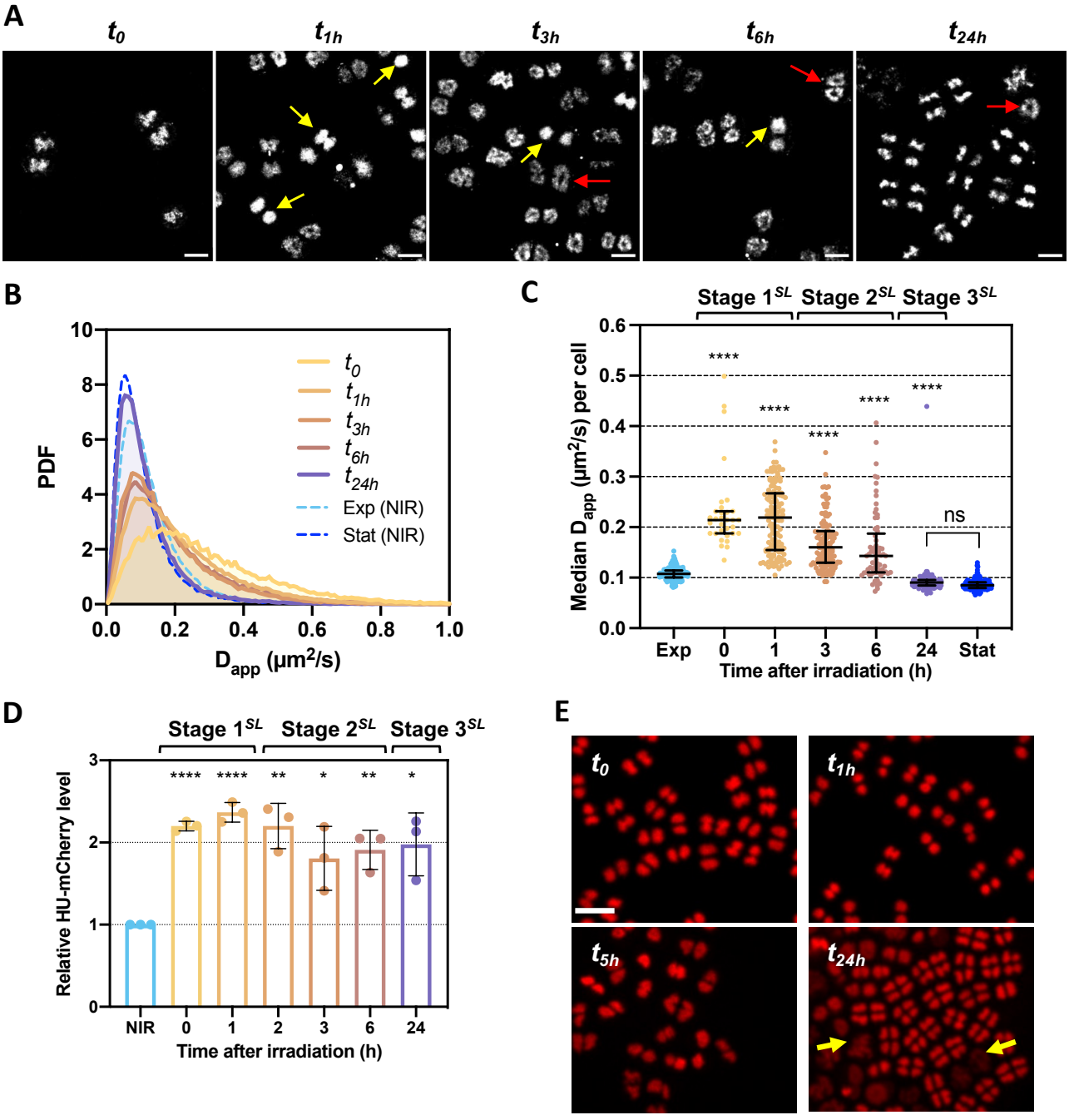

Figure 5

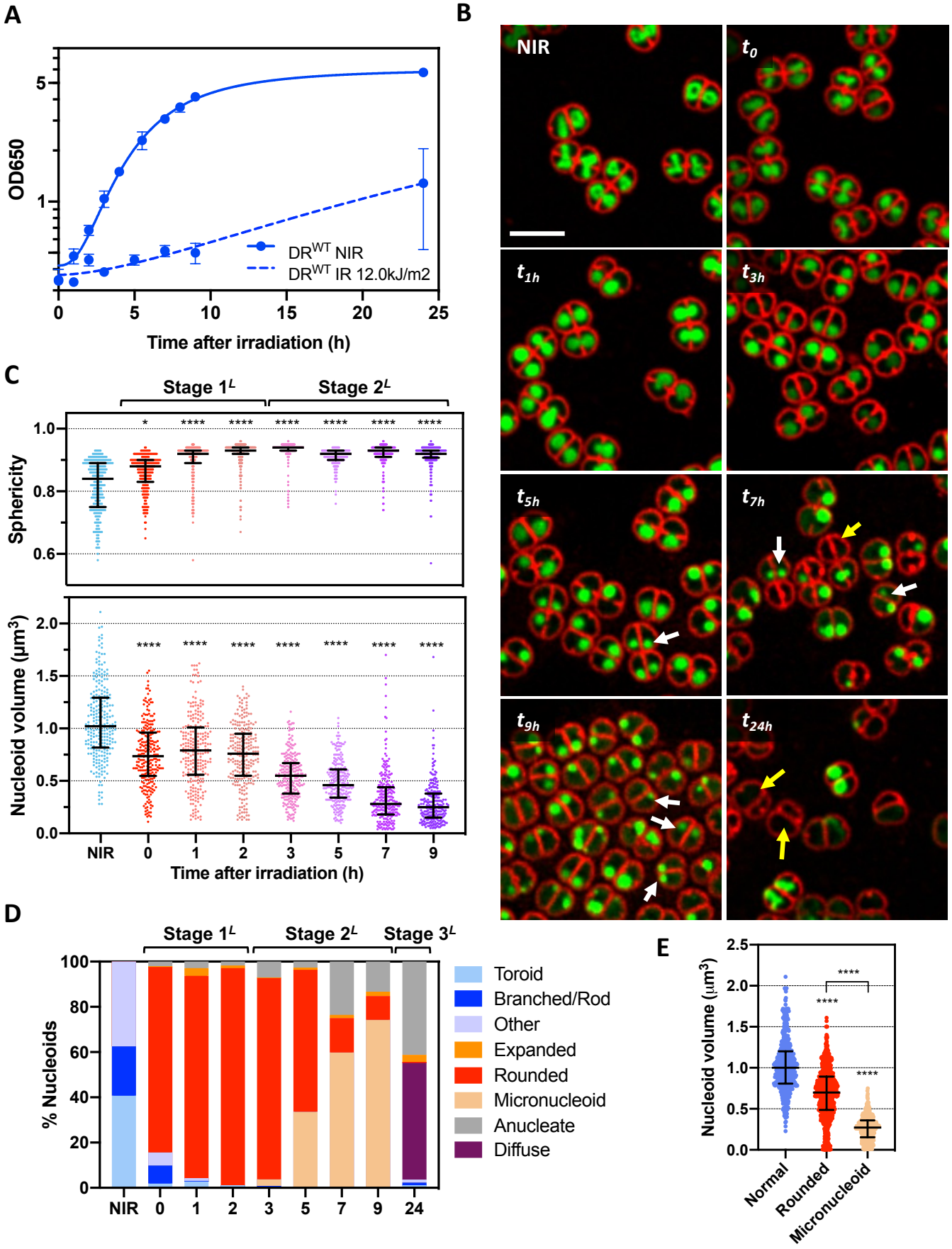

Figure 6

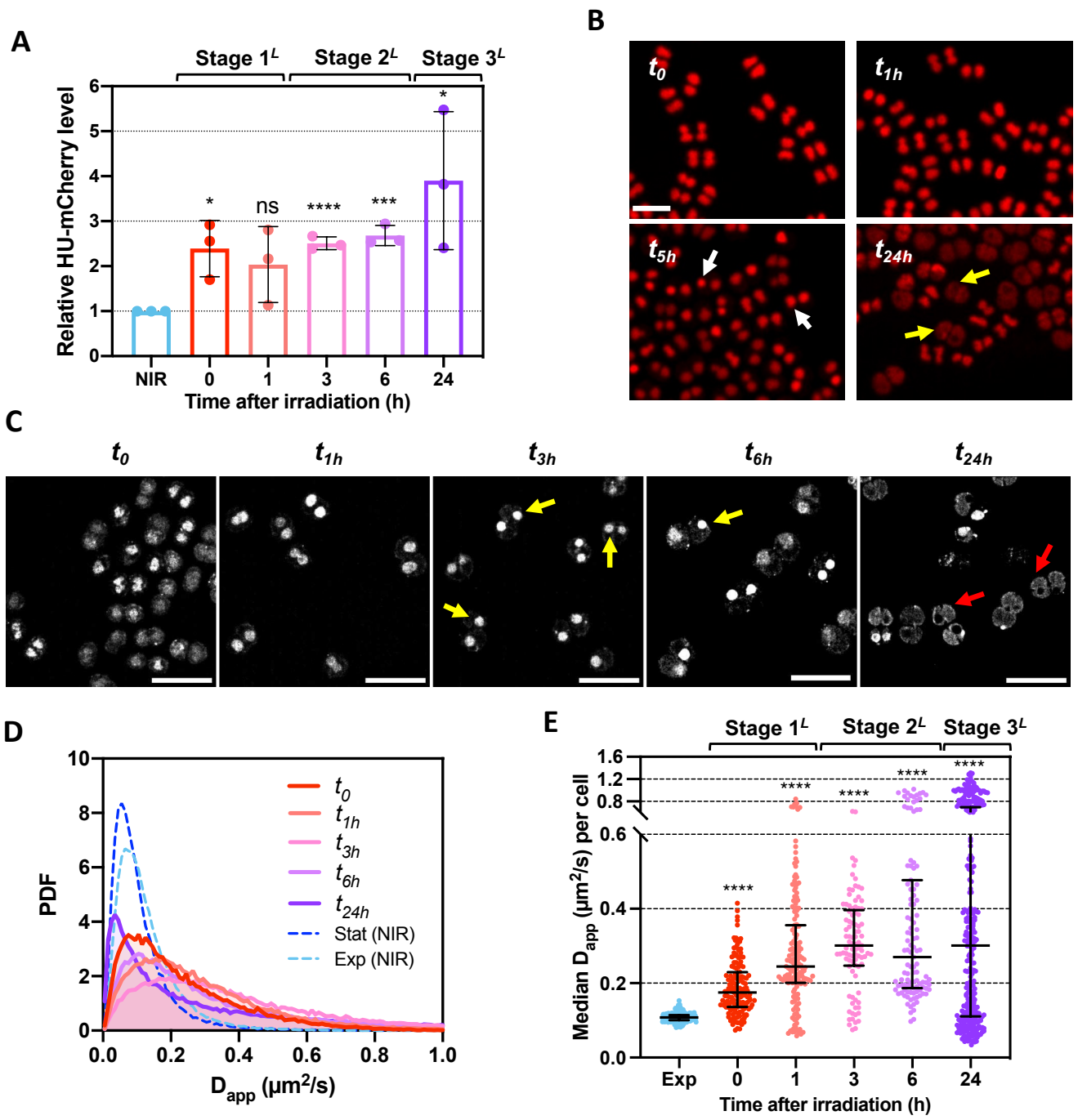

Figure 7

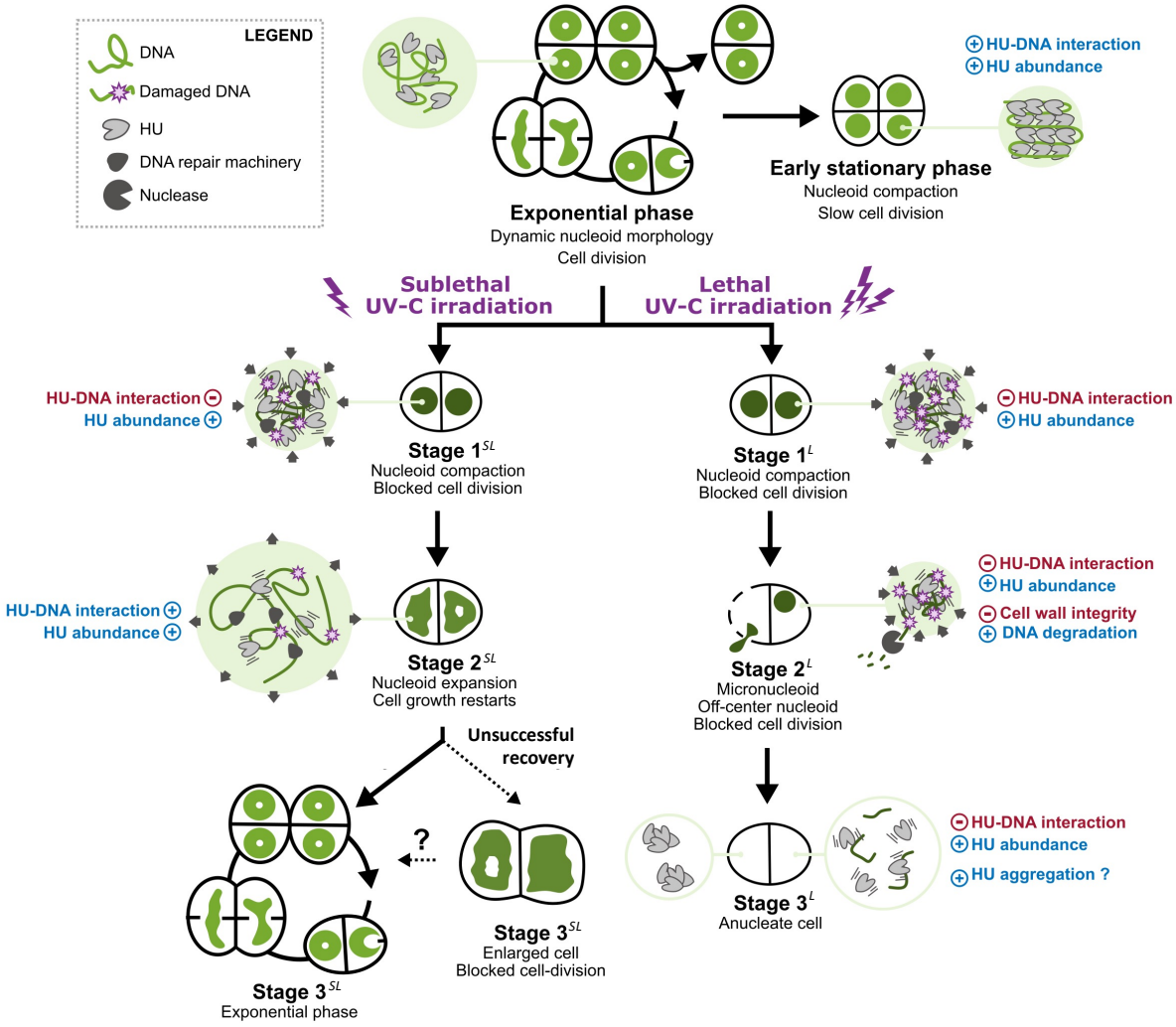

Chapter ??

Fluorophores & Labeling Methods for Fluorescence Microscopy

Jip Wulffelé
Institut de Biologie Structurale, CNRS, Université Grenoble Alpes, CEA, IBS

Dominique Bourgeois
Institut de Biologie Structurale, CNRS, Université Grenoble Alpes, CEA, IBS
Corresponding author : dominique.bourgeois@ibs.fr

1.1 Introduction

Fluorescence imaging has become an extremely powerful tool for biological studies. This is due to the unmatched sensitivity of the fluorescence physical process and the possibility to specifically label molecular targets in living samples using appropriate fluorophores. At the same time, the weakness of fluorescence microscopy is that fluorophores need to be introduced in the sample and may modify its functioning. Thus, a fluorescence-microscopy-based project always needs to start with the careful choice of the fluorescent markers and labeling strategies.

This chapter provides a general introduction to fluorophores for biological imaging. It is divided into three parts: basics of photophysics, fluorescent proteins and organic dyes. Fluorescent nanoparticles such as quantum dots are not discussed due

to space limitations. For the two classes of considered fluorophores, two main aspects are described: fluorescence (so-called "photophysical") properties, and labeling strategies, that is, how to attach a fluorophore to its target. We draw special attention to fluorophore requirements specific to super-resolution methods.

1.2 Basics of fluorophore photophysics

The photophysical behavior of a fluorophore is described by the Jablonski diagram shown in **Figure 1** (Lakowicz, 2006)**.** In the fluorescent state, absorption of a UV-visible photon in the singlet electronic ground state S_0 generates an almost instantaneous Frank-Condon transition to a vibrationally-coupled electronically excited state (S_1 or S_2), from which the fluorophore quickly relaxes (ps timescale) by internal conversion and/or vibrational relaxation to the lowest vibrational state of S_1. From there, fluorescence and non-radiative decay pathways compete (ns timescale) to bring back the fluorophore to vibrationally excited states in S_0. Alternatively, from S_1, intersystem crossing to the triplet state T_1 can occur (µs to ms timescale). T_1 is a "gate" for downstream photochemistry leading to the formation of transient (typically radical-based) dark states (ms to s timescale), or to photobleached states whereby the chromophore is irreversibly damaged.

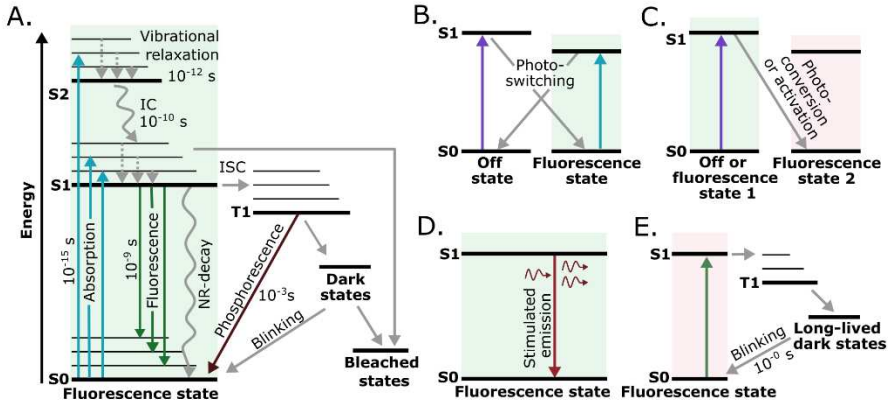

Figure 1. ***Jablonski diagrams*** *(A) General case. IC: Internal Conversion, ISC: Inter-System Crossing, NR: non-radiative. (B-E) Additional transitions specific to super-resolution methods: RESOLFT (B), PALM (C), STED (D) and STORM (E).*

In the fluorescent state, fluorescence brightness is defined as the product of the extinction coefficient at the excitation wavelength (efficiency of light absorption from S_0 to S_1) and the fluorescence quantum yield (probability that return to the ground

state occurs through photon emission). All other pathways starting from electronically excited states can be defined by associated "phototransformation" quantum yields (probability that the pathway in question takes place). Fluorescence quantum yields often exceed 0.5, whereas phototransformation quantum yields are orders of magnitude lower (e.g. ~10^{-3} for intersystem crossing). A key parameter is the so-called "photon budget" of a fluorophore, that is the total number of photons a fluorophore can emit before it photobleaches. The ns-long lifetimes of the S_1 state give rise to a strong environmental dependence of fluorescence processes. Indeed, in a matter of a few nanoseconds many biological events (molecular diffusion, protein tumbling, solvent reorganization) can occur that might modify the energy landscape sustaining the Jablonski diagram of **Figure 1**.

At the single-molecule level, any transition to a transient dark state gives rise to an interruption of fluorescence and is referred to as "blinking". Essentially, all fluorophores blink to some extent. The nature of dark states will be discussed later in the chapter.

Super-resolution methods (Sahl et al., 2017; Liu et al., 2022) rely on specific photophysical transitions (Figure 1B-E). Reversible photoswitching to a nonfluorescent but light-sensitive *off*-state that can be pumped back into the fluorescent state by blue-shifted illumination is at the basis of REversible Saturable OpticaL Fluorescence Transitions (RESOLFT) microscopy. Nonreversible photoactivation from a thermodynamically stable *off*-state to the fluorescent state, or photoconversion from one fluorescent state to another of a different color allow PhotoActivation Localization Microscopy (PALM). Enforcing return from S_1 to S_0 by stimulated emission is central to STimulated Emission Depletion (STED) microscopy. Stabilizing dark states so that they become very long-lived (s to min) is the concept behind Stochastic Optical Reconstruction Microscopy (STORM).

1.3 Fluorescent proteins

Fluorescent proteins (FPs) have revolutionized fluorescence microscopy (Dedecker et al., 2013). They are dubbed "genetically encoded fluorophores", which means that their gene can be fused to that of a protein of interest (POI), so that the FP-labeled POI is then expressed *in cellulo*. This offers ideal labelling specificity and compatibility with live cell imaging. The huge potential of FPs for fluorescence imaging was recognized by the chemistry Nobel Prize in 2008 awarded to Shimomura, Chalfie and Tsien. Shimomura was the first to isolate the Green Fluorescent Protein (GFP) from the jellyfish *Aequora victoria* in 1962 (Shimomura, 2009). Chalfie later demonstrated how GFP can be used as genetic label for biological research (Chalfie et al., 1994), and Tsien extended the FP color palette and contributed to our

mechanistic understanding of GFP fluorescence (Tsien, 1998). Their research, the discovery of FPs in different marine organisms (hydrozoan species like jellyfishes and anthozoan species like corals and anemones) (Matz et al., 1999) as well as extensive mutagenesis (Shu et al., 2006) have transformed FPs into the indispensable biological tool they are nowadays.

All GFP-like FPs have a molecular weight of about 30 kDa and share a similar structure consisting of a beta-barrel with a central helix which accommodates the (p-hydroxybenzylidene-imidazolinone) chromophore that is formed by three amino acids (S65, Y66 and G67 for wtGFP) (**Figure 2A**). The beta-barrel facilitates maturation of the chromophore and, after maturation, stabilizes it in position by van der Waals interactions, π-stacking interactions and an extensive hydrogen bond network, favoring fluorescence over non-radiative decay. By mutating the chromophore and/or the protein scaffold, engineering of GFP gave rise to FPs with a variety of photophysical behaviors and covering the entire visible spectrum. The rational design of FPs with specific properties, however, remains challenging as the effect of a mutation is difficult to predict and often depends on the presence or absence of other mutations. Other types of FPs (non-GFP-like) also exist, such as FPs derived from bacteriophytochromes, reaching into the infrared range (Chernov et al., 2017). These FPs, however, require exogenous chromophores and often suffer from a low fluorescence quantum yield. Thus, the quest for new FPs continues, searching for FPs that are brighter, redder, and more photostable. Below, we discuss the main properties, advantages and drawbacks of FPs that need to be considered when choosing a FP as fluorescent label (**Figure 2**).

Proper folding and maturation of the FP are needed for a high labelling efficiency. Misfolding of FPs may occur (as for any protein), notably under conditions that differ from those in which the (parent) FP is naturally expressed. A particular problem is the temperature difference between the cold environments in which FP-expressing organisms typically live versus the 30-37°C many bacteria and mammalian cells require. Maturation of the chromophore is a slow process which can take minutes to hours causing a delay in the appearance of fluorescence (Balleza et al., 2018). Thus to increase the labelling efficiency, efforts have been made to engineer FPs with optimized folding and maturation in bacterial and mammalian cells, resulting in variants such as αGFP (Crameri et al., 1996) or the well-known superfolder GFP (sfGFP) (Pédelacq et al., 2006).

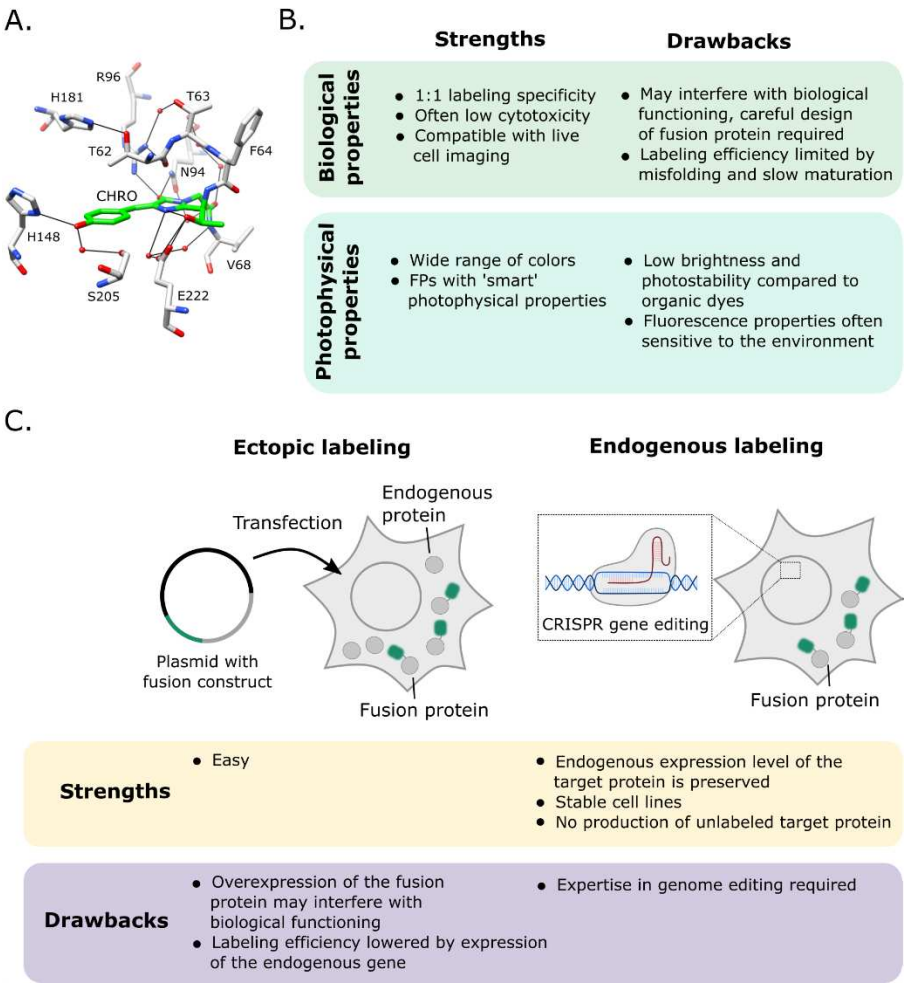

Figure 2. ***Labeling with FPs*** *(A) Structure and H-bond network (black lines) of the GFP chromophore (green) with nearby residues (grey) in the β-barrel. (B) Biological and photophysical strengths and drawbacks of FPs. (C) Strengths and drawbacks of labelling strategies with FPs.*

For biological studies it is critical that the labelling does not disturb the functioning of the labeled protein. This may arise because FPs are of substantial size (30 kDa), and may block interactions of the POI with other partners or ligands. Careful design of the fusion protein is therefore needed to avoid this issue. Another problem arises from the tendency of FPs to form oligomers, especially when working with anthozoan

FPs, which are obligate tetramers. Although large efforts have been made to produce fully monomeric FPs (Campbell et al., 2002), local concentrations in the cell can be extremely high (mM) and favor oligomerization. The OSER test allows researchers to evaluate the monomericity of a FP in the cellular environment (Costantini et al., 2012). The biological functioning of the sample may also be compromised by overexpression (or unregulated expression) of the FP-labeled protein, which is often the case with classical transfection (ectopic labelling). Furthermore, ectopic labelling results in a non-complete labelling efficiency as the non-labeled endogenous POI is also produced. These last two problems can be more easily overcome nowadays with the revolution of genome editing, based on CRISPR-Cas9, which offers the possibility to tag the endogenous gene, providing stable cell lines with up to 100% of the target protein labeled (case of homozygous edited cell lines) and preserving biological expression levels. Of note, to ensure optimal expression, codon optimization might be required, depending on the organism in which the FP is to be expressed.

To design the fusion protein (POI + FP), the FP can be placed at the C- or N-terminus of the POI, or in some cases may be inserted in the middle of the target gene by circular permutation. Placement of the FP needs to occur in such a way that the functioning of the target is optimally preserved. Factors to take into account, for example, are accessibility for ligands or interacting partners, and proper oligomerization. A linker needs to be designed to be inserted between the FP and the POI. The length of this linker must be carefully chosen as a linker that is too short may hinder the functioning of the target, while a linker that is too long may compromise the imaging resolution when super resolution methods are used. Finally, it has been found that for certain constructs, typically using anthozoan FPs, it can be advantageous for the expression and functioning of the fusion protein to replace the C- and N- termini of the FP by those of GFP, a trick called GFP-ization (Shaner et al., 2004).

Brightness and photostability are key features of fluorophores. FP brightness peaks in the yellow range where the best combination of a high extinction coefficient and a high fluorescence quantum yield is found. An important factor affecting the apparent brightness of FPs is the protonation state of the chromophore: neutral (protonated at the hydroxybenzylidene oxygen atom, typically nonfluorescent) or anionic (unprotonated at the oxygen atom, typically fluorescent). As a consequence, FP fluorescence is often sensitive to pH. In fact, the brightness of FPs is dependent on various environmental factors such as ionic strength or redox potential, which is often regarded as a drawback. However, this sensitivity can also been used to engineer FP-based biosensors (Dedecker et al., 2013).

FPs, unfortunately, are typically far less bright than organic fluorophores. This is partly explained by the large difference in extinction coefficient between FPs and organic dyes (e.g. 55000 $M^{-1}cm^{-1}$ for EGFP compared to 270000 $M^{-1}cm^{-1}$ for Alexa647). But the main reason why FPs give a lower signal is due to their relatively poor photostability (Cranfill et al., 2016). In fact, this may seem surprising given that the FP chromophore, hidden inside the β-barrel matrix, could be expected to be better protected from the environment as compared to organic dyes. Yet, the photobleaching quantum yield of FPs is typically one order of magnitude higher than that of organic dyes. How FPs bleach is incompletely understood, but it is known that it occurs by several mechanisms (Duan et al., 2013). The triplet state plays an important role in photobleaching processes for all fluorophores. In FPs, the T_1 lifetime is particularly long (ms) (Byrdin et al., 2018), giving more time for deleterious reactions and possibly at the origin of increased photobleaching. Reaction of T_1 with oxygen -which can generally still diffuse through the FP β-barrel- produces singlet oxygen, which may cause sulfoxidation of the FP and destruction of its fluorescent properties. At high laser intensities, T_1 or downstream dark states may absorb another photon, leading to photobleaching even in the absence of oxygen (Duan et al., 2013). Thus, a supra-linear relation is generally found between illumination intensity and photobleaching rate.

FPs typically can access multiple dark states, giving rise to highly complex blinking behaviors. Blinking can occur due to triplet state intersystem crossing followed by formation of short-lived or long-lived radical states, according to the mechanisms shown in **Figure 1**. In certain FPs, blinking may also arise from *cis-trans* isomerization of the chromophore (Zitter et al., 2019). These blinking behaviors can be strongly dependent on environmental or light illumination conditions. For example, radical state formation depends on the redox potential, and some dark states are light-sensitive, meaning that their lifetime can be reduced by suitable illumination.

Super-resolution techniques rely on the specific photophysical properties of so-called "phototransformable" FPs, whose photophysics can be controlled by illumination. Three types of phototransformable FPs are distinguished: photoactivatable, photoconvertible and photoswitchable FPs (**Figure 3**) (Adam et al., 2014). Photoactivatable FPs (PAFPs) can be switched irreversibly from a dark state to a fluorescent state by illumination with violet light. Photoactivation typically involves a change in the protonation state of the chromophore induced by decarboxylation of Glu222 (GFP numbering, a fully conserved residue located near the chromophore), favoring the fluorescent anionic state. Photoconvertible FPs (PCFPs) can be irreversibly switched from one color to another, which offers an advantage over

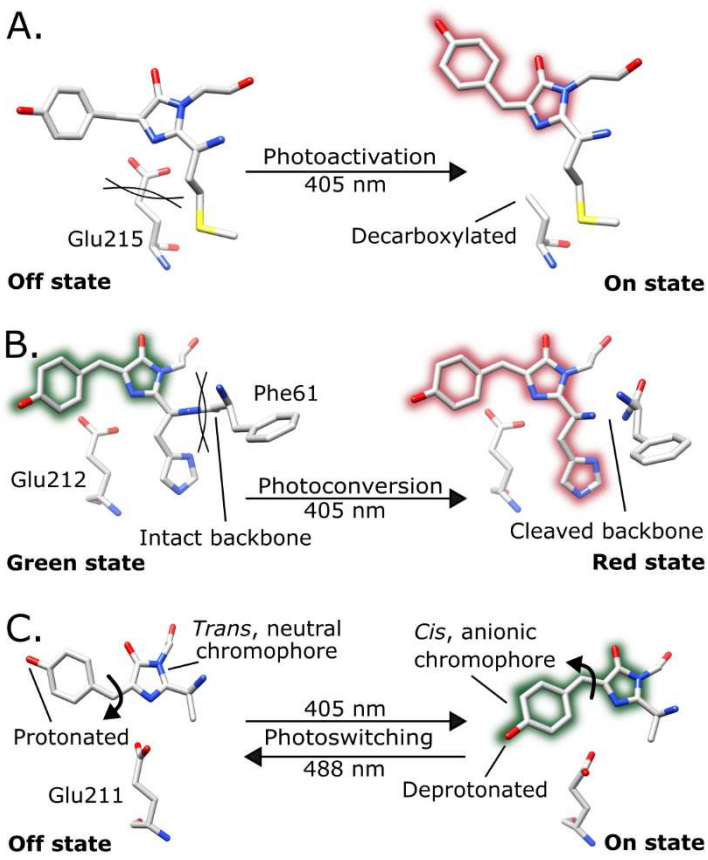

Figure 3. ***Phototransformations in FPs*** *(A) Photoactivation of PAmCherry is induced by absorption of 405 nm light, which causes decarboxylation of Glu222 leading to a rearrangement of the hydrogen bond network stabilizing the chromophore. (B) Photoconversion of mEos4b is induced by absorption of 405 nm light in the green state, which causes breakage of the peptide backbone near the chromophore extending the conjugated electron system leading to a red shift in the absorption and emission spectra. (C) Photoswitching of rsEGFP2 is controlled by absorption of 405 nm light (dark -> fluorescent) and 488 nm light (fluorescent -> dark), which induce cis-trans isomerization and protonation-deprotonation of the chromophore.*

PAFPs as both states are observable by fluorescence microscopy. Green-to-red PCFPs were discovered in anthozoan species. The underlying mechanism of photoconversion

is based on an elongation of the conjugated electron system that results from violet light-induced backbone breakage, but the details of this mechanism remain poorly understood. PCFPs display incomplete photoconversion (50-70%) which poses challenges for PALM experiments (Durisic et al., 2014). Popular PAFPs and PCFPs are PAmCherry (Subach et al., 2009) and the mEos variants (Nienhaus and Nienhaus, 2021), respectively. In contrast to PAFPs and PCFPs, the phototransformation of Reversibly Switchable FPs (RSFPs) is reversible as they can be switched back and forth between a dark and a fluorescent state. These FPs are used for nonlinear structured-illumination microscopy (NL-SIM) and RESOLFT microscopy. The switching of RSFPs is most often based on *cis-trans* isomerization of the chromophore, which is possible because in these proteins the chromophore is less restricted (Bourgeois and Adam, 2012). Unfortunately, this also means that RSFPs have a relatively low fluorescence quantum yield, especially the fast switching ones. An example of a popular RSFP today is rsEGFP2 (Grotjohann et al., 2012).

In summary, the 100% labelling specificity and compatibility with live cell imaging make FPs the preferred label for many microscopy experiments. However, FPs still need to be improved, notably in terms of brightness and photostability.

1.4 Organic dyes

In parallel with fluorescent proteins, there exists a huge plethora of organic fluorophores and fluorescent nanoparticles that are used for diverse applications in fluorescence imaging. Intense research continues to make those fluorophores more and more performant, and extensive reviews have been published recently to highlight advances (Lavis and Raines, 2008; Jin et al., 2018; Li and Vaughan, 2018). Here, we concentrate on basic features about organic dyes. **Figure 4** summarizes the main advantages and drawbacks of these fluorophores, which can be compared to those of fluorescent proteins described above.

Classifying organic fluorophores is a difficult exercise, but it is possible to distinguish five main subfamilies:

– Naturally occurring fluorophores such as nicotinamide adenine dinucleotide (NADH), flavins or some amino acids like tryptophan, phenylalanine or tyrosine.

– Polycyclic aromatics (e.g. pyrene), oxygen or nitrogen substituted bicyclic aromatics (e.g. coumarins or quinine, - a well-known and historical fluorophore used to render sodas fluorescent and make them appealing -)), indoles (e.g. DAPI or Hoechst, known for their ability to stain DNA). Typically, these fluorophores absorb and emit in the UV-blue region of the spectrum.

– Xanthene-derived fluorophores: this is the widest subfamily, starting with the well-known fluorescein and fluorescein isothiocyanate (FITC), and also all the rhodamine derivatives, including sulfo-rhodamine, carboxy rhodamine, silicon rhodamine, and boron substituted xanthenes (Bodipy dyes). They cover the whole visible range up to the near IR

– Polymethine-based fluorophores, referred to as cyanine dyes. Depending on the number of methines they also cover the visible range up to the near IR.

– Oxazine dyes, which are tri-aromatics bearing a nitrogen and an oxygen atom on the central ring, typically fluorescing in the red region of the spectrum

The three subfamilies of organic fluorophores mainly used in super-resolution fluorescence microscopy are rhodamine, cyanine and oxazine dyes, whose chemical structures are shown in **Figure 4A**. We note in passing that the above-mentioned subfamilies of organic fluorophores should not be confused with their brand names. For example, Atto 488, Alexa 555 and Janelia Farm (JF) 549 are all rhodamines, whereas Alexa 488 and Alexa 647 are rhodamine and cyanine dyes, respectively. Thus far rhodamine-based dyes have been most amenable to chemical engineering. One can cite the design of JF dyes bearing azetidine rings for improved brightness (Grimm et al., 2015), or deuteration procedures for improved photon budget (Grimm et al., 2021). Caged rhodamine dyes have also been devised to confer photoactivation properties, essential for approaches such as single-particle tracking PALM (sptPALM) (Grimm et al., 2016; Frei et al., 2019).

An important field of development is that of fluorogenic dyes, which only become fluorescent once bound to their target, allowing a drastic reduction of nonspecific background signals (Kozma and Kele, 2019). Fluorogenicity in rhodamines can be reached through the establishment of an equilibrium between a nonfluorescent spirolactone form (favored in nonpolar environment) and a fluorescent zwitterionic form (favored in polar environment, typically when bound to a substrate) such as in the case of carboxy-SiR650 (Lukinavičius et al., 2013). Many other fluorogenic dyes have been engineered such as lipid probes (Collot et al., 2018) or DNA-binding dyes (Rye et al., 1992). An elegant way to achieve fluorogenicity is to elicit fluorescence through a reduction in dye conformational flexibility upon binding a fluorogen activating protein (FAP) tag such as the protein FAST (Plamont et al., 2016).

Many developments have been carried out to optimize organic dyes for super-resolution microscopy (Li and Vaughan, 2018), in particular for STED and STORM. In STED, dye photostability and efficient singlet-state quenching by red-shifted light are key parameters (**Figure 1D**). In STORM, dark states, often anionic radicals or thiol adducts, are stabilized by adding a buffer that typically contains an oxygen

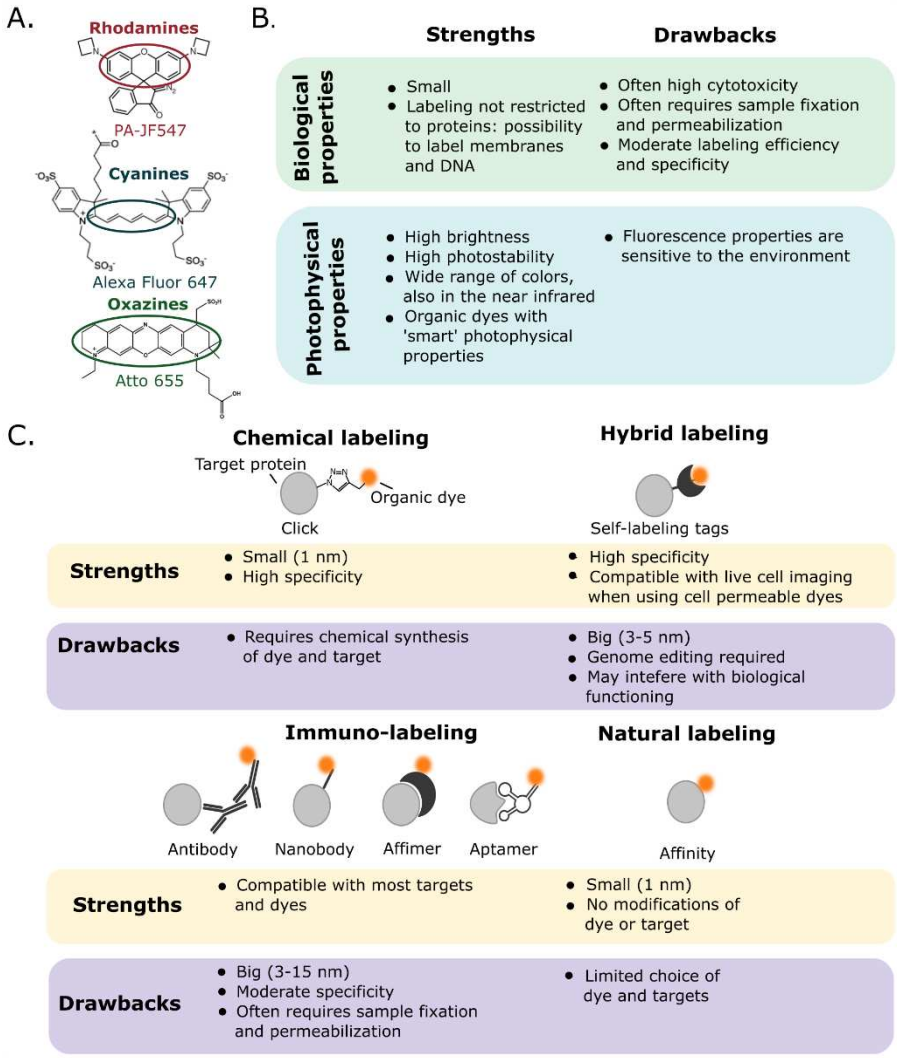

Figure 4. ***Labeling with organic fluorophores*** *(A) Example structures of organic dyes. (B) Biological and photophysical strengths and drawbacks of organic dyes. (C) Strengths and drawbacks of different labelling strategies with organic dyes.*

scavenging system such as glucose, glucose oxidase and catalase to remove oxygen and prevent triplet state quenching, as well as a highly concentrated reducing agent (for example mercaptoethylamine at 10-100 mM in the case of cyanine dyes) to

promote the formation of the dark state (**Figure 1E**). To avoid the necessity to use such a buffer, which is only compatible with fixed cells, oxazine dyes can be used in live cells (Vogelsang et al., 2009) and spontaneously blinking fluorophores have been developed that naturally achieve an equilibrium between a closed (nonfluorescent) and an open (fluorescent) form (Uno et al., 2014; Takakura et al., 2017).

The use of exogenously supplied organic dyes requires crossing of the biological membrane. Usually, this is achieved on fixed cells by membrane permeabilization using surfactants such as Triton-X100. Alternatively, many recently developed dyes have the capacity to cross intact plasma membranes (Grimm et al., 2015). Some of these dyes are fluorogenic and penetrate the cell in a nonpolar nonfluorescent form that shifts to a polar fluorescent form once binding to their target in the cytoplasm, as is the case for carboxylated silicon-containing rhodamine (Lukinavičius et al., 2013; Xue et al., 2015). Alternatively, some dyes might be attached to e.g. cell penetrating peptides (Pan et al., 2014).

An important aspect of organic fluorophores is that, as they are not protected from the solvent like, to some extent, fluorescent proteins, their photophysical behaviors strongly depend on the physicochemical environment. This can be an advantage in the case of e.g. fluorogenic dyes, but it also means that a fluorophore that performs well in a specific biological environment, may perform poorly in another, depending e.g. on pH or redox potential. A variety of anti-fading agents can also be added to the medium to improve photostability, and self-healing dyes have even been engineered, which are covalently linked to protective chemical groups (Altman et al., 2012).

Organic fluorophores are only valuable if they can be specifically attached to their biological target. Here, full genetically encoded labelling is not possible as with FPs, and a very diverse set of alternative labeling strategies have been developed over the years (**Figure 4C**). For a comprehensive recent review, see (Choquet et al., 2021).

Immunolabeling is a very widespread labeling strategy. Most commonly it is performed with antibodies, usually a primary antibody coupled to a secondary antibody to which the fluorophore is attached. The use of a pair of antibodies is justified by technical and cost considerations, as this allows using generic commercially available fluorophore-labeled secondary antibodies instead of having to design fluorophore attachment to every target-specific primary antibody. As a consequence, the entire label is very big, reaching ~10 nm in size, which constitutes a clear limitation to the achievable resolution in nanoscopy approaches. To reduce this size, nanobodies, which are derived from single chain antibodies produced by camelids (Hamers-Casterman et al., 1993) and have a molecular weight of ~15 kDa (about half of GFP), can be used, for example to recognize small tags appended to the

sequence of the target of interest (Virant et al., 2018). Alternatively, aptamers are RNA-based labels that can be designed by iterative combinatorial synthesis (SELEX method) to selectively recognize a ligand with very high affinity (Ellington and Szostak, 1990), while affimers are small proteins of about 12 kDa derived from cysteine proteases that can be designed by directed evolution to recognize a specific target (Woodman et al., 2005). Both aptamers and affimers are small labels appropriate for nanoscopy techniques, but require specific developments for each new target.

A nowadays highly popular labelling strategy consists in generating a fusion protein made of the target of interest linked to a protein tag displaying strong affinity for an organic fluorophore. Such a strategy is called hybrid labeling and can be performed with a number of tags such as Halo-Tag (Los et al., 2008), Clip-Tag (Gautier et al., 2008), Snap-Tag (Juillerat et al., 2003), or DHFR-Tag (Wombacher et al., 2010). Binding of the fluorophore to the tag can be covalent (Juillerat et al., 2003; Gautier et al., 2008; Los et al., 2008) or noncovalent (Wombacher et al., 2010). Fluorogen activating proteins (FAPs), described above, also belong to the class of hybrid-labeling tags. In contrast to e.g immunolabeling, but similar to labeling with fluorescent proteins, hybrid-labeled targets are ectopically (over)expressed, or their endogenous expression requires genetic engineering via e.g. CRISPR-Cas9 gene insertion.

Binding a fluorophore directly to the target in a highly compact manner is possible by employing chemical labelling, typically combining expansion of the genetic code to insert an unnatural amino acid (UAA) into the target, with click chemistry to attach a fluorophore in a biorthogonal way (Plass et al., 2011). By means of a tRNA/tRNA-synthetase pair, UAAs carrying strained alkyne or alkene side chains can be genetically incorporated at positions encoded by an Amber (TAG) STOP codon. Efficient labeling is then achieved with azide-bearing (fluorogenic) dyes by means of a click reaction under physiological conditions. Alternatively, click chemistry can be elegantly used to directly label an azide-bearing clickable metabolite which is added to the sample (Trouve et al., 2021).

Finally, in some cases direct labelling can be achieved by conjugating a fluorophore to a molecule that exhibit a natural affinity to the target: for example, phalloidin is a (poisonous) molecule classically used to irreversibly label actin in fixed cells, while Lifeact is a short peptide that can transiently label actin in live cells (Riedl et al., 2008).

In summary, the brightness, photostability and color tunability of organic dyes make them preferred labels for a wide diversity of imaging experiments, notably in

chemically fixed cells. However, despite significant recent progress, many organic dyes remain incompatible with live-cell experiments and may produce nonspecific staining.

1.5 Conclusion

The success of any biological fluorescence imaging experiment heavily depends on the choice of suitable fluorophores. Nowadays, there is a wide range of FPs and organic dyes available, which all have their own strengths and drawbacks. There is not one perfect fluorophore for all experiments. Instead, what is 'the best' fluorophore for an experiment depends on what is to be studied: a whole organism or a single cell; a live sample or a fixed sample; at room temperature or at cryogenic temperature. Likewise, there is still no ideal labeling strategy and every project requires its own optimization. Factors to consider are labeling specificity, labeling efficiency, preservation of biological function, compatibility with endogenous expression, compatibility with live-cell experiments and, finally, label size for compatibility with super-resolution approaches.

New developments are ongoing to improve the photophysics and labelling of fluorophores. Brightness and photostability are of key concern, especially for super-resolution techniques which often rely on the detection of single fluorophores. Labelling with FPs has been significantly improved by the invention of CRISPR gene editing, but misfolding, slow maturation and photobleaching still limit their effective labelling efficiency. On the other hand, organic dyes, although superior to FPs in brightness and photostability, still lack the 100% labelling specificity and full compatibility with live cell imaging in most cases. New developments lie ahead for fluorophores with improved photophysics and novel labelling strategies with higher efficiency and precision. They will provide the tools to further unravel the mysteries of life.

1.6 References

Adam, V., Berardozzi, R., Byrdin, M., Bourgeois, D. 2014. Phototransformable fluorescent proteins: Future challenges. *Current Opinion in Chemical Biology* 20: 92-102.

Altman, R.B., Zheng, Q., Zhou, Z., Terry, D.S., Warren, J.D., Blanchard, S.C. 2012. Enhanced photostability of cyanine fluorophores across the visible spectrum. *Nat Methods* 9: 428-9.

Balleza, E., Kim, J.M., Cluzel, P. 2018. Systematic characterization of maturation time of fluorescent proteins in living cells. *Nature Methods* 15: 47-51.

Bourgeois, D., Adam, V. 2012. Reversible photoswitching in fluorescent proteins: A mechanistic view. *Iubmb Life* 64: 482-491.

Byrdin, M., Duan, C., Bourgeois, D., Brettel, K. 2018. A Long-Lived Triplet State Is the Entrance Gateway to Oxidative Photochemistry in Green Fluorescent Proteins. *Journal of the American Chemical Society* 140: 2897-2905.

Campbell, R.E., Tour, O., Palmer, A.E., Steinbach, P.A., Baird, G.S., Zacharias, D.A., Tsien, R.Y. 2002. A monomeric red fluorescent protein. *Proc Natl Acad Sci U S A* 99: 7877-82.

Chalfie, M., Tu, Y., Euskirchen, G., Ward, W.W., Prasher, D.C. 1994. Green fluorescent protein as a marker for gene expression. *Science (New York, N.Y.)* 263: 802-805.

Chernov, K.G., Redchuk, T.A., Omelina, E.S., Verkhusha, V.V. 2017. Near-Infrared Fluorescent Proteins, Biosensors, and Optogenetic Tools Engineered from Phytochromes. *Chemical Reviews* 117: 6423-6446.

Choquet, D., Sainlos, M., Sibarita, J.-B. 2021. Advanced imaging and labelling methods to decipher brain cell organization and function. *Nature Reviews. Neuroscience* 22: 237-255.

Collot, M., Fam, T.K., Ashokkumar, P., Faklaris, O., Galli, T., Danglot, L., Klymchenko, A.S. 2018. Ultrabright and Fluorogenic Probes for Multicolor Imaging and Tracking of Lipid Droplets in Cells and Tissues. *Journal of the American Chemical Society* 140: 5401-5411.

Costantini, L.M., Fossati, M., Francolini, M., Snapp, E.L. 2012. Assessing the Tendency of Fluorescent Proteins to Oligomerize Under Physiologic Conditions. *Traffic* 13: 643-649.

Crameri, A., Whitehorn, E.A., Tate, E., Stemmer, W.P.C. 1996. Improved Green Fluorescent Protein by Molecular Evolution Using DNA Shuffling. *Nature Biotechnology* 14: 315-319.

Cranfill, P.J., Sell, B.R., Baird, M.A., Allen, J.R., Lavagnino, Z., de Gruiter, H.M., Kremers, G.-J. et al. 2016. Quantitative assessment of fluorescent proteins. *Nature Methods* 13: 557-562.

Dedecker, P., De Schryver, F.C., Hofkens, J. 2013. Fluorescent proteins: shine on, you crazy diamond. *Journal of the American Chemical Society* 135: 2387-2402.

Duan, C., Adam, V., Byrdin, M., Ridard, J., Kieffer-Jaquinod, S., Morlot, C., Arcizet, D. et al. 2013. Structural Evidence for a Two-Regime Photobleaching Mechanism in a Reversibly Switchable Fluorescent Protein. *Journal of the American Chemical Society* 135: 15841-15850.

Durisic, N., Laparra-Cuervo, L., Sandoval-Álvarez, Á., Borbely, J.S., Lakadamyali, M. 2014. Single-molecule evaluation of fluorescent protein photoactivation efficiency using an in vivo nanotemplate. *Nature Methods* 11: 156-162.

Ellington, A.D., Szostak, J.W. 1990. In vitro selection of RNA molecules that bind specific ligands. *Nature* 346: 818-822.

Frei, M.S., Hoess, P., Lampe, M., Nijmeijer, B., Kueblbeck, M., Ellenberg, J., Wadepohl, H. et al. 2019. Photoactivation of silicon rhodamines via a light-induced protonation. *Nature Communications* 10: 4580.

Gautier, A., Juillerat, A., Heinis, C., Corrêa, I.R., Kindermann, M., Beaufils, F., Johnsson, K. 2008. An engineered protein tag for multiprotein labeling in living cells. *Chemistry & Biology* 15: 128-136.

Grimm, J.B., English, B.P., Chen, J., Slaughter, J.P., Zhang, Z., Revyakin, A., Patel, R. et al. 2015. A general method to improve fluorophores for live-cell and single-molecule microscopy. *Nat Methods* 12: 244-50, 3 p following 250.

Grimm, J.B., English, B.P., Choi, H., Muthusamy, A.K., Mehl, B.P., Dong, P., Brown, T.A. et al. 2016. Bright photoactivatable fluorophores for single-molecule imaging. *Nature Methods* 13: 985-988.

Grimm, J.B., Xie, L., Casler, J.C., Patel, R., Tkachuk, A.N., Falco, N., Choi, H. et al. 2021. A General Method to Improve Fluorophores Using Deuterated Auxochromes. *JACS Au* 1: 690-696.

Grotjohann, T., Testa, I., Reuss, M., Brakemann, T., Eggeling, C., Hell, S.W., Jakobs, S. 2012. rsEGFP2 enables fast RESOLFT nanoscopy of living cells. *eLife* 1: e00248.

Hamers-Casterman, C., Atarhouch, T., Muyldermans, S., Robinson, G., Hammers, C., Songa, E.B., Bendahman, N., Hammers, R. 1993. Naturally occurring antibodies devoid of light chains. *Nature* 363: 446-448.

Jin, D., Xi, P., Wang, B., Zhang, L., Enderlein, J., van Oijen, A.M. 2018. Nanoparticles for super-resolution microscopy and single-molecule tracking. *Nature Methods* 15: 415-423.

Juillerat, A., Gronemeyer, T., Keppler, A., Gendreizig, S., Pick, H., Vogel, H., Johnsson, K. 2003. Directed evolution of O6-alkylguanine-DNA alkyltransferase for efficient labeling of fusion proteins with small molecules in vivo. *Chemistry & Biology* 10: 313-317.

Kozma, E., Kele, P. 2019. Fluorogenic probes for super-resolution microscopy. *Organic & Biomolecular Chemistry* 17: 215-233.

Lakowicz, J. 2006. *Principles of Fluorescence Spectroscopy*. Springer, Boston, MA.

Lavis, L.D., Raines, R.T. 2008. Bright Ideas for Chemical Biology. *ACS Chemical Biology* 3: 142-155.

Li, H., Vaughan, J.C. 2018. Switchable Fluorophores for Single-Molecule Localization Microscopy. *Chemical Reviews* 118: 9412-9454.

Liu, S., Hoess, P., Ries, J. 2022. Super-Resolution Microscopy for Structural Cell Biology. *Annual Review of Biophysics* 51: 301-326.

Los, G.V., Encell, L.P., McDougall, M.G., Hartzell, D.D., Karassina, N., Zimprich, C., Wood, M.G. et al. 2008. HaloTag: A Novel Protein Labeling Technology for Cell Imaging and Protein Analysis. *ACS Chemical Biology* 3: 373-382.

Lukinavičius, G., Umezawa, K., Olivier, N., Honigmann, A., Yang, G., Plass, T., Mueller, V. et al. 2013. A near-infrared fluorophore for live-cell super-resolution microscopy of cellular proteins. *Nature Chemistry* 5: 132-139.

Matz, M.V., Fradkov, A.F., Labas, Y.A., Savitsky, A.P., Zaraisky, A.G., Markelov, M.L., Lukyanov, S.A. 1999. Fluorescent proteins from nonbioluminescent Anthozoa species. *Nat Biotechnol* 17: 969-73.

Nienhaus, K., Nienhaus, G.U. 2021. Fluorescent proteins of the EosFP clade: intriguing marker tools with multiple photoactivation modes for advanced microscopy. *RSC Chemical Biology* 2: 796-814.

Pan, D., Hu, Z., Qiu, F., Huang, Z.-L., Ma, Y., Wang, Y., Qin, L. et al. 2014. A general strategy for developing cell-permeable photo-modulatable organic fluorescent probes for live-cell super-resolution imaging. *Nature Communications* 5: 5573.

Pédelacq, J.-D., Cabantous, S., Tran, T., Terwilliger, T.C., Waldo, G.S. 2006. Engineering and characterization of a superfolder green fluorescent protein. *Nature Biotechnology* 24: 79-88.

Plamont, M.-A., Billon-Denis, E., Maurin, S., Gauron, C., Pimenta, F.M., Specht, C.G., Shi, J. et al. 2016. Small fluorescence-activating and absorption-shifting tag for tunable protein imaging in vivo. *Proceedings of the National Academy of Sciences* 113: 497-502.

Plass, T., Milles, S., Koehler, C., Schultz, C., Lemke, E.A. 2011. Genetically Encoded Copper-Free Click Chemistry. *Angewandte Chemie International Edition* 50: 3878-3881.

Riedl, J., Crevenna, A.H., Kessenbrock, K., Yu, J.H., Neukirchen, D., Bista, M., Bradke, F. et al. 2008. Lifeact: a versatile marker to visualize F-actin. *Nat Methods* 5: 605-7.

Rye, H.S., Yue, S., Wemmer, D.E., Quesada, M.A., Haugland, R.P., Mathies, R.A., Glazer, A.N. 1992. Stable fluorescent complexes of double-stranded DNA with bis-intercalating asymmetric cyanine dyes: properties and applications. *Nucleic Acids Research* 20: 2803-2812.

Sahl, S.J., Hell, S.W., Jakobs, S. 2017. Fluorescence nanoscopy in cell biology. *Nature Reviews. Molecular Cell Biology* 18: 685-701.

Shaner, N.C., Campbell, R.E., Steinbach, P.A., Giepmans, B.N.G., Palmer, A.E., Tsien, R.Y. 2004. Improved monomeric red, orange and yellow fluorescent proteins derived from Discosoma sp. red fluorescent protein. *Nature Biotechnology* 22: 1567-1572.

Shimomura, O. 2009. Discovery of green fluorescent protein (GFP) (Nobel Lecture). *Angewandte Chemie (International Ed. in English)* 48: 5590-5602.

Shu, X., Shaner, N.C., Yarbrough, C.A., Tsien, R.Y., Remington, S.J. 2006. Novel chromophores and buried charges control color in mFruits. *Biochemistry* 45: 9639-9647.

Subach, F.V., Patterson, G.H., Manley, S., Gillette, J.M., Lippincott-Schwartz, J., Verkhusha, V.V. 2009. Photoactivatable mCherry for high-resolution two-color fluorescence microscopy. *Nature Methods* 6: 153-159.

Takakura, H., Zhang, Y., Erdmann, R.S., Thompson, A.D., Lin, Y., McNellis, B., Rivera-Molina, F. et al. 2017. Long time-lapse nanoscopy with

spontaneously blinking membrane probes. *Nature Biotechnology* 35: 773-780.

Trouve, J., Zapun, A., Arthaud, C., Durmort, C., Di Guilmi, A.M., Söderström, B., Pelletier, A. et al. 2021. Nanoscale dynamics of peptidoglycan assembly during the cell cycle of Streptococcus pneumoniae. *Current biology: CB* 31: 2844-2856.e6.

Tsien, R.Y. 1998. The green fluorescent protein. *Annu Rev Biochem* 67: 509-44.

Uno, S., Kamiya, M., Yoshihara, T., Sugawara, K., Okabe, K., Tarhan, M.C., Fujita, H. et al. 2014. A spontaneously blinking fluorophore based on intramolecular spirocyclization for live-cell super-resolution imaging. *Nature Chemistry* 6: 681-689.

Virant, D., Traenkle, B., Maier, J., Kaiser, P.D., Bodenhöfer, M., Schmees, C., Vojnovic, I. et al. 2018. A peptide tag-specific nanobody enables high-quality labeling for dSTORM imaging. *Nature Communications* 9: 930.

Vogelsang, J., Cordes, T., Forthmann, C., Steinhauer, C., Tinnefeld, P. 2009. Controlling the fluorescence of ordinary oxazine dyes for single-molecule switching and superresolution microscopy. *Proc Natl Acad Sci U S A* 106: 8107-12.

Wombacher, R., Heidbreder, M., van de Linde, S., Sheetz, M.P., Heilemann, M., Cornish, V.W., Sauer, M. 2010. Live-cell super-resolution imaging with trimethoprim conjugates. *Nature Methods* 7: 717-719.

Woodman, R., Yeh, J.T.-H., Laurenson, S., Ko Ferrigno, P. 2005. Design and validation of a neutral protein scaffold for the presentation of peptide aptamers. *Journal of Molecular Biology* 352: 1118-1133.

Xue, L., Karpenko, I.A., Hiblot, J., Johnsson, K. 2015. Imaging and manipulating proteins in live cells through covalent labeling. *Nature Chemical Biology* 11: 917-923.

Zitter, E.D., Thédié, D., Mönkemöller, V., Hugelier, S., Beaudouin, J., Adam, V., Byrdin, M. et al. 2019. Mechanistic investigation of mEos4b reveals a strategy to reduce track interruptions in sptPALM. *Nature Methods* 16: 707-710.